Numerical Analysis of Local Strain and Hydrogen Distribution Originating During Pitting Corrosion

Doctoral Thesis

Approved by the

Department of Mechanical Engineering

of the

Helmut-Schmidt-University

University of German Federal Armed Forces

for obtaining the academic degree of

Doktor-Ingenieurin (Dr.-Ing.)

presented by

Maria Christine Madigan

from Co. Limerick, Ireland

Hamburg, 2020

Committee members:

Prof. Dr.-Ing. Hans Hoffmeister

Prof. Dr.-Ing. Thomas Böllinghaus

Prof. Dr.-Ing. Thomas Klassen

Date of the oral defence:

13/09/2020

Numerical Analysis of Local Strain and Hydrogen Distribution Originating During Pitting Corrosion

Von der Fakultät für Maschinenbau
der Helmut-Schmidt-Universität
zur Erlangung des akademischen Grades einer Doktor-Ingenieurin
genehmigte

DISSERTATION

vorgelegt von

Maria Christine Madigan

aus Co. Limerick, Irland

Hamburg, 2020

Abstract

Supermartensitic stainless steels (SMSS) were developed in the 80's in order to replace the more expensive duplex stainless steels (DSS) and nickel alloys used in the offshore oil and gas industry. The good mechanical and corrosion resistance properties, along with their cost benefits made them an attractive alternative. SMSS use offshore originally consisted of downhole tubing but proved to be an alternative for combatting CO_2 corrosion and mildly sour conditions, compared to corrosion resistant alloy (CRA) materials. SMSS was therefore used as flowline materials. Especially the better weldability due to the low carbon content and the promising combination of mechanical properties of these materials, makes SMSS good candidates for other applications.

The risk of hydrogen assisted stress corrosion cracking (HASCC) may increase with increasing carbon (C) content in the steel, as the C may combine with chromium (Cr) ions present in the material. This in turn reduces the amount of Cr ions in the metal matrix which forms the passive layer which provides corrosion resistance. SMSSs have a reduced C content in order to reduce the risk of HASCC occurring when transporting sour service media. Additionally, the reduced C content also increases the weldability of the SMSS. Hydrogen concentration is one of the three key factors used in determining the susceptibility of a material to hydrogen assisted cracking (HAC), the other two being the local/ global mechanical load and the local microstructure. Additionally, a chromium content above approximately 12%, in addition to other alloying elements, such as molybdenum, reduces the susceptibility of a material to pitting corrosion. The presence of pits may cause high local stress and strain concentrations and additionally can cause local environments with high H^+ ion concentrations, which accumulates at regions of high stresses and strains. The main location for pitting corrosion on SMSS welded components is in the heat affected zone (HAZ), due to the altering of material properties during welding, however it is uncertain as to where in the pits the cracks initiate. This is because the regions of high strains and high hydrogen concentrations inside the pits are different for the various pit geometries. Pitting corrosion is both difficult to detect and predict making it more dangerous than uniform corrosion.

Experimental methods to measure the local hydrogen concentration in pits have proven difficult to establish, due to the small geometries involved. Additionally, the local mechanisms of initiation and propagation of HAC are not always thoroughly understood. Numerical modelling of hydrogen diffusion and HAC is therefore an alternative procedure to provide a better understanding of crack initiation and to investigate the origin of cracks in pits. This can be achieved by modifying Fick's law so the effect of various parameters on hydrogen distribution can be explored.

In this work, determining the pit geometry most susceptible to the regions of the highest strains was investigated firstly, and both the HAZ and the base material (BM) microstructures were assumed for numerical analysis. As a first approach, the specimens simulated are not real welds with different microstructures but are assumed to be homogeneous. Seven different pit geometries were modelled in 2D and 3D and have been subjected to a uniaxial load and a bending load. As expected, the depth of the pit influenced the uniaxial loading results with shallower pits producing the lowest total true strains in x-direction. For the bending loading condition however, the pit mouth diameter was the most important geometric aspect of the pit, with larger pit mouth diameters producing the lowest total true strains in x-direction. As another feature, the location of the maximum total true strains in x-direction for the 2D models were all located at the pit bottoms, but

the regions varied for the 3D models. The load carrying capacity of a specimen with a pit present was also investigated for both uniaxial and bending loading conditions for 2D and 3D. It was found that 3D models were able to withstand higher displacements for both loading conditions.

Various initial hydrogen conditions were applied to the surface of the pit and/ or the surface of the model in addition to an initial hydrogen concentration profile simulating an inhomogeneous hydrogen distribution created during pitting corrosion occurring inside the pit. The 3D pit geometries from the previous stage with the highest, lowest and medium maximum total true strains in x-direction were modelled. No load was applied during this stage of the work. Only the HAZ material was taken for numerical analysis for this stage and the normalised hydrogen concentrations at certain nodes in the model were recorded for each pit and boundary condition. The pit variable hydrogen concentration boundary condition was assumed most similar to real life anodic and cathodic reactions occurring in the pits. Therefore, the effect of this boundary condition was investigated for all pit geometries. Again, the geometry of the pits, including the depth of the pits, the slope at the bottom of the pits and the overall geometry of the pits, influenced the diffusion path of the normalised hydrogen concentration through the material.

The previous two steps were then combined and also an approximation of pit growth through the model was incorporated into the simulation for the HAZ material. At first, a uniaxial loading condition was applied to an unnotched specimen and after certain conditions were fulfilled various stages of approximate pit growth were applied. When the pits reached a certain depth, it was then assumed that the conditions in the pit were conducive to hydrogen uptake occurring in the pits and a varying normalised hydrogen concentration was applied to the pits. The critical hydrogen concentrations for increasing local strain in the pits were recorded.

Therefore, this work determined the pit geometries most susceptible to regions of maximum total true strains in x-direction and their locations, which may prove useful for non-destructive testing (NDT) of SMSS. Identifying the highest strained pit geometries early may result in more specific inspections to detect pits and prevent failure of the component. As HAC depends on the local interaction of the hydrogen concentration and the mechanical load in terms of strain, this work incorporated data previously evaluated into simulations to identify crack critical regions by the respective hydrogen concentration and strain level interactions.

Kurzzusammenfassung

Supermartensitische rostfreie Stähle (engl.: Supermartensitic Stainless Steels, SMSS) wurden in den 80‘er Jahren entwickelt, um die wesentlich teureren nichtrostenden Duplex-Stähle (engl.: Duplex Stainless Steels, DSS) und Nickellegierungen zu ersetzen, die in der Offshore-Öl- und Gasindustrie verwendet werden. Die guten mechanischen Eigenschaften, ihre hohe Korrosionsbeständigkeit in Zusammenspiel mit ihren ökonomischen Kostenvorteilen machten sie daher zu einer attraktiven Alternative. Ursprünglich wurden SMSS im Offshore-Bereich für die Verrohrung von Bohrlöchern eingesetzt, erwiesen sie sich aber im Vergleich zu den weiteren korrosionsbeständigen Werkstoffen (engl.: Corrosion Resistant Alloy, CRA) als eine Alternative unter Umgebungsbedingungen wie CO2-Korrosion und leicht sauren Bedingungen. SMSS werden daher als Rohrleitungswerkstoffe verwendet. Insbesondere gute Schweißeignung (aufgrund des niedrigen Kohlenstoffgehalts) in Verbindung mit den mechanischen Eigenschaften, machen die SMSS zu potentiellen Werkstoffkandidaten für andere Anwendungen.

Das Risiko einer wasserstoffunterstützten Spannungsrisskorrosion (engl.: Hydrogen Assisted Stress Corrosion Cracking , HASCC) kann sich mit zunehmendem Kohlenstoffgehalt im Stahl vergrößern, da sich der Kohlenstoff mit den im Werkstoff vorhandenen Chrom(Cr)-Ionen verbinden kann. Dies wiederum verringert die Menge an Cr-Ionen in der Metallmatrix, die die Passivschicht bildet, welche die Korrosionsbeständigkeit gewährleistet. SMSS haben einen reduzierten C-Gehalt, um das Risiko des Auftretens von HASCC beim Transport von sauren Betriebsmedien zu verringern. Zusätzlich erhöht der reduzierte C-Gehalt auch die Schweißeignung des SMSS. Die Wasserstoffkonzentration ist einer der drei Schlüsselfaktoren zur Bestimmung der Anfälligkeit eines Materials für wasserstoffunterstützte Risse (engl.: hydrogen assisted cracking, HAC). Die beiden anderen Faktoren sind die lokale/globale mechanische Belastung und die lokale Mikrostruktur. Darüber hinaus verringert in Chromgehalt von mehr als ca. 12%, zusätzlich zu weiteren Legierungselementen wie Molybdän, die Anfälligkeit eines Materials für Lochkorrosion. Diese kann zu hohen lokalen Spannungs- und Dehnungskonzentrationen führen und im Lochgrund zum Entstehen von lokalen Umgebungen mit hoher H+-Ionen-Konzentration führen (Ansäuerung des Lochelektrolyten), die sich dann in Regionen mit hohen Spannungen und Dehnungen ansammelt. Der häufigste Ort für Lochkorrosion an SMSS-geschweißten Bauteilen befindet sich in der Wärmeeinflusszone (engl.: Heat Affected Zone, HAZ), da sich die Werkstoffeigenschaften während des Schweißens massiv verändern. Es ist jedoch nicht abschließend geklärt, wo in durch Lochkorrosion entstandenen Materialschädigungen („Pits“), Risse entstehen. Dies liegt daran, dass Bereiche hoher Dehnungen und Wasserstoffkonzentration innerhalb einer Vertiefung stark von der Lochgeometrie abhängig sind. Lochkorrosion ist schwierig erkenn- und vorhersagbar, was sie gefährlicher macht als gleichmäßige Flächenkorrosion.

Experimentelle Methoden zur Messung der lokalen Wasserstoffkonzentration in Löchern haben sich aufgrund der kleinen Geometrie als nur bedingt anwendbar erwiesen. Darüber hinaus sind die lokalen Mechanismen der Initiierung und Ausbreitung von HAC nicht vollständig verstanden. Die numerische Modellierung der Wasserstoffdiffusion und der HAC ist hier ein alternatives Verfahren gegenüber Experimenten, um ein besseres Verständnis der Rissinitiierung zu erhalten und den Ursprung von Rissen als Folge der Pits zu untersuchen. Dies kann durch die

Modifizierung des Fickschen Gesetzes erreicht werden, so dass der Einfluss verschiedener Parameter auf die Wasserstoffverteilung untersucht und bewertet werden kann.

In dieser Arbeit wurde zunächst die Pit-Geometrie untersucht, die am anfälligsten für Bereiche mit höchsten Dehnungen ist. Für die numerische Analyse wurden sowohl die HAZ- als auch die Grundwerkstoff-Mikrostruktur (engl.: Base Material, BM) angenommen. In einem ersten Ansatz handelt es sich bei den simulierten Proben um homogene Werkstoffe (Gegensatz zu realen Schweißnähten mit unterschiedlichen Mikrostrukturen). Sieben verschiedene Pit-Geometrien wurden in 2D und 3D modelliert und einer einachsigen Zug- sowie Biegebeanspruchung ausgesetzt. Die Pit-Tiefe beeinflusste dabei die Ergebnisse hinsichtlich der niedrigsten wahren Gesamtdehnungen in x-Richtung im Fall von flachen Pits. Für die Biegebeanspruchung war jedoch der Pit-Öffnungsdurchmesser der wichtigste geometrische Aspekt, wobei größere Durchmesser die niedrigsten wahren Gesamtdehnung in x-Richtung erzeugten. Ein weiteres Merkmal war, dass sich die Lage der maximalen wahren Gesamtdehnung in x-Richtung bei den 2D-Modellen stets am Pit-Grund befand, diese Bereiche bei den 3D-Modellen jedoch variierten. Die Beanspruchbarkeit einer Probe mit einem vorhandenen Pit wurde ebenfalls für einachsige Zug- und Biegebeanspruchung in 2D und 3D untersucht. Es wurde festgestellt, dass die 3D-Modelle für beide Beanspruchungszustände höheren Verschiebungen erfuhren.

Zusätzlich zu einem anfänglichen auftretenden (durch die Lochkorrosion) inhomogenem Wasserstoffkonzentrationsprofil, wurden verschiedene Anfangsbedingungen für die initiale Wasserstoffverteilung auf der Oberfläche des Pits und des Modells angewendet. Dazu wurde die 3D-Geometrie des Pits aus der vorherigen Simulationsstufe mit den höchsten, niedrigsten und mittleren wahren Gesamtdehnungen in x-Richtung modelliert. Hierbei wurde noch keine mechanische Last aufgeprägt, zunächst nur die HAZ betrachtet und die normalisierten Wasserstoffkonzentrationen an bestimmten Positionen im numerischen Modell bestimmt. Es wurde dazu angenommen, dass eine variable Wasserstoffkonzentration den Folgen einer realen anodischen und kathodischen Teilreaktion im Pit entspricht. Daher wurde diese Randbedingung für alle Pit-Geometrien untersucht. Auch hier beeinflusste die Pit-Tiefe und Form des Pit-Grundes die Wasserstoffverteilung und damit den Diffusionsweg durch den Werkstoff.

Die beiden vorherigen Schritte wurden weiterführend kombiniert und das Pit-Wachstum in das Modell für die HAZ mit einbezogen. Dazu wurde zuerst wurde eine einachsige Beanspruchung definiert und auf eine ungekerbte Probe angewendet und das Pit-Wachstum in Abhängigkeit bestimmter Randbedingungen simuliert. Ab Erreichen einer bestimmten Pit-Tiefe, wurde angenommen, dass die die Wasserstoffaufnahme erleichtert wird und eine demensprechend variierende Wasserstoffkonzentration in der Simulation berücksichtigt. Die kritischen Wasserstoffkonzentrationen zur Erhöhung der lokalen Belastung in den Pits wurden aufgezeichnet.

In dieser Arbeit wurden Pit-Geometrien bestimmt, die aufgrund hoher Gesamtdehnungen in x-Richtung anfällige Bereiche für HAC darstellen. Die Vorhersage dieser Positionen kann sich als nützlich für die zielgerichtete zerstörungsfreie Prüfung (engl.: Non-Destructive Testing, NDT) von SMSS erweisen. Die frühzeitige Identifizierung am stärksten beanspruchter Pit-Geometrien, ist hilfreich zur Durchführung von zielgerichteten Inspektionen, um mögliche Pits frühzeitig zu erkennen und ein Versagen des Bauteils zu verhindern. Für die Bewertung HAC-Anfälligkeit wurden auf Basis numerischer Simulation mögliche risskritische Bereiche der Pits identifiziert und

deren Wechselwirkungen zwischen Wasserstoffkonzentration und mechanischer Beanspruchung (vor allem der Dehnung) beschrieben.

Acknowledgements

I want to begin by saying a heartfelt thank you to Prof. Dr.-Ing. Thomas Bollinghaus from the Bundesanstalt für Materialforschung und –prüfung (BAM) and Mr. Oddvar Deinboll from DNV GL, as without the agreement and support of these two gentlemen this work would never have been possible.

I am very grateful to Prof. Dr.-Ing. Hans Hoffmeister who has agreed to be my supervisor from the HSU. My colleagues from departments 9.0, 9.3 and 9.4 provided a lot of advice, guidance and also a very enjoyable working environment. Especially Dr.-Ing Tobias Mente who shared his time whenever he could. I want to also thank Dr.-Ing. Martin Mehlich and Christoph Münster at ISS, c/o HSU/ UniBw H. Ye both helped a lot with pitting discussions and providing information, no matter how busy ye were, I appreciate it. Frau Blackhart in the Faculty Administration at HSU/ UniBw H, thank you for helping me regarding the many documents and administrative part of submitting this thesis.

To the greatest colleagues, Maximillian Thomas, Eugen Wilhelm, Dr.-Ing. Thora Falkenreck and Jun.-Prof. Dr.-Ing. Michael Rhode. I am very lucky I got to spend these few years with ye in Berlin. Dr.-Ing. Oded Sobol, I will never forget the truly delicious cakes you made. A special thank you goes to the guys in the workshop, even though we never got a chance to work together the after lunch chats were always interesting.

To my family, Dad, Donie, Trisha and Dana, who don't always necessarily know what I'm doing but ye try. To Bernie for being with me throughout all my studies and even though I am far away we have never drifted apart. Last but not least, Alex. For being the most patient, calming and understanding person I know, and who makes a great cup of tea.

Maria Madigan Oslo, 2020

Table of Contents

1 Introduction

Over the past few decades, there has been an increased interest in martensitic and supermartensitic stainless steels (SMSS) for use in the oil and gas industry due to their good mechanical and corrosion resistance properties, along with their cost benefits [1]. SMSS has the potential to replace more expensive materials, such as Duplex Stainless Steel (DSS) and nickel alloys. SMSS are currently used in the oil and gas industry for onshore and offshore tubing applications, like flowlines.

Initially, early oil production used carbon steel as the material of choice, including carbon steel flowlines. The reason for this was oil tended to form a protective layer on the surface of the carbon steel, which hindered corrosion. However, as oil wells get depleted, increasing amounts of water are being produced in the oil, which leads to a more corrosive product. This in turn renders the protective oil film less effective. Alternatively, gas wells do not produce a protective oil film on the surface of the carbon steel. Cooling of the gas from the well temperature to surface temperature (i.e. sea or air temperature) causes the formation of condensation of water from vapour in the gas. This condensed water contains dissolved acid gases including CO_2 and H_2S while operating at high temperatures [2]. As a result of these dissolved acid gases, the pH of the medium is typically between 3.5 and 4.2 resulting in high corrosion rates of carbon steel, which can be up to several millimetre per year. Also, the presence of hydrogen in sour service increases the risk of incidents of hydrogen assisted failure which have been detected in sub sea oil and gas pipelines, structures and installations in the North Sea [3]. In offshore installations and subsea pipelines the main location of Hydrogen Assisted Stress Corrosion Cracking (HASCC) is in welded constructions due to the welding process altering the microstructure and therefor the properties of the base material (BM) [4]. Consequently, alternative materials need to be found which are especially capable of operating in deeper waters or able to handle aggressive media [5].

According to DNV [6], the predominant degradation mechanisms offshore steel structures are most susceptible to are corrosion and fatigue and the coupling of these two load types. Corrosion causes local damage to structures which can result in no major reduction in the overall safety level as long as regular inspection and maintenance programmes are implemented and appropriate actions taken based on the findings [7].

Localised corrosion normally takes place on materials which build passive layers. Upon the destruction of these passive layers the two predominant forms of localised corrosion are pitting and crevice corrosion, Figure 1.1. Crevice corrosion occurs in spaces between

mating materials, such as between a barnacle and the metallic material or between a washer and a test rack. However, pitting corrosion is a localised type of corrosion which may form at any imperfections on the surface of a metallic material, such as defects, grain boundaries or areas of stagnant electrolyte [8].

Figure 1.1: Localised and pitting corrosion on a stainless steel offshore pipeline [9].

Pitting corrosion has been studied for several decades [10]. Modelling pitting corrosion can however be difficult, in part due to the small geometries and to limitations in measurement techniques. However, currently finite element models of various pit geometries do exist but using ellipse or symmetric pit shapes instead of modelling real pit geometries is the norm in order to simplify the modelling process [11]. There are six different pit geometries specified by ASM [8], however the ellipse and shallow wide (or hemispherical) pits are modelled in most of the research [12-14], with the more complex yet true to life pits rarely modelled.

As an approach to fix this knowledge gap, first the strain distribution in the pit region of a model must be understood. For this, a displacement applied to a model with various pit geometries present was simulated. This was initially performed in 2D and then in 3D in order to investigate the difference in location of the region of maximum strain in both models. As the Heat Affected Zone (HAZ) has shown in previous research to be the area most susceptible to pitting corrosion [15, 16], this region along with the Base Material (BM), which is the largest region of a welded pipeline, are the materials of interest in this work.

The sour service media flowing through offshore pipelines, in addition to the separation of the cathodic potential reactions which will be mentioned in Chapter 2, makes pipelines more susceptible to HASCC. Therefore, the second stage of this work investigated the effect the presence of hydrogen has on the various pit geometries with varying hydrogen concentrations for the HAZ and BM. Various boundary conditions applicable to pipelines in a marine environment with pitting corrosion present were investigated, in order to determine the interaction between the hydrogen concentration, pit geometries and boundary conditions.

To determine the location of crack initiation in the presence of hydrogen in the various pits, the previous two steps of this work were combined. For these reasons a Slow Strain Rate Test (SSRT) was simulated where a constant strain rate of 1×10^{-5}mm/s, 1×10^{-6}mm/s and 1×10^{-7}mm/s were applied as a uniaxial load to a model with no pits present. When a certain strain in the material was reached it was then assumed pit initiation had begun, due to a break down in the passive layer of the material. The constant strain rate was still applied, and an approximation of pit growth was then modelled. When a certain pit depth was reached then hydrogen was introduced to the pit region and a critical hydrogen concentration (HD_{crit}) was calculated [16]. This combination of strain and hydrogen may lead to HASCC occurring in the pit. Unlike the previous two stages of this work, pit initiation and growth were modelled in this stage in order to accurately represent a SSRT in the presence of hydrogen.

2 Literature Review

2.1 Supermartensitic Stainless Steels

Since the first application of steel in steel structures in the 19th century the development of steel construction has been closely connected to advances in materials properties and production methods [17]. Important feats concerning strength, economy, design versatility, fabrication and erection techniques and service performance would never have been possible without advancements in steel. Steels are presently one of the most commonly used metals, with an average increase rate of approximately 5% per annum, according to Olsson and Landolt [18]. The development of steel is a continuous process due to the major role this material plays, with an annual production of more than a billion tonnes, which in turn improves the quality of daily life [19]. High strength steels are of particular interest due to their various advantages including economic advantages, reliable performance, environmentally friendly material and sustainability [17]. By increasing the strength of a steel, the various sectors can greatly benefit by a reduction in transport and fabrication costs which in turn lessens the environmental impact due to a reduction in emissions. For medium and long span bridges cost reductions of 20% can be achieved, according to Raoul [17]. The long lifetime and high recycling rate also ensure steels are one of the most sustainable materials.

In order to form a steel, Carbon (C) must be added to Iron (Fe) [19]. The inclusion of even a small amount of C, i.e. 0.1 - 0.2 wt.- %, has a significant effect on ferritic iron. This was known to blacksmiths even 2,500 years ago when iron was heated in a charcoal fire in order to absorb carbon by solid state diffusion [19]. However, the mechanisms of the adsorption of carbon into iron, which results in a soft metal becoming a very strong and tough alloy, have only recently been researched.

The material focused on in this work is a Supermartensitic Stainless Steel (SMSS) and the following chapters will provide more information on the production and formation of this material. Some background information as to why there was a need for this material to be developed and uses will also be presented. The microstructure of this material is then explored and finally the weldability of SMSS is discussed.

2.1.1 Stainless Steels

Stainless steels were invented more than a century ago by Monnartz [20] and may be defined as an iron based alloy which contains a minimum of approximately 10.5 wt.- % Chromium (Cr) and 1.2% Carbon (C), according to EN 10020 [21]. This is the minimum

required amount of Cr for the formation of a passive oxide layer, which leads to corrosion resistance in an unpolluted atmosphere [22]. Modern stainless steels contain other alloying elements in addition to Cr, depending on which properties are required, i.e. increase in hardness, tensile strength, ductility, corrosion resistance such as pitting and intergranular (IG) etc. While the hardness of the martensite class is determined by the carbon content, the hardenability is also dependent on alloying elements, as investigated by Lo et al. [23]. In order to achieve the desired properties, various alloying elements including Nickel (Ni), Manganese (Mn), Molybdenum (Mo), Copper (Cu) etc., may be added. Stainless steels are divided into four main groups based on their microstructure: ferritic, austenitic, martensitic and austenitic-ferritic (duplex) stainless steels. This work is based on supermartensitic stainless steel, therefore this material, and martensite in general, will be discussed in detail in the following chapters.

2.1.2 Production and Formation of Supermartensitic Stainless Steels

To form the martensite group of stainless steels, the steel is cooled from the austenite phase at a rate fast enough for the steel to supress the solid state transformation of the iron alloy from austenite into ferrite, i.e. fcc (face centred cubic) into bcc (body centred cubic). This cooling rate can be very high for plain carbon steels, but quite slow for a heavily alloyed steel which contains large concentrations of austenite stabilising solutes [19]. In fact, the time taken can be neglected, due to the very rapid nucleation and growth of martensite. This is demonstrated in the Koistenen and Marburger equation [24]:

$$f_M = 1 - e^{-0.011(M_s - T)} \tag{2.1}$$

Where:

f_M= Fresh Martensite,

M_s= Martensite start temperature (°C) and

T= Room Temperature (°C).

Equation (2.1) also shows that if the martensite transformation occurs at or below room temperature then there will be untransformed austenite remaining in the microstructure, this is referred to as retained austenite. These retained austenite phases are hydrogen trapping sites, according to Koistenen and Marburger [24]. Austenite additionally has a higher solubility for hydrogen, as do other interstitial and most substitutional elements, but most of this hydrogen is trapped at the austenite/ martensite interface or phase boundary. Hydrogen Assisted Cracking (HAC) may take place in the most susceptible martensitic phases resulting from high hydrogen concentration in the retained austenitic phases

diffusing into the neighbouring martensite under changing service conditions [25]. This will be discussed in more detail in Section 2.2.

Additionally, martensite can be created at very low temperatures where diffusion, including of interstitial atoms, is not possible. Therefore, martensite is referred to as a diffusionless, shear transformation which is crystallographic in nature as it is formed as a result of deformation of the austenite. This is due to the ability of martensite plates to grow rapidly in steel, 1100 ms^{-1}, and this high rate of growth is contrary to diffusion during transformation [19].

The formation of martensite is as a result of a suppressed diffusion and transformation process. This depends on the type of martensite: ε martensite or α' martensite, and when the chemical composition of martensite was measured it was found to be identical to the parent austenite [19]. In the formation of martensite, the atoms in the parent crystal are rearranged into a pattern more suitable for martensite, leading to an equivalent change in the macroscopic shape of the crystal which is undergoing transformation. Martensite is a supersaturated solid solution of carbon and other interstitials in ferritic iron [19]. Alloys with a low martensitic start temperature or with a high carbon concentration cause the atoms to order in a way that the crystal structure changes from Body Centred Cubic (BCC) to Body Centred Tetragonal (BCT). If the carbon content of the martensite is zero then the structure would be BCC and have no distortions [19]. However, martensite may contain both retained and annealing austenite between the martensitic laths. These are thin plates formed in alloys containing less than 0.6 wt.- % carbon, when the martensite is constrained by its surroundings, to minimise the strain energy due to deformation [26]. For automobile construction and in civil engineering structures, the lath martensite microstructure is the most important constituent in the high strength steel used [27]. Lath martensite consists of prior austenite grains, packets, blocks, sub-blocks and laths, Figure 2.1.

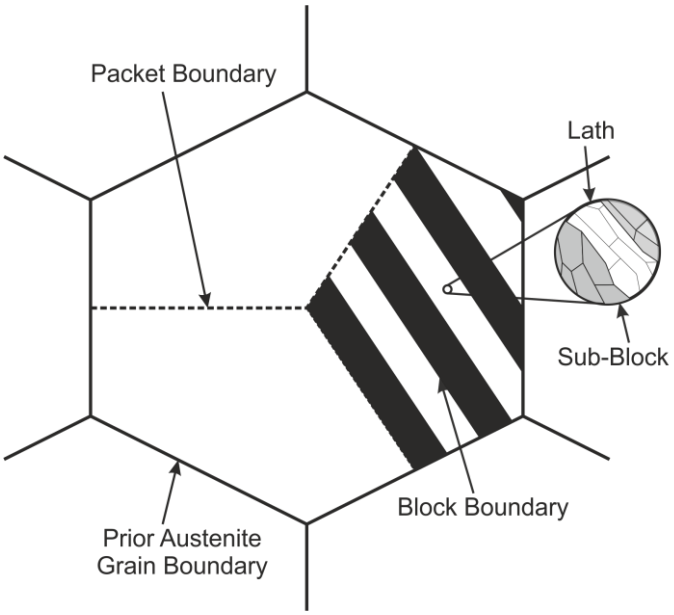

Figure 2.1: Martensitic microstructure [28].

Supermartensitic stainless steels were developed in the 80's in order to replace the more expensive duplex stainless steels (DSS) used in the offshore oil and gas industry [2]. This new material is cheaper as they contain less nickel and chromium, which are the most expensive elements in the material [29]. It was also due to improved steel production methods that this material was developed as it allowed a reduction in the carbon content in the range of 0.01 - 0.02 wt.- % and an increase in the molybdenum content of 2.0 - 4.0 wt.- % [30]. These alterations improve both the corrosion resistance and mechanical properties of the material, but the decrease in carbon content causes a reduction in the hardness of the material. To overcome this reduction in hardness a high amount of alloying elements, especially chromium, 11 – 14 wt.- % and nickel, 4 - 6 wt.- %, must be added to the material. For SMSS chromium increases the martensite start temperature, however the hardness is due to the presence of quenched martensite and nickel has the strongest effect on austenite formation in comparison to other elements [31]. Therefore, it was determined that in order to optimise the properties of SMSS there should be low C, approximately 13 wt.-% Cr and Ni added to martensitic stainless steel [2]. Several grades of 11 - 13 wt.- % Cr SMSS were developed, and the main application till now is in the oil and gas industry, as Oil Country Tubular Goods (OCTG) [32] but are also good candidates for other applications. At least 10.5 wt.-% Cr is needed in steels to provide a stable passive layer to achieve corrosion resistance. The intention is to uniformly precipitate the carbides and keep the matrix at Cr > 10.5%. Therefore, when the concentration of Cr is lower than 10.5 wt.-% then no stable passive layer forms and in the presence of a corrosive environment, then corrosion occurs. In order to determine the optimum level of Cr in SMSS

and to predict the microstructure formation of SMSS the Fe-Cr-C phase diagram should be consulted, Figure 2.2.

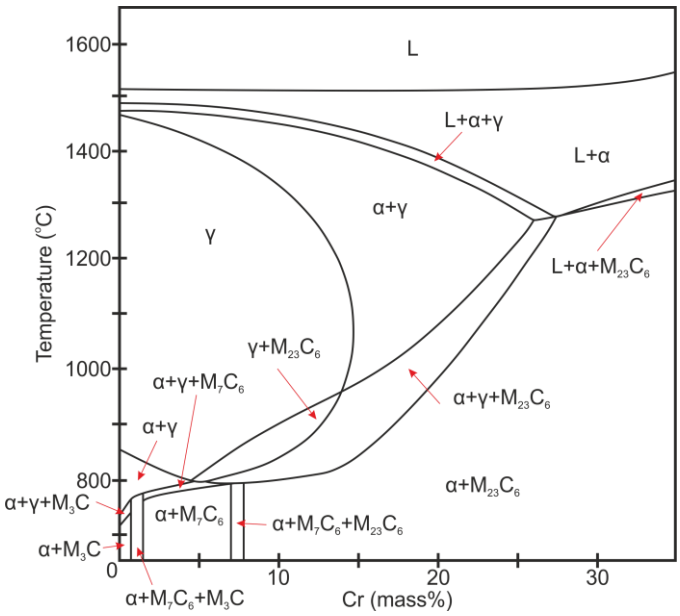

Figure 2.2: Phase diagram of Fe-Cr-C with 0.2 wt.- % C, based on Kondo et al. [31].

To achieve martensite without the presence of δ ferrite (α regions in Figure 2.2) for a steel with a chemical composition inside the austenite single phase region (γ) of Figure 2.2, at solution temperature, it is heated and austenitised then cooled to room temperature to transform to martensite. According to Figure 2.2, the Cr content should be lower than approximately 13 wt.- % in 0.2 wt.- % C steel. Increasing the Cr content to more than 13 wt.- % results in the formation of δ ferrite and this remains in the structure which detracts from the strength, hot workability and corrosion resistance to SCC of the steel, according to Kondo et al. [31]. It could be argued that an increase of C, which stabilises and expands the austenitic region in phase diagrams, along with the increase of Cr, in order to maintain the pure martensitic microstructure, may halt these reductions in properties. However, a decrease in toughness was observed due to the presence of increased Cr carbides, so increasing Cr while also increasing C is of no benefit to the microstructure [31].

As Cr and Ni are the major alloying elements of SMSS the microstructure formation can be described in relation to these alloying elements, using the phase diagrams for iron-chromium and iron-nickel, Figure 2.3. This phase diagram also indicates that above approximately 12 wt.- % Cr austenite will not be formed at any temperature. However, due to the presence of nickel the material can still be hardened due to the presence of a large austenite stabiliser region [33]. This is shown in Figure 2.3b where the γ region has been extended as a result of the increased nickel content and therefore the SMSS can still be

formed. These phase diagrams are useful as they determine the optimum amount of Cr, which promotes the formation of ferrite, and Ni, which promotes the formation of austenite. However, these phase diagrams are just for Fe-Cr and Fe-Ni steels and SMSS contains more alloying elements which additionally have an influence on the mechanical properties of the steel.

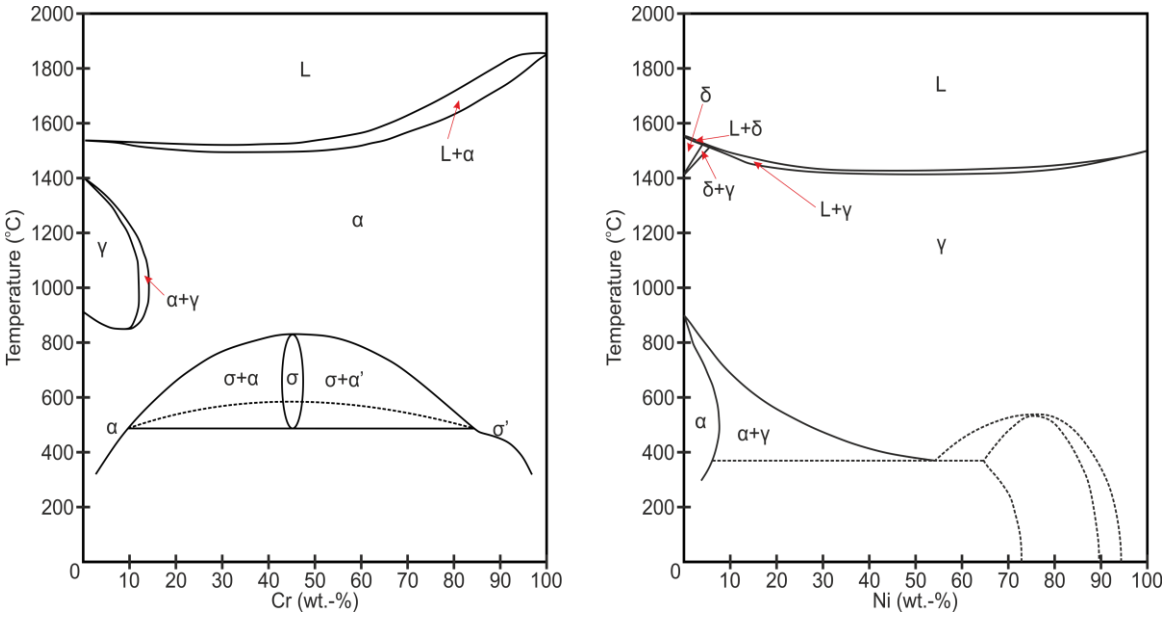

Figure 2.3: Major alloying element effects on microstructural formation of stainless steels for a) Fe-Cr and b) Fe-Ni equilibrium diagrams, based on Rabensteiner et al. [33].

These additional alloying elements include C and Mo, among others. As the Cr and Ni contents of SMSS are increased, the C and Mo contents are decreased to the range of 0.01 - 0.02 wt.- % and 2.0 - 4.0 wt.- % respectively, with the addition of Mo to improve the corrosion resistance and mechanical properties of the steel.

Various alloying elements may be added to improve the properties of SMSS and the role of each of the alloying elements is now summarised:

Carbon (C)

Carbon is added in low levels to stainless steels to increase the hardness and strength by heat treatment. The level of C added to Martensitic Stainless Steels (MSS) is intentionally increased to attain higher mechanical properties, such as hardness, and to develop the martensite phase by making these alloys heat treatable by quenching and tempering. However, C can combine with Cr, or Cr ions, to form chromium carbides, which reduces the amount of atomic Cr in the metallic matrix which forms the passive layer and provides corrosion resistance, according to Olsson and Landolt [18].

Chromium (Cr)

Cr is added to steel in order to obtain the corrosion resistance properties of stainless steel. Cr is the main element in the passive layer which is a stable oxide (Cr_2O_3) and has a very low corrosion rate. In neutral or alkaline environments passive films are often described as consisting of two layers. Marcelin et al. [34] found using XPS analysis that the passive films of a martensitic stainless steel are composed mainly of oxides, such as FeO, Fe_2O and Cr_2O_3, hydroxides, such as FeOOH and $Cr(OH)_3$, and contaminants such as C and O. The presence of Mo and Ni were also observed. XPS is X-ray photoelectron spectra and was carried out on a martensitic stainless steel passive film formed in contact with air. The presence of Cr in stainless steels therefore increases the corrosion resistance and restricts the growth of stable pitting corrosion, but only if at least 12 wt.- % is added, according to Bhadeshia and Honeycombe [19]. Cr restricts pitting propagation as its presence increases the pitting potential, as well as the Critical Pitting Temperature (CPT) and Critical Crevice Temperature (CCT). The presence of too much Cr in steels can have the opposite of the desired effect on steels by reducing the ductility, toughness and corrosion resistance due to the formation of intermetallic phases [19]. Additionally, martensitic chromium steels with a high chromium and low nickel equivalent have a tendency to form delta ferrite which influences the mechanical properties of the material. The presence of delta ferrite causes an increase in the ductility and toughness of the material, according to Schäfer [35]. However, dendritic carbide precipitations are also formed which are brittle and reduce both the ductility and toughness of the material. The presence of delta ferrite and dendritic carbide precipitations both decrease the strength of the steel and are undesirable [35]. Dendritic carbides should therefore be avoided as this phase reduces the mechanical properties of the steel, but delta ferrite without dendritic carbides can be tolerated.

Nickel (Ni)

Ni is an alloying element which stabilises the austenitic phase of the steel. The addition of other ferritising elements are counter balanced by the addition of Ni to achieve the austenite phase at high temperatures and to avoid the presence of δ ferrite islands in the material [36]. The presence of Ni also improves the toughness of the steel at low temperatures, promotes cross dislocation glide and can cause solid solution softening. Ni also reduces the M_s and A_1 (eutectoid) temperatures resulting in the presence of austenite after quenching and tempering which increase the corrosion resistance properties of the steel. As Ni is less oxidised than iron and Cr, there are high levels found in the metallic state in the region closest to the oxide/ metal surface [37].

Molybdenum (Mo)

The presence of Mo in stainless steels accelerates the formation of the passive layer and thus, improves the passivation behaviour [38]. In SMSS the presence of δ-ferrite in the Heat Affected Zone (HAZ) of welded joints increases the joints susceptibility to corrosion attack due to higher carbide precipitation. The welded joints and HAZ of SMSS consist of chromium and molybdenum carbide precipitations which have an influence on the susceptibility of the joints to corrosion attack. These precipitations are formed before the formation of austenite grain boundaries and are located at the prior austenite grain boundaries. During multipass welding these precipitations can also be found at the martensite/ δ ferrite phase boundaries [39]. PWHT can intensify the formation of these precipitations and also cause a decrease in the formation of intermetallic phases [40]. However, the presence of chromium and molybdenum carbides causes an increase in the hardness of the material. Mo is a ferrite former, therefore increasing the Mo content results in the Ni content having to be also increased, in order to maintain the desired microstructure [41].

Nitrogen (N)

Until recently N was an element considered harmful, even though it is always present in conventional metallurgical processes [42]. It has been shown that N stabilises the austenite and has a significant influence on the properties of the passive film, which in turn enhances the corrosion properties. It was reported that N may have an influence on localised corrosion due to the formation of chromium nitride and the depletion of free chromium in the steel matrix, which may affect the corrosion resistance of the material [43]. The solubility of the N is decreased by the presence of nickel, carbon, silicon and copper whereas chromium, manganese and molybdenum increase the solubility. When N is added below a temperature where CrN forms this results in a very high surface hardness, good wear resistance and excellent corrosion resistance, according to Li and Bell [43]. It is due to the higher strength, toughness and pitting corrosion resistance that high nitrogen grades of MSS are becoming more popular.

Manganese (Mn), Copper (Cu), Tungsten (W), Vanadium (V)

The addition of Mn has the benefit of increasing the solubility of N and Mo. The addition of Cu to highly corrosion resistance austenite increases the corrosion resistance and also provides anti-bacterial properties to the surface [37]. The presence of Cu also increases the machinability of the steel [44]. W is an element which only recently started being used as an alloying element in steels and has similar properties to Mo. The addition of V increases hardness as it causes carbides and nitrides to be formed at lower temperatures.

The alloys mentioned above are the most common alloys to be added to martensitic steels in order to form SMSS. Other alloys may of course be added but more alloys do not necessarily lead to improved mechanical and material properties. The development of this new steel will now be discussed.

2.1.3 Development of Supermartensitic Stainless Steels

As mentioned in Chapter 1, carbon steel was the material of choice in early oil and gas production. However, due to the need to drill new wells in previously undesirable locations there was a need to use materials capable of operating in different locations or conditions. These include deeper waters with High Pressure High Temperature (HPHT) wells, severe weather conditions, such as the artic, or able to handle the presence of sour service, which provide many challenges [45-48]. HPHT wells are defined as wells where the bottom hole pressure is greater than 1,000 bar and 177°C. This, along with well depths exceeding 1,000 m required a new high strength material while also exhibiting good corrosion resistance properties [49]. High Strength Low Alloy (HSLA) materials are usually used in these operations due to their good mechanical properties and due to the low alloy content, these are also not very expensive. The type of fluid flowing through the pipe is one factor which determines the type of corrosion the material may experience, including general or local corrosion or environmentally induced cracking. The other factors which determine corrosion type are the load applied and structural design of the component. Therefore, in selecting a material for oil and gas pipelines numerous parameters must be considered [50], including:

- Temperature of the fluid flowing through the pipe,
- Chloride concentration,
- Partial pressures of CO_2 and H_2S,
- Water composition,
- pH value and
- Flow rate.

As deciding on new materials is an expensive process including designing, manufacturing, testing etc. other methods were also considered in order to prevent corrosion in already established materials. It is common practice to control the pH of the media in flowlines by adding chemical inhibitors to the media [51]. Inhibitors are chemicals used in the oil and gas industry to protect the surface of metals to prevent corrosion. Chemical inhibitors work either by merging with the metal surface or by reacting with the impurities in the environment [52].

There are however disadvantages to this method [53], including:

- The well itself is not designed for injecting the chemical inhibitor,
- The corrosion rate is too high, even with the addition of the chemical inhibitor,
- The expense of purchasing the chemical inhibitor for the remaining lifetime of the well is too high to be feasible,
- The inhibitor injection system must be of a very high reliability, but this is not always guaranteed and
- Disposal of the chemical inhibitor in an environmentally friendly manner can be challenging.

Therefore, the development of Corrosion Resistant Alloy (CRA) materials were the next phase in new materials for the oil and gas industry [54].

CRAs have been used in flowlines since 1975 when the Dutch company NAM were the first company to use this material offshore, as CRAs not only have a higher reliability than carbon steel with inhibitors, but also have lower life cycle costs and environmental impact. In the period 1975-1980 seven flowlines internally clad with stainless steel AISI 316L and a total length of 7.7 km were installed [55]. It was well known that the standard austenitic stainless steels, such as AISI 304L and 316L, while not susceptible to corrosion, were however unsuitable for the high pressure environment of the flowlines, due to their low yield stress of 180 MPa minimum [2]. Therefore, in order to use austenitic stainless steel as a pipe material, thicker wall sections were required. It was for this reason that austenitic stainless steel was then developed as a cladding on much stronger backing steels, such as X52, which allowed a reduction of up to 50% in wall thickness compared to solid austenitic stainless steel, according to Smith and Celant [2]. This not only reduced the wall thickness but also weight, welding time and material costs. In addition to the seven internally clad flowlines, four duplex stainless steel lines with a total length of 13.3 km were installed. Two of these duplex lines were the first ever offshore CRA flowlines. The two duplex lines installed offshore contained 18 wt.- % Cr and were already used for some piping offshore due to the high resistance to CO_2 corrosion [2]. As duplex stainless steel has a higher yield stress than austenitic the wall thickness was greatly reduced, making these materials more economically feasible. However, duplex steels are much more expensive in comparison to other steels, due to the high alloy content.

By the end of 1990 over 238 km of DSS pipelines were selected for projects mostly in the Netherlands but also in the UK and Norwegian sectors of the North Sea, in the USA and also in Canada [2]. 1990 also saw the first application of the higher grade 25 wt.- % Cr superduplex stainless steel in flowlines. This superduplex not only has a higher yield stress

of 550 MPa but also offers greater corrosion resistance, including against H_2S, to some extent. Throughout the 90's more than 1,136 km of duplex stainless steels were installed with 91.1% being 22 wt.- % Cr, i.e. standard DSS of the 1.4462 type [2].

In parallel, the popularity of clad piping also increased with AISI 316L stainless steel as a cladding material being a direct technical alternative to DSS. As the conditions in oil and gas wells do not remain constant throughout the lifetime of the well and high demand results in more corrosive wells being drilled, this resulted in the flow media being too sour for AISI 316L clad pipe towards the end of the 80's [2]. One of the biggest advantages of clad piping is the ability to change only the cladding layer in contact with the flow medium for another alloy when the conditions inside the flowline change. From 1986 onward, nickel Alloy 825 clad pipe was the material selected for sour service conditions and by 1991 the amount of Alloy 825 clad pipes surpassed the amount of AISI 316L [2].

It was not until 1996 that the newly developed low carbon weldable grades of alloyed 13Cr martensitic stainless steel, "Super 13Cr" or supermartensitic stainless steel, significantly changed CRA flowline use. MSSs were first used in 1981 when Mobil installed pipelines in the Arun field in Indonesia. However, 12-13 wt.- % Cr steel is not commonly used as pipeline material as it has less weldability, which requires pre-heating and PWHT, compared to SMSS. The SMSS differed from MSS as the Cr content was increased while reducing the carbon content. Nickel was added in order to maintain the martensitic phase without δ ferrite and the addition of Mo increased resistance to localised corrosion and Stress Corrosion Cracking (SCC), according to Kondo et al. [56] as explained earlier. Over the next 13 years more than 28 km of SMSS was installed, including 9 km of pipelines in the Gulfaks Satellites and in the Asgard fields in the Norwegian sector of the North sea and in connecting the Sleipner platform with Statoils Loke satellite [57, 58]. SMSS had been used offshore for many years as downhole tubing and proved to be an economical choice for combatting CO_2 corrosion and mildly sour conditions, compared to other CRA flowline materials. SMSS has a lower alloy content than DSS but it also has the advantage of being able to be produced in bulk in the world's largest steel pipe production lines. These economic and production advantages lead to approximately 650 km of material being installed between 1996 and 2002 as flowlines [2]. In the period 2000-2004 it is estimated that 40% of flowlines are SMSS. Since 1975 2,400 km of CRA flowlines have been installed, 49% being DSS, 28% SMSS and 23% clad carbon steel [2]. It is expected that the percentage of SMSS will increase in the future to around 40% due to the good material properties in sour service and it is relatively inexpensive in comparison to the other CRA material options [2].

There are however disadvantages to the use of SMSS. When a new field is developed offshore, it is substantially cheaper to tie in new developments to existing infrastructure. As a result of this, one of the major costs of developing an offshore project is the costs involved in laying flowlines. This cost is increasing as the distance between a common production facility and the wells and manifolds are increasing, in the 1970s the average flowline was 3.5 km in length, in the 1980s this increased to 4.8 km and in the 1990s this increased again to 9 km [29]. However, when tie in operations are undertaken it is necessary for the pipe ends to be open for a short period of time, which is not ideal as SMSS are not seawater resistant. In order to minimise the risk of corrosion due to seawater, each end of the pipe is filled with a gel plug and 30 m of the inside of the pipe is coated with a wax [59]. Statoil has a specification stating that all seawater should be removed from SMSS pipelines within 7 days. An anchor accidently damaged a section of pipeline in the Åsgard field and this section of pipeline was partially filled with seawater, according to Olsen et al. [59]. This seawater remained in the pipeline for three months and when the pipeline was recovered from the seabed and inspected, deep pitting corrosion was present on the internal surface of the pipeline. This highlights that the inner and outer surfaces of the pipe are exposed to different corrosive environments. The inner surface is exposed to the media flowing through it which may be liquid or gas, sweet or sour etc. The outer surface is exposed to mud, earth, seawater and temperatures in the range of 5 to 40^{o}C. The outer surface may also be protected by cathodic protection (CP) in order to reduce surface corrosion. This may lead to hydrogen embrittlement depending on the cathodic current and the amount of hydrogen present in the steel if a failure occurs in the CP. This is explained in more detail in Section 2.2.

Presently, there is still ongoing research into the performance of CRA in sour service environments, as mentioned by Sridhar et al. [49] which is based on previous work by Rhodes [54] and Turnbull and Griffiths [60]. However, SMSS were developed for the offshore industry and are currently proving to be a viable replacement for other materials and methods including duplex stainless steels and cladding. There are disadvantages of using SMSS, including it being a new material compared to more established materials in the offshore industry. However, the advantages, including high corrosion resistance, less expensive than other materials with similar mechanical properties, outweigh these disadvantages and therefore SMSS is seen as a viable alternative to DSS or other materials. More information about the classification and specifications of SMSS is provided in the next section.

2.1.4 Grades and Compositions of Supermartensitic Stainless Steel

There are three grades of SMSS, divided in accordance to their level of alloying- Lean, Medium and High alloyed. These grades depend on the most important alloying elements which are Cr, Ni and Mo. The chemical compositions of the three different grades of SMSS are shown in Table 2.1 and are according to Akselsen and Aune [61]. The chemical composition and any tempering procedures will cause the mechanical properties of these steels to vary. These steels already have a combination of good mechanical properties and high mechanical strength, but heat treatment of these steels has a great influence on the mechanical properties as the amount of carbides in the quenched microstructure have an important influence on the hardness and corrosive properties.

The lowest martensite start temperature (150^{o}C) belongs to the high alloyed grade of SMSS and therefore these grades contain the highest amount of stable retained austenite. A decrease in Ms-temperatures of SMSS implies that the amount of retained austenite during cooling to room temperature in the welded component can be increased.

Table 2.1: Chemical compositions of the three different grades of SMSS [61].

Element	11Cr2Ni (Lean)	12Cr4.5Ni1.5Mo (Medium)	12Cr6.5Ni2.5Mo (High)
Cr (max%)	10.5 – 11.5	11.0 – 13.0	11.0 – 13.0
Ni (max%)	1.5 – 2.5	4.0 – 5.0	6.0 – 7.0
Mo (max%)	0.1	1.0 – 2.0	2.0 – 3.0
C (max%)	0.015		
Mn (max%)	2.0		
P (max%)	0.030		
S (max%)	0.002		
Si (max%)	0.4		
Cu (max%)	0.2 – 0.6		
N (max%)	0.012		

For use in the oil and gas industry welded SMSS pipelines are required to have a microstructural balance of tempered martensite and finely dispersed supercooled retained austenite with little to no supercooled delta (δ) ferrite present [62]. To achieve this specific microstructure, it is necessary to undergo heat treatment, as during welding small amounts of δ ferrite can form. δ ferrite transforms into austenite crystals at a temperature around

1,300°C and finishes around 1,200°C. The austenite to martensite transformation can lead to a martensitic microstructure with small amounts of supercooled retained austenite [62].

Heat treating these steels determines the amount of retained austenite present and this has a considerable effect on the yield stress, which is in the range $R_{p0.2}$ = 550 – 650 MPa and the tensile strength R_m= 850 MPa [63]. The ideal microstructure contains low carbon tempered martensite along with retained austenite. In order to achieve this microstructure, heat treatment consisting of austenising, cooling to room temperature to encourage martensite formation and finally single or double tempering [64].

The presence of the alloy Ni reduces the A_{c1} (temperature where austenite begins to form during heating) temperature and tempering treatments by about 50 – 70°C. Just above the A_{c1} temperature part reaustenisation will occur but without any transformation to martensite [65]. This forms a microstructure containing stable retained austenite between the martensite laths and along the prior austenite grain boundaries providing increased ductility and toughness. The amount of retained austenite present depends on the tempering cycle and can vary between 5 and 30 wt.- % [66]. Temperatures well above the A_{c1} temperature are not recommended as at these temperatures unstable austenite is formed. In a temperature range of 1,000 – 1,050°C these steels are austenitic and due to their good hardenability, the martensitic transformation can happen with air cooling.

PWHT can be applied in order to achieve better toughness properties. These can be achieved by subsequent intercritical tempering at 600°C, which is slightly above the A_{c1} temperature, according to Dalmau et al. [67]. This tempering causes the martensite to soften and the finely distributed austenite is precipitated along the prior austenite grain boundaries and the martensite interlath boundaries [62]. This tempering results in untransformed austenite which is responsible for the high toughness of this steel. However, this mechanism where the austenite increases the toughness properties of the steel, along with the thermal and mechanical stability of the austenite are not yet fully understood. There are several theories which attempt to explain this using a composite microstructure of tempered lath martensite with small austenite particles densely distributed along prior austenite grain boundaries and the martensite interlath boundaries. Some of these theories, according to Bilmes et al. [62], include:

Austenite acting as a crack blunter

This theory is based on assuming a crack propagating through the steel is hindered by the ductile Face Centered Cubic (FCC) austenite. However, it has been shown that austenite transforms to martensite just ahead of the crack tip, according to Fultz and Morris [68], who investigated the martensitic transformation of austenite particles in 9Ni steel. More

recent research suggests that austenite (FCC) transforms to martensite (BCC) during the fracture process. This corresponds to models based on transformation of austenite to martensite by localised Transformation Induced Plasticity (TRIP) [62]. It was also found that austenite behaves brittle and could not stop the crack from propagating in low carbon 13Cr-NiMo martensitic steels [62].

Austenite scavenging deleterious elements

Phosphorus (P) and Sulphur (S), which are considered to be grain boundary pollutants, are collected due to the presence of austenite, which in this case acts as a sink, and this leads to an increase in toughness as intergranular fracture is eliminated, according to Frear and Morris [69].

Austenite and the crystallographic cleavage impairment model

The martensite formed in highly strained regions in front of a crack tip may be different to the matrix and this can create a high angle boundary. The fracture surface when brittle fracture occurs then contains smaller facets due to the presence of the mechanically transformed austenite. Initiating cleavage cracks is more difficult due to the presence of more high angel boundaries, which in turn lowers the ductile to brittle transition temperature (T_B) in a manner similar to refining the grain size [69].

In order to estimate the austenite content at room temperature for various PWHT methods, the following Larson-Miller equation (2.2) can be used:

$$P_{LM} = T.[20 + \log t].10^{-3} \quad (2.2)$$

Where:

T = Tempering temperature (K) and

t = Duration (hours)

Figure 2.4 shows the effects of tempering on retained austenite in 13Cr4Ni0.5Mo and 13Cr6Ni1.5Mo supermartensitic stainless steels. It shows that most austenite forms at a P_{LM} value between 15.5 and 18 and remains stable during cooling to room temperature. Above a P_{LM} value of 18 the austenite becomes unstable and during cooling it transforms to untampered martensite [70].

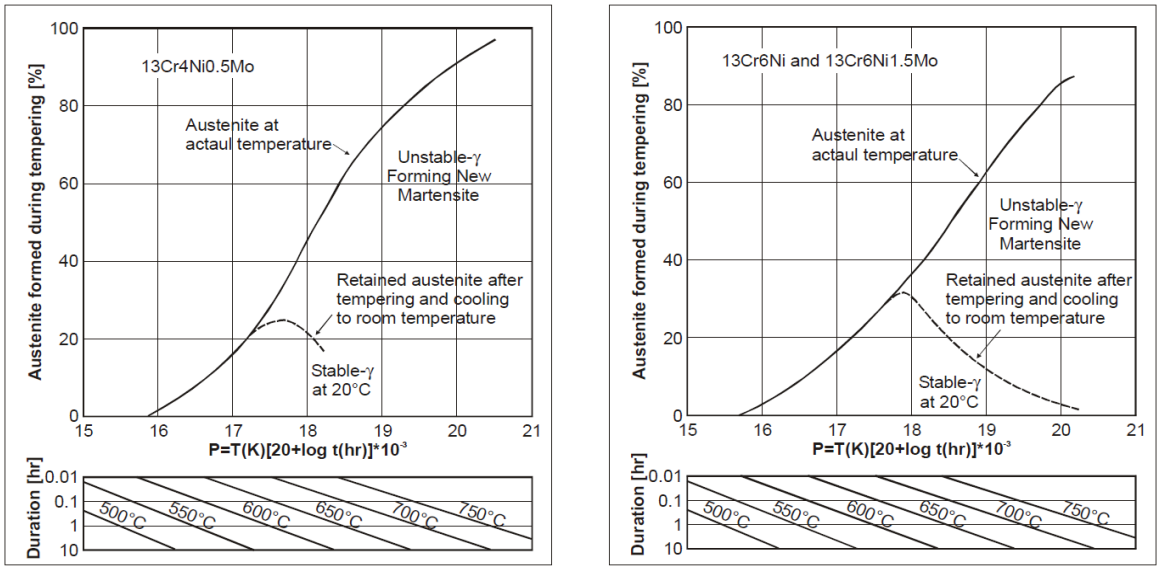

a) 13Cr4Ni0.5Mo system b) 13Cr6Ni1.5Mo system

Figure 2.4: Effects of PWHT conditions on austenite reformation in two different systems of supermartensitic stainless steel [70].

Additionally, the tempering temperature is an important factor of heat treating SMSS. This is due to temper embrittlement and a reduction in the corrosion resistance which can occur at intermediate tempering temperatures. Temper embrittlement is a reduction of toughness due to a metallurgical change which can occur in some low alloy steels resulting from long term exposure in the temperature range between 343 and 593ºC, according to API RP 571 [71]. Charpy impact tests revealed that this causes an upward shift in the ductile to brittle transition temperature. This reduction in toughness is not seen during operation but during start up and shut down, so the equipment that is temper embrittled may be at risk of brittle fracture [71].

The alloying elements determine the susceptibility of the steel to temper embrittlement with Manganese (Mn) and Silicon (Si) alloys the most susceptible. However, Ni-Cr martensitic steels are especially susceptible to tempering embrittlement when tempering is performed in the temperature region between 343 and 593ºC. Slow cooling through this temperature range is to be avoided. This shows that choosing the correct tempering temperature is an important factor to consider in the heat treatment process.

Mo carbonitride precipitations can also be formed, along with Cr precipitations, in the HAZ of SMSS. These precipitates can be mainly found at the prior austenite grain boundaries and the martensite/ δ-ferrite phase boundaries during multipass welding and can be increased by PWHT [72]. Carbide precipitates result from carbon matrix saturation and the tempering effect caused by ensuing welding passes. Therefore, Intergranular Stress Corrosion Cracking (IGSCC) can occur due to a reduction in the presence of Cr as a small

amount of Cr carbide precipitates are located at the prior austenite grain boundaries, according to Nakamichi et al. [73]. Böllinghaus et al. [74] shows that the HAZ is the region most susceptible to crack initiation due to the effects the welding process has on the weldments. As mentioned above, carbides precipitate alongside the martensite laths and the diffusion path of Cr and C out of the matrix is much shorter to the martensite laths than to the former austenitic grain boundaries. Therefore, IGSCC in SMSS is due to hydrogen enrichment at the former austenite grain boundaries as there is more space for hydrogen than alongside the martensite laths. This is also true if the carbides are equally distributed at the grain boundaries and the martensite laths. This will be discussed in more detail in later sections.

Secondary tempering can also be performed on SMSS. It was found that after secondary tempering is completed in a range between 520 to 720^{o}C and initial tempering undertaken up to 600^{o}C, the amount of retained austenite increases with increasing temperature. Initial tempering above 600^{o}C resulted in a decrease of retained austenite with increasing temperature, due to the reduction in concentration of austenite stabilising elements, such as Ni according to Zou et al. [75]. As a result of this, at room temperature less austenite is stabilised and the transformation of austenite to martensite during cooling is preferred. As previously mentioned, the presence of retained austenite at room temperature is an important factor in determining the mechanical properties of the SMSS, including Ultimate Tensile Strength (UTS), yield stress and elongation. This was investigated using new 17 wt.- %Cr supermartensitic- ferritic stainless steel specimens from a seamless tube with different heat treatments by Tavares et al. [76], Table 2.2. This table shows the % austenite formed from performing different heat treatments.

Table 2.2: Heat treatments on 17 wt.- %Cr SMSS specimens from a seamless tube

Specimen	%Austenite
Q	3.8
QT-300	0.0
QT-400	0.6
QT-500	1.2
QT-650	7.4
DT1	13.7

Where:

Q: Quenched at 1000^{o}C, no tempering

QT-300: Quenched at 1000^{o}C, tempered at 300^{o}C for 1 hour

QT-300: Quenched at 1000^{o}C, tempered at 400^{o}C for 1 hour

QT-300: Quenched at 1000°C, tempered at 500°C for 1 hour

QT-300: Quenched at 1000°C, tempered at 650°C for 1 hour

DT1: Quenched at 1000°C, double tempered at 670°C for 2 hours then 600°C for 2 hours

There are however ongoing discussions into how retained austenite influences the properties of MSS and SMSS, including the influence on hydrogen diffusivity [62, 77-79]. Due to its primarily martensitic structure, SMSS is susceptible to hydrogen embrittlement both related to welding, H_2S and CP. These steels are especially sensitive in the non-heat-treated condition, containing untempered martensite and unstable retained austenite. This is often the case in weld HAZ, where most of the HAC incidents occur. This will be discussed in more detail in Section 2.3.5.

2.1.5 Supermartensitic Stainless Steel as Welded/ Quenched

As mentioned previously, SMSS are a viable alternative to other HSLA steels, mainly used in the offshore oil and gas industry as they have excellent corrosion resistance, similar to carbon steels and MSS, while not being as expensive as duplex materials. SMSS were developed from MSS but with reduced carbon to enhance weldability and corrosion resistance. However, welding also plays an important role as it can influence toughness and resistance to cracking [80]. Due to the reduction in carbon content the martensite in the HAZ of SMSS is relatively soft and tough which increases the resistance to cold cracking in the HAZ of welds [36]. Researchers, such as Sebastián, Ramirez, Thibault, Tavares et al. [81-84] have found peaks of hardness may be present in the HAZ therefore it is necessary for SMSS welds, especially those operating in CO_2 and H_2S containing environments, to undergo PWHT in order to reduce these peaks of hardness in the HAZ.

One of the biggest advantages of SMSS is their weldability and the resulting mechanical and corrosion properties of the welded material. As mentioned, PWHT is required on SMSS but there is ongoing research into welding methods for SMSS to reduce the necessity for PWHT, which is both expensive and time consuming, while also increasing the reliability and economic value of these welding processes [40]. Therefore, new and advanced welding processes for SMSS have been investigated as substitutes to conventional processes as welding processes have a serious effect on the corrosion behaviour of the weldment. An example of new welding processes is the high power density processes. In these welding processes, the high heat input is confined to a small region along with the high cooling rates of high power density processes which promote dissolution and suppression of Cr-carbide precipitates, such as when electron beam welding is performed. Some advantages of this method of welding is that no PWHT needs

to be performed after electron beam welding and the weld is more resistant to corrosion [40]. Comparing the corrosion resistance and mechanical properties of high power density processes with more conventional methods, reveals better welded joints using the high power density processes [85]. It has also been found, however, that the HAZ region is not the most susceptible region to pitting corrosion in high power density process welds [86]. This is mainly due to the redissolution process of the Cr-carbide precipitates.

When welding MSS, and in turn SMSS, hydrogen is a well-known threat. Therefore, low hydrogen welding processes, consumables and welding procedures are considered during welding activities. In general, the same precautions against hydrogen ingress used during welding DSS were applied to MSS and in doing so the presence of cold cracking was minimised [57]. Base materials (BM) and weldments produced using the conventional welding methods of Submerged Arc Welding (SAW) and Gas Metal Arc Welding (GMAW) in sour service environments were investigated for SCC [87]. This is one main area being investigated along with developing matching consumables. Cracks, caused by the presence of hydrogen, have been found in the thermically altered region of SMSS tubes welded with super duplex consumables [88]. It is predicted that Ni based consumables will not encounter the same problem due to the slow diffusion rate of hydrogen in austenitic microstructures However, Electron Beam (EB) welded joints are more susceptible to embrittlement while undergoing hydrogen charging as a result of the high strength and hardness present in the microstructure of the weld.

Radial friction (RF) welding is an alternative welding process developed by The Welding Institute (TWI) as a “one shot” joining process and is a variation of the friction welding process [89, 90]. It has various advantages including fast welding times of less than 30 seconds, low operator skills required, high weld quality and reproducibility and dissimilar metals can be joined. The RF process has recently been applied to SMSS pipes and defect free high quality welds with mechanical properties similar to those of the BM can be reproduced without PWHT, according to Della Rovere et al. [90]. The RF welded regions also showed increased corrosion resistance due to the absence of Cr carbide precipitates caused by the welding process in comparison with the BM which was unaffected. However, the presence of delta ferrite was also observed, which reduces the corrosion resistance of the material and was found to neutralise any increase in corrosion resistance offered by the absence of Cr carbide precipitates, Della Rovere et al. [90]. The increased corrosion resistance was due to δ-ferrite formation at the weld interface [91].

To conclude, as SMSSs are still relatively new materials compared to more established materials used in offshore marine environments, such as DSS, there is still ongoing research and monitoring into their effectiveness and use in these environments. A lot of

research is also still focused on establishing optimal welding procedures and consumables for SMSS and how the weldments behave in different applications.

2.2 Hydrogen-Assisted Stress Corrosion Cracking and Material Degradation

2.2.1 Introduction

Welding can result in changes to the microstructure of the BM, resulting in the creation of the HAZ, which includes dissolution of precipitates, grain size effects and hardening. This can lead to many weld imperfections, including cracks. A specific type of crack which can occur are cold cracks, which form at temperatures < 450^{o}C and may be generated in the presence of hydrogen. The transport of hydrogen from its original location, internal or external, to another location within the material where critical degradation can occur is one of the most complex aspects of HAC. However, this is important to understand in order to predict the life of a component in the presence of hydrogen [92, 93]. Hydrogen can be absorbed into the component in various ways including during production (welding), processing and under service conditions, such as when CP is in use on the component.

A particular type of HASCC includes HAC, which occurs at temperatures lower than 100^{o}C [94]. An overview of the interaction of hydrogen with metals, which include absorption, desorption and diffusion is presented in the next chapters. These depend on the lattice diffusion, interaction of hydrogen with lattice defects, such as trapping, and the interaction of hydrogen atoms with the crystal lattice. SMSS may contain these crystal structures as the matrix structure or the substructure, which depends on the chemical composition of the material, if any heat treatment has been performed, etc. The various mechanisms and theories explaining how HAC occurs are then presented.

2.2.2 Hydrogen Transport Through the Metal

Transportation of atomic hydrogen through a metallic material is heavily influenced by the crystal structure of the material. Researchers have shown that the presence of hydrogen causes significant distortions in a metal matrix and these distortions may be lattice inter-atomic expansion or phase transformations, such as transformation of retained austenite [95-98].

It is therefore necessary to know the basic crystal structure of an iron matrix lattice, i.e. FCC or BCC crystal structure. These crystal structures provide interstitial sites for outside atoms, such as hydrogen. Interstitial sites can be divided into two groups:

1 Tetrahedral, with a coordination number of six and
2 Octahedral, with a coordination number of four.

The FCC crystal structure contains two different types of interstitial sites where a smaller atom, such as hydrogen, can be accommodated. The larger interstitial site is a hole at the centre of the cubic lattice structure and is surrounded by six atoms from the FCC lattice structure at the corners of an octahedral interstices, this is shown in Figure 2.5 (a). Figure 2.5 (b) shows the smaller interstitial site which consists of four atoms surrounding a tetrahedral interstice [99, 100].

The BCC crystal structure is less close packed than the FCC crystal but also contains two different interstitial sites. The smaller interstitial site is an octahedral interstice and is surrounded by six atoms, Figure 2.5 (c). The larger interstitial site is a tetrahedral interstice on the cubic face and is surrounded by four atoms, as seen in Figure 2.5 (d).

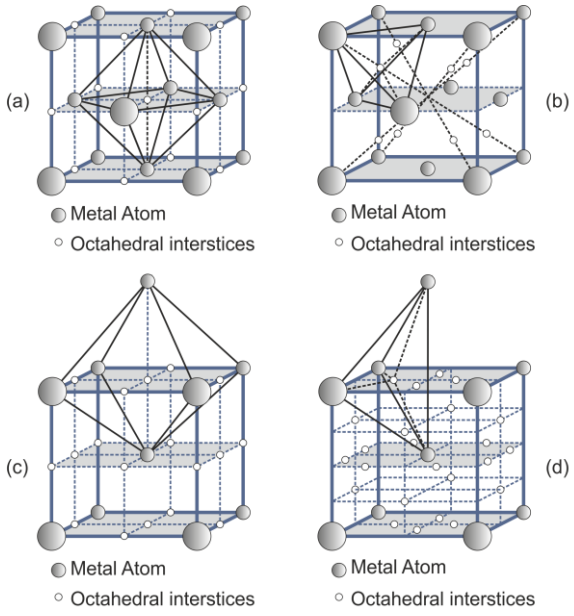

Figure 2.5: Schematic illustration showing interstitial spacing for foreign atoms such as hydrogen in iron matrix lattice of BCC- and FCC-crystal structures [99, 100].

As hydrogen is the atom with the smallest diameter it can occupy very small lattice sites. Therefore, when hydrogen is absorbed into a metallic lattice it can occupy octahedral or tetrahedral sites, depending on the lattice structure of the matrix. The FCC structure contains quite large interstitial sites and therefore has a higher hydrogen solubility.

However, the BCC structure is less condensed with a packing factor of 0.63 compared with 0.74 for the FCC structure. This results in hydrogen diffusing faster through the lattice with diffusion coefficients for BCC structures being four to five times higher than for FCC structures [101].

Hydrogen Absorption and Adsorption by Electrochemical Process/ Corrosion

Hydrogen diffusion requires gradients of hydrogen concentrations which are generated by the different sources of hydrogen. For welded components the sources of hydrogen uptake are either hydrogen uptake during welding or hydrogen uptake due to cathodic reactions in electrolytic solutions resulting from corrosion processes [102], Figure 2.6.

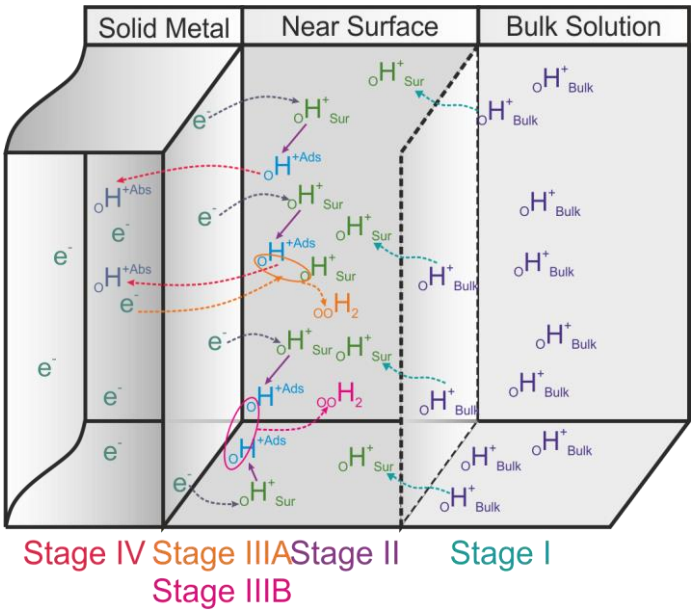

Figure 2.6: Consequence of hydrogen discharge and recombination at the electrochemical double-layer surface exposed to electrolytic solution with subsequent H^+ diffusion into the matrix material [103].

Hydrogen is present in many electrolytic environments in large quantities, such as in offshore facilities, gaseous hydrogen storage and acidic mediums in chemical industries. For this work the most relevant cause of hydrogen uptake is from sour service, H_2S-containg, environments as this hydrogen uptake may result in flowline failures in the oil and gas industry [104]. The process of hydrogen uptake on steel surfaces which are exposed to electrolytic solutions is divided into four stages: (I) the transport of hydronium/ hydroxide ions in the electrolyte to the specimen surface, (II) reduction and adsorption on the specimen surface and (IIIA) recombination to molecular hydrogen or (IIIB) absorption of atomic hydrogen in the bulk material or recombination, Figure 2.6. These stages are in accordance with the Volmer-Heyrovsky-Tafel mechanism [105] and will now be explained in more detail [106].

(I) Transport of hydronium/ hydroxide ions in the electrolyte to the specimen surface

This stage involves the mass transportation of hydrogen ions from the bulk electrolytic solution to the specimen surface. This produces hydrogen atoms from the electrolyte and H_3O_+ ions (in acid solutions) or OH_- ions (in alkaline solutions) are transported to the specimen surface which results in hydrogen being adsorbed. This can be described by the partial reaction in Equation (2.3), which is a reversible reaction.

$$H^+_{Bulk} \overset{k_1 \quad -k_1}{\longleftrightarrow} H^+_{Surface} \tag{2.3}$$

Where:

H^+_{Bulk}= Hydrogen present in the bulk solution,

k_1= Specific rate constant and

$H^+_{Surface}$= Hydrogen present on the surface of the material.

(II) Reduction and adsorption on the specimen surface

The next stage involves the reduction of positive hydrogen ions by consuming an electron from the anodic reaction to produce absorbed atomic hydrogen in a neutral solution. This is called the discharge reaction and is shown in Equation (2.4).

$$H^+_{Surface} + le^- \overset{k_2 \quad -k_2}{\longleftrightarrow} H_{Ab} \tag{2.4}$$

Where H_{Ab} is the hydrogen absorbed at the specimen surface.

If the solution is acidic (presence of oxonium ions H_3O^+) then H_3O^+ is reduced by electron acceptance, hydrogen discharge occurs, and the hydrogen is adsorbed at the specimen surface. This is called the Volmer mechanism and is shown in Equation (2.5).

$$H_3O^+ + e^- \rightarrow H_2O + H_{Ad} \tag{2.5}$$

Where H_{Ad} is the hydrogen adsorbed at the specimen surface.

But if the solution is alkaline, then self-hydrolysis of water occurs by electron acceptance (reduction) into hydroxide ions and atomic hydrogen. The hydrogen is adsorbed at the specimen surface and is shown in Equation (2.6)

$$H_2O + e^- \rightarrow OH^- + H_{Ad} \tag{2.6}$$

(IIIA) Recombination to molecular hydrogen

This stage involves the recombination of the adsorbed atomic hydrogen to form molecular hydrogen which then degasses through the liquid electrolyte. The desorbed hydrogen atoms can interact with each other resulting in molecular hydrogen in the Tafel recombination reaction as shown in Equation (2.7).

$$H_{ad} + H_{ad} \overset{k_3 \quad -k_3}{\longleftrightarrow} H_2 \uparrow \tag{2.7}$$

The Heyrovsky recombination reaction also generates molecular hydrogen. The general Heyrovsky recombination equation is shown in Equation (2.8), with the Heyrovsky recombination for acid and alkaline shown in Equations (2.9) and (2.10) respectively.

$$H^+_{Surface} + H_{Ab} + le \overset{k_3 \quad -k_3}{\longleftrightarrow} H_2 \uparrow \tag{2.8}$$

$$H_{Ad} + H_3O + e_- \rightarrow (H_2)_{Ad} + H_2O \tag{2.9}$$

$$H_{Ad} + H_2O + e_- \rightarrow (H_2)_{Ad} + OH_- \tag{2.10}$$

Hydrogen recombines to form molecular hydrogen more readily than atomic hydrogen is generated as hydrogen molecules are more energy stable than hydrogen atoms.

(IIIB) Absorption of atomic hydrogen in the bulk material

This final stage is the most significant reaction process for Hydrogen Assisted Stress Corrosion Cracking (HASCC) as this determines the rate of hydrogen uptake. The previous stage, the recombination process, requires a small activation energy but the dissociation of H_2 gas requires a high activation energy. However, for absorption only the H^+ ions move into the material, for which no activation energy is required. The H^+ ions are additionally attracted by the metal matrix, which is negatively charged due to anodic metal dissolution. Therefore, the majority of the hydrogen is adsorbed as an ion while recombination requires a small activation energy. The equilibrium condition for absorption of atomic hydrogen in the bulk material is shown in Equation (2.11).

$$H_{Ad} \overset{k_4 \quad -k_4}{\longleftrightarrow} H_{Ab} \tag{2.11}$$

The diffusion behaviour of hydrogen through a metallic material influences the crack propagation behaviour of HASCC. Therefore, understanding the stages in which hydrogen diffusion occurs can provide more information on various aspects required for the simulation of HASCC, including hydrogen subsurface concentrations and hydrogen diffusion coefficients, in order to accurately model and predict HASCC. Thus, the majority of the adsorbed H^+ is absorbed into the material while a smaller portion is degassed.

Hydrogen Effusion

Hydrogen effusion is the opposite process of hydrogen absorption and is very important to avoid hydrogen assisted material damage. Atomic hydrogen is adsorbed at the metal surface of the solid metal and electrolyte interface. The hydrogen atom then donates its electron to the metal lattice and the resulting proton is desorbed into the electrolyte. By releasing the hydrogen to the surrounding environment, the amount of hydrogen in the microstructure can be reduced, which reduces the risk of hydrogen assisted material damage. This reaction is shown in Equation (2.12) and is an inverse absorption mechanism:

$$H_{Ab} \rightarrow H_{Ad}^{+} + e^{-} \tag{2.12}$$

Recombination of the hydrogen on the surface of the metal can also occur in accordance with the inverse Volmer mechanism, Equation (2.3), Equation (2.4) for acids and Equation (2.5) for alkaline, which desorbs hydrogen into the electrolyte in gaseous form. The release of hydrogen from the metal surface can be influenced by various boundary conditions such as desorption sites on the metal surface can be occupied by other elements, i.e. oxygen. Various other factors including surface roughness, temperature or surface reactions resulting in the formation of an oxide layer, are also important for the effusion process [107, 108]. The effusion of hydrogen may be made more difficult by the presence of oxide or passive layers on the surface of the metal.

In the case of a metal/ gas interface, the hydrogen atoms desorb and recombine to form a molecular gas and mix with the surrounding gaseous environment. An example of this is the unavoidable leakage of high-pressure hydrogen storage tanks due to hydrogen permeation through the tank walls [109, 110].

Hydrogen Diffusion and Mobility

It is important to understand the atomic movement in materials associated with diffusion as diffusion is the basic mechanism for the modelling of HAC in this work. However, estimating the hydrogen transport behaviour in a specific material is quite difficult as various factors are involved, including lattice diffusion, the crystal structure of the metal and the characteristics of the microstructure. Steels in general consist of two phases: austenite (FCC crystal structure) and ferrite/ martensite (BCC/ BCT structure) which have different hydrogen diffusion characteristics. Hydrogen diffusion varies with every steel microstructure and depends on the morphology and the phase composition. Therefore, in order to determine effective diffusion coefficients and characteristics it is necessary to examine different microstructures of steel individually [111-113].

It has been well established that the diffusion coefficient of hydrogen in a ferritic microstructure is four to five times greater than in an austenitic microstructure [66, 114, 115]. The diffusion rate also depends on the morphology of the phases as alloys containing a continuous ferritic phase, such as rolled duplex steel, have a high hydrogen diffusion coefficient as the continuous ferrite provides a fast diffusion path, as long as hydrogen diffusion is in the rolling direction. However, alloys with a continuous austenite phase, such as welded duplex steel, where the austenite phase is concentrated around grain boundaries results in blocking of the diffusion path and therefor have a low hydrogen diffusion coefficient [116].

A review into the effect of different microstructures on hydrogen diffusion characteristics, based on various studies on hydrogen diffusion in steels, was undertaken [117]. The outcome of this review was the establishment of scatter bands for various steel microstructures. An example of the wide range of hydrogen diffusion coefficients for a martensitic microstructure is shown in Figure 2.7 [118]. It was discovered that the problem for the “low” diffusion rate at higher temperatures was insufficient temperature measurement during hot extraction as the sample never reached 800°C during effusion.

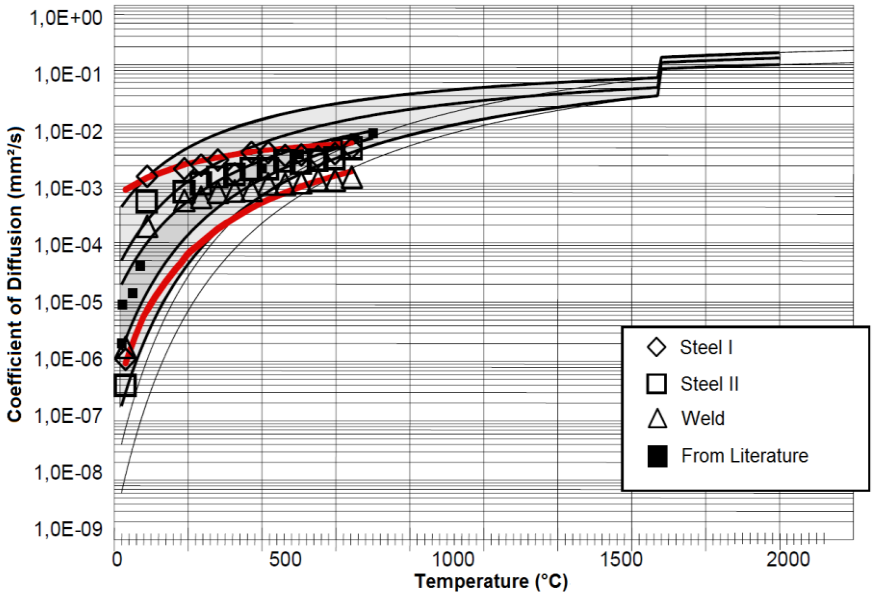

Figure 2.7: Published values of hydrogen diffusion coefficients in two types of SMSS as a function of temperature [118].

In martensitic structures hydrogen transport strongly depends on the dispersity of the retained austenite particles and the presence of precipitations, normally chromium carbides, as these can act as irreversible traps. It has been determined that fine precipitated carbides play the major role in hydrogen trapping, while dislocations only play a minor role, especially in the annealed state [119]. Therefore, the presence of carbides

greatly influences hydrogen transport through a metallic material. As martensitic stainless steels contain less austenite than duplex stainless steels, the hydrogen diffusion coefficient is higher for martensitic stainless steels than for duplex stainless steels.

The presence of austenite also affects HAC as retained austenite plays an important role in HAC, especially in SMSS which is the material this work investigated. The austenitic phase acts a hydrogen source when the material is subjected to a mechanical load as the austenitic phase has higher hydrogen solubility than the ferritic/ martensitic phase. This was determined by testing three different grades of SMSS, two low carbon pipelines and AISI 420, which showed that the presence of retained austenite in the material results in a greater loss in ductility of the material in the presence of hydrogen [120]. To investigate the influence of the quantity of retained austenite on the mechanical properties of the SMSS, different austenite content levels were created by heat treating. It was found that when the samples were exposed to an external load the hydrogen which was trapped in the austenitic phase was released. This hydrogen then diffused through the matrix and assisted in crack initiation and/ or propagation. These findings are especially critical for components in subsea applications with cathodic protection as the austenite phase might become charged with hydrogen over time. If this component is then subjected to plastic strain in an area of high stresses, such as a notch or pit, then HAC may occur.

Diffusion can also be explained mathematically and it has been agreed by a number of researchers [121-128] that diffusion of hydrogen through a metallic material can be explained using Fick's Law. Using this law, the chemical potential of hydrogen is considered and the flux of hydrogen passing through the specific plant can be expressed in terms of a concentration gradient. This concentration gradient is based on Fick's first law under the assumption of a constant hydrogen diffusion coefficient and is shown in Equation (2.13), [129].

$$J_H = D_{eff}\left(\frac{d[HD]}{dx}\right) \tag{2.13}$$

Where:

J_H= Hydrogen flux passing through the specific plane,

D_{eff}= Effective hydrogen diffusion coefficient,

d= Membrane thickness and

HD= Hydrogen concentration.

In real life conditions, hydrogen diffusion coefficients depend on various factors including position and temperature. These can be determined mathematically by using an Arrhenius relationship expressed as the general temperature dependency for a given activation

energy in order to formulate a common form of diffusion coefficient as shown in Equation (2.14), [130]:

$$D_{eff} = D_{H_0} exp\left(-\frac{Q}{R \cdot T}\right) \tag{2.14}$$

Where:

D_{H_0} = Hydrogen diffusion coefficient in the normal state,

Q= Barrier energy for hydrogen diffusion,

R= Universal gas constant (8.314 $Jmol^{-1}K^{-1}$) and

T= Absolute temperature.

A transient diffusion process consists of a variety of hydrogen concentrations at any one position as a function of time. In order to achieve this mathematically the flux of hydrogen must be modified by integrating second differential into Fick's first law. This is shown in Equation (2.15) and also in Figure 2.8, which describe the gradient of hydrogen entering through the entry surface and then escaping from the exit surface [130].

$$\frac{\partial J_{H_{diff}}}{\partial x} dx = J_{H_{out}} - J_{H_{in}} \tag{2.15}$$

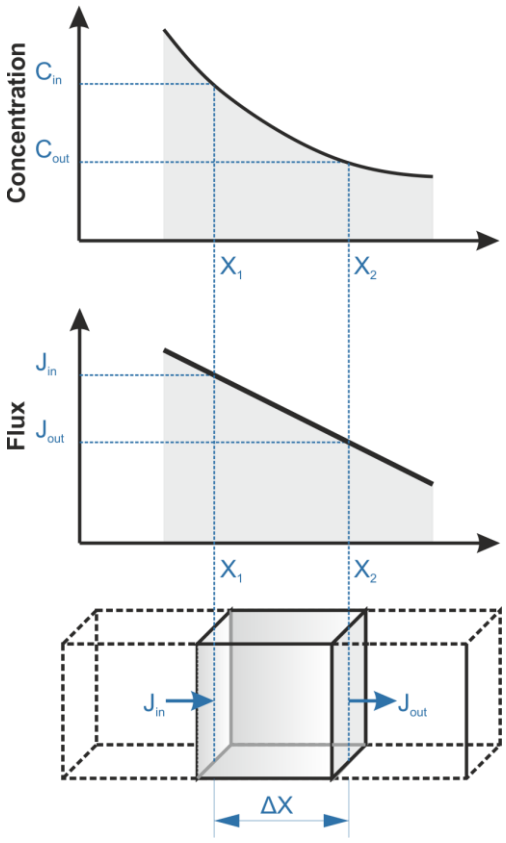

Figure 2.8: Schematic illustration of the basic principle of diffusion theory based on Fick's second law [130].

Assuming a constant hydrogen diffusion coefficient, the change in hydrogen concentration in the considered element with respect to time is shown by Equation (2.16):

$$\frac{\partial[HD]}{\partial t} = D_{eff}\left(\frac{\partial^2[HD]}{\partial x^2}\right) \tag{2.16}$$

Equation (2.16) is the principle equation to represent hydrogen diffusion in materials, which is based on an assumption of Fick's second law.

Hydrogen Trapping

As mentioned in Section 2.2.2, diffusible hydrogen occupies interstitial sites in the lattice (so-called lattice diffusion). However, hydrogen can also become trapped in lattice defects, including dislocations, vacancies, impurities, grain boundaries, second phase particles and voids [131], which can be seen in Figure 2.9.

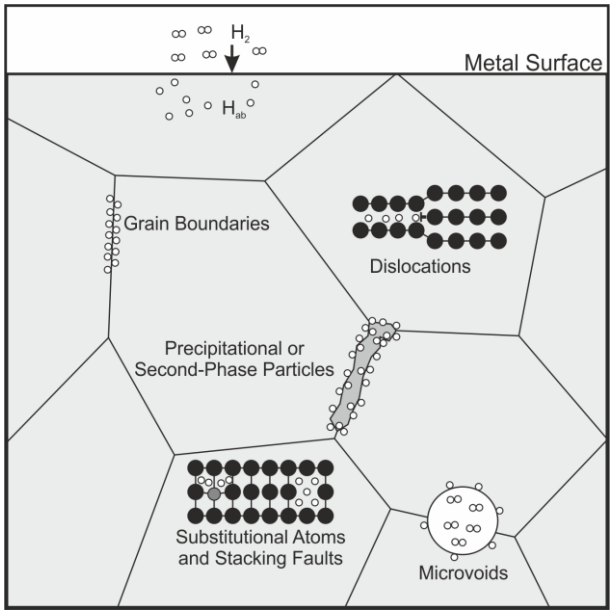

Figure 2.9: Graphical representation of general kinds of trapping sites interacting with dissolved atomic hydrogen [131].

The distribution of hydrogen inside the metal lattice is influenced by the interaction between the single hydrogen atoms with defects and inhomogeneities in the lattice, resulting in hydrogen remaining longer in the defects than in the interstitial site due to the energy benefits [132]. This results in an inhomogeneous distribution of hydrogen throughout the material, with the majority of hydrogen concentrated at trap sites. A higher number and density of traps increases the solubility but lowers the diffusivity of hydrogen in the microstructure, therefore a higher number of homogenously distributed traps increases the capacity of hydrogen in the steel.

The trapping theory was first proposed by McNabb and Foster in the 1960's [133] and came from observations that hydrogen diffusion in a metallic material does not correspond to Fick's law of diffusion. They noted that the different traps required different amounts of energy to release the trapped hydrogen atoms, this energy is the trap binding energy. They also noticed that the hydrogen free energy in the trap, $E_{B\ Trap}$, is lower than in the lattice interstitial sites, $E_{Lattice}$, as seen in Figure 2.10 [134, 135]. It is assumed that the hydrogen in the lattice (Y) combines with the hydrogen present in the traps (X) and are in equilibrium with no interaction between the atoms in the lattice and in the traps. The hydrogen can however escape if an activation energy, E_A, is sufficiently high and the hydrogen is released and can continue as lattice diffusion.

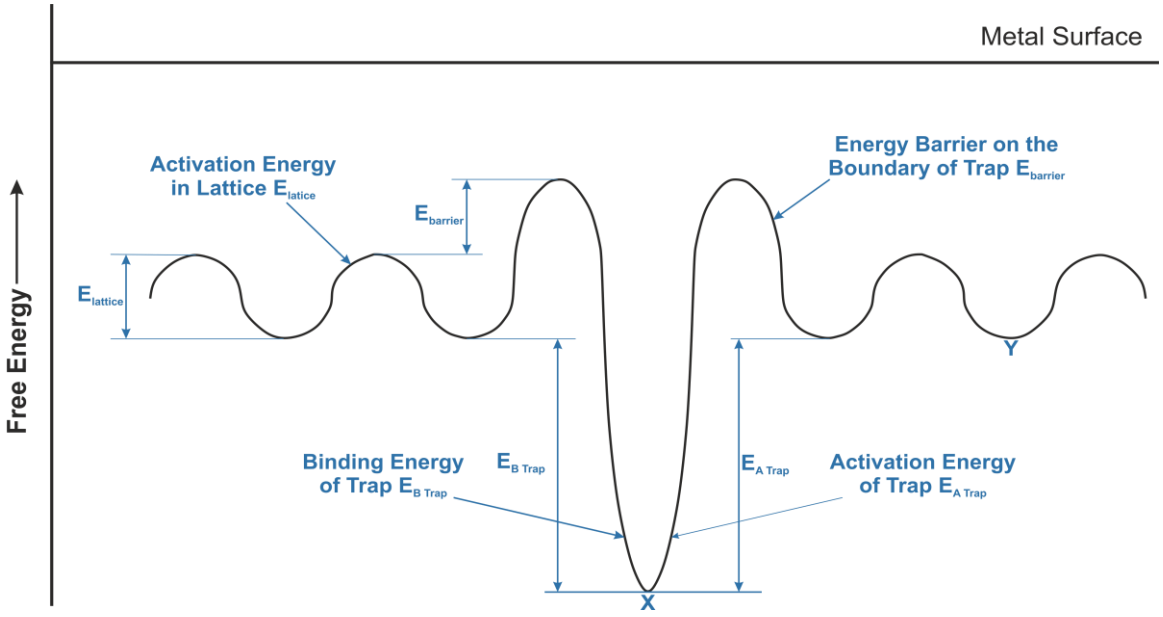

Figure 2.10: The energy level of hydrogen around trap sites [134, 135].

The binding energy, or activation energy, can be used to classify hydrogen traps into different groups which are characterised by the energy amount required to release hydrogen from a certain trap. The ability of a hydrogen atom to be released from a trap site is called the reversibility of a trap. It is easier for a hydrogen atom to be released by an attractive trap than from a physical trap as only small jump increments are required to be released from an attractive trap, but a physical trap requires one big jump. The mean jump increments of hydrogen depend on temperature- so called reversible traps will release hydrogen constantly at elevated temperatures, but irreversible traps will only release hydrogen above a certain temperature.

These have been classified by Pressourye [136] and Bernstein [124] into three groups:

- Traps with negligible effect during hydrogen diffusion,

- Reversible traps- part time trapping effect and a binding energy of ≤ 30 kJ/mol. These have the largest effect on delayed hydrogen diffusion both in steady and non-steady state diffusion and
- Irreversible traps- which trap hydrogen permanently and have a binding energy of > 50 kJ/mol. These traps have a major effect on non-steady state diffusion and after saturation these traps only play a minor role in the diffusion process.

Reversible traps are both a sink and source of hydrogen and at elevated temperatures act as solute hydrogen. However, irreversible traps are only a hydrogen sink as very high temperatures are required to release hydrogen from the trap sites.

Hirth separated the traps even further and included different precipitates or atom-hydrogen interdependencies [137]. His main difference was to separate the traps by their different trap binding energies:

- Weak/ reversible traps have a binding energy range of $0 \leq E_A \leq 30$ kJ/mol and
- Strong/ irreversible traps have a binding energy > 65 kJ/mol.

An intermediate range also exists between the strong and weak traps.

Pressouyre [136] additionally divides the hydrogen traps, this time in accordance with the nature of the trapping process into:

- Attractive traps- these are a region of the lattice where hydrogen atoms are subjected to an attracting force such as an electric field, stress field, temperature gradient or chemical potential gradient. Stress fields are usually concentrated at the vicinity of defects such as dislocations, crack tips, etc.
- Physical traps- these are sites in the lattice where a diffusing hydrogen atom will be randomly trapped, rather than being attracted. These trap sites are due to modifications of the ideal crystal lattice high angle grain boundaries, voids, etc. Hydrogen is more likely to stay in physical traps than in interstitial lattice sites due to the favourable energy conditions.
- Mixed traps- these are the most common type of hydrogen traps as in most cases a combination of attractive and physical traps exist. An edge dislocation is an example of a mixed trap with the stress field present being a form of attractive trap and the lattice distortion being a form of physical trap.

The trapping sites in SMSS were investigated according to three different hydrogenation methods: electrochemical charging, gaseous phase charging and introduction of hydrogen

through the welding process [138]. To introduce hydrogen during the welding process, hydrogen was present in the shielding gas. It was found that all trapping sites were reversible and the binding energy was calculated to be < 10 kJ/mol [138]. It was also found that the welding process caused the hydrogen trap sites to be located deeper in the material than in the electrochemical charging process. However, the concentration of hydrogen introduced during the electrochemical charging process was up to twice as much as during the welding process [138]. These are important factors in the trap theory of HAC.

The trap theory of HAC describes the influence of three major factors on the possibility of HAC occurring. The extent and type of so-called embrittlement depends on the combination of these three factors [139]:

- How hydrogen enters the metallic material and how it diffuses internally, such as dislocations, interstitial diffusion, high diffusivity paths,
- The location of hydrogen before testing- internal hydrogen vs. external hydrogen,
- The type of trap site- reversible or irreversible.

An example of this is the susceptibility of any material to HAC is related to the traps present in the material, especially for reversible traps as these are both hydrogen sources and sinks [140]. The traps create or reduce the presence of hydrogen rich regions, which affect the hydrogen transport characteristics. The presence of traps, both reversible and irreversible, cause a reduction in the diffusion coefficient of hydrogen, causing a reduction in the number of hydrogen enriched regions. However, irreversible traps have a large hydrogen capacity and form hydrogen concentration areas. Stresses also concentrate around defects and the combination of these may make the material susceptible to HAC [124]. For reversible traps if the location of hydrogen before testing is external to the material and the dislocation carries a constant initial hydrogen concentration, then all traps are hydrogen sinks. If the initial concentration of hydrogen begins to decrease at a certain dislocation, then the reversible traps begin to act as hydrogen sources. When a reversible trap acts as a hydrogen source and the hydrogen is transported by dislocations, then the material is more susceptible to HAC. This is due to the hydrogen sources charging the dislocations as they move and the dislocation reaches the defect, such as crack tips, with more hydrogen present, introducing more hydrogen to the defect [140]. Cracking will then occur in the region where the critical hydrogen concentration is reached first. The critical hydrogen concentration is the minimum hydrogen concentration in a certain trap which causes crack initiation. This corresponds to hydrogen pressure and/ or stresses applied to surpass the cohesive strength, which is lowered due to the presence of hydrogen.

2.2.3 Controlling Mechanisms of Hydrogen Assisted Cracking

HAC is mainly described as the degradation of the mechanical properties of a given material in the presence of hydrogen. The resulting interaction between hydrogen atoms and the metal lattice can lead to failure of the component at lower stresses than the yield strength of the material, which makes establishing the reliability of a component difficult to predict. The reason is that typically the ductility is more influenced compared to the allowable stress level. This risk of HAC in steels leads to enormous challenges concerning material selection for a wide range of applications but especially in energy generation related fields and offshore/ marine environments [141]. Examples of cases which were as a result of HAC include: fracture of aircraft components, leakage from gas filled pressure vessels, delayed fracture in various high strength steels, blisters/ fish eyes in steel components [142]. Martensitic/ bainitic microstructures are in particular susceptible to HAC [143, 144] but HAC is not only a problem in high strength steels but has also been found in titanium, nickel and aluminium [145-147].

The HAC mechanism consists of a series of processes which occur before and during service and which may lead to component failure [137, 148-151]. The lifetime of such components is controlled by three factors: the local/ global mechanical load, the local microstructure and the hydrogen concentration. These are the three key factors used to determine the interdependencies in HAC models which are used to explain the degradation process, Figure 2.11.

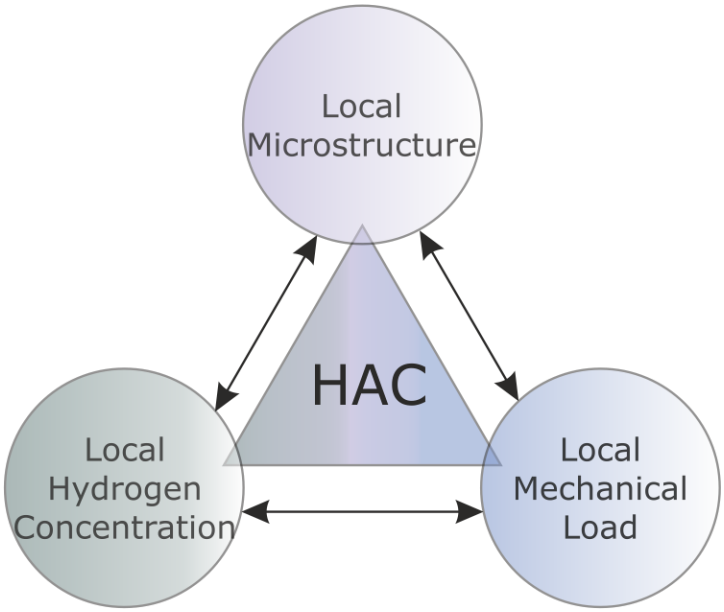

Figure 2.11: The three key factors effecting HAC.

The local microstructure consists of both the microstructure and the crystal structure. The microstructure includes the chemical composition, phase distribution, orientation, grain

size and grain and phase boundaries. However, the crystal structure consists of the lattice structure, (FCC, BCC, etc.) and structural defects including dislocations, twining, etc.

The local mechanical load can be separated into local and global stresses or into internal and external stresses and is influenced by production and service conditions. Residual stresses may have been introduced during the production process, welding process or service.

The local hydrogen concentration is the amount of diffusible and trapped hydrogen present in the material. It is important to know the source of the hydrogen- if it enters during production, such as welding, or during service, such as a failure in the CP. The critical hydrogen concentration, a combination of hydrogen diffusion at a maximum possible load, which leads to component failure depends on addition factors, such as martensitic materials with high hardness values are more susceptible to HAC than austenite materials with higher ductility and may fail in the presence of lower hydrogen concentrations.

Despite various studies into HAC, the mechanisms are not fully understood as there are many factors affecting the type and consequences of the process. Various mechanisms explaining HAC are present in literature, however the mechanisms which are most likely the cause of HAC for this material are presented in the following pages. These mechanisms of HAC are based on differing opinions as critical events associated with interactions between local mechanical loads and local hydrogen concentrations for HAC occur on the atomic scale at the crack tip. The most dominant mechanisms for steel subjected to a mechanical load in the presence of dissolved hydrogen are the Hydrogen Enhanced De-Cohesion (HEDE) [152], Hydrogen Enhanced Localised Plasticity (HELP) [23, 150, 151, 153-155] mechanisms and Adsorption Induced Dislocation Emission (AIDE) [156, 157]. A basic understanding of the general HAC mechanisms, in addition to the hydrogen uptake and diffusion processes mentioned in the previous sections, along with the determination of mechanical loads may assist in explaining the phenomenon of HAC. The verification of theories is very difficult but there is general agreement that no one mechanism of those currently existing is applicable to all materials, microstructures and hydrogen environments. Instead, every HAC event must be individually investigated to establish the circumstances and failure mechanism. It is agreed that on the atomic scale there is more than one active mechanism involved in the HAC degradation process. The most common approaches are now presented and discussed.

Hydrogen Enhanced Decohesion (HEDE)

The hydrogen enhanced decohesion (HEDE) or Decohesion Model, was developed by Trojano et al. in 1960 [158] as theories at that time, including the pressure theory, were

unable to accurately explain experimental results of hydrogen embrittlement. This mechanism explains the hydrogen effect based on the atom scale. The dissolved hydrogen atoms in the metal matrix compound decrease the strength of the cubic cleavage planes as the hydrogen atoms deliver their electrons to the 3d-orbitals of the iron atoms and become protons in the metal matrix. The filling of the 3d-orbitals increases the inter atomic spacing which in turn decreases the cohesive force between the atomic nuclei. This explains why the fracture of steel in a hydrogen containing environment appears brittle as in response to the applied stress, it is easier for the material to remove iron-iron bonds than undergo plastic deformation [158]. The disadvantage of this mechanism is that it describes crack propagation and not crack nucleation.

The presence of tri-axial stresses at the tip of a crack causes an increase in elastic stresses in this region which results in an increase of the local hydrogen concentration in this region. This increase in local hydrogen concentration at the crack tip in turn causes another increase in the stress concentration in this region. This continues until the hydrogen concentration exceeds the critical hydrogen concentration causing crack propagation resulting from an increase in local stresses and decrease in cohesive force in the crack tip region. Once the crack leaves the region where hydrogen has accumulated it encounters a region of plastic deformation and stops. This process can be repeated many times which eventually leads to discontinuous propagation.

Oriani modified this model and determined that the fracture energy of the material will be lowered due to a reduction in the cohesive strength by dilatation of the atomic lattice resulting from interstitial hydrogen [152]. The assumption is that the presence of hydrogen moves the energy barrier down for grain boundary or cleavage plane decohesion which results in fracturing being initiated in the area of highest hydrostatic stress, which is located at a distance from the crack tip. This mechanism can be explained mathematically where crack propagation can occur if the maximum local tensile stress ahead of the crack tip, σ'_{max}, at the location directly ahead of the crack tip which is normal to the plane of the crack, equals the maximum cohesive resistive force of the metal per unit area of the cracking plane. This can be explained as Equation (2.17) [152]:

$$\sigma'_{max} = n \cdot F_m \cdot [HD] \tag{2.17}$$

Where:

n= Number of metal atoms per unit area of the cracking plane and

F_m= Maximum cohesive resistive force of iron atoms.

The presence of larger hydrostatic and/ or shear stresses will lead to an increased accumulation of dissolved hydrogen present in front of the crack tip, which explains the

effect of hydrogen concentration on crack propagation. This accumulation occurs up to equilibration state while there is a noted decrease in the maximum cohesive drag force [158], which is shown in Figure 2.12. This shows that the crack only grows elastically and therefore has no losses as a result of plastic deformation.

An advantage of this mechanism is that it is based on the assumption that diffusion is necessary in order to transport hydrogen to the critical strain region in front of the crack tip. This in turn can also explain delayed cracking where the importance of hydrogen is based on the possible risk of delayed cracking even within hours or days. A disadvantage of this mechanism is that it is limited as it assumes only sharp cracks and in BCC-metals.

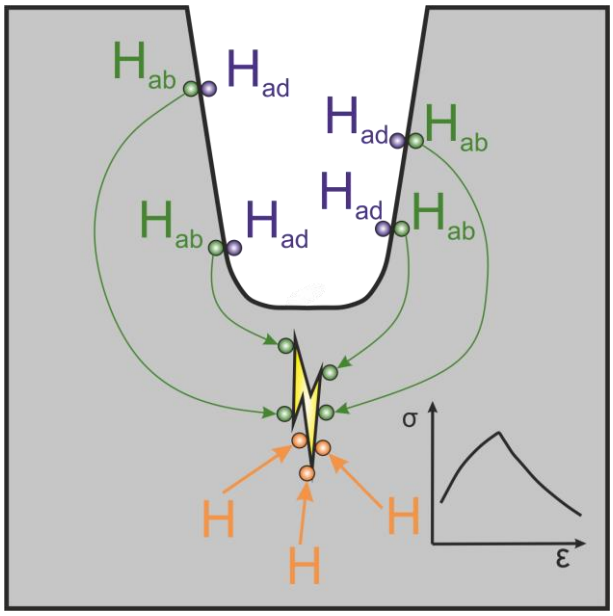

Figure 2.12: Decohesion theory caused by dissolved hydrogen atoms [152].

Hydrogen Enhanced Localised Plasticity (HELP)

The Hydrogen Enhanced Localised Plasticity (HELP) mechanism includes all metallurgical effects which may cause a change in the local plasticity of a material in the presence of hydrogen. Siros [159] and Sofronis [154] developed the HELP theory, which explains the interaction of dislocations with hydrogen. This mechanism is based on the theory that hydrogen can cause two contradictory effects: hardening and softening which was reported by Nelson in 1983 [160]. Hardening means that the material undergoes strain-hardening and softening means that the material undergoes strain-softening. These depend on the chemical composition of the steel grade which shows that the different alloying elements used cause a change in the mechanical behaviour of the steel in the presence of hydrogen.

Hardening can be caused by hydrogen diffusing into highly stressed area and this hydrogen limits the number of dislocations present [160]. This results in decreased plasticity at the crack tip and may lead to brittle fracture in the material.

Softening can be caused by the presence of hydrogen clouds, Cottrell atmosphere model, around both nucleating dislocations and obstacles to dislocations, located in the region in front of the crack tip. These clouds shield the dislocations from the elastic stress field of any obstacle present and therefore reduce the interaction energy between the dislocation and obstacles. This results in dislocation movements requiring less energy and the dislocations can also move at lower levels of applied stress. In order to increase the velocity of propagation and to continue propagating, the dislocations must carry the hydrogen environment with them. This results in local hydrogen concentrations being driven by the motion of dislocations and the hydrogen accumulates at the crack tip, which causes deformation to occur near the crack tip [161, 162].

The enhanced mobility of dislocations in the presence of hydrogen was proven by Robertson in the late 1990's using Transmission Electron Microscopy (TEM) [163]. Samples were deformed in situ in a vacuum or in the presence of hydrogen. The TEM imagining showed the mobility of a dislocation was increased in the presence of hydrogen. The influence of hydrogen and the enhanced mobility of dislocations, which is explained by the HELP mechanism, Figure 2.13. Figure 2.13 a) shows that crack growth occurs in the plastic region ahead of the crack tip due to the combining of microvoids, in the absence of hydrogen. Figure 2.13 b) shows that crack propagation and growth occur at the crack tip as a result of severe local deformation, in the presence of hydrogen.

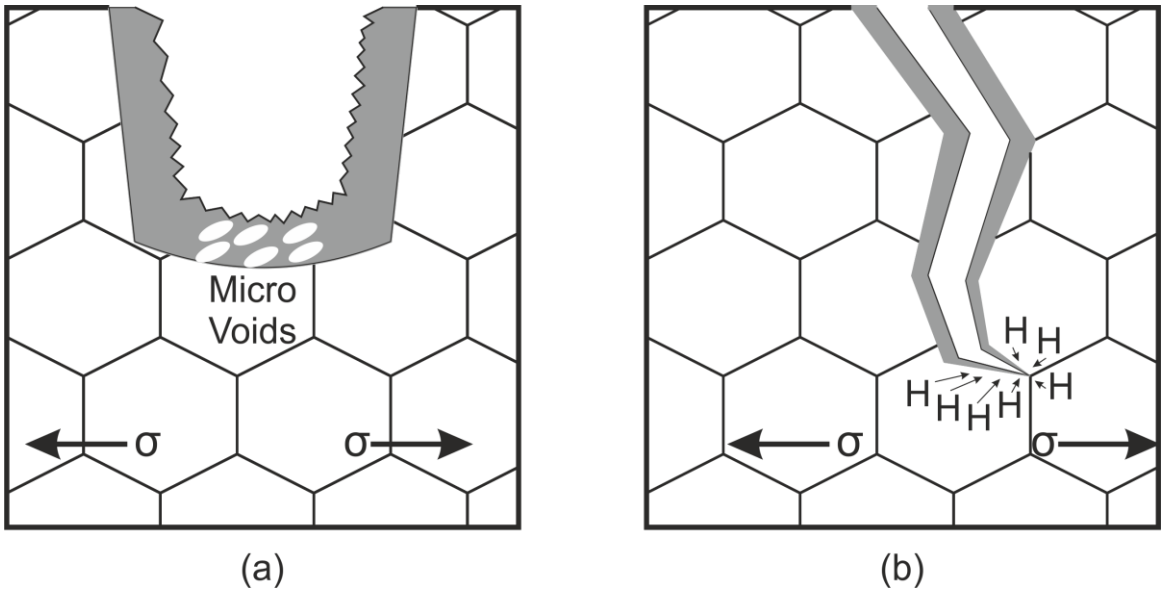

Figure 2.13: Crack propagation in high strength steels a) In the absence of hydrogen and b) In the presence of hydrogen [160].

This mechanism results in local ductile failure with the cracks having ductile fracture surfaces, such as Microvoid Coalescence (MVC) and dimples may also be present. The cracks produced by this mechanism are usually Transgranular (TG) cracks, however, when hydrogen is concentrated along grain boundaries then intergranular cracks may also be present [164].

There are some limits to this mechanism, including the main metallurgical factors influencing the hydrogen dependent improved slip processes have not yet been clearly identified. Also, this mechanism does not explain the presence of cleavage characteristics on the fracture surface due to HAC. Therefore, this mechanism is unable to be applied to these cases.

Adsorption Induced Dislocation Emission (AIDE)

The Adsorption Induced Dislocation Emission (AIDE) mechanism was first proposed by Lynch in the mid 1980's [156, 157] and is a combination of some basic principles of both the HELP and HEDE mechanisms, but is more complex. The brittle intergranular and transgranular cleavage like fracture surfaces of metal specimens tested in various liquid and gaseous hydrogen environments were compared. The fracture surfaces of the specimens tested in the gaseous hydrogen environment showed evidence of slip, dimples and tear ridges, which are evidence of enhanced dislocation activity. This resulted in determining that crack growth occurred where adsorbed hydrogen atoms near the crack tip cause the interatomic bonds to weaken and this aids the nucleation and movement of dislocations [156, 157].

The presence of the stresses required for formation of the emission of dislocations increase the nucleation activity in the plastic zone ahead of the crack tip. As part of the nucleation of a dislocation firstly a dislocation core is formed by shearing of several atomic layers. The next part of this process is the formation of microvoids ahead of the crack tip, as well as nucleation and growth of voids at second phase particles. This results in the formation of small voids at particles or slip band intersections [161].
In an inert environment, ductile crack growth occurs due to dislocations which nucleated in the plastic zone ahead of the crack tip and regress at the crack tip surface, therefore limiting crack growth. This is due to only a small amount of dislocations originating from sources near the crack tip actually intersect the crack tip, resulting in crack advancement. It is therefore necessary for large strains to be present in front of the crack tip in order for crack growth to occur. This also results in the presence of small dimples within large dimples being produced on the fracture surface, as the formation of large voids first requires nucleation and growth of smaller voids between the larger voids [161].

The presence of adsorbed hydrogen causes additional weakening of the interatomic bonds in several atomic layers. This results in crack propagation and crack opening for the AIDE mechanism occurring at lower strains and the fracture topography is characterised by the presence of dimples. These dimples are not the same as “fish eyes” which are found in embrittled areas where quasi-cleavage fracture occurs and develop at non-metallic inclusions and are not covered by the AIDE mechanism. “Fish eyes” are embrittled areas where quasi-cleavage fracture occurs which are described by three characteristic properties [165, 166]:

1. Quasi-cleavage fracture surface in the presence of hydrogen,
2. Mostly round or oval shaped in an embrittled area surrounding a metallic inclusion,
3. Surrounded by a ductile fracture surface.

All the sub processes of the AIDE mechanism are explained in Figure 2.14. The crack paths produced by the AIDE mechanism are intergranular or transgranular, depending on where the dislocation movement and void formation occurred.

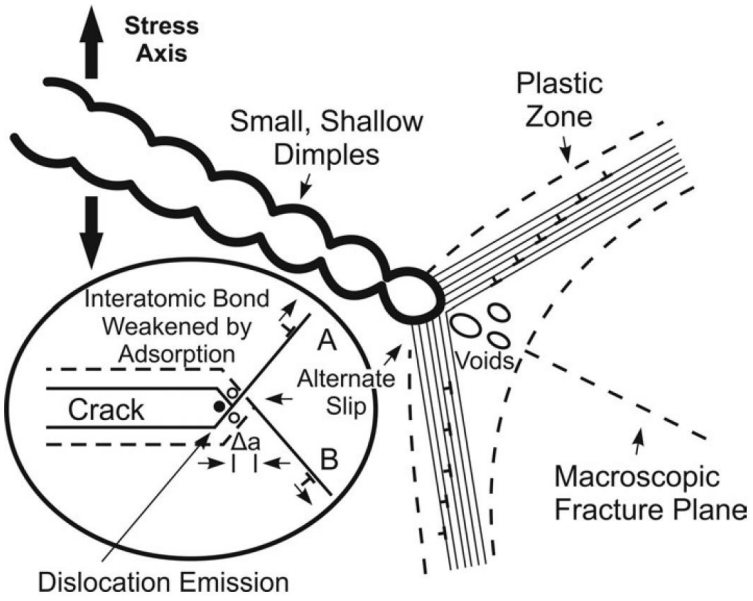

Figure 2.14: A schematic illustration of the AIDE mechanism involves alternate-slip from crack tips facilitating coalescence of cracks with voids formed in the plastic zone ahead of cracks [157, 161].

The presence of hydrogen causing a reduction in the necessary stress required for dislocation nucleation to occur was proven by Barnoush and Vehoff using a nanoindentation technique called the “pop-in load” [153, 167, 168]. This was due to reductions in the shear modulus, dislocation line energy and stacking fault energy and these observations confirm that the AIDE mechanism is a combination of some basic principles of both the HELP and HEDE mechanisms.

2.2.4 Locations of Crack Formation and Cracking

There are three ways to apply a force which enables a crack to propagate:

(I) Mode I: Opening Mode (a tensile stress normal to the plane of the crack),

(II) Mode II: Sliding Mode (a shear stress acting parallel to the plane of the crack and perpendicular to the crack front) and

(III) Mode III: Tearing Mode (a shear stress acting parallel to the plane of the crack and parallel to the crack front).

Mode I occurs when an external tensile stress is applied normal to the faces of the crack. This causes displacement of the crack surface perpendicular to the leading edge of the crack. Mode II occurs when an external shear stress is applied normal to the leading edge of a crack. The crack surface is displaced to the plane of the crack and is perpendicular to the leading edge of the crack. Model III occurs when an external shear stress is applied parallel to the leading edge of a crack. The displacement of the crack surface is in the planer direction of the crack and parallel to the leading edge of the crack. These three modes are shown in Figure 2.15.

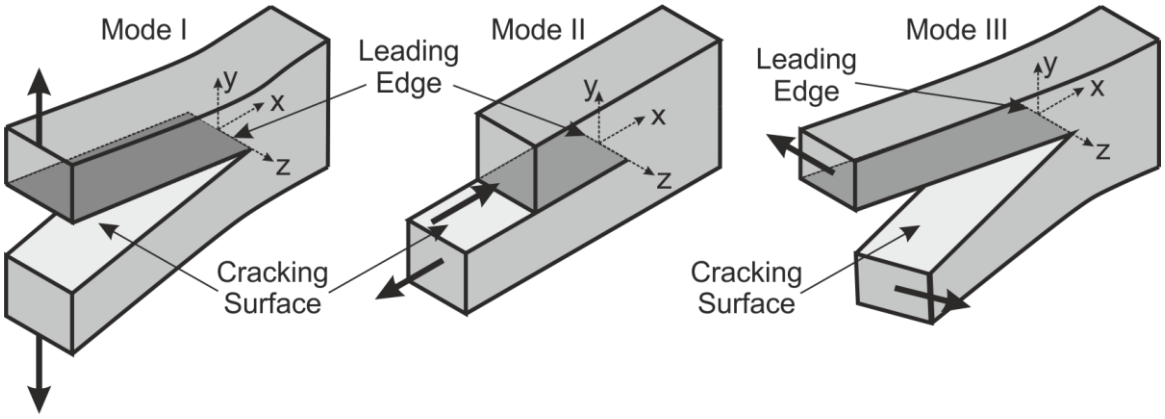

Figure 2.15: Graphical illustration of the three modes of cracking [169].

All calculations for crack propagation focus on Mode I as this mode is the most important mode for technical applications [169, 170]. The stress intensity factor, K_I, for Mode I is most likely to determine the stress/ strain field around the crack tip. The critical value of stress intensity generated by the stress/ strain distribution in front of the crack tip, K_{IC}, is a material property and can be calculated as Equation (2.18) [169]:

$$K_{IC} = \sigma_{crit}\sqrt{\pi \cdot a} \tag{2.18}$$

Where:

σ_{crit}= Critical tensile stress of Mode I required for the crack to propagate and

a= Actual crack length.

In general, the stress intensity can be expressed as a function of the specimen's geometry as shown in Equation (2.19), [170]:

$$K_I = \sigma\sqrt{\pi \cdot a} \cdot f(a, W) \tag{2.19}$$

Where:

f= Coefficient of friction and

W= Work.

The material will fail when the stress intensity factor, K_I, reaches the critical value of stress intensity. However, degradation of material properties, such as by environment-material-load interactions, can cause the critical value of stress intensity to be decreased.

As mentioned, there are three modes of cracking, there are also three ways in which a crack can propagate in the presence of hydrogen. HASCC is a time-dependent phenomenon which depends on the hydrogen diffusion process and also on the mechanical load [171], as shown in Figure 2.18. Therefore, three stages of crack propagation in metallic materials have to be considered in a cracking process in the presence of hydrogen, as shown in Figure 2.16. Crack propagation is usually divided into 3 phases:

Phase 1) Crack Incubation

This is the first cracking stage where significant dislocation movement or plasticity, especially on the local scale, is required to initiate crack propagation in the material. Nucleation and formation of a microcrack takes place which continues to propagate if the local stress/ strain reaches the critical value. For example, the presence of hydrogen may reduce the yield stress and the initial flow stress of pure iron at temperatures higher than 200 K [172, 173]. Therefore, a sufficient local hydrogen concentration is able to facilitate the mobility of screw dislocation by enhancing double-kink nucleation with promotion of slip planarity. For edge dislocations, dissolved hydrogen hinders the kink motion.

In alloyed steels the presence of a local hydrogen concentration may cause failure of the material due to enhanced dislocation formation or the formation of voids at grain boundaries or the interface of second phase particles [172]. During this stage, the characteristic of crack propagation is described as the crack propagation rate as a function of stress intensity levels. Crack nucleation appears if the local stress intensity reaches the threshold stress intensity value, K_{th}, which is affected by the presence of hydrogen. The rate of crack propagation during Phase 1 is high compared to the rate during stable crack growth, Phase 2, Figure 2.16. Fractographic analysis of Phase 1 may show intergranular or quasi-cleavage (QC) fracture surfaces [172]. Figure 2.17 shows that intergranular

cracking is a function of hydrogen concentration as the crack length increases with increasing hydrogen concentration for the intergranular cracking region of the graph.

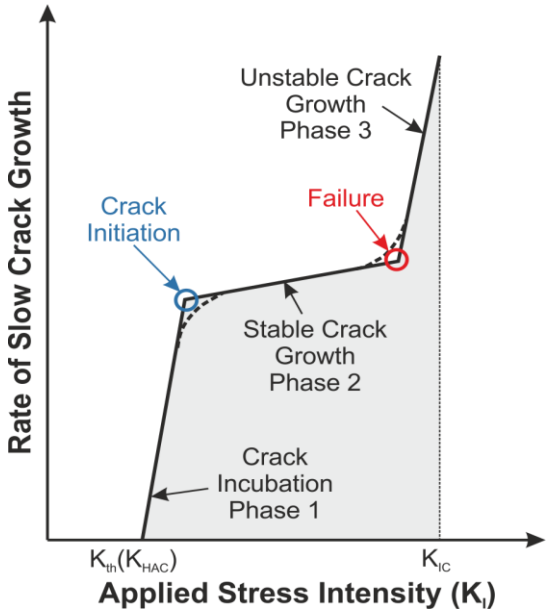

Figure 2.16: Kinetics of the crack propagation as a function of stress intensity for hydrogen assisted cracking, according to Hirth [172].

Phase 2) Stable Crack Growth

In Phase 2 a macroscopic crack propagates in a stable manner at stress levels which are higher than the threshold stress intensity value, K_{th}, but lower than the critical stress intensity value, K_{IC}, Figure 2.16. The presence of hydrogen at the crack tip can influence the crack propagation by degrading the material properties. In order to continue propagating, a necessary local hydrogen concentration must be present in the region ahead of the crack tip for a specific stress intensity level. If the necessary local hydrogen concentration levels are not present when the local stress continually increases, then this can lead to unstable crack propagation. Therefore, it can be determined that the kinetics of stable crack growth is strongly linked to the transportation of hydrogen from the newly exposed crack surface to the region ahead of the crack tip. This is due to hydrogen must be present for stable crack growth during Phase 2 [160]. As fracture occurs at the lowest rate of crack propagation during this phase, the lifetime of components is dominated by this phase. Fractographic analysis of Phase 2 may show transgranular or mixed mode tearing and quasi-cleavage fracture surfaces [172]. Figure 2.17 shows that in phase 2 as the hydrogen concentration decreases the local strain increases with increasing crack length for the cleavage-like cracking region of the graph.

Phase 3) Unstable Crack Growth

In Phase 3 the stress intensity ahead of the crack tip is greater than the critical stress intensity value, K_{IC}, which can be reduced in the presence of a larger hydrogen concentration. This final stage of crack propagation is dependent on high stress intensity levels, due to the increased crack length, or the presence of local stress/ strain in front of the crack tip. The fracture surfaces are less susceptible to hydrogen degradation than Phase 2, therefore the fractographic analysis of Phase 3 may show MVC [160] or TG ductile rupture due to the growth of holes [172]. Microvoid coalescence is seen in Figure 2.17 when the local strain increases with decreasing hydrogen concentration.

However, if the same loading conditions are applied to a material which is sensitive to hydrogen, then the local load capacity is reduced by the presence of hydrogen. Martensitic steels have an especially high sensitivity to hydrogen, due to its lower deformability. In these microstructures a low hydrogen concentration is sufficient to cause damage and even failure [174]. It is possible in SMSS exposed to hydrogen to get a change in the fracture topography from IG to QC fracture to ductile fracture as a result of MVC [16]. The local hydrogen concentration and the local elongation affects the fracture topography and Figure 2.17 shows the fracture topography at various stages of the interaction between local strains and local hydrogen concentrations.

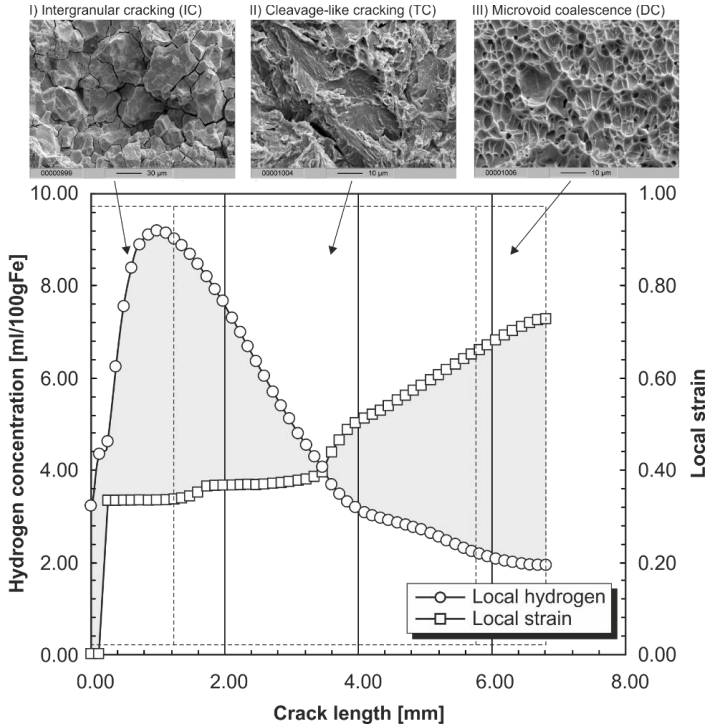

Figure 2.17: Change in fracture topography as a function of local hydrogen concentration and local stress in a supermartensitic stainless steel, from Viyanit [16].

Crack initiation in Figure 2.17 is represented as intergranular cracking. This may occur at phase or grain boundaries as the separation strength is lower in these regions than in the grain. The strain is low, but a high concentration of hydrogen is present which can further reduce the separation strength at the phase or grain boundaries. This process can also be accelerated due to the presence of high amounts of hydrogen trapped at phase or grain boundaries [16, 162]. The hydrogen concentrations are highest at the material surface due to the presence of pressurised hydrogen or electrochemical hydrogen absorption.

As the crack continues to propagate the crack fracture topography can change into Transcrystalline (TC) or QC cracking. A lower hydrogen concentration that the earlier stage is sufficient but the strain, i.e. at the crack tip, has increased. As the strain increases and the hydrogen concentration decreases the crack propagation changes to being more ductile. The increasing strain also causes the crack velocity to increase and due to the transport behaviour of hydrogen, or the inability of hydrogen to continue to follow the crack tip, less hydrogen diffuses to the crack tip. The increasing crack depth and speed of crack propagation results in no new hydrogen being transported to the crack tip and only the hydrogen which is already present in the microstructure contributes to failure [16, 162].

An alternative to the more commonly used explanation of the degradation of material properties affected by HAC described using the crack propagation rate dependent on stress intensity levels, as shown in Figure 2.16, is Figure 2.18.

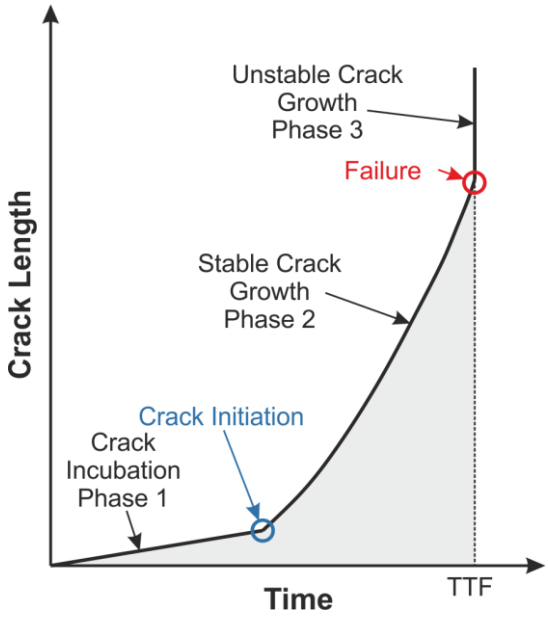

Figure 2.18: General relationship of crack length versus time for describing material properties under the condition of hydrogen assisted cracking, according to Hirth [172].

This new figure describes crack length as a function of time and may also be used to describe crack propagation behaviour in materials. Figure 2.18 is more useful for lifetime

prediction of components as it represents directly the time to failure (TTF) of components under specific test conditions. The effects of hydrogen on the mechanical properties of high strength steels was investigated [158] and it was found that the total lifetime of these steels is controlled by an incubation period for crack initiation and for stable crack growth.

During the investigation of failures of high strength steel components, it was discovered that the loss in ductility negatively affects the lifetime of these components. It can therefore be determined that the characteristics of crack growth caused by HAC can be explained as hydrogen degrades the material properties in the form of ductility rather than in the form of strength, as noted by Böllinghaus et al. [175]. The reason for this is shown in Figure 2.19, where it can be seen that for the presence of 1 ml of hydrogen, the maximum stress capacity is reduced by 20%, while the maximum strain capacity is reduced by 80%, compared to no hydrogen present. This is caused by dislocation interactions as previously explained. The graph in Figure 2.19 represents high strength structural steels with a yield stress of 690 MPa or higher. As SMSS has a similar strength, then the principle of this graph is easily transferable.

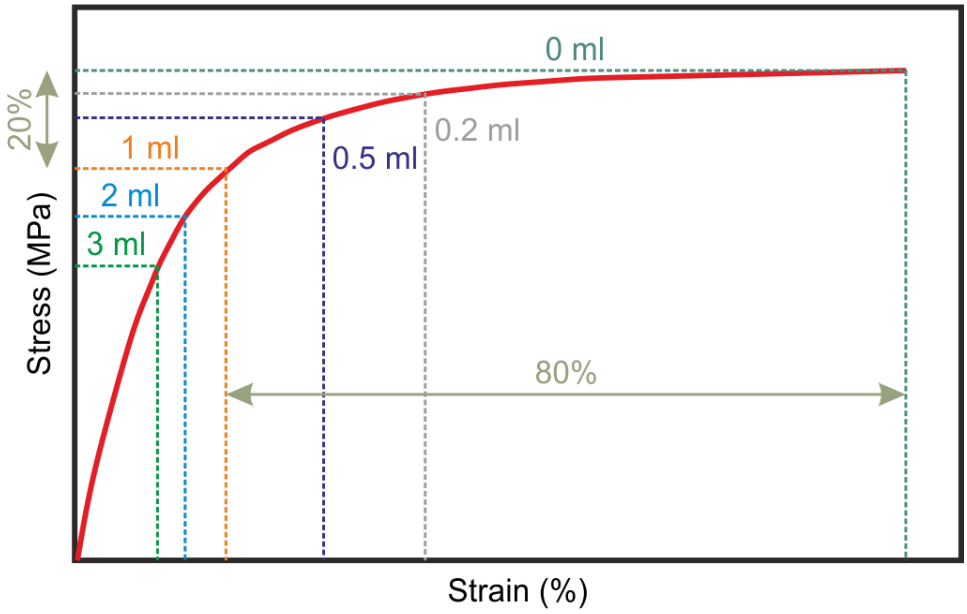

Figure 2.19: Graph showing the influence the presence of hydrogen has on the strength and ductility of a high strength structural steel, based on Böllinghaus et al. [175].

2.2.5 Local Strain Calculations

The local strain rate, $\dot{\varepsilon}_{loc}$, is difficult to calculate accurately, however, Lidbury determined that it can be determined based on the global strain rate, $\dot{\varepsilon}_{glob}$, for various notch geometries [176]. This plays an important role in determining the behaviour of crack propagation and is shown in Equation (2.20):

$$\dot{\varepsilon}_{loc} \approx \frac{\pi}{2(1-c)\varepsilon_{ys}} \cdot \left(\frac{\bar{a}}{a_{IC}}\right) \cdot \left(\frac{\sigma_{ys}}{\sigma_{max}}\right)^2 \cdot \dot{\varepsilon}_{glob} \quad (2.20)$$

Where:

c= Hardening index,

ε_{ys}= Yield strain of the material,

a= Actual crack length and

σ_{ys}= Yield stress of the material.

Using this equation, Lidbury reasoned that the ratio between local and global strain rates for alloyed steels is in the range 10 to 20 $\left(10 \leq \frac{\dot{\varepsilon}_{loc}}{\dot{\varepsilon}_{glob}} \leq 20\right)$. This ratio also includes the actual crack tip length and can be simplified to Equation (2.21):

$$\dot{\varepsilon}_{loc} = K_{lid} \cdot \dot{\varepsilon}_{glob} \quad (2.21)$$

Where K_{lid} is Lidbury's constant factor.

In order to reduce the amount of variables for estimating the local strain rate as a function of the global strain rate the K_{lid}-factor, $\left(\frac{\dot{\varepsilon}_{loc}}{\dot{\varepsilon}_{glob}}\right)$, can be utilised as a simple variable instead of more complicated variables. This is especially useful when creating numerical finite element simulations of HASCC as there are currently various equations for calculating the local and global strain rates.

The relationship between local and global strain rates for different crack and notch geometries (A – D), was investigated using finite element analysis and is presented in Figure 2.20 [177].

Figure 2.20 shows that at higher values of global strain the notched specimens cause a greater influence on the fracture behaviour. For the specimen with the longest notch, the K_{lid}-factor, $\left(\frac{\dot{\varepsilon}_{loc}}{\dot{\varepsilon}_{glob}}\right)$ will be up to 20. This may also be applied to pitting as deeper notches with small pit mouth diameters should behave similar to notch A and if these pits grow, then notch B in Figure 2.20 and a shallow pit with a larger pit mouth diameter should behave similar to notch C.

To conclude, a combination of the HEDE and HELP mechanisms is the most feasible explanation of the degradation process involved in steels subjected to a mechanical load in the presence of dissolved hydrogen.

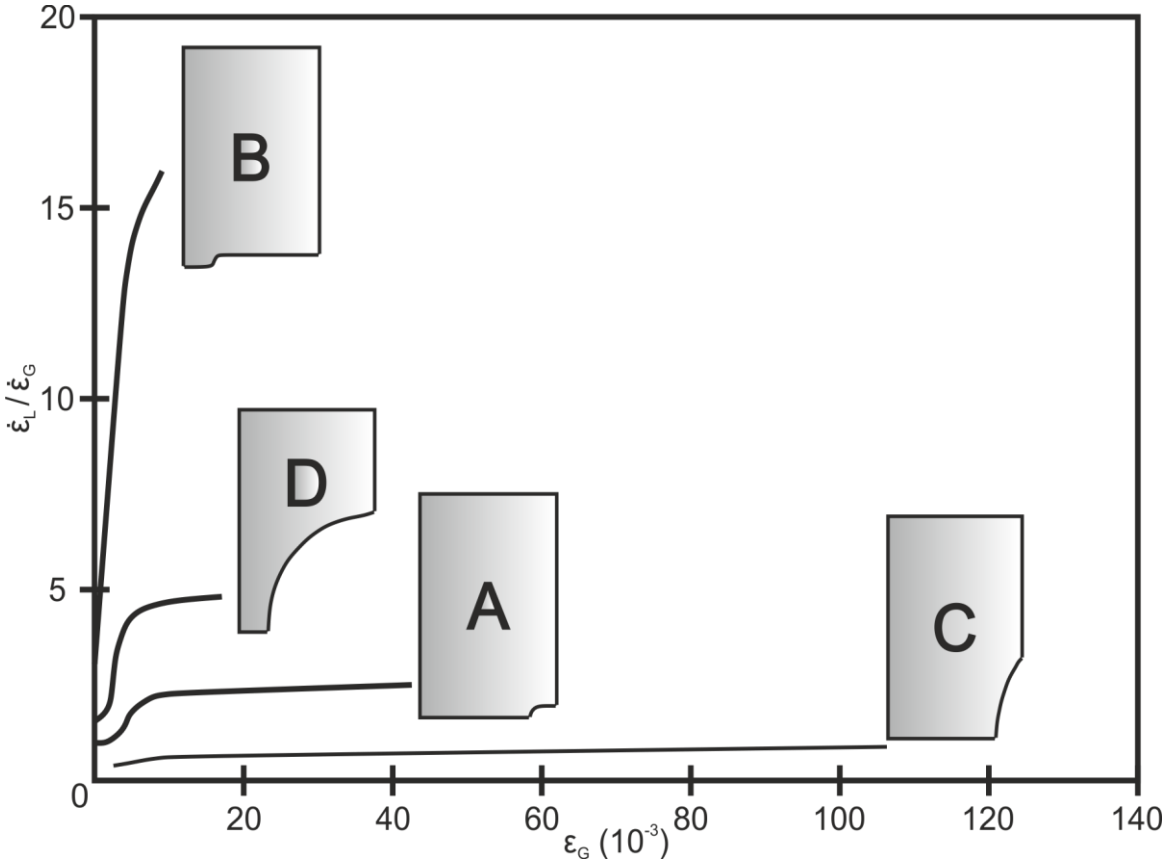

Figure 2.20: Relationship between local and global strain rates as a function of global strain taking account of effects of notched forms [177].

2.3 Pitting Corrosion and Hydrogen Assisted Stress Corrosion (HASCC)

2.3.1 Introduction

The various types of corrosion have been categorised in a NACE (National Association of Corrosion Engineers) publication into eight forms of corrosion in three different groups [178]. These are as follows:

Group I: Corrosion easily identified using visual examination.

1 Uniform corrosion- categorised by an even, regular loss of surface metal from the surface.
2 Localised corrosion- where all or most of the metal loss occurs at isolated areas. Crevice corrosion is considered a particular form of pitting due to localised differences in the environment.
3 Galvanic corrosion- caused by electrical contact between dissimilar conductors in an electrolyte.

Group II: Corrosion damage which may require additional means of examination for identification.

4 Velocity effects- these include: erosion–corrosion (a form of attack caused by high velocity flow); cavitation (caused at even higher flow by collapsing bubbles formed at areas of low pressure in a flowing stream); and fretting (caused by vibratory motion of two surfaces in close contact under load).
5 Intergranular corrosion- occurs at the grain boundaries in the metal microstructure (intergranular, exfoliation).
6 Dealloying corrosion- the selective dissolution of one component of an alloy.

Group III: Corrosion specimens should be verified by microscopy.

7 Cracking phenomena- including corrosion fatigue (a mechanical phenomenon heightened by nonspecific corrosive environments) and environmental cracking (brittle failure is induced in a normally ductile material under tensile stress in an environment specific for the alloy system).
8 High-temperature corrosion- including scaling and internal attack.

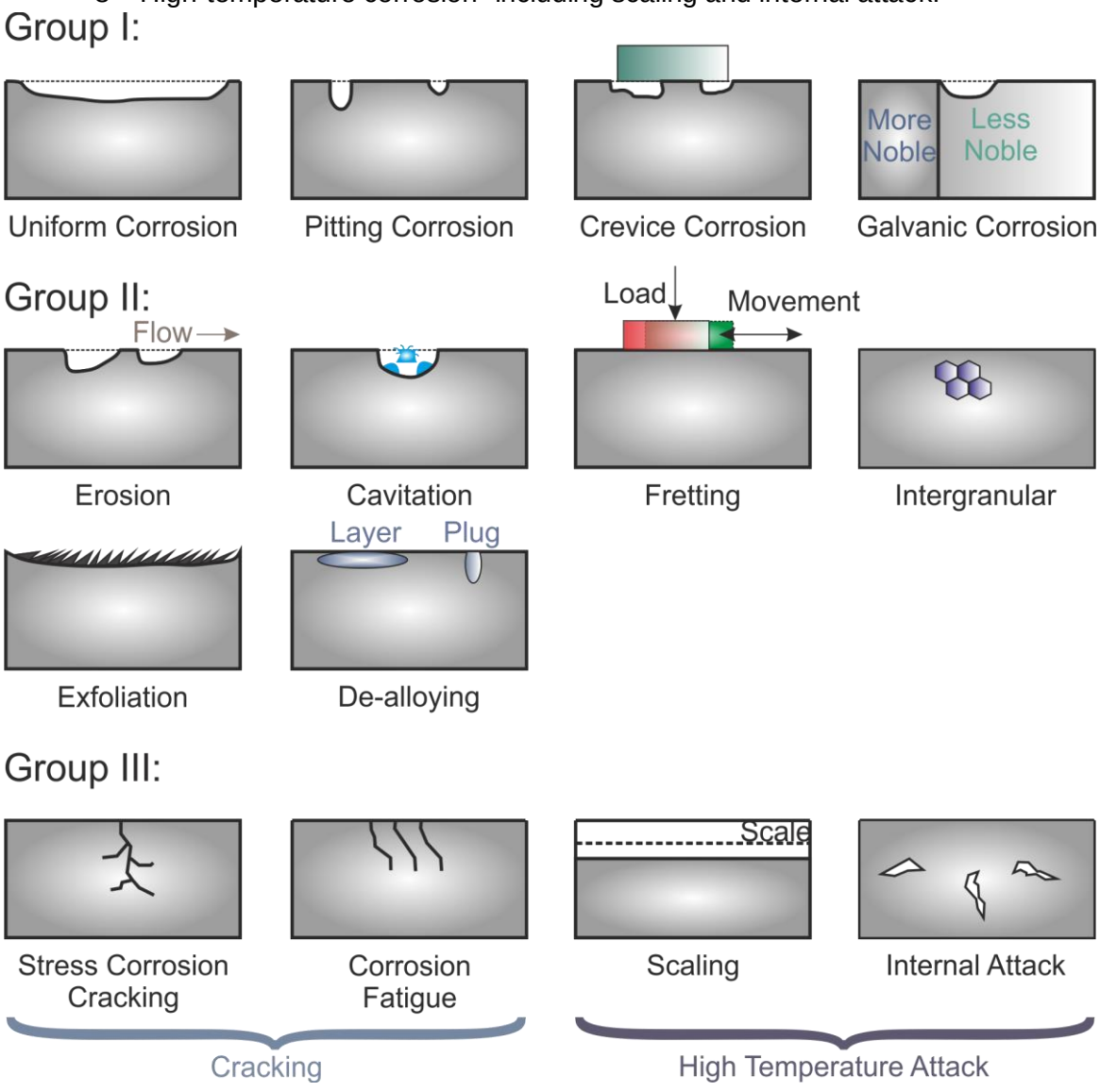

Figure 2.21: Main forms of corrosion attack regrouped by ease of identification [178].

As mentioned in the previous section, materials in marine environments are more susceptible to corrosion. Marine environments contain approximately 3.5% sodium chloride which facilitates localised corrosion, including pitting corrosion [179]. SMSS in marine oil and gas pipelines have relatively low Cr and Mo contents, and are therefore more susceptible to localised corrosion than DSS. This pitting corrosion, from Group I in Figure 2.21, is one of the primary causes of damages of these metallic alloys. While these pits are grouped as “Identifiable by visual inspection” detecting these pits can sometimes prove difficult, not only due to their small size but these pits are often covered with corrosion products [179, 180].

After immersing low alloyed steels in seawater, pit initiation can occur very quickly [181, 182]. There is a significant increase in pit depth after a preliminary period of exposure which can last from a few weeks to years, depending on water temperature and other environmental factors [181]. The cause of increasing maximum pit depth has been partly linked to the anaerobic conditions which develop on the inner surface of the pit, which can be favourable to corrosion [183-185]. Recently, increasing attention has been paid to the likely participation of microbiological influences in addition to the more well-known marine environment factors, which include material composition, seawater chemistry, pH, dissolved oxygen content, salinity, galvanic interactions, temperature and fluid velocity characteristics [186, 187]. The microbiological influences, however, include the effects of the existence of suitable bacterial colonies and the availability of both energy sources (electron transfer) and nutrients, which are necessary to sustain bacterial metabolism [188]. The presence of bacteria inside the pit may facilitate acceleration of subsurface pit growth even though the mouth of the pit becomes plugged, due to a build-up of material, or clogging in general. This type of subsurface pitting corrosion is especially dangerous as it is not visible to the naked eye and may appear as general corrosion. Therefore, the frequency and depth of the pitting corrosion is unknown.

Leaks and ruptures due to internal sour corrosion in tubing and pipelines are oftentimes caused by large, wide pits and pit clusters [189]. The average local corrosion rates were up to 10 mm/ year in the middle of the pits with surrounding areas uniformly corroded which had been protected by condensed hydrocarbons or corrosion product films. Groups of smaller pits can merge into larger and wider pits as they grow, which further increases the danger of the presence of pitting corrosion.

Steel structures such as ships, offshore platforms and land-based structures are susceptible to various types of damage as they age and have been exposed to environmental and loading conditions. Corrosion and fatigue cracking may be the two most important types of damage in aging structures. In such cases, structures that were

originally adequate may become marginal later in life or even reach the catastrophic failure state. It is of vital importance to estimate the residual strength of damaged structures for many reasons. For instance, it is important to seek rational standards for the structural integrity of aging structures without economic penalties with respect to the repair and maintenance costs incurred over the life cycle of the structure, while risk or reliability assessment schemes are normally applied for that purpose [190].

Corrosion damage is the most widely reported primary cause of ultimate strength reduction of engineering structures, including civil, nuclear, aerospace and naval structures [191-201]. Oil and gas production has encountered problems as a result of corrosion since the early history of the industry. Corrosion results in significant costs due to repair and replacement of infrastructures [202]. This also forces unplanned shutdowns and causes disastrous incidents that result in environmental contamination and human casualties. NACE (National Association of Corrosion Engineers) in 2008 estimated that the total costs related to all types of corrosion is $276 billion in the United States [203]. Corrosion of onshore oil and gas transmission pipelines covers $7 billion of this total [203]. Through near misses, incidents, forced shutdowns, accidents etc. several industries have come to realise that lack of corrosion management can be very costly and that through proper corrosion management, significant cost savings can be achieved over the lifetime of an asset [204].

Additionally, according to DNVGL-RP-F116 [205] there are 1069 steel lines operating in the North Sea. The total number of incidents which resulted in a leakage, reported between the years 1971 to 2001, is 651, Figure 2.22. As the figure shows, 40% of the accidents were related to corrosion, which consists of both internal and external corrosion, with 7 and 14 incidents respectively. Five incidents were not specified and were therefore reported as “Unknown”. 17 incidents were related to anchor (12%) and impact damages (14%). The material damages were related to weld and steel defects.

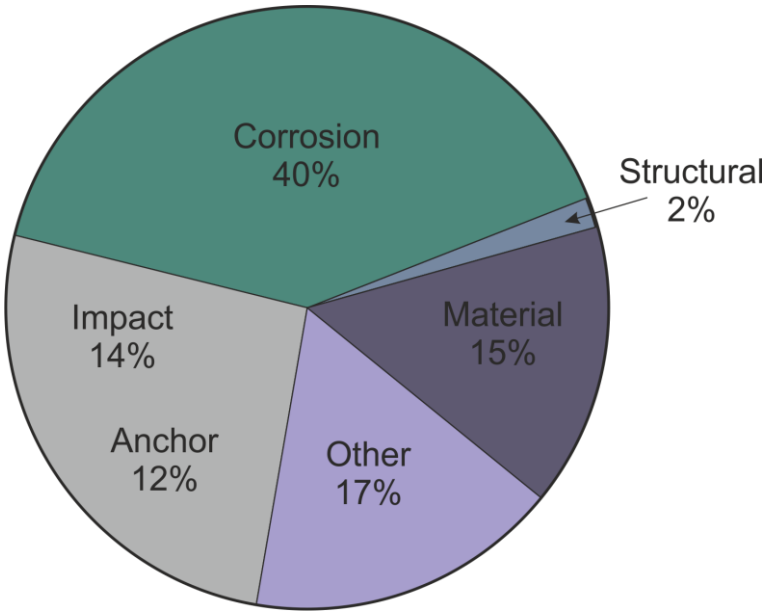

Figure 2.22: Operating steel pipelines incidents resulting in leakages in the North Sea, according to DNV GL [205].

As shown in Figure 2.22, corrosion incidents are the main cause of failures on steel pipelines. Figure 2.23 is an overview of the pipelines where the different types of corrosion incidents were located.

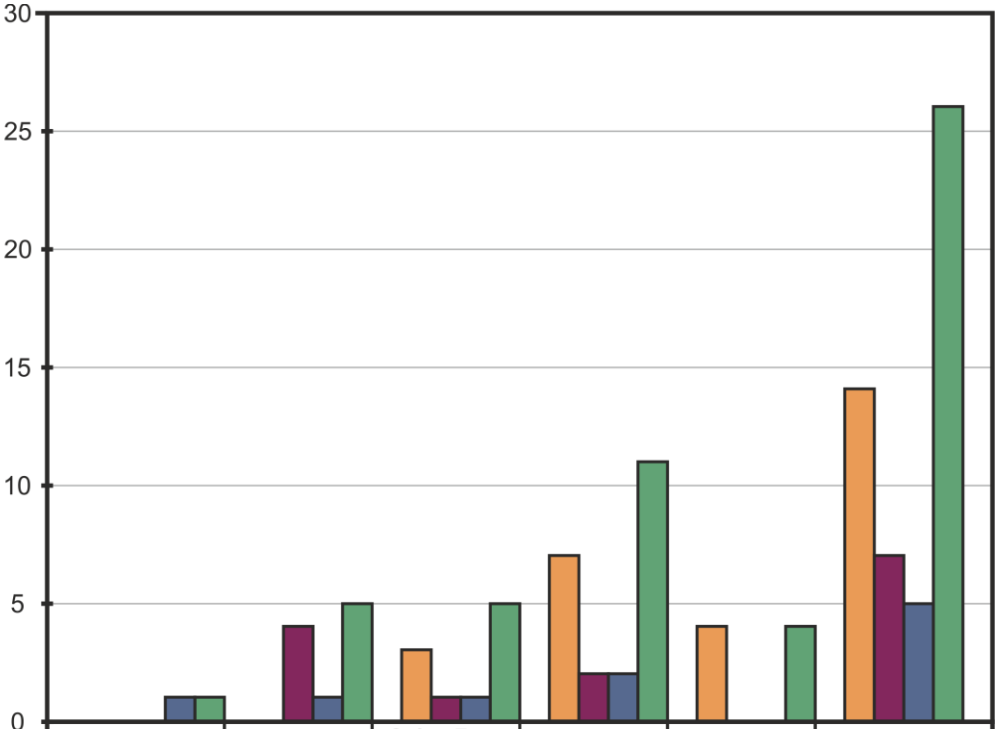

	Platform	Riser	Safety Zone	Mid Line	Well	Total Incidents
Internal Corrosion	0	0	3	7	4	14
External Corrosion	0	4	1	2	0	7
Unknown	1	1	1	2	0	5
All Corrosion Types	1	5	5	11	4	26

Figure 2.23:Location of corrosion failures on steel pipelines, according to DNV GL [205].

The highest frequency of external corrosion incidents occurred in the splash zone on the risers. However, most of the internal corrosion failures were located in the midline of the steel pipeline with the unknown corrosion incidents being randomly distributed along the pipelines.

Pitting corrosion is a form of localised corrosion which produces cavities and/ or holes in the material that may lead to perforation. Due to difficulties in detecting and predicting pitting corrosion, it is determined to be more dangerous than uniform corrosion. The failure of an entire engineering system can be caused by the presence of a small, narrow pit with minimal overall metal loss [206]. The understanding and prediction of corrosion damage is a very important aspect for the structural integrity of metal alloys.

Mild and high strength low alloy structural steels are extensively used in modern infrastructure systems, including ships, pipelines, offshore platforms and tanks. Many of these are exposed to harsh oceanic environments where pitting corrosion is more likely to occur. Loss of containment due to the presence of pitting corrosion is a major cause of accidents in liquid and natural gas pipelines [207-209]. This may occur when the protective coatings or cathodic protection systems become ineffectual. While internal pressure is the predominant load for onshore and shallow water pipelines, ultra-deep pipelines must be designed to maintain function due to the additional presence of external pressure [210-212]. Changing from low to high alloyed materials is necessary in order to minimise material loss and costs due to corrosion. However, this change causes other corrosion types to be considered, i.e. if high alloyed passivating materials are chosen then pitting corrosion is the mostly likely and prominent corrosion type, in seawater environments but also especially internally due to harsh, multiphase, partly sour service conditions.

Many SMSS pipelines are present in a marine environment, under saline conditions. This requires perforation due to pitting corrosion to be an important design criterion [181, 213, 214]. However, pitting corrosion is a difficult phenomenon to overcome due to its complex nature, but it represents an important limitation to the safe and reliable use of many alloys in various industries. Engineering manuals take into account, to a certain extent, losses due to corrosion in the design of pipelines [215, 216]. These documents however do not deal with corrosion damage under applied stresses, including uniaxial and bending loading conditions. As mentioned previously, pitting corrosion may perforate the pipe wall resulting in a loss of containment, but it may also lead to a reduction in the local wall thickness which is enough to cause local structural failure resulting in leakage. Additionally, the presence of pits may result in local stress concentrations which may then initiate structural cracking or tearing of the wall when an external load is applied [217, 218].

The structural response of pipelines subject to pitting corrosion are commonly investigated using one of two methods: research into the loads around the pits and research into the load bearing capacity of a metal with pitting corrosion present. An example of the first method is to develop a relationship between the maximum stress around a pit, the pit aspect ratio and the applied tensile stress, which are based on a series of three-dimensional numerical models of pits [219]. The pit aspect ratio is a ratio of the pit depth to pit mouth diameter and is used to define the severity of a pit. Another example is investigating the relationship between stress concentration and shape parameters for different shapes of pits, in this case the pits were semi-ellipsoidal [220] and a diagram is shown in Figure 2.24. The A, B and C values were varied to model varying pit mouth diameters and depths. Regarding strain in the material with pitting corrosion present, Turnbull et al. [221] found that localisation of the plastic zone occurs beneath the pit mouth at high stress levels and not at the pit bottom as previously assumed.

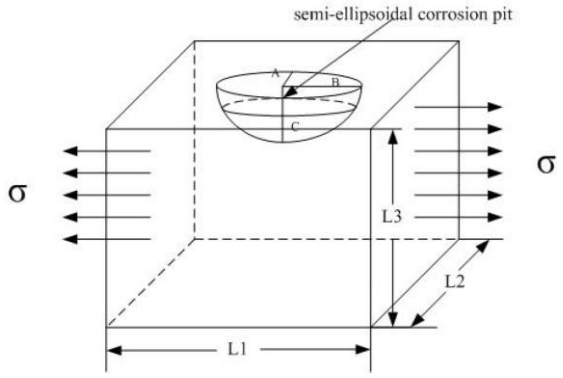

Figure 2.24: Semi-ellipsoidal pit geometry as researched by Mu et al. [220].

The second method investigates the strength of the material with pitting corrosion present. The study into the strength of corroded pipes under applied loads is also applicable to the investigation of flat plates affected by pitting corrosion [222]. Investigations into the structural strength of flat plates with corrosion pits present is especially applicable to the hull structures of ships. Examples of these investigations include the effects of corrosion pits on buckling of plates [223], strength of plates under biaxial compression [224], strength of plates under shear stresses [190] and the relationship between global and local stresses, such as for plate bending, as influenced by plate size, pit dimension and pit intensity, as investigated by Yu [225].

In this work the first method is considered the appropriate option, especially the method used by Turner et al. [221] as the magnitude and location of the strains in the region around the various pit geometries are of interest. This is due to the interaction of hydrogen with the regions of highest strains, which will be explained in further detail in Section 2.3.5. Investigating the relationship between global and local stresses, as mentioned by Yu [225]

is altered to investigating the relationship between global and local strains and is also part of this work.

The following sections will discuss the mechanisms behind how pit growth occurs and the locations most susceptible to the formation of pits. The locations in the material where crack initiation may occur are then presented, (Pit bottom? Sides of the pit?) and the propagation of these cracks is then discussed. HASCC developing from the presence of pits and how to simulate this, are the last items to be discussed.

2.3.2 Controlling Mechanisms of Pit Formation and Growth

Pitting corrosion occurs when there is an intense attack at localised sites on the metal surface. These localised sites corrode faster than the rest of the metal surface and is a result of the breakdown of the protective passive layer on the metal surface at these localised sites. There are two main reasons why the passive layer fails:

- Exposure to a chemical environment of the local area could remove protective layers such as oxides or metal salt films and
- Build-up of elastic strain in the oxide until the strain energy density exceeds the surface fracture energy of the oxide, which leads to failure [226].

Strain, instead of stress, is investigated as at the interface of a massive metal with a thin scale the strain is continuous while also an observable quantity [227]. Stresses are only applied via the metal substrate to the scale. If the substrate is already stressed beyond yield, then no additional stresses are able to be applied to the scale. This is shown in Equation (2.22) [227]:

$$\varepsilon > \varepsilon_m = \frac{\sigma_m}{E_m} \tag{2.22}$$

Where:

ε = Strain in the oxide,

ε_m = Strain in the substrate metal,

σ_m = Stress in the substrate metal and

E_m = Young's modulus of the substrate metal

Equation (2.22) shows that the strain in the metal can continue to increase, however the stress in the oxide cannot. When exposed to a tensile load the oxide begins to break apart into little islands due to the presence of local flaws, Figure 2.25. These islands float on the metal surface as the strain increases in the metal and the metal yields at the surface in the

gaps between the islands. The strain in the metal is then allowed to increase but the local strain in the metal oxide islands is limited to ε_m [227].

For metals exposed to a compressive load, the formation of islands is not present as the strain can be relieved by yielding of the substrate and also mild bucking of the scale, Figure 2.26. Some scale cracking may be present but it is unlike any detachment of the scale will occur and will therefor remain a protective layer [227].

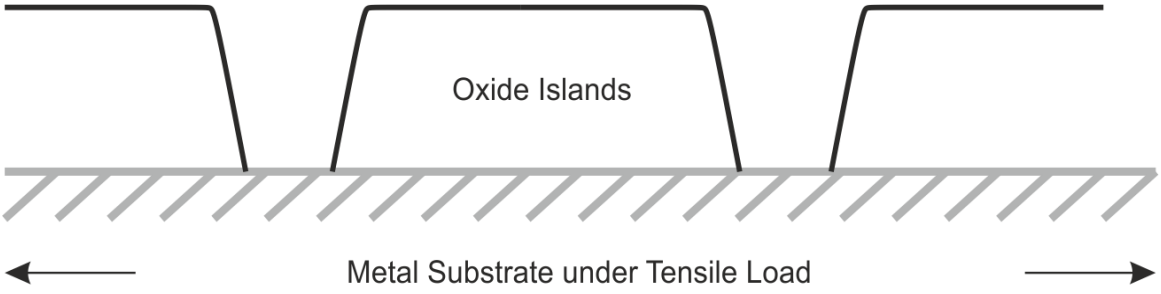

Figure 2.25: Cracking of oxide layer and formation of islands when the protective oxide is exposed to a tensile load [227].

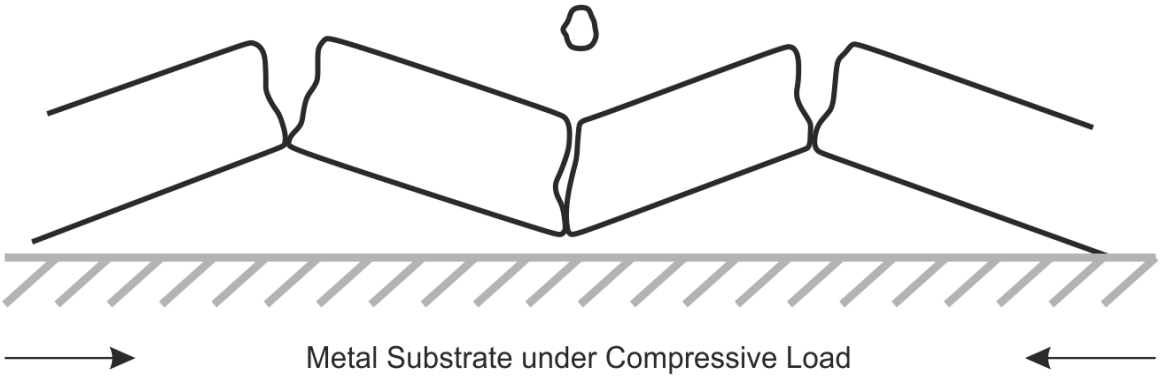

Figure 2.26: Buckling of oxide layer when the protective oxide is exposed to a tensile load (tension region) [227].

Once the passive layer has been compromised, then corrosion can begin. There are many pitting corrosion theories but these can be divided into two well-known broad groups, which depend on the passivity model considered [209]. One theory assumes that pitting is the result of competitive adsorption between oxygen and halide anions. The second theory assumes the presence of a passive film is necessary, with local breakdown of the passivity occurring during pitting. It is also well-known that pitting initiates at surface inhomogeneities, physical or chemical, which include inter-metallic phases, non-metallic inclusions, grain boundaries, dislocations, defects or mechanically damaged sites [186, 228]. These are referred to as pit nucleation sites. Once the corrosion protection layer breaks down locally, corrosion is possible in these areas [229, 230].

Corrosion pits generally occur due to some chemical or physical heterogeneity on the surface of the material with many variables of the metal–environment system, such as alloy composition and microstructure, composition of the surrounding media and temperature all being involved in the pitting process. Pit nucleation occurs at the microscopic level and some metals show preferential sites of pit nucleation [231].

Based on these two theories, the pitting mechanism considered in this work is the second theory mentioned above, where there is a local breakdown in the passive film protecting the surface of the material, resulting in pitting. The series of events occurring in this pitting method is as follows:

1. Local breakdown occurs in the oxide layer formed on the surface of stainless steel in order to protect against corrosion [181].
2. Dissolved salt anions, such as chloride, thiosulphate and bromide anions, present in the aqueous media surrounding the specimen, can interfere with the formation of the passive film leading to vacancies in the metal oxide matrix [232, 233]. In oil field applications the chloride ions present increase the rate of pitting corrosion as chlorides bind to cations which enhance their solubility in aqueous media. This exposes bare metal to the aggressive aqueous environment. Local metal dissolution may occur at pit nucleation sites.
3. The remaining metal surface, with undamaged protective film, acts as a cathode. These regions provide counter electrodes to the pit region which causes the exposed metal in the pit to dissolute. This results in increasing the depth of the pit if the repassivation of the material occurs at a slower rate than the dissolution occurring inside the pit. Corrosion products, including Cr and Fe hydroxides are formed which can cause plugging of the pit mount.
4. The plugging of the pit mouth causes a change in pH inside and around the pit as oxygen is prevented from entering the pit and therefore hydrolysis of cations occurs inside the pit. The process of hydrolysis of cations is shown in Equations (2.23) - (2.24), [234]. The hydrogen produced as a result of hydrolysis does not recombine entirely [228] and may enter the metallic structure using the various hydrogen adsorption mechanisms discussed previously in Chapter 2.2.2.

$$Me \rightarrow Me^{+2} + 2e^{-}(Anode) \tag{2.23}$$

$$Me^{+2} + 2H_2O \rightarrow Me(OH)^{+} + H^{+} \tag{2.24}$$

$$2Me^{+2} + H_2O + OH^{-} \rightarrow 2Me(OH) \quad + H^{+} \tag{2.25}$$

The anodic reactions occurring in a pit when the bulk solution is an aqueous environment are shown in Equations (2.26) to (2.32) from Hoffmeister and Böllinghaus [185]:

Reactions occurring in bulk water where surface corrosion potential is established:

$$O_2 + 2H_2O + 4e^- = 4OH^- \quad (2.26)$$

$$H_2 = 2H^+ + 2e^- \quad (2.27)$$

Reactions occurring in the Fe_3O_4 pit surface layer:

$$3Fe + 4H_2O = Fe_3O_4 + 8H^+ + 8e^- \quad (2.28)$$

$$H^+ + e^- = H_{liquid} \quad (2.29)$$

Reactions occurring in the Fe^{++} H^+ OH^- active layer:

$$6Fe^{++} + 8H_2O = 2Fe_3O_4 + 14H^+ + H_2 + 2e^- \quad (2.30)$$

$$2H^+ + 2e^- = 2H_{liquid}/H_2 \quad (2.31)$$

Hydrogen diffusing further into the metal and crack propagation:

$$H_{liquid} = H_{metal} \quad (2.32)$$

The above equations are based on a model developed by Hoffmeister and Böllinghaus [185], which describes the local anodic reactions occurring in a pit and is also shown in Figure 2.27. It can be assumed that the pit bottom is the anode, as shown in Figure 2.27, which dissolves according to Equation (2.23) and is also illustrated in Figure 2.28. The subsequent metal ions then react with the water in the pit- hydrolysis as shown in Equation (2.24). Hydrolysis decreases the pH in the pit and creates an acidic environment, Equation (2.25). If chloride ions are present, these will then travel into the pit in order to balance the charge neutrality. The acidic chloride environment created in the pit causes the pit to continue to grow [10].

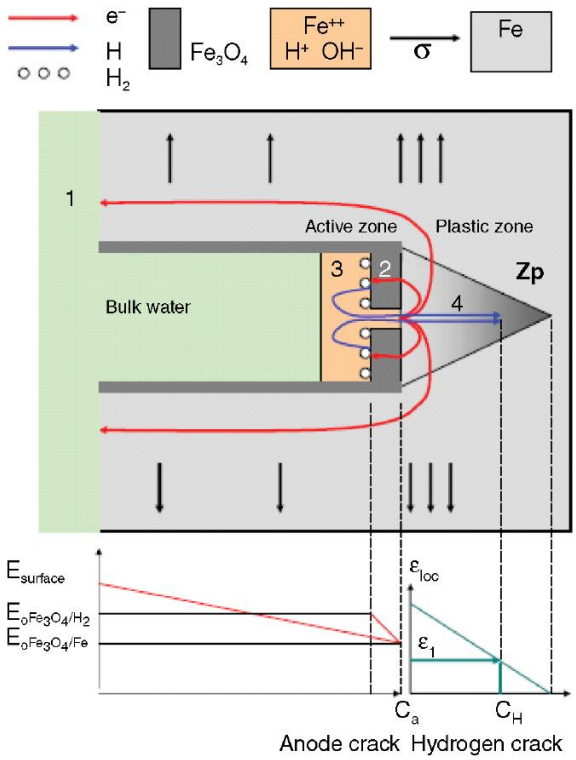

Figure 2.27: Principle of local acidification and crack propagation as developed by Hoffmeister and Böllinghaus [185].

The dissolution of the metal in the bottom of the pit is the anode and the passive film on the sides of the pit are the cathodes. The electrons then travel from the pit bottom to the sides of the pit with the metal ions released into the electrolyte. The hydrogen is then adsorbed into the sides of the pit, Figure 2.28.

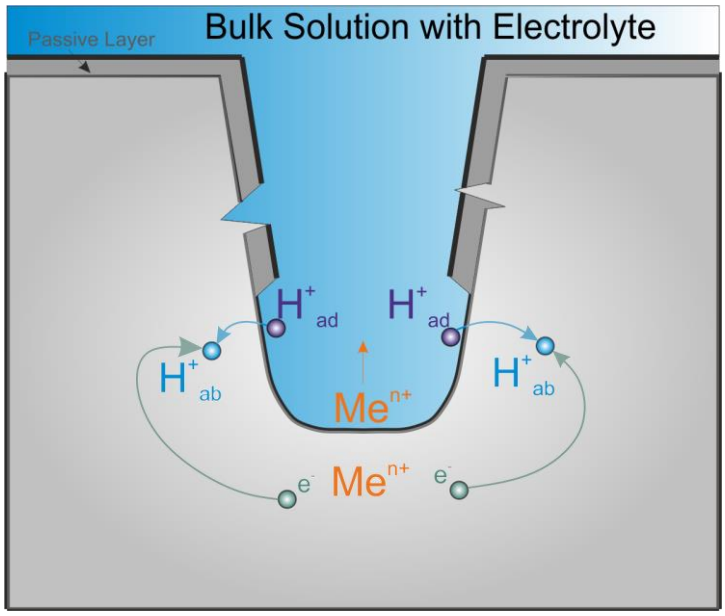

Figure 2.28: Hydrolysis and hydrogen adsorption occurring in a pit.

The tendency of a metal or alloy to undergo pitting is characterised by its critical pitting potential, as illustrated in Figure 2.29. If chloride ions are present, then the passive film suffers localised attack and pitting initiates at a well-defined potential called the critical pitting potential (E_{pit}) [235]. The critical pitting potential is also referred to as the breakthrough potential, breakdown potential or rupture potential. However, stable pits can form at potentials higher than E_{pit}. E_{pit} can be defined in several ways, such as the potential below which pits do not nucleate and above which stable pits can survive and grow. E_{pit} is also defined as the applied potential necessary to maintain a salt film in a small open pit. At E_{pit} and higher potentials, metastable pits can become stable pits. Another definition is that above E_{pit} the passive film is locally unstable and repassivation is not possible, but at and just below E_{pit} metastable pits can grow. Metastable pits are pits which grow for a limited time but then repassivation occurs and the pits therefore stop growing. The pitting potential indicates initiation of stable pits which can grow and propagate. Metastable pits have a limited lifetime. This is due to the concentrated acidic chloride solution, which promotes pit propagation, has not yet developed within the metastable pit. Therefore, the metastable pit can be repassivated. Metastable pits are commonly of micron size and have a lifetime of the order of seconds or less [236].

The stable pits then grow at potentials higher than the repassivation potential (E_r), which is lower than E_{pit}. E_r is defined as the potential below which neither stable nor metastable pits can grow and above which metastable pits can form and nucleated pits can grow [228]. Although E_{pit}, is a characteristic property of a given metal or alloy, the value of E_{pit} for a given metal depends on the chloride concentration. For any specific chloride concentration, the more positive the critical pitting potential then the more resistant the metal or alloy is to pitting. However, E_{pit} is not the only parameter which should be used to determine the resistance to pitting attack. Other important parameters are the density of pits and their propagation rate, which will determine the depths of pits and as a result of this, the lifetime of the structure [237]. E_{corr} is the pitting potential where corrosion is initiated.

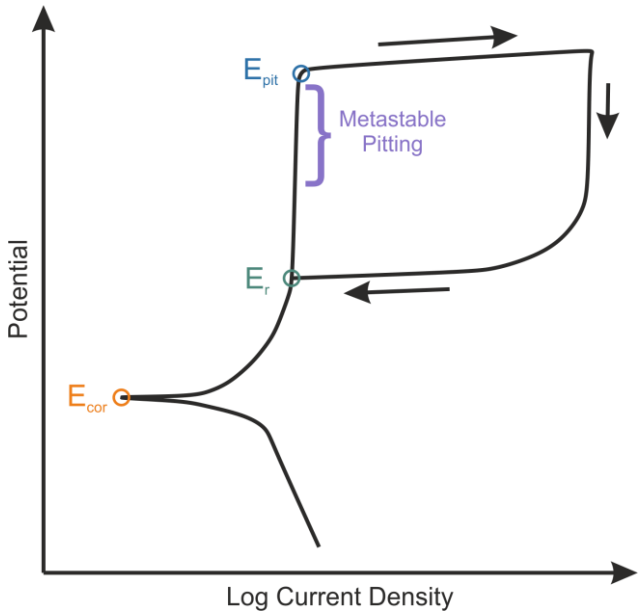

Figure 2.29: Anodic polarisation curve showing the critical pitting potential for a passive metal [228].

2.3.3 Locations of Pit Formation

As explained in Chapter 2.1 welded pipelines are widely used in a variety of applications. For pitting corrosion in welds the largest pit depths have been linked to certain factors, including: surface finish, thermal stresses and variations in grain structures between the Weld Metal (WM), HAZ and BM for both mild and stainless steels [238-240]. Upon investigation, the most severe pitting corrosion was observed near the welds, in the HAZ [209]. Although SMSS weldments suffer from pitting corrosion in the HAZ, it is still under investigation as to why this region is more susceptible to such corrosion than the adjacent parent material or weld metal. One explanation, among others, may be that the more severe pitting in the HAZ has been due to the microstructure of the material and the material properties [241, 242]. As mentioned previously, in SMSS the Ni content is between 4 wt.-% to 6 wt.-% and the C is reduced to a content as low as 0.01 wt.-%. This reduced C content increases the materials weldability. After welding annealing may occur for hours on 13% Cr steels, with the aim to achieve a uniformed distribution of carbides. It is the HAZ of multipass welds which is often the critical point in pitting resistance, as inhomogeneous passive layers, associated with poor shielding and annealing colours accompanying welding in combination with, for example, some underlying microstructural effect [242].

Viyanit [16] developed a basic numerical model for HASCC in steel welds. The approach was based on the three local influences on HAC from Figure 2.11. Crack incubation, slow

crack growth, final unstable rupture and the interaction between mechanical loads and hydrogen transport were all simulated in the model. The major findings of this work concluded that a higher hydrogen concentration can dominate crack growth at lower residual strains. It was also found that the HAZ is the most crack susceptible area, due to high concentrations of hydrogen diffusing from the BM to the HAZ [15, 243]. This work was performed on a smooth surface, so pitting corrosion was not considered. This research was conducted using a full scale test facility and the resulting image of a cracked weld in a pipe, where the crack initiated in pits in the HAZ, can be seen in Figure 2.30. It was in the HAZ that such pitting attacks were observed, with less frequent observations in the WM and with none observed in the as delivered BM. Therefore, the failure of SMSS by a combination of pitting and HASCC may additionally be associated with the pH and the reduction in potential inside the pits. This is due to hydrogen uptake inside in the pit as a result of hydrolysis occurring inside the pit.

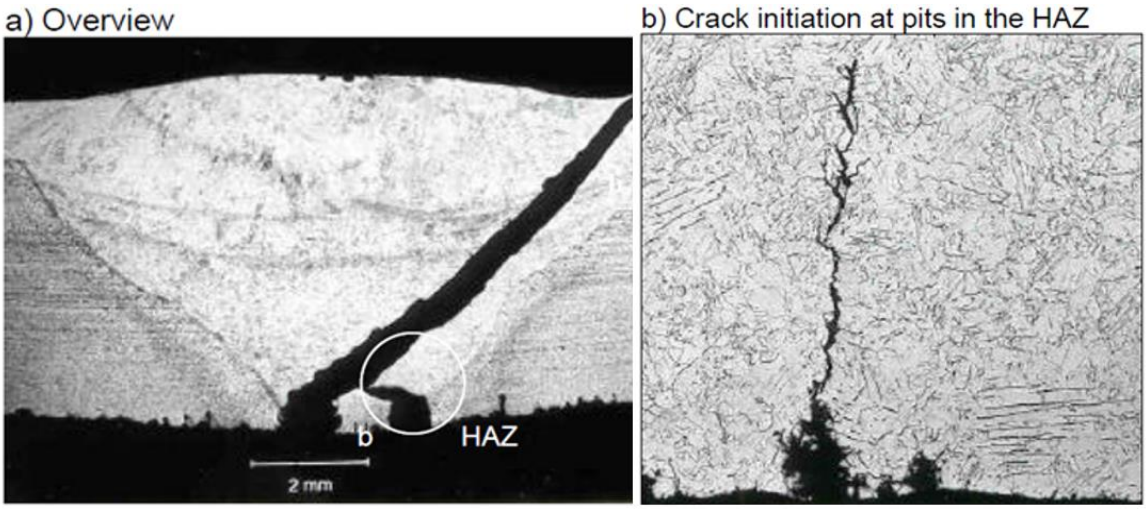

Figure 2.30: a) Microstructure of a cracked weld in a pipe and b) where the crack initiated in pits in the HAZ [74].

An example of HASCC originating from pits was in 2001 in the Jade gas field in the Norwegian sector, when cracks and leaks were noticed during installation and service start-up of two SMSS flowlines. Detailed investigations were performed on a circumferential weld sample to compare to previous failures with the same filler material type. This was done to determine why brittle failure occurred at the crack initiation area. It was found that the original fracture was related to HAC as the SMSS flowlines had never been in operation. Therefore, they were not exposed to the cathodic protection for a significant amount of time to allow electrochemical hydrogen uptake in concentrations which would result in cracking. It was determined that an inter-run lack of fusion was the primary origin of the failure, with the fracture spreading from both sides of the lack of fusion

to the top and root of the weld. Also, hydrogen uptake had occurred during the welding process as a result of leaks in the TIG torch cooling systems, which caused hydrogen contamination of the welds during onshore orbital welding [244]. The crack then proceeded to propagate into the weld metal and then shifted towards the HAZ due to a quenched HAZ, which can have a hydrogen diffusion coefficient five times higher than in the BM. Cracking was also observed to initiate at pits in the HAZ, which corresponds to a low pitting corrosion resistance due to the presence of carbide precipitation and oxide layers produced during welding [74].The presence of pitting corrosion can be disastrous for various marine environment structures such as ships, tanks and containers. Pitting corrosion may also occur on pipelines and flowlines in the presence of seawater, which can erode the passive oxide layer protecting the pipeline, but also has to be considered in welds. Laser welds must be especially considered as these welds in particular show a less developed oxide layer than the stainless steel base materials [245].

Therefore, the main area of interest in this work is not in the weld material but in the nearby heat affected zone. This also determines that the model created previously in [15, 16, 243] does not accurately reflect the process of HASCC in SMSS in detail. This work aims to develop a model which more accurately reflects the process of HASCC in SMSS initiation from pitting corrosion and is illustrated in Figure 2.31, which is an adapted version of Figure 2.11. The corrosion process consists of both passive layer breakdown and localised corrosion. This image shows that various additional parameters can have an effect on HAC and is not just limited to local microstructure, local mechanical load and local hydrogen concentration. Pitting corrosion has an influence on the local microstructure of the material and as the pit geometry changes, with increasing depth in particular, and this in turn has an influence on the local mechanical load due to the change in geometry of the specimen. The pit behaves as a notch where high stress and strain concentrations accumulate, which may occur at the tip of the notch, which is the bottom of a pit. This is also the area where high local hydrogen concentrations can be found. The high concentration of stresses and strains accumulating at the pit bottom is commonly found in 2D simulations, but 3D simulations are becoming more common and the higher stressed and strained regions are then more commonly found located at the sides of the pits. More information on the simulation of HAC can be found in Section, 2.3.5.

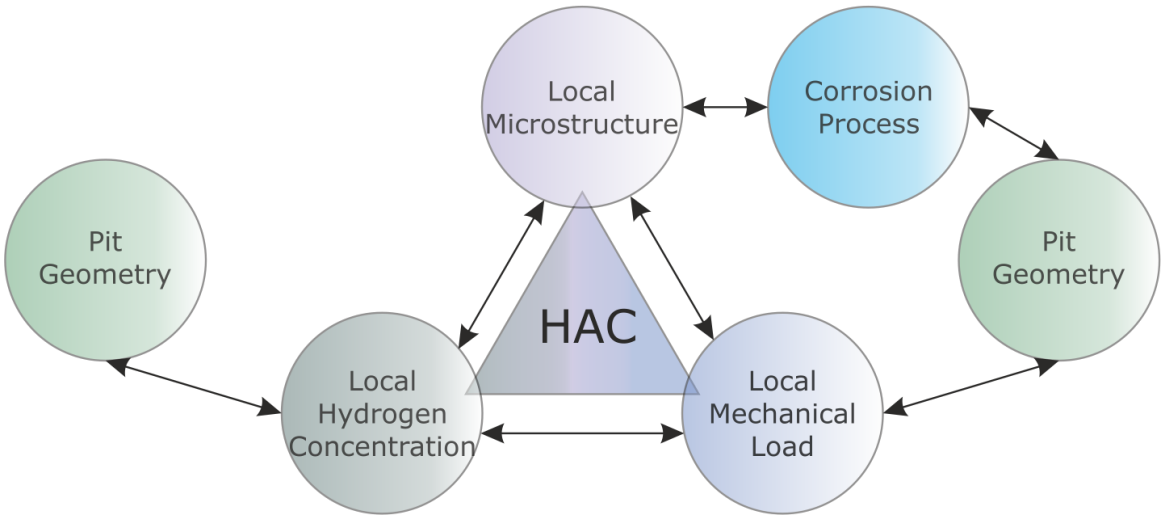

Figure 2.31: The three local parameters affecting HAC.

The presence of pitting is not a requirement to stop using equipment, even though it may lead to lack of containment. Pitting is investigated during surveys and inspections of offshore equipment and also vessels, both the location and frequency. DNVGL-CG-0182 [246] has a pitting intensity diagram, Figure 2.32, which is used to determine the minimum acceptable remaining thickness of a hull plate without the need for repair. The minimum acceptable remaining thickness of a hull plate without the need for repair is then determined as:

- For plates with a pitting intensity of less than 20%, using Figure 2.32, the minimum remaining thickness in pitting shall be as a minimum, Equation (2.33), [246]:

  $$t_{min} = 0.6 \cdot t_{orig} \quad (2.33)$$

  Where:

  t_{min}= Minimum thickness in mm including a margin for further corrosion until next hull survey and

  t_{orig}= Original "as built" thickness in mm.

- For plates with a pitting intensity of 100%, which is general or uniform corrosion, the average remaining thickness in the worst cross section through the pitting in a hull plate should not be less than the minimum thickness for general corrosion, which is Equation (2.34), [246]:

  $$t_{min} = k \cdot t_{orig} \quad (2.34)$$

  With k being the diminution coefficient depending on the equipment being investigated and varies from 0.7 to 0.8

- For intermediate pitting intensities, a linear interpolation between the two instances above is used to determine the average acceptable remaining thickness.

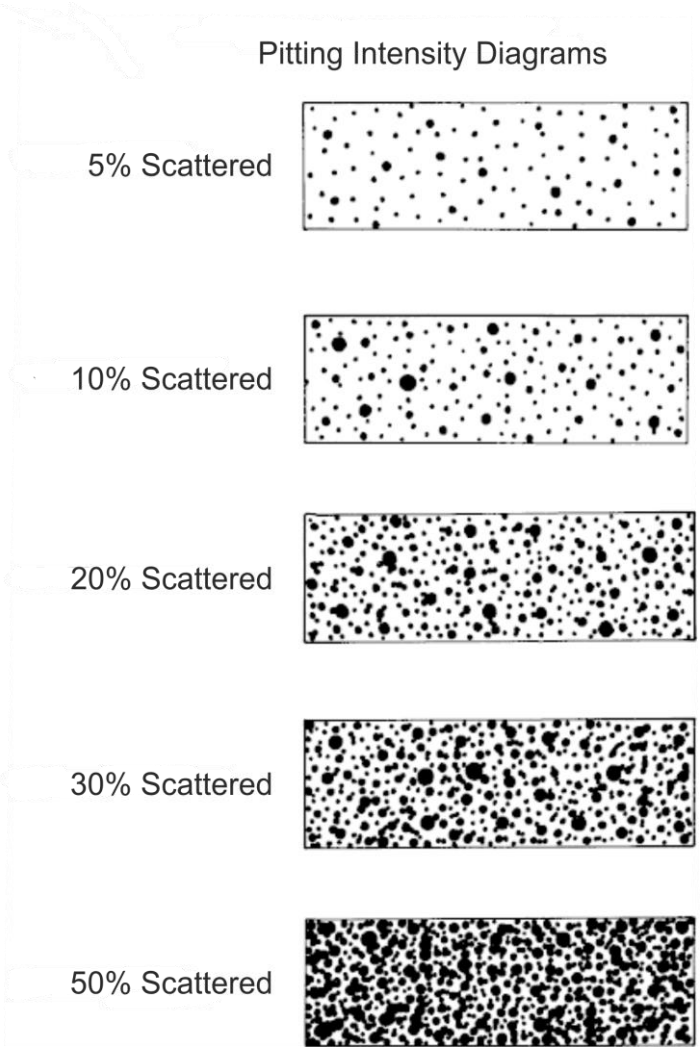

Figure 2.32: Pitting Intensity diagram from DNVGL-CG-0182 [246].

2.3.4 HASCC as a Consequence of Pitting Corrosion

In many engineering applications the occurrence of pitting may be closely followed by SCC, as is the case for Open Circuit Potential (OCP) where SCC generally starts from pre-existing corrosion types or defects on the material surface. This is especially applicable to pitting or crevice corrosion as an aggressive medium can be created at the bottom of a pit or gap, due to a decreased oxygen content and potential drop. The subsequent crack initiation is not just a result of anodic dissolution of the metal, but the separation of the cathodic partial reaction is the cause of the increase in hydrogen absorption in the material. The locally accumulated hydrogen at the bottom of the pit or gap can result in the degradation of the ductility of the material, and in turn assist crack initiation due to the additional high stresses and strains in these regions. SCC in OCP

conditions mostly occur in aqueous electrolytes, especially Cl ion containing electrolytes. This reaction is always accompanied by hydrogen absorption due to the local cathodic partial reaction and therefore this type of corrosion is termed Hydrogen Assisted Stress Corrosion Cracking (HASCC). Pits are mostly found at the origin of fracture surface of test specimens as well as machinery parts, so it was investigated if pit initiation in turn initiates the formation of cracks [247]. This is due to pitting providing the necessary requirements of a high stress or strain concentration and an aggressive local solution. In order to maintain high standards, there has been great effort to understand and model the evolution of damage in practical systems [248-252]. Extensive research has therefore been undertaken to produce reliable laboratory data [253, 254], but a more knowledgeable foundation based on understanding how cracks initiate and propagate in the early stages of failure development is a necessary requirement. The essential steps in the overall process of crack initiation and development involve; pit initiation, pit growth, the transition from a pit to a crack, short crack growth and long crack growth. However, a reliable prediction of the complete damage process in engineering components would require a quantitative understanding of each stage. Several deterministic (mechanistic based) models [255-257] have been developed to address SCC initiation and propagation in low-pressure steam turbine disc steels. In these models, the pit-to-crack transition is based on requirements determined by Kondo [247] which states that the pit depth must be greater than a threshold depth and that the crack growth rate must exceed the pit growth rate, as shown in Equations (2.35) and (2.36). It is also assumed that the pit is still growing.

$$\Delta K \geq \Delta K_{th} \tag{2.35}$$

$$\left(\frac{dc}{dt}\right)_{crack} \geq \left(\frac{dc}{dt}\right)_{pit} \tag{2.36}$$

Where:

ΔK= Stress intensity factor,

ΔK_{th}= Threshold stress intensity factor,

$\left(\frac{dc}{dt}\right)_{crack}$= Crack growth rate and

$\left(\frac{dc}{dt}\right)_{pit}$= Pit growth rate.

It was determined that a stable crack will initiate and propagate from an actively growing pit if the threshold stress requirement for crack development is exceed and if the crack growth rate is larger than the rate at which the pit surface dissolves. When the length of the crack, which is propagating from the pit, is equal to the depth of the pit, then the pit is also considered as part of the crack (pit to crack transition).

It is however difficult to determine how a crack develops from a corrosion pit due to limitations in visualisation and measurement techniques [248]. Turnbull et all [258] investigated pit and crack morphology in a 3-NiCrMoV disk steel in an aqueous chloride solution using a combination of a serial metallography technique and 3D imaging. This investigation showed finger-like cracks propagating from pits in addition to pits with depths greater than the associated cracks. X-ray tomography is another method used to investigate pit to crack transition. This method creates a 3D visualisation of the pit [259, 260], crack [261-265] or defect. Horner et al. [248] investigated the pit to crack transition in a 3-NiCrMoV turbine disk steel using focus-tube x-ray tomography and combined these measurements with results from a Finite Element Analysis (FEA) of the stress and strains associated with pit models. The images from the x-ray tomography showed that the preferred crack initiation site is on the pit wall, close to the pit mouth, Figure 2.33.

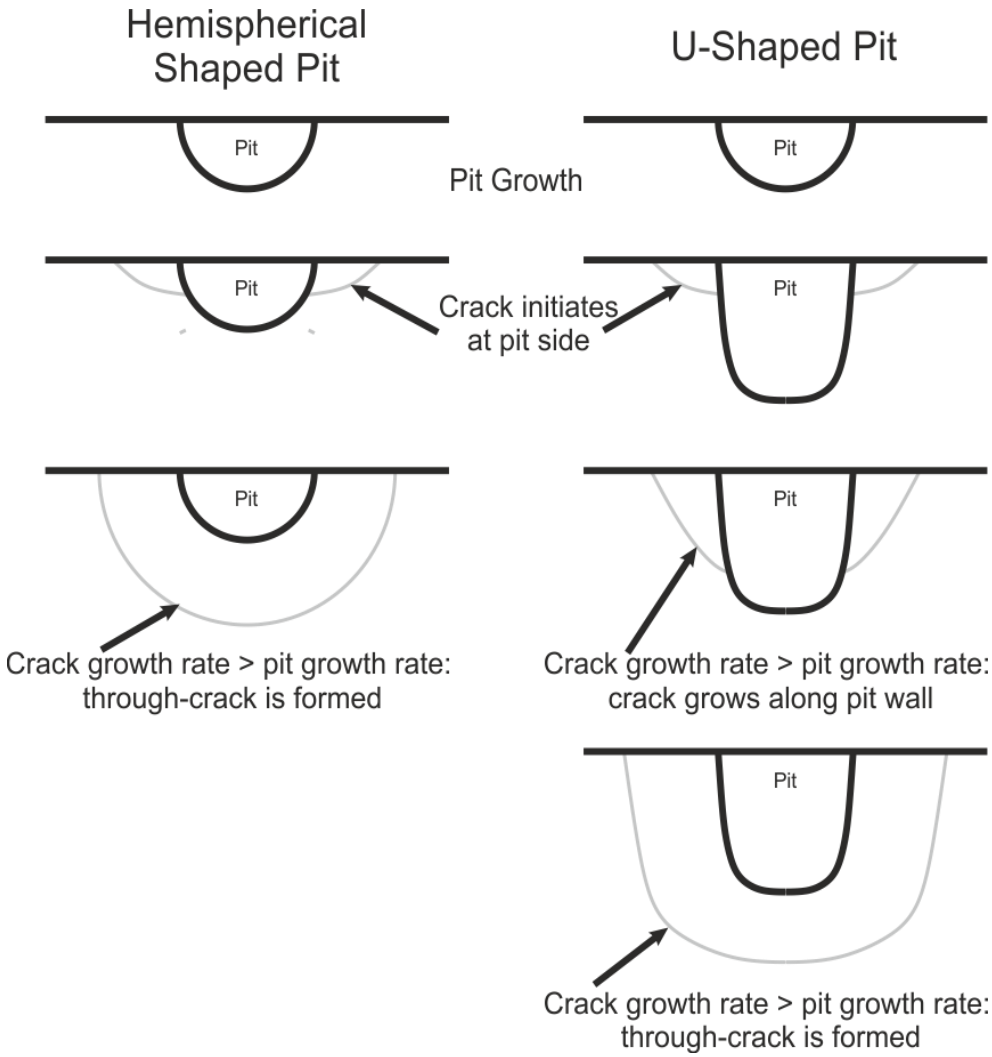

Figure 2.33: Schematic illustrating pit-to-crack transition and subsequent crack evolution in the steam turbine disc-aqueous chloride solution system [248].

Data from the FEA showed plastic strain just below the pit mouth. This explains crack nucleation in the region close to the pit mouth as a growing pit in an applied stress field creates a dynamic strain in the nearby material.

It is necessary to investigate the effects the depth, size and shape of the pits have on the stresses and strains present in the pit and region alongside the pit. This is due to the presence of a pit on the surface of a component causes an increase in the local stress field. This increase in stress causes a reduction in the load carrying capacity of the component. It is presented in various research that the pit depth is an important characteristic of failure, and the deeper the pit the more drastic the consequences of failure [221, 266]. There are numerous works investigating the effect of high stress concentrations on the effect of pitting and crack growth but as previously mentioned, the strains in the region close to the pit mouth also contribute to crack propagation and growth.

The presence of cracks in offshore structures and pipelines can result in catastrophic failures. Over the last years several incidents of hydrogen induced failure have been reported in sub sea oil and gas pipelines and installations in the North Sea [3, 66].

For austenitic and duplex stainless steels for example, the bulk hydrogen content can be measured with reasonable accuracy with established methods like e.g. melt extraction. It has however proven difficult to establish experimental methods for measurement of local hydrogen concentration. Up to the present date the hydrogen assisted local fracture mechanisms in the vicinity of a crack are not well understood either. Numerical modelling of hydrogen diffusion and HAC is thus an alternative method of investigation. By modifications of Fick's law, the effect of different parameters on the time dependent hydrogen distribution can be investigated. This work however, modelled crack critical conditions in terms of local strains and a normalised hydrogen concentration and is explained later in Chapter 4.

Additionally, the presence of notches or pits, which cause high local stress and strain concentrations, as well as residual stresses after welding can all contribute to the local accumulation of hydrogen [66]. This is in addition to the separation of the cathodic reactions as described in Section 2.3.2 and also mentioned at the start of this chapter. In the presence of pitting or crevice corrosion the fatigue life and fatigue limit can no longer exist under corrosion fatigue conditions, according to experiments and service experience [252]. The fatigue life of a defect-free component or specimen can be divided into two phases: crack initiation and crack propagation. The influence of corrosion on crack initiation is greater than on crack growth, but only if SCC or hydrogen embrittlement are

excluded. The presence of a corrosive media can increase the crack propagation rates by a factor of 3 to 5 [267].

For high strength structural steels, it is well known that HAC may occur at low hydrogen concentrations due to the possibility of hydrogen uptake during fabrication or welding or due to service conditions, such as corrosion reactions. Initiation and propagation of HAC is based on the interaction between three local parameters- hydrogen concentration, local microstructure and mechanical load, as shown previously in Figure 2.11.

2.3.5 Numerical Simulation of HASCC

Numerical simulations currently exist where crack initiation occurs in a pit, as the evolution of stress corrosion cracks from pits is important for many industrial applications. This however continues to be a challenge in both measurement and prediction. The early foundations of this investigation were developed by Kondo [268] and more recently by Turnbull [269] who determined that the evolution of a stress corrosion crack from a pit is a complex process. Pitting corrosion has been a research topic for many years but according to Bhandari et al. [270] the structural failure due to pit characteristics is still not understood fully and certain factors need further investigation, including pit depth, precise assessment of strength in and around the pit and the environment surrounding pitting. These however prove difficult to assess accurately due to the small geometries involved. The existing models also do not take into account hydrogen uptake in the pit or these models are purely to investigate stresses and strains.

There are currently various researchers investigating pitting corrosion and/ or SCC, including Anantha et al. [271], Cerit [206, 266], Eksi [272], Hoehbusch et al. [14], Horner et al. [248], Mai et al. [12, 13], Turnbull [221], Wang and Han [273] and Xiang et al. [274]. All of this research, apart from Mai et al. and Wang and Han, simulated 3D pits, but Mai et al. and Wang and Han simulated 2D pits. Most researchers model the ellipse or hemispherical shaped pits, however Cerit, modelled a secondary pit at the bottom of the main pit [275], Eksi modelled pits (d) and (e) from ASM [8], Mai et al. investigated three different pit geometries and Xiang et al. additionally modelled a “butterfly” shaped pit which is a V shaped notch with a rounded pit bottom. All of these researchers investigated the stresses in a pit, with Anantha, Horner, Turnbull and Xiang additionally investigating the strains present in the pits. Mai et al, Turnbull and Xiang modelled stable pits but also pit growth, with the other researchers modelling stable pits only. Investigations into the electrochemical reactions and hydrolysis occurring in the pits are also ongoing by Hoffmeister [185] and Mehlich [276].

No literature during this work has been found regarding numerical simulation of the effect the presence of hydrogen has on crack initiation and the location of crack initiation in pits in a loaded SMSS specimen. Wei et al. [277] investigates the presence of hydrogen around a crack tip in a specimen with a wedge shaped notch, but this investigates the stresses in the region around a crack tip and not in a pit. Anand et al. [278] also investigated a notched specimen but this was a bending load applied to a ferritic steel to investigate the strains present, Figure 2.34.

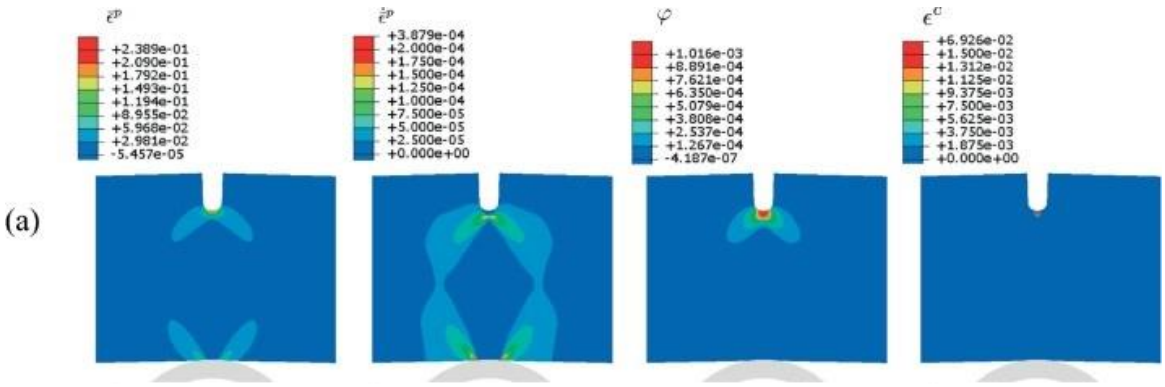

Figure 2.34: Contour plots of equivalent tensile plastic strain, equivalent tensile plastic strain rate, internal variable and craze strain for a bending load applied to a ferritic steel, from Anand et al. [278].

Diaz et al. [279] simulated hydrogen embrittlement in a notched high strength steel, as shown in Figure 2.35.

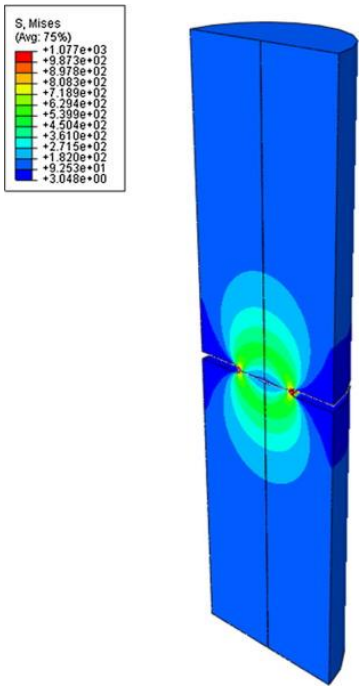

Figure 2.35: Equivalent stress of the beginning of load in a notched high strength steel from Diaz et al. [279].

Anantha et al. [271] investigated the strains in hemispherical shallow and deep pits and compared the results to where cracks initiated in experimental samples. These results are shown in Figure 2.36.

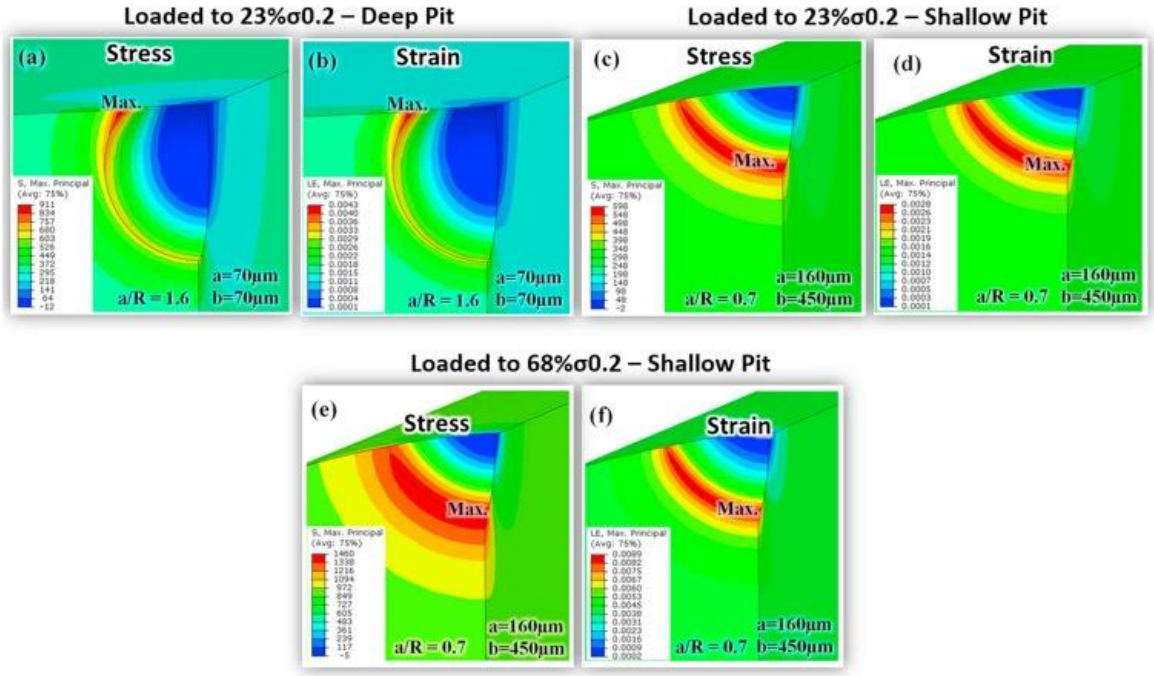

Figure 2.36: Strains in hemispherical shallow and deep pits from Anantha et al. [271].

Creating a numerical simulation to accurately model formation and growth of various geometry pits in a loaded SMSS specimen in the presence of a bulk electrolyte seems to be a concept which has not yet been created.

In order to create this model, the following information is required:

- Information on the rupture of the passive layer,
- Information on the growth of pits and
- Information on the geometries of stable pits.

Rupture of the passive layer

As mentioned in Section 2.3.2 there are two mechanisms which may cause the passive layer to fail- chemical or mechanical. In this work it is assumed that breakdown of the passive layer occurs due to the displacement subjected to the specimen during the SSRT. One method to determine when the passive layer fails, is to use the Young's modulus of the Cr_2O_3 passive layer. This value can be found in literature and the strain where failure occurs can then be calculated using Equation (2.37):

$$E = \frac{\sigma}{\varepsilon} \tag{2.37}$$

To use this method, the Young's modulus of the Cr_2O_3 passive layer must be determined. Values obtained generally contain a large scatter range [227]. This is in part due to problems with measuring the mechanical properties of brittle materials. Therefore, the most common method to determine the Young's modulus of a brittle oxide layer is to perform the measurements on scales or single crystals, instead of bulk oxides. Table 2.3 shows Young's modulus values for Cr_2O_3 in bulk oxides at room temperature, apart from Nicholls et al. [280]., who performed their tests on a single crystal.

Table 2.3: Values for Youngs Modulus in literature.

Youngs Modulus (E) (GPa):	Source:
272	Tortorelli [281]
283	Robertson and Manning [227]
283*	Nicholls et al. [280]
229 ± 22	Nicholls et al. [280]

* Single crystal

Growth of pits

The time taken from the breakdown of the passive layer to the formation of a stable pit must then be investigated. Due to the small geometries of the pits it is very difficult to get accurate values for this as the passive layer breakdown and growth of the pits cannot be observed without interrupting the experiment. Therefore, the values in Table 2.4 have been determined using the acoustic emission method. This method involves recording the noise generated by the initiation and growth of pits and from the number of counts and short and resonant AE signals recorded.

Table 2.4: Pit growth information from literature.

Passive Layer Breakdown (s):	Pit Growth (s):	Source:
120	1500 - 9000	Calabrese et al. [282]
Unknown	615600	Horner et al. [248]
Unknown	130 a)	Scheiner et al. [283]
Unknown	215 b)	Scheiner et al. [283]
300	126000	Kim et al. [284]
1500	800	Fregonese et al. [285]
Unknown	1200	Park et al. [286]

a) To a pit radius of 180µm

b) To a pit radius of 600µm

Information on the geometries of stable pits.

According to ASM [8], there are six different types of stable pits: (a) Narrow and deep, (b) Elliptical, (c) Wide and shallow, (d) Subsurface, (e) Undercutting, (f) Shapes determined by microstructural orientation, Figure 2.37.

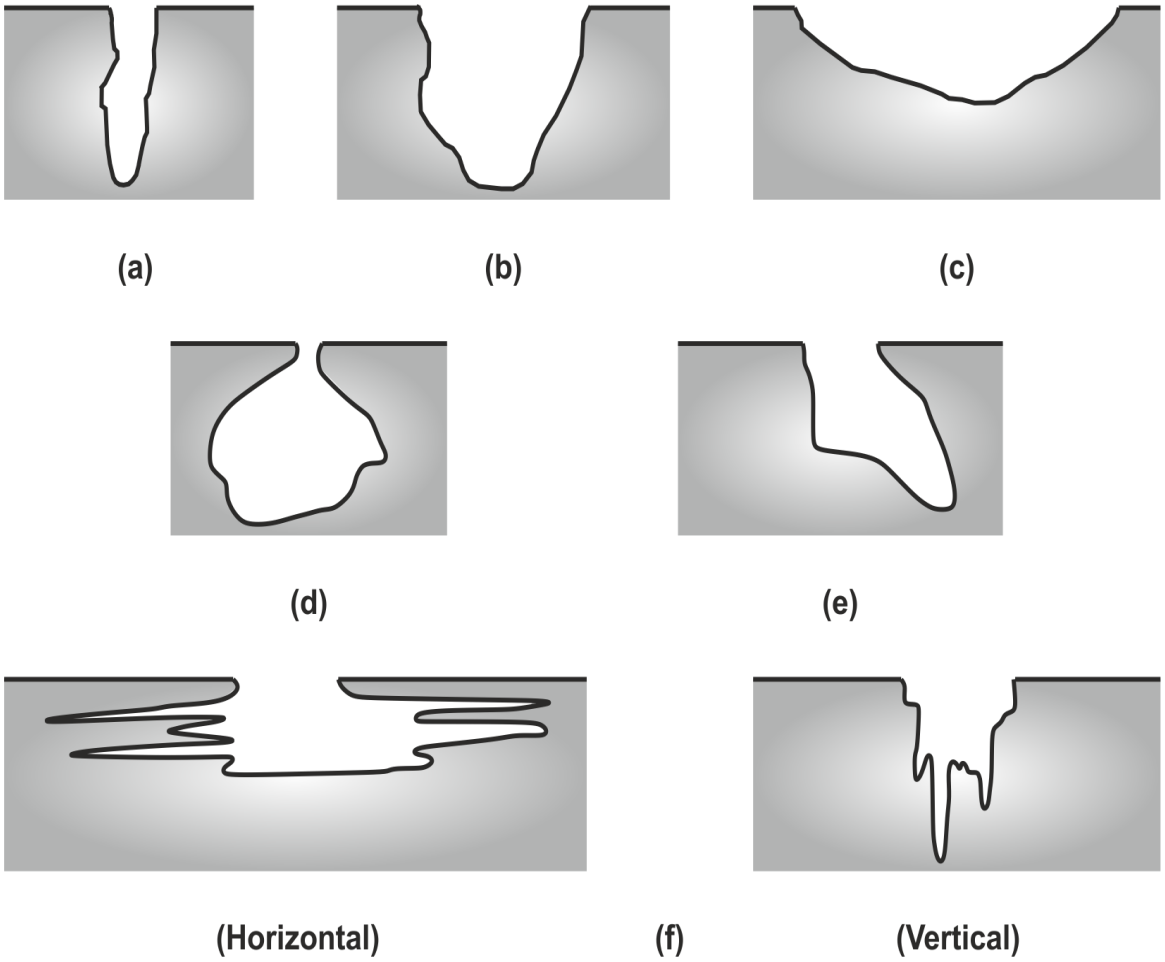

Figure 2.37: Variations in the cross-sectional shape of pits (a) Narrow deep, (b) Elliptical, (c) Wide shallow, (d) Subsurface, (e) Undercutting, (f) shapes from [8].

The most commonly modelled pit shapes are the elliptical (b) and wide shallow (or hemispherical) (c) pit shapes. The reason for this may be they can be modelled easier due to their symmetry. This is also an advantage regarding computing time as half or even a quarter of the pit can be modelled instead of the complete pit. In order to model as accurately as possible, the various pit geometries, the depth of the stable pit and the radius at the mouth of the pit are needed. Various researchers have modelled stress or strain accumulation in pits or completed experiments to investigate the pits formed when submerged in a bulk solution. Mai and Soghrati investigated 2D pits in metallic materials, Figure 2.38, based on the plane stress assumption subjected to a uniaxial load. They found

that both the maximum von Mises stress and maximum principal normal strain occur at the pit bottom [12]. In this research hydrogen was not considered in the simulations.

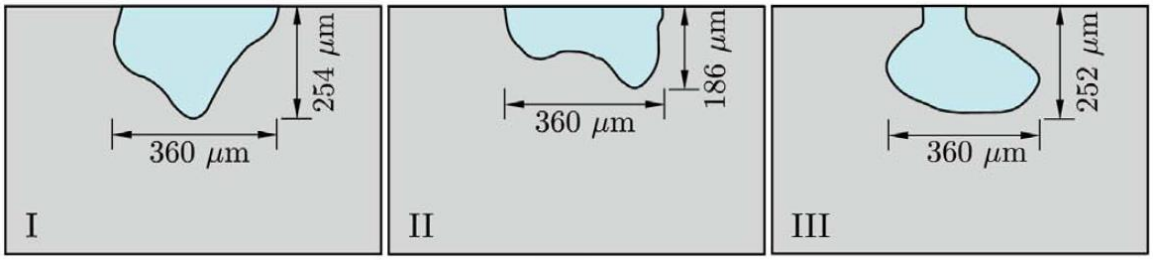

Figure 2.38: Pit geometries investigated by Mai and Soghrati [12].

Hoehbusch et al. [14] examined 3D spherical, bullet pit geometries in the stainless steel 1.4462, under axial and cyclic loads. The diameter (2r) of the corrosion pits modelled varied from 0.01 mm to 0.5 mm and the ratios of depth (t) to radius were 1, 2 and 4. The main aspect of interest in this research was the first principle stresses and not the strains. The max principle stresses were found to be located on the wall of the pit perpendicular to the applied load and not at the pit bottom. These pits were not exposed to an electrolyte containing hydrogen, so no hydrogen was considered in this research.

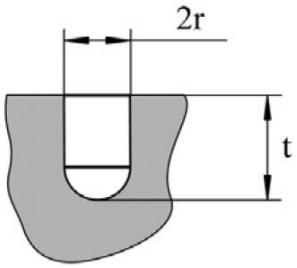

Figure 2.39: Spherical and bullet pit geometries modelled by Hoehbusch et al. [14].

Xiang et al. [274] studied four different 3D pit shapes in a 13-14.5% Cr steel subjected to an axial load, not in the presence of hydrogen. The radius of the hemispherical pit was 100μm, the butterfly pits were 125μm x 100μm, the bullet pits were 250μm x 125μm and the semi-ellipsoid pits were c x b with c and b being four different depths and diameters of pits which were: 50μm x 100μm, 75μm x 100μm, 125μm x 100μm and 150μm x 100μm. Pit growth was also modelled in this research and for both static and growing pits the location of the maximum strain was found to be near the mouth of the pit or the shoulder.

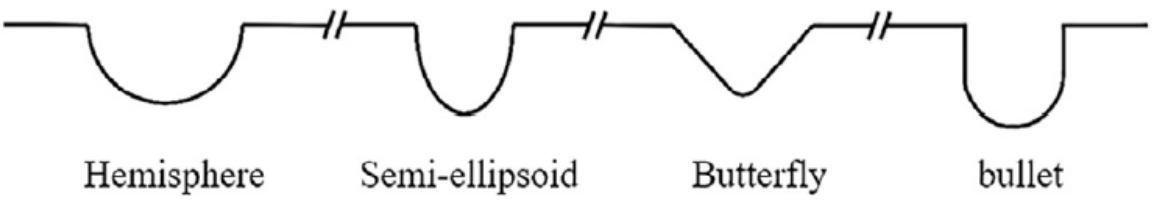

Figure 2.40: The various pit geometries modelled by Xiang et al. [274].

Calabrese et al. [1] did not model pit geometries, instead the corrosion behaviour of a 13%Cr martensitic stainless steel under tensile load in an acidified chloride solution in the presence of thiosulphate ions at room temperature was evaluated by the acoustic emission technique. The applied tensile stress was equal to 80% of the 0.2% yield strength of the material and was applied to a tensile specimen in accordance with NACE TM0177 method A. It was found that all specimens failed between 300 and 400 hours with pit dimensions all very similar with a pit radius of about 325µm and depth of 420µm. It was also found that the high hydrogen reduction rate allowed hydrogen diffusion into the martensitic matrix where trapping occurred at irreversible traps. The high hydrogen content in the martensitic matrix may then be responsible for the microplasticity and transgranular cleavage front at the pit tip where intergranular brittle fracture might occur.

Fregonese et al. [287] investigated the corrosion behaviour of AISI 316L which is an austenitic stainless steel with 17.2% Cr. The experiments were conducted at room temperature in a 3% NaCl solution. Tests conducted for less than 8 hours still had the pitting cap intact but tests for longer than 8 hours showed the metallic cap collapsing. The falling down of the metallic cap was understood to be the stopping of the development of the pits and a change in corrosion type which then became a more uniform corrosion type. Hydrogen bubbles were produced during this experiment, but the origin of these bubbles in the pit was not investigated.

Hariramabadran et al. [271] considered an AISI 420 martensitic stainless steel, with a Cr content of 13.8%, subjected to a tensile load at room temperature in a 0.3 M NaCl solution. The pits were then modelled as spherical shaped pits the depths of the pits modelled varied from 26µm to 334µm and radii of 20µm to 430µm. The deeper pits were found to have locations of maximum stress and strain at the pit mouth region, but the shallow pits had highest stresses and strains distributed along the pit surface/ walls. It was also found during experimental investigations that the presence of hydrogen accelerated both corrosion and cracking processes. Additionally, the heavier loaded conditions showed less deformation which suggested hydrogen embrittlement acted together with SCC resulting in rapid failure. These factors were not considered in the numerical simulations and therefore the numerical simulations contained no hydrogen.

Horner et al. [248] examined a 3NiCrMoV disk steel from an ex-service steam turbine disc. The specimens were then loaded to a percentage of the 0.2% proof stress at 90°. Three dimensional X-ray microtomographic images of the pits generated during this experiment were found to have cracks which develop predominately at the shoulder of the pit near the pit/ surface interface. A hemispherical shaped pit with depth of 100µm and a U shaped pit of depth 500µm and 333µm pit mouth radius were then modelled. A uniform stress was

then applied to the surface of the specimen and no bulk electrolyte containing hydrogen was included in this simulation. These models also showed that maximum strains occur at the pit wall just below the pit mouth.

Park et al. [286] conducted experiments on type 304 and 306 stainless steels in neutral chloride solutions containing thiosulfate concentrations varying from 0.01 to 55 mM and 1 to 100m M of chloride. Pits of 30 – 35µm deep and a radius of 200 – 300µm were formed after 2 hours.

Fregonese et al. [285] undertook additional acoustic emission experiments on two types of 316L austenitic stainless steels in a 3% NaCl solution acidified to a pH of 2 at room temperature. For the 316L sheet specimen which underwent potentiostatic testing the time delay was 1000 – 2500 s and produced 3 – 4 large pits of diameter 1.5 – 2 mm. The time delay is assumed to correspond to when pit growth begins. The 316L bar specimen had a time delay of 1500 s and produced hundreds of small pits of diameter < 500 µm. The 316L bar specimen then underwent galvanostatic testing with a time delay of 1800 – 3500 s which produced 5 – 20 pits of diameters 500 – 800 µm. Hydrogen bubbles were generated during the experiments but the origin of these bubbles in the pits was not investigated.

Mazille et al. [288] conducted acoustic emission tests on an AISI 316L austenitic stainless steel, with 17% Cr, at room temperature in 3% NaCl solution acidified to a pH of 2. Most of the pits produced in this experiment had a diameter < 200µm after 7 hours of tests, however some pits reached diameters of 300 – 400µm. The acoustic emission test produced bubbles of hydrogen, but the origin of these bubbles was not part of the research.

Turnbull and Zhou carried out tests on a 3NiCrMoV steam turbine disc steel as cylindrical tensile test specimens self loaded to 90% of 0.2% yield stress. These were additionally exposed to deaerated pure water, aerated pure water and aerated water containing 1.5 ppm of chloride ions. All of the water was at a temperature of 90^{o}C. For the deaerated pure water specimens, the maximum pit depths were found to range between 186µm and 218µm. For the aerated pure water specimens, the maximum pit depths varied from 168µm to 433µm. The specimens in aerated 1.5ppm Cl^- had pit depts ranging from 861µm to 1117µm. The depths of the pits in the 1.5ppm Cl^- solution is a lot larger than the other solutions. No cracks were found in the deaerated pure water specimens, but cracks were found to initiate in aerated water between 13 and 19 months. For the 1.5ppm Cl^- solution cracks were found to initiate in less than 7 months. Cracks found in the 1.5ppm Cl^- solution had depths greater than the corresponding pit depth but cracks were also found which were smaller than the corresponding pit. This suggests that cracks did not necessarily originate in the pit bottoms. The presence of hydrogen was not included in this research.

The information above is summarised in Table 2.5.

Table 2.5: Stable pit geometries from literature.

Radius (µm):	Depth (µm):	Bulk Solution:	Temp (°C):	Load:	Pit Geometry Information:	Source:
180	300	None	-	Uniaxial	b, d and e from Figure 2.37	Mai and Soghrati [12]
5 - 250	Ratio vs Radius (1, 2, 4)	None	-	Uniaxial, cyclic	Spherical, bullet shapes	Hoehbusch et al. [14]
50 – 250	100 - 125	None	Room	Uniaxial	4 different shapes	Xiang et al. [274]
325	420	NaCl, CH3COOH, Na2S2O3	Room	Uniaxial	From AE induced pits	Calabrese et al. [1]
-	200	NaCl	Room	None	From AE induced pits	Fregonese et al. [287]
26 – 334	20 – 430	NaCl	Room	Uniaxial	Spherical	Hariramabadran et al. [271]
50 - 333	100 - 500	Aerated water, Cl-	90	Uniaxial	Hemispherical, U-shaped	Horner et al. [248]
100 – 150	30 - 35	NaCl, Na2S2O3	Room	None	Not specified	Park et al. [286]
1.5 – 2 mm < 500, 500 – 800µm	-	NaCl, HCl	Room	None	3 or 4, Hundreds 5 - 20	Fregonese et al. [285]
100 – 200	-	NaCl	Room	None	Not specified	Mazille et al. [288]
-	186 - 218	Deaerated pure water	90	Self loaded	Width/Depth ratio increases with pit depth	Turnbull and Zhou [254]
-	168 – 433	Aerated pure water	90	Self loaded	Width/Depth ratio increases with pit depth	Turnbull and Zhou [254]
-	861 - 1117	Aerated Cl-	90	Self loaded	Width/Depth ratio higher than pure water	Turnbull and Zhou [254]

It can be seen that not all pit geometries from Figure 2.37 have been mentioned. It can also be noted that combining the presence of hydrogen from a bulk solution or addressing the partial reactions in a pit are not considered in any of the research mentioned above. The combination of strains and hydrogen or even stresses and hydrogen in pits have not

been found in the covered literature. However, using the above information obtained from literature, modelling of hydrogen uptake in a pit during an SSRT can be performed. This is explained in detail in Chapter 4.

3 Research Overview

3.1 Summary of Literature

Supermartensitic stainless steels (SMSS) were developed in order to provide resistance to corrosion while maintaining a high mechanical strength, which has the advantages of weight and cost savings, for use in maritime environments [76]. Corrosion is a major cause of structural deterioration in maritime structures, which can affect the lifetime of the components and may result in disastrous consequences, such as loss of containment, if a failure occurs [270]. As welding is the preferred method of joining offshore pipes and structures, the HAZ region especially needs to be investigated, as mentioned in the literature study in Chapter 2 this region is most susceptible to HASCC [15, 243]. In view of the literature presented in the previous chapter, the following points can be made:

1. Drilling for oil and gas has noticed an increase in sour service in the flowlines which increases the risk of corrosion, especially pitting corrosion and subsequent Hydrogen Assisted Stress Corrosion Cracking (HASCC). Research is ongoing into how corrosion resistance alloys perform in sour service environments but SMSSs are proving to be a viable alternative to other offshore materials, including Duplex Stainless Steels (DSS) and Corrosion Resistance Alloys (CRA) [48, 60]. SMSS have an increased Cr content but decreased C content with the addition of Mo to increase the corrosion resistance properties, especially against localised and SSC corrosion [56]. The decreased carbon content in SMSS also enhances the weldability of the material, which can then influence the toughness and resistance to cracking of the material [80].
2. HASCC occurs when hydrogen is transported from the source of the hydrogen, i.e. during production (welding), processing and under service conditions (i.e. CP or the separation of the cathodic partial reaction resulting in locally accumulated hydrogen in pits and cracks), to a location in the material where critical degradation can occur. Substantial research has been conducted into this topic [133, 154, 156, 158, 159], and is still ongoing, but no single method has been determined to definitively cover this degradation method. However, this is important to understand in order to predict the lifetime of a component in the presence of hydrogen [92, 93]. The effects of hydrogen on the mechanical properties of high strength steels were investigated [158] and it was found that the total lifetime of these steels is controlled by an incubation period for crack initiation and for stable crack growth [158]. It was also found by Böllinghaus et al. [175] that the lifetime of

components depends on ductility loss. These researchers also noted that the presence of hydrogen causes a greater reduction in strain in a material than stresses, showing that the presence of hydrogen influences ductility more than strength of a material, Section 2.2.4.

3. Pitting corrosion is a type of localised corrosion [178], but difficulties in detection and prediction means it may be more dangerous than uniform corrosion as these pits often are of very small size but also may be covered with corrosion products, causing subsurface pitting [179, 180]. SMSS are used in various offshore and marine environments where pitting corrosion is likely to occur, leading to failure [207]. These failures may be brought about due to a variety of reasons, including when protective coatings fail. This exposes the metal surface to the medium being transported in the pipeline which may lead to the decrease of oxygen and pH in the pit resulting in hydrogen ingress into the pit, increasing the risk of HASCC. Two main methods are used to investigate the response of pipes subjected to pitting corrosion- researching stress distribution around pits [219] or researching the strength of a metal with pitting corrosion already present [222]. Strain can also be investigated in a material with pitting corrosion present as localisation of the plastic zone occurs beneath the mouth of the pit at high stresses [221].
4. Pitting corrosion can be divided into two groups- a result of competitive adsorption between oxygen and halide anions or a result of breakdown of the passive layer [209]. For the second theory, in order for pitting corrosion to occur, the first stage is the breakdown of the passive layer covering the material. This can occur due to chemical or mechanical conditions. A harsh chemical environment can remove the passive layer or elastic strains in the oxide can cause fracture [226].This however may be due predominately to the high temperatures present in heat exchangers. Strain is investigated over stresses as strains in the material increase even after yield, Equation (2.22) and strain is also an observable quantity [227]. However, there is general agreement that initiation and growth of pitting corrosion can be approximately divided into four stages, as described above. The HAZ region of SMSSs is more susceptible to pitting corrosion than the WM or BM [241]. Based on the literature review, one theory for this considers the microstructure of the material and the differences in material properties [242]. The formation of oxide scales or annealing colours during welding combined with some microstructural defect, may also cause pitting corrosion in the HAZ [242].
5. The presence of pits provides high stress and strain concentrations, so it has been investigated if pit initiation is linked to the formation of cracks [247, 253, 254]. The steps involved in crack initiation from a pit are: pit initiation and growth, transition

from pit to crack, short crack growth and finally long crack growth. One theory explaining how a crack grows from a pit states that the pit depth must be greater than a threshold depth, the crack growth rate must exceed the pit growth rate and the pit is assumed to still be growing [247]. Due to limits in measurement techniques it is difficult to explain exactly how a crack initiates from a pit [248]. However, x-ray tomography has shown that cracks initiate on the pit sides near the pit mouth and not at the pit bottom as previously thought. Crack initiation close to the pit mouth is therefore explained as a region of dynamic strain resulting from a pit growing in an applied stress field [248]. This may indicate that previous theories stating that crack initiation occurs at the pit bottom are no longer valid.

6. The presence of pits reduces the load carrying capacity of a component, due to an increase in the local stress field in the pit region, as stated in the literature review. The depth, size and shape of pits all have an effect on the stresses and strains present in the pit and the region around the pit. Most of the research into pitting and crack growth investigates the stresses in the pit and pit region [12-14, 247, 269] but strain has a greater influence on the lifetime of components in the presence of hydrogen. Few researchers are investigating the influence of strain in pits [221, 248, 271, 274] but these existing numerical simulation models do not take into account hydrogen uptake in the pit or these models are purely to investigate stresses and strains. Few researchers also take into account the various ASM pit geometries [8] with just Cerit [206], Eksi [272], Mai et al. [12, 13] and Xiang [274] investigating pits other than the ellipse and hemisphere shapes.

It can therefore be concluded from the present literature that a numerical model can be created and using this, perform numerical simulations to accurately model formation and growth of pits with various geometries. This approach seems to be a better concept to understand the transition from pitting corrosion into hydrogen assisted stress corrosion cracking. As seen from the literature review, the individual aspects such as stress or stain locations in various pit geometries, hydrogen diffusion or hydrolysis in pit are investigated but have not yet been combined. As an initial goal, such modelling techniques should provide a deeper insight into where in the various pit geometries crack initiation might occur, as due to the small geometries and limits in measurement techniques, this is currently difficult to predict. The first application of such modelling might be applied to various SMSS components in offshore and maritime industries, as for instance flowlines. With continuous further development, such models may provide an increased understanding of the pit to crack transitions and finally, may assist in developing sufficient life cycle engineering to prevent failure over long-term service of respective components.

3.2 Research Goals

For the reasons stated above, the main aim of this work is to provide some further fundamental steps into numerical modelling of pitting corrosion in terms of strain (and stress) distributions and in terms of hydrogen concentrations developed in such pits. As an approach towards this, it is reasonable to create a numerical model to approximate various idealised pit geometries. For this, the NACE [289] standardised SSRT specimen has been selected. Figure 3.1 provides an overview of the parameters investigated during this work.

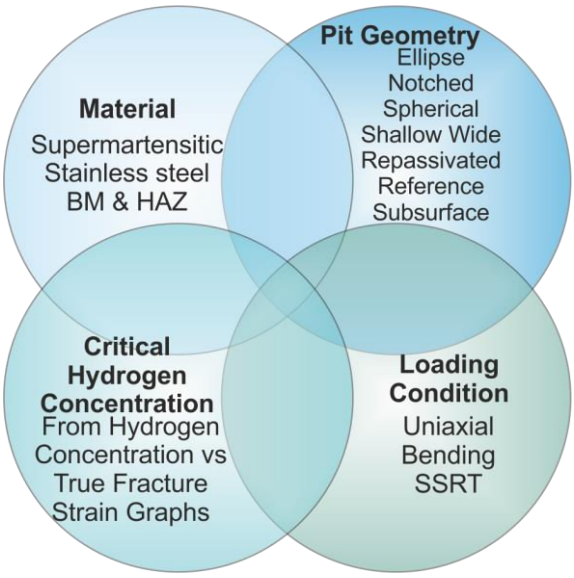

Figure 3.1: Investigated parameters.

This work can be divided into the four main components seen in Figure 3.1, which corresponds to the extends three local parameters affecting HAC in Figure 2.31:

- Material,
- Pit geometry,
- Loading condition and
- Hydrogen concentration.

The current work is located in the intersecting region of all four investigated parameter circles in Figure 3.1.

The design of experiments methodology, developed by Taguchi, was incorporated into this work to some extent. The design of experiments method is a structured approach in order to collect output data by varying key input variables to a system. The output data can be analysed and approximate models in order to predict outputs as a function of inputs can be determined [290]. This method was utilised by investigating all pit geometries in the first stage of this work and from these results determining the pit geometries with the highest,

lowest and average strain values. Only these three pit geometries were investigated in the following two stages. Additionally, various boundary conditions were investigated in stage two of this work and the boundary condition which was determined to be most similar to real life applications, from those boundary conditions investigated in this work, was chosen to be investigated in the final stage of this work.

Pit geometry

These shapes and dimensions are based on the standard pit shapes in the ASM corrosion handbook [8] and work conducted by Mai et al. [12]. The repassivation pit is however based on research conducted by Cerit [275], and Mehlich [291], and occurs when corrosion stops for some time but then conditions change, causing a new pit to form at the bottom of the previous pit. This new pit formation may be due to a limited time for repassivation and this work investigates which conditions of local hydrogen production within the pit and additional mechanical loading may result in HASCC starting from such normally quite deep pits.

The reference pit was created to a specific geometry to investigate the impact the pit mouth diameter and pit depth have on the stresses and strains around the pit. As seen in Figure 3.2, all the pit geometries are idealised versions.

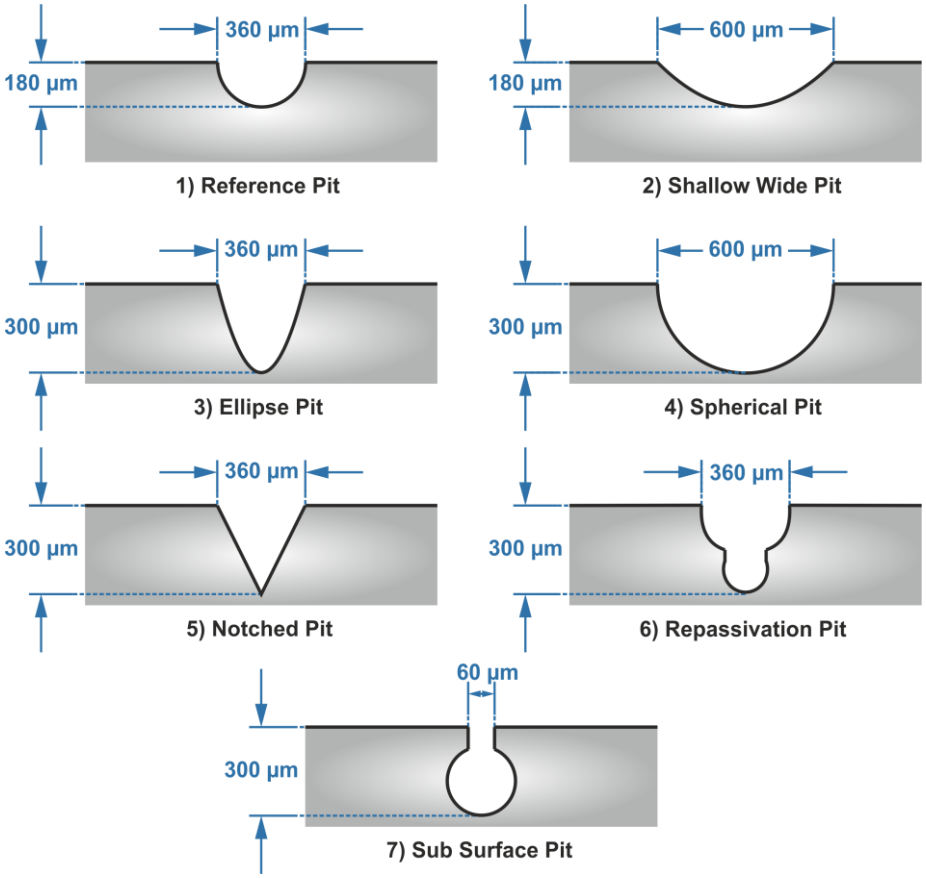

Figure 3.2: Pit geometries [8], [12] and [275].

Loading condition

Uniaxial loading shows a tensile test which is a standard test in engineering to provide standard data such as the ultimate tensile strength and to generate stress-strain curves. In this work a uniaxial load was applied to the model for the first and final stages. In the first stage of this work a strain rate of 1×10^{-6} mm/s was applied and in the final stage three strain rates of 1×10^{-5} mm/s, 1×10^{-6} mm/s and 1×10^{-7} mm/s were applied. Time dependent pit formation and growth was however not included in this work.

The bending loading condition was developed in order to investigate how the material behaves such as when a SMSS pipeline is laid from a reel on a vessel to the seabed or a pipeline is resting on an uneven seabed. A real pipeline section was not investigated however, the same standardised NACE specimen used in the uniaxial loading condition was also subjected to the bending loading condition. This was to investigate if the local stresses and strains inside the same pit geometry develop differently when a uniaxial or bending loading condition is applied.

Crack criterion

The hydrogen concentration used in this work is also based on previous work by Viyanit [16], which is based on work by Böllinghaus et al. [175]. This work, however, investigates the application of a normalised hydrogen concentration to various boundary conditions and the previous work investigated the actual hydrogen concentration dissolved in the various weld microstructures.

Hydrogen Assisted Cracking (HAC) is time based and involves local interaction between hydrogen concentration and strain distribution. This work however did not model increased hydrogen absorption due to increased strain with time. As a criterion for potential crack initiation the failure criteria of the material is required for the simulation in order to determine when crack initiation will occur, Figure 3.3.

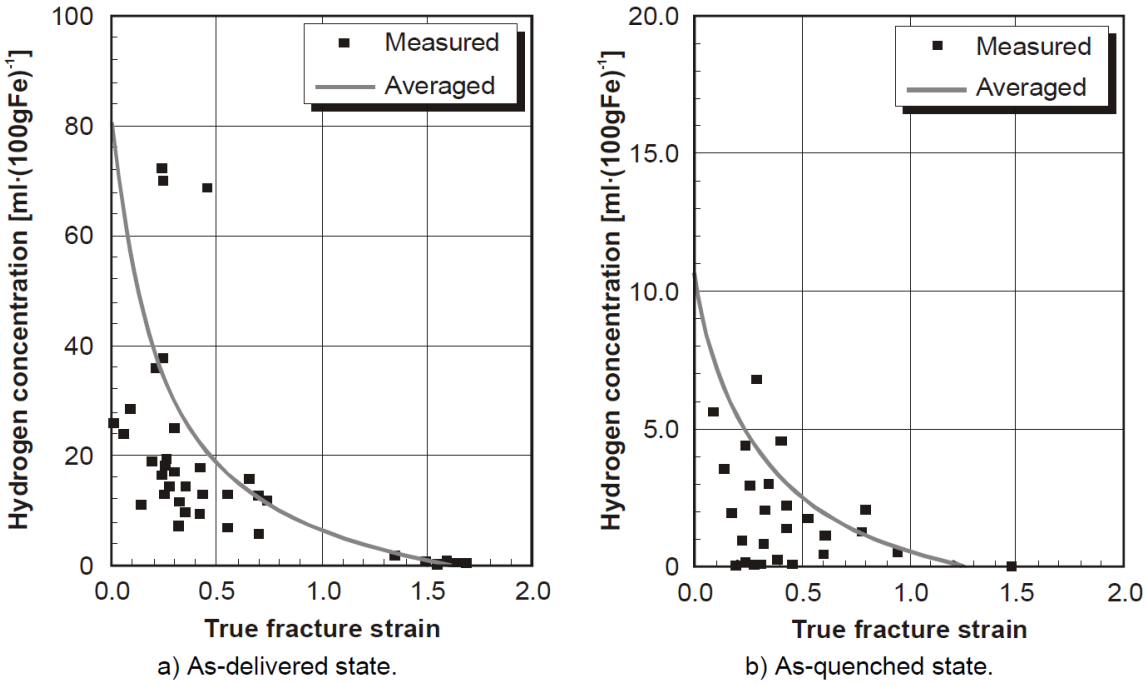

Figure 3.3: Critical hydrogen concentration vs true fracture strain of SMSS for a) As delivered and b) As quenched states [16].

As previously shown in earlier research by Viyanit [16] and Böllinghaus et al. [175] and also as an overall summarising approach, the degradation of the ductility represented by the various points can be approached using the graphs in Figure 3.3. This can also be expressed in equation form [16], with Equation (3.1) used for the as delivered state and Equation (3.2) used for the as quenched state:

$$[HD]_{crit} = 64.2490exp(-4.5 \cdot \varepsilon_{true}) - (9.9447 \cdot \varepsilon_{true}) + 16.3060 \quad (3.1)$$

$$[HD]_{crit} = 6.3410exp(-5.2 \cdot \varepsilon_{true}) - (3.5953 \cdot \varepsilon_{true}) + 4.5320 \quad (3.2)$$

4 Developing the Finite Element Model

The use of numerical methods and geometric modelling are increasing popular in various industries, such as maritime, offshore, oil and gas etc. The main reason being, it is becoming cheaper, faster and more accurate to utilise the Finite Element Method (FEM) that it is to do laboratory experiments [292]. In this work, the commercially available finite element program “ANSYS” is utilised to determine the interaction between local strain and hydrogen in a supermartensitic stainless steel exposed to a bulk electrolyte. This chapter describes the principle procedures of the finite element method using the direct method to couple structural and diffusion analyses to develop a numerical finite element model.

The nodes and elements are essential parts of building a finite element model and before meshing can begin the element type must be defined. In order to select a suitable element type, the geometry of the model and the boundary conditions must be considered. As this work investigates both a displacement force and a concentration of hydrogen being applied to a model, the coupled field analysis model in ANSYS can be used for simulations. The coupled field analysis combines analyses from different engineering disciplines and physics fields which may interact to solve a global engineering problem. Coupled analysis is when the input of one field analysis is dependent on the results from a different analysis. The process for a coupled field analysis depends on the fields being coupled, but these methods can be divided into two distinct methods, as described below:

The Sequential Method involves two or more sequential analyses, all belonging to different fields. The results from one analysis can be applied as loads to another analysis and therefore the fields are coupled. This is carried out by creating files which prepare the single mesh for a given analysis. The database is then configured to perform a solution. A new analysis file is then read into the database where the coupled field loads are transferred, and the second analysis is solved. Coupling occurs by issuing commands to read the coupled load terms from one analysis to another. This occurs across a node-node similar mesh interface. An advantage to the sequential method is that it is more efficient and flexible as the two or more analyses can be performed independently of each other.

The Direct Method involves just one analysis which uses a single coupled field element type. This element type contains all the necessary DoF necessary for the complete analysis. Coupling is achieved by calculating element matrices or element load vectors which contain all the necessary terms. An advantage to the direct coupling method is that the elements are specifically formulated to directly solve the coupled field interactions.

In this work the direct method was used for simulating the specimen undergoing an SSRT test surrounded by a bulk solution. This direct method used the structural- diffusion coupling mode selected in ANSYS.

4.1 General Remarks

As mentioned, SMSS will be the material investigated during this work. The chemical composition for the material investigated in this work is shown in Table 4.1 and is based on research performed by Viyanit [16].

Table 4.1: Chemical composition of supermartensitic stainless steel used in this work [16].

	Composition (wt.-%)						
	C	**Cr**	**Ni**	**Mo**	**Mn**	**S+P**	**N**
Base Metal	0.015	12.35	4.48	1.41	1.11	0.026	0.013

As mentioned previously in Chapter 2 the HAZ is the region where it is most likely cracks will occur from a pit in welded SMSS. This HAZ region along with the largest region in a welded pipeline, which is the BM, will be investigated in this work. The material used in this work is also the same material used in previous research by Viyanit [16]. The mechanical properties used in the previous research are shown in Table 4.2.

Table 4.2: Material properties used in this work.

	Ultimate Tensile Strength (MPa)	Yield Stress (MPa)
Base Material	870	770
Heat Affected Zone	1060	870

The information from bilinear stress strain graphs was used in the simulations. These bilinear stress-strain graphs are also from Viyanits previous research [16]. Additionally, a density of $7.9025*10^{-3}$ g/mm^3, Poisson's ratio of 0.27 and Young's modulus of 210 GPa are also applied to all models, from Viyanits previous research [16]..

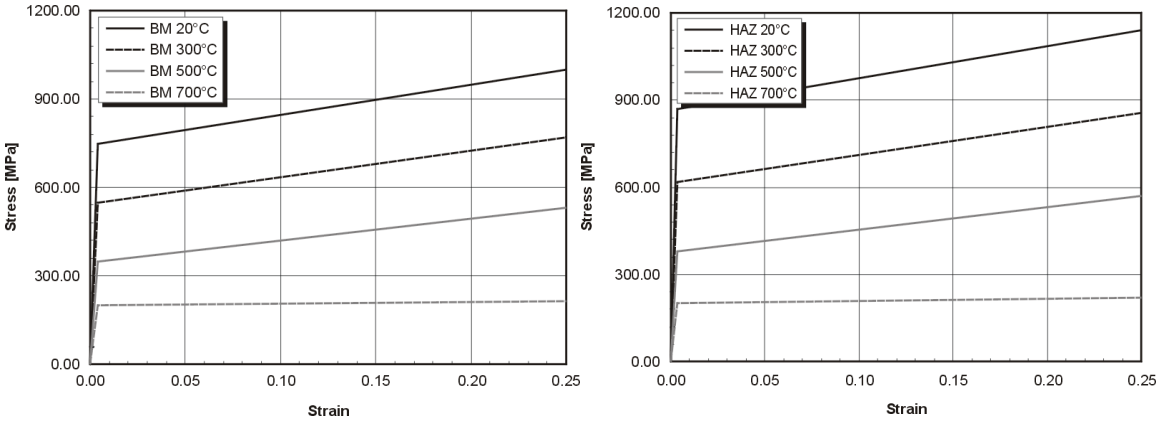

Figure 4.1: Bilinear stress strain graph of base material (L) and heat affected zone (R) used in this work [16].

Some basic aspects must be clarified before describing the modelling process used in this work in more detail:

1. This work has been divided into three different stages. The first stage consists of a simulated structural analysis in both 2D and 3D for the BM and HAZ to determine the regions of maximum total true strain in the x-direction in the different pit geometries at a constant strain rate. The second stage is comprised of a simulated hydrogen diffusion analysis where the 3D HAZ pitted sample was exposed to a bulk solution at several different boundary conditions. The third and final stage is a combination of the previous two stages where the unpitted 3D HAZ model was exposed to the same constant strain rate as in Stage 1, while in the presence of the same bulk solution from Stage 2. This simulates a slow strain rate test with the test specimen surrounded by a bulk solution, for example seawater. In this final stage an approximation of pit growth was also simulated, and the region of high local strains and highest normalised hydrogen concentrations were also determined.
2. The material properties used in these simulations are from the BM and HAZ of supermartensitic stainless steel. It has been explained in Chapter 2 that the HAZ is the area in a welded material most susceptible to cracking. Therefore, this HAZ region and also the BM, which is the largest region of a pipeline, were taken for numerical analysis, for both 2D and 3D models, in this work.
3. The calculation of the critical hydrogen concentration (HD_{crit}) is based on the formulas previously used by Viyanit [16], Equations (3.1) and (3.2) in Section 3.2. In these formulas the true total mechanical strain is used to calculate the critical hydrogen concentration needed for crack initiation for all nodes in the area of interest for all time steps

4. The 2D and 3D, both unpitted and pitted, models, are created using the same process. This ensures limited variation between models. This ensures the only (geometrical) differences are the pit shapes.
5. The element shapes used in this work were triangular shaped elements for 2D analysis and tetrahedral shaped elements for 3D analysis. There are no restrictions for choosing element shapes, however brick shaped elements are less stiff in bending than tetrahedral shaped elements. Tetrahedral shaped elements were chosen due to the complex geometries around the pit region where it proved very difficult to mesh with brick shaped elements, but tetrahedral shaped elements provided an adequate mesh.
6. In finite element modelling the size of the mesh can determine the accuracy of the results. Therefore, in the specimen modelled in this work the finest mesh is located in the region closest to the pit, with the mesh getting more coarse the further away from the pit. This has the advantage of using less nodes than if the same fine mesh was used for the full model, which in turn reduces the computing time of the simulations, while still maintaining accuracy of results. This mesh was chosen as HAC is a result of the local interaction between the microstructure and the local mechanical load, while being exposed to a hydrogen concentration, as shown in Figure 2.11 in Section 2.2.3.

4.2 Modelling and Meshing of the Models

The model used in all of the simulations in this work was created based on the recommendations in NACE TM0177-96 for the testing of metals subjected to tensile stresses for resistance to cracking failure in low pH aqueous environments containing H_2S [289]. This standard contains four different test methods:

- Method A- The standard tensile test,
- Method B- The standard bent beam test,
- Method C- The standard C-ring test and
- Method D- The standard Double Cantilever Beam (DCB) test.

From these four methods, Method A has been chosen for applying a uniaxial load in this work and the subscale specimen from NACE TM0177-96 is the specimen modelled. For bending, Method B should be chosen along with the corresponding specimen but the subscale specimen from Method A was again used for bending to be able to directly compare between the two loading conditions. This provides information about the mechanical load distribution in the uniaxial specimens and bending specimens and a direct

comparison between the difference in the magnitudes of these loads and also where the highest strained regions for both loading conditions are located. The NACE TM0177-96 subscale specimen consists of a gauge section of diameter 3.81 mm and a length of 25.40 mm. The overall length of the specimen is 78 mm with head diameters of 8.0 mm. It is recommended that the radius of curvature at both of the ends of the gauge section is a minimum of 15.0 mm to avoid high stress concentrations in this region. These specifications can be seen in a drawing of the specimen in Figure 4.2.

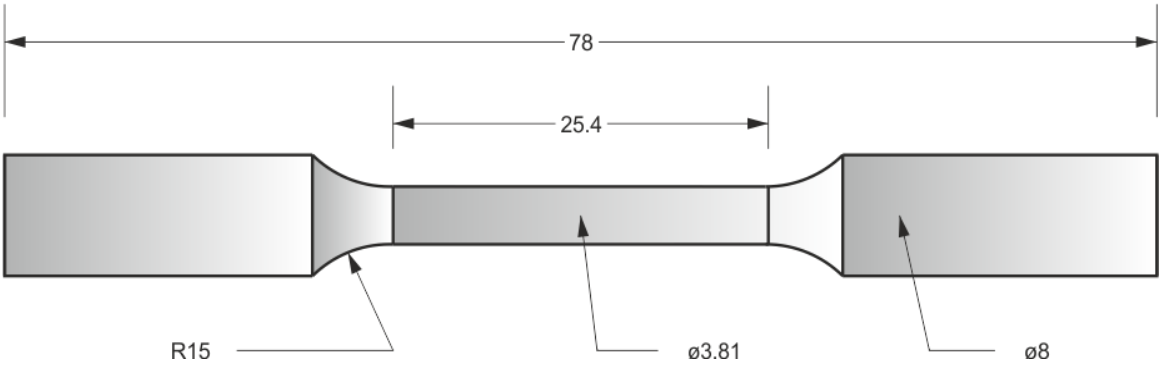

Figure 4.2: NACE TM0177-96 Subscale Specimen [289].

The first step in this work was to create a finite element model according to the dimensions of the standard specimen in Figure 4.2. There are two commonly used methods in order to create a finite element model and they are:

- Top Down Modelling and
- Bottom Up Modelling.

Table 4.3 provides and overview of both the advantages and disadvantages of these two commonly used methods.

Table 4.3: Advantages and disadvantages of top down and bottom up modelling [293].

Advantages	Disadvantages
Top Down Modelling	
Sometimes the only feasible way to model 3D solid volumes with complex geometries.	User must have a good understanding of meshing, otherwise ANSYS may not be able to generate the mesh.
Low level of user data input required.	For simple models, top down modelling may be laborious.
Features such as extrusion, dragging and rotation are possible. These are not possible when working directly with nodes and elements.	Large amounts of CPU are required.
Areas or volumes can be easily altered using Boolean operations to achieve the desired shape.	
Bottom Up Modelling	
User has complete control of placement and numbering of nodes and elements.	Extremely tedious for solving real engineering design applications, especially if 3D is required
For simple problems, this is the quickest way to generate a mesh	Design optimisation and modification of meshing elements is quite difficult.

In this work the top down method was used. This is mainly due to the complex geometry of the pits, which will be modelled not only in 2D but also in 3D. The major advantage of using the top down method is that the finite element mesh can be very fine around the area of interest, where the pits are located, while the rest of the model has a relatively coarse mesh. In this work, due to the geometry of the specimen, symmetric boundary conditions can be applied in order to achieve the same results using less nodes and elements. Symmetric boundary conditions are used when the geometry, material properties and loading conditions in a model have mirror symmetry. In order to model this tensile test, the full specimen in Figure 4.2 is not required to be modelled, only one quarter of this specimen is sufficient. However, for the bending loading condition, a half specimen must be modelled in order to accurately apply the loads. The quarter model of NACE TM0177-96 in 2D, which the uniaxial load will be applied to is shown in Figure 4.3 and the half model, which the bending load will be applied to, is shown in Figure 4.4**.**

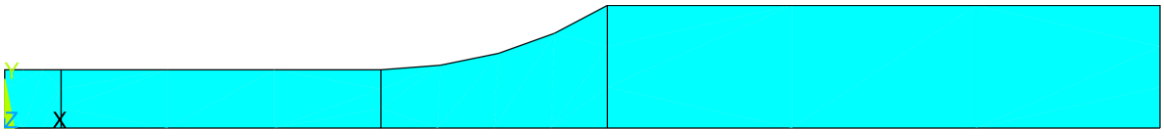

Figure 4.3: 2D quarter model of NACE TM0177-96 in 2D.

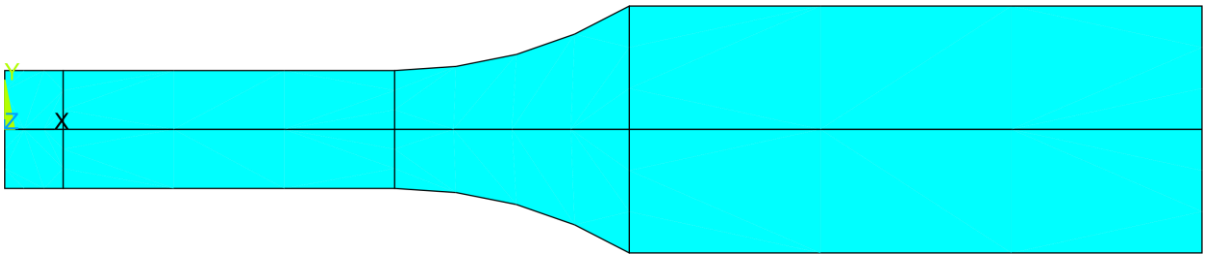

Figure 4.4: 2D half model of NACE TM0177-96 in 2D.

In order to obtain the desired accurate results, the correct elements with the appropriate Degrees of Freedom (DoF) must be chosen. For the 2D structural analysis PLANE183 triangle elements were chosen and applied to the NACE TM0177-96 specimen in Figure 4.3 above and the mesh was generated. PLANE183 elements are higher order 2D, 8 or 6 node elements, Figure 4.5. Advantages of this element type is that it is a higher order element and is very capable of modelling irregular meshes with minimal to no reduction in accuracy of results. Each node of this element has two degrees of freedom- translations in the nodal x- and y-directions. This element may be used as a plane element (plane stress, plane strain and generalised plane strain) or as an axisymmetric element and is capable of handling large deflections and large strain capabilities.

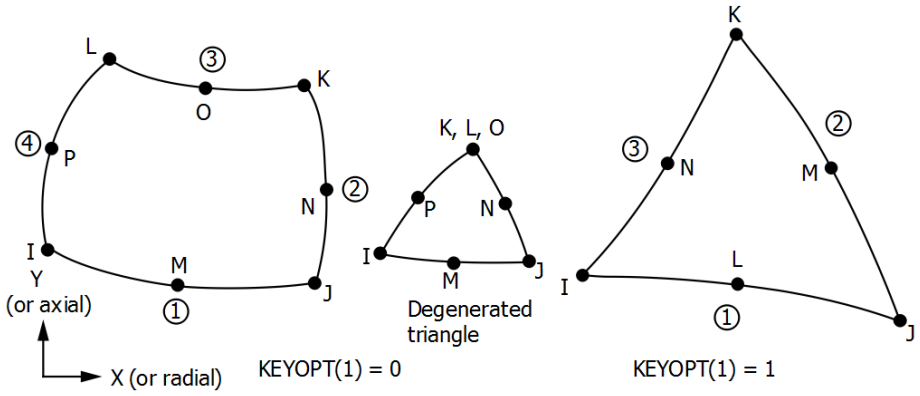

Figure 4.5: PLANE183 Elements [294].

As explained in Section 4.1, the size of the mesh determines the accuracy of the results but also if the elements are lower or higher order elements. PLANE183 elements are higher order elements, due to the presence of midside nodes, which leads to small errors for the solution if all parameters (geometry, boundary conditions, materials) are suitably smooth. In the meshed quarter model, there are 3,586 nodes and 1,697 elements. This model is split into 3 different regions with varying mesh size in each, Figure 4.6. The smallest mesh size is 0.1 mm and is located at the centre of the full model. The rest of the gauge length is meshed in 0.3 mm size elements and the rest of the model has the largest size mesh of 1 mm elements.

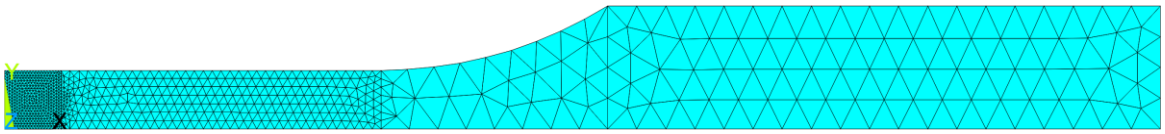

Figure 4.6: Meshed 2D quarter model of NACE TM0177-96.

The pit shapes being investigated were removed from the submodel and the submodel was meshed. The same mesh from Figure 4.6 was used for the submodel mesh, however the mesh size was 0.01 mm in the region directly beside the pit and 0.03 mm in the next region. An example of a pit (ellipse) in a submodel with the mesh applied is shown in Figure 4.7. The submodel with the mesh applied for all pits in 3D can be seen in in Figure 4.12.

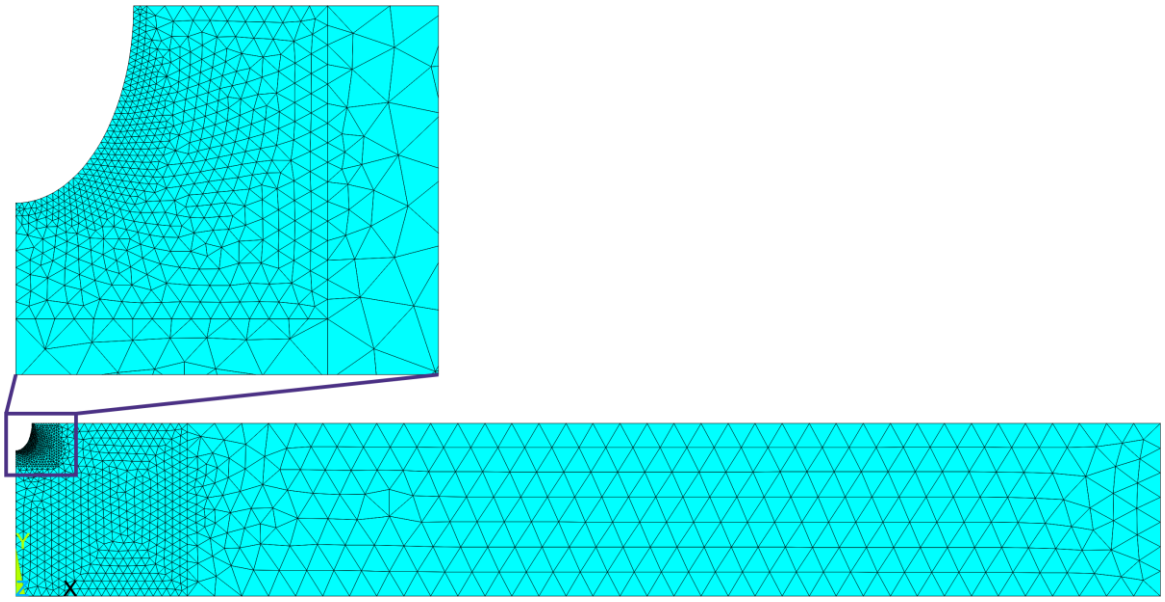

Figure 4.7: Meshed 2D uniaxial loading submodel with ellipse pit.

The number of nodes and elements in each submodel with a different pit geometry located in the centre, and also the unpitted submodel for comparison, is shown in Table 4.4.

Table 4.4: Number of nodes and elements in the unpitted 2D uniaxial submodel and also with the seven pit geometries.

Pit Geometry	Number of Nodes	Number of Elements
Unpitted	3,102	1,481
Reference	5,363	2,590
Shallow Wide	5,509	2,660
Ellipse	5,549	2,680
Spherical	5,468	2,637
Notched	5,345	2,580
Repassivation	6,055	2,932
Subsurface	5,848	2,821

After the uniaxial loading conditions were modelled, the next step was to generate the mesh for the bending model. The resulting meshed model is shown in Figure 4.8 and this meshed half model contains 6,973 nodes and 3,378 elements. Triangular shaped elements are less stiff in bending than square shaped elements. However, this is a higher order element type and due to the presence of midside nodes the accuracy can still be maintained and any differences in results are minimal.

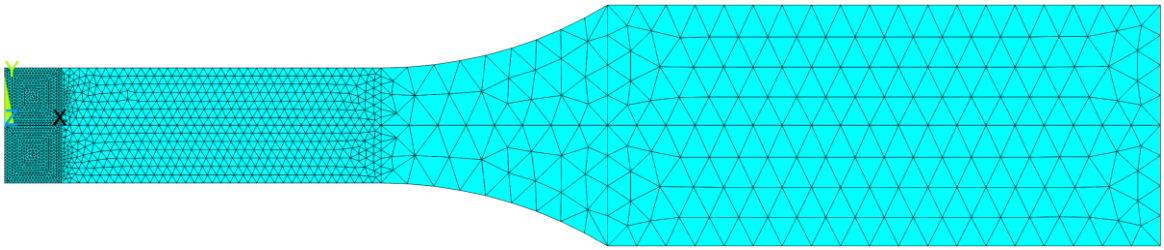

Figure 4.8: Meshed half model of NACE TM0177-96 in 2D.

After the 2D bending simulation was completed on the unpitted half models, the same pits and mesh used in the 2D uniaxial loading condition were then included in the 2D bend submodel. The number of nodes and elements in the submodel with different pit geometries located in the centre of the model, also the unpitted submodel for comparison, are shown in Table 4.5.

Table 4.5: Number of nodes and elements in the unpitted 2D bending submodels and also with the seven pit geometries.

Pit Geometry	Number of Nodes	Number of Elements
Unpitted	6,973	3,378
Reference	8,376	4,079
Shallow Wide	8,523	4,150
Ellipse	8,563	4,170
Spherical	8,491	4,132
Notched	8,359	4,070
Repassivation	9,065	4,420
Subsurface	8,846	4,303

The modelling and simulation procedure is the same for 3D as for 2D, however some changes need to be implemented to account for the additional z-direction. Another element type with the desired DoF must be selected for meshing in 3D. SOLID187 elements were chosen as this element is suitable for modelling irregular meshes, is a higher order 3D, 10 node element with each node having three degrees of freedom at each node- translations in the nodal x-, y- and z- directions. This element is capable of large strain and deflections, and also plasticity [294]. The geometry, node locations and coordinate system for the SOLID187 element are shown in Figure 4.9.

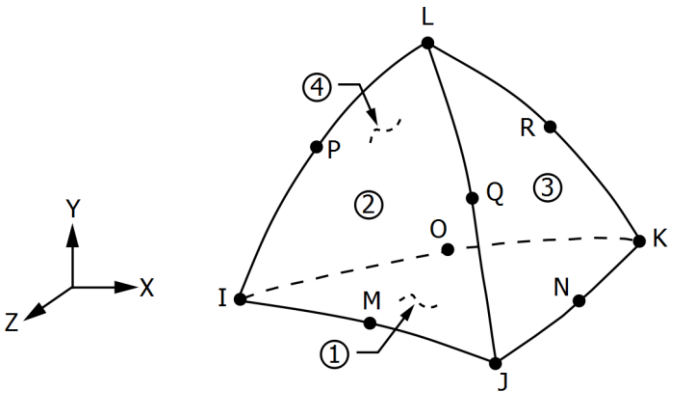

Figure 4.9: SOLID187 Element [294].

A similar mesh as used in the 2D model was applied to the 3D model, Figure 4.10. In the meshed 3D one eight model there are 9,6619 nodes and 6,6993 elements. The model is designed so the model is located in the positive axis direction for all three axes.

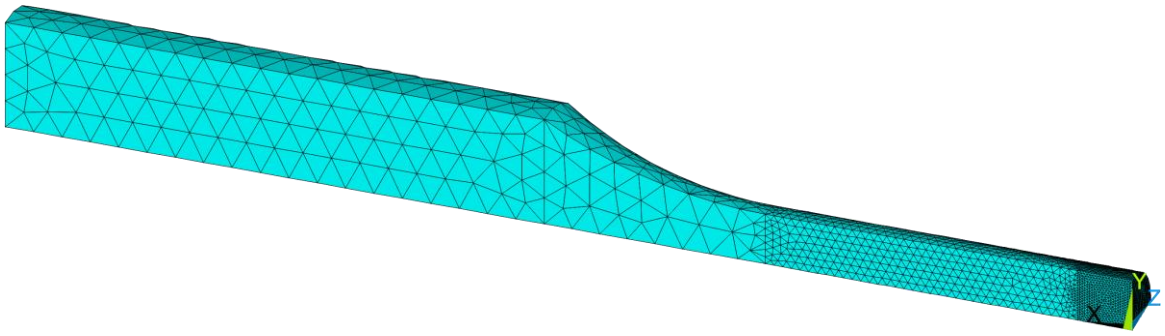

Figure 4.10: Meshed 3D one eight model of NACE TM0177-96.

After the unpitted 3D uniaxial load simulations were complete, the same pits used in the 2D models were also used in the 3D models and these seven different pit geometries are shown in Figure 4.12. However, extra volumes had to be created in the submodel to achieve smooth transitions between the various mesh sizes, Figure 4.11.

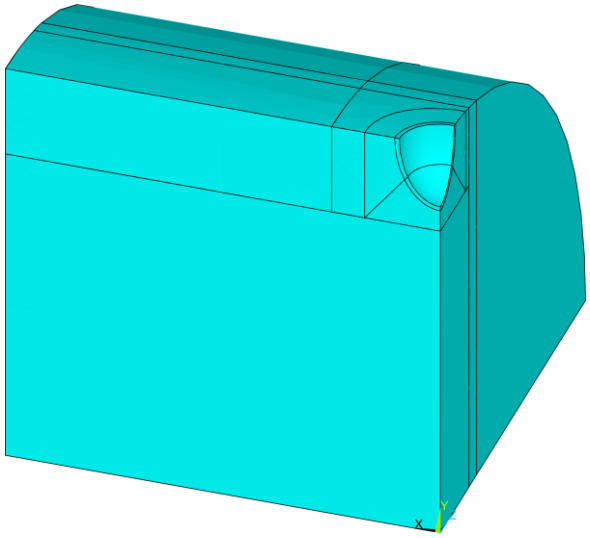

Figure 4.11: Additional volumes in the centre region of the 3D NACE TM0177-96 submodel.

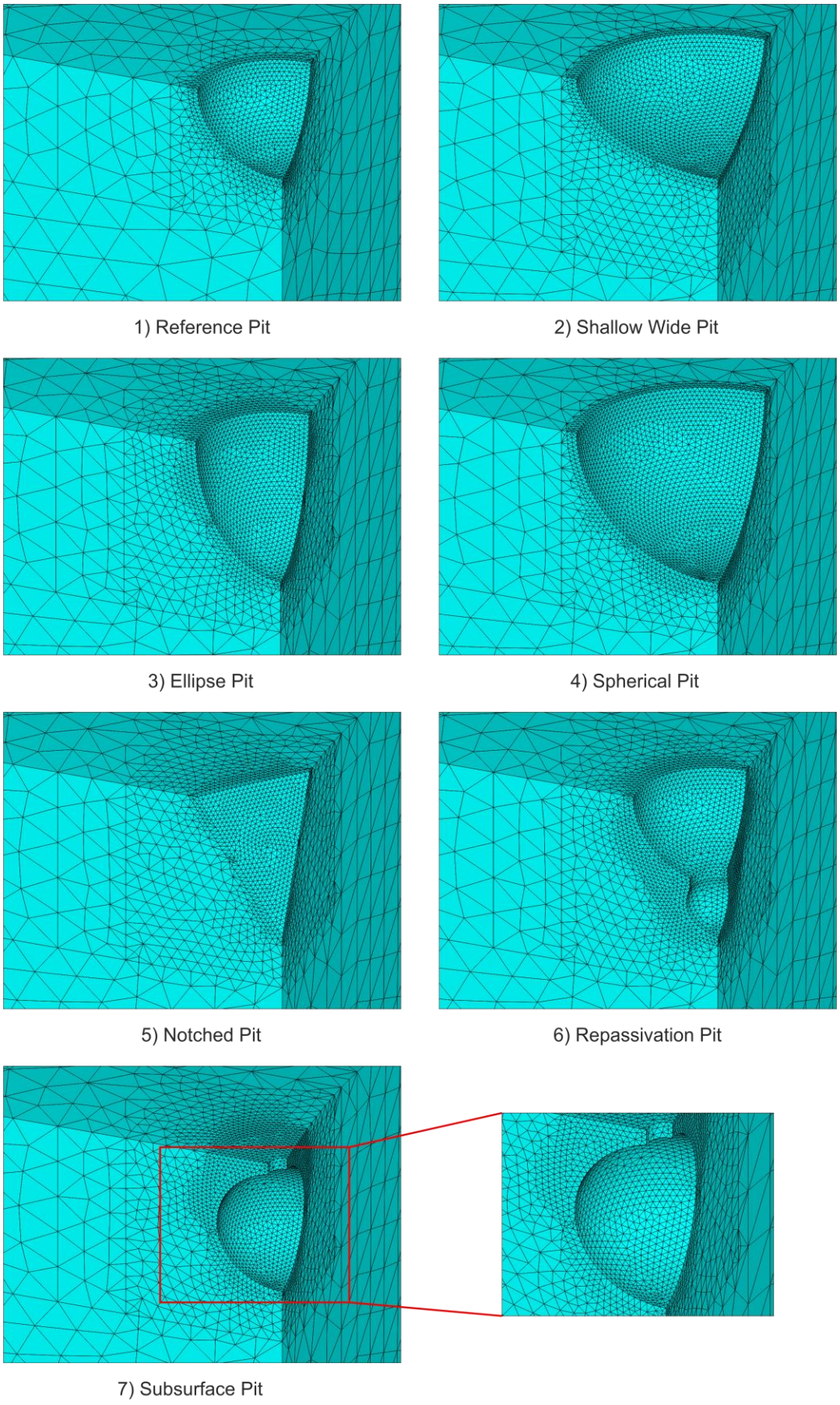

Figure 4.12: Meshed 3D pits.

An example of a pit (ellipse) in a submodel with the mesh applied is shown in Figure 4.13. The volumes located directly in the pit region have a mesh of 0.01 mm, the same as in the 2D model. The circular region behind this volume has a mesh of 0.03 mm, again as in the 2D model. The rest of the volumes located in the top right figure in Figure 4.13 were meshed with 0.1 mm elements, similar to the 2D model, with the remaining length of the specimen meshed with 0.3 mm elements. This ensures the 3D models are created in a similar manner to the 2D models to make direct comparison easier.

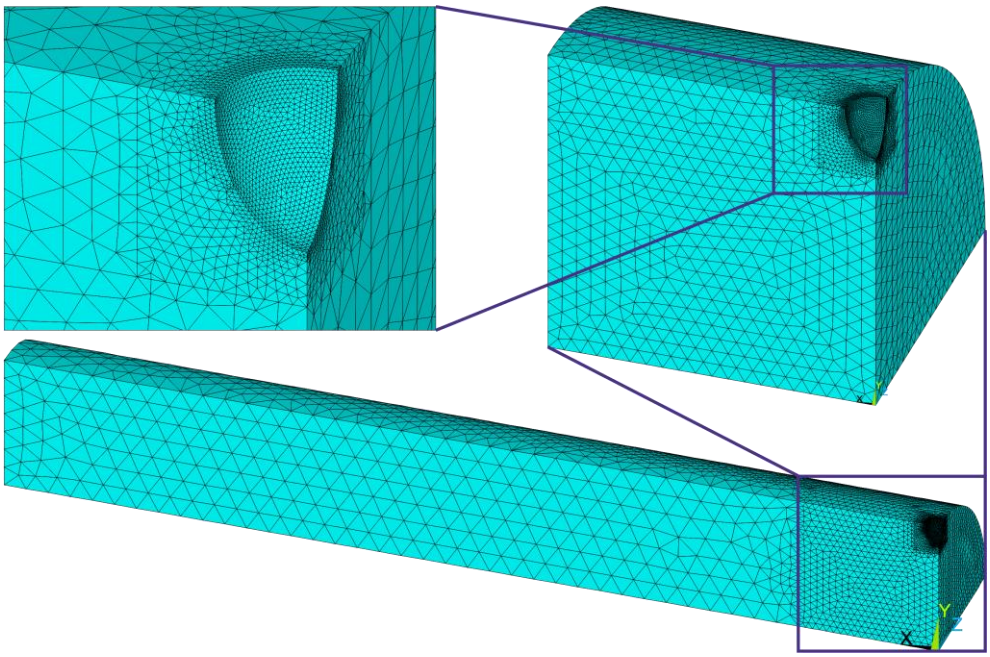

Figure 4.13: Meshed 3D uniaxial loading submodel with ellipse pit.

The number of nodes and elements in each 3D uniaxial submodel with a different pit geometry, and also the unpitted submodel for comparison, is shown in Table 4.6.

Table 4.6: Number of nodes and elements in unpitted 3D uniaxial submodels and also with the seven pit geometries.

Pit Geometry	Number of Nodes	Number of Elements
Unpitted	92,246	64,417
Reference	127,892	88,846
Shallow Wide	162,901	113,999
Ellipse	160,854	112,633
Spherical	167,405	116,663
Notched	150,974	105,872
Repassivation	182,783	128,982
Subsurface	182,359	128,408

As carried out previously for the 2D model, a larger model also had to be created for the 3D bending simulation. This model is a quarter model of the full 3D NACE TM0177-96 specimen. The same elements used in the 3D uniaxial loading condition, SOLID187, were applied to the 3D bending quarter model. The resulting meshed model is shown in Figure 4.14. In this meshed 3D unpitted quarter model there are 187,301 nodes and 132,232 elements.

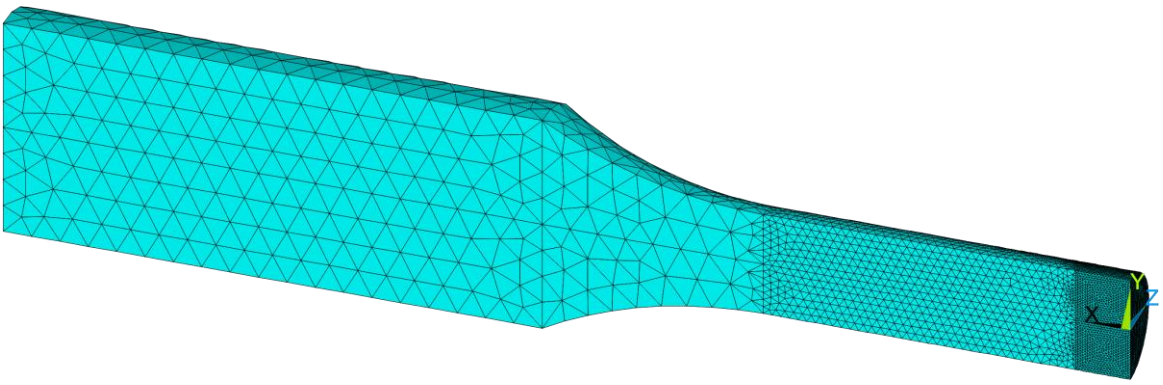

Figure 4.14: Meshed one quarter model of NACE TM0177-96 in 3D.

After the 3D bending simulation was completed on the unpitted quarter models, the same pits and mesh used in the 3D uniaxial loading condition were then included in the 3D bend submodel. The number of nodes and elements in each 3D bending submodel with a different pit geometry, and also the 3D unpitted bending submodel for comparison, are shown in Table 4.7.

Table 4.7: Number of nodes and elements in 3D bending submodels with the seven pit geometries.

Pit Geometry	Number of Nodes	Number of Elements
Unpitted	179,229	127,228
Reference	226,203	159,534
Shallow Wide	259,742	183,604
Ellipse	262,982	186,200
Spherical	266,217	187,732
Notched	252,161	178,745
Repassivation	284,784	202,451
Subsurface	275,857	195,492

For the diffusion analysis, the material properties and the mesh applied to these models are the same as described above for the structural analysis modelling. However, a different

element type has to be applied as SOLID187 elements are unable to perform diffusion analysis. Instead, SOLID227 elements were used, which are 3D 10 node coupled- field solid elements with each node having up to five DoFs and concentration. This element also has structural capabilities including elasticity, plasticity, large strain and large deflection [294]. The Structural- Diffusion key option was chosen for analysis. The geometry, location of nodes and the coordinate system for SOLID227 are shown in Figure 4.15.

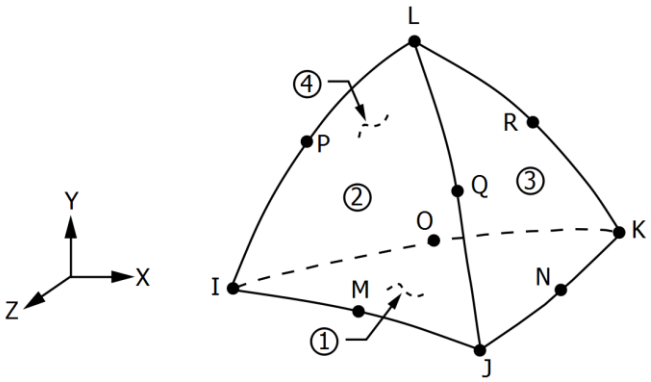

Figure 4.15: SOLID227 Element [294].

Only the pitted 3D one eight models, Figure 4.13, were investigated, however, as 3D models provide more accurate representations of the diffusion of hydrogen through the material for each step. Additionally, due to the curved geometry of the specimen modelled, the 3D representation is considered more accurate regarding applying hydrogen concentrations in the various boundary conditions. They are also more accurate in showing the locations where the maximum concentration of hydrogen will be present, especially in the regions around the pits. The submodels were chosen as the boundary conditions applied to these models would have the same hydrogen presence in the region around the pit, which is the region of interest in this work, as for the same boundary conditions if they were applied to the quarter models. This creates a more optimised model which produces the same results but with a reduction in computational time. The pit shapes modelled are the same as previously modelled, Figure 4.12.

4.3 Boundary Conditions and Loads Applied

4.3.1 Structural Analysis

Structural analysis is divided into uniaxial and bending loading conditions, HAZ and BM material properties and unpitted and pitted models for both 2D and 3D. The main aims of this stage are:

- To determine if a submodel is sufficient to achieve the same results as a full or smaller model,
- To see the influence the various pit geometries have on strains in the model and
- To compare the results of 2D simulations to 3D simulations, in particular the location of the highest strained regions in the various pits.

In this work the BM and HAZ of a SMSS are investigated. The material properties have been explained in Section 4.1 and these are applied to the all models. Certain assumptions were also applied to the models, including: it was assumed to be a homogeneous material and the simulations were carried out at room temperature. As bilinear stress strain curves were used for this work, the BISO (Bilinear Isotropic Hardening Specifications) material model was used and plane stress is the element behaviour selected for investigation. The plane stress element behaviour has been used by previous researchers, including Mai et al. [12] and Wang and Han [273] who also investigated the presence of strains in 2D pitted specimens. The BISO material model was used as the graph for the material properties used are bilinear (two slope) true stress strain curves, Figure 4.1. This material model is slightly less accurate than, for example multilinear isotropic hardening. However, the BISO option is faster and the full stress strain curve for the material is not required as the stresses experienced in the model are not increasing far beyond the yield point and therefore a linear approximation of the true stress strain curve can be applied.

Once the material properties are applied, the boundary conditions must be fixed, and the desired load is then applied. For the structural analysis a tensile test is simulated, where a displacement is applied to the head end of the model. These loads are applied in a manner which results in 100% of the yield stress (770 MPa for the BM and 870 MPa for the HAZ) globally in the model. This represents the limit of performance of mechanical components as these are the maximum forces that can be applied without permanent deformation of the material. Additionally, 66% of yield for the HAZ material was also investigated for this stage of the work in accordance with ASME B31.1 [295], the results of which are in Appendix A. The displacement applied is determined by the number of time steps specified and the desired strain rate, in order to reach 100% of the desired yield stresses globally in the model. The strain rate was set to $1x10^{-6}$ mm/s, which is the critical strain rate for promotion of SCC in stainless steels in chloride environments [296], [8] and is recommended in NACE TM0177-96 [289]. There were 10 time steps used and these were divided into 100 substeps. A total displacement of 0.1096 mm was applied to the 2D HAZ quarter uniaxial model and a displacement of 0.809 mm was applied to the 2D HAZ

half bending model, as these values achieved 100% global yield stress in the models. While a total displacement of 0.0966 mm was applied to the 2D BM quarter uniaxial model and a displacement of 0.0984 mm was applied to the 2D BM half bending model. The same displacements were also applied to the 3D models to directly compare the 2D and 3D models as the only difference is the extra z-dimension and therefore also the element type.

The symmetric boundary conditions constrain the 2D uniaxial model in the x- (orange) and y- (green) directions at the centre of the model, Figure 4.16. However, for the 3D model a new symmetric boundary condition in the z-direction was also applied, Figure 4.17.

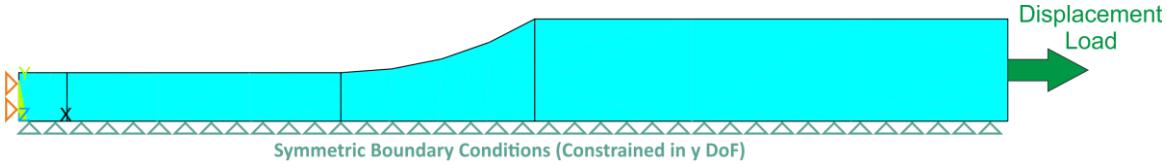

Figure 4.16: 2D quarter model with symmetric boundary conditions and uniaxial displacement applied.

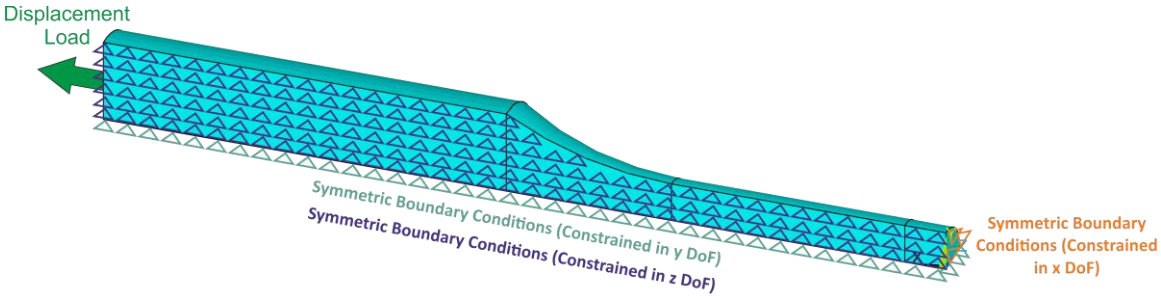

Figure 4.17: One eight model with symmetric boundary conditions and bending displacement applied.

The maximum component stress, principal stress and total mechanical strain (elastic and plastic strain) all in the models x-direction, including the node numbers where these occur, were recorded. As cracks grow perpendicular to the applied load, the most important loads to consider are those which cause crack initiation in the y-direction. These are the loads which are applied in the x-direction, therefore the total true strain in x-direction was investigated. The displacement values of the nodes at the end of the gauge length in the x- and y-directions were also recorded to a table.

The same material properties, mesh, symmetric boundary conditions and strain rate from the global model were then applied to the submodels. However, instead of applying a displacement to the end of the models, the x- and y displacement values from the same position on the larger models were applied to the submodels. The red line on the global models, Figure 4.18 and Figure 4.19, indicates the nodes where the x- and y displacement

values, and z- displacement for the 3D models, were recorded in order to apply these values to the nodes where the red line is located on the submodel. This ensures that the strain rate and loading conditions on the submodel are the same as on the global model, with the only difference being the geometry of the model. This was to investigate if a smaller submodel provides the same results as the larger model, using less nodes and elements and therefore also less computing time. In the meshed 2D submodel model there are 3,102 nodes and 1,481 elements where there are 9,2246 nodes and 6,4417 elements in the 3D submodel.

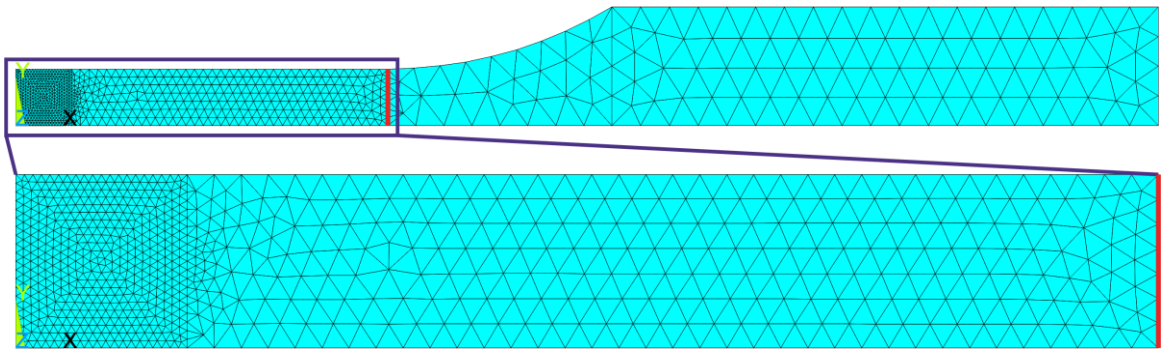

Figure 4.18: Meshed 2D quarter model (top) with submodel region (bottom).

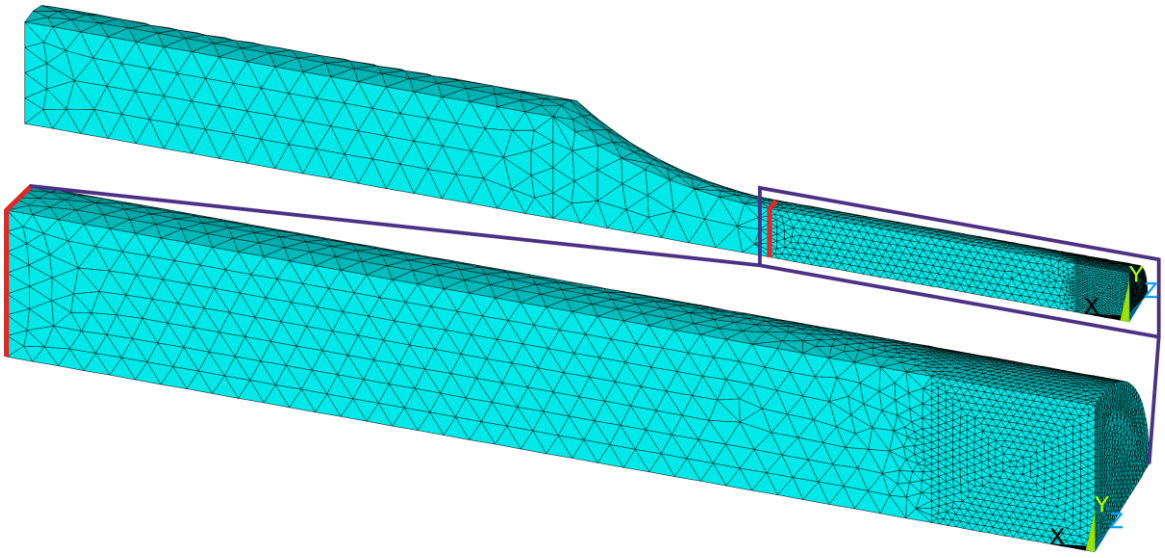

Figure 4.19: The meshed one eight model with the submodel region.

The location of the 2D and 3D submodels in comparison to the full NACE TM0177-96 specimen are shown in Figure 4.20 and Figure 4.21 respectively, with the boundary conditions and displacement applied. The 2D submodel boundary conditions are located in the same regions as the quarter model, Figure 4.16. and the 3D submodel boundary conditions are applied to the same regions as the 3D one eight model, Figure 4.17.

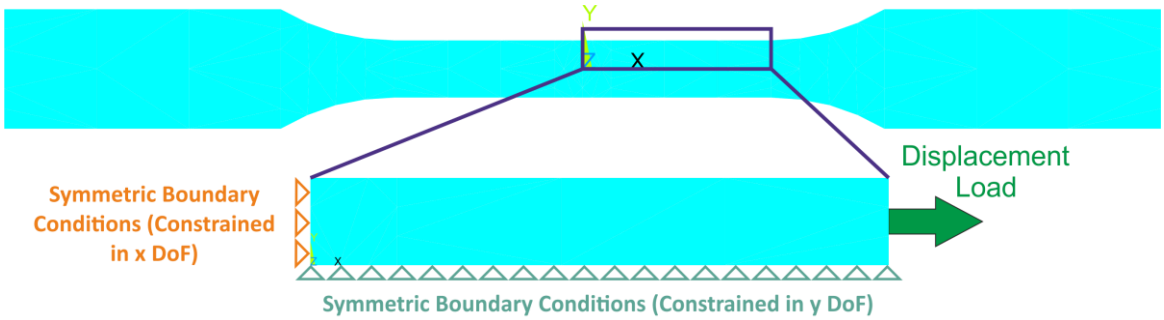

Figure 4.20: Full 2D NACE TM0177-96 specimen (top) with 2D uniaxial submodel and boundary conditions (bottom).

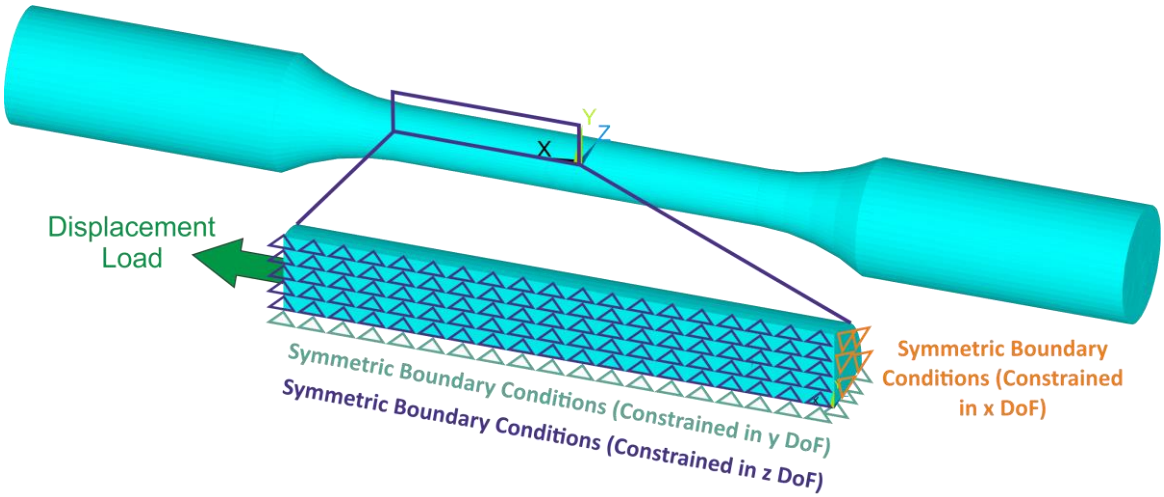

Figure 4.21: Full 3D NACE TM0177-96 specimen (top) with 3D uniaxial submodel and boundary conditions (bottom).

Once the 2D and 3D submodels with pits were created, the same material properties, boundary conditions and uniaxial loading conditions were applied as those applied to the unpitted 2D and 3D submodels. This ensures a direct comparison can be made between the unpitted and pitted uniaxial load models, as the only variable is the presence of a pit. The 2D and 3D models can also be compared as the only difference is the presence of an additional z-axis in the 3D model.

To investigate bending, symmetric boundary conditions were also applied to this model, in the x-direction but only at the centre of the model which constrains the centre of the model in the x-direction. The centre of the model must, however, also be constrained in the y-direction to avoid rigid body motion of the complete model when the bending load is applied in the -y-direction. Therefore, the node at the very centre of the model, location (0,0) is also constrained in the y-direction. The location of this node is shown in grey in Figure 4.22. For the 3D model no symmetric boundary condition in the y-direction was required. The centre of the model must be constrained, as for the 2D model, therefore, the nodes at

the very centre of the model along the neutral fibre are also constrained in the y-direction. The locations of these nodes are shown in grey in Figure 4.23.

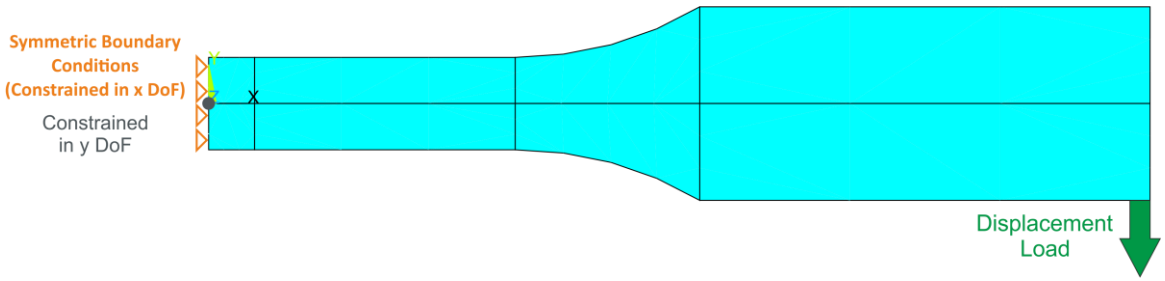

Figure 4.22: 2D half model with symmetric boundary conditions and bending displacement applied.

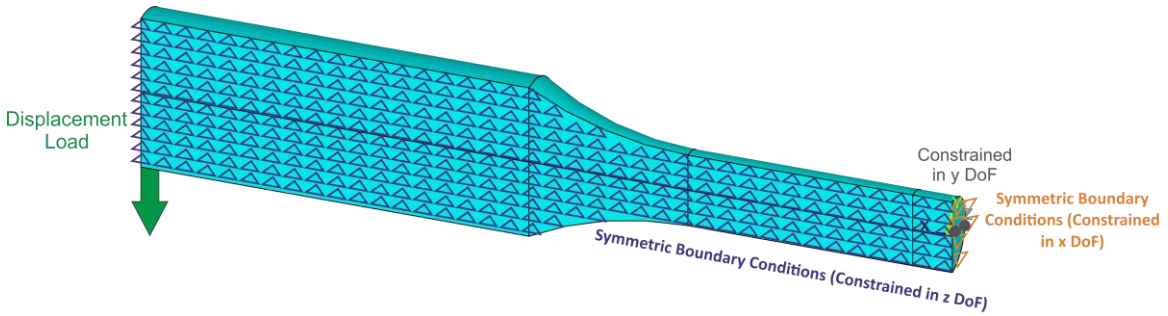

Figure 4.23: One quarter model with symmetric boundary conditions and bending displacement applied.

The loading condition in these bending models is a displacement applied to the nodes at the end of the head end of the model in a -y-direction [215]. This location was chosen to apply the load in order to create a resulting tensile load on the upper surface of the model. This is the region where the pits will be modelled, as for the uniaxial load models. As explained in Section 2.3.2 previously, the oxide layer on a model subjected to a bending load only buckles and does not crack in the compressive region. Therefore, the loads have been applied in order to create a tensile region on the surface in the area where the pits will be located.

The same number of time steps and strain rate applied to the uniaxial loading conditions were applied to the 2D and 3D bending loading conditions in order to reach 100% of the yield stress globally in the BM and HAZ 2D models.

The displacement values of the nodes located at the end of the gauge lengths in the 2D and 3D models in the x- and y-directions, and z-direction for the 3D models, were recorded to a table. These x-, y- and z-displacement values are then applied to the nodes located at the end of the submodel regions, as previously explained for the uniaxial submodels. In the meshed 2D submodel there are 3,102 nodes and 1,481 elements and the location of

this submodel in comparison to the full NACE TM0177-96 specimen is shown in Figure 4.24, with the boundary conditions and bending displacement applied. The submodel boundary conditions are located in the same regions as the 2D half model, Figure 4.22.

In the meshed 3D submodel there are 179,229 nodes and 127,228 elements and the location of the 3D bending submodel in comparison to the full 3D NACE TM0177-96 specimen with boundary conditions and displacement applied is shown in Figure 4.25. The submodel boundary conditions are located in the same regions as the 3D one quarter model, Figure 4.23.

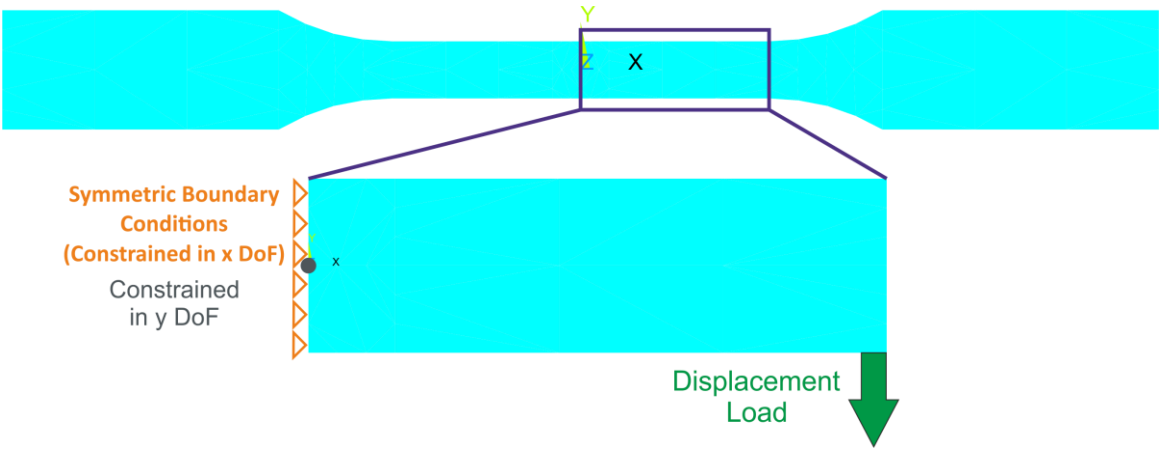

Figure 4.24: Full 2D NACE TM0177-96 specimen (top) with 2D bending submodel and boundary conditions (bottom).

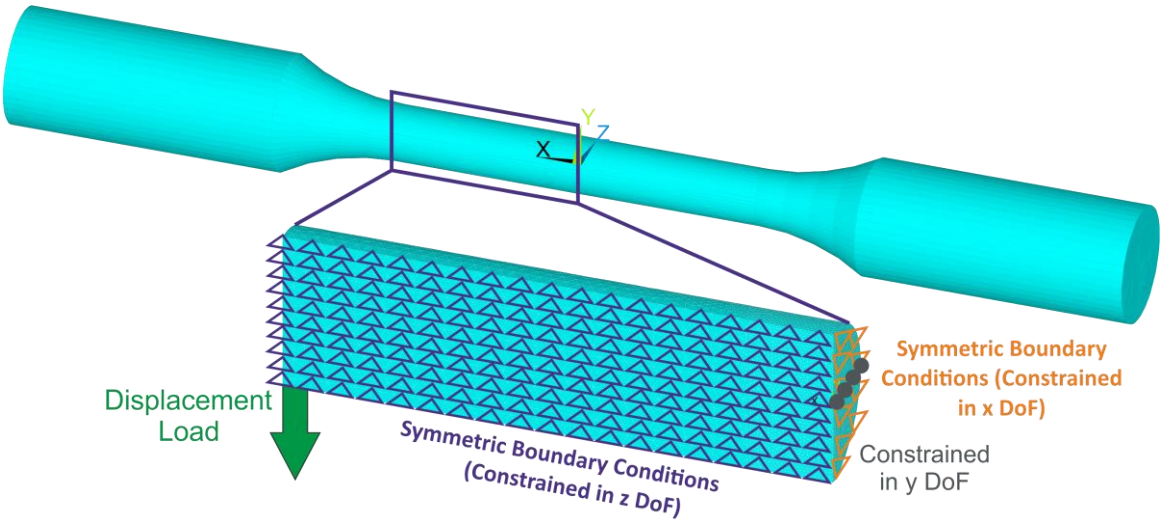

Figure 4.25: Full 3D NACE TM0177-96 specimen (top) with 3D bending submodel and boundary conditions (bottom).

As for the uniaxial loading condition, once the 2D and 3D submodels with pits were created, the same material properties, boundary conditions and bending loading conditions were applied as those applied to the unpitted 2D and 3D submodels.

The influence of the presence of a pit on the load carrying capacity of the material was investigated next. A displacement was again applied to the unpitted model over a number of time steps and the resulting displacement applied to the submodel, as in Figure 4.19. The same material properties and strain rate as used previously were applied, however there was a difference in the number of time steps applied to reach the desired yield stress. These displacement models had a time increment of 966s which was 10 times smaller than the time increments for the earlier models. This time increment size was utilised as the same displacements were applied to the pitted submodels and when the pitted submodel reached the desired local yield stress, which occurred in the pit, the simulation aborts. This smaller time step size is used in determining what percentage of the unpitted loading condition a pitted model can withstand before the desired yield stress is reached, in comparison with the unpitted model.

As with the 2D model, a displacement was applied to the 3D meshed quarter model and the displacement values applied to the submodel, as in Figure 4.19. The same material properties, strain rate and geometry were used as applied to the earlier 3D quarter and half models, however these displacement models had a time increment of 966s which was 10 times smaller than the time increments for the earlier models. This is the same as experienced by the 2D models. These displacement values were then applied to the uniaxial and bending pitted 3D submodels and the simulation was aborted when 100% of yield stress was reached.

To ensure the model set up where the displacement is applied to both ends, as used in the simulations above, is comparable to tensile tests or SSRT, where the displacement is applied to one end only with the other end fixed, two models with both of these boundary conditions were modelled. Symmetric boundary conditions are applied in the y-direction of this model, therefore only the top half of the NACE TM0177-96 specimen is required for these simulations.

The first simulation involves fixing the 3D half model at one end, Figure 4.26. The nodes at the end of the head end of the model are all fixed in the x-direction, as shown using red circles in Figure 4.26. However, in order to prevent movement in the y- and z-directions, the nodes located at the centre of both ends of the model, as shown by dark squares, are constrained in both the y- and z-directions. The same mesh, material properties, load steps and strain rate were applied as to the 3D uniaxial loading condition. However, the displacement applied is twice as large as the displacement previously applied to one end of the 3D one eight model, as this whole displacement is applied to one end of the model only and not divided between both ends of the model.

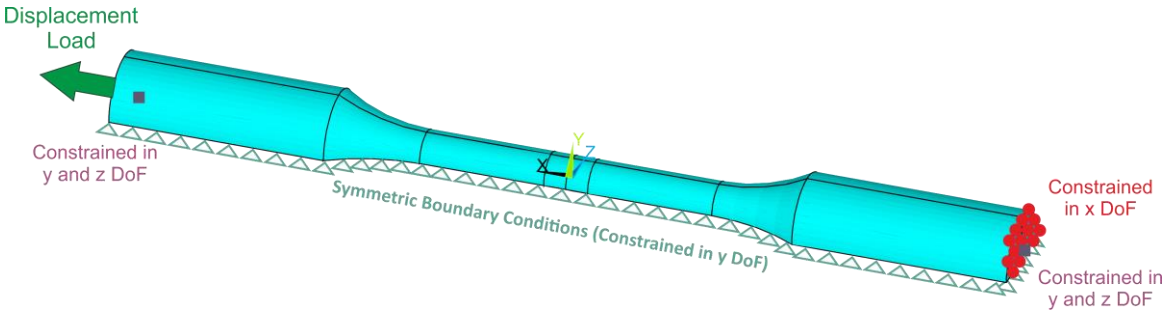

Figure 4.26: Displacement applied to one end of the 3D half model with other end fixed.

The boundary conditions were then altered, with no constraints applied in the x-direction at the very end of the model, however the y- and z-direction constraints remained. The same displacement as applied to the 3D uniaxial one eight model was applied, this time to both ends of the model, Figure 4.27.

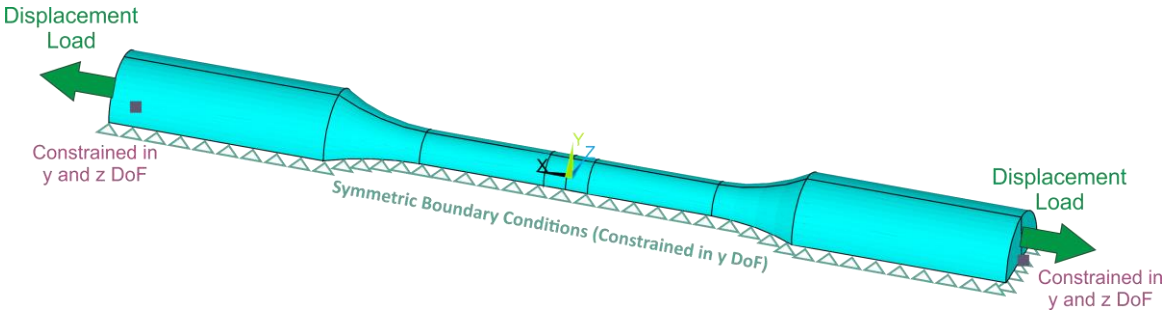

Figure 4.27: Displacement applied to both ends of 3D half model.

It was found that the stress and strain values recorded in both models were the same, therefore ensuring that the uniaxial and bending models above are representative of tensile tests and SSRT. The next stage of this work was to incorporate a pit shape from Figure 4.12 into the half model and apply boundary conditions. This is to investigate if the results in the models used in the sections above are comparable to a full half model loaded at both ends. An ellipse pit was chosen and removed from the half model. The mesh applied was the same as applied to the 3D uniaxial and 3D bending models and can be seen in Figure 4.28. The displacements and boundary conditions from Figure 4.26 and Figure 4.27 were then applied.

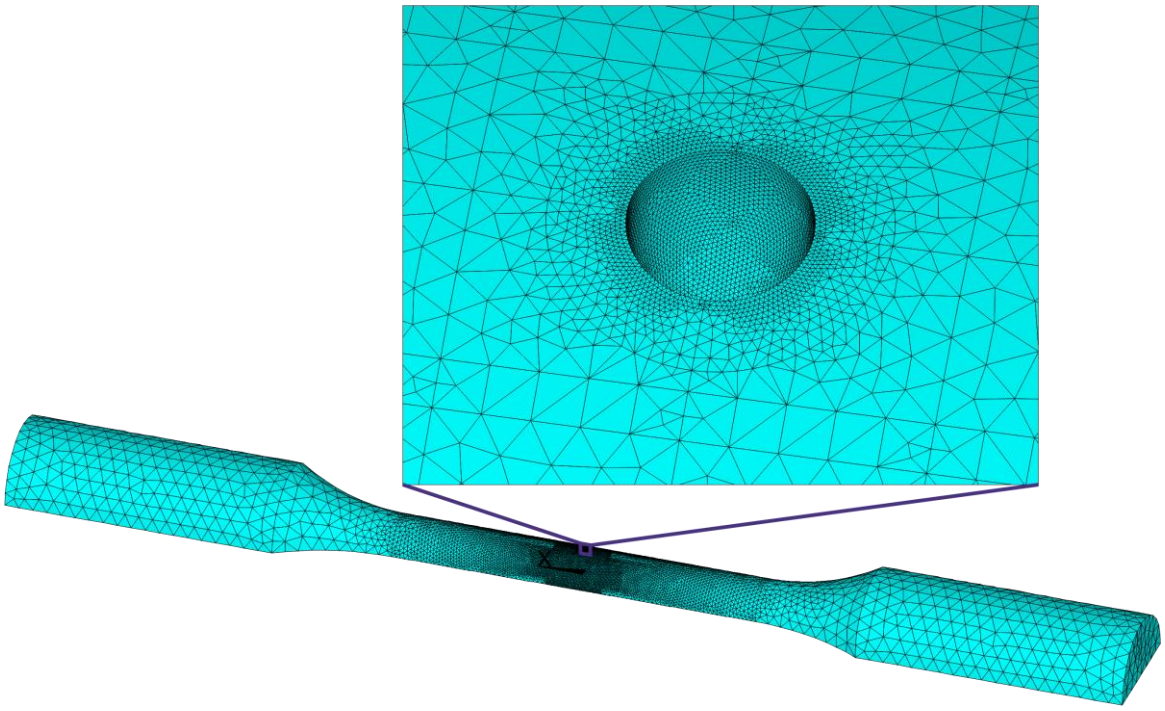

Figure 4.28: 3D half model with ellipse pit.

The number of nodes and elements in the unpitted 3D half model and also in the 3D half model with an ellipse pit are shown in Table 4.8.

Table 4.8: Number of nodes and elements in the unpitted 3D half model and also with an ellipse pit.

Pit Geometry	Number of Nodes	Number of Elements
Unpitted	375,203	267,020
Ellipse	858,053	620,578

This was the final simulation in the first stage of this work involving structural analysis. The numerical procedure calculations undertaken in ANSYS in order to undertake these structural analysis simulations are now described in detail.

After the 2D and 3D models mentioned above have been meshed a displacement is applied for both uniaxial and bending simulations. The displacement method mentioned above is commonly used for stress and strain analysis problems in ANSYS. In this method it is assumed that nodal displacements are unknown variables and are related to nodal forces by a stiffness matrix. The basic equation for the entire model can be expressed using the global stiffness Equation (4.1) [293]:

$$\{F\} = [K]\{U\} \tag{4.1}$$

Where:

$\{F\}$ = Column vector of global nodal forces,

$[K]$ = Global stiffness matrix, determined by geometry, material and elemental properties and

$\{U\}$ = Column vector of nodal displacements.

Every element applied to a meshed model has a certain number of nodes. The displacement function of these nodes can be described using three Gaussian displacement components at each node of the element, in a cartesian coordinate system, where the shape functions map the geometry of every element to the global coordinate system.

Therefore, the stiffness matrix which describes the behaviour of individual elements can be developed using the principle of virtual work. This states that the work done by a set of forces which are in equilibrium and moving through a set of small, compatible displacements is zero. For deformable bodies, this is shown in Equation (4.2):

$$\delta W = \delta W_{int} + \delta W_{ext} \tag{4.2}$$

Where:

δW= Total virtual work,

δW_{int}= External virtual work and

δW_{ext}= Internal virtual work

Equation (4.2) is very important for the approximate solutions for displacement, stress and strain in the finite element method. This equation must also apply to any virtual displacements and corresponding virtual strains where the displacement boundary conditions are applied. The behaviour of the individual elements can be described using the element stiffness equation, Equation (4.3):

$$\{f\} = [k]\{u\} \tag{4.3}$$

Where:

$\{f\}$ = Column vector of elemental nodal forces,

$[k]$ = Element stiffness matrix, determined by geometry, material and elemental properties.

$\{u\}$ = Column vector of unknown element nodal displacements.

All of the element equations, Equation (4.3), for each individual element are added together in order to get the global stiffness Equation (4.1). The determinant of the global stiffness matrix $[K]$ in the global stiffness equation is zero, therefore it is a singular matrix. To remove this, boundary conditions are applied to the model in order to avoid rigid body motion by constraining the model. The required equations can then be solved for the

unknown variables at each node, such as the displacement. The stresses and strains can then be solved as these can be expressed in terms of displacement.

For strain analysis an elastic- plastic model is assumed, as an elastic component of strain is still present even during plastic deformation. An elastic- plastic model assumes the total deformation can be divided into an elastic part and a plastic part. Equation (4.4) shows when the plastic part, plasticity, occurs:

$$\sigma - \sigma_y > 0 \tag{4.4}$$

Where:

σ= Stress and

σ_y= Yield stress.

The increment of plastic strain is determined by Equation (4.5):

$$\Delta\varepsilon_{eq}^{pl} = \frac{\sigma - \sigma_y}{3G + H} \tag{4.5}$$

Where:

$\Delta\varepsilon_{eq}^{pl}$= Increment of equivalent plastic strain,

H= Plastic hardening at the beginning of the increment where $H = \frac{\delta\sigma_y}{\delta\varepsilon_{eq}^{pl}}$ and

G = Shear modulus where $G = \frac{E}{2(1+v)}$

Therefore, at time t + Δt, Equation (4.5) can be rewritten as Equation (4.6) to determine the incremental plastic strain:

$$\Delta\varepsilon_{eq}^{pl}{}_{new} = \Delta\varepsilon_{eq}^{pl}{}_{old} + \Delta\varepsilon_{eq}^{pl} \tag{4.6}$$

The equivalent elastic strain is calculated using Equation (4.7):

$$\sigma_{eq} = E\varepsilon_{eq}^{el} \tag{4.7}$$

Where:

σ_{eq}= Equivalent stress,

ε_{eq}^{el}= Equivalent elastic strain and

E= Young's modulus.

The total mechanical strain in a model is then determined using Equation (4.8):

$$\varepsilon_{eq}^{tm} = \varepsilon_{eq}^{el} + \varepsilon_{eq}^{pl} + \varepsilon_{eq}^{cr} \tag{4.8}$$

Where:

ε_{eq}^{tm}= Equivalent total mechanical strain and

ε_{eq}^{cr}= Equivalent creep strain.

Equivalent creep strain is not considered in this work as the stresses and temperatures are not high enough for creep to have any great influence on the total mechanical strain. Equation (4.8) can be rewritten as Equation (4.9):

$$\varepsilon_{eq}^{tm} = \varepsilon_{eq}^{el} + \varepsilon_{eq}^{pl} \tag{4.9}$$

4.3.2 Diffusion Analysis

The second part of this work consisted of investigating the effects different boundary conditions have on the unloaded model. In this case, four different boundary conditions where hydrogen uptake to the model would occur are considered and they are:

- Hydrogen uptake just on the model surface,
- Hydrogen uptake just in the pit,
- Hydrogen uptake on the model surface and in the pit and
- Variable hydrogen concentration uptake just in the pit.

These models had no hydrogen initially present in the models and were exposed to the hydrogen from the bulk electrolyte for the same duration of time- 1,728,000 seconds or 20 days. This was to ensure that hydrogen diffusion would occur in the models, but the model would not be saturated with hydrogen. The diffusion of hydrogen through the model can also be investigated for each boundary condition. This is important as the presence of hydrogen requires a lower stress or strain value in order to initiate cracking so knowing how hydrogen diffuses through a material will determine the regions of high hydrogen concentration.

In Section 4.3.1 it was determined that a submodel can provide similar accurate data as a full or smaller model. Therefore, for this stage of the work a submodel was used for all simulations. Additionally, for this stage hydrogen diffusion in 2D models was not undertaken as 3D models show the diffusion paths of the hydrogen more accurately, especially in the region around the pit. It was determined from Section 4.3.1, that the subsurface pit geometry would have a high accumulation of local strains due to the sharp geometry at the pit mouth and the shallow wide pit would have lower strains due to the more smooth geometry. Therefore, these “best” and “worse” case pit shapes, along with the ellipse shaped pit, were chosen as the pit shapes for this stage of this work, as hydrogen accumulated in the regions of highest stresses and strains. The ellipse shaped pit was chosen as this is similar to the bullet shaped pit modelled by researchers and

mentioned in Figure 2.40 in Section 2.3.5, but also has a geometry where an average accumulation of local strains for all the pit geometries is assumed will occur.

There is no loading condition applied, as this stage of the work is to investigate the diffusion of hydrogen through the 3D HAZ submodels and to investigate what effect the pit geometries have on the hydrogen profile of the models. For the four boundary conditions it is assumed that no hydrogen is initially present in the models, therefore the only hydrogen source is from the bulk electrolyte. The reference temperature is the same as for the previous models, room temperature. As previously explained in Chapter 2 the HAZ is the area of the SMSS pipeline where it is most probable that cracks initiating from pits in the presence of hydrogen may occur. For this reason, only the HAZ was investigated during this stage of the work and not also the BM. The diffusion coefficient for the HAZ is 1.8 10^{-5} mm^2/s [16]. Hydrogen concentrations of 7, 4 and 1 ml·(100gFe)$^{-1}$ are assumed to be transferred from the bulk solution to the model for the HAZ. These values correspond to approximately 100%, 1% and 0.25% H_2S saturation [297] and represent the maximum hydrogen concentration value of the graph in Figure 3.3 in Section 3.2, the lowest non zero value and the mid value to correspond with the ideology of design of experiments, respectively. In order to calculate diffusion, the ANSYS software uses a normalised concentration, where the applied concentration is normalised against the saturation concentration of the material. This normalised concentration is shown in Equation (4.10).

$$\bar{C} = \frac{C}{C_{sat}} \tag{4.10}$$

Where:

$\bar{C}$= Normalised concentration,

C= Applied concentration and

C_{sat}= Saturation concentration, which is the maximum concentration applied as a subsurface concentration in the material.

This results in the same diffusion for all three different hydrogen concentrations. Therefore, only the 7 ml·(100gFe)$^{-1}$ hydrogen concentration was investigated as a worst case scenario. The normalised hydrogen concentration is explained in more detail, along with the ANSYS equations used in this simulation, at the end of this section. The subsurface concentration used in these simulations was initially 0.

The normalised hydrogen concentrations at the nodes for three different paths were recorded, for all boundary conditions at each time step. The location of these nodes is shown in Figure 4.29. The path of the nodes along path A was selected as when a load is

applied to a specimen and a crack initiates in a pit, then these cracks generally grow along the axis perpendicular to the applied load, which will be along the nodes selected for Path A. Therefore, the hydrogen concentration in front of the pit, if a crack were to initiate in the pit and grow, is recorded by these nodes. The nodes along path B were chosen to monitor the depth the hydrogen diffuses into the model when applied to the surface. Pits may also grow wider instead of just deeper, so the nodes along path C were selected in case this were to occur. These nodes can also be used to determine how far into the material the hydrogen diffuses when a normalised hydrogen concentration is applied to the pit. Further information on the boundary conditions applied is provided next.

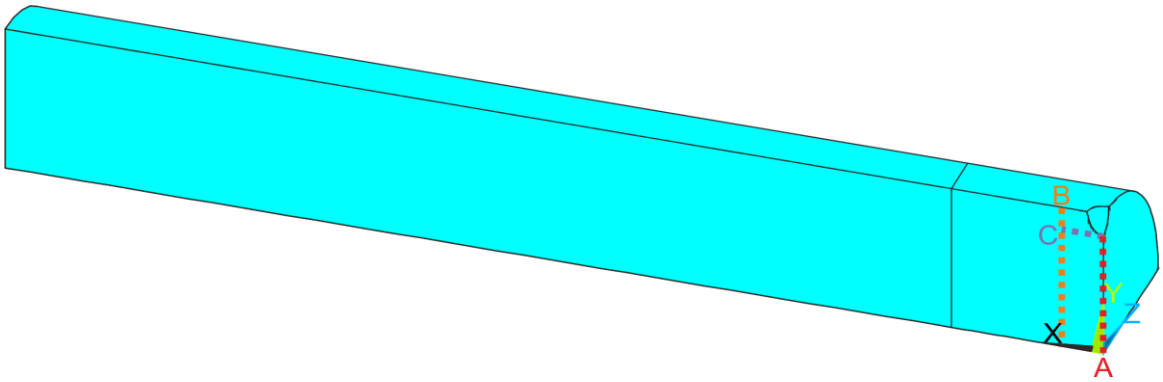

Figure 4.29: Path of nodes where hydrogen concentration was recorded.

Surface Hydrogen Boundary Condition

A normalised hydrogen concentration was supplied to the full surface of the model only, Figure 4.30. This boundary condition is to simulate a component exposed to a bulk solution with a pit located on the surface, however plugging of the pit has already occurred therefore no hydrogen from the bulk solution continues entering the pit.

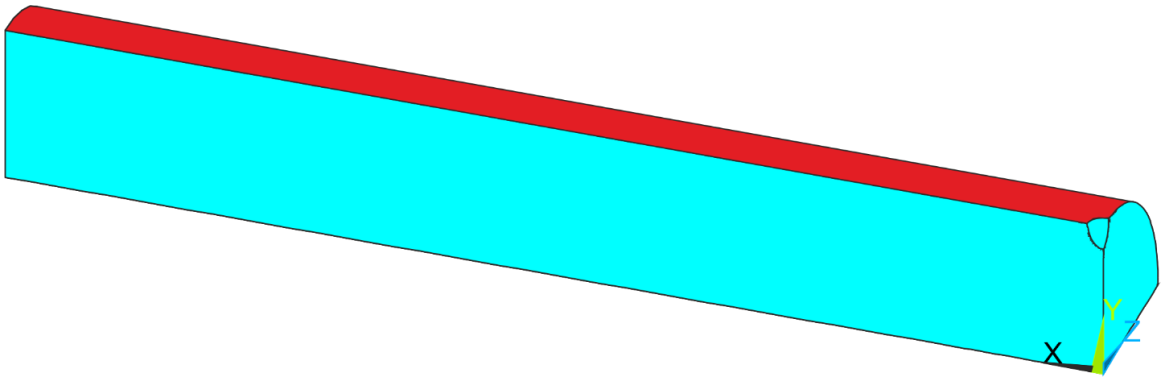

Figure 4.30: One- eight submodel, base material, with hydrogen applied to the surface.

Pit Hydrogen Boundary Condition

For this boundary condition a normalised hydrogen concentration was supplied to the pit region only, Figure 4.31. This boundary condition is to simulate a component exposed to a bulk solution with a pit located on the surface. The pit however has become plugged and this results in hydrolysis occurring in the pit region only.

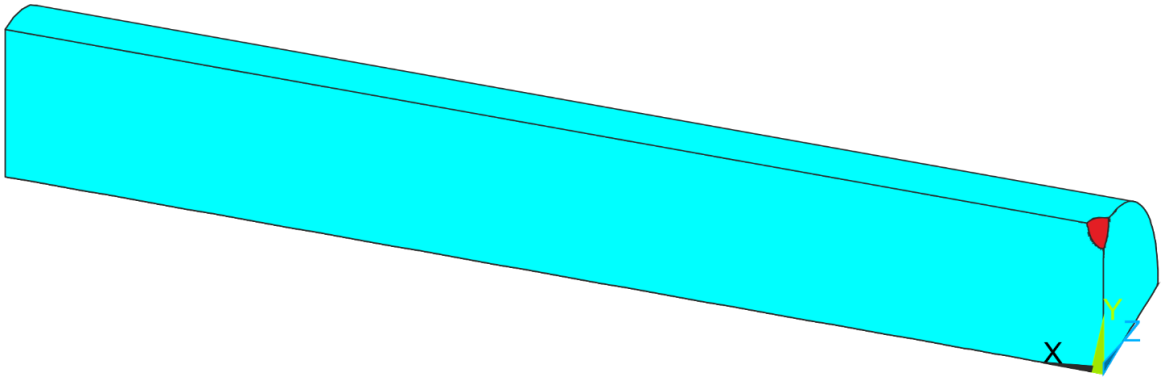

Figure 4.31: One- eight submodel, base material, with hydrogen applied to the pit.

Surface and Pit Hydrogen Boundary Condition

For this boundary condition a normalised hydrogen concentration was supplied to the full surface of the model and also the pit region, Figure 4.32. This boundary condition is to simulate a component exposed to a bulk solution with an open pit located on the surface.

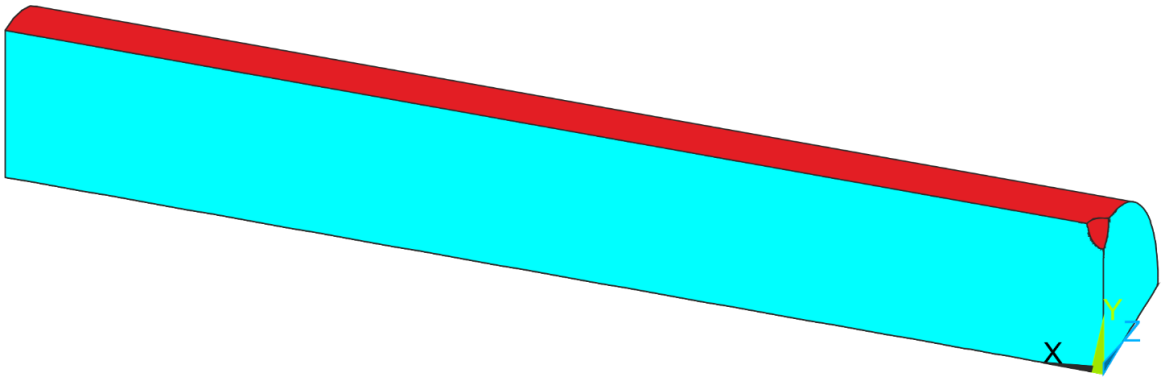

Figure 4.32: One- eight submodel, base material, with hydrogen applied to the surface and pit.

In this boundary condition it is assumed that plugging of the pit has not yet occurred, but the bulk electrolyte is providing hydrogen to both the surface of the model and to the pit.

Pit Varying Hydrogen Concentration Boundary Condition

The above boundary condition, Figure 4.31, was then modified to provide a more realistic representation of the local reactions occurring in the pit, based on the model developed by Hoffmeister and Böllinghaus [185] in Figure 2.27

The normalised hydrogen concentration is not uniformly distributed in the pit but has higher concentrations in certain regions of the pit, as explained previously in section 2.3.2. This normalised distribution inside the pit varies from 0 at the pit mouth to 1 in the centre of the pit, back to 0 at the bottom of the pit, Figure 4.33. The normalised hydrogen concentration applied to the pit may diffuse out of the material through the surface of the material. However, the diffusion of the varying normalised hydrogen concentration through the material was chosen to be investigated and this includes effusion from the material.

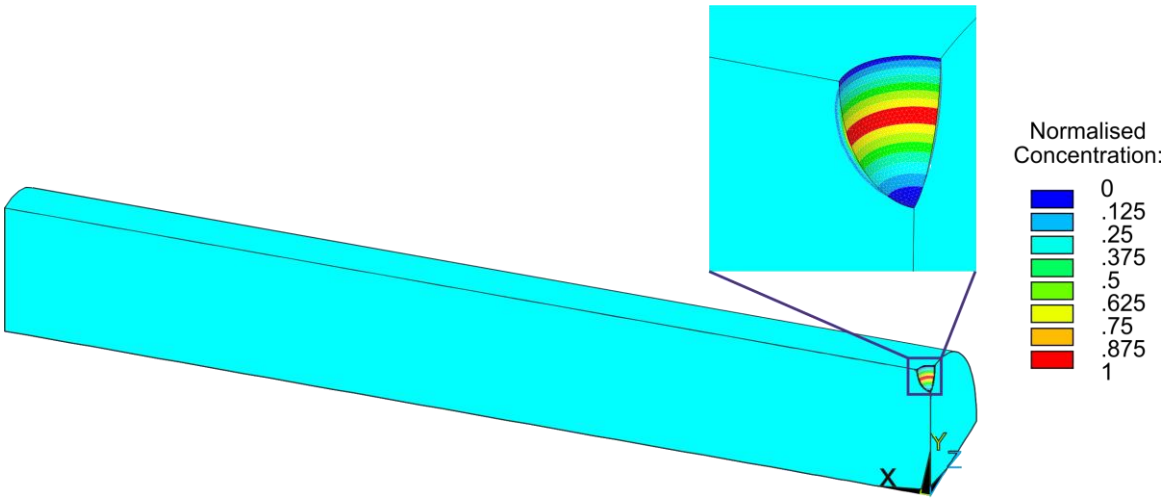

Figure 4.33: One- eight submodel, base material, with a varying hydrogen concentration applied to the pit.

An explanation of the numerical procedure calculations undertaken in ANSYS, from the ANSYS user handbook [294], is presented in detail next.

In order to apply the boundary conditions mentioned above to the model, the Thermal-Diffusion analysis was selected. The temperature remains constant for the analysis, at room temperature, but there is no diffusion only analysis in ANSYS, only coupled analyses such as thermal- diffusion and structural- diffusion. Therefore, the thermal part of the analysis is constant and not changing. This is show in Equations (4.11) and (4.12) below, where Equation (4.11) is Fick's first law and (4.12) is the thermal- diffusion equation where the diffusion flux, $\{J\}$, is coupled to temperature.

$$\{J\} = -[D]\nabla C + \{v\}C \tag{4.11}$$

$$\{J\} = -[D]\nabla C - \frac{[D]CQ}{kT^2}\nabla T \tag{4.12}$$

Where:

$\{J\}$= Diffusion flux vector,

$[D]$= Compliance matrix, which is $[D] = \begin{bmatrix} D_{xx} & 0 & 0 \\ 0 & D_{yy} & 0 \\ 0 & 0 & D_{zz} \end{bmatrix}$, where D_{xx}, D_{yy} and D_{zz} are the diffusivity coefficients in the x, y and z directions of the elements,

C = Concentration,

$\{v\}$= Transport velocity vector,

∇= Gradient operator, where $\nabla = \left\{\frac{\partial}{\partial_x}\frac{\partial}{\partial_y}\frac{\partial}{\partial_z}\right\}^T$,

Q= Particle heat of transport,

k= Boltzmann constant and

T= Absolute temperature, where $T = T_c + T_{off}$, and T_c is the current temperature and T_{off} is the offset temperature.

As the temperature remains constant in the diffusion analysis, Equation (4.11) will be the diffusion equation used in this simulation.

4.3.3 Combined Structural and Diffusion Analysis

The final stage of this work was to combine the previous stages, i.e. to apply both a displacement and normalised hydrogen concentration to the model in order to combine the structural and diffusion analysis. The aim was to simulate a SSRT test with the model exposed to a varying normalised hydrogen concentration in the pit. The same strain rate applied to the structural analysis model, 1x10^{-6} mm/s, was applied to this model. Additional strain rates of 1x10^{-5} mm/s and 1x10^{-7} mm/s were also applied to investigate the influence the increasing and decreasing strain rates have on the model.

One major difference between this simulation and the previous simulations is that a stable pit is not assumed to be present in the model. The model at the beginning of the simulation has no pit present, but as a result of a breakdown in the passive layer, due to the total mechanical strain in the passive layer reaching more than 0.1% yield, a pit begins to form. In this simulation the passive layer is not modelled, it is just assumed to rupture at 0.1% yield of the HAZ material. A pit then grows through various stages of idealised pit growth to reach a stable pit, Figure 4.12. These pit geometries are also idealised versions of pit geometries. The shallow wide, ellipse and subsurface pit geometries are again chosen for this stage of the work and the geometries for each pit stage are shown in Table 4.9, where

“Pr” is the pit radius at the mouth of the pit in µm and “Pd” is the depth of the pit in µm. Figure 4.34 to Figure 4.36 show the five different stages of pit growth used in this work for the shallow wide, ellipse and subsurface pits. It was not possible to model the pit growing continuously, instead an incremental increase from one pit size to the next was treated in a step wise manner. Therefore, the pit geometries and meshes were designed so as each pit geometry is removed, using the ANSYS ekill command, the next pit has the same mesh as the previous. This idealised pit growth method has been utilised by Turnbull et al. [221, 298] and Xiang et al. [274] but these researchers only modelled hemisphere or bullet shaped pits, Figure 2.40. As the pit mouth radius for the subsurface pit is very small in comparison to the shallow wide and ellipse pits, a narrow deep pit geometry was chosen as the initial pit in this pit growth model. This narrow deep pit geometry was researched by Cerit et al. [266] and is also similar to the narrow deep pit geometry in Figure 2.37. Turnbull [221] modelled pit growth in three steps, as did Xiang [274]. However Mai et al. [13] modelled pit growth in seven stages and Bhandari [270] in four stages. It was chosen to model five stages of pit growth for this work as an approximation of pit growth can be modelled and additionally hydrogen uptake in the pit as certain conditions have to be reached before hydrogen can diffuse into the pit, as previously mentioned in Section 2.3.2, Equations (2.23) to (2.32). These equations were not implemented into this model, however it was assumed that these conditions would not occur in the first pit but would occur at a later stage, Figure 4.37. The pit growth modelled is an assumption as a first approach as this has not previously been undertaken, as indicated above.

Table 4.9: Different pit geometries at each simulated idealised pit growth stage.

Stage of pit growth	Shallow Wide		Ellipse		Subsurface	
	Pr in µm	Pd in µm	Pr in µm	Pd in µm	Pr in µm	Pd in µm
1	60	60	60	60	10	60
2	120	90	120	120	20	120
3	180	120	160	180	30	180
4	240	150	170	240	30	240
5	300	180	180	300	30	300

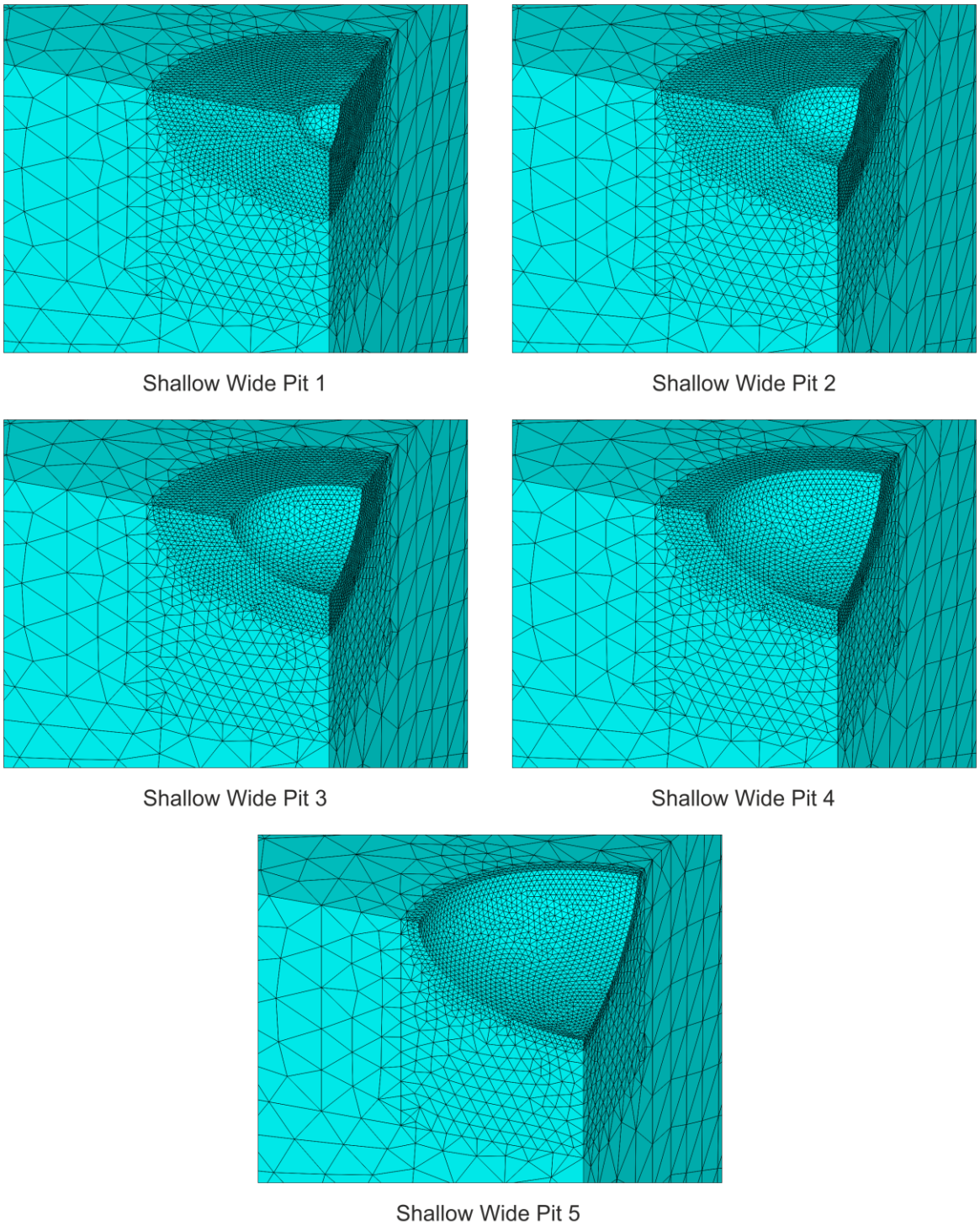

Figure 4.34: Simulated stages of pit growth for shallow wide pit.

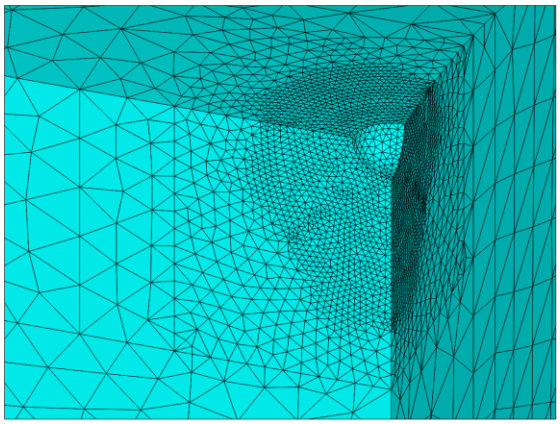

Ellipse Pit 1

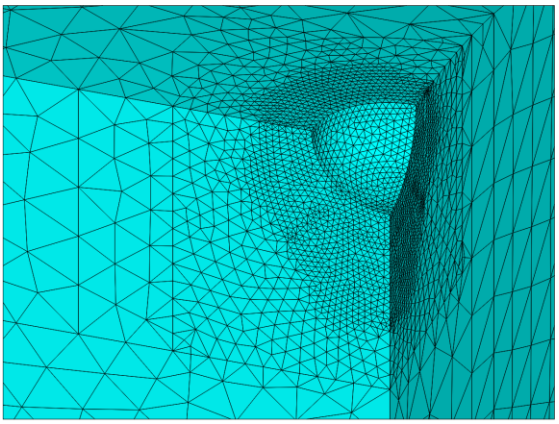

Ellipse Pit 2

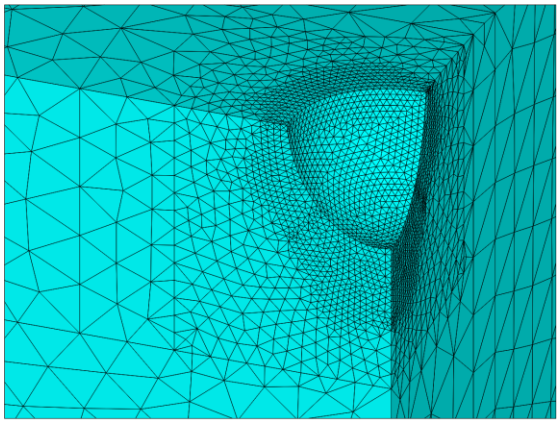

Ellipse Pit 3

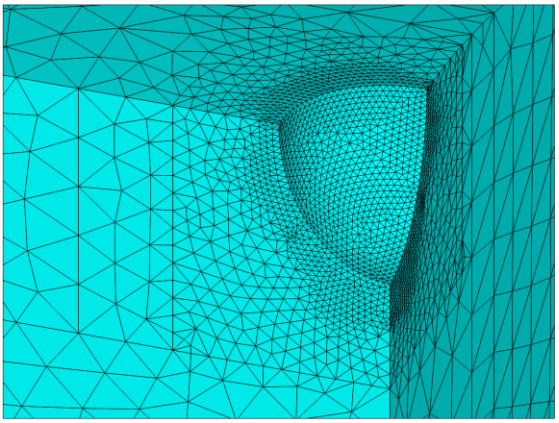

Ellipse Pit 4

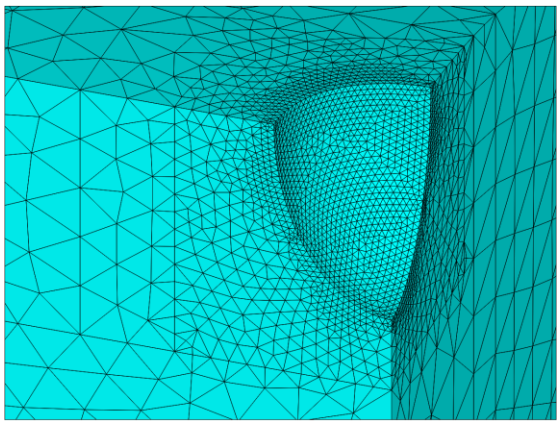

Ellipse Pit 5

Figure 4.35: Simulated stages of pit growth for ellipse pit.

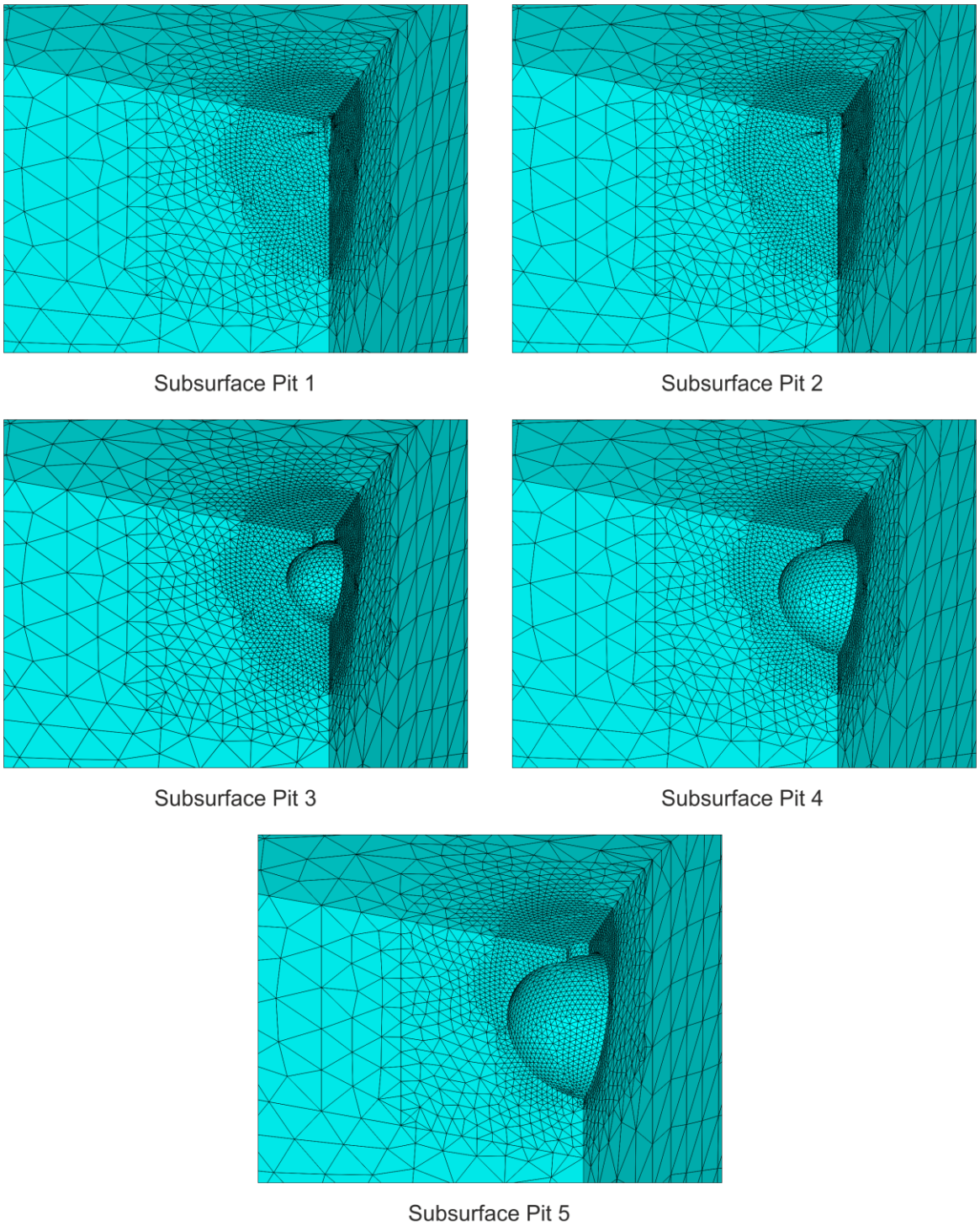

Figure 4.36 Simulated stages of pit growth for subsurface pit.

The submodel and boundary conditions in Figure 4.21 were also used in this stage of the work. The same material properties and strain rate as previously applied were also applied to this model. The model was loaded in the x-direction until 0.1% of the yield stress was reached, as explained in Section 3.2, which corresponds to breakdown of the passive layer. This is shown as the Incubation Stage in Figure 4.37, along with the boundary

conditions applied during this stage. The model was continued to be loaded and the first stage of idealised pit growth was simulated by removing the elements of the first pit volume from the model after a certain time. The total time assumed for the pit to grow to the final pit depth was 9000 seconds. This value was chosen from Table 2.4 in Section 2.3.5 as it seems the most applicable to this work and is shown in Figure 4.37 as Pit 1. This model was designed with five different pit sizes, so the time taken for each pit to grow is 1800 seconds. The second pit was then deleted after straining the model for 1800 seconds after breakdown of the passive layer occurred with the same strain rate, Pit 2 in Figure 4.37. The third pit was then deleted after an additional 1800 seconds but it was assumed that the appropriate conditions had been reached for hydrogen uptake to occur in a plugged pit. Therefore, a variable normalised hydrogen concentration was applied to the pit, as seen in Figure 4.33, with the red region being where a normalised hydrogen concentration of 1 is applied and the blue region where a normalised concentration of 0 is applied. The boundary conditions applied to this pit, Pit 3, and the following stages are shown in Figure 4.37. The application of a normalised hydrogen concentration to the model while also applying a displacement was repeated for pits 4 and 5 with the same strain rate and variable hydrogen concentration also applied to these pits, Pit 4 and Pit 5 in Figure 4.37. This was undertaken in order to perform a direct coupled analysis including strain assisted diffusion. When the last pit has been deleted the load and variable hydrogen concentration continues to be applied for an additional 900 seconds. This ensures hydrogen diffusion into the model will occur and will provide an insight as to how this appears.

The same normalised hydrogen concentration, where the applied hydrogen concentration of 7 $ml \cdot (100gFe)^{-1}$ was normalised against the saturation concentration of the material, was applied to all pit geometries and stages. Additionally, the same hydrogen distribution, where the highest normalised hydrogen concentration value of 1 occurs at the middle of the pit and the lowest normalised hydrogen concentration value of 0 occurring at the pit mouth and bottom, was also applied to all pit geometries and stages. As the pits grow the region where the highest normalised hydrogen concentration is located, also increases. This may account for an increase in the acidification in the pit, but this region may also be further increased in subsequent simulations but was kept proportional to the pit depth in this work.

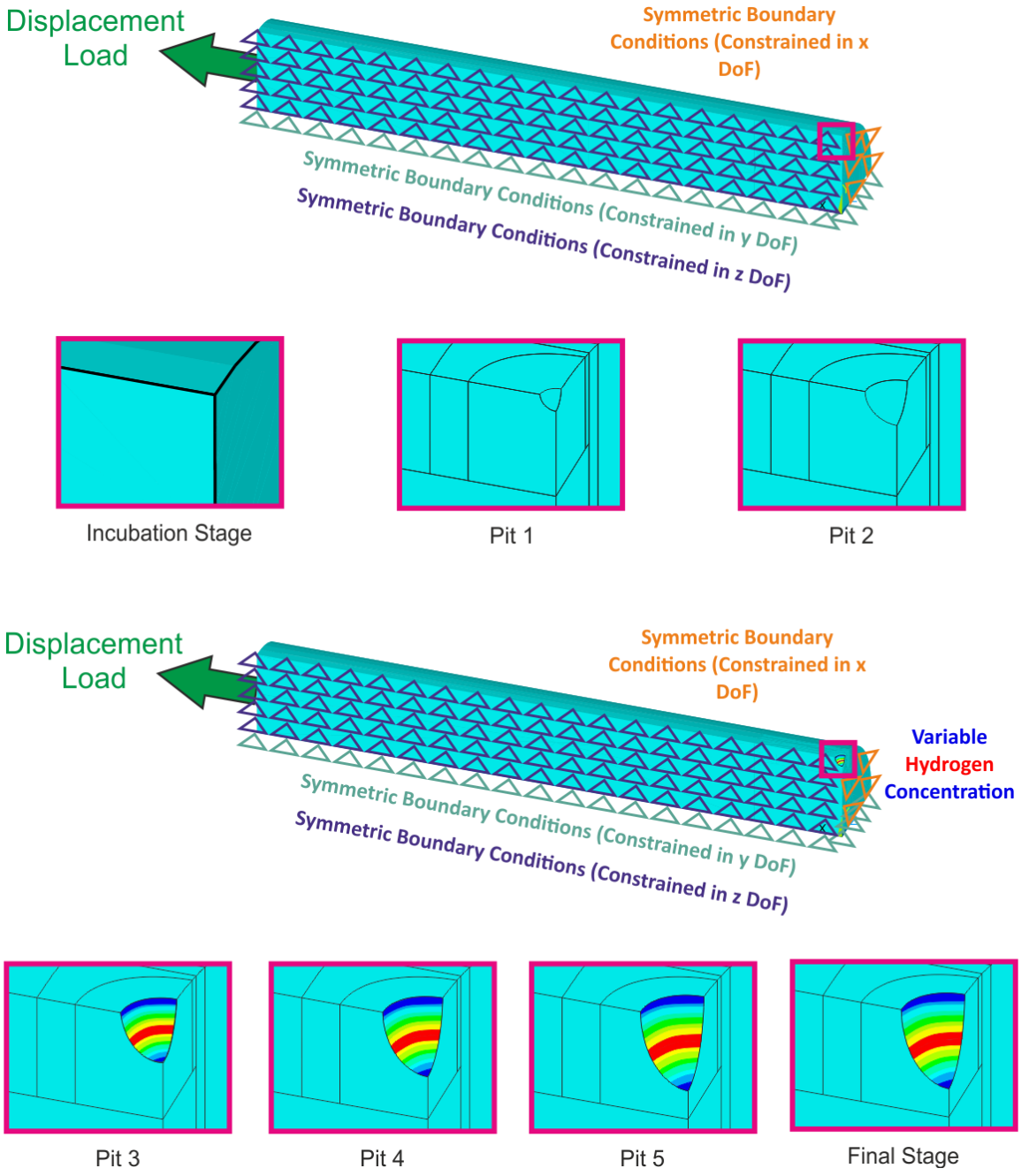

Figure 4.37: Different stages during the direct coupled strain dependent diffusion (red region is normalised hydrogen concentration = 1.0 and blue = 0.0).

The background of the finite element analysis used in this final stage is presented next and is from the ANSYS user handbook [294].

In a coupled structural-diffusion analysis the total strain consists of both plastic and elastic strains, Equation (4.13).

$$\{\varepsilon\} = \{\varepsilon^{el}\} + \{\varepsilon^{di}\} \tag{4.13}$$

Where:

$\{\varepsilon\}$= Total strain vector, where $\{\varepsilon\} = \{\varepsilon^{el}\} + \{\varepsilon^{di}\} = \left[\varepsilon_x \varepsilon_y \varepsilon_z \varepsilon_{xy} \varepsilon_{yz} \varepsilon_{xz}\right]^T$,

$\{\varepsilon^{el}\}$= Elastic strain vector and

$\{\varepsilon^{di}\}$= Diffusion strain vector.

5 Results and Discussion

5.1 Structural Analysis Model

As previously mentioned in Chapter 2, the HAZ is the region where it is most likely that crack initiation from pits will occur. Therefore, the results for the HAZ only are presented in this chapter, with the results from the BM presented in Appendix A.

5.1.1 2D Structural Analysis

2D Uniaxial Structural Analysis for Unpitted Heat Affected Zone (HAZ)

The highest stressed and strains regions in the 2D HAZ one quarter unpitted model subjected to an x-direction uniaxial (UA) load until 100% yield stress was reached, can be seen in Figure 5.1 and Figure 5.2. The location of the max stresses and total true strains in x-direction for the model are in the same location, which falls just outside the margins of the gauge length. In experiments however, the gauge length, or experimental length, region of the sample is the region of interest, which is therefore why this region was chosen to be the 2D UA HAZ submodel. Table 5.1 shows the displacement values applied to the global model and the resulting maximum stresses and total true strains in x-direction for the 2D HAZ one quarter model. As the material is below yielding, the technical and true stresses are the same and will therefore be referred to as "stress".

Table 5.1: Displacement values applied to 2D UA HAZ one quarter model and resulting total true strain and stress results.

Displacement (x) (mm)	Total True Strain in x-direction	Stress in X-direction (MPa)	% Yield
0.1096	0.0041	870	100

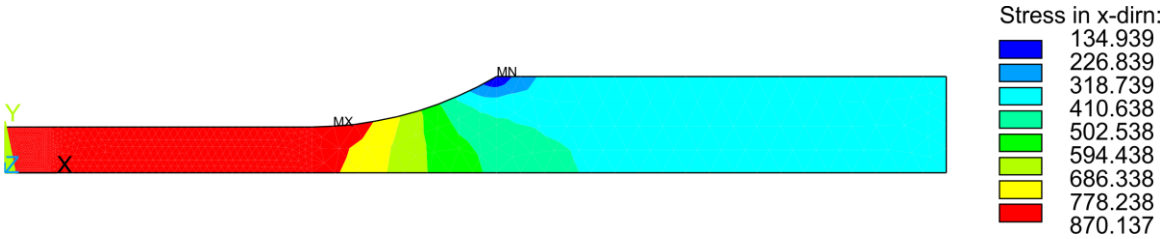

Figure 5.1: 2D one quarter model maximum stress in x-direction for 100% of HAZ yield stress applied as uniaxial displacement.

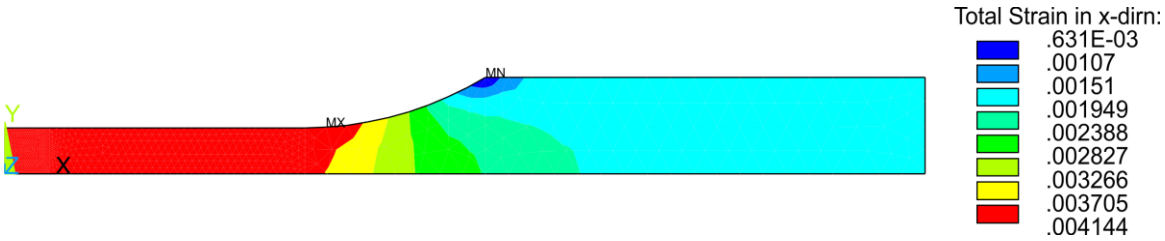

Figure 5.2: 2D one quarter model maximum total true strain in x-direction for 100% of HAZ yield stress applied as uniaxial displacement.

A graph depicting the increase of displacement, maximum total true strain and stress in x-direction with increasing time, Figure 5.3, show that these three parameters increase linearly with increasing time over 120,000 seconds.

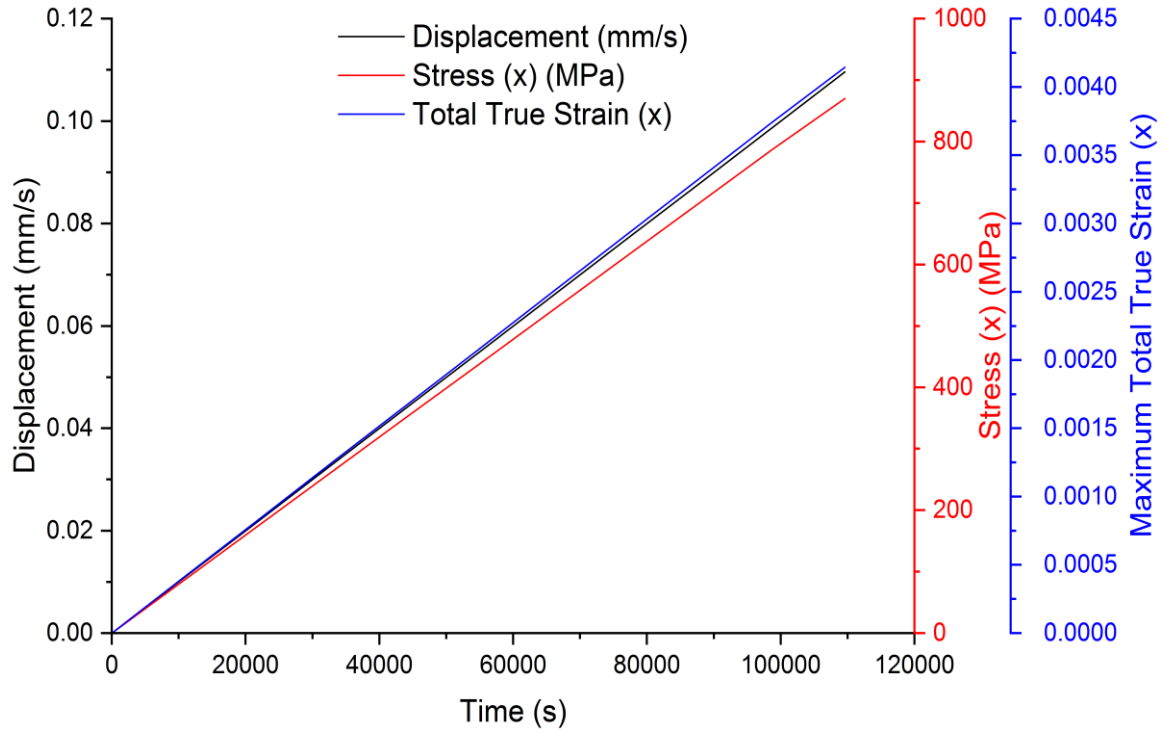

Figure 5.3: Displacement, maximum total true strain and stress in x-direction vs time for the 2D one quarter model for 100% of HAZ yield stress applied as uniaxial displacement.

The 2D HAZ one quarter model and the gauge length region selected from the 2D HAZ one quarter model, along with their corresponding maximum x-direction stress and total true strain results, can be seen in Figure 5.4 and Figure 5.5. The 2D UA HAZ submodel with the x- and y-displacements from the 2D HAZ one quarter model applied and the corresponding maximum x-direction stress and total true strain results can be seen in Figure 5.6 and Figure 5.7. Table 5.2 shows the global displacement applied to the 2D HAZ submodel and the resulting stress and total true strain in the x-direction.

Table 5.2: Displacement values applied to 2D UA HAZ submodel and resulting total true strain and stress in x-direction results.

Displacement (x) (mm)	Total True Strain in x-direction	Stress in X-direction (MPa)	% Yield
0.05015	0.0041	865	99

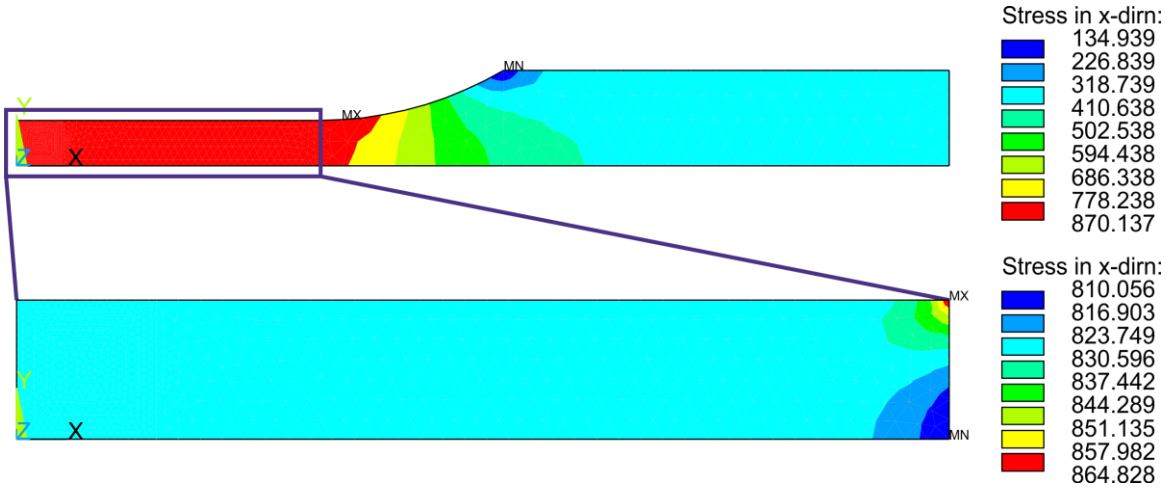

Figure 5.4: 2D one quarter model maximum stress in x-direction for 100% of HAZ yield stress applied as uniaxial displacement and selected gauge length region shown on the 2D one quarter model.

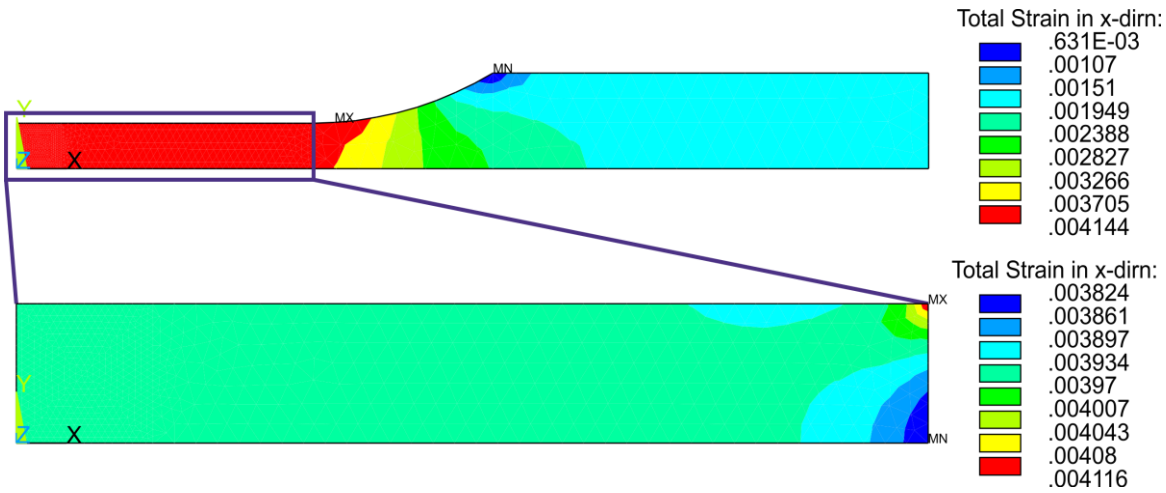

Figure 5.5: 2D one quarter model maximum total true strain in x-direction for 100% of HAZ yield stress applied as uniaxial displacement and selected gauge length region shown on the 2D one quarter model.

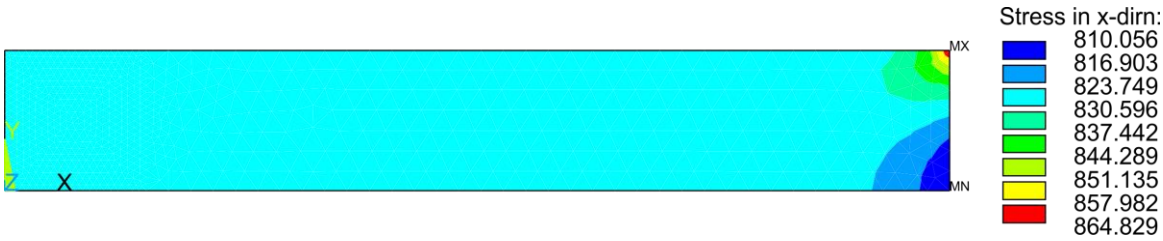

Figure 5.6: 2D UA submodel maximum stress in x-direction for 100% of HAZ yield stress applied as uniaxial displacement to 2D one quarter model.

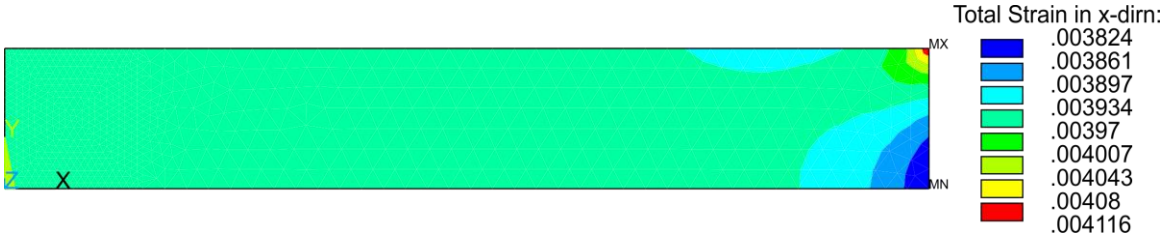

Figure 5.7: 2D UA submodel maximum total true strain in x-direction for 100% of HAZ yield stress applied as uniaxial displacement to 2D one quarter model.

As seen in Figure 5.4 to Figure 5.7, the maximum x-direction stress and total true strain values in the 2D UA HAZ submodel are the same as the maximum x-direction stress and total true strain values for the selected gauge length region. The reason the maximum x-direction stress in the 2D UA HAZ submodel is not the exact same value as in the 2D HAZ one quarter model, but is slightly reduced, is due to the highest stressed region in the 2D HAZ one quarter model being located slightly outside the selected gauge length region. As previously explained however, the gauge length is the region of interest. Therefore, in the subsequent simulations involving a 2D HAZ one quarter model loaded to 100% of yield stress, the 2D UA HAZ submodel is used in place of the 2D HAZ one quarter model.

2D Uniaxial Structural Analysis for Pitted HAZ

From the simulation results above, the next stage of this work involved removing the various pit geometries from the 2D UA submodels only. These pit geometries have been shown in Figure 3.2 in Section 3.2. As the focus of this work relates to the total true strain in the x-direction in the material, instead of the stress in x-direction, the maximum total true strain in the x-direction in the pits in the 2D UA HAZ submodel are presented in Figure 5.9. The maximum total true strain in the x-direction values in Table 5.3 correspond to a load of 100% yield stress in the unpitted submodel.

Table 5.3 shows the maximum strains in x-direction for the various pit geometries and have been sorted from lowest to highest. The pit aspect ratio for each pit is also shown in Table 5.3. The pit aspect ratio is a ratio of the pit depth to pit mouth diameter and is used to define the severity of a pit.

Table 5.3: Lowest maximum total true strain in x-direction to highest for all seven pit geometries, in the uniaxially loaded 2D UA HAZ submodel and the pit aspect ratios.

Pit Geometry	Maximum Total True Strain in the x-direction	Pit Aspect Ratio
Unpitted	0.0041	-
Shallow Wide	0.028801	0.3
Reference	0.058532	0.5
Spherical	0.06465	0.5
Subsurface	0.11372	10
Ellipse	0.136392	0.83
Repassivation	0.41869	0.83
Notched	0.453797	0.83

The maximum total true strain in x-direction for all pit geometries in the 2D HAZ submodel are presented in Figure 5.8 as a function of time. The maximum total true strain in x-direction for all pit geometries occur in the pit bottoms. Unlike the maximum total true strain in x-direction results for the unpitted 2D HAZ quarter model in Figure 5.3, the strains for the pitted geometries do not increase linearly over time. This may be due to the specimen being loading past the yield point of the material.

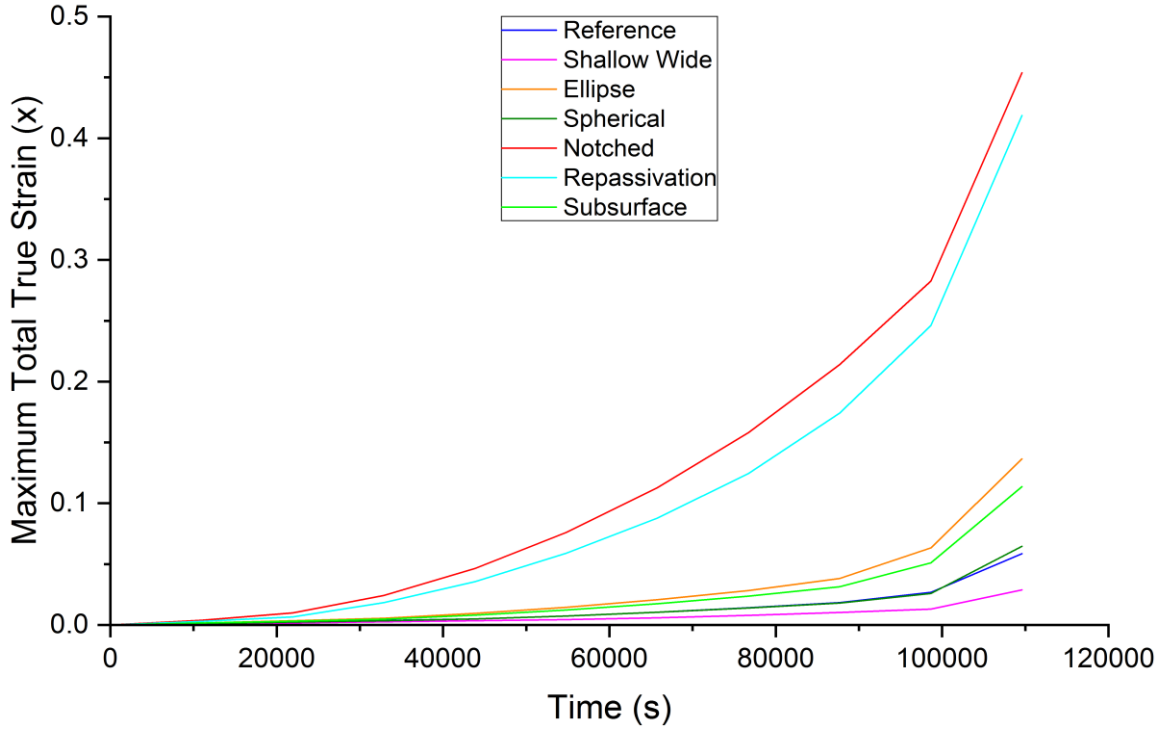

Figure 5.8: Maximum total true strain in x-direction vs time for all pit geometries in the 2D HAZ submodel.

As seen in Figure 5.9, the location of the maximum total true strains in the x-direction in all of the seven different pit geometries, occur at the bottom of the pits, as also recorded by Mai et al. [12]. Table 5.3, Figure 5.9 and Figure 5.10 show that the shallow wide pit has the lowest maximum total true strain in x-direction value, 0.029, with the reference pit having the second lowest value, 0.059. These pits are the only pits to have a pit depth of 180 µm and are the shallowest pits modelled. Due to the different pit mouth diameters of 600 µm for the shallow wide pit and 360 µm for the reference pit, this results in a pit aspect ratio of 0.3 for the shallow wide pit and 0.5 for the reference pit. The pit aspect ratio of 0.3 is the smallest for all of the pits, making this the least severe pit, and corresponds to the lowest maximum total true strain in x-direction value in the 2D UA HAZ submodel subjected to a uniaxial x-direction displacement.

The spherical pit is the only additional pit with the same pit mouth diameter as the shallow wide pit, 600 µm, which is the largest pit mouth diameter modelled. The pit aspect ratio for the spherical and reference pits is the same at 0.5. This may show that for a uniaxial x-direction displacement, the depth of the pit is the most important geometric aspect, with a shallow pit producing lower maximum total true strain in x-direction values in pits.

The ellipse, repassivation and notched pits all have a pit aspect ratio of 0.83 and these are the pits with the highest maximum total true strain in x-direction values of 0.136, 0.419 and 0.454 respectively. However, there is a difference of 0.035 between the highest maximum total true strain in x-direction value in the notched pit and the second highest value in the repassivation pit, while the ellipse pit maximum value is 3 times lower than the repassivation pit. This also shows that pit geometry determines the maximum total true strain in x-direction value in pits as the ellipse pit has curved sides and pit bottom while the notched pit has a sharp angle at the pit bottom. While the snowman pit also has curved pit sides and no sharp angles at the pit bottom, the geometry is not as smooth as the ellipse pit, nor as sharp as the notched pit. This may explain why the highest maximum total true strain in x-direction value of this pit is not as high as the notched pit, even though the pit aspect ratios are the same. This indicates that the whole geometry of the pit, not just the pit mouth diameter and depth, are important geometric parameters. In fact, the highest maximum total true strain in x-direction value in the ellipse pit is closer to the subsurface pit value of 0.114 than the repassivation pit, with a difference of 0.023 instead of a factor of 3. This is despite the subsurface model having a pit aspect ratio of 10, but this is predominately due to the pit mouth having a diameter of only 60 µm. Again, this shows that the geometry of the pit plays an important role in the magnitude of the maximum total true strain in x-direction values in the pit as it seems that the smoother the transition

from pit sides to pit bottom, the lower the maximum total true strain in x-direction values are in the pits.

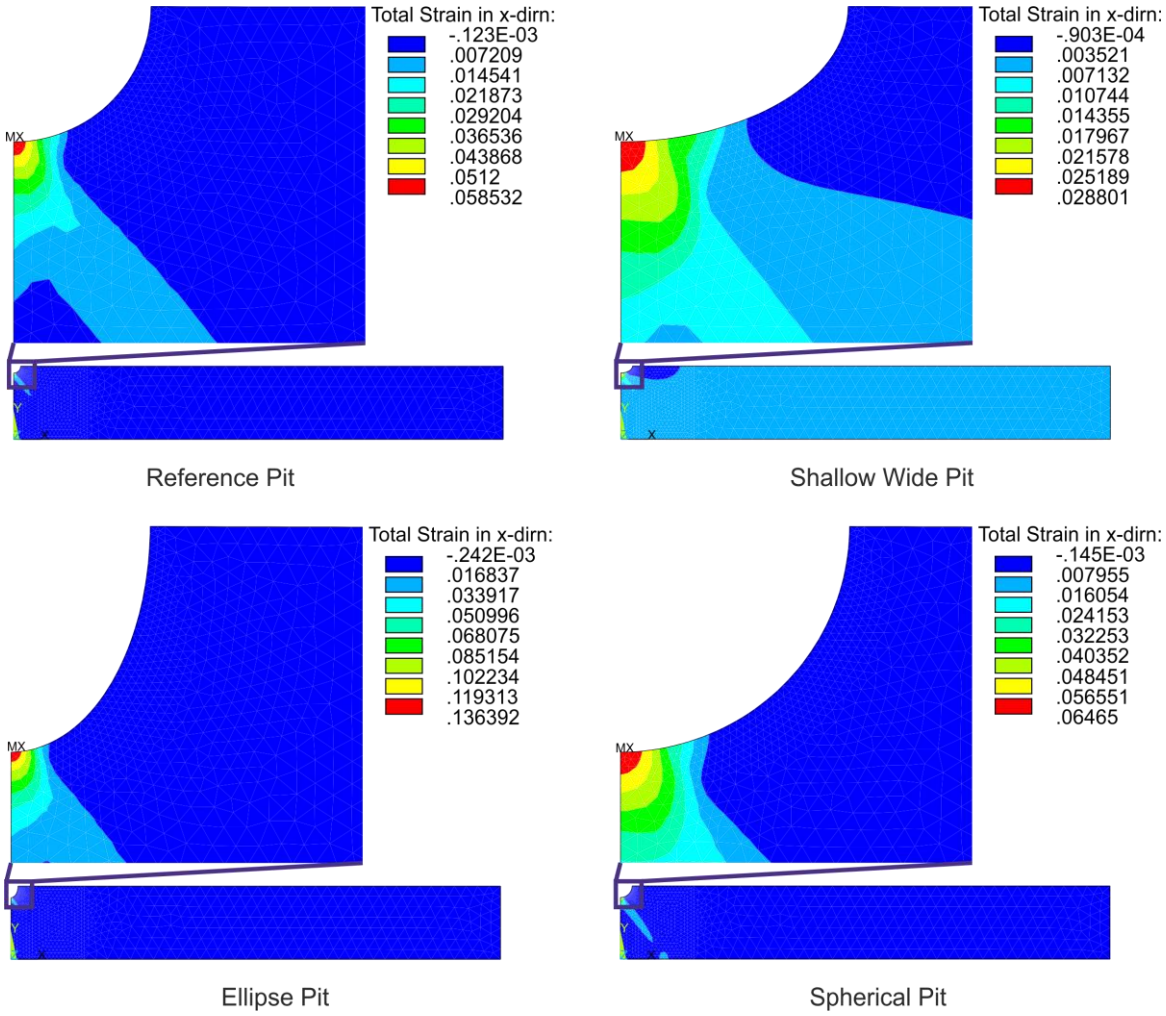

Figure 5.9: 2D UA HAZ submodel with reference, shallow wide, ellipse and spherical pits total true strain in x-direction results.

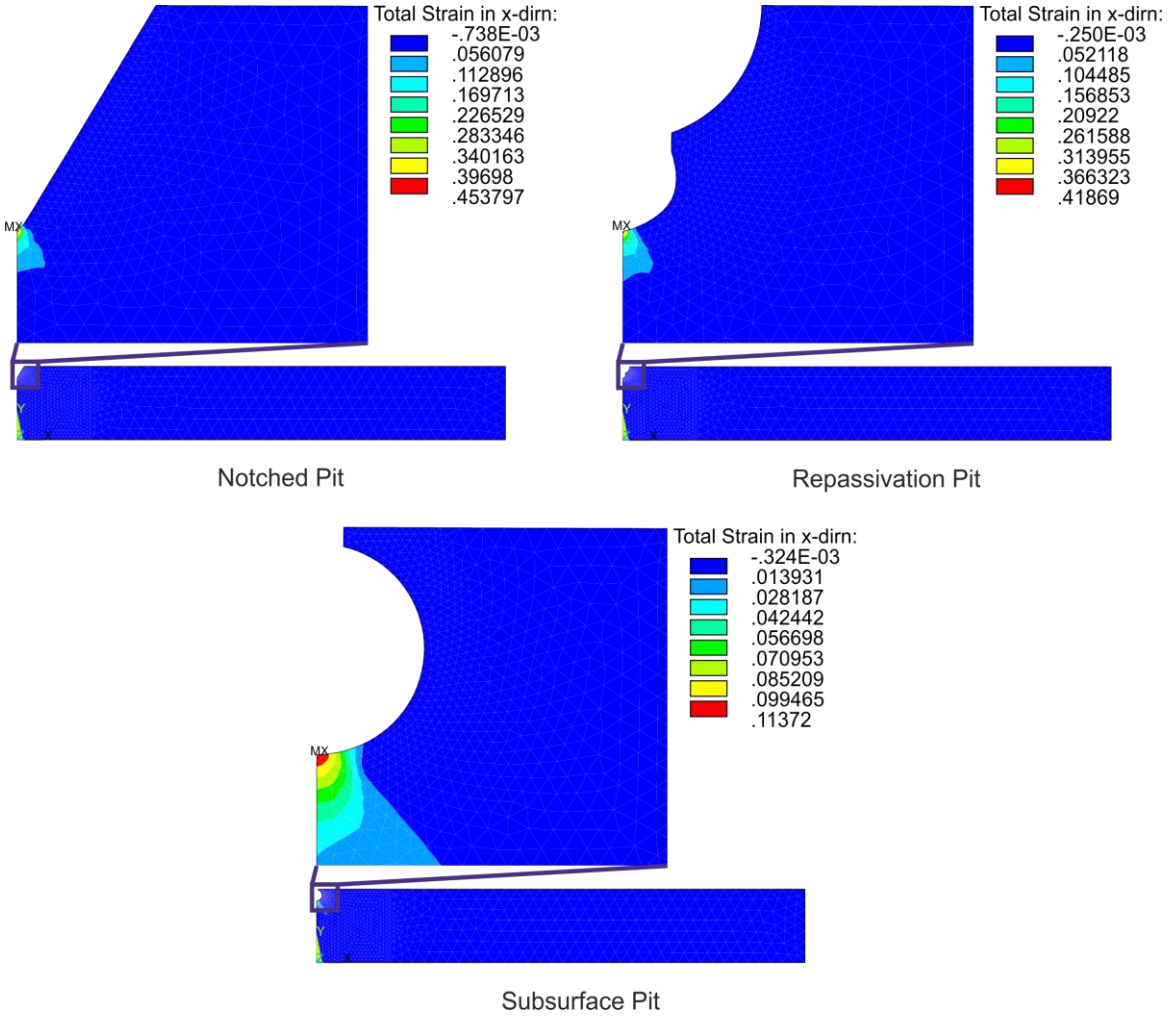

Figure 5.10: 2D UA HAZ submodel with notched, repassivation and subsurface pits total true strain in x-direction results.

2D Uniaxial Structural Analysis for Unpitted Base Material (BM)

The 2D UA (Uniaxial) BM model of one quarter of the real specimen and the gauge length region selected from the 2D UA BM one quarter model, along with their corresponding maximum x-direction stress and total true strain results, can be seen in Figure 5.11 and Figure 5.12. As for the HAZ simulation, the location of the max stresses and total true strains in x-direction for the model are in the same location, which falls just outside the margins of the gauge length. Table 5.4 shows the displacement values applied to the global model and the resulting maximum stresses and total true strains in x-direction for the 2D UA BM one quarter model.

Table 5.4: Displacement values applied to 2D UA BM one quarter model and resulting total true strain and stress results.

Displacement (x) (mm)	Total true strain in x-direction	Stress in X-direction	% Yield
0.0966	0.0037	770	100

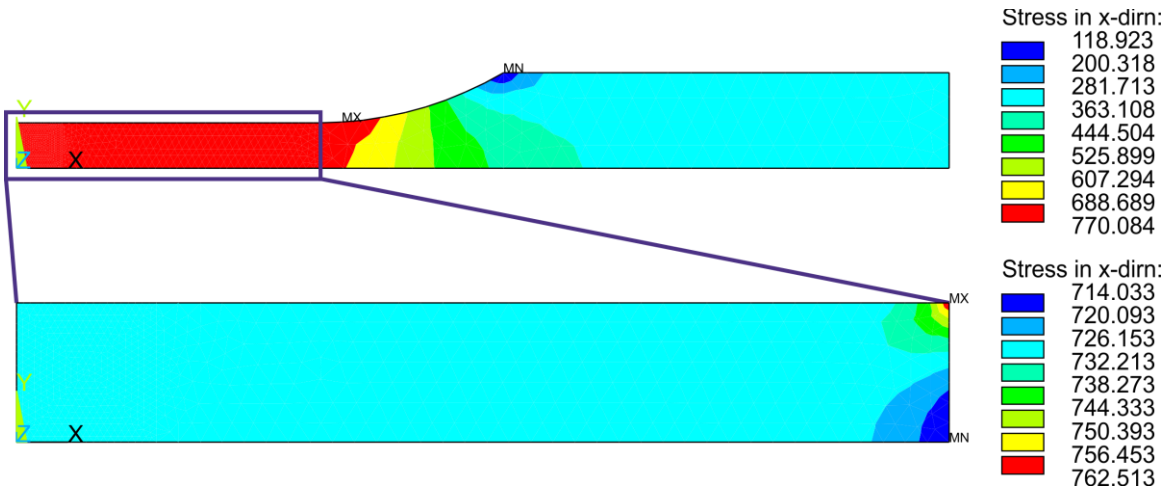

Figure 5.11: 2D one quarter model maximum stress in x-direction for 100% of BM yield stress applied as uniaxial displacement load and selected gauge length region shown on the 2D one quarter model.

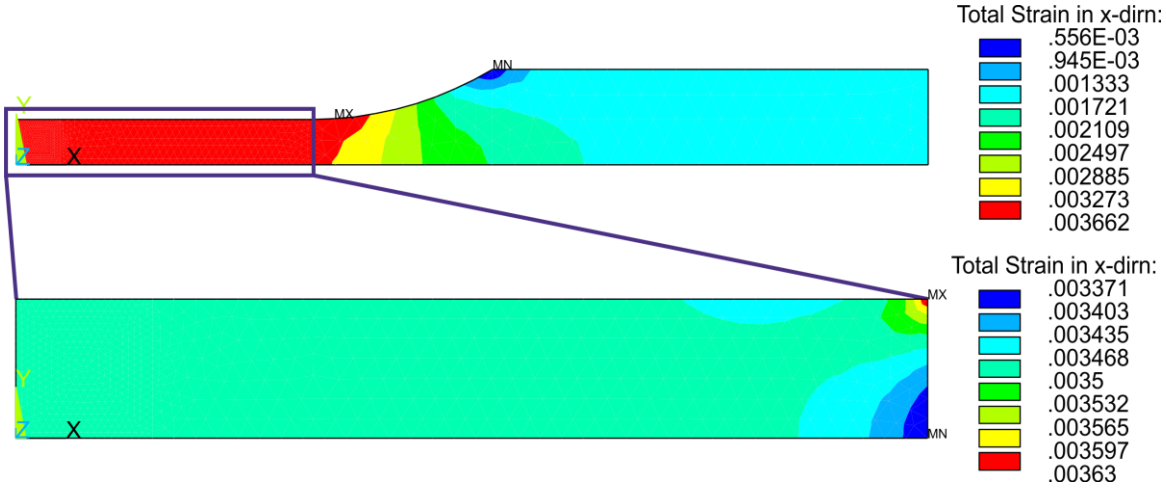

Figure 5.12: 2D one quarter model maximum total strain in x-direction for 100% of BM yield stress applied as uniaxial displacement load and selected gauge length region shown on the 2D one quarter model.

The 2D UA BM submodel with the x- and y-displacements from the 2D UA BM one quarter model applied and the corresponding maximum x-direction stress and total true strain results can be seen in Figure 5.13 and Figure 5.14. Table 5.5 shows the global

displacement applied to the 2D UA HAZ submodel and the resulting stress and total true strain in the x-direction.

Table 5.5: Displacement values applied to 2D UA BM submodel and resulting total true strain and stress results.

Displacement (x) (mm)	Total true strain in x-direction	Stress in X-direction	% Yield
0.044197	0.0036	763	100

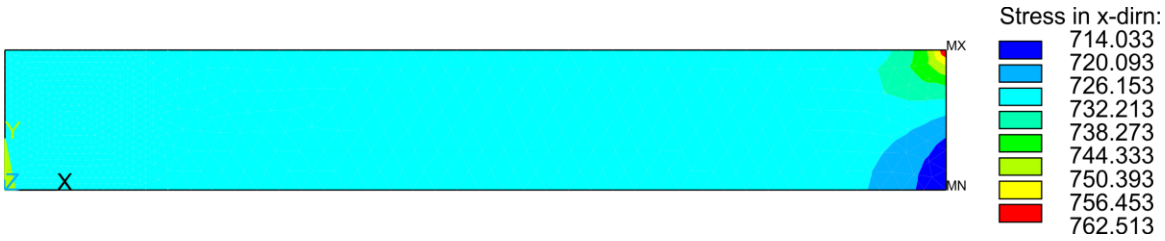

Figure 5.13: 2D UA submodel maximum stress in x-direction for 100% of BM yield stress applied as uniaxial displacement load to 2D one quarter model.

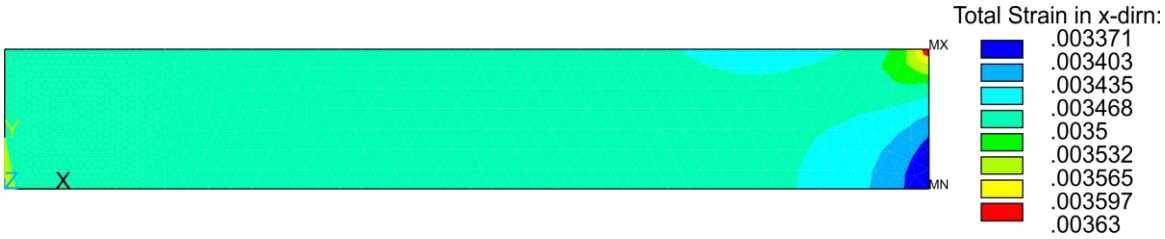

Figure 5.14: 2D UA submodel maximum total strain in x-direction for 100% of BM yield stress applied as uniaxial displacement load to 2D one quarter model.

As for the 2D UA HAZ model, the maximum x-direction stress and total strain values in the 2D UA BM submodel are the same as the maximum x-direction stress and total strain values for the selected gauge length region. Again, there is a slight variation in the values for the maximum stresses and total true strains x-direction as the locations in the one quarter models are located slightly outside the gauge length region, as for the HAZ simulations described previously. Therefore, in the subsequent simulations involving a 2D UA BM one quarter model loaded to 100% of yield stress, the 2D UA BM submodel is used in place of the 2D UA BM one quarter model.

The results for the total true strain in the x-direction for the 2D UA BM submodels seen in Figure 5.11 to Figure 5.14 correspond to the results in Figure 5.4 to Figure 5.7. For both materials the locations of the maximum and minimum strains in the 2D one quarter model, selected gauge length region and the submodel are all in the same regions. However, the

maximum x-direction stress and total strain values for the HAZ simulations are greater than for the BM simulations as the strength of the HAZ material is greater.

2D Uniaxial Structural Analysis for Pitted Base Material (BM)

The same pit geometries used in the HAZ simulations were also investigated for the BM. The maximum total strain in x-direction in the pits in the BM are presented in Figure 5.16 and Figure 5.17. These maximum total strain in x-direction values correspond to a 100% yield stress in the unnotched 2D BM model. Table 5.6 shows the maximum strains in x-direction for the various pit geometries and have been sorted from lowest to highest and the pit aspect ratio.

Table 5.6: Lowest maximum total strain in x-direction to highest for all seven pit geometries in the uniaxially loaded 2D UA BM submodel and the pit aspect ratios.

Pit Geometry	Maximum Total Strain in the x-direction	Pit Aspect Ratio
Shallow Wide	0.024189	0.3
Reference	0.049687	0.5
Spherical	0.055787	0.5
Subsurface	0.098193	10
Ellipse	0.121112	0.83
Repassivation	0.34663	0.83
Notched	0.396307	0.83

The maximum total true strain in x-direction for all pit geometries in the 2D UA BM submodel are presented in Figure 5.16 as a function of time. All of the maximum total true strain in x-direction for all pit geometries occur in the pit bottoms. Similar to the maximum total true strain in x-direction results for the pitted 2D HAZ quarter model in Figure 5.8, the strains for the pitted geometries do not increase linearly over time. This again may be due to the specimen being loading past the yield point of the material.

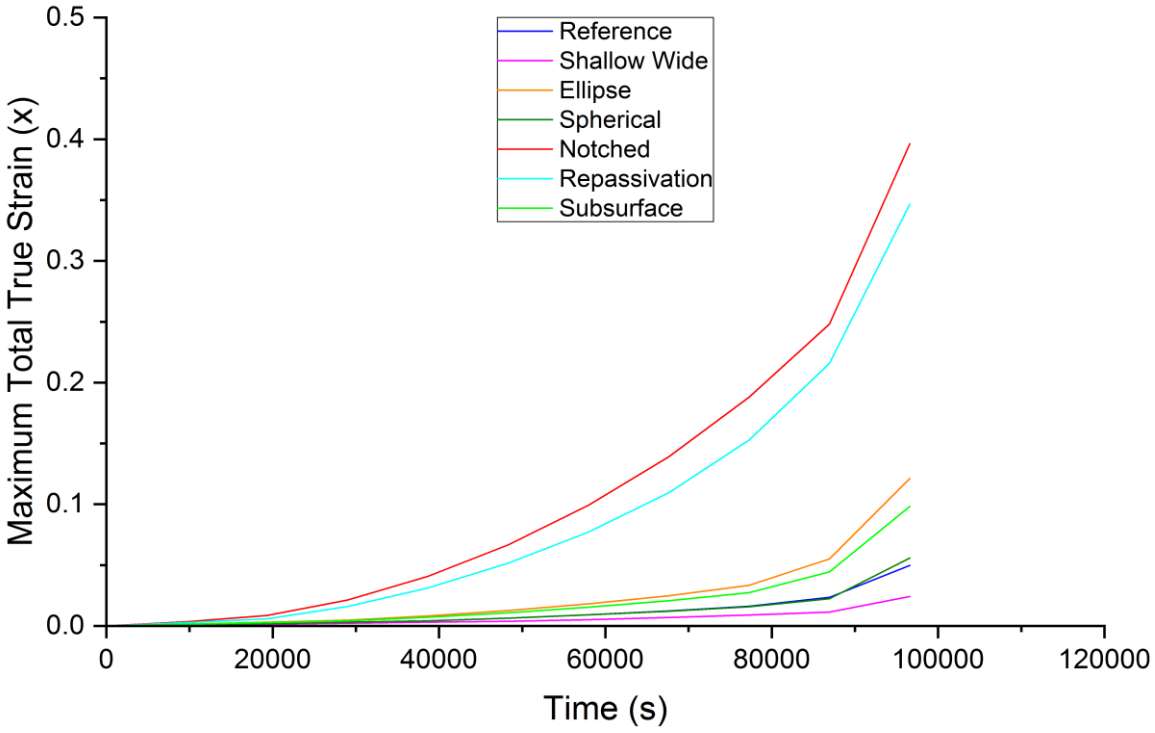

Figure 5.15: Maximum total true strain in x-direction vs time for all pit geometries in the 2D BM submodel.

As seen in Figure 5.16 and Figure 5.17, the location of the maximum total strain in x-direction in all of the seven different pit geometries, again occurs at the bottom of the pits. Similar to the HAZ values mentioned above, Table 5.6, Figure 5.16 and Figure 5.17 show that the shallow wide pit has the lowest maximum total strain in x-direction value, 0 024189, with the notched pit having the highest value, 0.396307. The maximum total strain in x-direction values for the BM material are ranked in the same order as for the HAZ. This again shows that for a uniaxial x-direction displacement load the depth of the pit is the most important geometric aspect of the pit, with a shallow pit producing lower maximum total strain in x-direction values in pits. These results again show that the geometry of the pit plays an important role in the magnitude of the maximum total strain in x-direction values in the pit as it seems that the smoother the transition from the pit sides to the pit bottom, the lower the maximum total strain in x-direction values are in the pits.

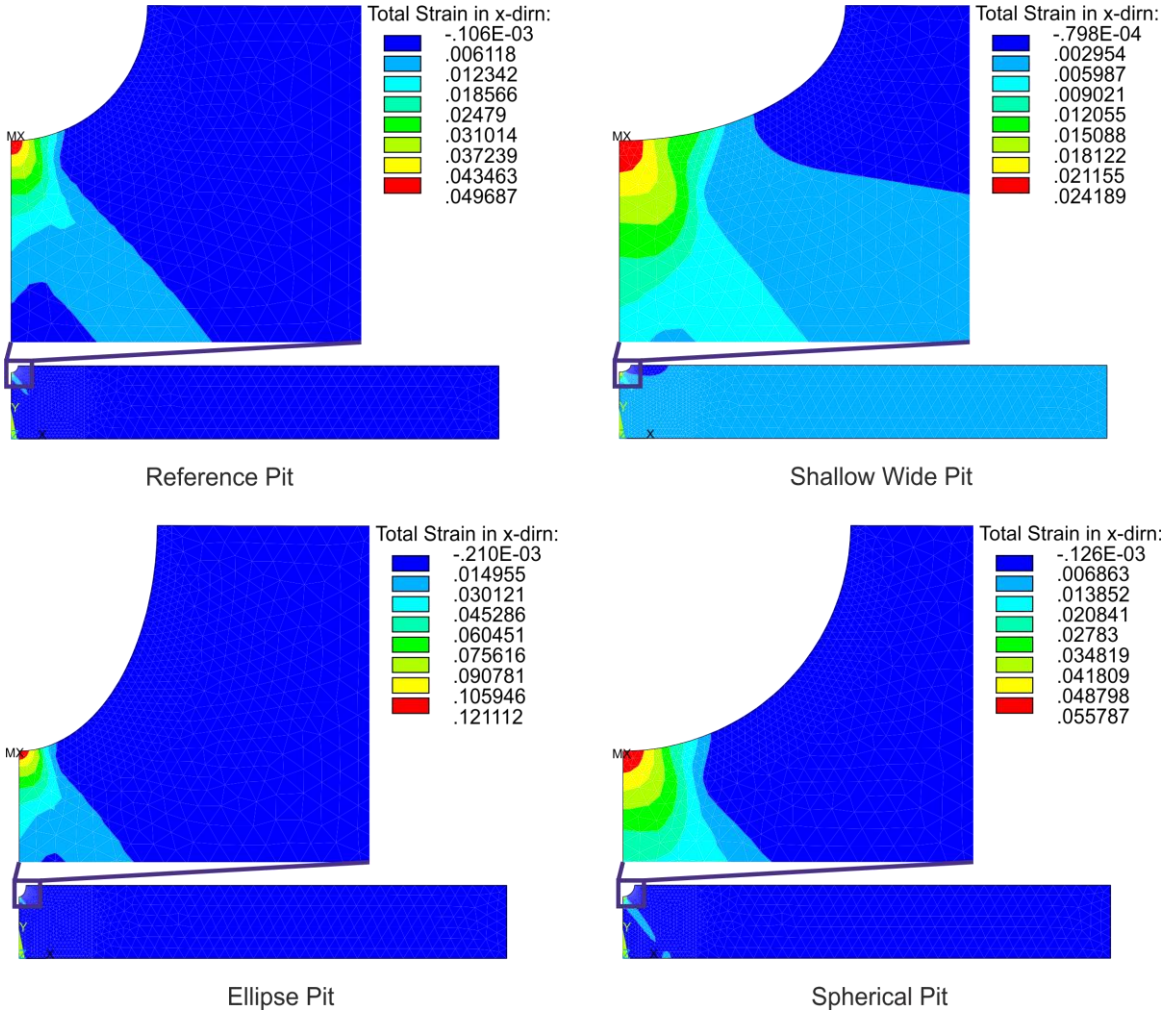

Figure 5.16: 2D UA BM submodel with reference, shallow wide, ellipse and spherical pits total strain in x-direction results.

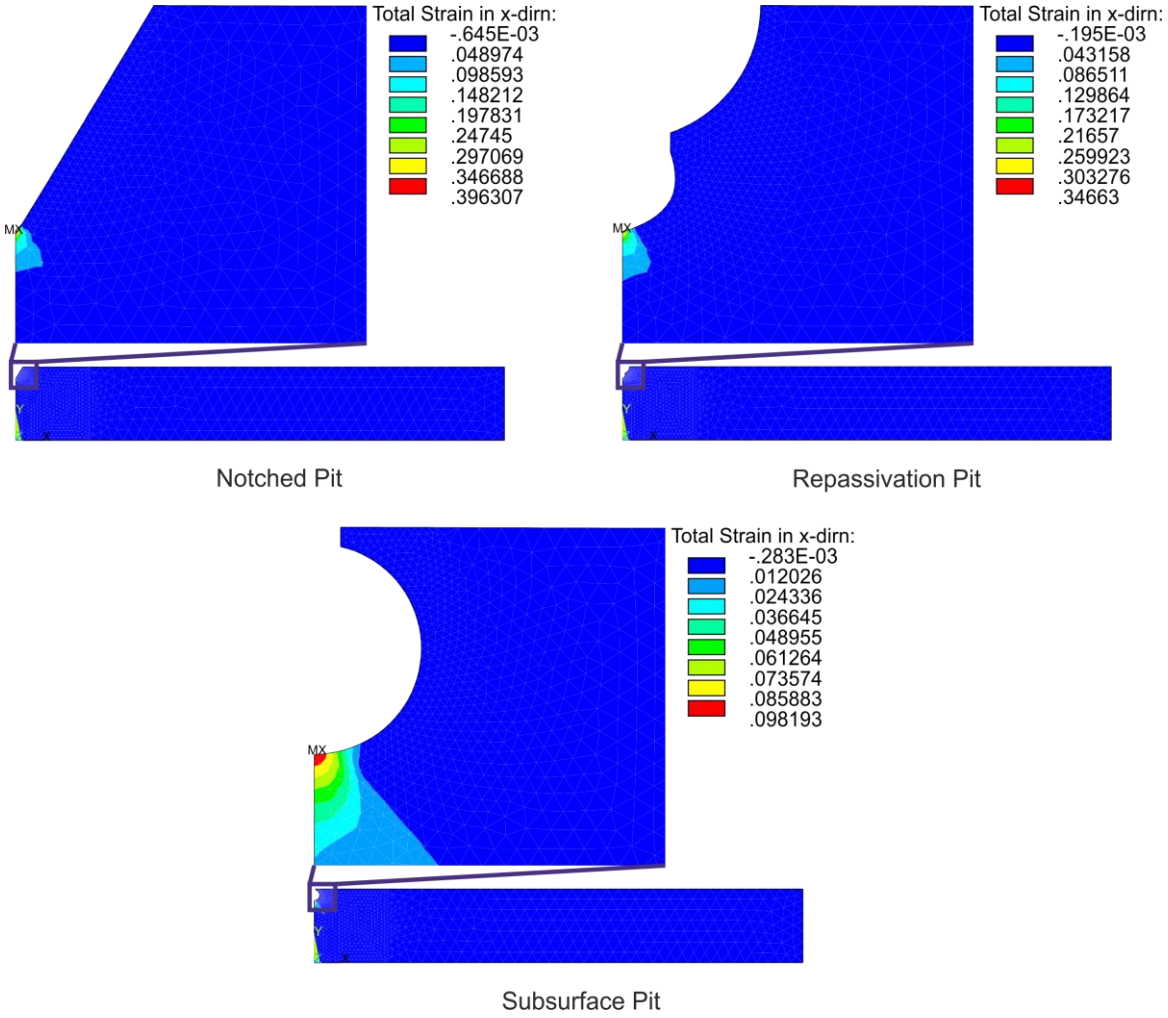

Figure 5.17: 2D UA BM submodel with notched, repassivation and subsurface pits total strain in x-direction results.

The pitting information above for both HAZ and BM can also be presented graphically, as shown in Figure 5.18. These graphs show for both HAZ and BM, both repassivation and notched pit geometries have consistently higher local strains for all corresponding global strain values compared to the other pit geometries. The shallow wide pit has the lowest local strains for all corresponding global strain values. The reference and spherical pits have similar curves, but the spherical pit has the higher final local strain value. This again shows the depth of the pit is the most important geometric aspect of the pit, with a shallow pit producing lower local strains for all corresponding global strain values. The local and global strains in Figure 5.18 for the HAZ material are higher than for the BM. This may be due to the strength of the HAZ is greater than for the BM, as previously explained.

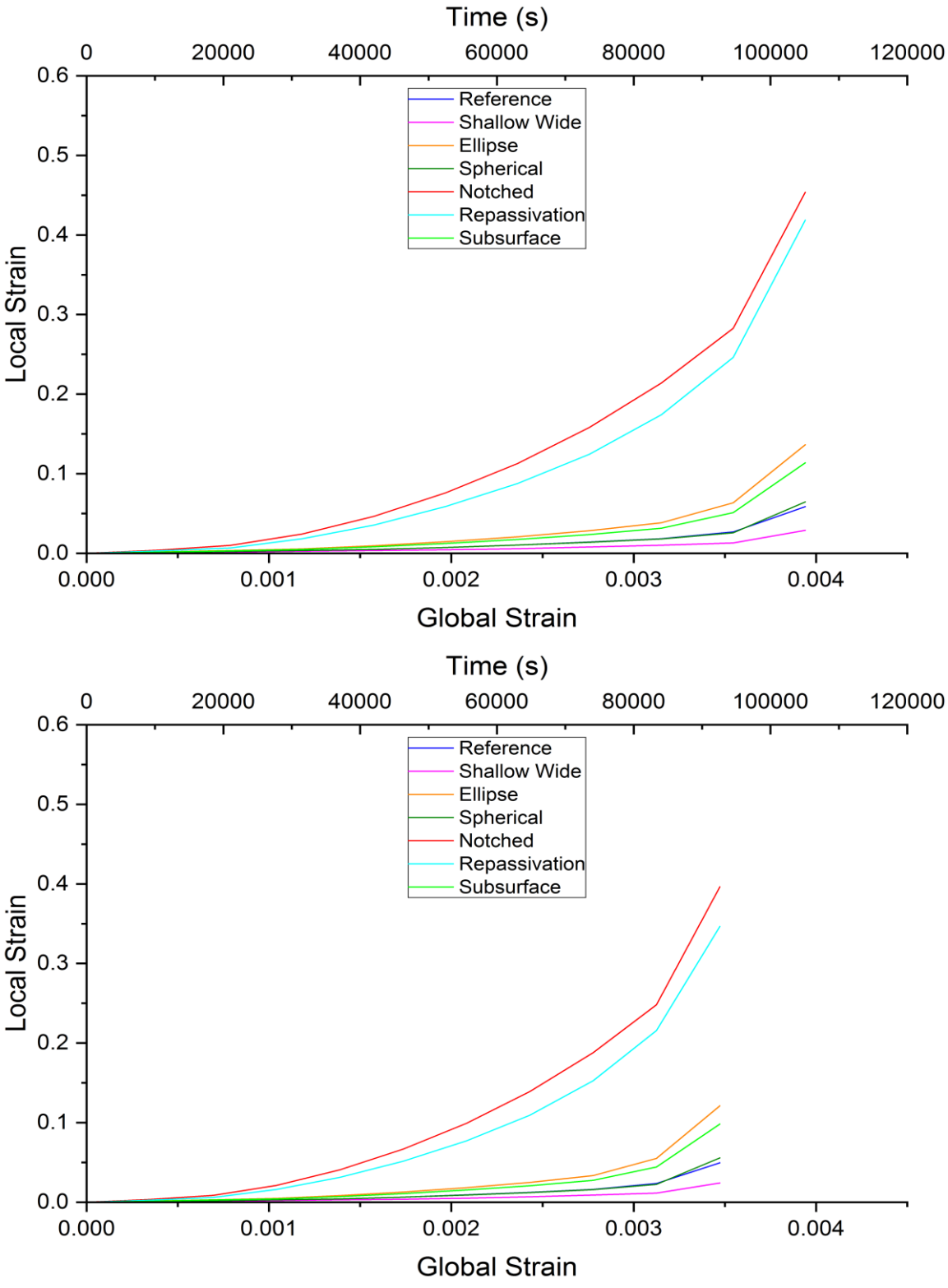

Figure 5.18: Graph of global vs local strains for all pit geometries in the 2D UA HAZ (Top) and BM (Bottom) submodel.

Time-dependent pit growth is not modelled in this stage of the work, nor is this shown in Figure 5.18. The same pit geometry is present for the duration of the time for all pit

geometries modelled. This is to investigate the increase in local strain compared to the gradually applied global strain over a certain time period.

The order of the pits with the lowest to highest maximum total true strain in x-direction is the same for the BM material, Table 5.6, as for the HAZ material, Table 5.3. The location of the highest total true strain in x-direction for the 2D BM pit geometries, Figure 5.16 and Figure 5.17, are the same for the 2D HAZ pit geometries, Figure 5.9 and Figure 5.10, which is at the pit bottom. Additionally, the location of the highest total true strain in x-direction for the 2D HAZ pit geometries with 66% of the load applied, Figure A.1 and Figure A.2 in Appendix A are also in the pit bottom. The order of the pits with the lowest to highest maximum total true strain in x-direction for the 66% loaded 2D HAZ pit geometries is however different to Table 5.3. For the 66% loaded pit geometries the spherical pit has a higher maximum total true strain in x-direction than the reference pit. Figure 5.18 shows that the spherical and reference pits have similar global strain and local strain values, however after 100% of the load has been applied the reference pit has the higher value. This is however not the case when 66% of the load is applied, as seen in Figure A.3. This information shows the importance of graphs such as Figure 5.18, where the global and local strain information for all stages of the numerical simulation is presented and not just the final stage, as in Table 5.3.

The results of this 2D investigation correlate with the results obtained by both Mai et al. [12] and Wang and Han [273]. These researchers also found that the location of the highest strains is in the pit bottom. As a weakness of such previous investigations, the exact materials used in these simulations were not specified, however Mai et al. used a “metallic material” and Wang and Han used a stainless steel. Both researchers used more realistic pit geometries instead of idealised versions with smooth walls and bottom as used in this work and modelled pit growth in addition. The pit geometries modelled by Mai et al. are shown in Figure 2.38 in Section 2.3.5 and the pit geometry modelled by Wang and Han is a spherical pit with unsmooth sides and bottom.

Mai et al. discovered that the pit morphology greatly affects the SCC nucleation site, the subsequent path and the time taken for SCC initiation. It was also found in the results presented above that the pit morphology certainly influenced the magnitude of the strains present in the pit. Mai et al. also discovered that cracks can nucleate and evolve for short periods of time when subjected to a tensile load. However, only a single sharp crack will continue to grow as the rest of the cracks arrest due to relaxation of stresses and strains as a result of the main crack propagating.

Wang and Han applied a tensile stress of 200 MPa to a model and no stress to an additional model and investigated the growth of the pits. It was found that the pit grows more quickly in depth with a load applied and leads to an increase in strain in the pit bottom.

Therefore, the research of Mai et al. and Wang and Han show that in order to model SCC the shape of the pit and if a load is applied or not are vital factors in determining if cracks will occur in pits. This is also found in the results presented above, as the geometry of the pits certainly have an effect on the local strains present in the pit, with a smoother transition from pit sides to bottom having lower strains than sharper geometries.

However, some more information is provided already at this point, for instance, regarding the locations of maximum strains in additional pit geometries than previously shown elsewhere. It seems that most research concentrates the stresses in a pit and not the strains so there is limited literature available to investigate strains in 2D pit geometries while subjected to a tensile load. It can only be emphasised that the local strains are much more important to evaluate with respect to subsequent hydrogen assisted cracking (HAC), as hydrogen reduces the ductility more than the strength of a material, i.e. embrittles the material. In addition, the literature published by Mai et al. and Wang and Han however contained only pit geometries b, d and e from Figure 2.37 in Section 2.3.5 and a spherical pit geometry. This work additionally investigated pit geometry c from Figure 2.37 in Section 2.3.5 along with a notched pit and a repassivation pit. The repassivation pit is a pit geometry which may be found during inspections of SMSS as these pit geometries are formed when a pit stops growing but then conditions change, and a new pit may form at the bottom of the existing pit. Therefore, this work provides information regarding the locations of maximum strains located in additional pit geometries than available previously.

To summarise the above findings, the present investigation of the various 2D pit geometries under uniaxial loading shows that the location of highest strains in the pit geometries modelled are <u>all</u> located in the pit bottom. Therefore, it can be stated that:

- *Using a smaller submodel, instead of modelling the whole specimen geometry, produces comparable results.*
- *The presence of a pit in a model produces high local total strain in the x-direction values in the pit region when loaded in the x-direction. Due to high local strains in the pit bottom, HAC is more likely to occur in this region for all pit geometries modelled in 2D, in accordance with Mai et al. [12, 13] and Wang and Han [273].*
- *The pit depth is the most important geometric aspect of the pit, with deeper pits producing higher values.*

2D Bending Structural Analysis for Unpitted HAZ

As a step further, the same model of a round NACE small scale tensile specimen has been subjected to a bending load. This normally does not completely comply to the real bending during the laying of SMSS pipelines on seabeds which is undertaken by reeling and dereeling of the tubular structures. This introduces triaxial bending loads into the material by tension and compression in the axial, radial and tangential direction. However, it might at least be compared to axial bending during operation and shutdowns over long free spans, due to variations in soil conditions and temperature differences.

As a first approach, bending loads have also been investigated for the present contribution, and not just the more commonly modelled uniaxial loads. Under uniaxial loading conditions tensile stresses are present throughout the material, but when a bending load is applied tensile stresses are only present on the top surface of the material. Therefore, the location of the highest tensile stress and total true strain in x-direction regions in the 2D HAZ model of one quarter of the real specimen were investigated as part of this work. Table 5.7 shows the displacement values applied and the resulting maximum stresses and total true strains in x-direction for the 2D HAZ bend one half model. The maximum stress and total true strain in x-direction regions in the unpitted HAZ 2D half model subjected to a bending load can be seen in Figure 5.19 and Figure 5.20.

Table 5.7: Displacement values applied to 2D HAZ bend one half model and resulting total true strain and stress results.

Displacement (y) (mm)	Total True Strain in x-direction	Stress in X-direction (MPa)	% Yield
0.913	0.00414	870	100

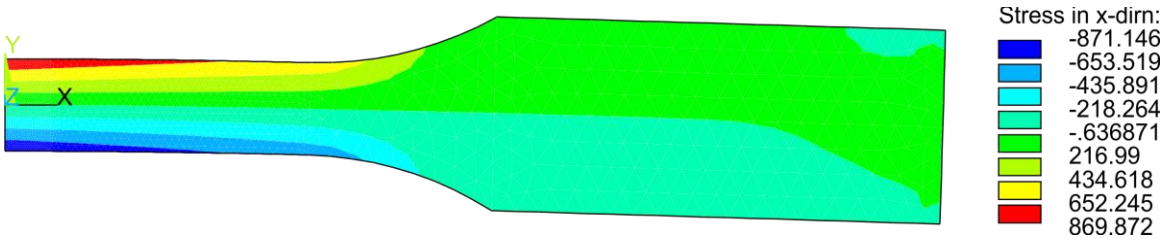

Figure 5.19: 2D half model maximum stress in x-direction for 100% of HAZ yield stress applied as bending displacement.

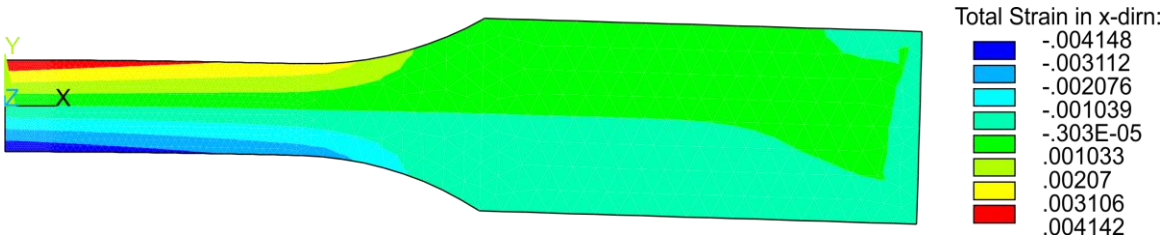

Figure 5.20: 2D half model maximum total true strain in x-direction for 100% of HAZ yield stress applied as bending displacement.

A graph depicting the increase of displacement, maximum total true strain and stress in x-direction with increasing time, Figure 5.21, show that these three parameters increase linearly with increasing time over 1,000,000 seconds. This is the same as for the uniaxially loaded specimen in Figure 5.3.

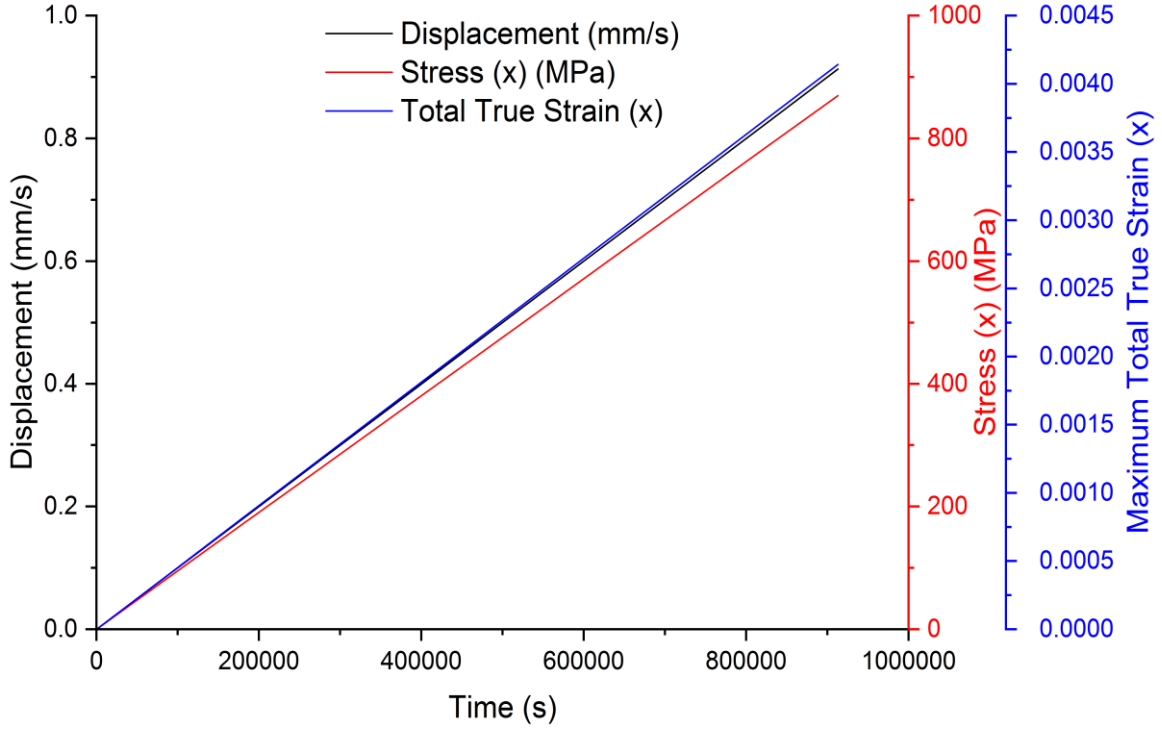

Figure 5.21: Displacement, maximum total true strain and stress in x-direction vs time for the 2D one quarter model for 100% of HAZ yield stress applied as a bending load.

The 2D HAZ half model and the selected gauge length region with corresponding maximum x-direction stress and total true strain results can be seen in Figure 5.22 and Figure 5.23. Figure 5.24 and Figure 5.25 show the 2D HAZ bend submodel with the x- and y-displacements from the 2D HAZ half model applied and corresponding maximum x-direction stress and total true strain results. Table 5.8 shows the displacement values applied to the 2D HAZ bend submodels and the resulting stresses and total true strains in the x-direction.

Table 5.8: Displacement values applied to 2D HAZ bend submodel and resulting total true strain and stress results.

Displacement (y) (mm)	Total True Strain in x-direction	Stress in X-direction (MPa)	% Yield
0.15914	0.00414	870	100

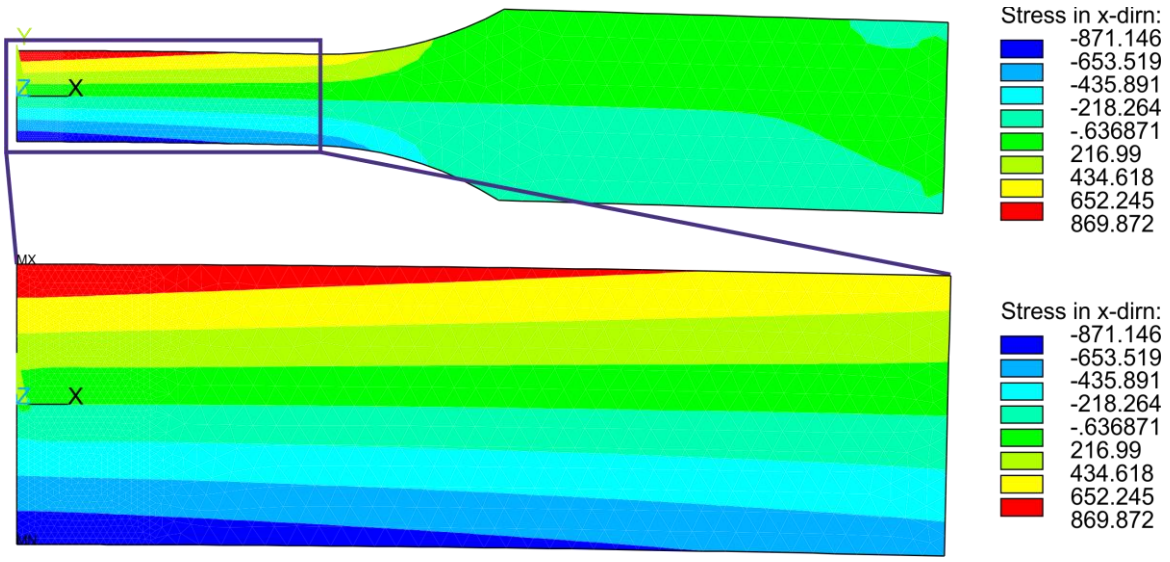

Figure 5.22: 2D half model maximum stress in x-direction for 100% of HAZ yield stress applied as bending displacement and selected gauge length region shown on the 2D half model.

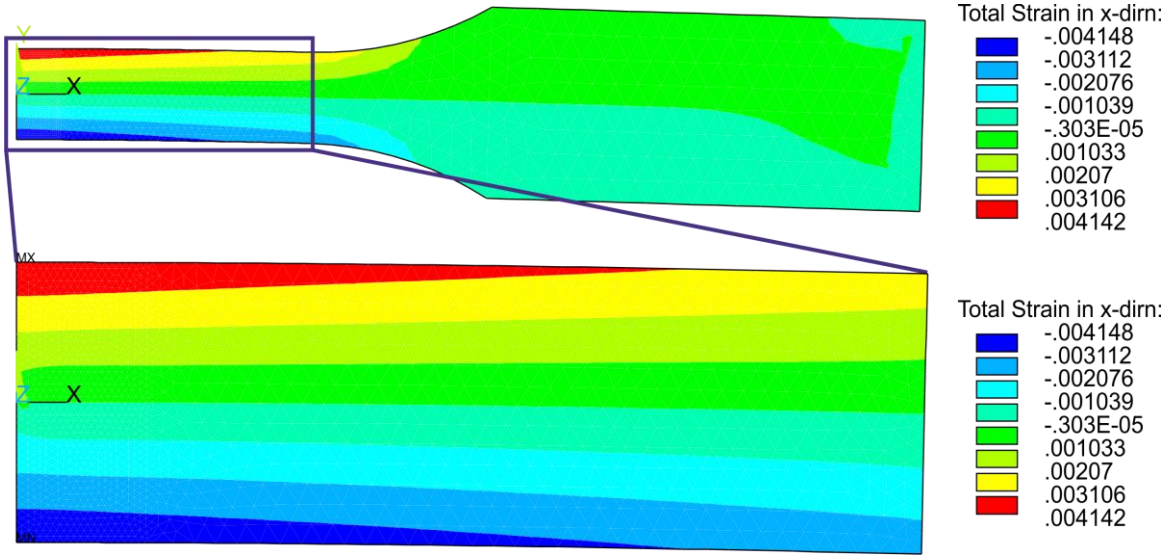

Figure 5.23: 2D half model maximum total true strain in x-direction for 100% HAZ yield stress applied as bending displacement and selected gauge length region shown on 2D half model.

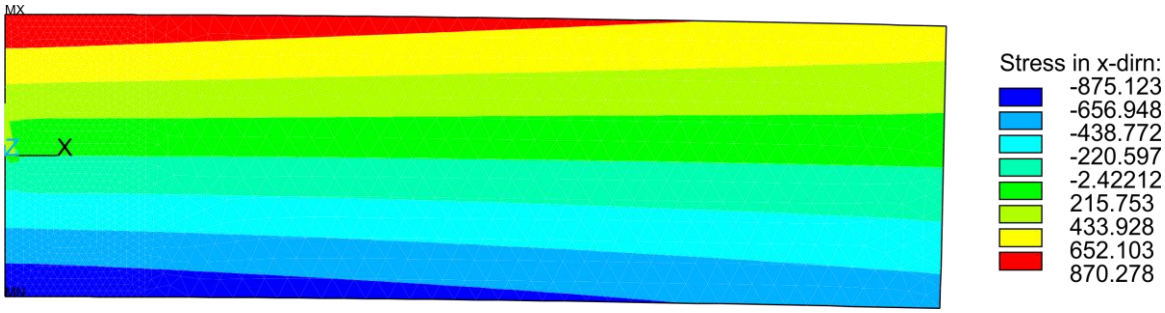

Figure 5.24: 2D bend submodel maximum stress in x-direction for 100% of HAZ yield stress applied as bending displacement to 2D half model.

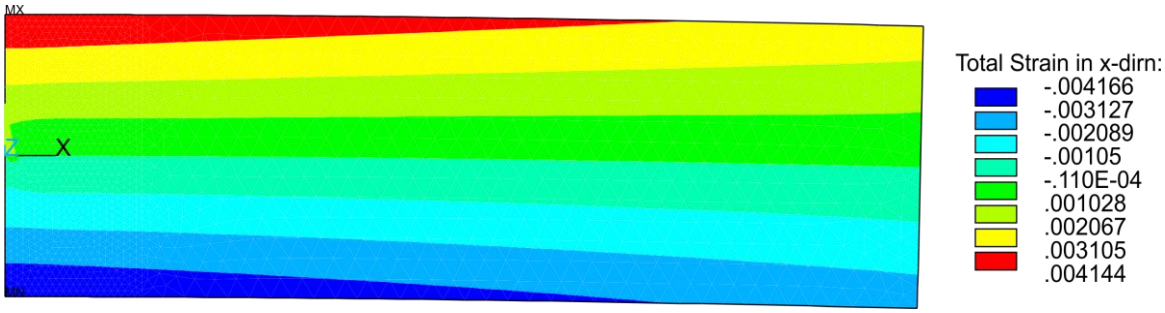

Figure 5.25: 2D bend submodel maximum total true strain in x-direction for 100% of HAZ yield stress applied as bending displacement to 2D half model.

As seen in Figure 5.22 to Figure 5.25 the maximum stress and total true strain in x-direction values in the 2D HAZ bend submodel are equal to the maximum stress and total true strain in x-direction values in the 2D HAZ half model. The location of these maximum values is in the same region for both models. For this reason, in the subsequent simulations involving a 2D HAZ half model with a -y-direction load applied to simulate bending, until 100% of yield stress is reached, the 2D HAZ bend submodel will be used in place of the 2D HAZ half model.

The results for the total true strain in the x-direction for the 2D BM bend submodels can be seen in Figures A.7 to A.10 in Appendix A. Similar to the 2D UA results, these 2D BM bending results correspond to the HAZ results in Figure 5.22 to Figure 5.25 with the regions of maximum and minimum total true strains in x-direction being located in the same region for the 2D half model, selected gauge length region and the submodel, respectively.

2D Bending Structural Analysis for Pitted HAZ

Similar to the uniaxial (UA) models, the maximum total true strain in x-directions in the pits in the 2D HAZ bend submodel are presented in Figure 5.27 and Figure 5.28. These strain values correspond to a 100% yield stress in the unpitted 2D HAZ half model. The location of the maximum total true strain in x-direction in all of the seven different pit geometries with a bending load applied to the 2D HAZ bend submodel again occurs at the bottom of

the pit. Table 5.9 shows the maximum strains in x-direction for the various pit geometries and have been sorted from lowest to highest. The pit aspect ratio for each pit is also shown.

Table 5.9: Lowest maximum total true strain in x-direction to highest for all seven pit geometries in the bending loaded 2D HAZ 2D bend submodel and pit aspect ratio.

Pit Geometry	Maximum Total true strain in the x-direction	Pit Aspect Ratio
Unpitted	0.00414	-
Shallow Wide	0.013078	0.3
Spherical	0.021364	0.5
Reference	0.024816	0.5
Subsurface	0.038213	10
Ellipse	0.047472	0.83
Repassivation	0.211922	0.83
Notched	0.264356	0.83

The maximum total true strain in x-direction for all pit geometries in the 2D bend HAZ submodel are presented in Figure 5.26 as a function of time. All of the maximum total true strain in x-direction for all pit geometries occur in the pit bottoms, as for the uniaxial simulations. Unlike the maximum total true strain in x-direction results for the unpitted 2D HAZ quarter model in Figure 5.21, the strains for the pitted geometries do not increase linearly over time, similar to the uniaxial loading condition. This again may be due to the specimen being loading past the yield point of the material.

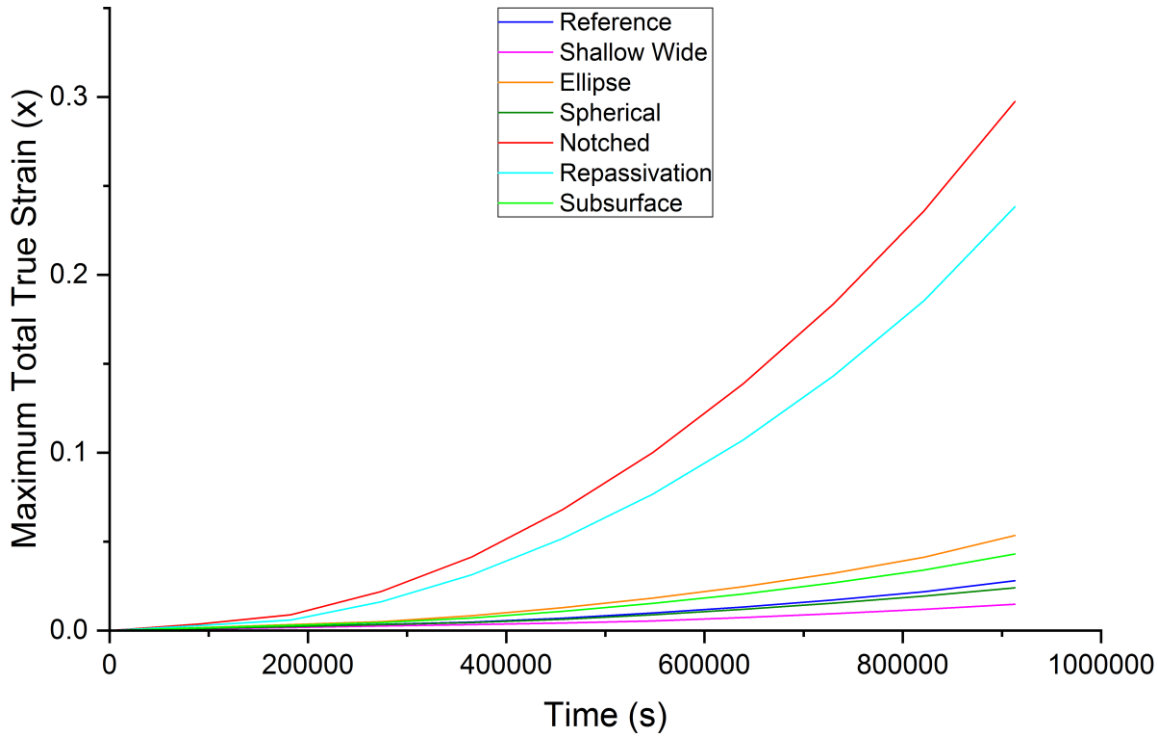

Figure 5.26: Maximum total true strain in x-direction vs time for all pit geometries in the 2D bend HAZ submodel.

Table 5.9, Figure 5.27 and Figure 5.28 show that the shallow wide pit again has the lowest maximum total true strain in x-direction value, 0.014. However, when a bending load is applied, the spherical pit has the second lowest value, 0.021, and not the reference pit, as in Table 5.3. The shallow wide and spherical pits have a pit mouth diameter of 600 µm, however the shallow wide pit is not as deep as the spherical pit, with depths of 180 µm and 300 µm respectively. This results in a pit aspect ratio of 0.3 for the shallow wide pit but a ratio of 0.5 for the spherical pit. This shows that for a bending load a large pit mouth and shallow pit depth, which produces the lowest pit aspect ratio, results in the lowest maximum total true strain in x-directions in the pits. This can also be seen in the reference pit, which is the only other shallow pit modelled which has the same pit depth of 180 µm as the shallow wide pit, but the pit mouth diameter is only 360 µm. The pit aspect ratio for the reference pit is the same as for the spherical pit, 0.5. This further shows that for a bending load the pit mouth diameter is the most important geometric aspect of the pit, with a larger pit mouth diameter producing lower maximum total true strain in x-direction values in pits.

The ellipse, repassivation and notched pits all have a pit aspect ratio of 0.83 and these are the pits with the highest maximum total true strain in x-direction values. However, there is only a difference of 0.05 between the highest maximum total true strain in x-direction value in the notched pit and the second highest value in the repassivation pit while the ellipse pit

maximum value is 4.5 times lower than the repassivation pit. Similar to the uniaxial loading, this shows that the geometry of the pit plays an important role in the magnitude of the maximum total true strain in x-direction values in the pit, as it seems the smoother the transition from the pit sides to the pit bottom, the lower the maximum total true strain in x-direction values are in the pits.

In comparison to the 2D HAZ submodel with pit geometries removed and a uniaxial load applied, the order of the pit geometries is similar. When a uniaxial load is applied, the reference pit shape has a lower maximum total true strain in x-direction than the spherical pit, but this is reversed when a bending load is applied. It can therefore be concluded that for a uniaxial x-direction displacement the depth of the pit is the most important geometric aspect of the pit, with a shallow pit producing lower maximum total true strain in x-direction values in pits. In comparison, for a bending load the pit mouth diameter is the most important geometric aspect of the pit, with a larger pit mouth diameter producing lower maximum total true strain in x-direction values in pits.

The maximum total true strain in x-direction values when a uniaxial x-direction displacement is applied are much higher than when a -y-direction bending displacement is applied, Table 5.3 and Table 5.9. This is due to the application of the loads as the x-direction uniaxial load is applied to the x-direction only, with minimal resulting loads in the y-direction due to shrinkage. The -y-direction bending loading condition, however, has a load also applied in one direction only, but due to the boundary conditions a bending moment is set up in the model, which causes loads in both the x- and y-directions. Additionally, this may be a reason why the displacements applied to the bending models, Table 5.7 and Table 5.8 are significantly higher than the displacements applied to the UA models, Table 5.1 and Table 5.2 in order to reach 100% yield stress in the x-direction.

As cracks which initiate in pits grow perpendicular to the applied load, the most important loads to consider are those which cause the crack to grow in the -y-direction. These are the loads which are applied in the x-direction. Therefore, for the bending loading condition, even though the load is applied in the -y-direction, the results which are considered in this work are the same as considered for the 2D uniaxial loading condition, which is the total true strain in x-direction.

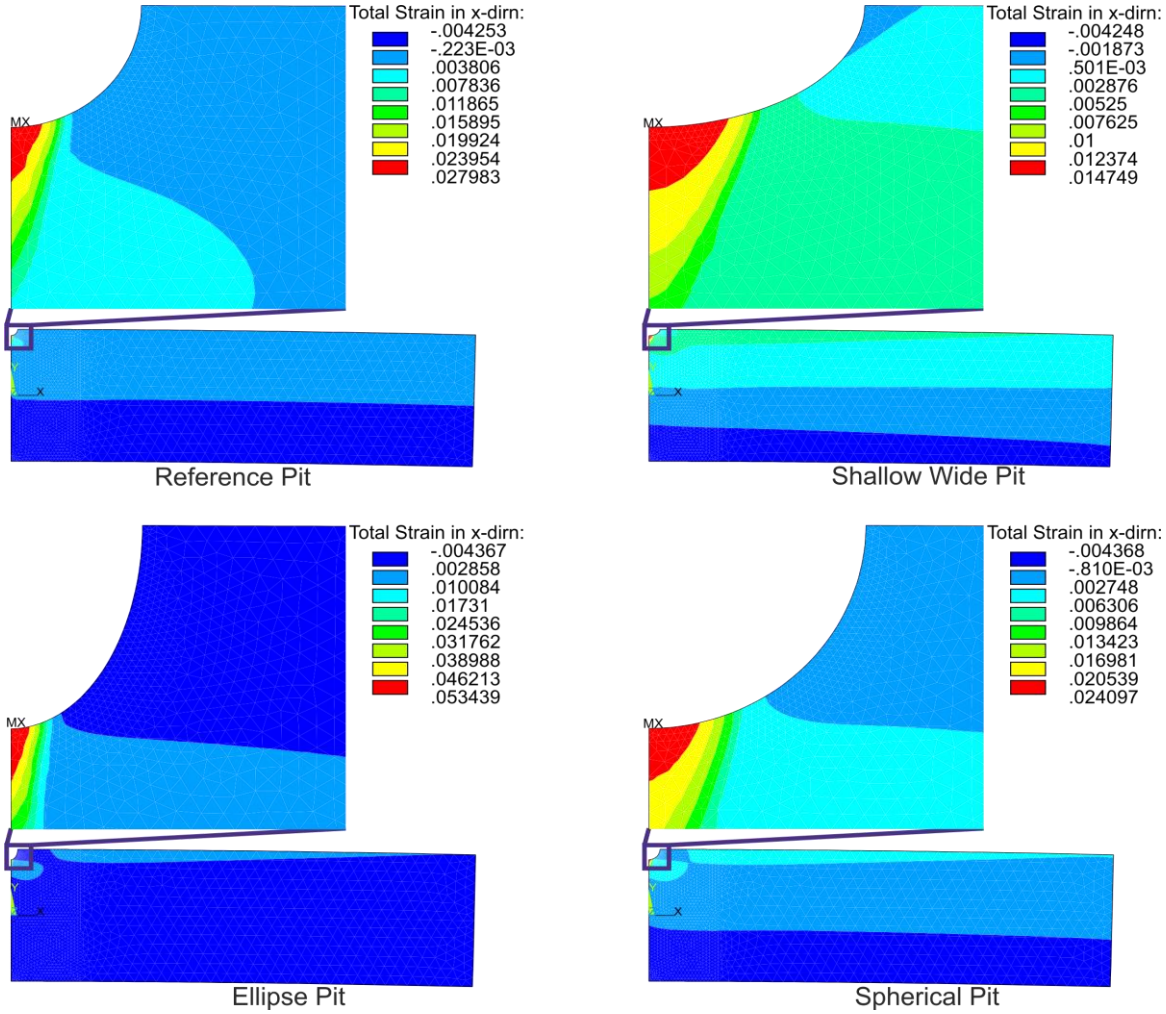

Figure 5.27: 2D HAZ bend submodel with reference, shallow wide, ellipse and spherical pits total true strain in x-direction results.

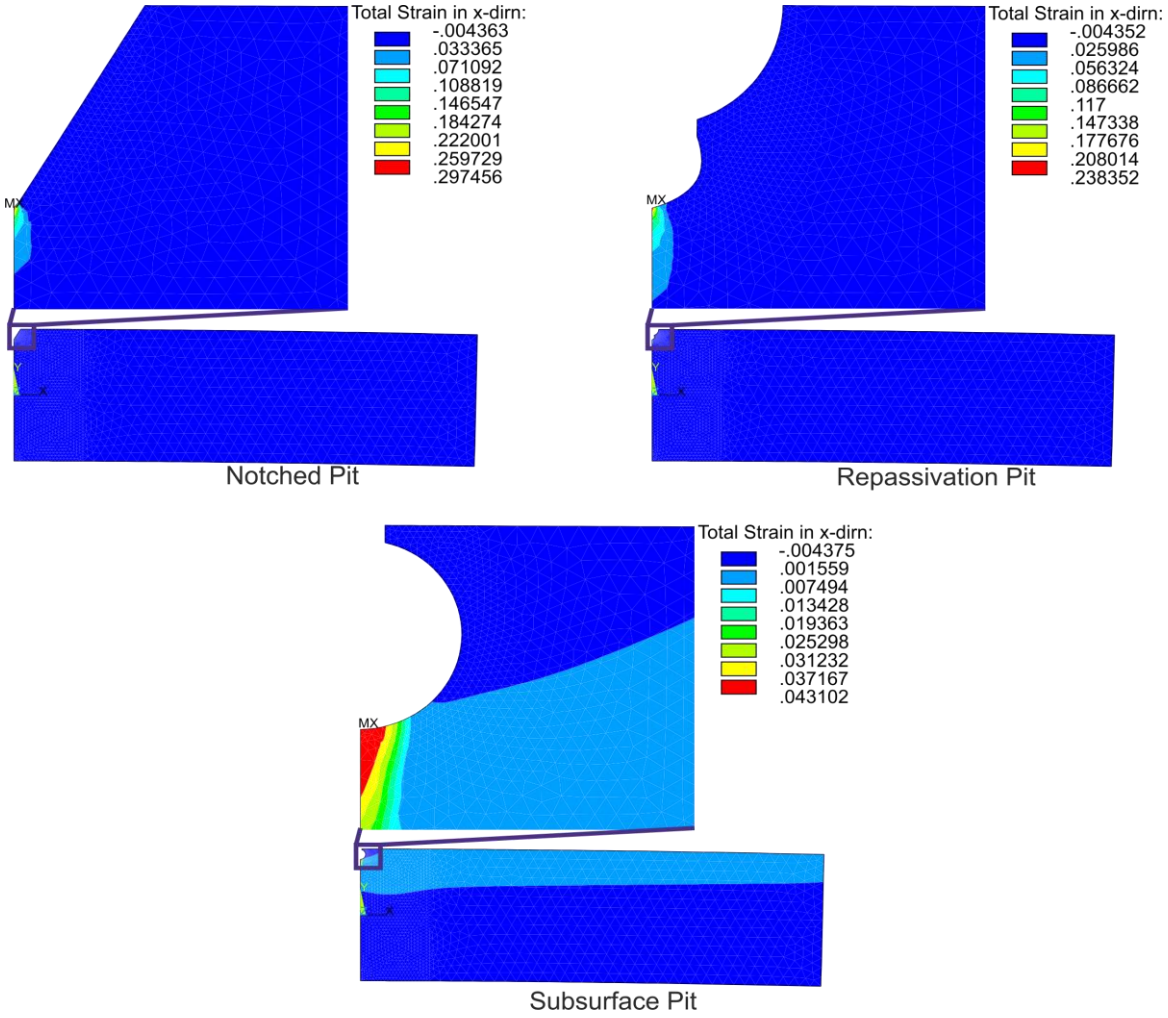

Figure 5.28: 2D HAZ bend submodel with notched, repassivation and subsurface pits total true strain in x-direction results.

2D Bending Structural Analysis for Unpitted Base Material (BM)

The 2D bend BM model of one half of the real specimen and the gauge length region selected from the 2D bend BM one half model, along with their corresponding maximum x-direction stress and total true strain results, can be seen in Figure 5.29 and Figure 5.30. As for the HAZ simulation, the location of the max stresses and total true strains in x-direction for the model are in the same location, which is the top surface of the centre region of the gauge length. Table 5.10 shows the displacement values applied to the global model and the resulting maximum stresses and total true strains in x-direction for the 2D bend BM one half model.

Table 5.10: Displacement values applied to 2D bend BM one quarter model and resulting total true strain and stress results.

Displacement (x) (mm)	Total true strain in x-direction	Stress in X-direction (MPa)	% Yield
0.809	0.0037	770	100

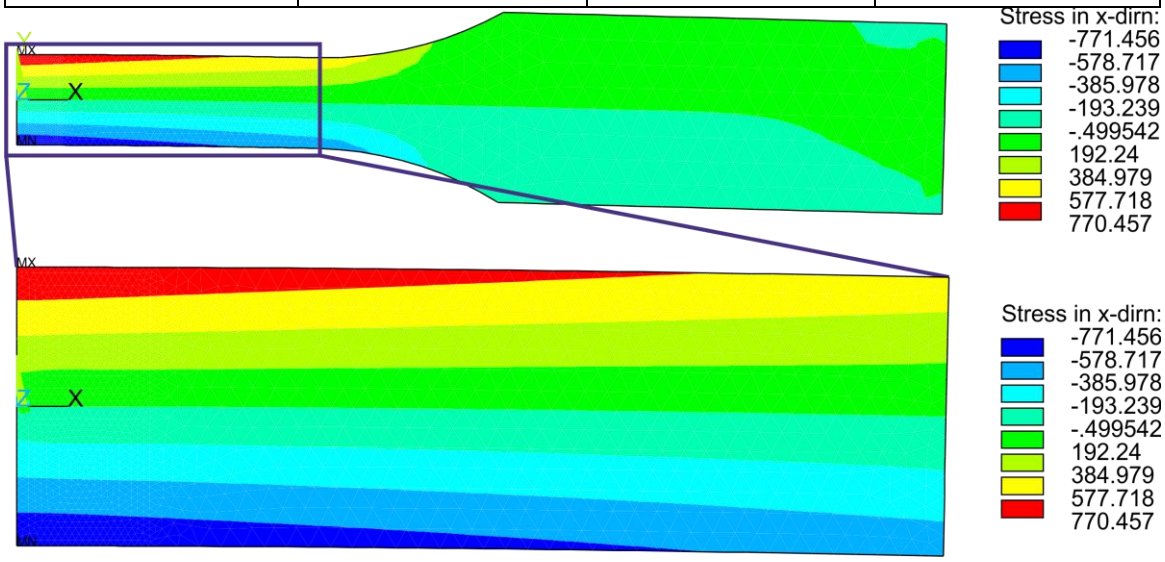

Figure 5.29: 2D half model maximum stress in x-direction for 100% BM yield stress applied as bending displacement and selected gauge length region shown on the 2D half model.

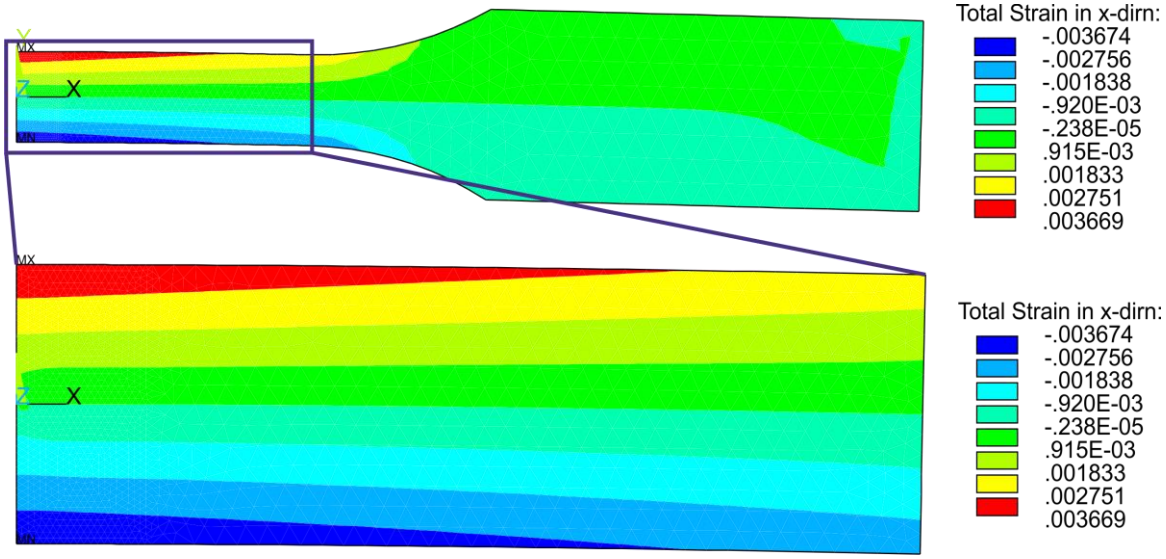

Figure 5.30: 2D half model maximum total true strain in x-direction for 100% of BM yield stress applied as bending displacement and selected gauge length region shown on the 2D half model.

The 2D bend BM submodel with the x- and y-displacements from the 2D bend BM one half model applied and the corresponding maximum x-direction stress and total true strain results can be seen in Figure 5.31 and Figure 5.32. Table 5.11 shows the global

displacement applied to the 2D UA HAZ submodel and the resulting stress and total true strain in the x-direction.

Table 5.11: Displacement values applied to 2D BM bend submodel and resulting total true strain and stress results.

Displacement (x) (mm)	Total true strain in x-direction	Stress in X-direction (MPa)	% Yield
0.141984	0.0037	771	100

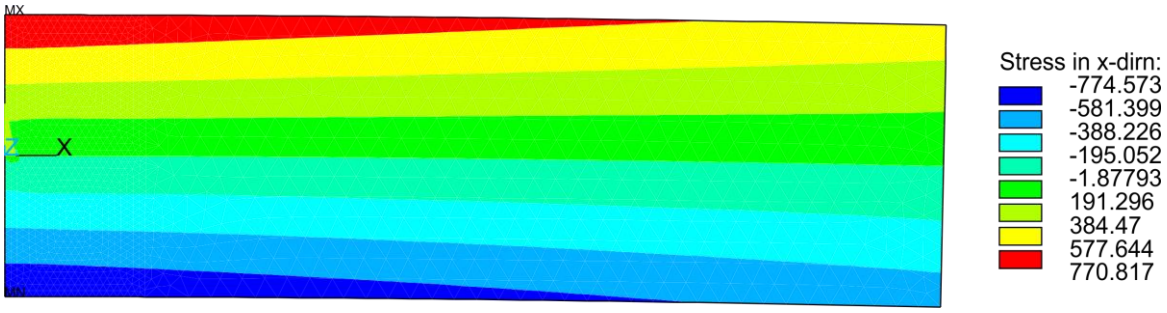

Figure 5.31: 2D bend submodel maximum stress in x-direction for 100% of BM yield stress applied as bending displacement to 2D half model.

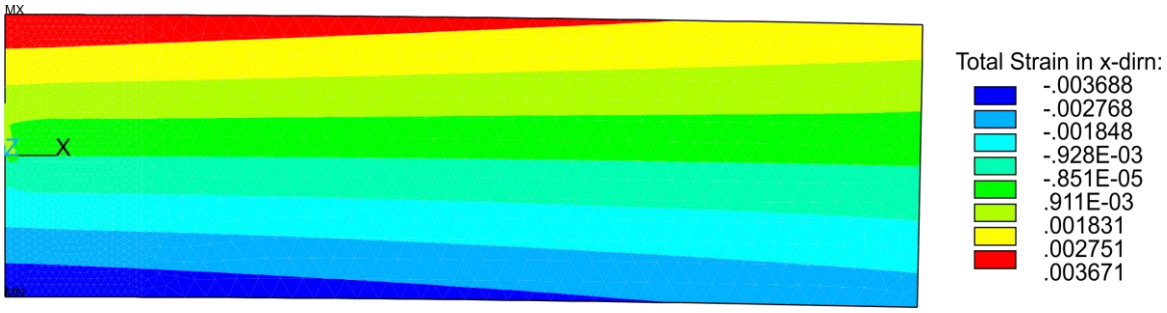

Figure 5.32: 2D bend submodel maximum total true strain in x-direction for 100% of BM yield stress applied as bending displacement to 2D half model.

The maximum x-direction stress and total strain values in the 2D bend BM submodel are the same as the maximum x-direction stress and total strain values for the selected gauge length region. This is the same as for the 2D bend HAZ submodel and also for the uniaxial loading conditions. Therefore, in the subsequent simulations involving a 2D bend BM one quarter model loaded to 100% of yield stress, the 2D bend BM submodel is used in place of the 2D bend BM one quarter model.

The results for the total true strain in the x-direction for the 2D bend BM submodels seen in Figure 5.29 to Figure 5.32 correspond to the results in Figure 5.22 to Figure 5.25 for the 2D bend HAZ submodels. For both materials the locations of the maximum and minimum strains in the 2D one half model, selected gauge length region and the submodel are all in

the same regions. However, the maximum x-direction stress and total strain values for the HAZ simulations are greater than for the BM simulations as the strength of the HAZ material is greater. This was also found for the uniaxial loading condition.

2D Bending Structural Analysis for Pitted Base Material (BM)

The maximum total true strain in x-direction in the pits in the 2D bend BM submodel are presented in Figure 5.34 and Figure 5.35. These maximum total strain in x-direction values correspond to a 100% yield stress in the unnotched 2D BM model. The location of the maximum total strain in x-direction in all of the seven different pit geometries, again occurs at the bottom of the pits. Table 5.12 shows the maximum strains in x-direction for the various pit geometries and have been sorted from lowest to highest. The pit aspect ratio for each pit is also shown.

Table 5.12: Lowest maximum total true strain in x-direction to highest for all seven pit geometries in the bending loaded 2D HAZ 2D bend submodel and pit aspect ratio.

Pit Geometry	Maximum Total true strain in the x-direction	Pit Aspect Ratio
Unpitted	0.0037	-
Shallow Wide	0.013078	0.3
Spherical	0.021364	0.5
Reference	0.024816	0.5
Subsurface	0.038213	10
Ellipse	0.047472	0.83
Repassivation	0.211922	0.83
Notched	0.264356	0.83

The maximum total true strain in x-direction for all pit geometries in the 2D bend BM submodel are presented in Figure 5.33 as a function of time. All of the maximum total true strain in x-direction for all pit geometries occur in the pit bottoms, as for the bend HAZ and uniaxial simulations. Unlike the maximum total true strain in x-direction results for the unpitted 2D HAZ quarter model in Figure 5.26, the strains for the pitted geometries do not increase linearly over time, similar to the uniaxial loading condition, due to the specimen being loading past the yield point of the material.

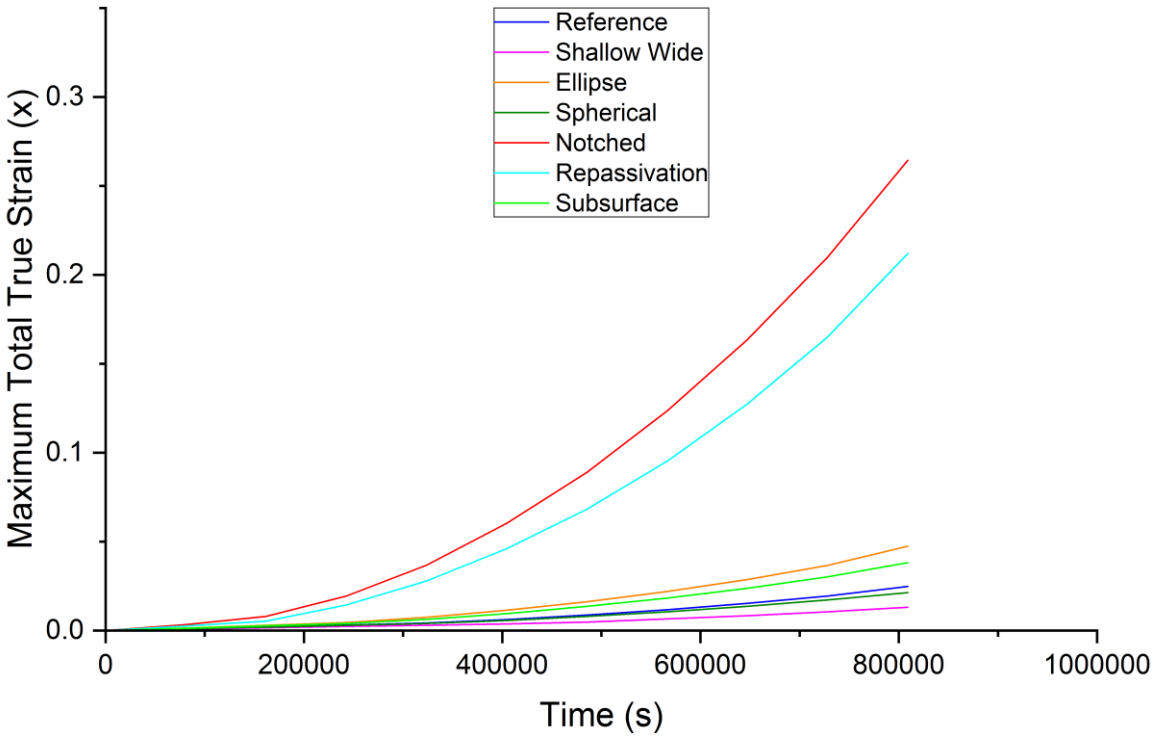

Figure 5.33: Maximum total true strain in x-direction vs time for all pit geometries in the 2D bend BM submodel.

Similar to the HAZ values, Table 5.12, Figure 5.34 and Figure 5.35 show that the shallow wide pit has the lowest maximum total strain in x-direction value, 0.013078, with the notched pit having the highest value, 0.264356 .The maximum total strain in x-direction values for the BM material are ranked in the same order as for the HAZ. This again shows that for a displacement load applied in the -y-direction the pit mouth diameter is the most important geometric aspect of the pit, with a large pit mouth diameter producing lower maximum total strain in x-direction values in the pits. These results also show that, similar to the uniaxial loading condition, the geometry of the pit plays an important role in the magnitude of the maximum total strain in x-direction values in the pit as it seems the smoother the transition from pit sides to pit bottom, the lower the maximum total strain in x-direction values are in the pits.

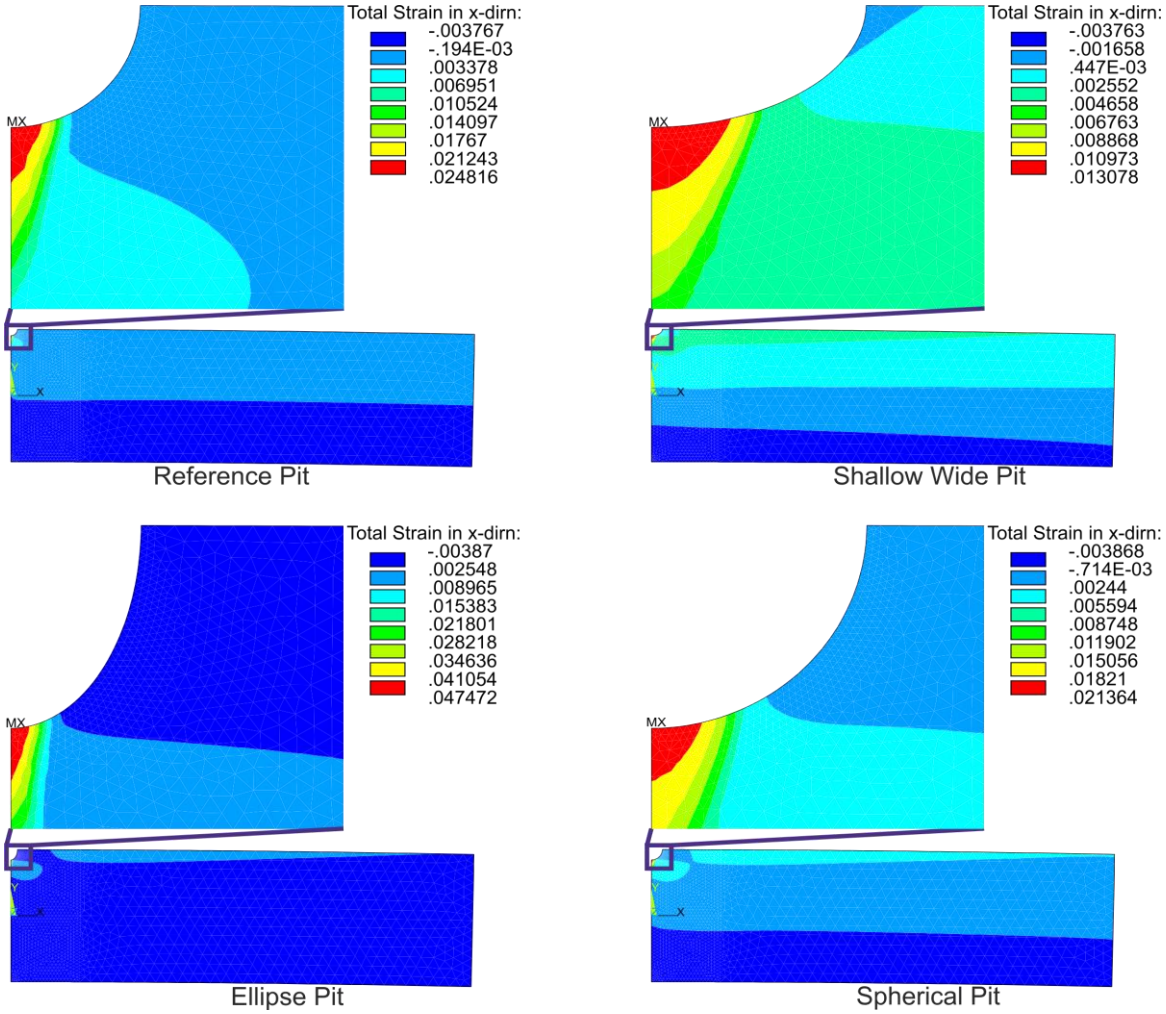

Figure 5.34: 2D BM bend submodel with reference, shallow wide, ellipse and spherical pits total true strain in x-direction results.

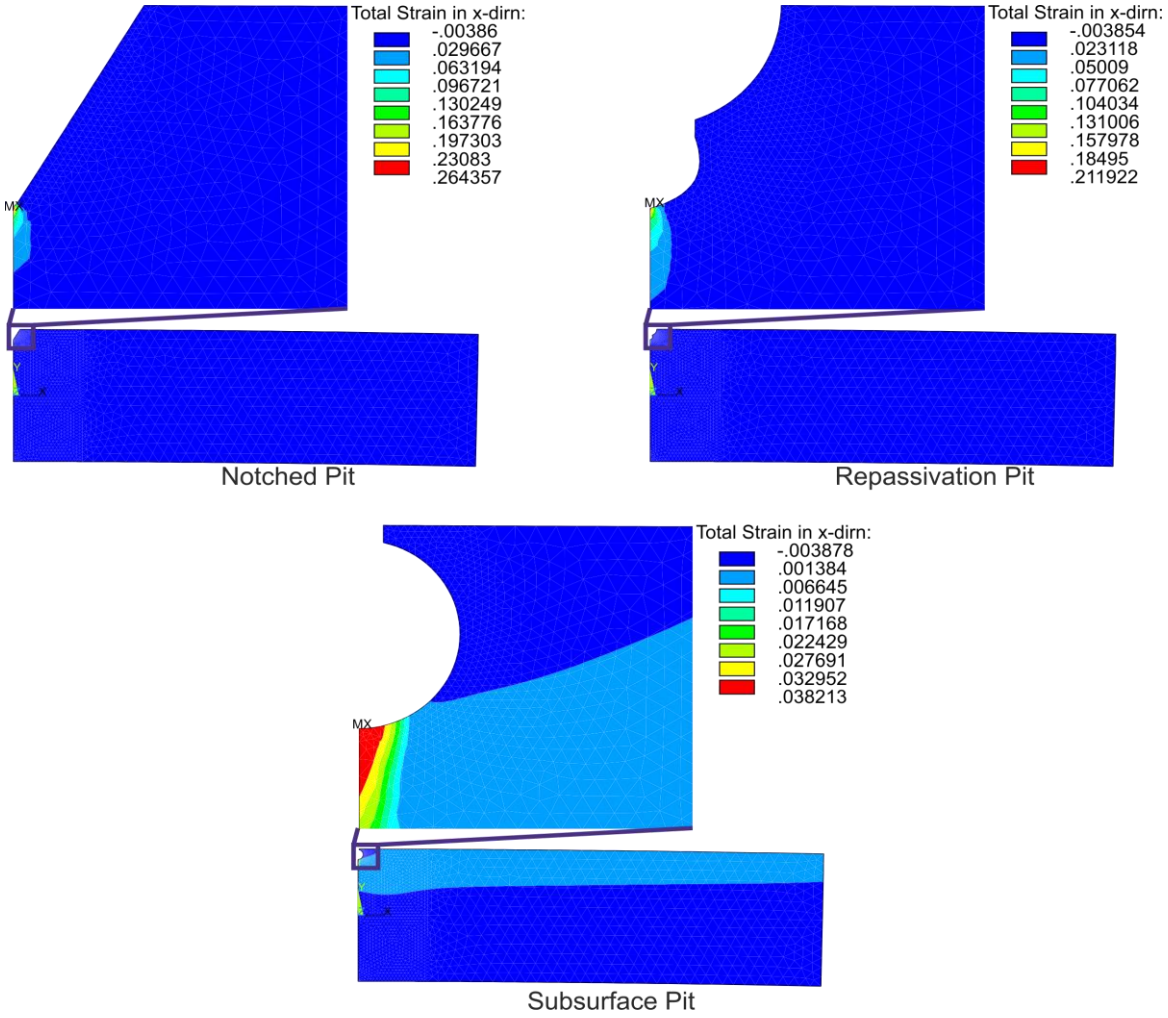

Figure 5.35: 2D BM bend submodel with notched, repassivation and subsurface pits total true strain in x-direction results.

This information is also presented in the graph in Figure 5.36. This graph again shows both repassivation and notched pit geometries have consistently higher local strains for all corresponding global strain values compared to the other pit geometries. The shallow wide pit has the lowest local strains for all corresponding global strain values. However, for bending the spherical pit has higher local strain values than the reference pit for a significant amount of global strain values. This collaborates the finding that for bending the pit mouth diameter is the most important geometric aspect of the pit, with a larger pit mouth diameter producing lower local strains for all corresponding global strain values. Similar to the 2D UA simulation, time-dependent pit growth is not modelled in this stage of the work

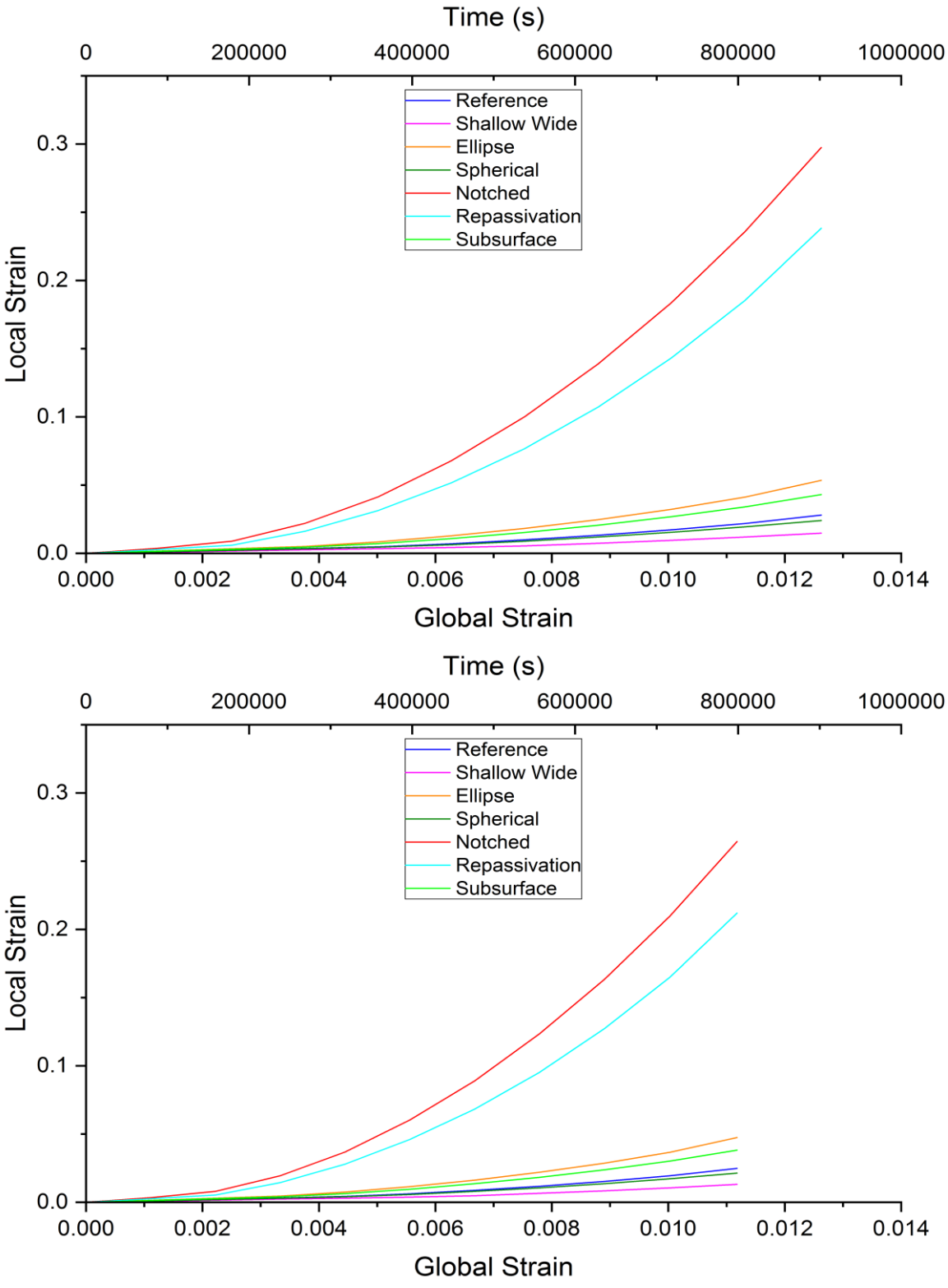

Figure 5.36: Graph of global vs local strains for all pit geometries in the 2D bend HAZ (Top) and BM (Bottom) submodel.

As for the uniaxial loading condition, the total true strain in the x-direction for the 2D BM bend pitted submodels has the same order for the 2D HAZ bend model, Table 5.9, as for the 2D BM bend model, Table 5.12. Additionally the locations of the highest maximum total

true strain in x-direction for the 2D HAZ bend model, Figure 5.27 and Figure 5.28, are located in the same region as for the 2D BM bend model, Figure 5.34 and Figure 5.35, which is the pit bottom. This is the same region as for the 2D UA loading condition. For the 66% loading condition the order of lowest to highest strains is the same as the 2D BM and 2D HAZ models, Table A. 1 and the location of the highest maximum total true strain in x-direction for all pits is again located at the pit bottoms, Figure A.1 and Figure A.2. From Figure 5.36, it can be seen that the order of lowest to highest maximum total true strain in x-direction is consistent for all corresponding global strain values and does not alter as for the uniaxial (UA) loading condition.

The vast majority of numerical simulation research into loading conditions applied to pitted models investigate just the uniaxial loading condition. Nakai et al. [299] investigated in-plane compressive loads and bending moments applied to plates with circular pits present. One of the key findings of this research was that the ultimate strength of the material is most vulnerable to the presence of corrosion pits. This may be due to a significant increase in the local stresses and strains in the pit in comparison to the global stresses and strains. This was also observed in this current work as the maximum total true strain in x-direction for the pits subjected to a uniaxial loading condition, Table 5.3 and Table 5.6, are significantly higher than the maximum total true strain in x-direction in the pits when a bending loading condition is applied, Table 5.9 and Table 5.12. This was evident throughout the entire loading of the specimens, as shown in Figure 5.18 for the uniaxial loading condition and in Figure 5.36 for the bending loading condition. This may be a reason why most researchers only investigate the uniaxial loading condition and not bending in addition. However, this is also dependent on the pit geometry and therefore various pit geometries should also be considered and modelled.

To summarise the above findings, the present investigation of the various 2D pit geometries under bending loading shows that the location of highest strains in the pit geometries modelled are <u>all</u> located in the pit bottom. Therefore, it can be stated that:

- *Similar to the uniaxial loading condition, using a smaller submodel, instead of modelling the whole specimen geometry, produces comparable results.*
- *Similar to the uniaxial loading condition, the presence of a pit in a model produces high local total strain in the x-direction values in the pit region when loaded in bending. Due to high local strains in the pit bottom HAC is more likely to occur in this region for all pit geometries modelled in 2D.*
- *The pit mouth diameter is the most important geometric aspect as wider pit mouth diameters produce lower total strain in the x-direction values.*

2D Load Analysis

Another approach to investigate the severity of the various pit geometries was undertaken by investigating the percentage of a displacement load applied to an unnotched specimen, a pitted specimen can withstand, before reaching the yield strength of the material locally. The displacements applied to the unpitted 2D UA quarter models which resulted in 100% yield stress in the BM and HAZ models are shown in Table 5.13. The same displacement was applied to the pitted specimens and the percentage load taken to reach 100% yield stress in the material, in addition to the corresponding displacement in x-direction, were recorded. These percentage load values and corresponding displacements are shown in Table 5.13, ranked from highest to lowest percentage load.

Table 5.13: Table of percentage load for 2D unpitted and pitted specimens for uniaxial loading condition to 100% of BM and HAZ yield stresses and corresponding displacements.

Pit Geometry:	% Unpitted Load Until 100% YS BM:	BM displacement (mm):	% Unpitted Load Until 100% YS HAZ:	HAZ displacement (mm):
Unpitted:	100	0.1096	100	0.0500
Shallow Wide:	49	0.0216	48	0.0240
Spherical:	36	0.0159	35	0.0175
Reference:	35	0.0153	35	0.0175
Subsurface:	27	0.0119	26	0.0130
Ellipse:	24	0.0106	24	0.0120
Repassivation:	14	0.0062	14	0.0070
Notched:	10	0.0044	10	0.0050

From Table 5.13 it can be seen that a shallow wide pit in a 2D submodel with a uniaxial loading condition applied, can withstand a load which is approximately 49% of the load applied to the unpitted 2D submodel. However, a notched pit for BM and HAZ 2D submodel can only withstand a load that is 10% of the load applied to the unpitted 2D submodel. This pit geometry was modelled with a small, sharp angle at the pit bottom and was considered as a “worst case”. This “worst case” scenario is however unlikely to occur during service condition/ environmental change, but in reality, it could be regarded as an unintended notch or as a kind of pre-crack. However, the repassivation shaped pit, which can withstand a load that is 14% of the load applied to the unpitted 2D submodel may be visible during inspections. This pit geometry can occur, for example, when there is a change in

service conditions in a pipeline, so a pit begins to grow. The service conditions then return to normal operating conditions so the pit stops growing but then another change occurs so a new pit begins to grow in the bottom of the previous pit, as explained by Cerit [275]. Therefore, during inspections it may be useful to have an overview of “best” to “worst” pits as the presence of a notched or repassivation pit will cause failure of the component a lot quicker than a shallow wide pit and should therefore be avoided under all circumstances.

In Table 5.3 it was discovered that the shallow wide pit is the pit geometry with the lowest maximum total true strain in x-direction when a uniaxial load is applied to the 2D UA submodels for both BM and HAZ. The pit that has the next lowest maximum total true strain in x-direction when a uniaxial load is applied to the 2D UA submodels for both BM and HAZ is the reference pit. However, Table 5.13 shows that the spherical pit and not the reference pit can withstand the next highest percentage of the load applied to the unpitted 2D BM submodel. For the HAZ however, both spherical and reference pits failed at the same percentage load. It may be that both pits fail at the same load percentage for both BM and HAZ, but the load step sizes were slightly too large to record this.

The 2D bending models were then investigated, with a displacement in the -y-direction applied in a greater number of substeps to reach 100% of the yield stresses of the BM and HAZ 2D model. The percentage load applied to the pitted 2D bend submodels which resulted in 100% yield stress in the unpitted model for both BM and HAZ are shown in Table 5.14, ranked from highest to lowest percentage load until failure. The corresponding displacements in x-direction are also shown.

Table 5.14: Table of percentage load for 2D unpitted and pitted specimens of bending loading condition to 100% BM and HAZ yield stresses and corresponding displacements.

Pit Geometry:	% Unpitted Load Until 100% YS BM:	BM displacement (mm):	% Unpitted Load Until 100% YS HAZ:	HAZ displacement (mm):
Unpitted:	100	0.00183	100	0.00193
Shallow Wide:	58	0.00129	58	0.00141
Spherical:	44	0.00103	44	0.00114
Reference:	42	0.00099	42	0.00110
Subsurface:	33	0.00081	33	0.000890
Ellipse:	30	0.00074	30	0.00083
Repassivation:	17	0.00044	17	0.00049
Notched:	12	0.00032	12	0.00036

Similar to the UA loading condition, a shallow wide pit in a 2D submodel with a bending loading condition applied can withstand the highest load in comparison to the other pit geometries investigated during this work. The bending load a shallow wide pit can withstand is 58%, for both BM an HAZ, of the load applied to the unpitted 2D bend submodel. This value is greater than the percentage load the shallow wide pit can withstand when a uniaxial load is applied. All of the pit geometries are able to withstand greater comparison loads when a bending load is applied in contrast to a uniaxial load, confirming the findings of Nakai [299] who investigated a circular pit. As for the uniaxial loading condition, the presence of a notched or repassivation pit will cause failure of the component quicker than a shallow wide pit and should be avoided under all circumstances.

The above findings, the present investigation of the 2D load analysis, can be summarised as follows:

- *The notched and repassivation pits can withstand the lowest uniaxial and bending loads, with the shallow wide pit able to withstand the highest loads.*
- *The information provided in Table 5.13 and Table 5.14, may prove useful to NDT operators for inspection and planning as certain pit geometries have higher total strain in the x-direction values than others and may need additional monitoring. This may include more frequent inspections and the use of NDT.*

5.1.2 3D Structural Analysis

3D Uniaxial Half Model

As a first control check to ensure the models used in the simulations in sections 5.1.1 and 5.1.2 provide accurate results in comparison to a model loaded at both ends as during a tensile test, a half model was created, as explained in Section 4.3.1. A displacement was applied to this model in two different manners according to Figure 4.26 and Figure 4.27. The results of the application of these displacements are shown in Figure 5.37 to Figure 5.42, which show the displacement applied, resulting stresses and strains in the models.

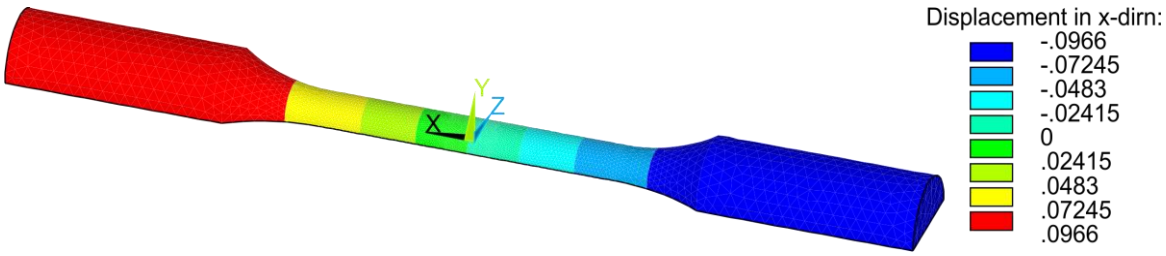

Figure 5.37: Displacement in x-direction applied to both ends of 3D half model.

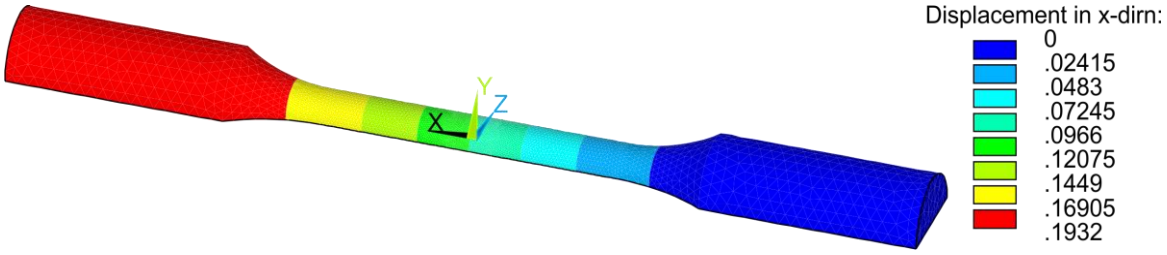

Figure 5.38: Displacement in x-direction applied to one end of 3D half model.

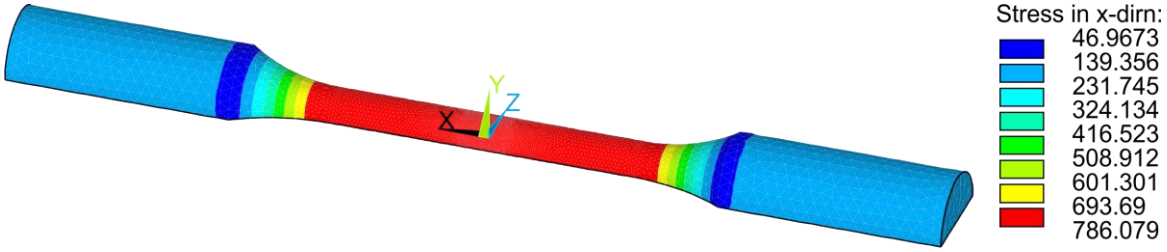

Figure 5.39: Stress in x-direction for displacement applied to both ends of 3D half model.

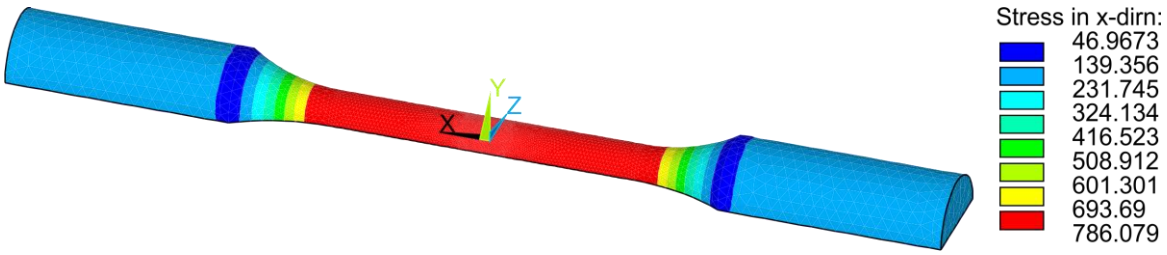

Figure 5.40: Stress in x-direction for displacement applied to one end of 3D half model.

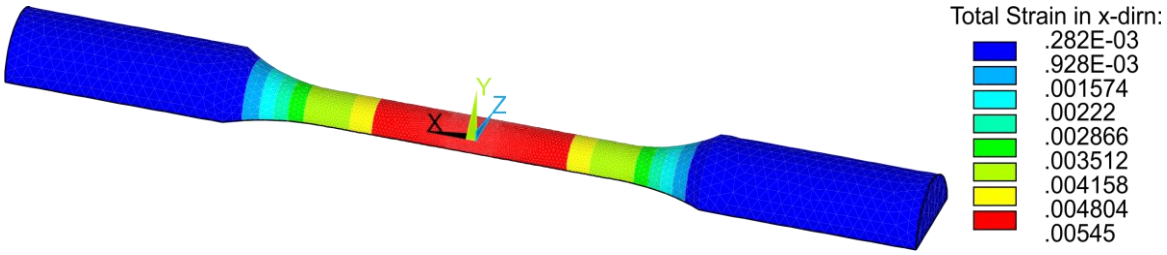

Figure 5.41: Strain in x-direction for displacement applied to both ends of 3D half model.

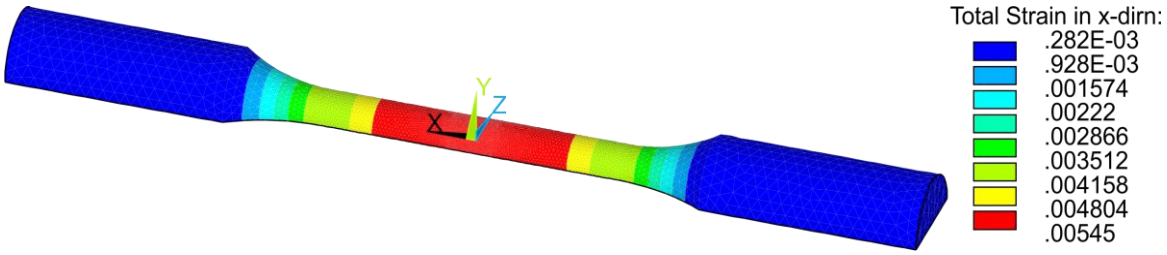

Figure 5.42: Strain in x-direction for displacement applied to one end of 3D half model.

Figure 5.37 to Figure 5.42 show that there is no difference in the values for the stresses or total true strains in the x-direction, or the regions where they occur, between the two different models. These values are summarised in Table 5.15.

Table 5.15: Stress and total true strain in x-direction results for displacement applied to both ends and one end only.

Stress in x-direction (MPa)		Total true strain in x-direction	
Displacement applied to both ends	**Displacement applied to one end**	**Displacement applied to both ends**	**Displacement applied to one end**
786	786	0.005	0.005

A pit was then introduced into the geometry to investigate if there are any discrepancies between the loading conditions when a pit is present. Figure 5.43 to Figure 5.46 show the resultant stresses and strains in the full 3D half model and also in the pit region for the two loading conditions. For both stresses and total true strain in the x-direction, Figure 5.43 to Figure 5.46, show that there are no differences between the magnitude or location of the stresses and total true strain in the x-direction between the two loading conditions. Additionally, the 3D BM UA submodel with an ellipse pit which had a load applied corresponding to 100% yield stress of the unpitted 3D BM UA submodel is shown in Figure 5.47. From this it can be seen that the stresses and total true strain in the x-direction for the pit in the submodel are slightly higher, but not significantly so, than for both of the half models, 1038 MPa vs 967 MPa and 0.0442 vs 0.0439 respectively. These values are summarised in Table 5.16.

Table 5.16: Stress and total true strain in x-direction results for displacement applied to both ends and one end only for pitted half model and pitted submodel.

Stress in x-direction (MPa)			Total true strain in x-direction		
Applied to both ends (Half Model)	**Applied to one end (Half Model)**	**Applied to both ends (Submodel**	**Applied to both ends (Half Model)**	**Applied to one end (Half Model)**	**Applied to both ends (Submodel**
967	967	1038	0.0442	0.0442	0.0439

The location of the max stresses and total true strain in the x-direction for all models were also located in the same regions- at the bottom of the pit for the stresses and at the pit side near the mouth for the total true strains. These results confirm that the usage of a submodel with sufficient symmetric boundary conditions and the load applied to one end only produces comparable results to a model loaded at both ends, as performed in a tensile test.

The results for the 3D half model in Figure 5.43 and Figure 5.44, however also show high stresses in the vicinity of the pit. This indicates that cracking does not necessarily occur in the pit bottom.

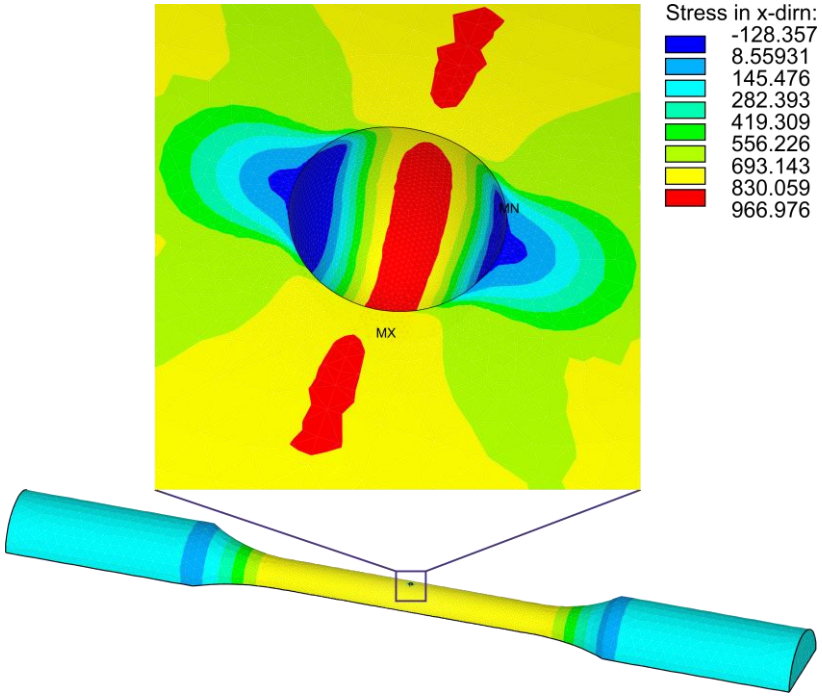

Figure 5.43: Stress in x-direction for displacement applied to both ends of 3D half model with ellipse pit.

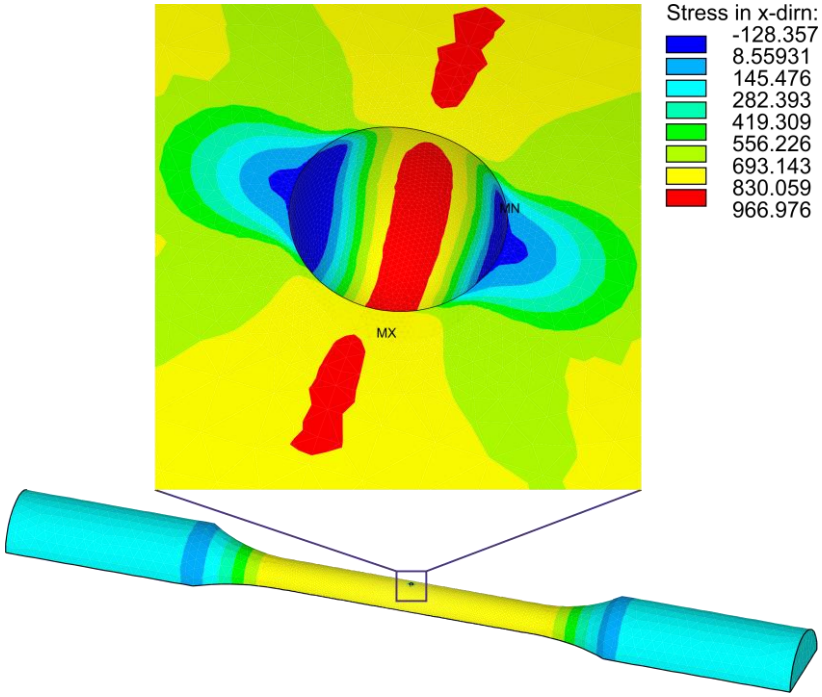

Figure 5.44: Stress in x-direction for displacement applied to one end of 3D half model with ellipse pit.

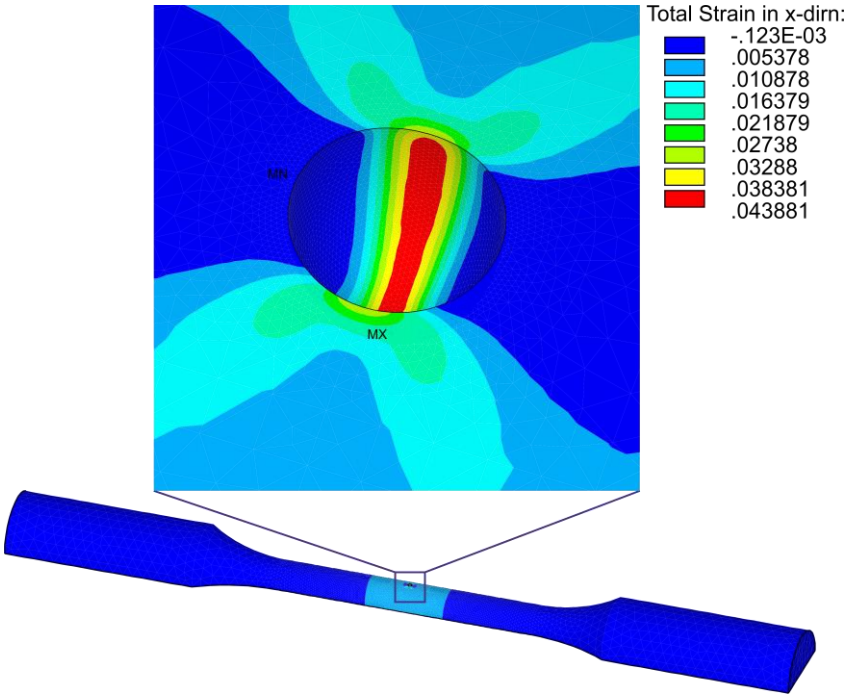

Figure 5.45: Total true strain in x-direction for displacement applied to both ends of 3D half model with ellipse pit.

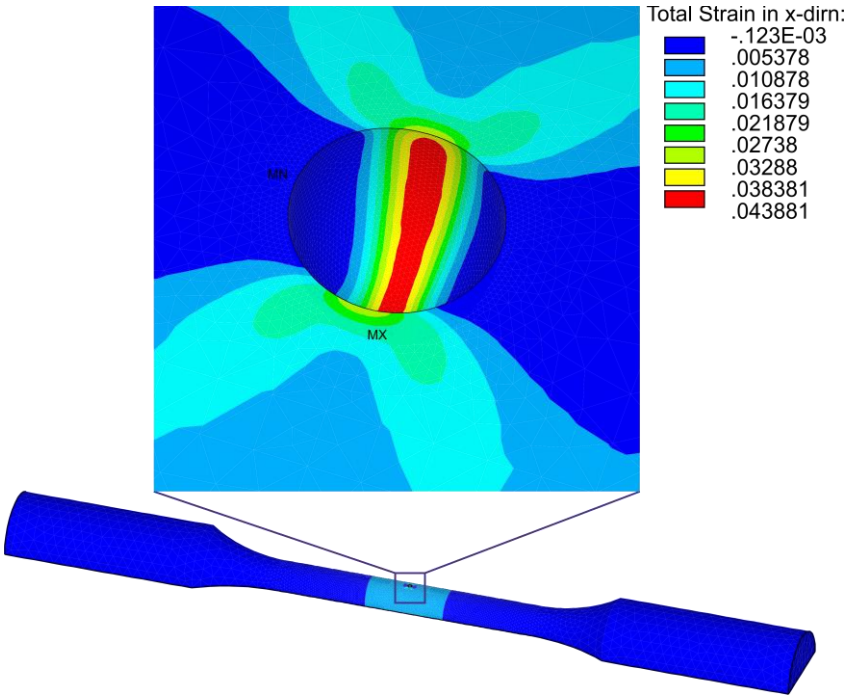

Figure 5.46: Total true strain in x-direction for displacement applied to one end of 3D half model with ellipse pit.

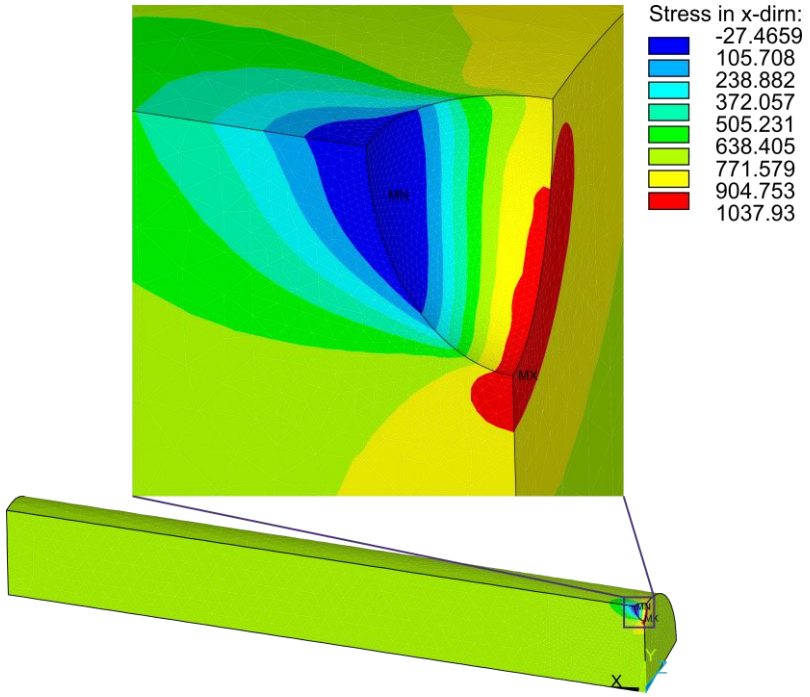

Figure 5.47: Stress in x-direction for ellipse pit in 3D BM UA submodel with load applied in x-direction corresponding to 100% yield stress in the unpitted 3D UA submodel.

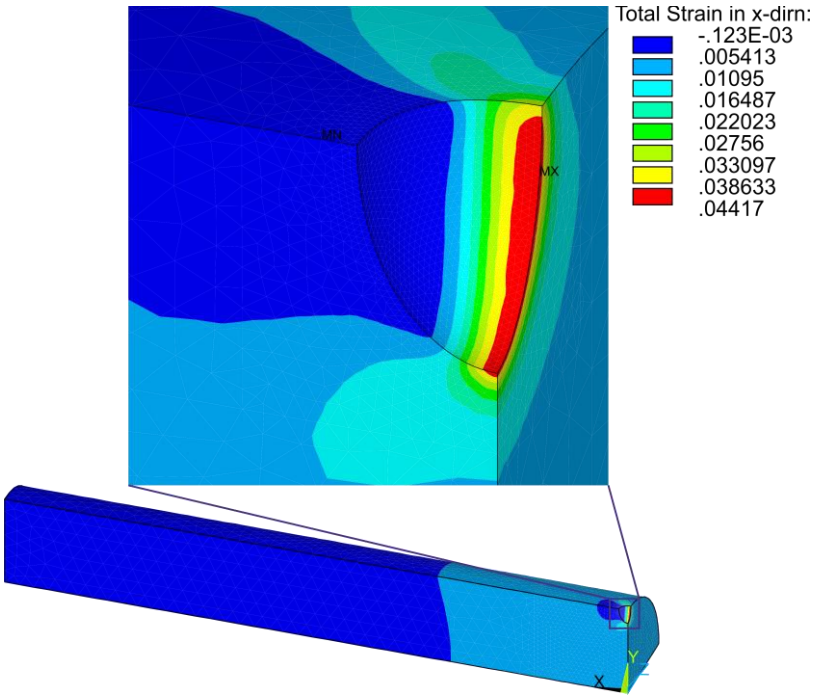

Figure 5.48: Total true strain in x-direction for ellipse pit in 3D BM UA submodel with load applied in x-direction corresponding to 100% yield stress in the unpitted 3D UA submodel.

The above findings, the present investigation of the 3D Uniaxial half model, can be summarised as follows:

- *A uniaxial loading condition was applied to one end of a 3D half model and the other end was fixed due to symmetric boundary conditions. The stress and strain results were compared to a specimen loaded at both ends. Both of these models showed the same results for maximum stresses and strains in the x-direction.*
- *An elliptical shape pit was then introduced to the half models and the stresses and total strain in the x-direction for the pit in the one eight submodel are slightly higher than for the two half models which have the same values, an increase of 100 MPa for stress and an increase of 0.000289 for total strain in the x-direction. These increases are not significant but the smaller one eight submodels can therefore be considered more conservative in comparison to the half models.*

3D Uniaxial Structural Analysis for Unpitted HAZ

The next phase of this work was to investigate when the same x-direction uniaxial (UA) displacement as applied to the 2D models is applied to a 3D model. The highest stresses and strains regions in the 3D HAZ model of one eight of the real specimen unpitted model subjected to the same x-direction uniaxial load as the 2D model modelled previously, Figure 5.1, can be seen in Figure 5.49 and Figure 5.50. The location of the maximum x-direction stress is similar to the 2D HAZ one quarter model and falls just outside the margins of the gauge length. The maximum total true strain in x-direction is not located in the same region as the 2D HAZ one quarter model but is located towards the fixed end of the model, Figure 5.50. The maximum x-direction stress and strain values are increased slightly- 870 MPa vs 888 MPa and 0.004 vs 0.006 for 2D and 3D respectively. Table 5.17 shows the displacement value applied, which is the same as applied to the 2D model in Table 5.1, and the resulting maximum stresses and total true strains in x-direction for the 3D HAZ UA one quarter model. The same strain rate over time in terms of displacement was applied to all specimens in both 2D and 3D for uniaxial and bending loading conditions. This results in a % Yield value of 102 in Table 5.17.

Table 5.17: Displacement values applied to 3D HAZ UA one quarter model and resulting total true strain and stress results.

Displacement (x) (mm)	Total True Strain in x-direction	Stress in X-direction (MPa)	% Yield
0.1096	0.0062	888	102

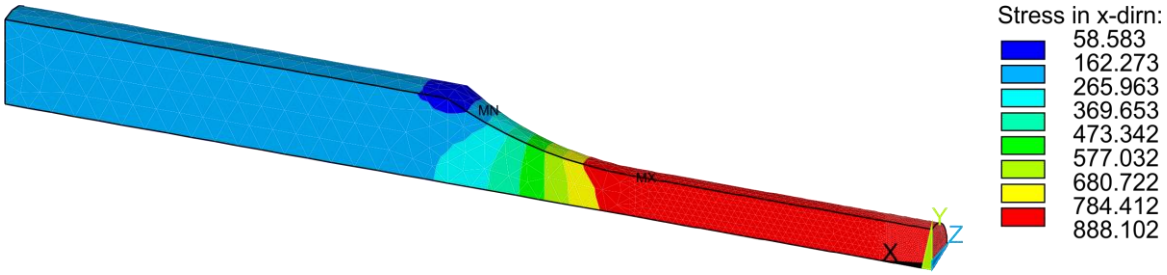

Figure 5.49: 3D quarter model maximum stress in x-direction for 100% of HAZ yield stress applied as uniaxial displacement to 2D model.

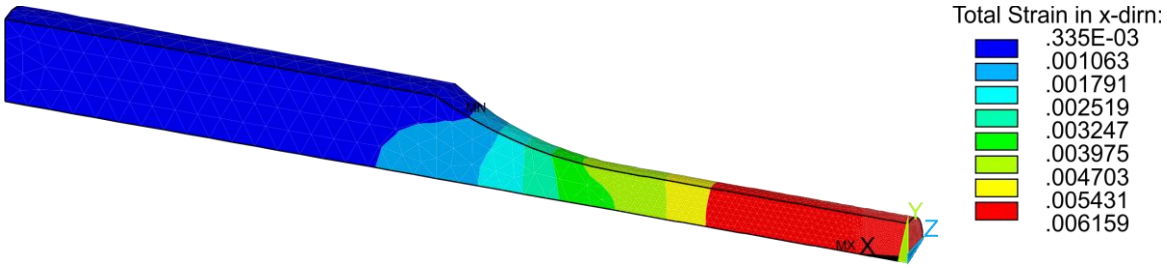

Figure 5.50: 3D quarter model maximum total true strain in x-direction for 100% of HAZ yield stress applied as uniaxial displacement to 2D model.

A graph depicting the increase of displacement, maximum total true strain and stress in x-direction with increasing time, Figure 5.51, show that these three parameters increase linearly with increasing time up to approximately 90,000 seconds. From 90,000 seconds onwards only displacement increases linearly, with the stresses noting a very slight increase but the maximum total trues strains have a large increase. This may be due to the yield strength of the material being reached around 90,000 seconds and after this the yield strength has been surpassed.

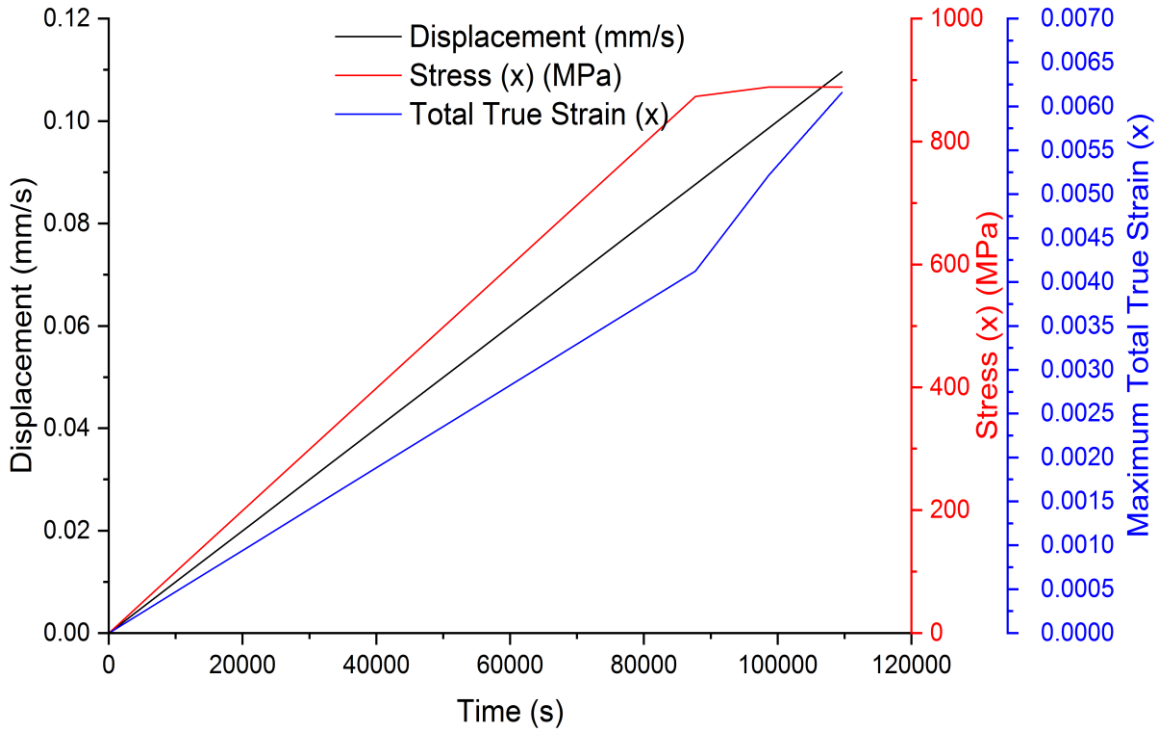

Figure 5.51: Displacement, maximum total true strain and stress in x-direction vs time for the 3D one quarter model for 100% of HAZ yield stress applied as uniaxial displacement.

The 3D HAZ one eight model and selected gauge length region with maximum x-direction stress and total true strain results can be seen in Figure 5.52 and Figure 5.53. The 3D UA HAZ submodel with the x-, y- and z-displacements from the 3D HAZ one eight model applied and the corresponding maximum x-direction stress and total true strain results can be seen in Figure 5.54 and Figure 5.55. Table 5.18 shows the displacement values applied to the 3D HAZ UA submodels and the resulting stresses and total true strains in the x-direction.

Table 5.18: Displacement values applied to 3D HAZ UA submodel and resulting total true strain and stress results.

Displacement (x) (mm)	Total True Strain in x-direction	Stress in X-direction (MPa)	% Yield
0.071188	0.0062	886	102

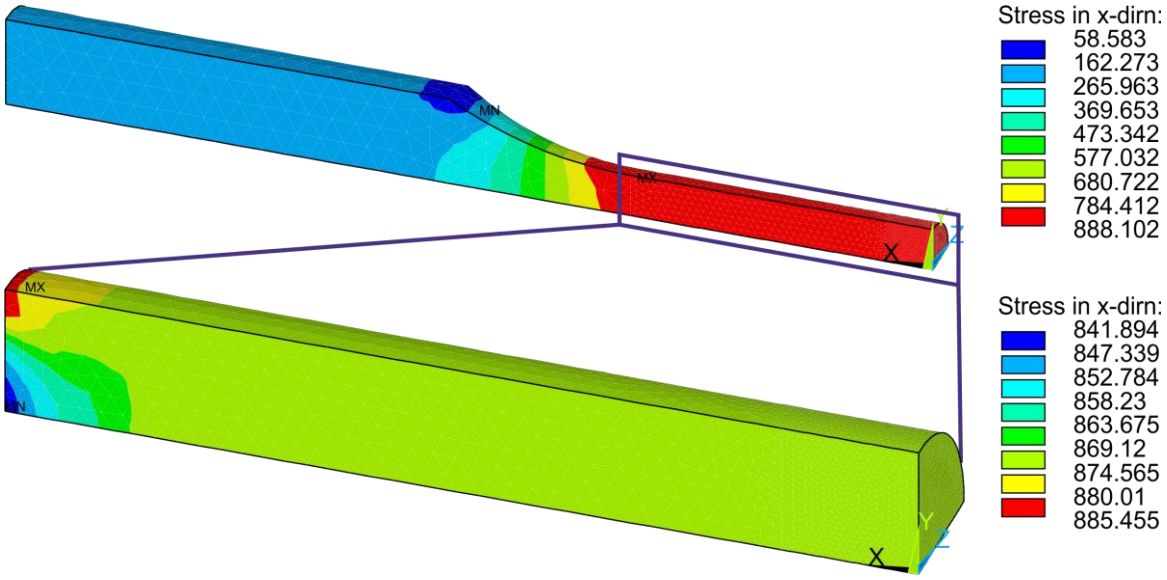

Figure 5.52: 3D one eight model maximum stress in x-direction for 100% of HAZ yield stress applied as uniaxial displacement to 2D model and selected gauge length region shown on the 3D one eight model.

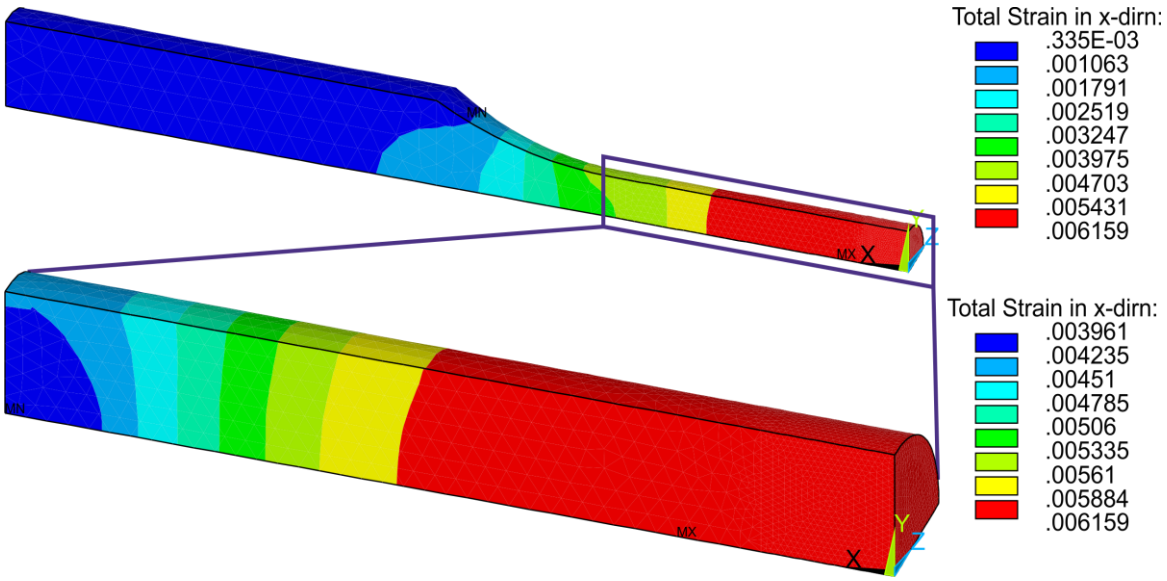

Figure 5.53: 3D one eight model maximum total true strain in x-direction for 100% of HAZ yield stress applied as uniaxial displacement to 2D model and selected gauge length region shown on the 3D one eight model.

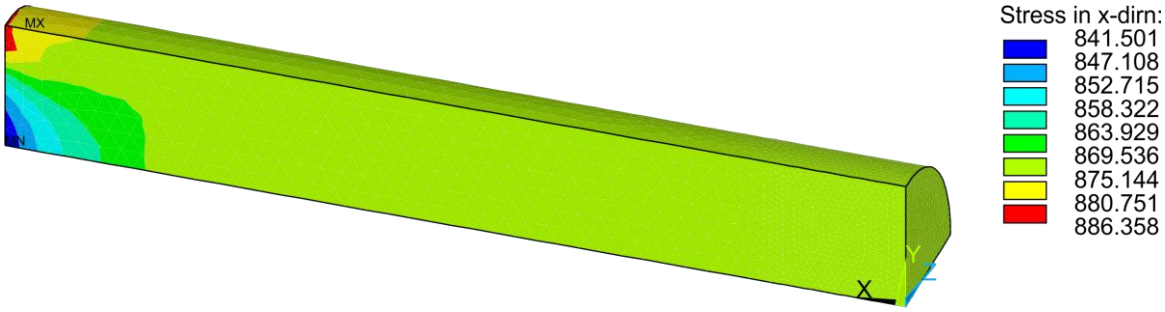

Figure 5.54: 3D UA submodel maximum stress in x-direction for 100% of HAZ yield stress applied as uniaxial displacement to 2D model.

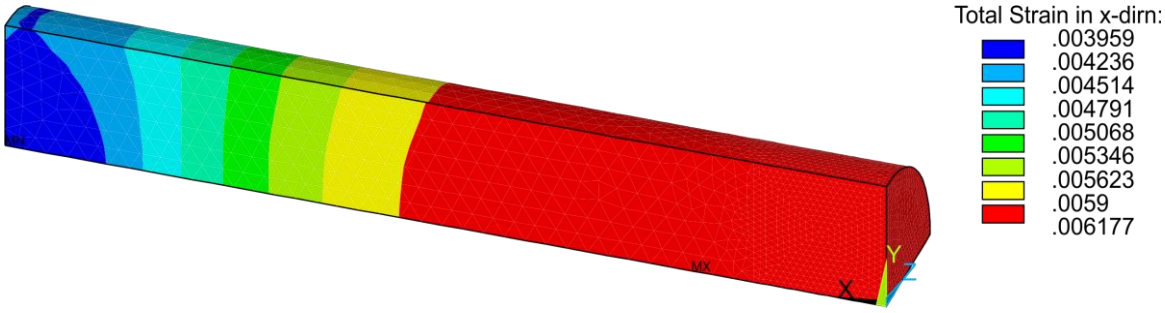

Figure 5.55: 3D UA submodel maximum total true strain in x-direction for 100% of HAZ yield stress applied as uniaxial displacement to 2D model.

As seen in Figure 5.52 to Figure 5.55, the maximum x-direction stress and total true strain values in the 3D HAZ UA submodel are similar to the maximum x-direction stress and total true strain values for the selected gauge length region within the 3D HAZ one eight model. Therefore, in the subsequent simulations involving a 3D HAZ one eight model loaded to 100% of HAZ yield stress applied as uniaxial displacement to the 3D HAZ one quarter model, the 3D HAZ submodel is used in place of the 3D HAZ one eight model. These findings also correspond to the 2D simulation results where the maximum x-direction stress and total true strain values for the one eight model are located outside the selected gauge length region.

3D Uniaxial Structural Analysis for Pitted HAZ

The 3D pits used in this stage of the work are shown in Figure 4.12. For 3D analysis the total true strain in the x-direction in the pits is again the main result of interest, Figure 5.57 and Figure 5.58. Similar to the 2D analysis in Figure 5.9 and Figure 5.10, the region of high total true strain in the x-direction are located in the pit bottom for the pit geometries investigated, Figure 5.57. However, unlike the 2D analysis this region extends from the pit bottom to the pit mouth perpendicular to the loading direction. The pit geometries in Figure 5.58 have more severe geometries with the region of high total true strain in the x-direction located not at the pit bottom. Table 5.19 shows the maximum strains in x-direction for the

various pit geometries and have been sorted from lowest to highest along with the pit aspect ratio for the uniaxially loaded 3D HAZ UA pitted submodels.

Table 5.19: Lowest maximum total true strain in x-direction to highest for all seven pit geometries in the uniaxially loaded 3D HAZ UA pitted submodel and the pit aspect ratios.

Pit Geometry	Maximum total true strain in the x-direction	Pit Aspect Ratio
Unpitted	0.0062	-
Shallow Wide	0.028350	0.3
Reference	0.031112	0.5
Spherical	0.045219	0.5
Ellipse	0.050012	0.83
Repassivation	0.089721	0.83
Notched	0.163195	0.83
Subsurface	0.237126	10

The maximum total true strain in x-direction for all pit geometries in the 3D HAZ submodel are presented in Figure 5.56 as a function of time. Similar to the maximum total true strain in x-direction results for the pitted 2D HAZ quarter model in Figure 5.8, the strains for the pitted geometries do not increase linearly over time, which again may be due to the specimen being loading past the yield point of the material.

Figure 5.56 also shows that the influence of overyielding the material can be excluded from explaining why the notched pit is the pit geometry with the highest maximum total true strain in x-direction for the 2D pit geometries, but the subsurface pit has the maximum value for 3D. Using the values presented in Table 5.19 alone, the issue of overyielding the material might be considered. However, Figure 5.56 shows that the notched pit already behaves less severe than the subsurface pit before yielding occurs at 90000 s.

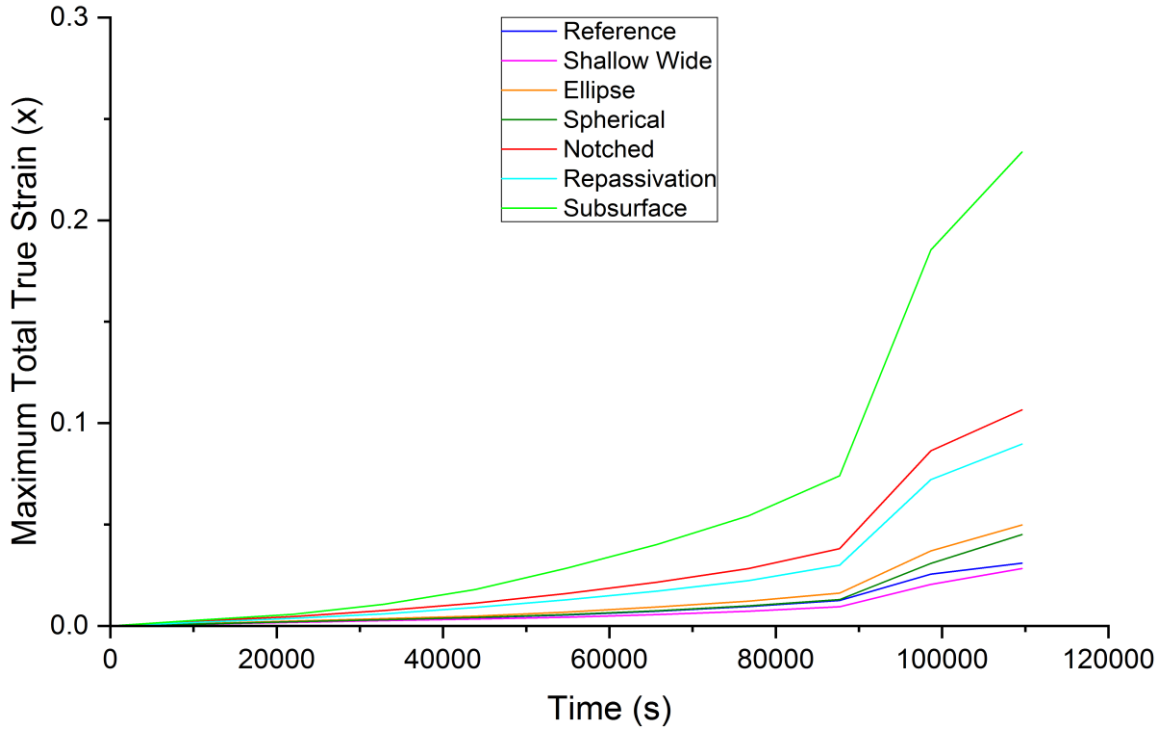

Figure 5.56: Maximum total true strain in x-direction vs time for all pit geometries in the 3D HAZ submodel.

From Table 5.19, Figure 5.57 and Figure 5.58 it can be seen that not only the locations of the maximum total true strain in the x-direction, but also the pit order is different to the 2D results in Table 5.3. The shallow wide, reference and spherical pits still have the lowest maximum total true strain in the x-direction values. However, in the 2D HAZ submodel the subsurface pit had the next highest value (number four), but for the 3D HAZ submodel the subsurface pit has the highest of all maximum total true strain in the x-direction values. The subsurface pit also has the highest pit aspect ratio, meaning it has the most severe pit geometry of all the pit geometries modelled. Table 5.19 shows that for uniaxially loaded 3D HAZ submodels the pit aspect ratio for the lowest to highest strained pits are also in increasing order. This may indicate that for 3D pits the pit aspect ratio is a more accurate indication of severity of a pit geometry than for 2D. This is due to the pit aspect ratios were not in increasing order for the uniaxially loaded 2D HAZ submodels in Table 5.3.

As the top three ranked pits for the uniaxially loaded 3D HAZ submodels are the same as for the 2D HAZ submodel, this also shows that for 3D models the depth of the pit is again the most important geometric aspect of the pit, with a shallow pit producing lower maximum total true strain in x-direction values in the pits. It is however interesting that the location of the maximum total true strain in x-direction values in the 3D repassivation and subsurface pits are located at the transition from vertical to rounded pit geometry but in the 2D pits, the maximum total true strain in x-direction values are located at the bottom

of the pits. This is due to the highest stresses and strains in a pitted model will occur perpendicular to the applied load. As 2D models do not show the plane perpendicular to the load, the regions of maximum stresses and strains are not accurately indicated. Therefore, it is recommended to use 3D models for increased accuracy. Stresses and strains tend to accumulate at regions of sharp edges or corners and therefore the location of the maximum total true strain in x-direction values in the 3D repassivation and subsurface pits are at the transition from vertical to rounded pit geometries. This is another indication that the 3D model for uniaxially loaded HAZ submodels provides more accurate information on the location of the maximum total true strain in x-direction values than the uniaxially loaded 2D HAZ submodel.

The location of the maximum total true strain in x-direction for the uniaxially loaded 3D HAZ submodel with a notched pit geometry is located at the side of the pit and not at the sharp geometry at the pit bottom, as occurs in 2D. This is again due to the plane perpendicular to the loading direction being absent in 2D. This pit geometry varies from the other pit geometries as it neither has a smooth, curved transition along the depth of the curve nor a sharp vertical region as in the other pit geometries. This shows that the 3D geometry is a more accurate indicator of the location of the maximum total true strain in x-direction.

The 3D geometry is therefore recommended to model the maximum strain in the x-direction values for all of the pit geometries. The displacement applied to both the 2D and 3D HAZ unpitted quarter or one eight models is the same, 0.1096 mm, and the subsequent displacements recorded at the end of the gauge length region are applied to the pitted 2D and 3D submodels. However, the strains in the 3D HAZ pitted submodels, Table 5.19, are all lower than in the 2D HAZ pitted submodels, Table 5.3. This may be explained by the use of the plane stress element behaviour used in this work and also by Mai et al. [12] and Wang and Han [273] who also investigated the presence of strains in 2D pitted specimens.

However, after noticing the discrepancies between the 2D and 3D values for maximum total true strain in x-direction, with the 2D values being higher than the 3D values, all element behaviours calculated in ANSYS were applied to the 2D reference pit geometry from Figure 3.2 as a control check, Table 5.20. This table shows the displacement applied in the x-direction to achieve 100% yield stress in the pit and the corresponding local strain values for the various element behaviours. It was found that the total true strain in x-direction 2D values which were closest to the 3D values for the reference pit geometry were achieved using the plane strain element behaviour. For the stress in x-direction, the axisymmetric values were the closest to the 3D values. It is therefore recommended that

when modelling pit geometries in 2D in order to investigate the maximum total true strain in x-direction that the plane strain, not the plane stress, element behaviour is selected. Additionally, in contrast to the available literature, Mai et al. [12] and Wang and Han [273], it is recommended to model in 3D and not 2D as the selection of the correct element behaviour plays an important role in achieving accurate results.

Table 5.20: Displacement, total true strain and stress values in x-direction for all element behaviours in ANSYS for 2D reference pit.

	Displacement (x) (mm)	Total True Strain in x-direction	Stress in X-direction (MPa)
3D Model	0.071188	0.031112	1177.890
2D Plane Stress	0.05	0.058532	1011.304
2D Axisymmetric	0.05	0.013380	1274.082
2D Plane Strain	0.05	0.027374	1391.366
2D Plane Stress with Thickness	0.05	0.58532	1011.304
2D Generalised Plane Strain	0.05	0.02172	1301.845

The 3D displacement value in Table 5.20 is higher than the displacement values for the 2D models. The same displacements were applied to the 3D models as to the 2D models to directly compare the models as the only difference is the extra z-dimension and therefore also the element type. The higher displacement value for the 3D model may be as a result of 3D plasticity.

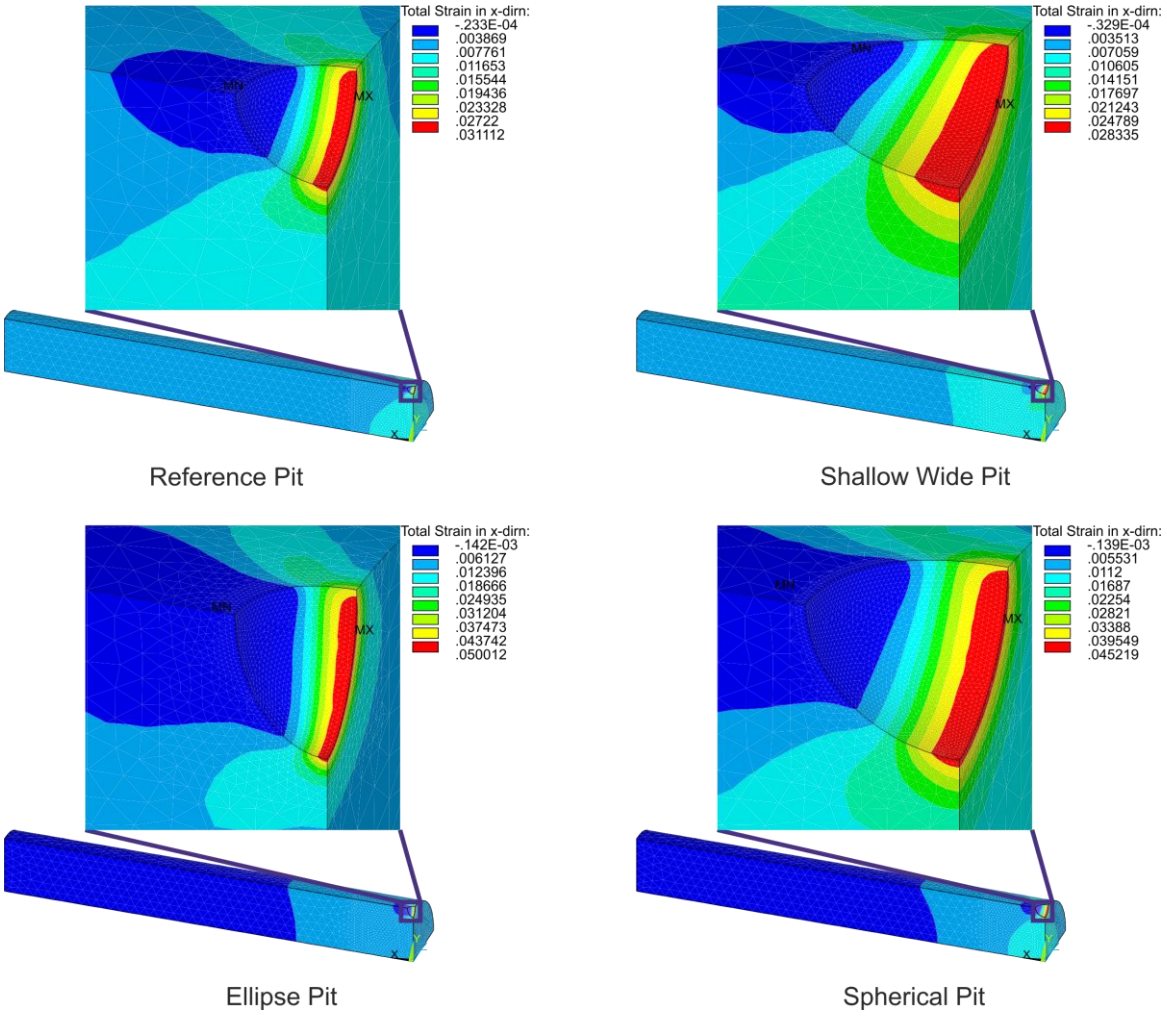

Figure 5.57: 3D HAZ UA submodel with reference, shallow wide, ellipse and spherical pits total true strain in x-direction results.

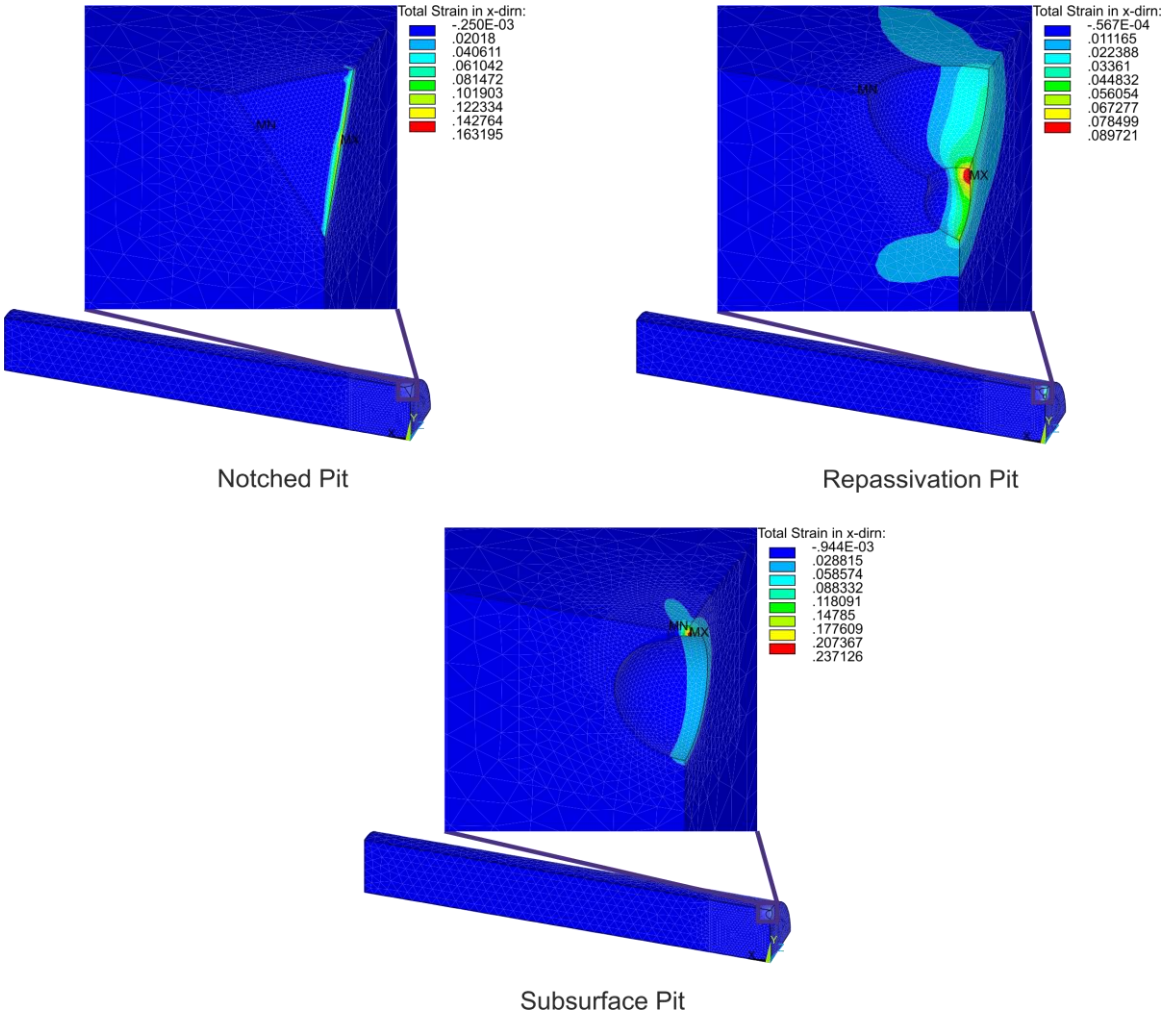

Figure 5.58: 3D HAZ UA submodel with notched, repassivation and subsurface pits total true strain in x-direction results.

3D Uniaxial Structural Analysis for Unpitted Base Material (BM)

The highest stresses and strains regions in the 3D BM uniaxial (UA) one eight unpitted model and selected gauge length region subjected to the same x-direction uniaxial load as the 2D model modelled previously, can be seen in Figure 5.59 and Figure 5.60. The location of the maximum x-direction stress is similar to the 2D BM one quarter model and falls just outside the margins of the gauge length. Similar to the 3D HAZ simulation described previously, the maximum total true strain in x-direction is not located in the same region as the 2D BM one quarter model but is located towards the fixed end of the model, Figure 5.60. The maximum x-direction stress and strain values are increased slightly- 770 MPa vs 786 MPa and 0.004 vs 0.005 for 2D and 3D respectively. Table 5.21 shows the displacement value applied, which is the same as applied to the 2D model in Table 5.4, and the resulting maximum stresses and total true strains in x-direction for the 3D UA BM one quarter model.

Table 5.21: Displacement values applied to 3D BM UA one eight model and resulting total strain and stress results.

Displacement (x) (mm)	Total true strain in x-direction	Stress in X-direction	% Yield
0.0966	0.0054	786	102

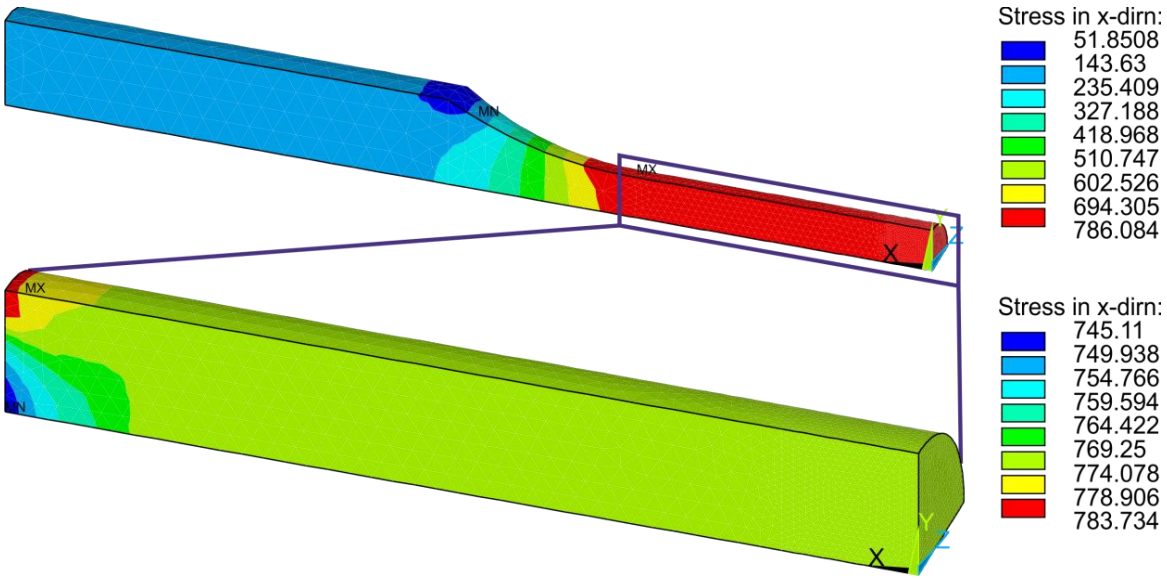

Figure 5.59: 3D one eight model maximum stress in x-direction for 100% of BM yield stress applied as uniaxial displacement load to 2D model and 3D UA submodel region shown on the 3D one eight model.

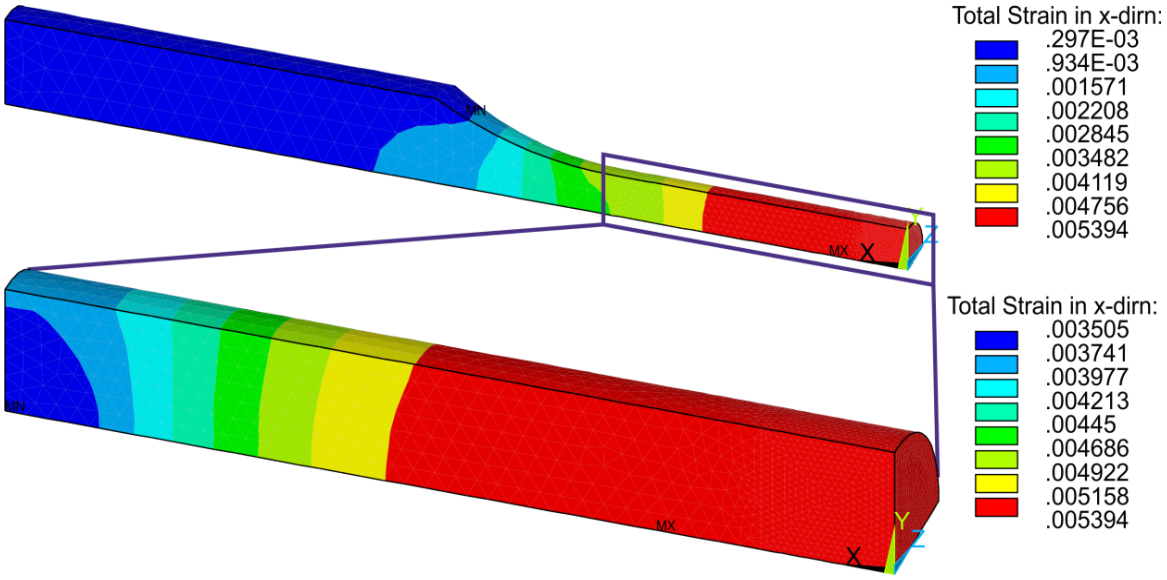

Figure 5.60: 3D one eight model maximum total strain in x-direction for 100% of BM yield stress applied as uniaxial displacement load to 2D model and 3D UA submodel region shown on the 3D one eight model.

The 3D UA BM submodel with the x-, y- and z-displacements from the 3D UA BM one eight model applied and the corresponding maximum x-direction stress and total true strain results can be seen in Figure 5.61 and Figure 5.62. Table 5.22 shows the global displacement applied to the 3D UA HAZ submodel and the resulting stress and total true strain in the x-direction.

Table 5.22: Displacement values applied to 3D BM UA submodel and resulting total strain and stress results.

Displacement (x) (mm)	Total true strain in x-direction	Stress in X-direction	% Yield
0.062602	0.00541	785	102

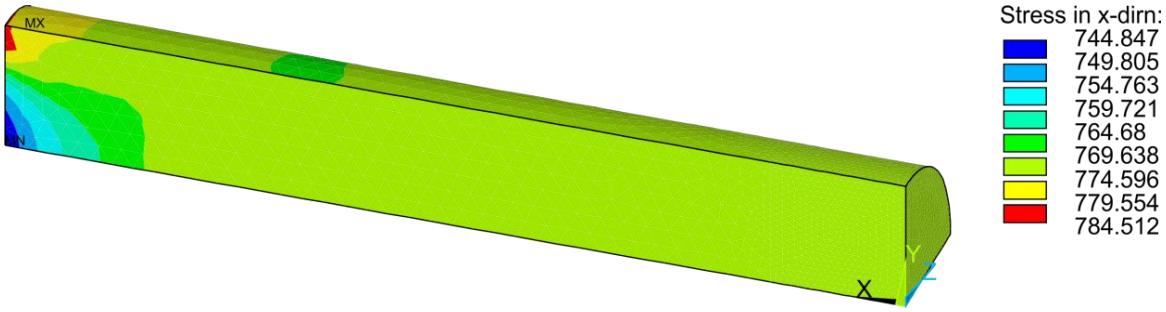

Figure 5.61: 3D UA submodel maximum stress in x-direction for 100% of BM yield stress applied as uniaxial displacement load to 2D model.

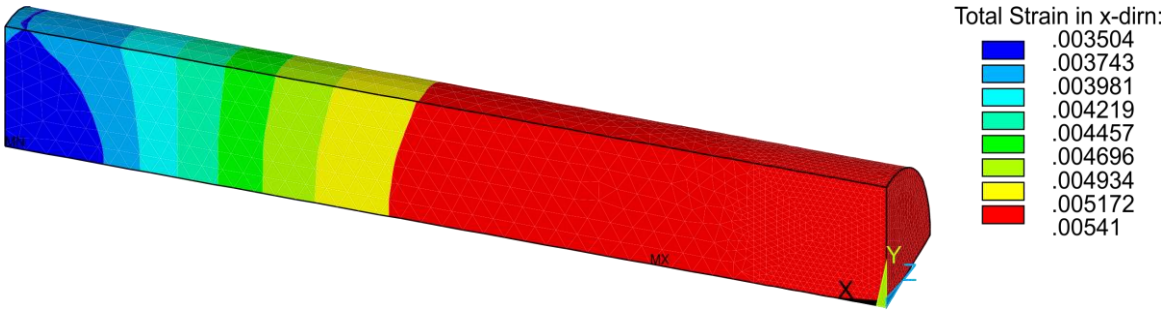

Figure 5.62: 3D UA submodel maximum total strain in x-direction for 100% of BM yield stress applied as uniaxial displacement load to 2D model.

Similar to the 3D HAZ model, the maximum x-direction stress and total strain values in the 3D UA BM submodel are comparable to the maximum x-direction stress and total strain values for the 3D UA BM submodel region within the 3D BM one eight model, Figure 5.59 to Figure 5.62. Therefore, in the subsequent simulations involving a 3D BM model loaded to 100% of BM yield stress applied as a uniaxial displacement to the 2D BM one quarter model, the 3D BM submodel is used in place of the 3D BM one eight model.

3D Uniaxial Structural Analysis for Pitted Base Material (BM)

The same 3D pit geometries used for the HAZ simulations were also removed from the BM model. The total true strain in the x-direction in the pits is again the main result of interest, Figure 5.64 and Figure 5.65. Similar to the 2D UA analysis in Figure 5.16 and Figure 5.17, and the 3D UA HAZ results in Figure 5.57 and Figure 5.58, the region of high total true strain in the x-direction are located in the pit bottom, for the pit geometries in Figure 5.64. However, unlike the 2D analysis this region extends from the pit bottom to the pit mouth perpendicular to the loading direction. The pit geometries in Figure 5.65 have more severe geometries with the region of high total true strain in the x-direction located not at the pit bottom, which is also what was found for the 3D UA HAZ simulations. Table 5.23 shows the maximum strains in x-direction for the various pit geometries and have been sorted from lowest to highest, along with the pit aspect ratio for the uniaxially loaded 3D HAZ UA pitted submodels.

Table 5.23: Lowest maximum total strain in x-direction to highest for all seven pit geometries in the uniaxially loaded 3D BM UA submodel and the pit aspect ratios.

Pit Geometry	Maximum Total Strain in the x-direction	Pit Aspect Ratio
Shallow Wide	0.024881	0.3
Reference	0.027254	0.5
Spherical	0.039662	0.5
Ellipse	0.044170	0.83
Repassivation	0.078978	0.83
Notched	0.143586	0.83
Subsurface	0.209971	10

The maximum total true strain in x-direction for all pit geometries in the 3D BM submodel are presented in Figure 5.63 as a function of time. Similar to the maximum total true strain in x-direction results for the pitted 2D BM quarter model in Figure 5.15 and for the pitted 3D HAZ one eight model in Figure 5.56, the strains for the pitted geometries do not increase linearly over time, which may be due to the specimen being loaded past the yield point of the material.

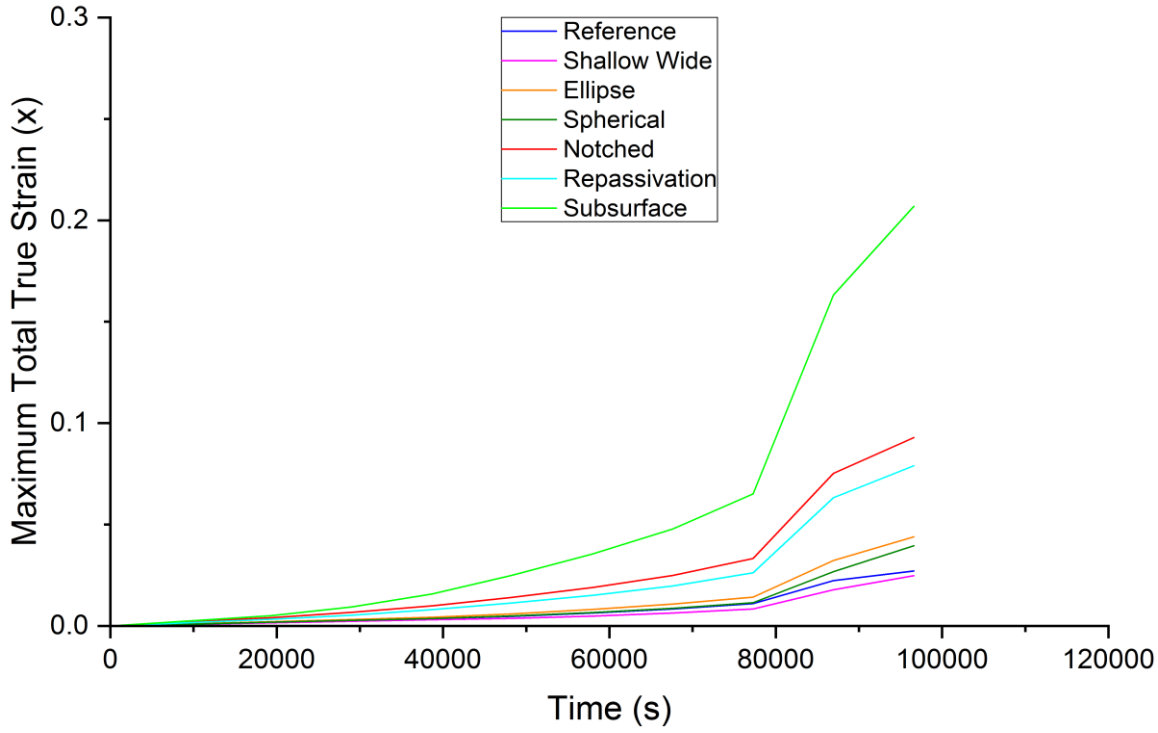

Figure 5.63: Maximum total true strain in x-direction vs time for all pit geometries in the 3D BM submodel.

Similar to the 3D HAZ results in Table 5.19, Figure 5.64 and Figure 5.65 for the BM show that the shallow wide pit has the lowest maximum total strain in x-direction value, 0.024881, with the subsurface pit having the highest value, 0.209971. The maximum total strain in x-direction values for the 3D HAZ material are ranked in the same order as for the 3D BM. This again shows that for a uniaxial x-direction displacement load the depth of the pit is the most important geometric aspect of the pit, with a shallow pit producing lower maximum total strain in x-direction values in pits. This applies to both 2D and 3D models in addition to BM and HAZ material properties.

The locations of the maximum total strain in x-direction are also the same in the BM 3D submodel as the HAZ 3D submodel with the ellipse, spherical, shallow wide and reference pits having the maximum total strain in the x-direction occurring at the side of the pit, near the pit mouth. The notched pit has the maximum total strain in the x-direction at the side of the pit. This might again be as a result of the additional z-dimension, which provides more accurate information than 2D models. The location of the maximum total strain in the x-direction in the repassivation pit occurs at the vertical intersection between the larger top pit and smaller bottom pit. For the submodel pit, the maximum total strain in the x-direction is present also at the vertical intersection between the pit mouth region and the larger subsurface region of the pit.

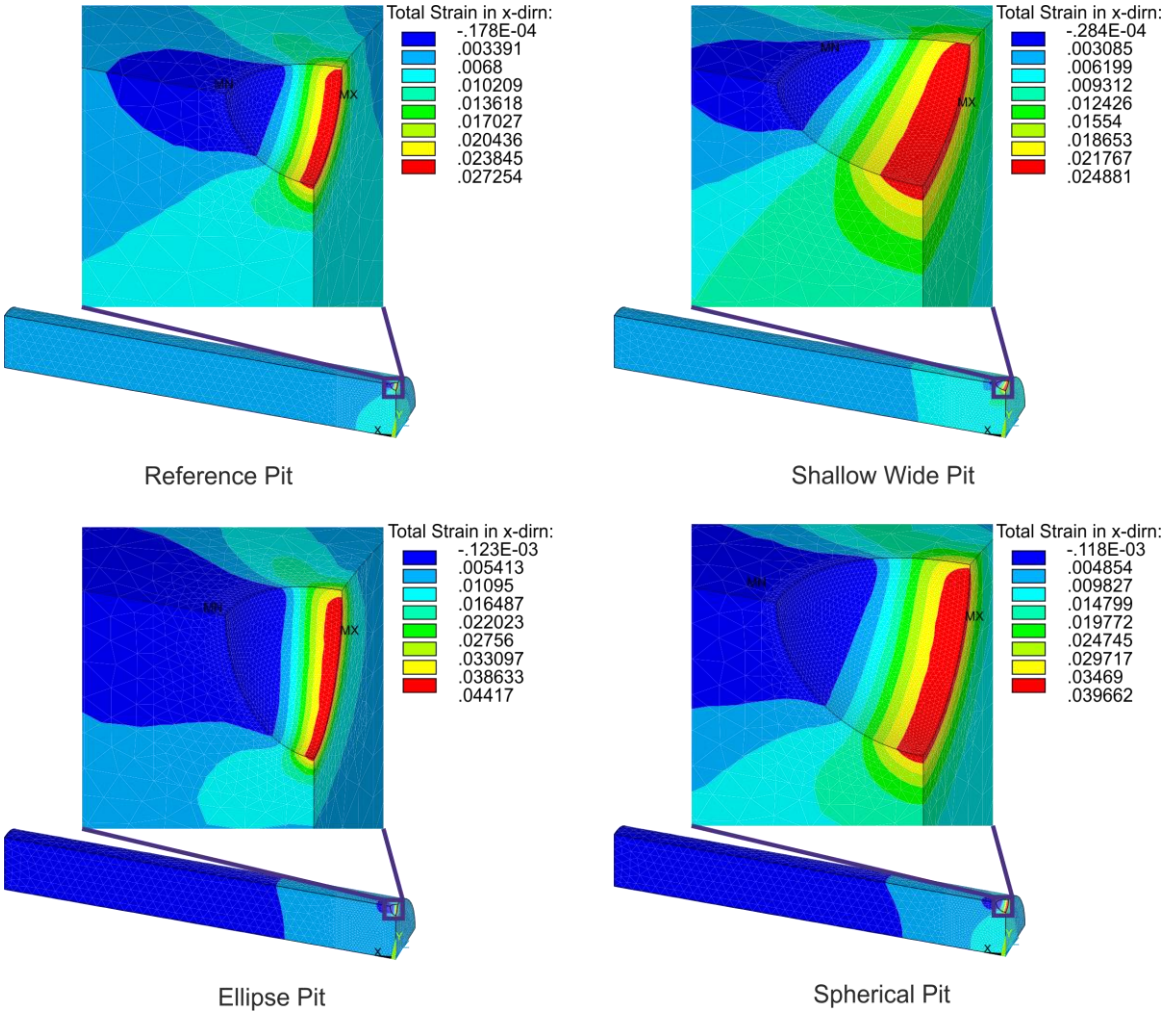

Figure 5.64: 3D BM UA submodel with reference, shallow wide, ellipse and spherical pits total strain in x-direction results.

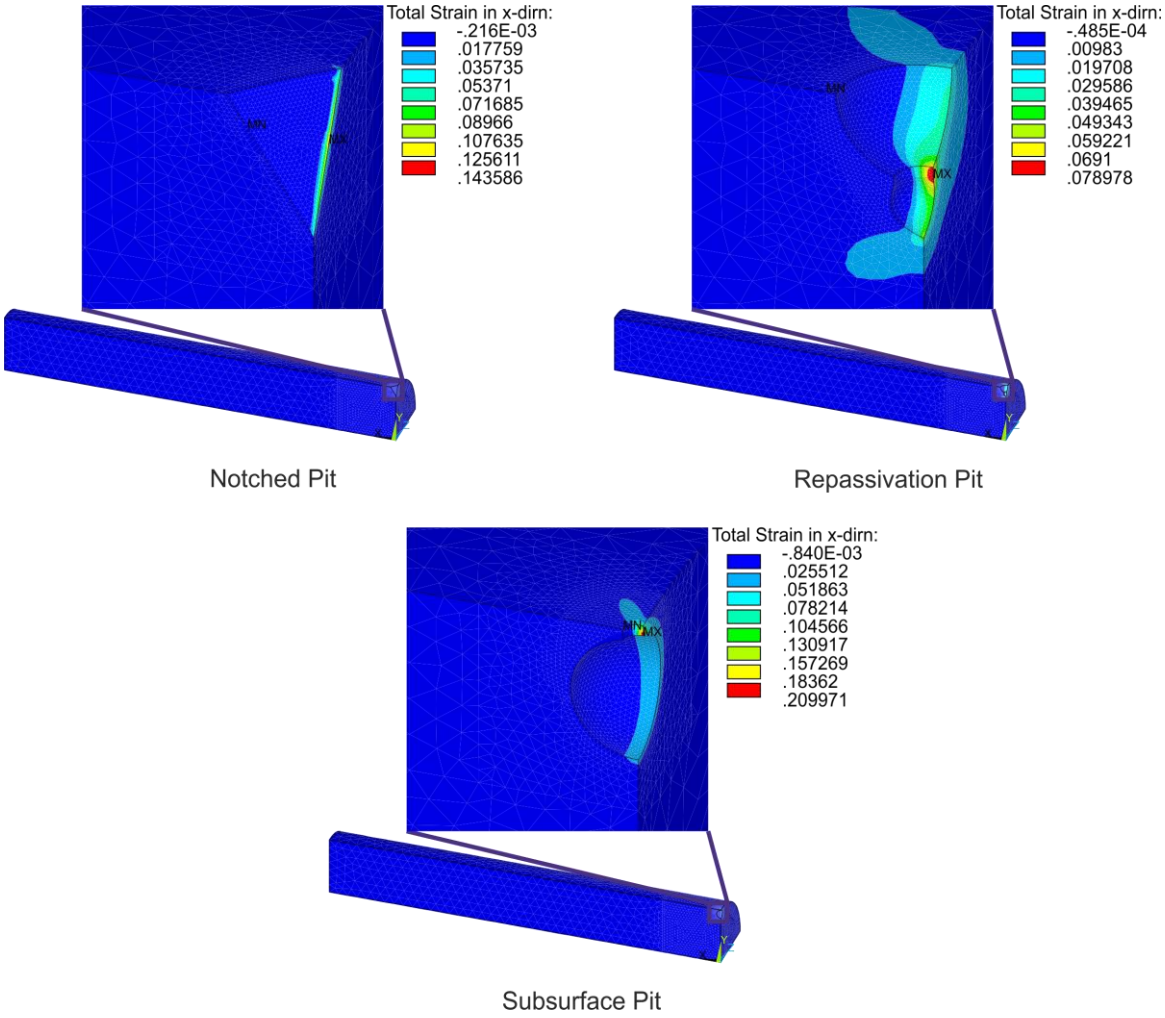

Figure 5.65: 3D BM UA submodel with notched, repassivation and subsurface pits total strain in x-direction results.

This information is also presented in the graph in Figure 5.67. All the curves for the 3D pits have lower local strains for all corresponding global strain values than for the 2D pits, Figure 5.18, which may be due to the plane stress element behaviour option. The pit with the highest global vs local strain curve for the 2D HAZ and BM models, the notched pit, is also included in the graphs in Figure 5.66. The curve for the 2D notched pit is significantly higher than the highest curve for the 3D pit, the subsurface pit. Similar to the 2D simulations, time-dependent pit growth is not modelled in this stage of the work.

It must again be stated that the 3D values are more accurate however, as the location of the highest strains in x-direction are located on the plane perpendicular to the applied load, which is absent in the 2D model. Figure 5.66, however, also shows that the shallow pits have lower local strains for all corresponding global strain values, as also seen in Figure 5.18. Unlike Figure 5.18, where the notched pit geometry had the highest global vs local strain curve, the subsurface pit has the highest local strains for all corresponding global strain values. This may be due to the sharp geometry in the pit mouth region and also the

smaller pit mouth radius results in the highest pit aspect ratio for the subsurface pit. Due to the difference in the pit shapes exhibiting the highest local strains in 2D, the notched pit, and in 3D, the subsurface pit, it is recommended that 3D modelling is preferable over 2D modelling. It must also be noted that perhaps the modelling applied by others may be misleading regarding the effects of pit geometry.

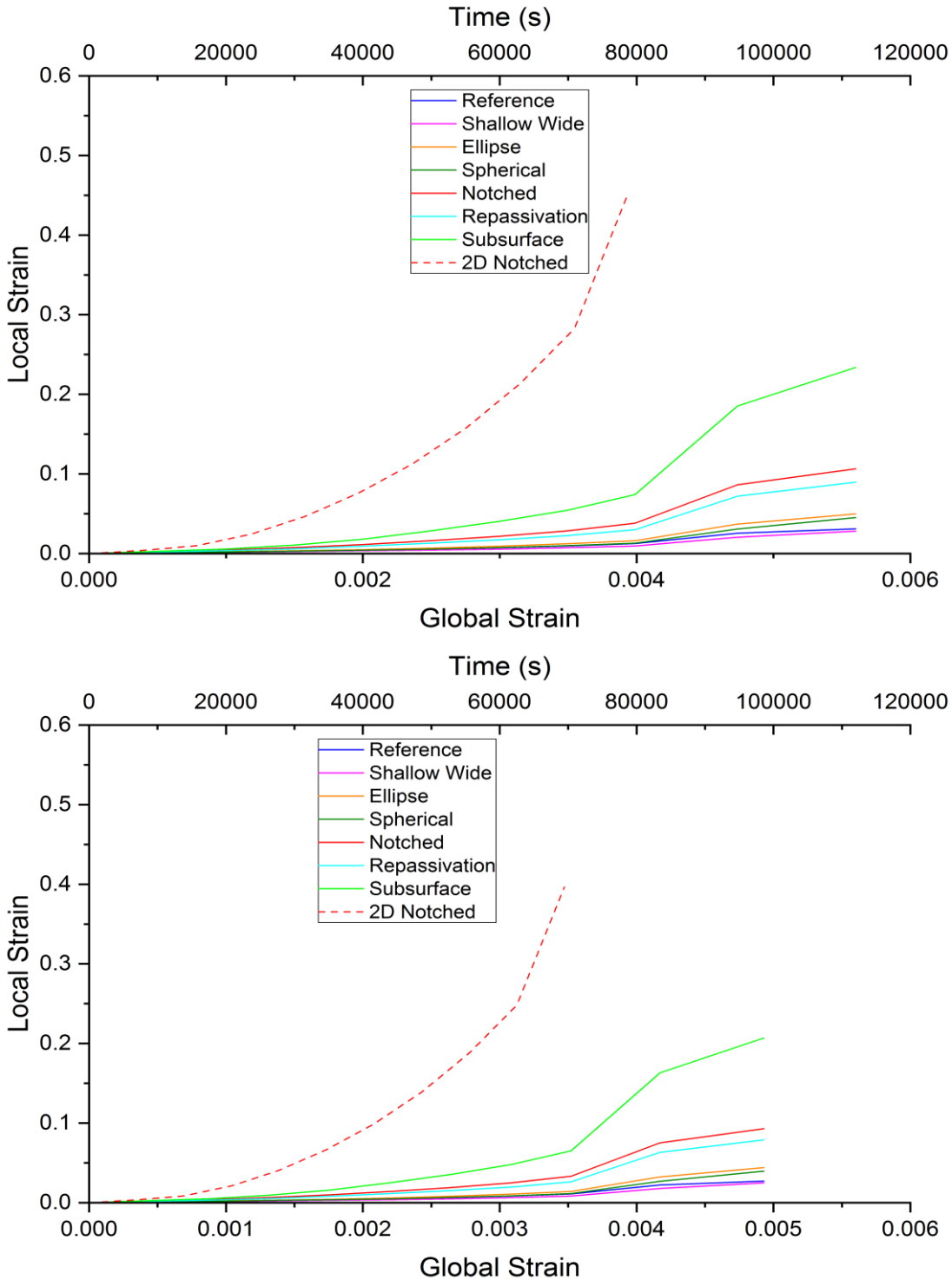

Figure 5.66: Graph of global vs local strains for all pit geometries in the 3D UA HAZ (Top) and BM (Bottom) submodel.

The highest to lowest maximum total true strain in x-direction occurs in the same order for the BM material pits, Table 5.23, as for the HAZ material pits, Table 5.19. Additionally, the location of the highest maximum total true strain in x-direction occurs in the same location for both the BM material, Figure 5.64 and Figure 5.65, and the HAZ material, Figure 5.57 and Figure 5.58. These locations differ to the location of the highest maximum total true strain in x-direction in the 2D models, for both the BM, Figure 5.16 and Figure 5.17 and HAZ materials, Figure 5.9 and Figure 5.10. In the 2D models the location of the highest maximum total true strain in x-direction for all pit geometries was in the bottom of the pit. For the 3D models none of the pit geometries had the location of the highest maximum total true strain in x-direction in the pit bottom. This may again indicate that the 3D models provide a more accurate indication of the regions of the highest maximum total true strain in x-direction and is therefore recommended over 2D modelling.

The results for 66% of the yield stress in the 3D UA HAZ pitted submodel can be seen in Figure A.21 and Figure A.22 in Appendix A. The location of the maximum total true strain in the x-direction for the 3D HAZ UA pitted submodel loaded to 66% of yield stress occur in regions similar to Figure 5.57 and Figure 5.58, which are for 100% yield stress. The subsurface, repassivation and notched pits all have maximum total true strain in the x-direction located in the same regions in both 100% and 66% yield models. The remaining pits have maximum total true strain in the x-direction located at the pit side near the pit mouth for 100% yield stress loading condition. However, for the 66% yield model the maximum total true strain in the x-direction are located slightly higher, more towards the pit mouth, Figure A.21 and Figure A.22. The table showing the order of the seven pit geometries from lowest maximum total true strain in the x-direction to highest for the 66% yield uniaxially loaded 3D HAZ UA pitted submodels, Table A. 12, is in the same order as for the 100% yield uniaxially loaded 3D HAZ UA pitted submodel, Table 5.19. Additionally, the graph of global vs local strains for all 3D pit geometries loaded to 66% of yield for the HAZ material, Figure A. 23, follow the same curves as for the 100% loaded specimens, Figure 5.66, until the 100% yield curve reaches 66% of yield.

Most researchers investigate the presence of stresses in a pit, but the few researchers mentioned have at least considered more the strains and their locations in the pits. Also, not all of the pit geometries modelled in this contribution have been investigated elsewhere. To make the results regarding the pit geometries and location of the strains inside the pits more readily available, such information is summarised in Table 5.24.

Table 5.24: Summary of below findings for uniaxial loads on 3D pitted specimens.

Pit Geometry:	Location of Maximum Strains (100% Yield):	Location of Maximum Strains (66% Yield):
Reference	Side of pit, near pit mouth	Near pit mouth
Shallow Wide	Side of pit, near pit mouth	Near pit mouth
Ellipse	Side of pit, near pit mouth	Near pit mouth
Spherical	Side of pit, near pit mouth	Near pit mouth
Notched	Along pit sides	
Repassivation	Vertical intersection between pits	
Subsurface	Near pit mouth, vertical section	

The results are described in more detail and compared to literature in the following paragraphs.

The ellipse, spherical, shallow wide and reference 3D pits all have the maximum total true strain in the x-direction occurring at the side of the pit, near the pit mouth. Cerit [206], Horner et al. [248] and Xiang et al. [274] also noted the location of the highest strained regions occur near the pit mouth for 3D models. Xiang et al. [274] also noted that a 3D notched pit has the maximum total true strain in the x-direction at the side of the pit. However, Xiang et al. modelled a “butterfly” shaped pit, Figure 2.40, with a rounded pit bottom, so the location of the maximum strains in this model were also located on the sides of the pits but more towards the pit bottom than the sides, as in Figure 5.57. The findings from various researchers regarding the pit shapes investigated and the corresponding location of maximum strains for 3D pit geometries are presented in Table 5.25.

Table 5.25: Pit geometry and location of maximum strains for 3D pit geometries.

Pit Geometry:	Location of Maximum Strains:	Source:
Wide- Shallow	Pit mouth	Cerit [206]
Hemispherical	Near pit mouth	Cerit [206]
Narrow- Deep	Near pit mouth but further down pit wall	Cerit [206]
Hemispherical	Near pit mouth	Horner et al. [248]
U-Shaped	Near pit mouth	Horner et al. [248]
Butterfly	Pit sides near pit bottom	Xiang et al. [274]
Submodel	Near pit mouth, vertical section	Eksi [272]
Shallow Hemisphere*	Along pit sides	Anantha et al. [271]
Deep Hemisphere*	Near pit mouth	Anantha et al. [271]
Shallow Hemisphere'	Along pit sides	Anantha et al. [271]
Deep Hemisphere'	Along pit sides	Anantha et al. [271]

* For strains of 23% of yield.

' For strains of 66% of yield

The location of the maximum total true strain in the x-direction in the repassivation pit occurs at the vertical intersection between the larger top pit and smaller bottom pit. For the submodel pit geometry, the maximum total true strain in the x-direction is present also at the vertical intersection between the pit mouth region and the larger subsurface region of the pit, Figure 5.58. This was also observed by Eksi [272], with the location of the maximum strained regions for all of the subsurface pits modelled being also in the pit mouth region.

Anantha et al. [271] investigated a shallow and deep hemispherical pit geometry and found the highest strained regions were concentrated near the pit mouth for the deep pit geometry and along the pit walls for the shallow pit geometry, for strains of 23% yield strength. Additionally, the strains in the deeper pit were higher than for the shallow pit. However, when a load of 66% yield strength was applied, the highest strained regions were more distributed along the pit walls, similar to Figure 5.57. However, for the remaining pits in Figure 5.58 the maximum total true strains in x-direction are still concentrated in one region only for these remaining pit geometries, but this is not at the pit mouth.

The above findings from literature and from the work on 100% yield 3D pitted models, does not correspond to the findings on 66% of the applied HAZ in this work, Figure A.21 in Appendix A. For the reference, shallow wide, ellipse and spherical pit geometries the

location of the highest maximum total true strains in x-direction when 66% of the yield stress is applied were found to be located more towards the pit mouth than along the pit walls. For the notched, repassivation and subsurface pit geometries the location of the highest maximum total true strains in x-direction were located in the same regions as for the 100% loaded pits, Figure 5.58.

To summarise the above findings, the present investigation of the various 3D pit geometries under uniaxial loading shows that the location of highest strains in the pit geometries modelled are not located in the pit bottom for any pit geometry. Therefore, it can be stated that:

- *The local mechanical loads in terms of strains differ largely for the various pit geometries with respect to height, location and direction.*
- *It may be recommended to model the pit geometries used in this work in 2D using the plane strain element boundary condition as the resulting highest total true strains in x-direction resemble the 3D values most accurately, Table 5.20.*
- *Already from the aspect of local mechanical loading in the pits, HAC initiating from such pits does not necessarily occur at the pit bottom, as frequently anticipated elsewhere, Mai et al. [12, 13] and Wang and Han [273]. Due to high local strains HAC is more likely to occur near the pit mouth for the reference, shallow wide, ellipse, spherical and subsurface pit geometries. It also becomes more likely to occur along the pit wall for the notched pit geometry and at the intersection of the first and second pit for the repassivation pit geometry.*

3D Bending Structural Analysis for Unpitted HAZ

The highest stressed and strained regions in the 3D HAZ model of one quarter of the real specimen unpitted model subjected to the same -y-direction bending load as the 2D HAZ model modelled previously, can be seen in Figure 5.67 and Figure 5.68. The location of the maximum x-direction stresses and strains are the same as in the 2D model, however the values are increased slightly- 869 MPa vs 880 MPa and 0.0041 vs 0.0042 for 2D and 3D respectively. This may again be due to the plain strain elemental behaviour used in the 2D models, instead of the more accurate true stress behaviour, as summarised in Table 5.20. Table 5.26 shows the displacement values applied and the resulting maximum stresses and total true strains in x-direction for the 3D HAZ bend one quarter model.

Table 5.26: Displacement values applied to 3D HAZ bend one quarter model and resulting total true strain and stress results.

Displacement (y) (mm)	Total True Strain in x-direction	Stress in X-direction (MPa)	% Yield
0.913	0.0042	880	101

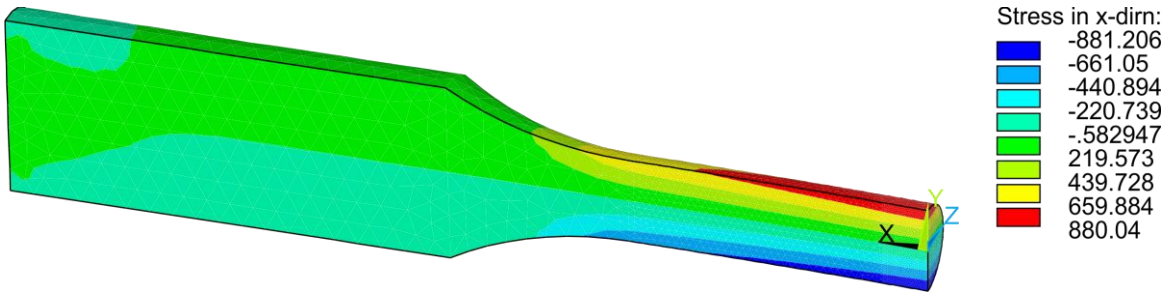

Figure 5.67: One quarter model maximum stress result for 100% of HAZ yield stress applied as bending displacement.

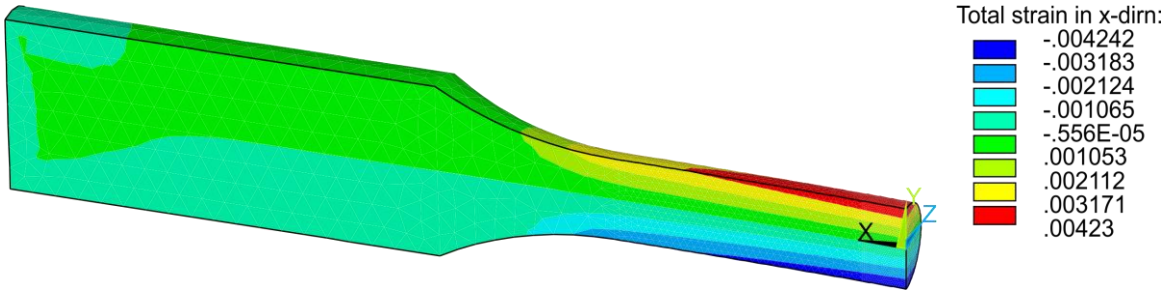

Figure 5.68: One quarter model maximum total true strain result for 100% of HAZ yield stress applied as bending displacement.

The 3D HAZ one quarter model selected gauge length region and corresponding maximum x-direction stress and total true strain results can be seen in Figure 5.69 and Figure 5.70. The 3D bend HAZ submodel with the x-, y- and z-displacements from the 3D HAZ one quarter model applied and the corresponding maximum x-direction stress and total true strain results can be seen in Figure 5.71 and Figure 5.72. Table 5.27 shows the displacement values applied to the 3D HAZ bend submodels and the resulting stresses and total true strains in the x-direction.

Table 5.27: Displacement values applied to 3D HAZ bend submodel and resulting total true strain and stress results.

Displacement (y) (mm)	Total True Strain in x-direction	Stress in X-direction (MPa)	% Yield
0.16415	0.0042	880	101

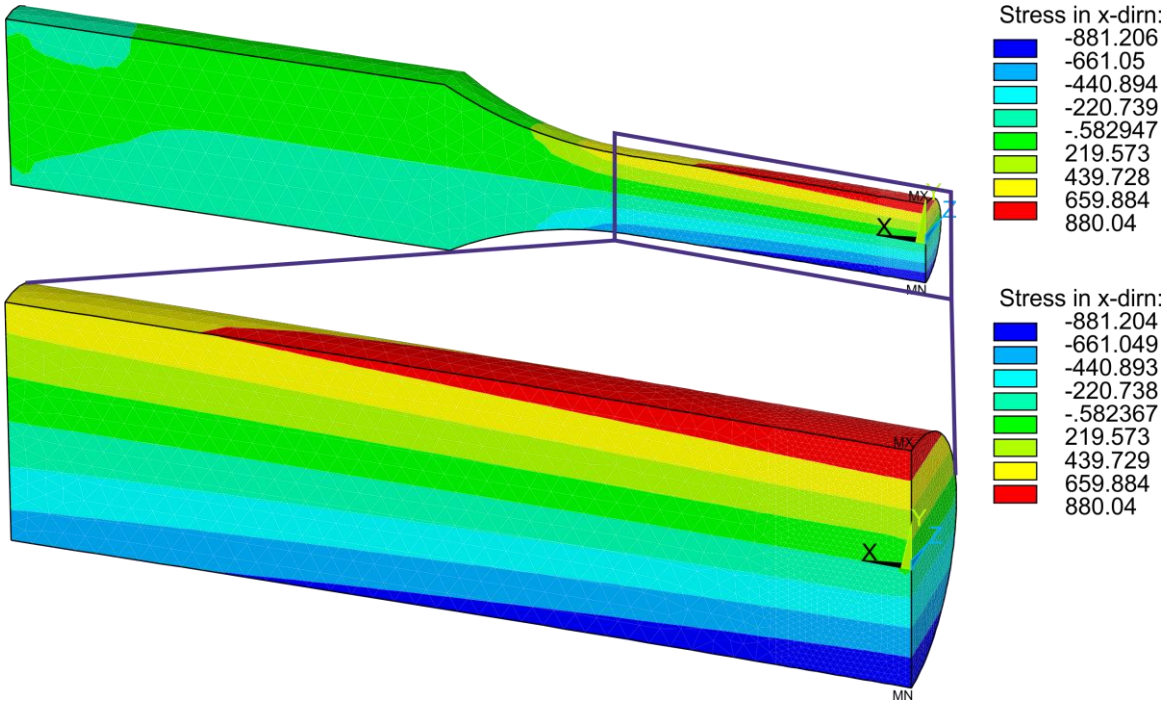

Figure 5.69: One quarter model maximum stress result for 100% HAZ yield stress applied as bending displacement and selected gauge length region shown on the full half specimen.

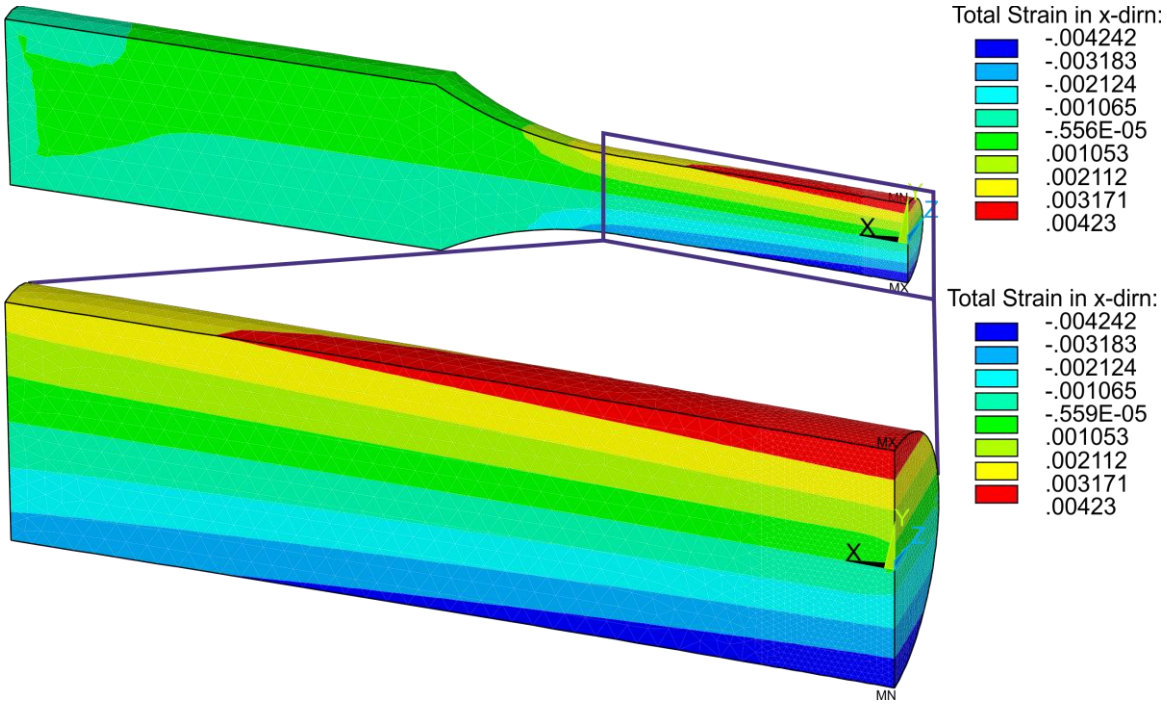

Figure 5.70: One quarter model maximum total true strain result for 100% HAZ yield stress applied as bending displacement and selected gauge length region shown on full half specimen.

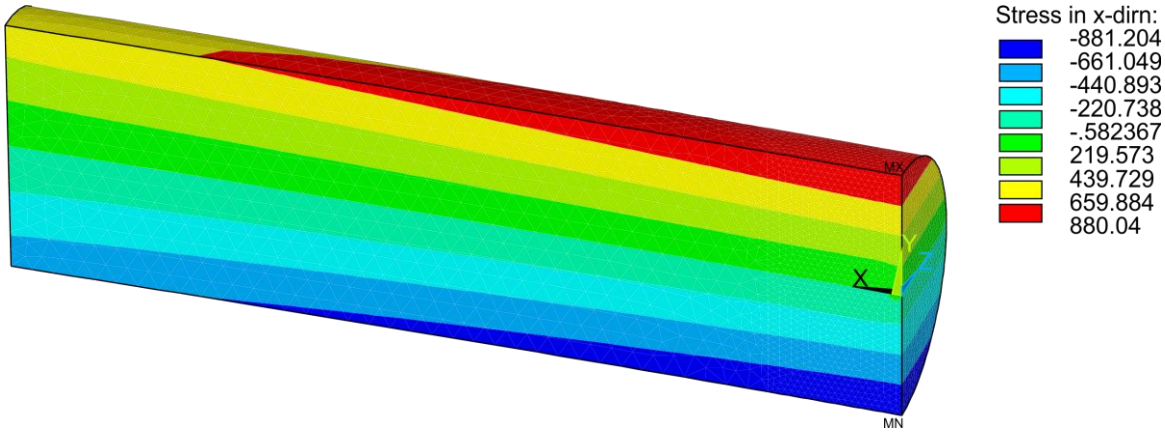

Figure 5.71: Submodel maximum stress result for 100% of yield stress applied as bending displacement to HAZ one quarter model.

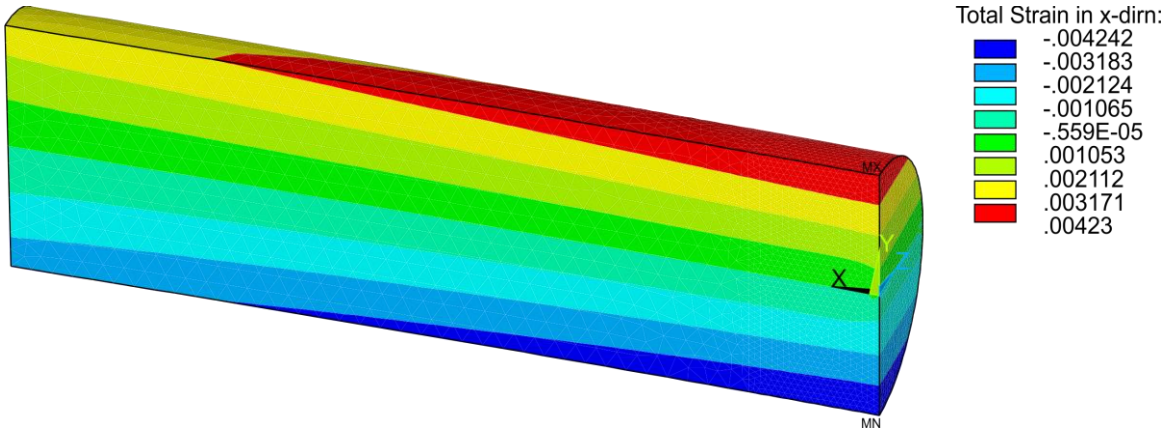

Figure 5.72: Submodel maximum total true strain result for 100% of yield stress applied as bending displacement to HAZ one quarter model.

As seen in Figure 5.69 to Figure 5.72, the maximum stress and total true strain in x-direction values for the 3D HAZ bend submodel are equal to the maximum stress and total true strain in x-direction values in the 3D HAZ half model. The location of these maximum values is in the same region of both models. For this reason, in the subsequent simulations involving bending until 100% of yield stress is reached, the 3D HAZ bend submodel will be used in place of the 3D HAZ quarter model.

3D Bending Structural Analysis for Pitted HAZ

For 3D HAZ bending analysis the total true strain in the x-direction in the pits is again the main result of interest, Figure 5.74 and Figure 5.75. Similar to the uniaxial (UA) loading condition, the regions of high total true strain in the x-direction are located in the pit bottoms. For the 2D analysis in Figure 5.27 and Figure 5.28, the region of high total true strains in the x-direction are also located in the pit bottom. However, unlike the 2D models this region extends from the pit bottom to the pit mouth perpendicular to the loading direction, Figure 5.74 and Figure 5.75. However, none of the 3D pit geometries have a

maximum total true strain in the x-direction occurring at the bottom of the pit. The regions with the maximum total true strain in the x-direction are the same as for the UA loading condition. Table 5.28 shows the maximum strains in x-direction for the various pit geometries and have been sorted from lowest to highest. The pit aspect ratio for each pit is also shown.

Table 5.28: Lowest maximum total true strain in x-direction to highest for all seven pit geometries in the bending loaded 3D HAZ bend pitted submodel and the pit aspect ratios.

Pit Geometry	Maximum Total true strain in the x-direction	Pit Aspect Ratio
Unpitted	0.0042	-
Shallow Wide	0.009431	0.3
Spherical	0.012403	0.5
Reference	0.012712	0.5
Ellipse	0.015937	0.83
Repassivation	0.027858	0.83
Notched	0.061354	0.83
Subsurface	0.078442	10

The maximum total true strain in x-direction for all pit geometries in the 3D bend HAZ submodel are presented in Figure 5.73 as a function of time. Similar to the maximum total true strain in x-direction results for the pitted 2D HAZ quarter model in Figure 5.26, the strains for the pitted geometries do not increase linearly over time, which again may be due to the specimen being loading past the yield point of the material.

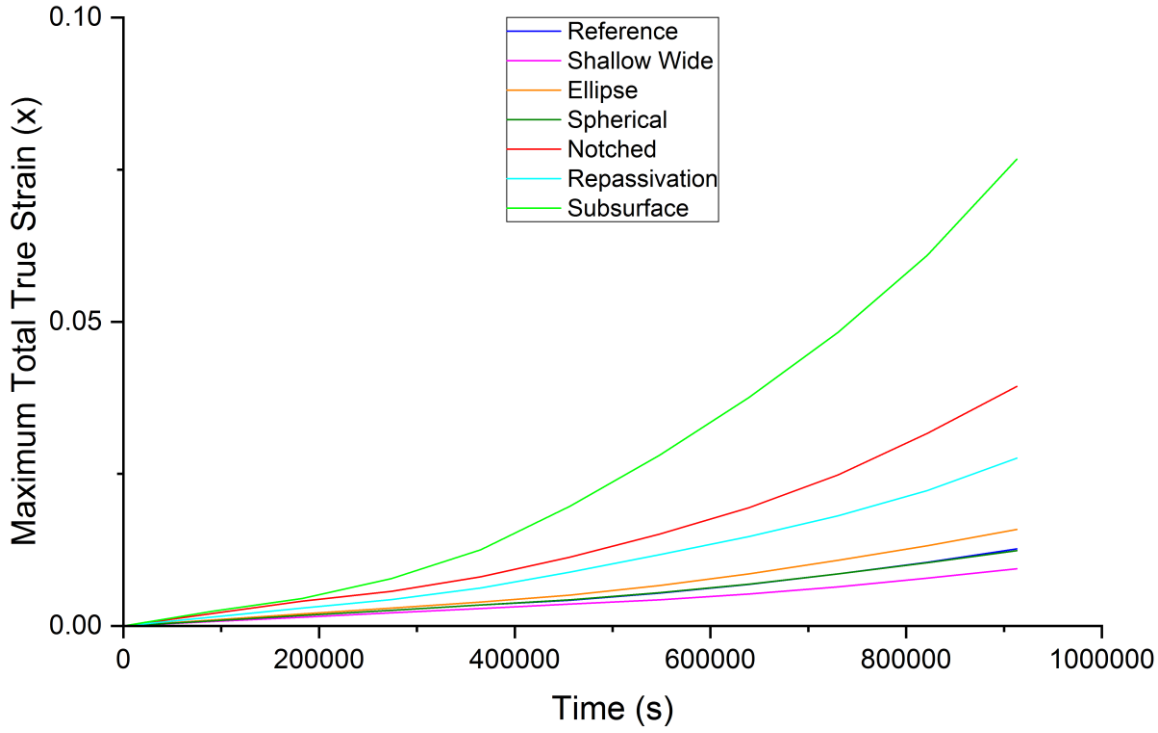

Figure 5.73: Maximum total true strain in x-direction vs time for all pit geometries in the 3D bend HAZ submodel.

As observed for the 3D UA HAZ pits in Figure 5.57 and Figure 5.58, the 3D HAZ pitted specimens loaded under bending in Figure 5.74 and Figure 5.75, and Table 5.28 also have a different order to their 2D counterparts, in Figure 5.27, Figure 5.28, and Table 5.9. As previously found for the 2D HAZ bend submodel, the subsurface pit in the 3D HAZ bend submodel has the highest maximum total true strain in x-direction value. This may be due to for bending, as previously found, a large pit mouth and shallow pit depth, which produces the lowest pit aspect ratio, results in the lowest maximum total true strain in x-direction in the pits. As the subsurface pit has the smallest pit mouth diameter and resulting from that also the highest pit aspect ratio, this may explain why the subsurface pit geometry experiences the highest maximum total true strain in x-direction when a bending load in the -y-direction is applied to the 3D HAZ submodel.

The three pits with the lowest maximum total true strain in x-direction are the same as for the 2D HAZ bending submodel, which are the shallow wide, spherical and reference pits. This further shows that for a bending load the pit mouth diameter is the most important geometric aspect of the pit, with a larger pit mouth diameter producing lower maximum total true strain in x-direction values in pits, both for 2D and 3D HAZ bend submodels. As the pit mouth diameter is also a factor in determining the pit aspect ratio, it is understandable that the pit ratio order in Table 5.28 are in increasing order. This might again indicate that pit aspect ratio is more accurate for 3D models than 2D models as the

pit aspect ratios were not in increasing order for the bending loaded 2D HAZ bend submodels in Table 5.9.

The locations of the highest total true strains in x-direction are the same as for the 3D UA HAZ submodel, for the notched, repassivation and submodel pit geometries, Figure 5.58 and Figure 5.75. This additionally shows that the geometries of the pits, for example sharp edges and vertical regions in the pits, are important in determining the regions of maximum total true strains in x-direction when a displacement is applied. The location of the highest total true strains in x-direction for the reference, shallow wide, ellipse and spherical pit geometries are located slightly more towards the pit mouth for the 3D HAZ bending submodel, Figure 5.74 than for the 3D UA HAZ submodel, Figure 5.57. This may be due to the region of highest tensile loads for the bending loading condition being concentrated on the top surface of the specimen but for the uniaxial loading condition the tensile load is distributed evenly through the specimen.

The highest total true strains in x-direction, Table 5.28, for the 3D HAZ bending loading condition are lower than the highest total true strains in x-direction for the 2D HAZ bending loading condition, Table 5.9. This is the same as for the uniaxial loading condition and may also be explained by the use of the plane stress element behaviour for 2D simulations, in accordance with various other researchers.

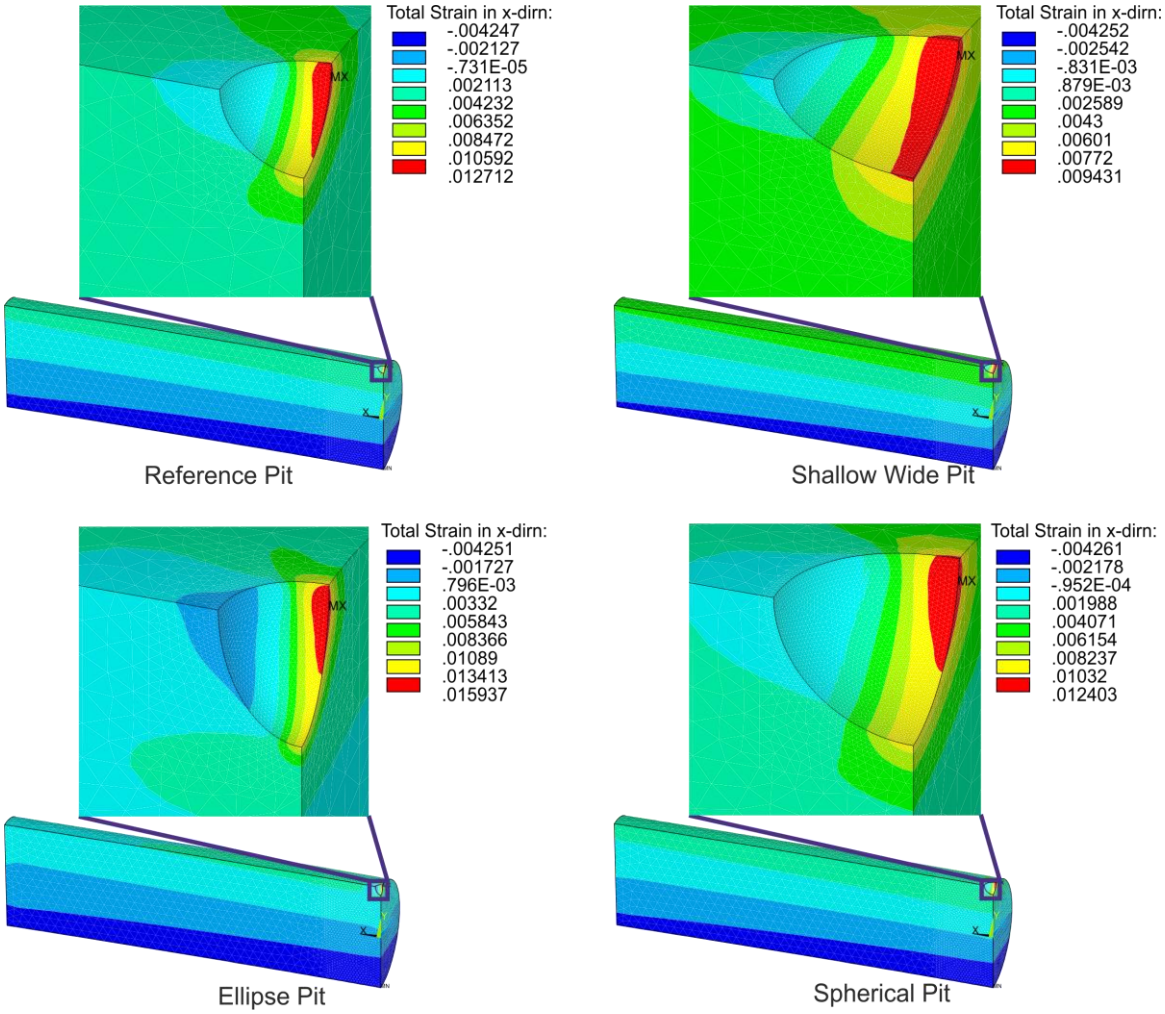

Figure 5.74: 3D HAZ bend submodel with reference, shallow wide, ellipse and spherical pits total true strain in x-direction results.

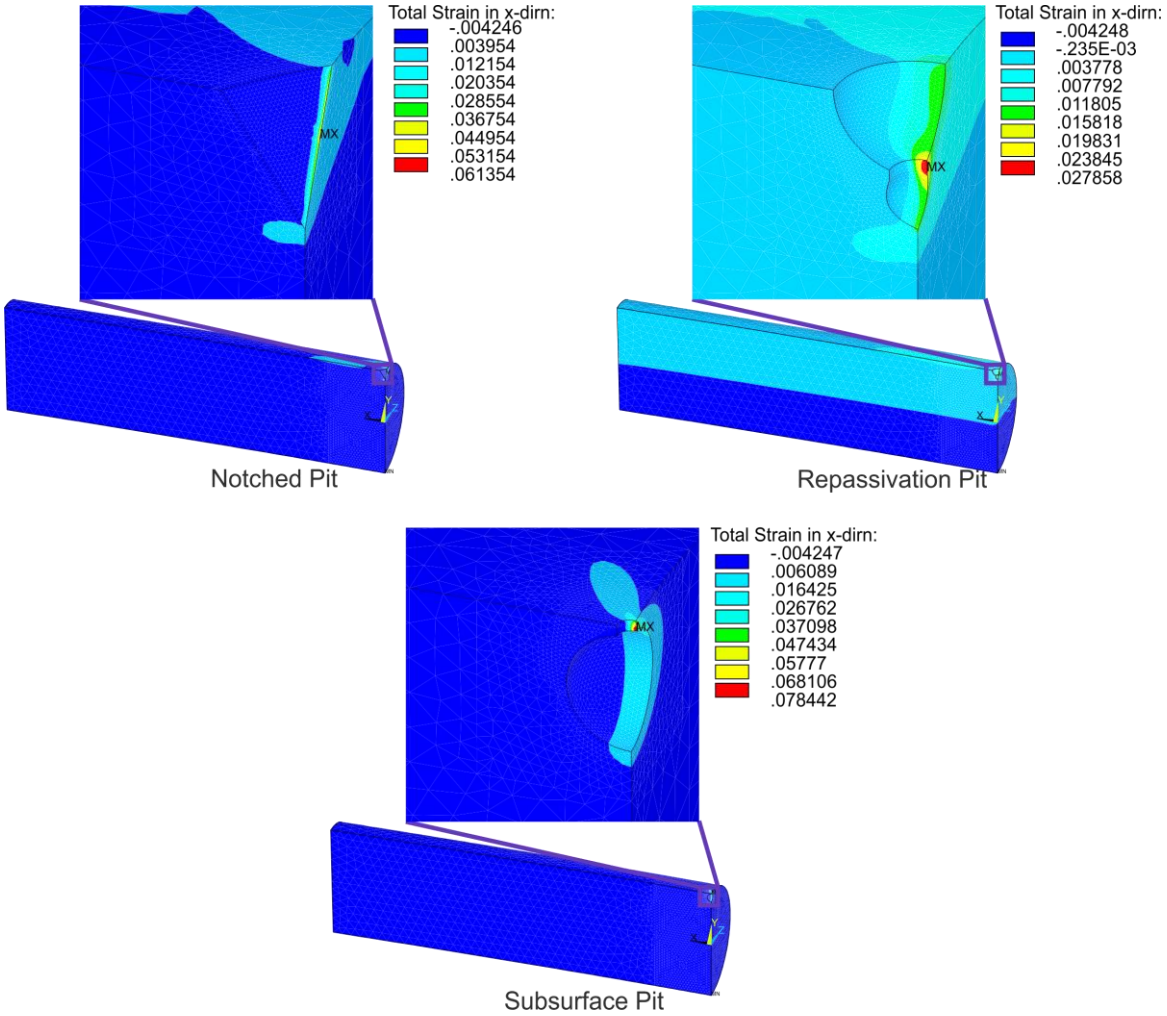

Figure 5.75: 3D HAZ bend submodel with notched, repassivation and subsurface pits total true strain in x-direction results.

3D Bending Structural Analysis for Unpitted Base Material (BM)

The 3D bend BM one quarter model and the gauge length region selected from the 3D bend BM one quarter model, along with their corresponding maximum x-direction stress and total true strain results, can be seen in Figure 5.76 and Figure 5.77. As for the 2D simulations, Figure 5.22, Figure 5.23, Figure 5.29 and Figure 5.30 and the 3D HAZ simulation, Figure 5.69 and Figure 5.70, the location of the max stresses and total true strains in x-direction for the model are in the same location, which is the top surface of the centre region of the gauge length. Table 5.29 shows the displacement values applied to the global model and the resulting maximum stresses and total true strains in x-direction for the 3D bend BM one quarter model.

Table 5.29: Displacement values applied to 3D BM bend one quarter model and resulting total strain and stress results.

Displacement (x) (mm)	Total Strain in x-direction	Stress in X-direction	% Yield
0.539	0.0025	527	68
0.809	0.0038	779	101

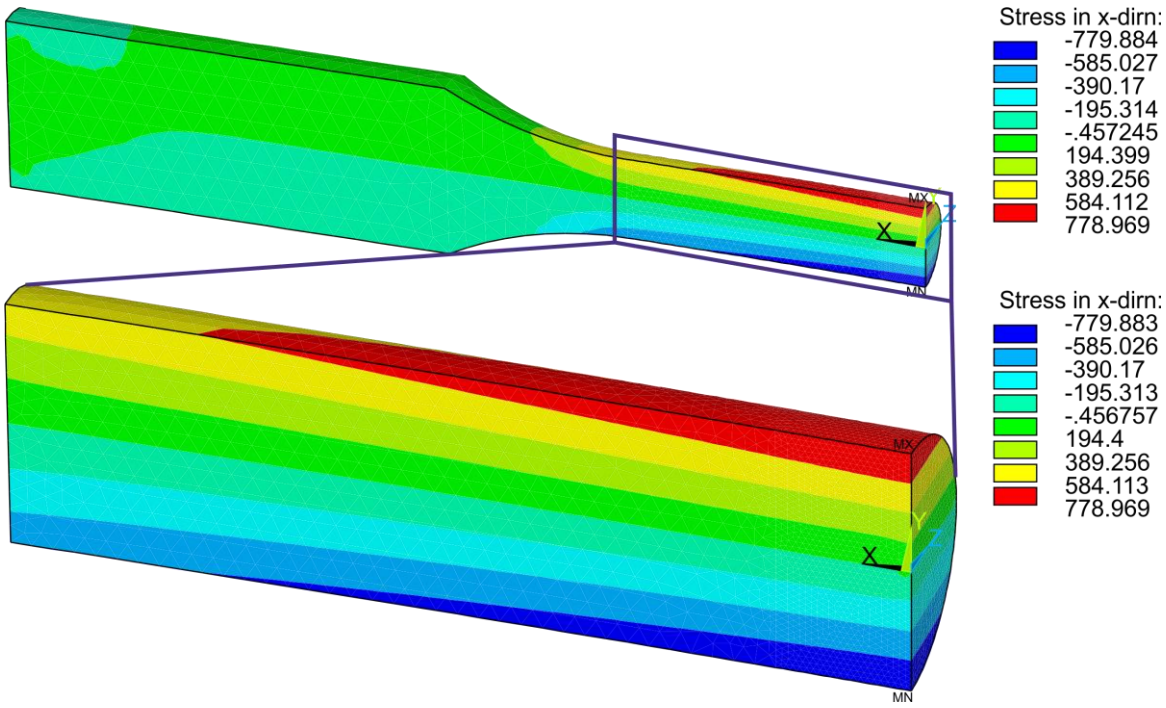

Figure 5.76: One quarter model maximum stress result for 100% of BM yield stress applied as bending displacement load and submodel region shown on the full half specimen.

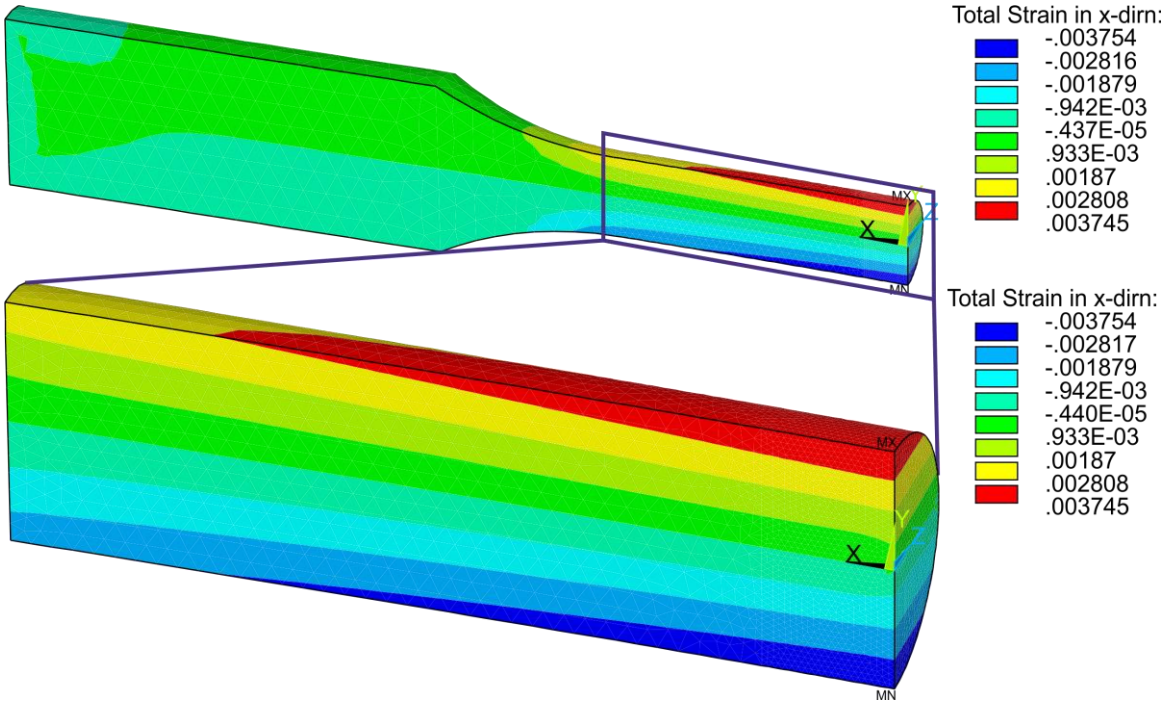

Figure 5.77: One quarter model maximum total strain result for 100% of BM yield stress applied as bending displacement load and submodel region shown on the full half specimen.

The 3D bend BM submodel with the x-, y- and z-displacements from the 3D bend BM one quarter model applied and the corresponding maximum x-direction stress and total true strain results can be seen in Figure 5.78 and Figure 5.79. Table 5.30 shows the global displacement applied to the 3D UA HAZ submodel and the resulting stress and total true strain in the x-direction.

Table 5.30: Displacement values applied to 3D BM bend submodel and resulting total strain and stress results.

Displacement (x) (mm)	Total Strain in x-direction	Stress in X-direction	% Yield
0.096592	0.0025	527	68
0.145311	0.0038	779	101

The location of the maximum x-direction stress and total strain values and their location in the 3D BM bend submodel are the same as the maximum x-direction stress and total strain values for the 3D BM bend submodel region within the 3D BM half model. Therefore, in the subsequent simulations involving a 3D BM quarter model loaded to 100% of yield stress, the 3D BM bend submodel is used as a viable alternative to the 3D BM bend quarter model. The maximum x-direction stress and strain values are increased slightly-

770.457 MPa vs 778.969 MPa and 0.003669 vs 0.003745 for 2D and 3D respectively. This may be due to using plane stress as the element behaviour in 2D modelling instead of the more accurate plane strain. It is again recommended to model in 3D, not 2D for more accuracy.

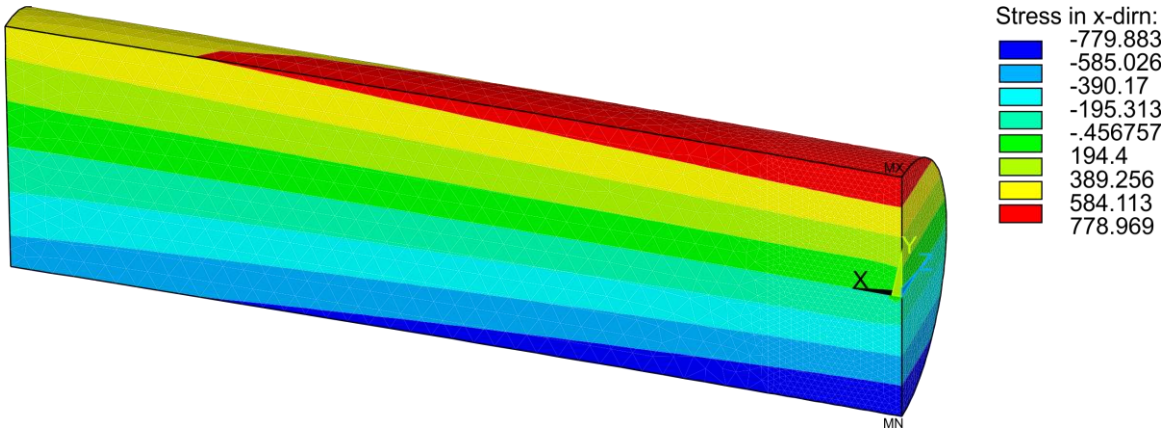

Figure 5.78: Submodel maximum stress result for 100% of yield stress applied as bending displacement load to BM one quarter model.

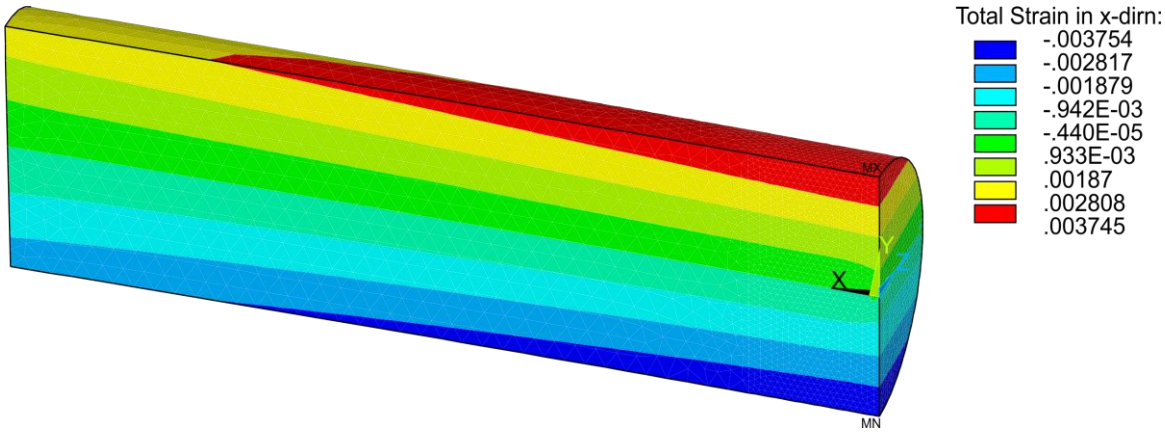

Figure 5.79: Submodel maximum total strain result for 100% of yield stress applied as bending displacement load to BM one quarter model.

3D Bending Structural Analysis for Pitted Base Material (BM)

The maximum total strain in x-direction in the pits in a 3D BM bend submodel of the real specimen are presented in Figure 5.81 and Figure 5.82. These strain values correspond to a 100% yield stress in the 2D unnotched BM specimen with a displacement load applied in the -y-direction. Table 5.31 shows the maximum strains in x-direction for the various pit geometries and have been sorted from lowest to highest. The pit aspect ratio for each pit is also shown.

Table 5.31: Lowest maximum total strain in x-direction to highest for all seven pit geometries in the bending loaded 3D BM bend submodel and the pit aspect ratios.

Pit Geometry	Maximum Total Strain in the x-direction	Pit Aspect Ratio
Shallow Wide	0.008357	0.3
Spherical	0.010993	0.5
Reference	0.011266	0.5
Ellipse	0.014127	0.83
Repassivation	0.024685	0.83
Notched	0.054478	0.83
Subsurface	0.069844	10

The maximum total true strain in x-direction for all pit geometries in the 3D bend BM submodel are presented in Figure 5.80 as a function of time. Similar to the maximum total true strain in x-direction results for the pitted 2D BM quarter model in Figure 5.33, the strains for the pitted geometries do not increase linearly over time, which again may be due to the specimen being loading past the yield point of the material.

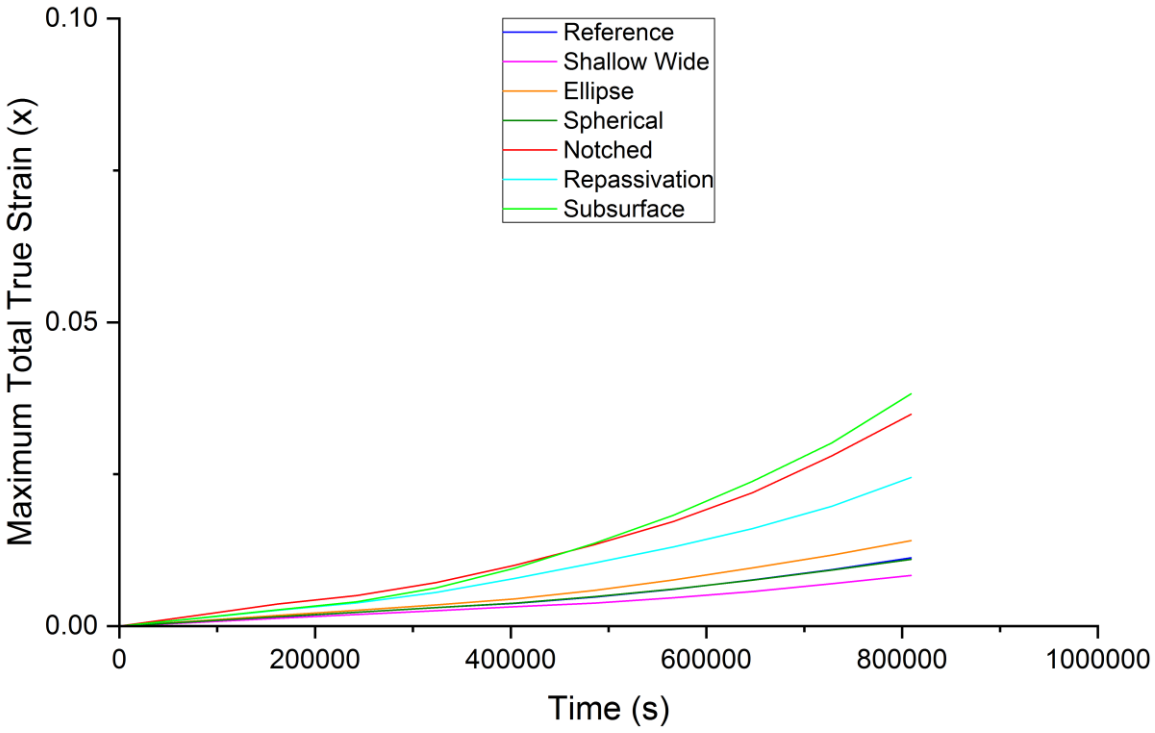

Figure 5.80: Maximum total true strain in x-direction vs time for all pit geometries in the 3D bend HAZ submodel.

Similar to the HAZ values in Table 5.28, Figure 5.81 and Figure 5.82 show that the shallow wide pit has the lowest maximum total strain in x-direction value, 0.008357, with the

subsurface pit having the highest value, 0.069844.The maximum total strain in x-direction values for the BM material are in the same order as for the HAZ. This again shows that for a displacement load applied in the -y-direction the pit mouth diameter is the most important geometric aspect of the pit, with a large pit mouth diameter producing lower maximum total strain in x-direction values in pits.

The locations of the maximum total strains in x-direction are the same as for the 3D UA submodels and the 3D HAZ submodel. This additionally shows that the geometries of the pits, for example sharp edges and vertical regions in the pits, are important in determining the regions of maximum total strains in x-direction.

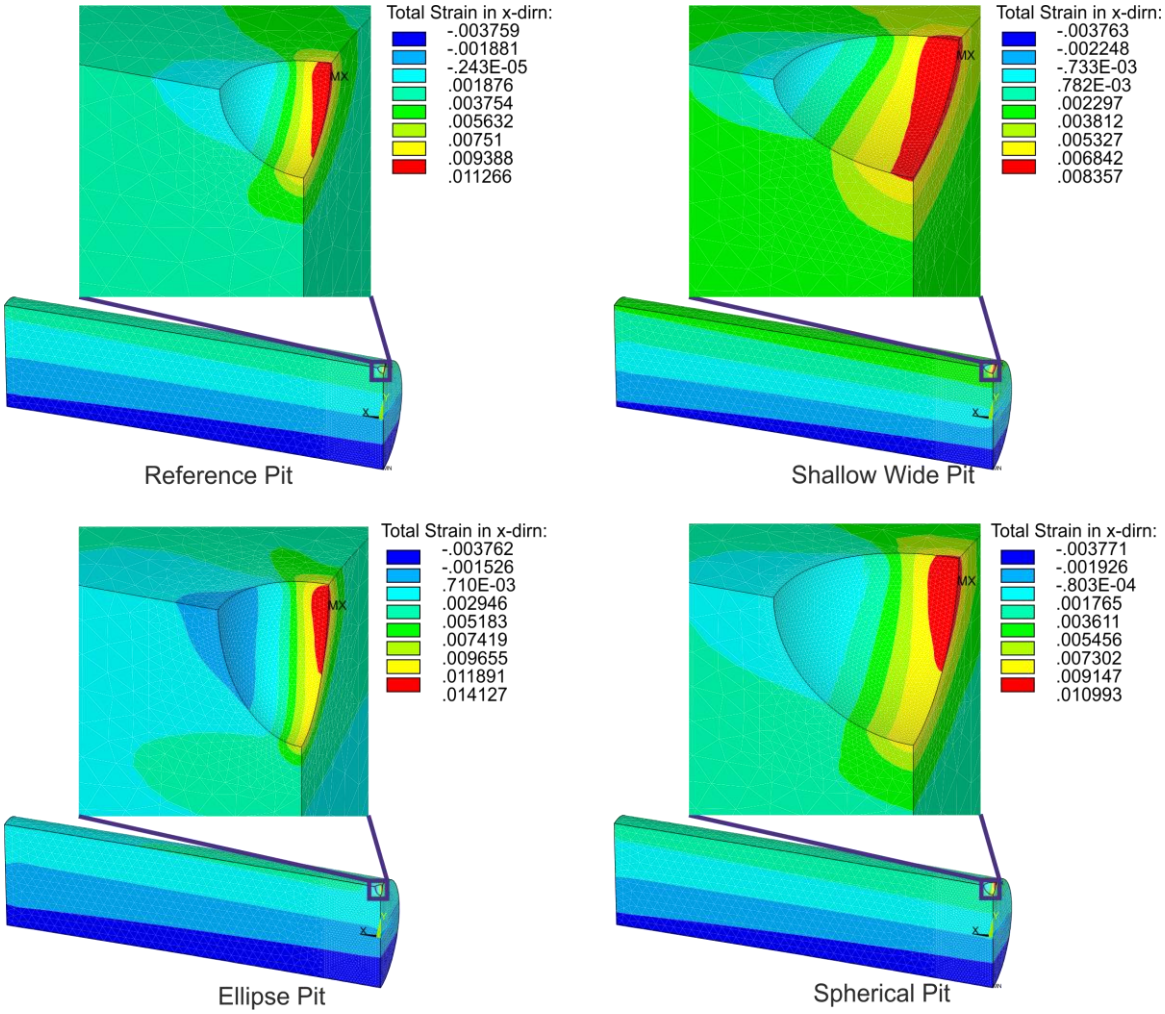

Figure 5.81: 3D BM bend submodel with reference, shallow wide, ellipse and spherical pits total strain in x-direction results.

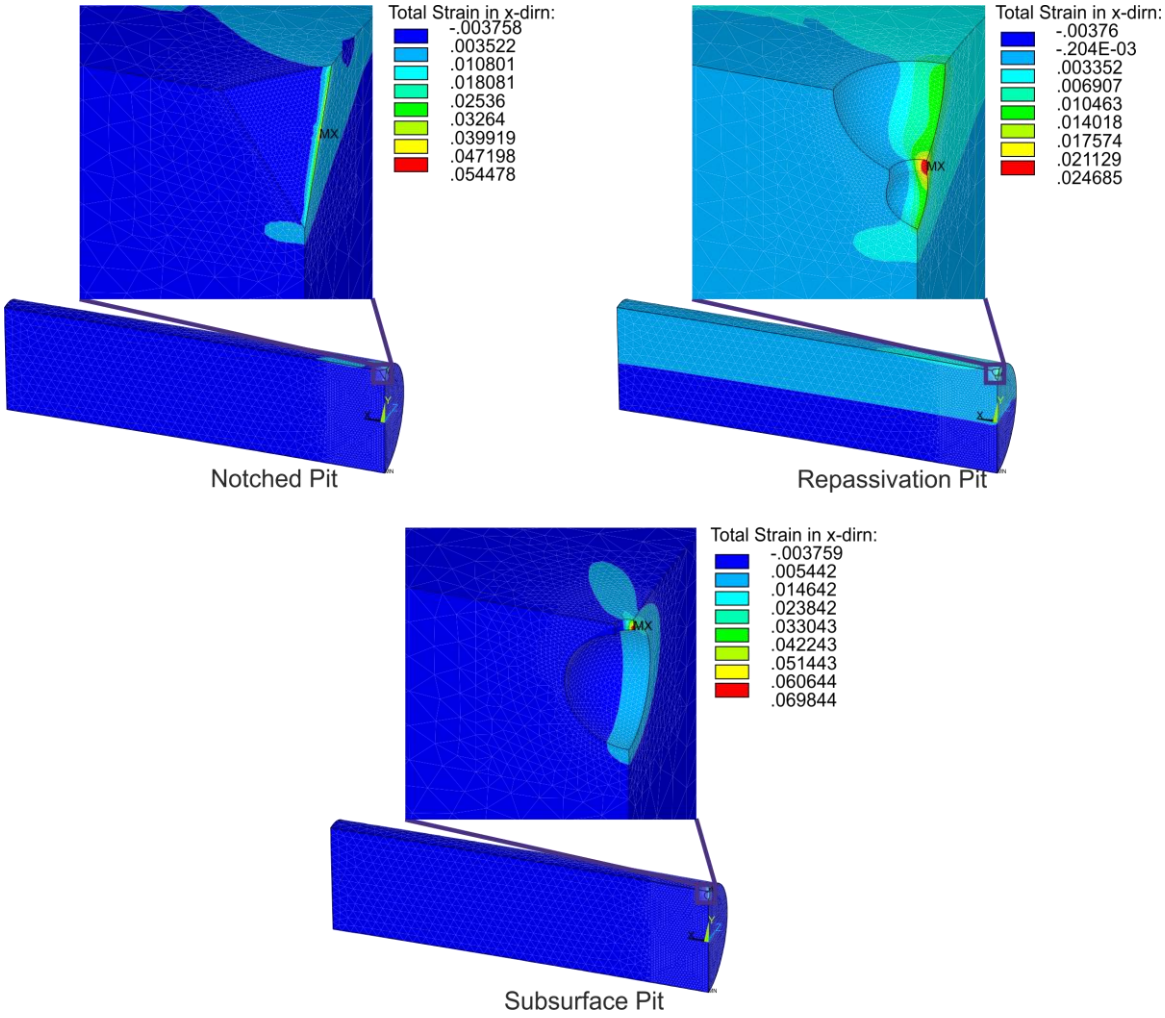

Figure 5.82: 3D BM bend submodel with notched, repassivation and subsurface pits total strain in x-direction results.

This information is also presented in the graph in Figure 5.83. All of the curves for the 3D pits have lower local strains for all corresponding global strain values than for the 2D pits, Figure 5.36, which may again be due to the plane stress element behaviour option. The pit with the highest global vs local strains curve for the 2D HAZ and BM bending models, again the notched pit, is also included in the graphs in Figure 5.83. The curve for the 2D notched pit is significantly higher than the highest curve for the 3D pit, the subsurface pit. Similar to the 2D simulations, time-dependent pit growth is not modelled in this stage of the work.

Figure 5.36 shows that the spherical and reference pits have very similar curves, but the spherical pit geometry has slightly lower local strain values. The shallow wide pit has the lowest local strain values and both shallow wide and spherical pits have the same pit mouth diameter. This shows for bending the most important geometric aspect of the pit is the pit mouth diameter. Using this presumption, the subsurface pit with the lowest pit mouth diameter has the highest local strains for all corresponding global strain values. Figure

5.36 however, shows the notched pit geometry had the highest global vs local strain curve, but Figure 5.83 shows the subsurface pit has the highest local strains for all corresponding global strain values, as also observed for the 3D uniaxial simulations. This may be due to the sharp geometry in the pit mouth region and also the smaller pit mouth radius results in the highest pit aspect ratio for the subsurface pit. Due to the difference in the pit shapes exhibiting the highest local strains in 2D, the notched pit, and in 3D, the subsurface pit, it is recommended that 3D modelling is preferable over 2D modelling. It must also be noted that perhaps the modelling applied by others may be misleading regarding the effects of pit geometry.

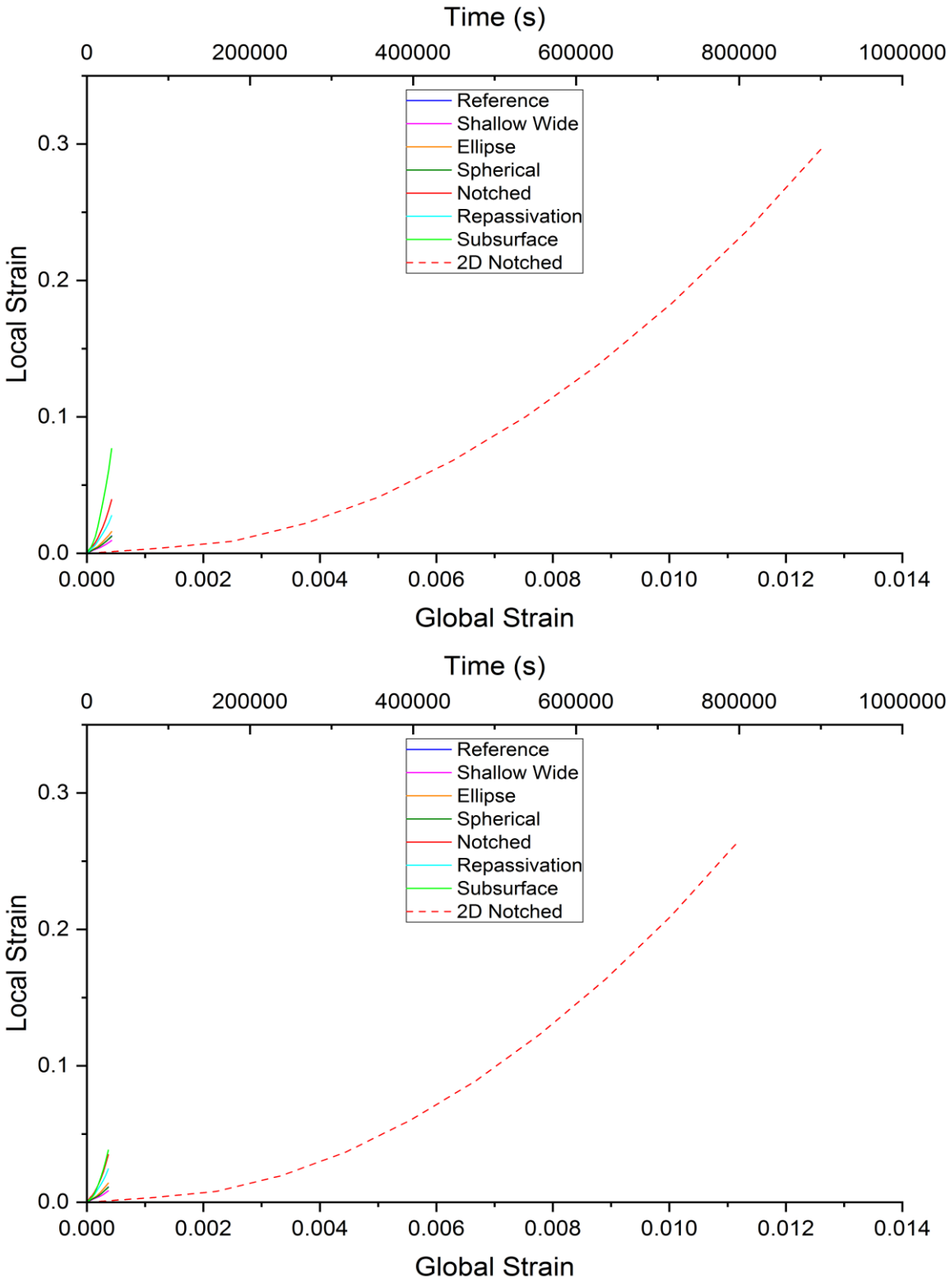

Figure 5.83: Graph of global vs local strains for all pit geometries in the 3D bend HAZ (Top) and BM (Bottom) submodel.

The highest to lowest maximum total true strain in x-direction occurs in the same order for the BM material pits, Table 5.28, as for the HAZ material pits, Table 5.31. Additionally, the location of the highest maximum total true strain in x-direction occurs in the same location

for both the BM material, Figure 5.81 and Figure 5.82, and the HAZ material, Figure 5.74 and Figure 5.75. As noticed already for the uniaxial loading condition, these locations differ to the location of the highest maximum total true strain in x-direction in the 2D models, for both the BM, Figure 5.34 and Figure 5.35 and HAZ materials, Figure 5.27 and Figure 5.28. In the 2D models the location of the highest maximum total true strain in x-direction for all pit geometries was in the bottom of the pit. For the 3D models none of the pit geometries had the location of the highest maximum total true strain in x-direction in the pit bottom. This may again indicate that the 3D models provide a more accurate indication of the regions of the highest maximum total true strain in x-direction and is therefore recommended over 2D modelling.

The results for 66% of the yield stress in the 3D HAZ bend pitted submodel can be seen in Figure A.24 and Figure A.25 in Appendix A. The pit order for the 66% 3D bend pitted submodels, Table A. 14, are the same as for the 100% loaded 3D HAZ bend pitted submodel, Table 5.28. Additionally, the location of the maximum total true strain in the x-direction for the 3D HAZ bend pitted submodel loaded to 66% of yield stress occur in regions similar to Figure 5.74 and Figure 5.75. Similar to the UA models, the subsurface, repassivation and notched pits all have maximum total true strain in the x-direction values located in the same regions in both 100%, Figure 5.74 and Figure 5.75 and 66% models, Figure A.24 and Figure A.25. The remaining pits have maximum total true strain in the x-direction located at the pit side near the pit mouth for 100% yield stress loading condition, but for the 66% model the maximum total true strain in the x-direction are located slightly higher, more towards the pit mouth. This was also found for the 3D uniaxially loaded specimens mentioned earlier. It therefore seems that the location of the maximum total true strain in the x-direction for the 66% loaded specimens for both uniaxial and bending loading conditions, are located more towards the pit mouth region than the 100% loaded specimens. This indicates that the region of the pit, which is most susceptible to HAC, changes with increasing load. As described for the 3D uniaxial loading condition, this is similar to what was discovered by Anantha et al. [271], except this research only applied a uniaxial load with a maximum load of 66%$\sigma_{0.2}$ and discovered the maximum strains in slightly different regions. That research did however observe that the location of the maximum strains varies with increasing load.

Most researchers investigate uniaxial bending conditions only, apart from Nakai et al. [299] who investigated bending loads on circular cone pit geometries, but mainly considered the stresses and the strains were not the priority of this research . Therefore, none of the pit geometries modelled in this contribution have been investigated elsewhere. Nor was literature found which investigates strains in pit geometries subjected to a bending loading

condition. To make the results regarding the pit geometries and location of the strains inside the pits more readily available, such information is summarised in Table 5.32.

Table 5.32: Summary of below findings for bending loads on 3D pitted specimens.

Pit Geometry:	Location of Maximum Strains (100% Yield):	Location of Maximum Strains (66% Yield):
Reference	Side of pit, near pit mouth	Near pit mouth
Shallow Wide	Side of pit, near pit mouth	Near pit mouth
Ellipse	Side of pit, near pit mouth	Near pit mouth
Spherical	Side of pit, near pit mouth	Near pit mouth
Notched	Along pit sides	
Repassivation	Vertical intersection between pits	
Subsurface	Near pit mouth, vertical section	

The results are described in more detail and compared to literature in the following paragraphs.

As mentioned previously for the 2D bending condition, most researchers only investigate the uniaxial loading condition and only few researchers, such as Nakai et al. [299], additionally investigate a bending loading condition. This is due to the material being more vulnerable to the presence of corrosion pits under a uniaxial loading condition than under a bending loading condition. This is highlighted in the results tables for maximum total true strains in x-direction for this work where the uniaxial results for the 3D pit geometries, Table 5.19 and Table 5.23, are much larger than for the bending results, Table 5.28 and Table 5.31. These tables are combined in Table 5.33 to easier compare the maximum total true strain in the x-direction for the various pit geometries, loading condition and materials.

Table 5.33: Maximum total true strain in the x-direction for the various pit geometries, loading condition and materials.

	Maximum total true strain in the x-direction			
	HAZ		BM	
Pit Geometry	**Uniaxial Load**	**Bending Load**	**Uniaxial Load**	**Bending Load**
Reference	0.031112	0.012712	0.027254	0.011266
Shallow Wide	*0.028350*	*0.009431*	*0.024881*	*0.008357*
Ellipse	0.050012	0.015937	0.044170	0.014127
Spherical	0.045219	0.012403	0.039662	0.010993
Notched	0.163195	0.061354	0.143586	0.054478
Repassivation	0.089721	0.027858	0.078978	0.024685
Subsurface	**0.237126**	**0.078442**	**0.209971**	**0.069844**

However, as the pit geometries modelled in this work are pit geometries not commonly modelled by researchers, it was decided to investigate both uniaxial and bending loading conditions. This work also confirms the research by Nakai et al. [299] that the uniaxial bending condition produces higher total maximum strains in x-direction than the bending loading condition, however the location of these highest maximum strains in x-direction vary for the two loading conditions.

To summarise the above findings, the present investigation of the various 3D pit geometries under bending loading shows that, similar to the uniaxial loading condition, the location of highest strains in the pit geometries modelled are <u>not</u> located in the pit bottom for any pit geometry. Therefore, it can be stated that:

- *Similar to the uniaxial loading condition, the local mechanical loads in terms of strains differ largely for the various pit geometries with respect to height, location and direction.*
- *The location of the highest maximum strains in x-direction for the bending loading condition occur more towards the pit mouth than for the uniaxial loading condition. Therefore, if HAC were to occur under a bending loading condition the crack might initiate more toward the pit mouth than further along the pit wall, as for the uniaxial loading condition.*

3D Load Analysis

Next, the effect of the presence of the pits on the overall loading condition was considered. The displacements applied to the unpitted 3D UA models of one eight of the real specimen which resulted in 100% yield stress in the BM and HAZ models are shown in Table 5.34. The same displacement was applied to the pitted specimens and the percentage load taken to reach 100% yield stress in the material, in addition to the corresponding displacement in x-direction, were recorded. These percentage load values and corresponding displacements are shown in Table 5.34, ranked from highest to lowest percentage load.

Table 5.34: Table of displacement percentage values for 3D unpitted and pitted specimens for uniaxial loading condition to 100% of BM and HAZ yield stresses and corresponding displacements.

Pit Geometry:	% Unpitted Load Until 100% YS BM:	BM displacement (mm):	% Unpitted Load Until 100% YS HAZ:	HAZ displacement (mm):
Unpitted:	100	0.044738	100	0.050588
Shallow Wide:	60	0.026834	60	0.030342
Reference:	51	0.022807	51	0.025789
Spherical:	50	0.022360	50	0.025283
Ellipse:	43	0.019228	43	0.021742
Repassivation:	27	0.012072	27	0.013650
Subsurface:	18	0.008047	18	0.009099
Notched:	11	0.004918	11	0.005560

Table 5.34 shows that again the shallow wide pit withstands the largest displacement compared to the other pit geometries and the notched pit withstands the least. All of the pits, except the subsurface pit ,were able to withstand larger percentage loads compared to the 2D models in Table 5.13, 18% vs 27% respectively. For this reason, it is recommended to model the subsurface pit geometry in 3D and not 2D for accurate results.

The shallow wide and reference pits have very similar values in both Table 5.34 and Table 5.13. The 3D simulation is more accurate but there is only a 1% difference between the values in both tables so it may be sufficient to say that both of these pits will fail after the same percentage load is applied for the same loading conditions. In Figure 5.65 the subsurface pit geometry had the region of highest strain of all the pit geometries. However,

Table 5.34 shows that the notched pit geometry will reach 100% yield stress of the unpitted model before the subsurface pit.

The percentage of load applied to the unpitted 3D bend one quarter model which caused failure in the various pitted 3D bend submodels for both BM and HAZ are shown in Table 5.35, ranked from highest to lowest percentage load until failure.

Table 5.35:Table of displacement percentage values for 3D unpitted and pitted specimens for bending loading condition to 100% of BM and HAZ yield stresses and corresponding displacements.

Pit Geometry:	% Unpitted Load Until 100% YS BM:	BM displacement (mm):	% Unpitted Load Until 100% YS HAZ:	HAZ displacement (mm):
Unpitted:	100	0.038969	100	0.043841
Shallow Wide:	58	0.022837	58	0.025725
Reference:	49	0.019336	49	0.021788
Spherical:	48	0.018946	49	0.021788
Ellipse:	42	0.016603	42	0.018712
Repassivation:	28	0.011107	28	0.012524
Subsurface:	17	0.006762	17	0.007627
Notched:	11	0.004382	11	0.004944

The shallow wide pit in a 3D submodel with a bending loading condition applied, can withstand the highest load in comparison to the other pit geometries investigated during this work. Similar to the UA 3D loading results in Table 5.34, the notched pit geometry can withstand the lowest load. This is also evident in the 2D bending load pit geometry order from Table 5.14, where the shallow wide pit can withstand the highest load and the notched pit the lowest. However, similar to Table 5.28, the percentage of load the subsurface pit can withstand has drastically decreased in comparison to the 2D submodel results in Table 5.14. The notched pit also fails at a lower percentage load than the 2D, but this is only a decrease of 1%, 12% to 11%, while the subsurface pit decreases from 33% to 17% which is quite significant. The information in Table 5.34 and Table 5.35 may prove especially useful for NDT operators as they provide information on the reduction in load the presence of a pit causes.

It was observed that the 2D submodels with the pit geometries were able to withstand more load when a uniaxial load in the x-direction was applied, Table 5.13, compared to when a bending load in the -y-direction was applied, Table 5.14. When the submodel and

pits are modelled in 3D however the opposite is the case. Most of the pits can withstand an increase of 1% - 2% load in bending opposed to uniaxially loaded. The exceptions are the repassivation pit which can withstand a 1% greater uniaxially applied load, and the notched pit which withstood the same percentage load for both loading conditions. This is due to the plane represented by the 2D model is not the plane with the maximum total true strain in x-direction results for the model. Therefore, the 2D model does not accurately depict the maximum total true strain in x-direction and to investigate this, a 3D model must be used.

The above findings, the present investigation of the 3D load analysis, can be summarised as follows:

- *Similar to the 2D load analysis, the shallow wide pit is able to withstand the highest loads. However, the notched and subsurface pits can withstand the lowest uniaxial and bending loads.*
- *The information provided in Table 5.34 and Table 5.35, may prove useful to NDT operators for inspection and planning as certain pit geometries have higher total strain in the x-direction values than others and may need additional monitoring. This may include more frequent inspections and the use of NDT.*

These first results are the local mechanical load factor of the HAC triangle from Figure 2.11 and provide an insight into the local strain distribution in the various pits. This is important information as, explained in Chapter 2, it was in the HAZ material where it was found that cracks initiate from pits more frequently than in the BM or WM.

5.2 Diffusion Analysis

This diffusion analysis consists of a hydrogen concentration of $7ml \cdot (100gFe)^{-1}$ which was normalised, from values of 1 to 0, and applied to the various boundary conditions explained in Section 4.3.2 for a duration of 20 days. The normalised concentration value of 1 corresponds to $7ml \cdot (100gFe)^{-1}$, or 100% of the hydrogen concentration is applied with a normalised concentration value of 0 corresponding to 0% applied hydrogen, with the applied hydrogen values varying linearly between these two values. All of these boundary conditions are applied to the shallow wide, ellipse and subsurface pits, with just the varying pit boundary condition applied to all pit geometries. This boundary condition is considered the most accurate to simulate hydrogen uptake in the pit**,** according to Hoffmeister and Böllinghaus [185], and is therefore applied to all pits. This is however an idealised depiction of hydrogen concentration and does not take into account pH drop and oxygen depletion in the pits.

The hydrogen concentration at the A, B and C paths, mentioned previously in Figure 4.29 in section 4.3.2, were recorded after 20 days for all three pits and are presented in Figure 5.85, Figure 5.87, Figure 5.89 and Figure 5.91. The “Y-Coordinate” x-axis applies to the y-coordinate values recorded for points A and B and the “X-Coordinate” x-axis applies to the x-coordinate values recorded for points C. The 0 x- and y-coordinate values for points A and C correspond to the origins of the paths which are located directly at the pit bottom. The 0 y-coordinate value for point B corresponds to the surface of the model. The locations and directions of these paths are indicated using arrows in Figure 5.84. The B node path is at the same location for all pit geometries, whereas both the A and C node paths vary as the origin for these paths is at the pit bottom, so a deeper pit has a shorter A path.

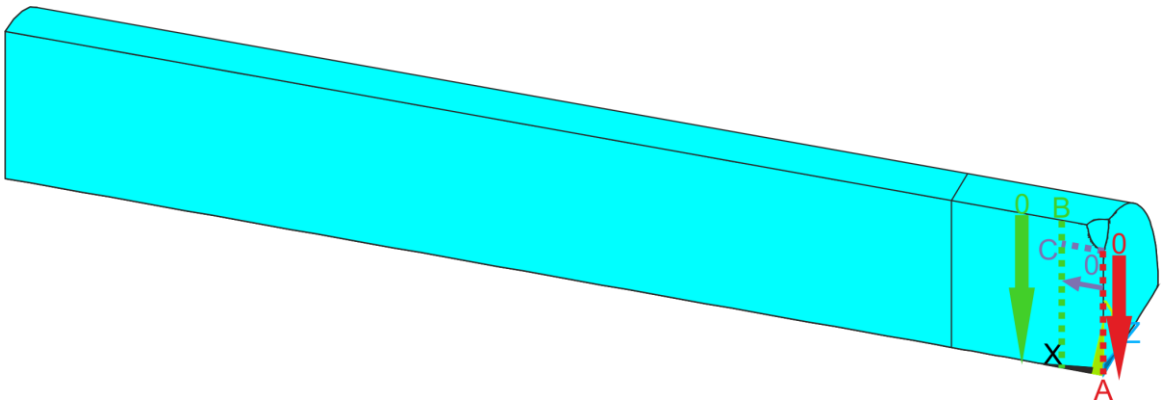

Figure 5.84: A, B and C node paths.

The main aims of this stage of the work are:

- To see the influence the various pit geometries have on the hydrogen diffusion through the 3D HAZ submodel and
- To create an overview of how the hydrogen diffuses through the 3D HAZ submodel without any load applied by recording the hydrogen concentrations at three different locations in the 3D HAZ submodel.

5.2.1 Influence of the Surface Hydrogen Boundary Condition

The first boundary condition investigated was a normalised concentration of hydrogen applied to the surface of the model only. The graph of normalised hydrogen concentration values for the A, B and C node paths for a normalised hydrogen concentration applied to the surface for the shallow wide, ellipse and subsurface models is shown in Figure 5.85.

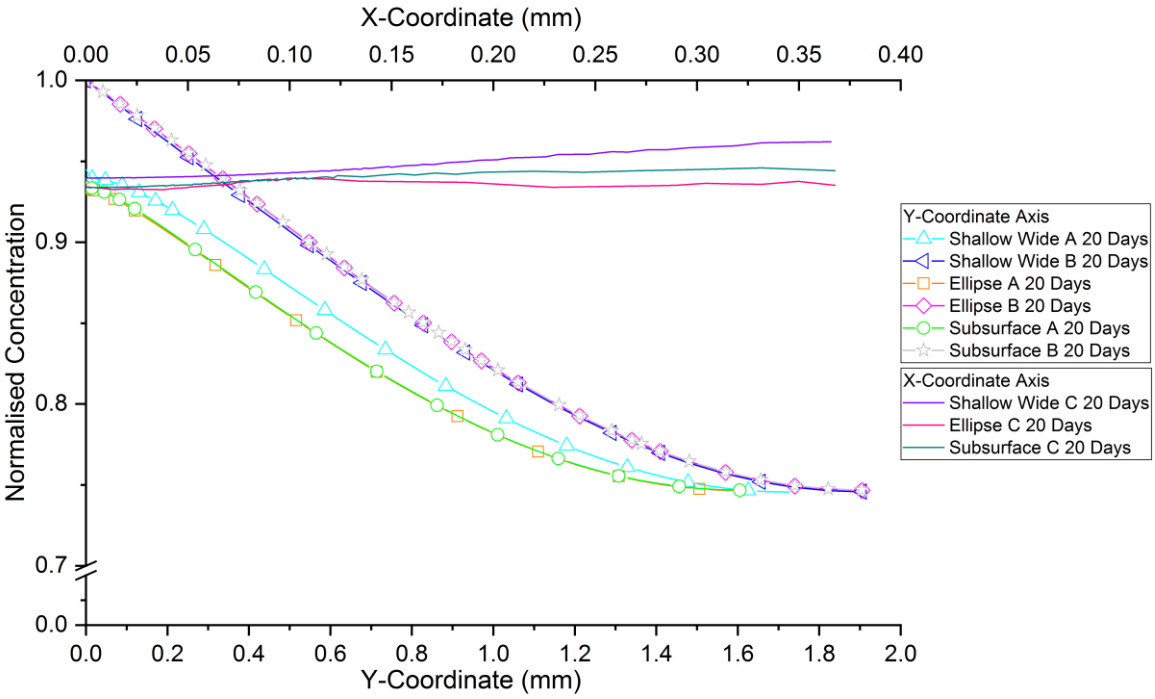

Figure 5.85: Graph of location vs normalised hydrogen concentration for the shallow wide, ellipse and subsurface pits exposed to a normalised hydrogen concentration applied to the surface after 20 days.

The shape of the curves for path A for the three pit geometries in Figure 5.85 begin with a slope less steep than the remainder of the graph. This indicates the region around the pit bottom has a high normalised concentration of hydrogen. The normalised hydrogen concentration values then decrease in curves similar to the curves for path A in Figure 5.89, which shows the influence of the hydrogen applied to the pit in Figure 5.89 is no longer a major influence on the normalised hydrogen concentration recorded by the nodes along path A. Therefore, at a certain depth the normalised hydrogen concentration is the same whether the hydrogen was applied to the surface and the pit or just the surface.

The shape and values for the curves for path B in Figure 5.85 are very similar to the curves for path B in Figure 5.89. This is because the location of the nodes along path B is an appropriate distance away from the pit and at the same location for all three pit geometries. Therefore, the normalised hydrogen concentration applied to the pit for the surface and pit boundary condition should not have any major effect on the normalised hydrogen concentration recorded by the nodes along path B. It is only the normalised hydrogen concentration applied to the surface that is recorded by these nodes for both boundary conditions. Therefore, the nodes for path B curves for the surface and pit and surface boundary conditions are the same.

The curves for path C for the surface boundary condition all have a lower normalised hydrogen concentration in the region directly beneath the pit bottom than further away from the pit. This indicates that the hydrogen has a longer diffusion path in order to diffuse around the pit before being recorded by the nodes at location C, directly beneath the pit bottom. Further away from the pit bottom however, the hydrogen can diffuse straight through the material and for this reason the normalised hydrogen concentration for the curves for path C increase with increasing distance from the pit bottom. This shows the geometry of the pits can have an influence on the distribution of the normalised hydrogen.

The shallow wide pit has less steep pit sides and therefore the curve for path C for the shallow wide pit has the highest normalised hydrogen concentration values of the three curves. This may be due to the proximity of the pit bottom to more nodes along path C, so the hydrogen diffuses to more nodes along path C faster. Path C begins at the pit bottom for all pit geometries so even though the shallow wide pit has the shallowest pit depth, by having path C for all geometries located at the bottom of each pit the geometry will be more of an influencing factor on the curves in in Figure 5.85 than time. The geometries of the ellipse and subsurface pits are also different and Figure 5.85 indicates that the normalised hydrogen concentration for both curves increase with increasing distance from the pit bottom and then begin to the reach an almost constant normalised hydrogen concentration value. The ellipse curve for path C reaches this almost constant value before the subsurface curve for path C as the ellipse pit is less wide and less flat in the bottom region of the pit than the subsurface pit. The nodes further away from the pit bottom for the subsurface pit are influenced by the hydrogen diffusing around the sides of the wider subsurface pit than the same nodes for the less wide and flat ellipse pit. This results in a curve for path C increasing for a greater distance along the x-axis for the subsurface pits than for the ellipse pits.

Figure 5.86 shows the hydrogen distribution from the surface through the three models after 20 days. The final normalised hydrogen distribution is the same for all three different pit geometries but is also very similar to the normalised hydrogen concentration distribution in Figure 5.90 for the surface and pit boundary condition. The initial hydrogen concentration applied is shown in Figure B.6 in Appendix B.

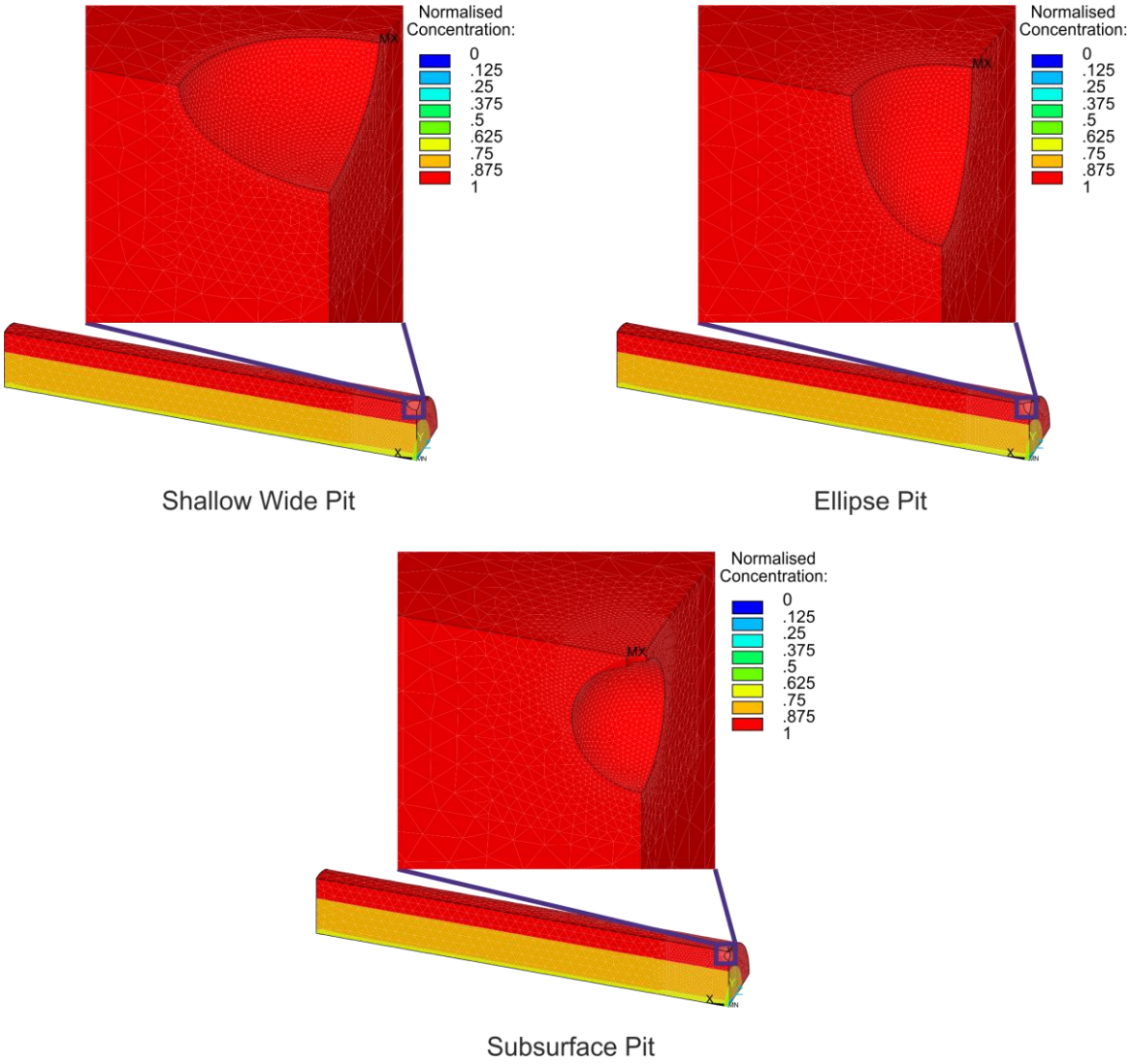

Figure 5.86: Shallow wide, ellipse and subsurface pits normalised hydrogen concentration models exposed to a normalised hydrogen concentration applied to the surface after 20 days.

5.2.2 Influence of the Pit Hydrogen Boundary Condition

A normalised hydrogen concentration was next applied to the pit region only of the shallow wide, ellipse and subsurface pit surfaces for 20 days. The graph for the normalised hydrogen concentration at A, B and C node paths for all three pit geometries is shown in Figure 5.87.

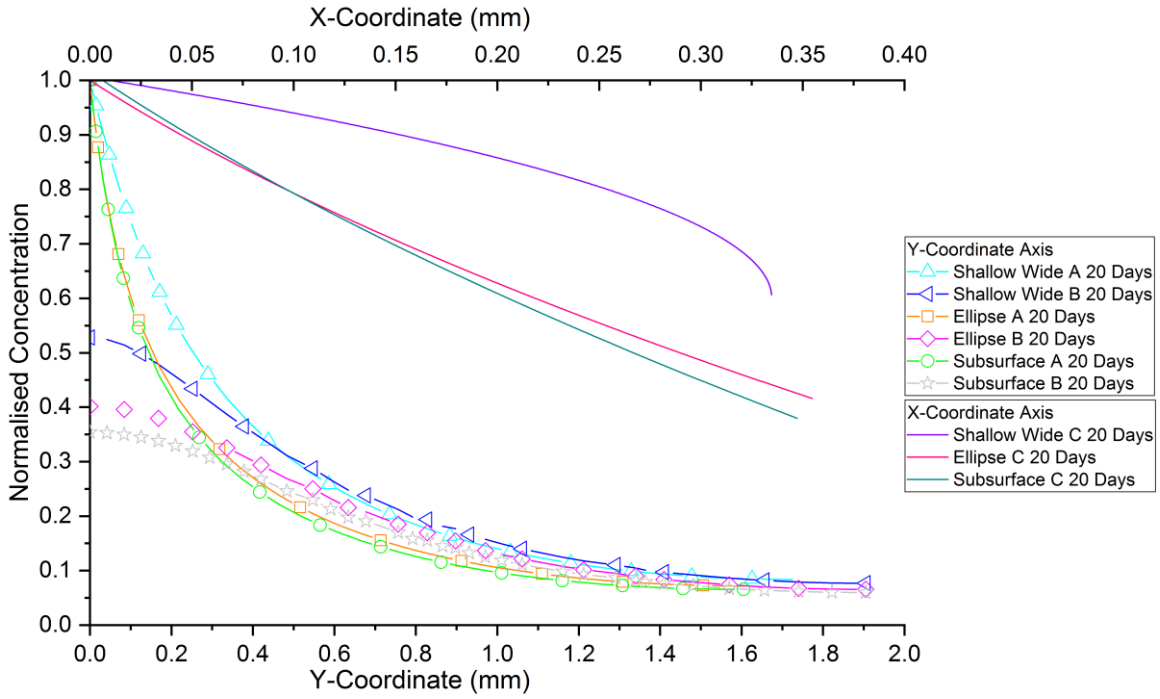

Figure 5.87: Graph of location vs normalised hydrogen concentration for the shallow wide, ellipse and subsurface pits exposed to a normalised hydrogen concentration applied to the pit after 20 days.

It would be assumed that due to the same normalised hydrogen concentration being applied to the three pits with the same diffusion coefficient of the material that the resulting curves would be very similar, as the pit depth is no longer an influence. However, the curves for path A in Figure 5.87 show that the shallow wide pit has much higher hydrogen concentration values for the same distance below the pit bottom than the other two curves. Figure 5.88 also shows that the depth of maximum concentration region for the shallow wide pit is greater than the two other pits. This may again be due to the geometry of the shallow wide pit having a flatter pit bottom region which results in more of the hydrogen applied to the pit bottom to be able to diffuse vertically into the region below the pit bottom, following the geometry of the pit, as also seen in the surface and pit boundary condition. As the shallow wide pit also has a greater surface area than the other two pits in this work, more hydrogen is introduced into the material over time, which causes an increase in the concentration level of hydrogen present at the same distance beneath the shallow wide pit than for the other two pits.

Additionally, the surface and pit and surface boundary conditions show the subsurface and ellipse pits have the same shaped curves for path A. However, for the pit boundary condition, these curves are only the same for the initial section of the graph, but the ellipse curve then has higher hydrogen concentration values from approximately 0.1 mm onwards, Figure 5.87. The opposite would be expected as the flatter, less steep

subsurface pit bottom may facilitate easier hydrogen diffusion in a vertical direction directly below the pit bottom than the steeper ellipse pit. However, Figure 5.88 shows that the hydrogen diffusion from the pit is affected by the geometry of the whole pit and not just the pit bottom, which may explain the slightly higher normalised hydrogen concentration values for the ellipse pit curve for path A than for the subsurface pit curve for path A.

The curves for path B for all three pits follow a similar pattern with a steady decrease in normalised hydrogen concentration, with the shallow wide pit having the steepest curve compared to the ellipse and subsurface pits. The higher initial normalised hydrogen concentration for the shallow wide pit is due to this pit geometry having the largest pit mouth radius of all three pits and this influence is also shown in Figure 5.88. The ellipse pit has the second largest pit mouth radius and has the second highest initial hydrogen concentration value, with the subsurface pit having the lowest initial value. The shallow wide pit also has the steepest slope of all three pits as the hydrogen diffuses parallel to the pit geometry, Figure 5.88, with the ellipse pit having the next steepest slope with the subsurface pit having a slightly less steep slope.

The curve for path C for the shallow wide pit however has the least steep slope of all three curves, but this is also due to the hydrogen diffusion following the geometry of the pits. The normalised hydrogen concentration decreases with increasing distance from the pit and the flatter shallow wide pit bottom geometry results in more nodes along path C being exposed to higher normalised hydrogen concentration values close to the pit bottom. The subsurface pit curve for path C has the steepest curve for path C which is again a combination of the hydrogen following the pit geometry, leading to higher initial normalised hydrogen concentration values than the ellipse pit. However, the normalised hydrogen concentration values for the subsurface pit then fall below the ellipse pit values. This is due to the pit mouth radius which causes more hydrogen to diffuse in the x-direction for the ellipse pit than for the subsurface pit, Figure 5.88.

Figure 5.88 shows the hydrogen distribution from the surface through the three models after 20 days with the initial hydrogen concentration applied shown in Figure B.14 in Appendix B.

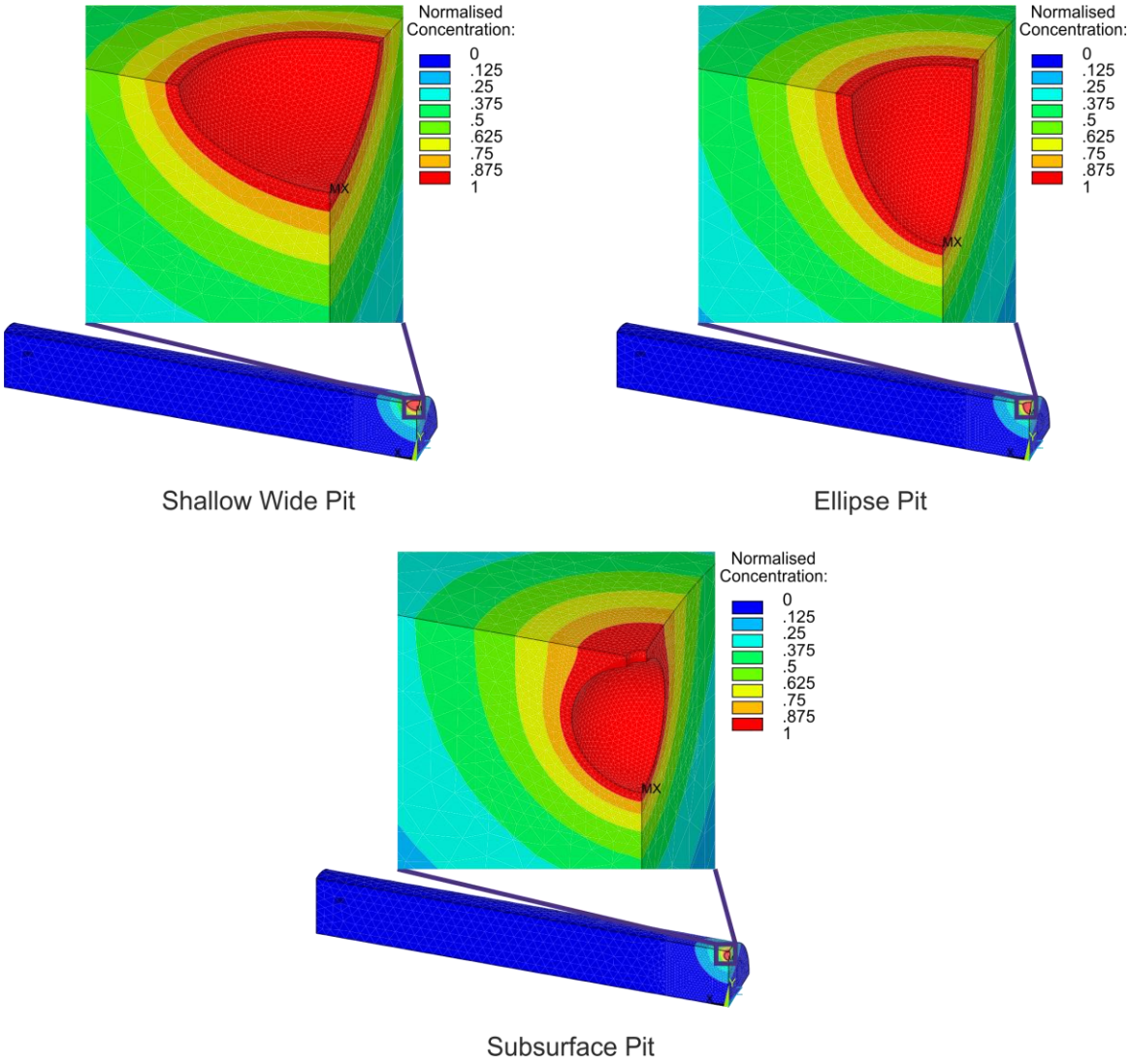

Figure 5.88: Shallow wide, ellipse and subsurface pits normalised hydrogen concentration models exposed to a normalised hydrogen concentration applied to the pit after 20 days.

5.2.3 Influence of the Surface and Pit Hydrogen Boundary Condition

The surface and pit boundary condition was then investigated, with a normalised hydrogen concentration applied to both the surface and the pit. The hydrogen concentration distribution in all three pits after 20 days can be seen in Figure 5.90. The initial hydrogen concentration distribution after one time step can be seen in Appendix B.

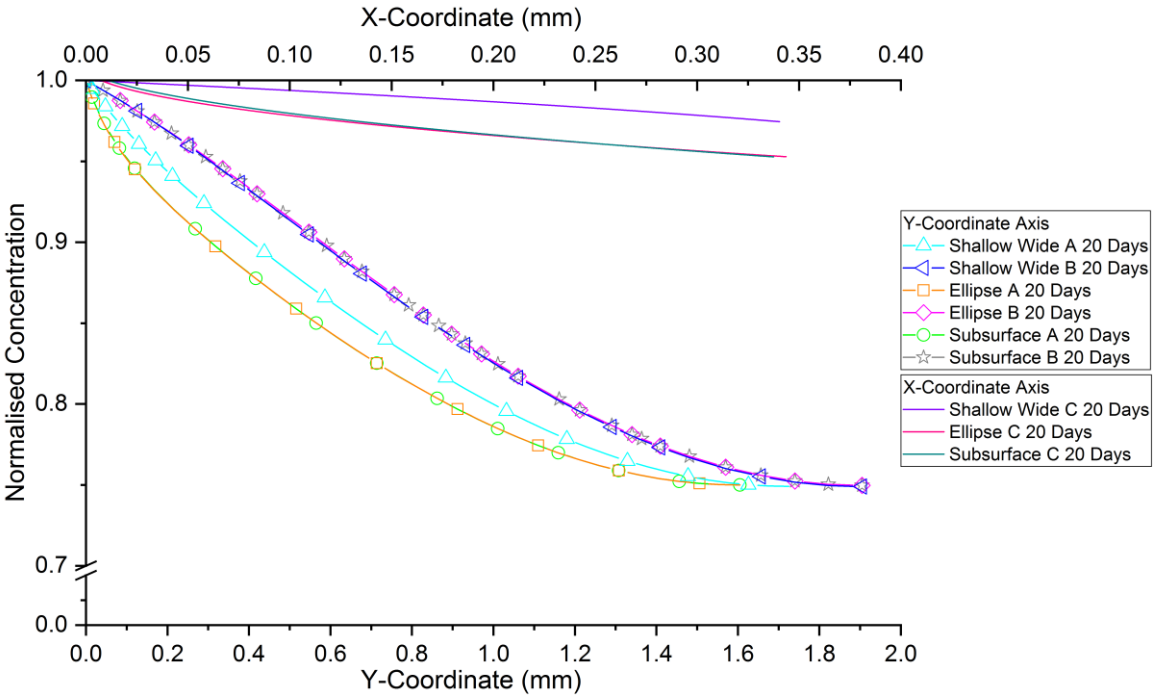

Figure 5.89: Graph of location vs normalised hydrogen concentration for the shallow wide, ellipse and subsurface pits exposed to a normalised hydrogen concentration applied to the surface and pit after 20 days.

Figure 5.89 shows that the hydrogen distribution profiles for both the ellipse and subsurface pits are very similar shapes for all three diffusion paths. This is due to the hydrogen applied to the pit bottom being the predominant hydrogen source recorded by the nodes along path A at the beginning. The hydrogen applied to the surface will be the predominant hydrogen source recorded by these nodes when it has diffused to the same depth as the pit hydrogen source. This is a result of the surface hydrogen diffusing vertically down through the material, whereas the hydrogen applied to the pit follows the same curvature as the pits. As the ellipse and subsurface pits are the same depth, 300 μm, then the nodes in path A will record hydrogen concentration values along exactly the same path and should yield similar results.

The shallow wide pit however has a shallower depth of 180 μm. The beginning of the curve for the nodes along path A for the shallow wide pit should follow the curve for the nodes along path A for the ellipse and subsurface pits, until a certain distance is reached where the hydrogen concentration applied to the shallower pit bottom combines with the hydrogen applied to the surface. However, the hydrogen concentration values for the shallow wide pit at the same distance from the pit bottom as the ellipse and subsurface pits are consistently higher. As the depth of the shallow wide pit is less than for the other two pits, the hydrogen applied to the surface of the specimen will reach the bottom of the pit, and therefore the nodes on path A, before the other two pits, resulting in higher

normalised concentration values recorded for the shallow wide nodes on path A than the ellipse or shallow wide pits.

The curves for the nodes on path B are the same for all three pits as the hydrogen concentration applied to the surface will diffuse through all models at the same rate. The location of the nodes on path B is a sufficient distance away from the pits, so the hydrogen applied to the pits does not reach these nodes on path B before the hydrogen applied to the surface does. Therefore, only the hydrogen concentration applied to the surface is recorded for these locations, which is the same for all three pit geometries.

Figure 5.89 shows that the ellipse and subsurface pit curves for the nodes on path C are very similar, but for the shallow wide curve for the nodes on path C the normalised hydrogen concentration values are higher. The geometries of the ellipse and subsurface pits at the pit bottom are very similar with curved surfaces, ensuring the hydrogen diffusion from the pit sides near the pit bottom for both models will follow similar paths. The hydrogen concentration values at the beginning of the curve for the nodes on path C for the subsurface pit are slightly higher than for the ellipse pit, which may be as a result of the subsurface pit having a slightly “flatter” pit bottom than the ellipse pit. The subsurface pit bottom is therefore located slightly closer to the nodes recording the hydrogen concentration values for the curves for the nodes on path C. However, the shallow wide pit bottom is even “flatter” than the subsurface pit, meaning the subsurface pit bottom is located even closer to the nodes recording the hydrogen concentration values for the curve for nodes on path C. This results in consistently higher normalised hydrogen concentration values for all subsurface nodes on path C. The shallow wide pit is also less deep than the ellipse and subsurface pits, therefore the surface hydrogen will diffuse to the nodes on path C locations before the ellipse or subsurface pits resulting in higher nodes on path C normalised hydrogen concentration values for the shallow wide pit.

Figure 5.90 shows the hydrogen distribution through the three models after 20 days, which is quite similar in the pit region for all three models. The initial hydrogen concentration applied is shown in Figure B.1 in Appendix B.

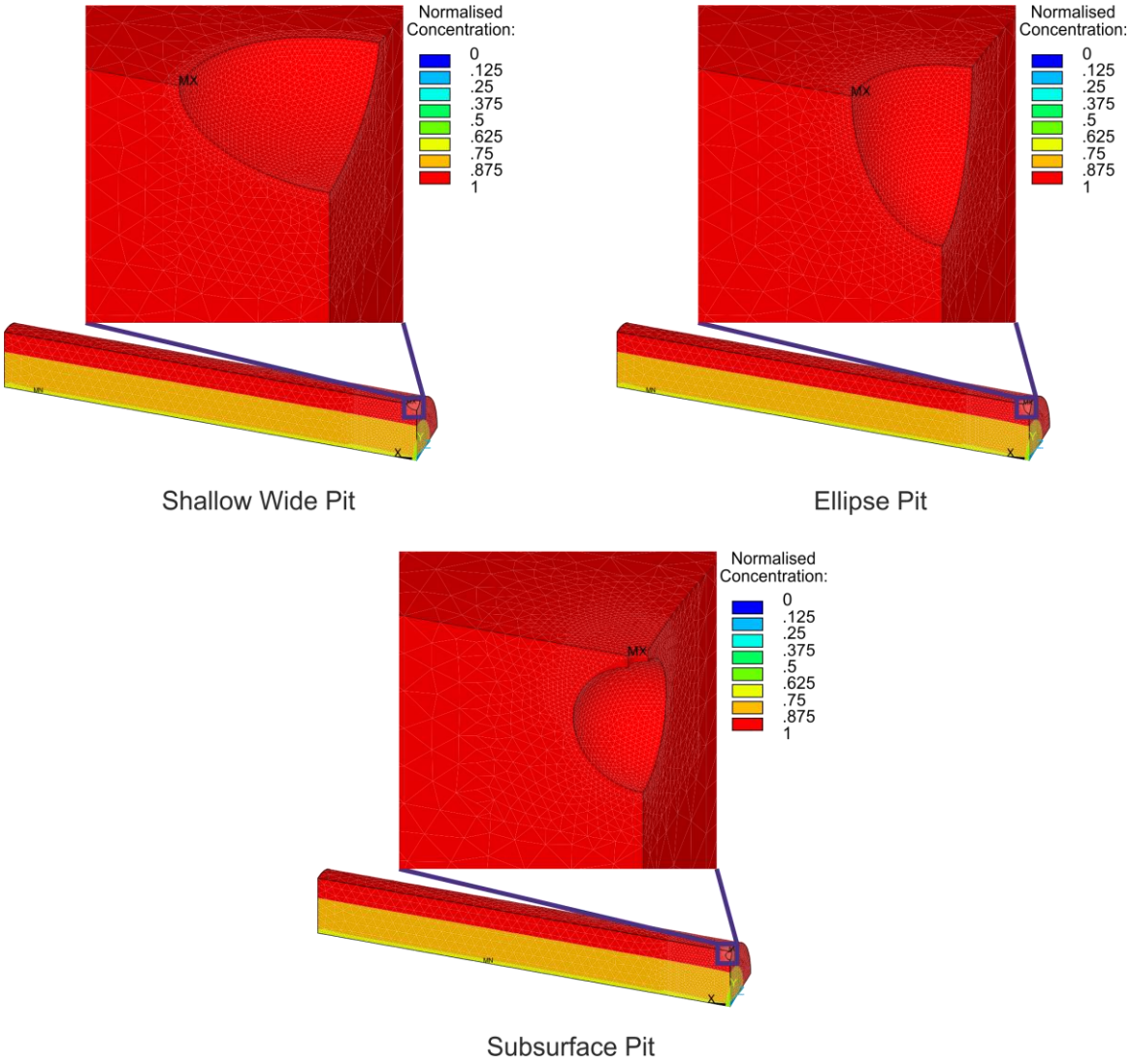

Figure 5.90: Shallow wide, ellipse and subsurface pits normalised hydrogen concentration models exposed to a normalised hydrogen concentration applied to the surface and pit after 20 days.

5.2.4 Influence of the Pit Varying Hydrogen Concentration Boundary Condition

The last boundary condition investigated was the pit varying hydrogen concentration boundary condition, where a normalised concentration of 1 was applied to the centre region of the pit, varying to 0 at the pit mouth and pit bottom. Instead of just the shallow wide, ellipse and subsurface pits, all pits were investigated. As previously explained in Section 4.3.2, Modelling and Meshing of the Models, and Section 5.2, Diffusion Analysis, the varying normalised hydrogen concentration in the pit is considered the most accurate depiction of pitting corrosion, with hydrogen uptake occurring at the middle of the pit, as explained in Section 2.3.2 Controlling Mechanisms of Pit Formation and Growth, Figure 2.27. The simulation used in this work however is an idealised version of hydrogen uptake

in a pit. Therefore, this boundary condition was applied to all seven pit geometries from Figure 4.12 and can be seen in Figure 5.91.

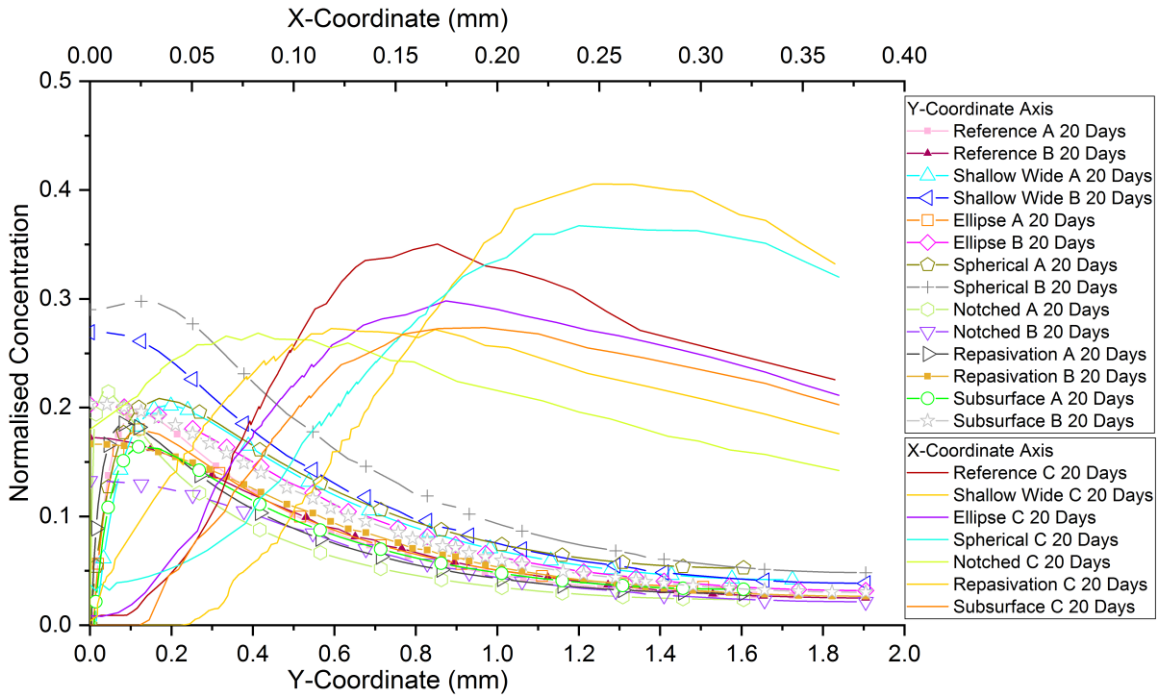

Figure 5.91: Graph of location vs normalised hydrogen concentration for all pits exposed to a varying normalised hydrogen concentration applied to the pit after 20 days.

The A, B and C curves in Figure 5.91 follow the same path for all different pit geometries. The highest values for all curves for paths A, B and C are for the shallow wide and spherical pits, with the notched and repassivation values having the lowest values for all curves. This may be due to the spherical and shallow wide pit geometries are the two pits with the largest regions for a normalised hydrogen concentration of 1, due to the large radius of the pit mouth, Figure 5.92. This creates the longest diffusion path for hydrogen to the be transported to reach certain regions. The notched and repassivation pits in contrast have very narrow regions for a normalised hydrogen concentration of 1 through the model in the z-direction, Figure 5.92 and Figure 5.93, and this may explain the low normalised hydrogen concentration values at all of the nodes for paths A, B and C locations.

Figure 5.92 and Figure 5.93 show the hydrogen distribution after 20 days with the initial varying hydrogen concentration applied to all pits shown in Figure B.20 and B.21 in Appendix B.

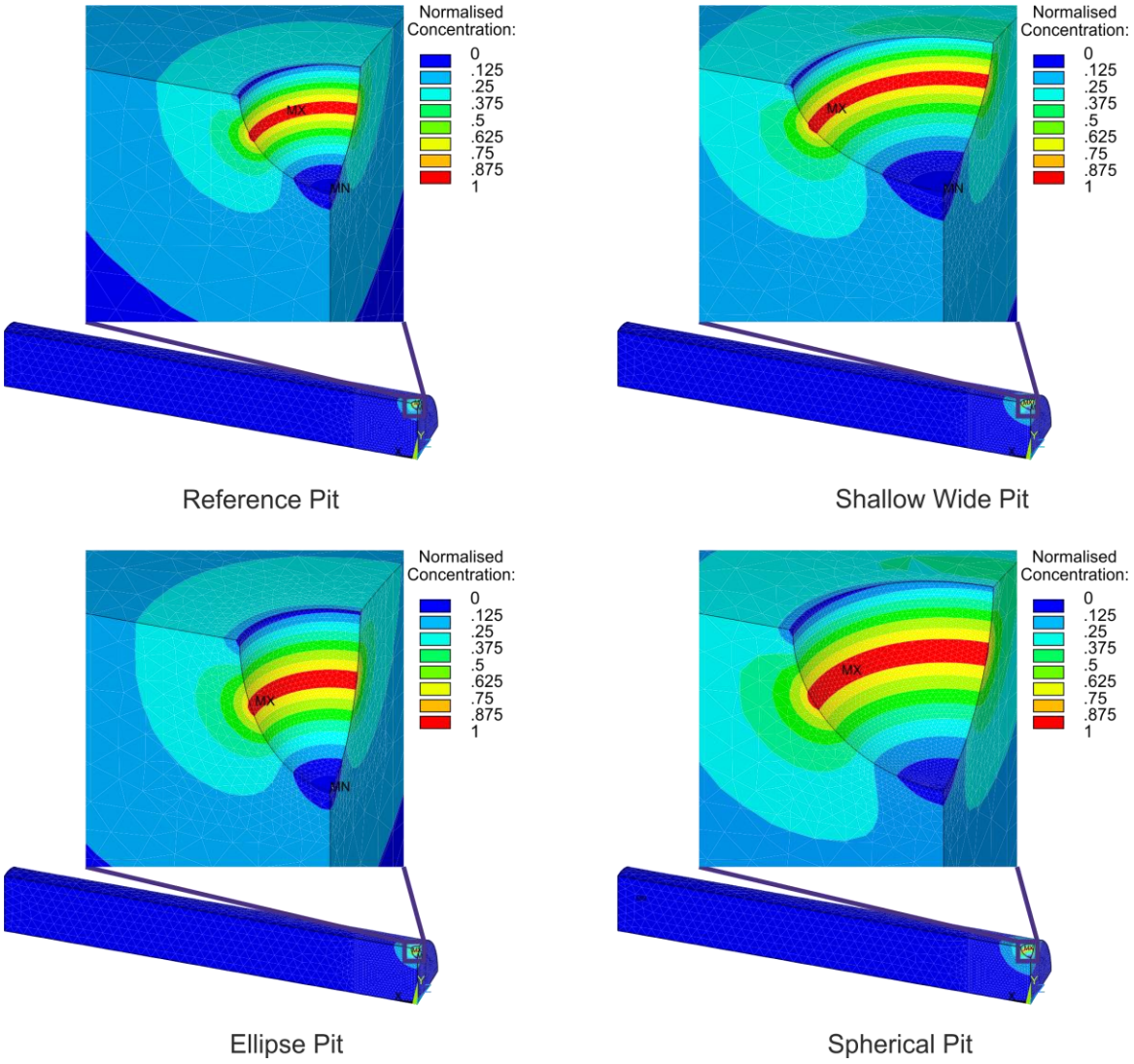

Figure 5.92: Reference, shallow wide, ellipse and spherical pit geometries exposed to a varying normalised hydrogen concentration after 20 days.

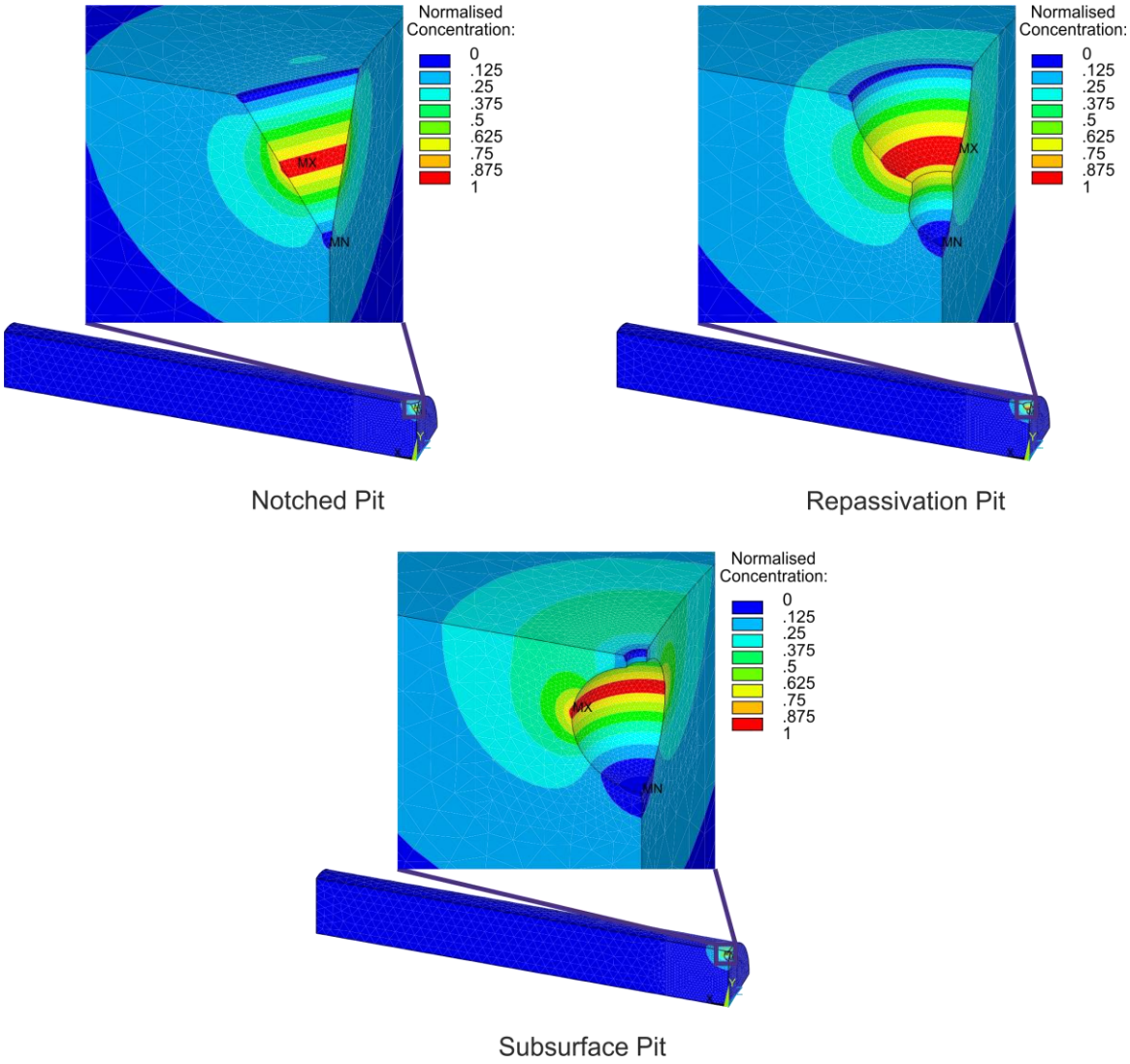

Figure 5.93: Notched, repassivation and subsurface pit geometries exposed to a varying normalised hydrogen concentration after 20 days.

Most researchers consider the diffusion of hydrogen through an unpitted specimen or in a pre-cracked specimen. However, very few investigate the diffusion of hydrogen through a specimen with a pit or a notch present. Additionally, most researchers also investigate loaded conditions as HAC is an accumulation of local hydrogen concentration and the local mechanical load, which in this work corresponds to the regions of highest strains. However, the diffusion of the hydrogen through an unloaded specimen with the various pit geometries present gives an overview of the hydrogen diffusion paths for each pit geometry for the various boundary conditions. As seen in Section 5.1.2, the location of the highest strained region changes with the varying pit geometries. Therefore, the diffusion of the hydrogen through a specimen with the various pit geometries present gives an overview of the hydrogen concentration that may be present in the region of highest strains

for each pit geometry for the various boundary conditions. This information may be combined in order to prevent HAC and is discussed in Section 5.3.

Some researchers, such as Capelle et al. [300, 301] however, do investigate the affect the presence of a notch has on the hydrogen present in an unloaded specimen. The hydrogen influence on pipeline metals API X52, X70 and X100, was investigated by Capelle et al. [300, 301]. It was discovered for the API X52 [300] material using a hydrogen discharging process, that the efficiency of the hydrogen permeation in the notched metal is low and depends on the time of exposure. However, when this metal is loaded during fracture tests of a notched section of the pipeline material, it was discovered that the hydrogen charging of the material was significantly increased. It was noted that the difference between the hydrogen concentrations in stressed metal can exceed more than five times the hydrogen concentration in unloaded metal. The notch was a 45^{o} V shaped notch with a notch radius at the bottom of 0.15 mm, located on the outside of the pipeline. This penetration was found to change the mechanism of local fracture at the notch. It was also found that the radius of the notch tip, in combination with the hydrogen concentration, affects the local elasoplastic zone at the notch tip where hydrogen tends to accumulate and where cracks might initiate. In comparing the API X52, X70 and X100 materials [301] it was found that the resistance to hydrogen absorption was highest for the X100 steel and decreased with decreasing strength of steel. This may be due to dislocations are more pinned by precipitates which are introduced to achieve the high strength.

In the work presented in this thesis different pit geometries were investigated and the simulated hydrogen distribution path was found to vary for the different pit geometries. This was found to be influenced by the whole pit geometry and not just the notch tip radius, as mentioned by Capelle et al. [300, 301]. However, the material investigated in this work is SMSS and Capelle et al. investigated API X52 (a ferrite-bainite microstructure), X70 (a polygonal ferrite microstructure with small martensitic- austenitic particles at grain boundaries) and X100 (a ferritic-bainitic microstructure).

From the present state of hydrogen distribution analyses in the vicinity of the various pit geometries, it can be summarised that:

- *The geometries of the pits have an influence on the hydrogen distribution for all boundary conditions investigated.*
- *The shallow wide pit consistently experiences the highest normalised hydrogen concentration on all node locations in comparison to the ellipse and subsurface pits, for both the surface and surface and pit boundary conditions, due to shorter diffusion paths to the pit bottom. This may be a modelling artefact, but it may also*

indicate that shallower pits are more susceptible to hydrogen uptake and initiation of HASCC. This, however, is outside the scope of this contribution.

- *At a certain depth, the normalised hydrogen concentration is the same whether the hydrogen was applied to the surface and the pit or just the surface, due to the hydrogen diffusing from the surface combining with the hydrogen applied to the pit. This is still time dependent and as the shallow wide pit is the least deep pit, this combination will occur before the other two pits, resulting in higher normalised hydrogen concentration values at a depth equal to or greater than the pit depth.*
- *As the same normalised and varying hydrogen concentration values were applied to all pit geometries, it was expected to see a similar diffusion path in all three pits, as the depth of the pit is no longer an influence on the resulting hydrogen diffusion path. It was found that the geometry of the whole pit, and not just the bottom of the pit, affected the distribution path of hydrogen through the material.*

The results presented in this section provide the information for the local hydrogen concentration factor of the HAC triangle from Figure 2.11. These results show how a normalised concentration of hydrogen diffuses through the material when several different boundary conditions and pit geometries are investigated. As discovered in Section 5.1, the regions in the pits where the highest maximum total true strains in x-direction are located are near the pit mouth. Therefore, the application of a normalised hydrogen concentration in this vicinity, as applied in all boundary conditions in this work, may cause HAC.

5.3 Combined Structural and Diffusion Analysis

5.3.1 Approach to Modelling of HAC Initiated in Idealised Pit Geometries

For seven idealised pit geometries, the local mechanical load factor has been investigated in Section 5.1 and the local hydrogen concentration factor has been investigated in Section 5.2. Therefore, the final part of this work is to combine these two key factors affecting HAC in order to get an indication of the location where HASCC might be initiated. This can then be achieved for a given microstructure, as for instance the HAZ microstructure being homogenous in a SSRT specimen, which completes the HAC triangle from Figure 2.11. The simulation of the altering compliance mechanically and with respect to hydrogen absorption and diffusion has to be left to future studies. As previously mentioned in Section 4.3.3, and similar to Section 5.2, only three pit geometries, the shallow wide, ellipse and subsurface, were investigated in this part of the work. These are considered to contain the least, average and highest maximum total true strain in x-direction values for all the pit geometries investigated in this work, as this is an engineering approach. The various remaining pit geometries may be investigated in future work.

The final stage of this contribution involved combining the findings from the previous two stages in order to model pit initiation, idealised pit growth and hydrogen uptake in the pits. It has to be emphasised that this is meant as an engineering approach towards future directions of the pitting – HASCC transition modelling. For instance, the increasing acidification and increasing hydrogen production during pitting have not yet been included into such modelling and has, as mentioned, to be incorporated perhaps at a later stage.

Crack propagation has not been considered in the models developed in this work. However, the regions where crack initiation is most likely to occur have been identified. Also, first approaches have been undertaken to define the time of such crack intuition by applying the respective critical hydrogen concentration resulting from the time-dependent and continuously increasing local strain and comparing this to the simulated actual hydrogen concentrations. In other words, the time and location of potential crack initiation inside the respective pits can be determined, if the local hydrogen concentration exceeds the critical hydrogen concentration, dependent on the actual local strain.

Further margins of such an engineering approach are explained in the following points:

- As the homogenous local microstructure of all models and as the most prone region for pitting corrosion and subsequent HASCC, the HAZ microstructure of a specific SMSS has been taken, i.e. taking the above mechanical and hydrogen diffusion

properties. In contrary to this, real welds would have various microstructures with different mechanical compliances, as well as solubilities and diffusion abilities.

- To model an approximation of pit growth using a combination of volumes and element kill commands for the shallow wide, ellipse and subsurface pits. For the various pit geometries, some stages of pit growth with the corresponding total strain in x-direction and normalised hydrogen concentrations are shown.
- The effect of different strain rates on the local strain and normalised hydrogen concentration is also investigated in this work. Lower strain rates entail that hydrogen diffuses deeper into the material, as diffusion is time based. Therefore, if HAC does occur, the local hydrogen concentration reaches the critical hydrogen concentration value so crack propagation can occur without requiring any additional hydrogen to diffuse to the regions in front of the crack tip. For high strain rates hydrogen does not have sufficient time to diffuse into the material or to the crack tip so the critical hydrogen concentration has not been reached at the crack tip. Therefore, the total strain in x-direction, or local strain, is also presented as a curve in Figure 5.104, Figure 5.115 and Figure 5.126, for the three different pit geometries and three strain rates investigated. These graphs show how the local strain increases with increasing time for all strain rates, with the strain rate of $1x10^{-5}$ having the highest gradient or steepest slope. The critical hydrogen concentration for each strain rate was also calculated using Viyanit [16] Equation (3.2) in Section 3.2 to determine the critical hydrogen concentration for each strain rate.
- To assume a varied normalised hydrogen concentration profile in the pits, as this probably occurs during pitting due to separation of the cathodic reactions and the anodic metal dissolution at the pit tip.
- In order to determine the critical locations for potential HAC initiation, the critical hydrogen concentration dependent on the localised strain in the pits is calculated. The critical hydrogen concentration for each stage when hydrogen is applied to the pit is also shown, using Equation (3.2) from Section 3.2. From these graphs the critical hydrogen concentration for the corresponding local strain and pit geometry can be determined. Therefore, the critical hydrogen concentration needed in order for HAC to be initiated in these pits under the loading conditions investigated in this research are known.
- To try to assign such conditions to the time and to deduce a preliminary time to failure of such specimens, in terms of crack initiation, by achieving such critical conditions.

The results for this final stage of this work will now be explained for the shallow wide pit, the ellipse pit and finally the subsurface pit geometries.

5.3.2 Shallow Wide Pit

The shallow wide pit has the location of the highest maximum total true strain in x-direction at the pit mouth for the first and second pits but then the location of the highest maximum total true strain in x-direction moves to the pit bottom, Figure 5.94 to Figure 5.98. The normalised hydrogen concentration profiles for the various pit stages for the shallow wide pit are shown in Figure 5.99 to Figure 5.103. As previously mentioned in Section 4.3.3, for each strain rate applied the model was loaded in the x-direction until 0.1% of the yield stress was reached. The total time assumed for the pit to grow to the final pit depth was 9000 seconds and this model was designed with five different pit sizes, so the time taken for each pit to grow is 1800 seconds.

As the location of the highest normalised hydrogen concentration is located across the middle of the pits, the shallower the pit the closer the highest normalised hydrogen concentration is located towards the pit mouth. For the shallow wide pit, the interaction of the maximum local strain in x-direction and the highest normalised hydrogen concentration may result in HAC for pit 2, Figure 5.95 and Figure 5.100, as both of these regions are located close to the pit mouth. However, for pit 3, Figure 5.96 and Figure 5.101, the highest maximum total strain in x-direction is located directly at the pit bottom, which is located further from the location of the highest normalised hydrogen concentration than if the highest maximum total strain in x-direction were to be located near the pit mouth. The value of the highest maximum total strain in x-direction for pit 3 however, is larger than for pit 2 so even in the presence of a lower normalised hydrogen concentration HAC may still occur.

The total true strain in x-direction, or local strain, is also presented as a graph in Figure 5.104, for the three different strain rates investigated. This graph shows how the local strain increases with increasing time for all strain rates, with the strain rate of $1x10^{-5}$ having the highest gradient or steepest slope. The critical hydrogen concentration for each stage when hydrogen is applied to the pit is also shown, using Equation (3.2) from Section 3.2. From this graph the critical hydrogen concentration for the corresponding local strain for the shallow wide pit can be determined. Therefore, the critical hydrogen concentration needed in order for HAC to be initiated in the shallow wide pit under the loading conditions investigated in this work are known. This knowledge can determine the minimum allowable hydrogen concentration which may be present without the possibility of HAC occurring.

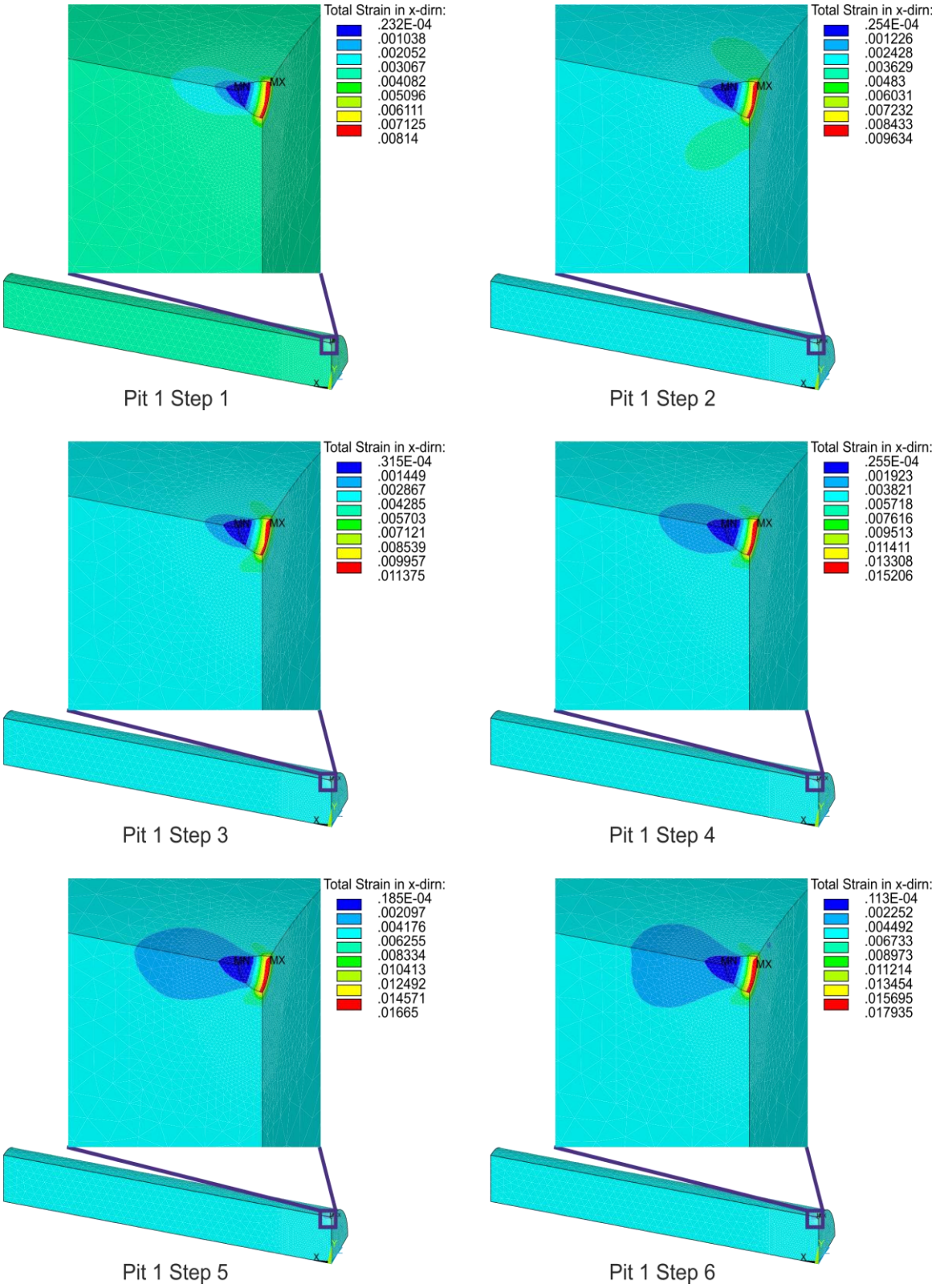

Figure 5.94: Total true strain in x-direction for shallow wide pit 1.

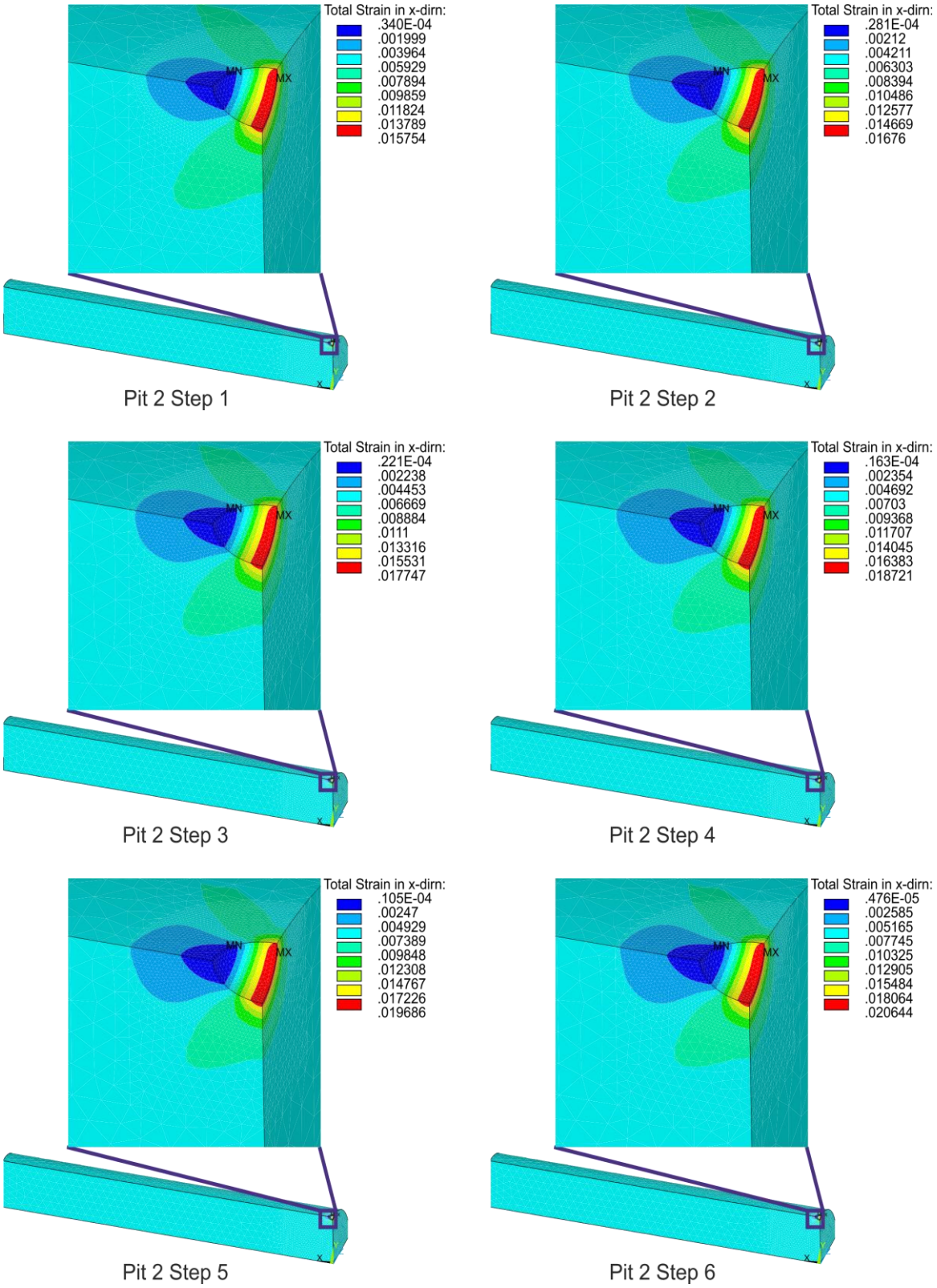

Figure 5.95: Total true strain in x-direction for shallow wide pit 2.

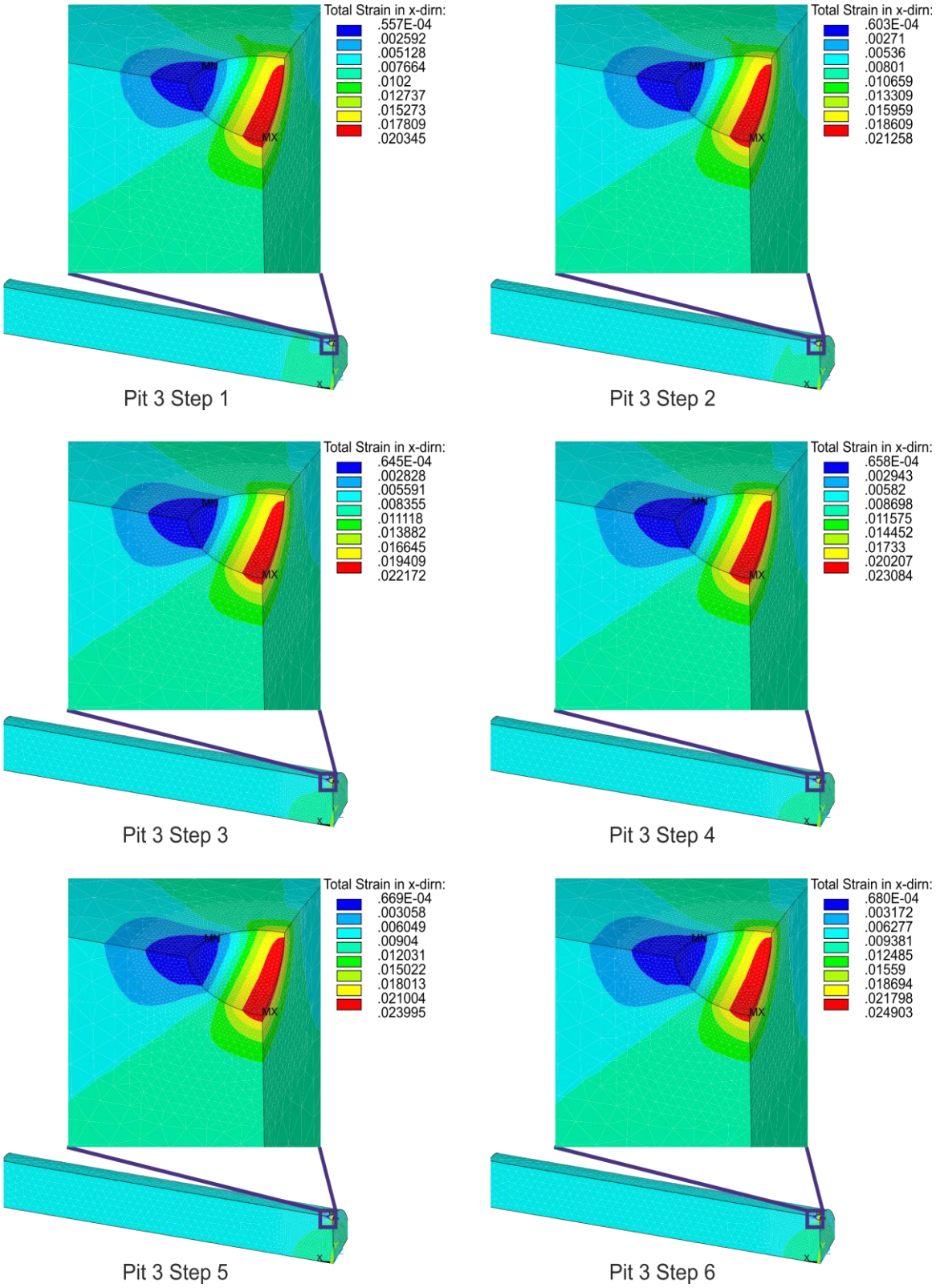

Figure 5.96: Total true strain in x-direction for shallow wide pit 3.

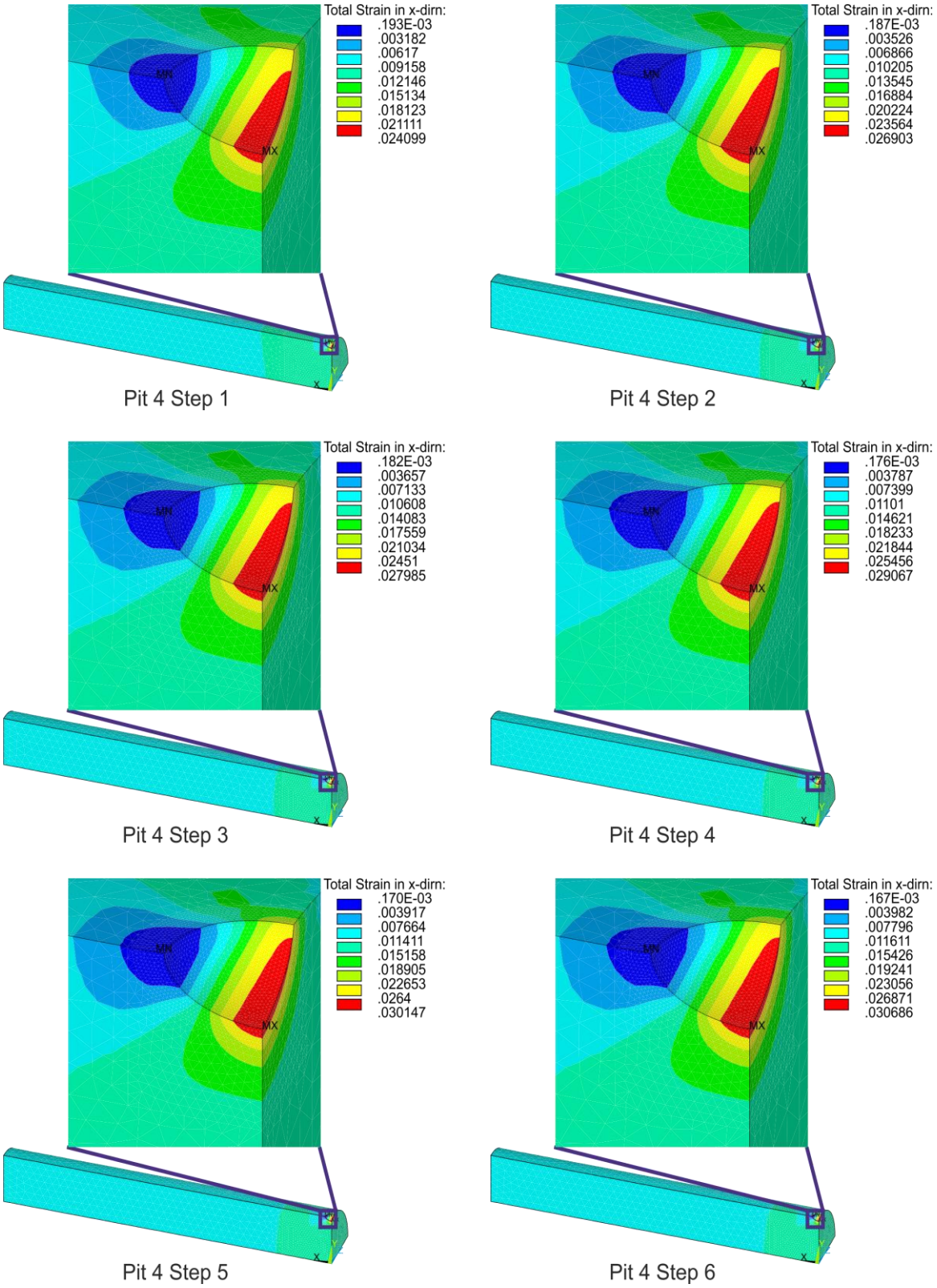

Figure 5.97: Total true strain in x-direction for shallow wide pit 4.

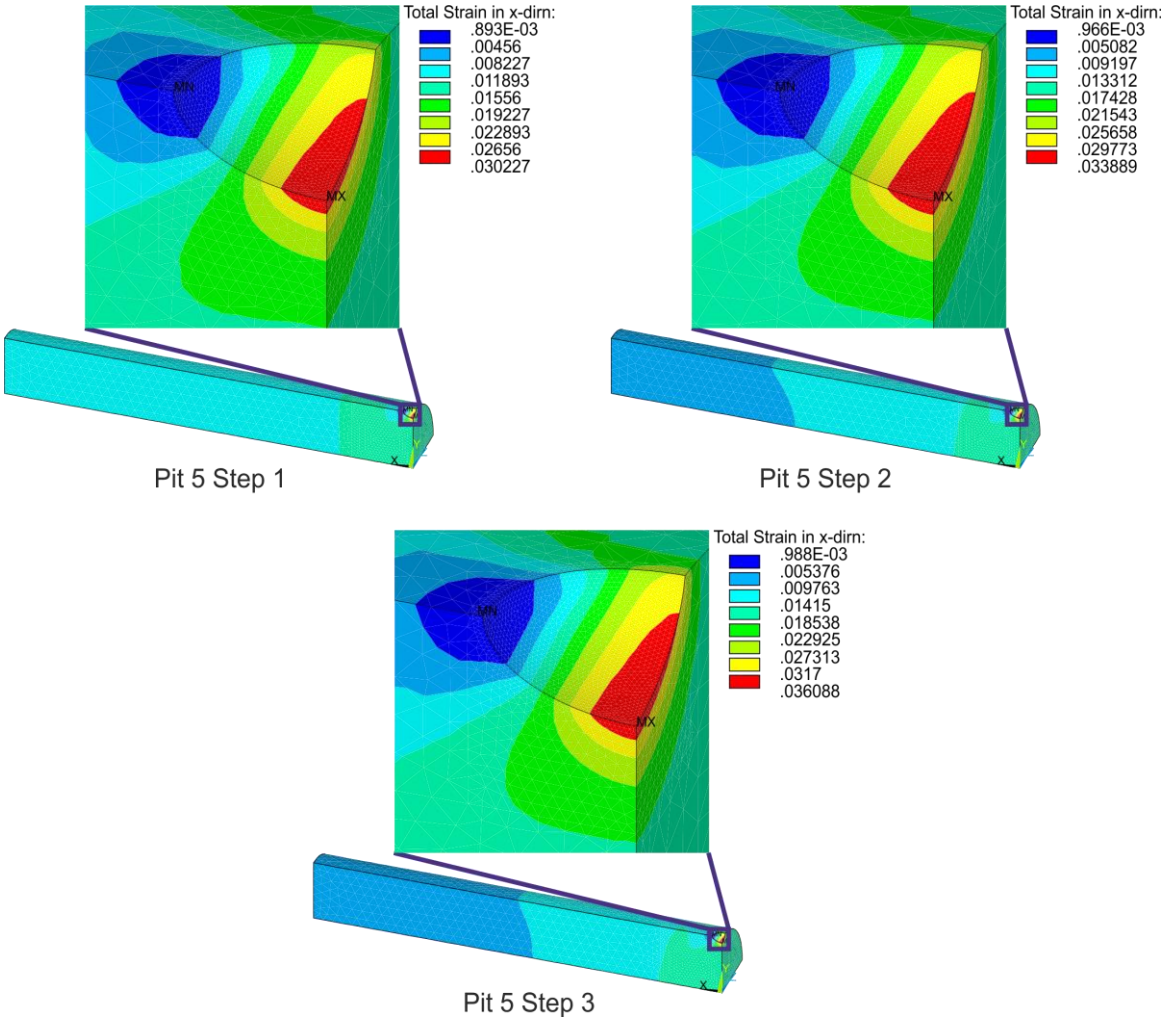

Figure 5.98: Total true strain in x-direction for shallow wide pit 5.

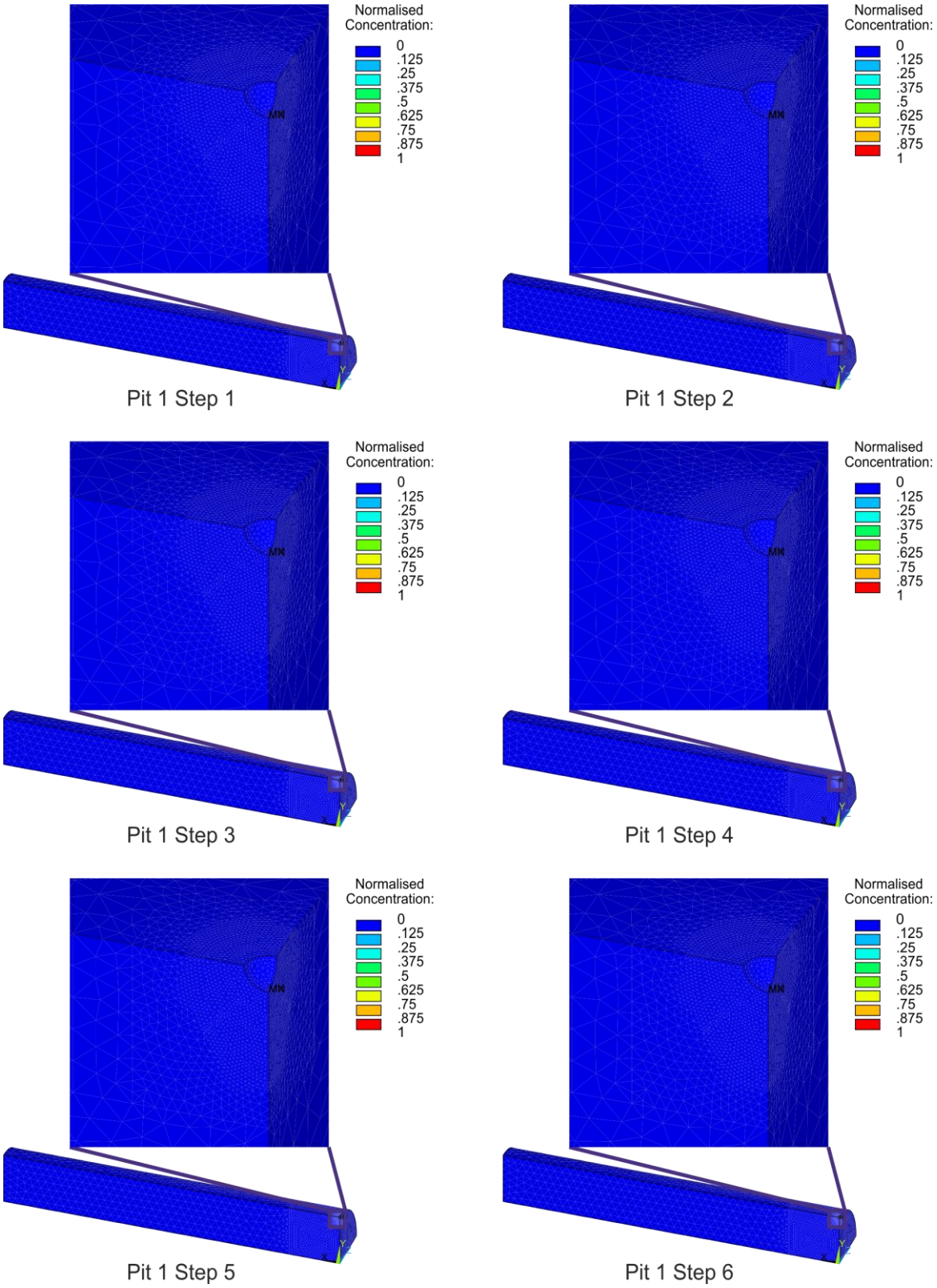

Figure 5.99: Normalised hydrogen concentration for shallow wide pit 1.

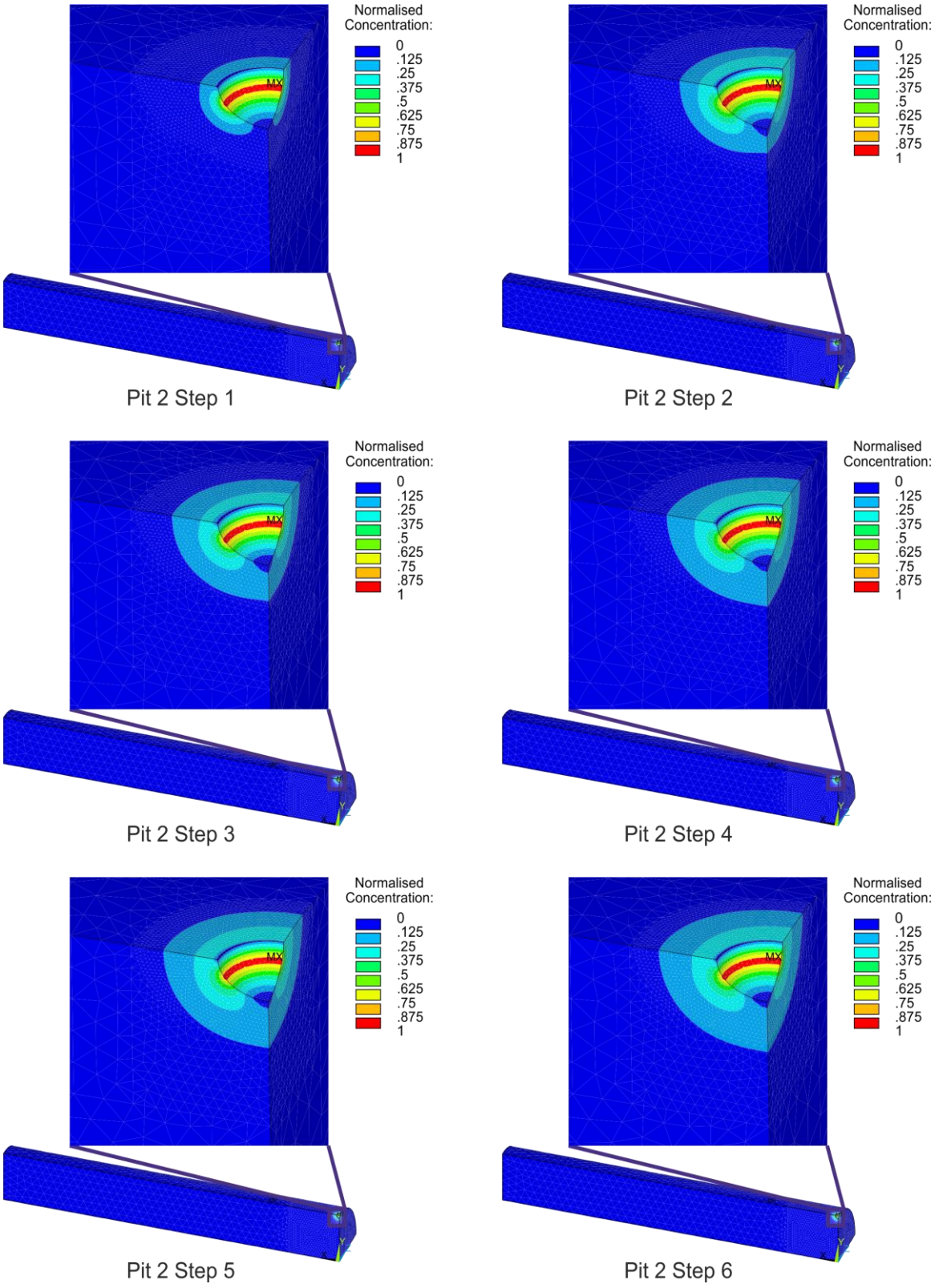

Figure 5.100: Normalised hydrogen concentration for shallow wide pit 2.

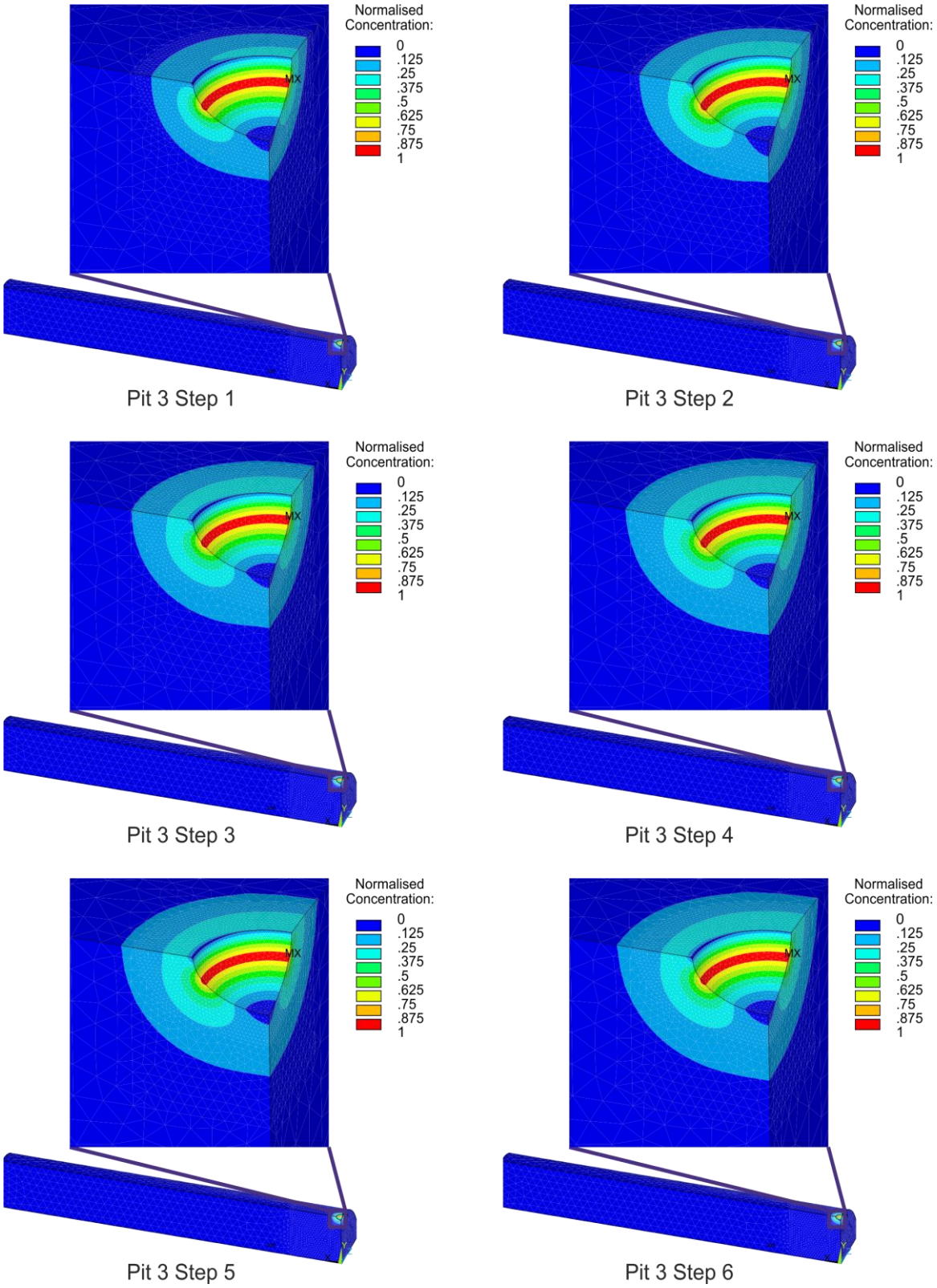

Figure 5.101: Normalised hydrogen concentration for shallow wide pit 3.

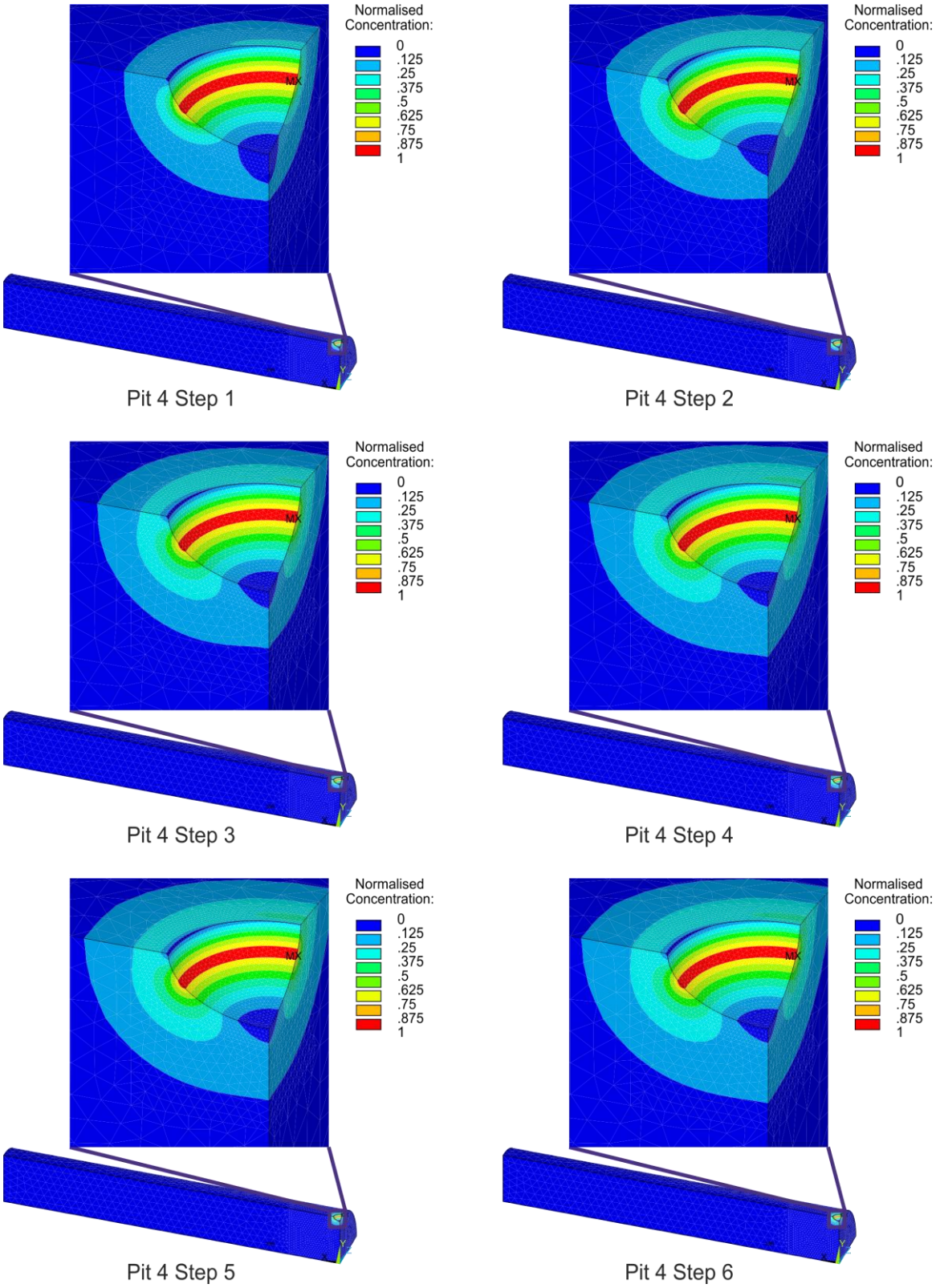

Figure 5.102: Normalised hydrogen concentration for shallow wide pit 4.

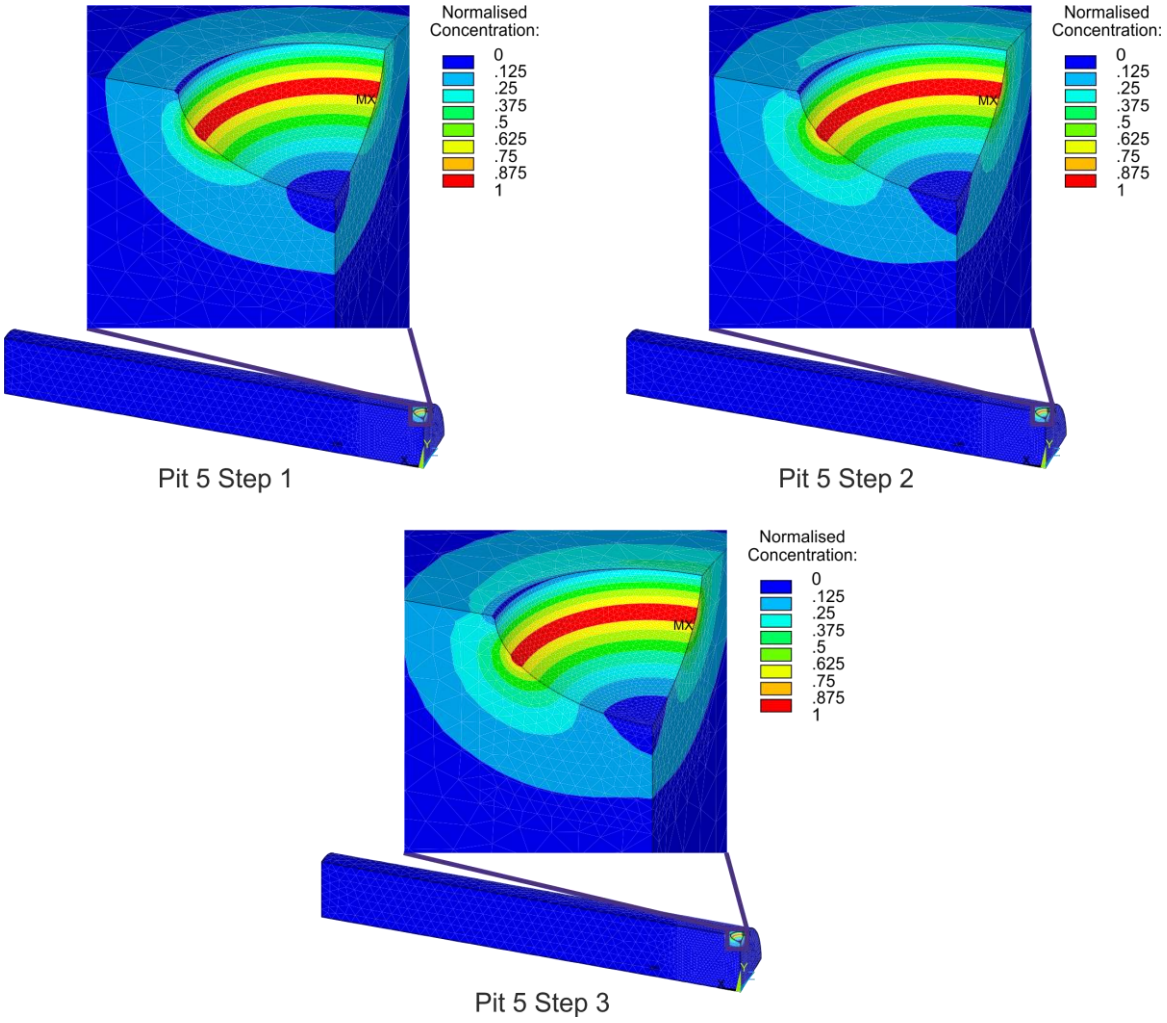

Figure 5.103: Normalised hydrogen concentration for shallow wide pit 5.

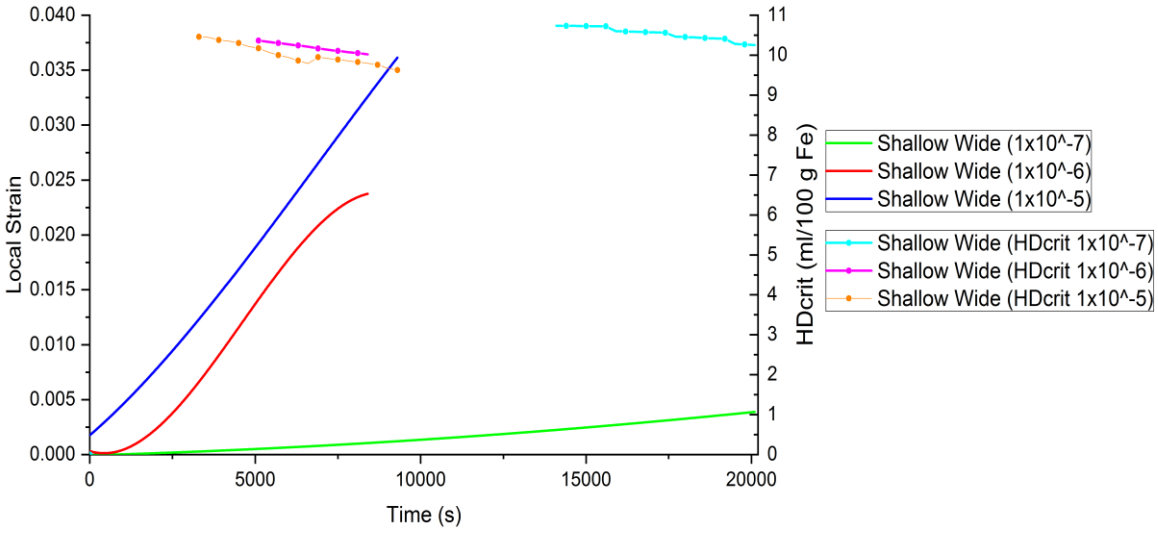

Figure 5.104: Graph of local strain vs time and HDcrit vs time for shallow wide pit.

Using Figure 5.104, the critical hydrogen concentration for a certain local strain in the shallow wide pit can be determined for the three different strain rates. If the hydrogen concentration remains below the critical value for the local strain in the shallow wide pit at that certain time, then HAC should not occur. However, if the local strain or critical hydrogen concentration values are higher, then HAC most likely will occur.

5.3.3 Ellipse Pit

For the ellipse pit the location of the highest maximum total true strain in x-direction for all pit stages is located on the side of the pit, towards the pit mouth, Figure 5.105 to Figure 5.109. The normalised hydrogen concentration profiles for the various pit stages for the ellipse pit are shown in Figure 5.110 to Figure 5.114. The pit was loaded as described above for the shallow wide pit.

As for the shallow wide pit, the shallower the pit the higher the risk of the critical hydrogen concentration being located where the highest maximum total true strain in x-direction is also located. However, the deeper the pit, the higher the highest maximum total true strain in x-direction values, requiring a lower critical hydrogen concentration to initiate HAC.

The local strain is also presented as a graph in Figure 5.115, for the three different strain rates investigated. This graph again shows how the local strain increases with increasing time for all strain rates, with the strain rate of $1x10^{-5}$ having the highest gradient or steepest slope with the critical hydrogen concentration for each stage when hydrogen is applied to the pit also shown. The critical hydrogen concentration for the corresponding local strain for the ellipse pit can now be determined which in turn can identify the minimum allowable hydrogen concentration which may be present without the possibility of HAC occurring.

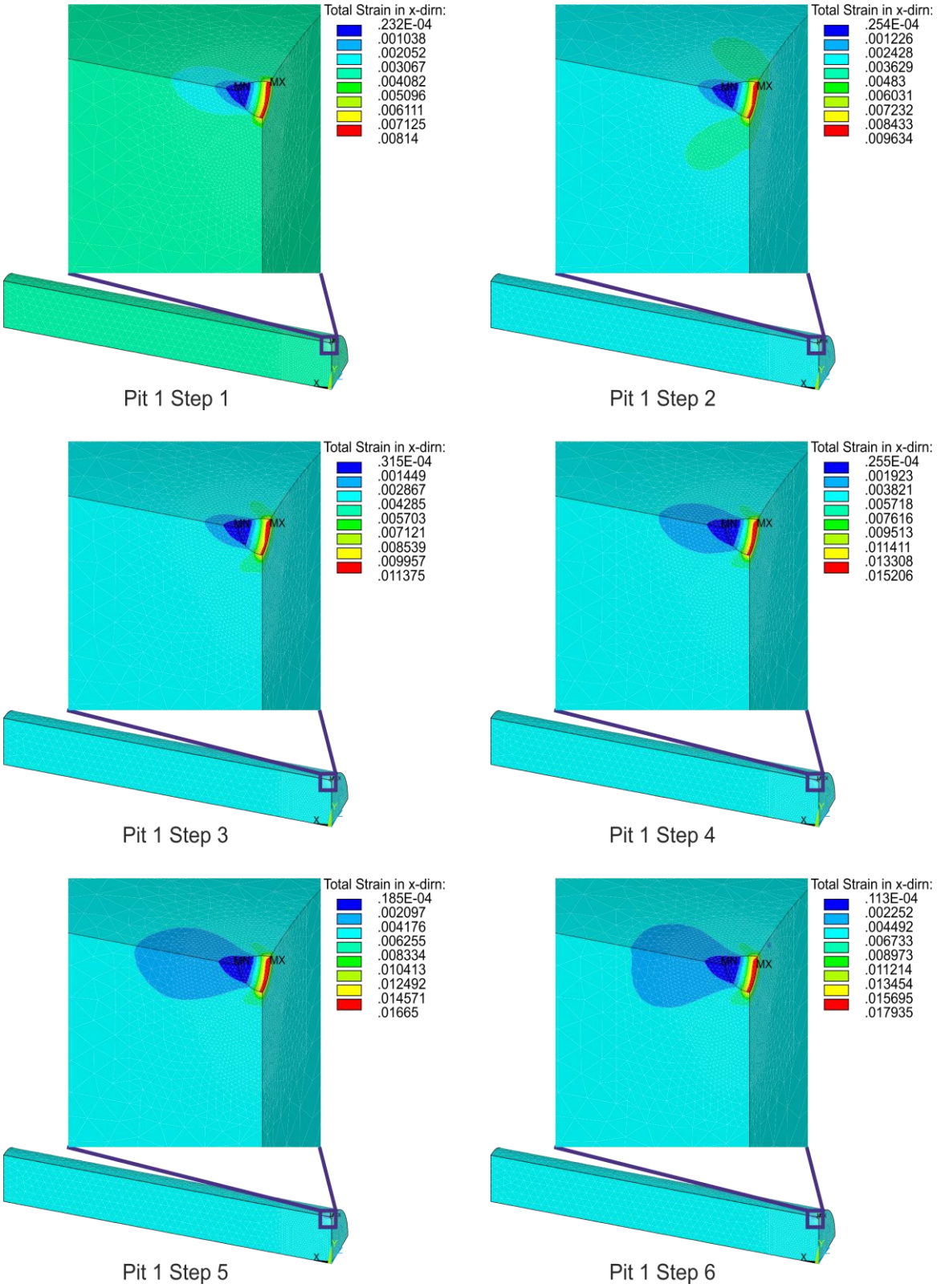

Figure 5.105: Total true strain in x-direction for ellipse pit 1.

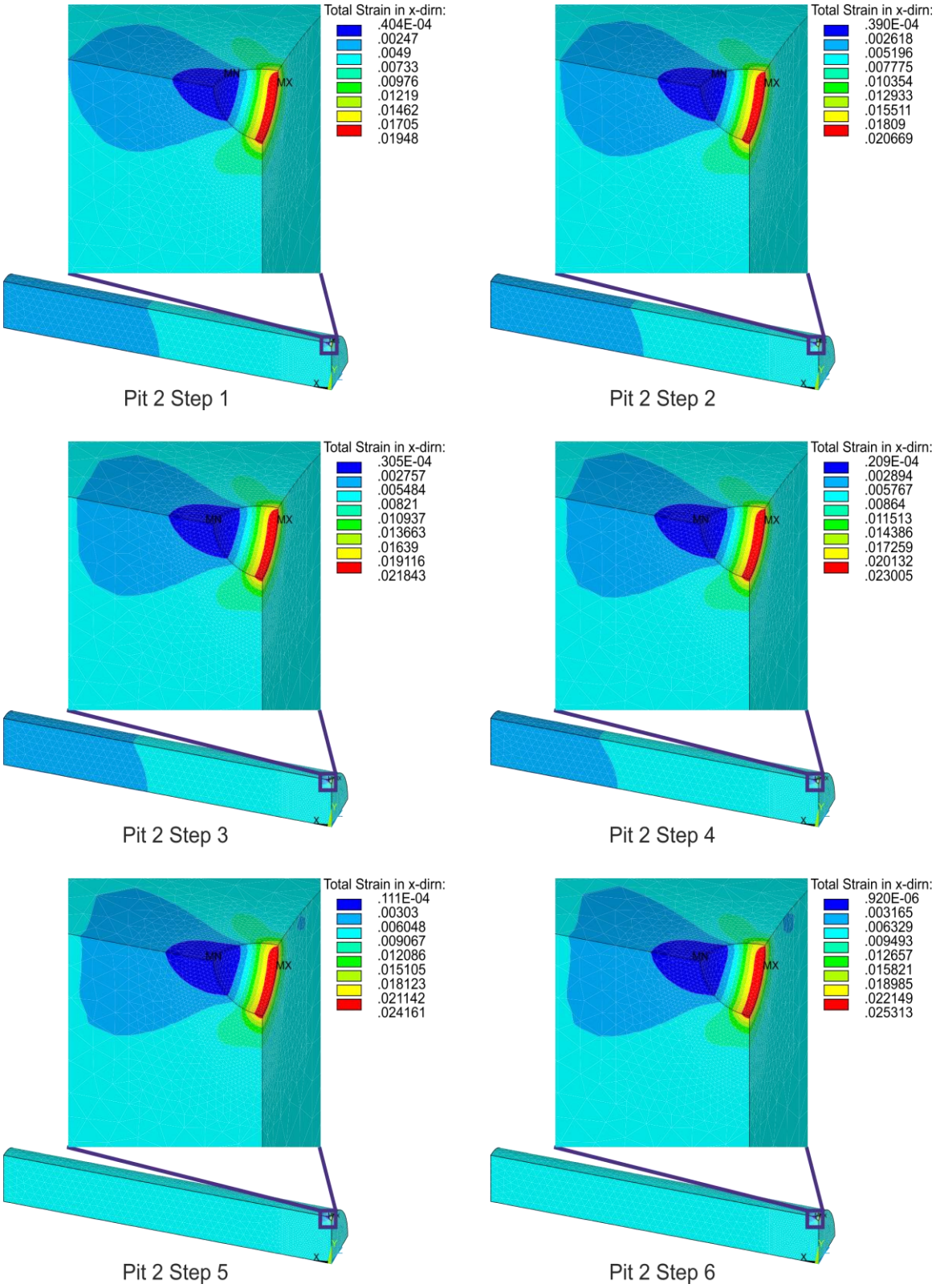

Figure 5.106: Total true strain in x-direction for ellipse pit 2.

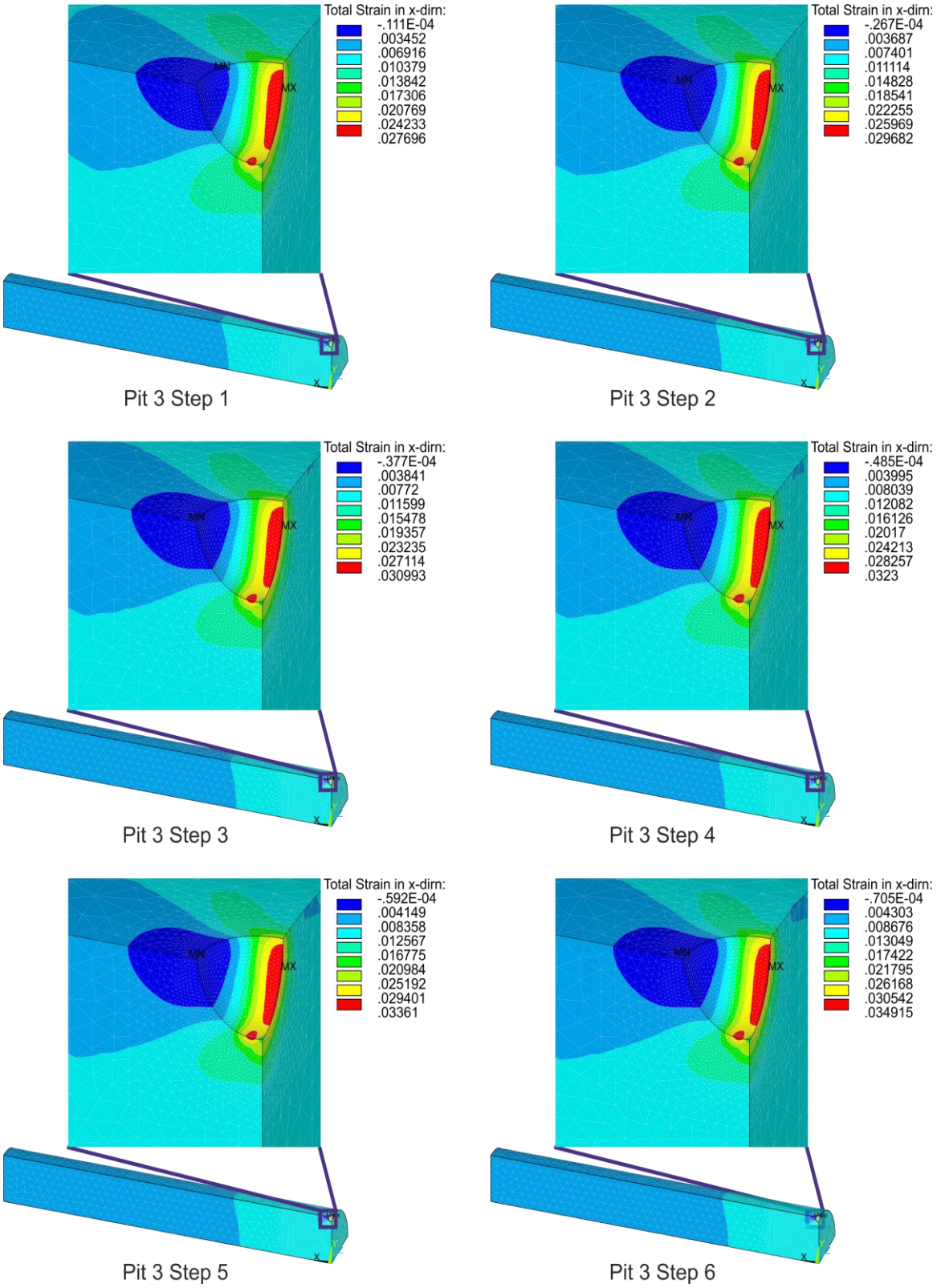

Figure 5.107: Total true strain in x-direction for ellipse pit 3.

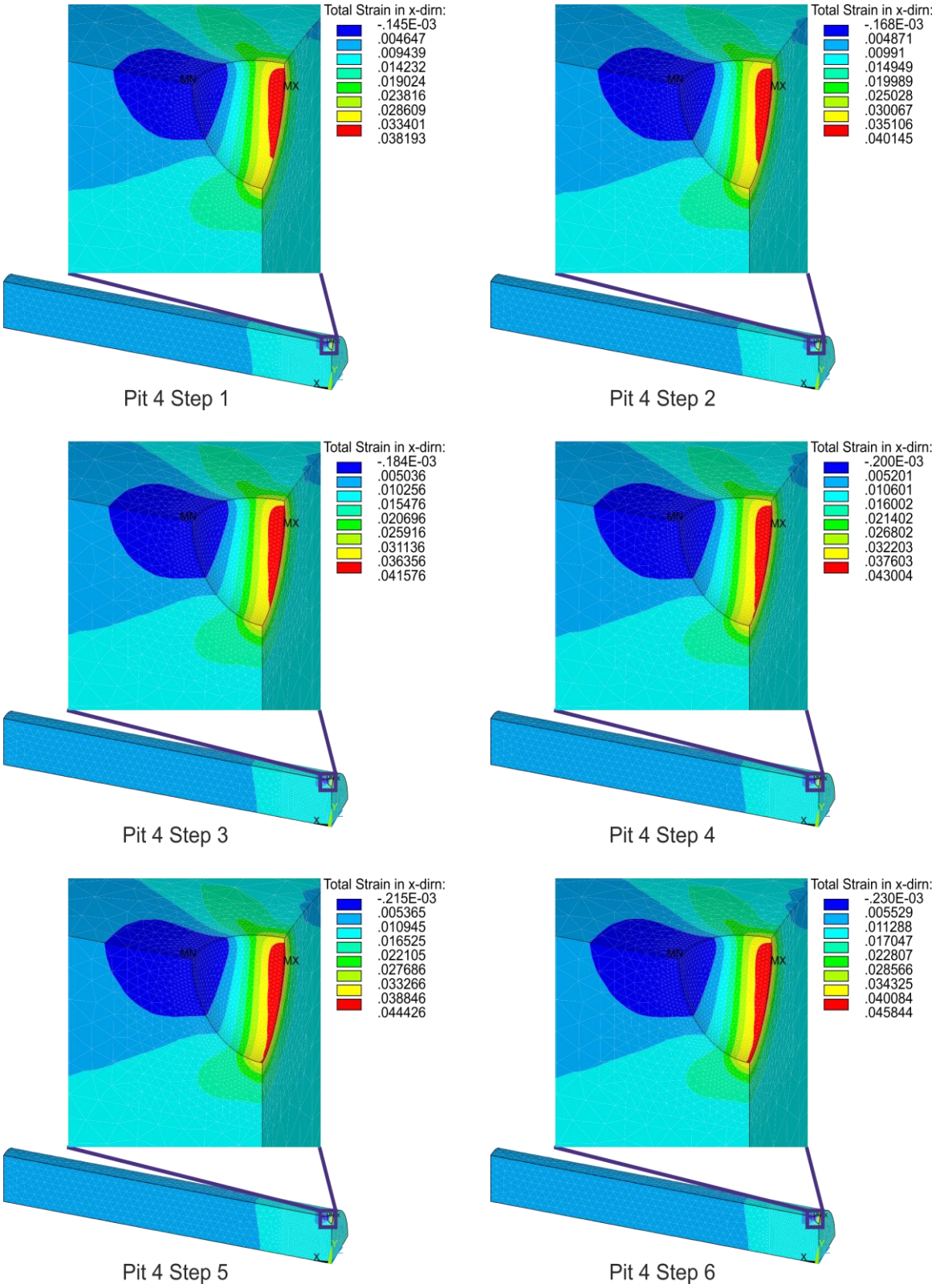

Figure 5.108: Total true strain in x-direction for ellipse pit 4.

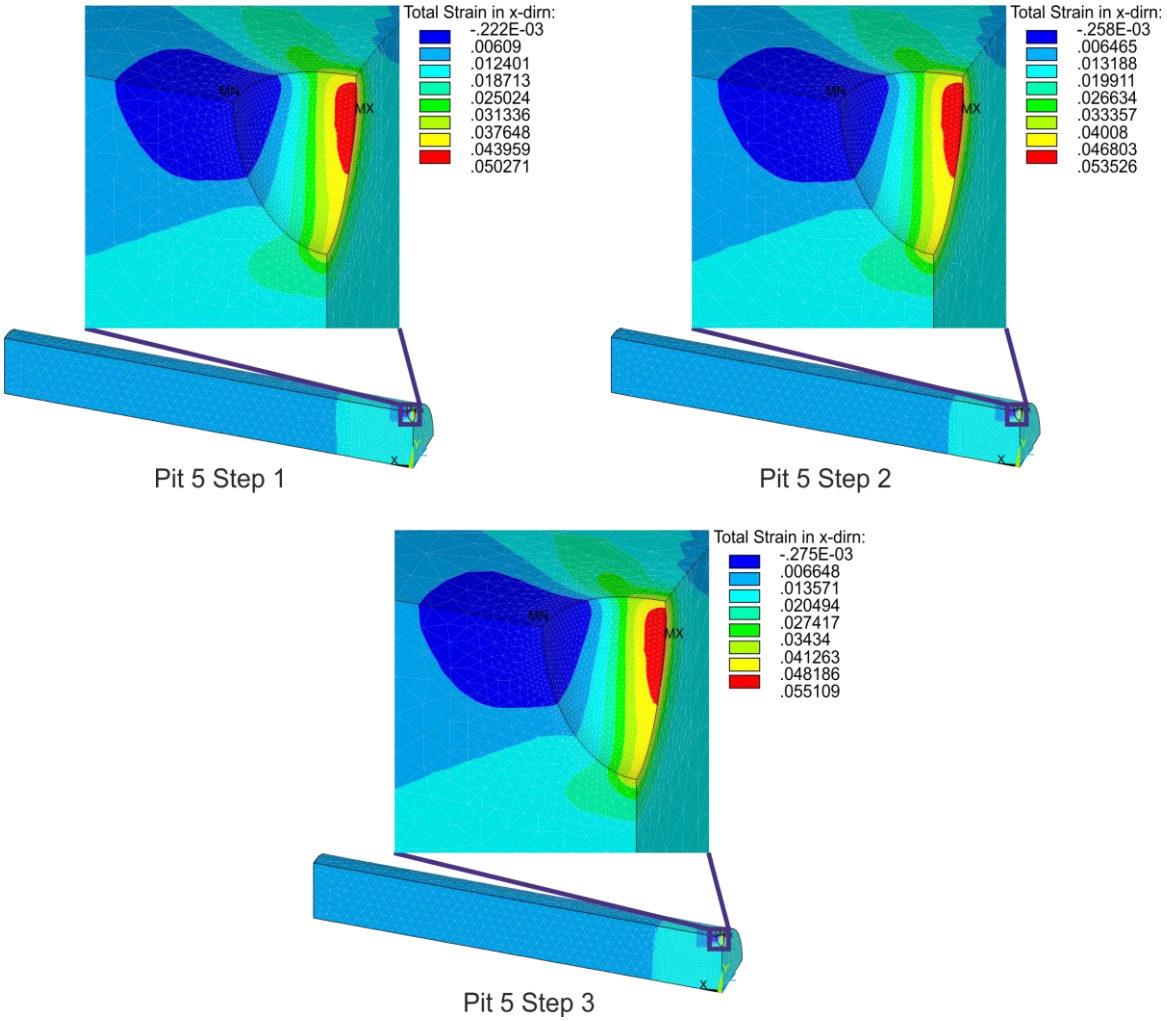

Figure 5.109: Total true strain in x-direction for ellipse pit 5.

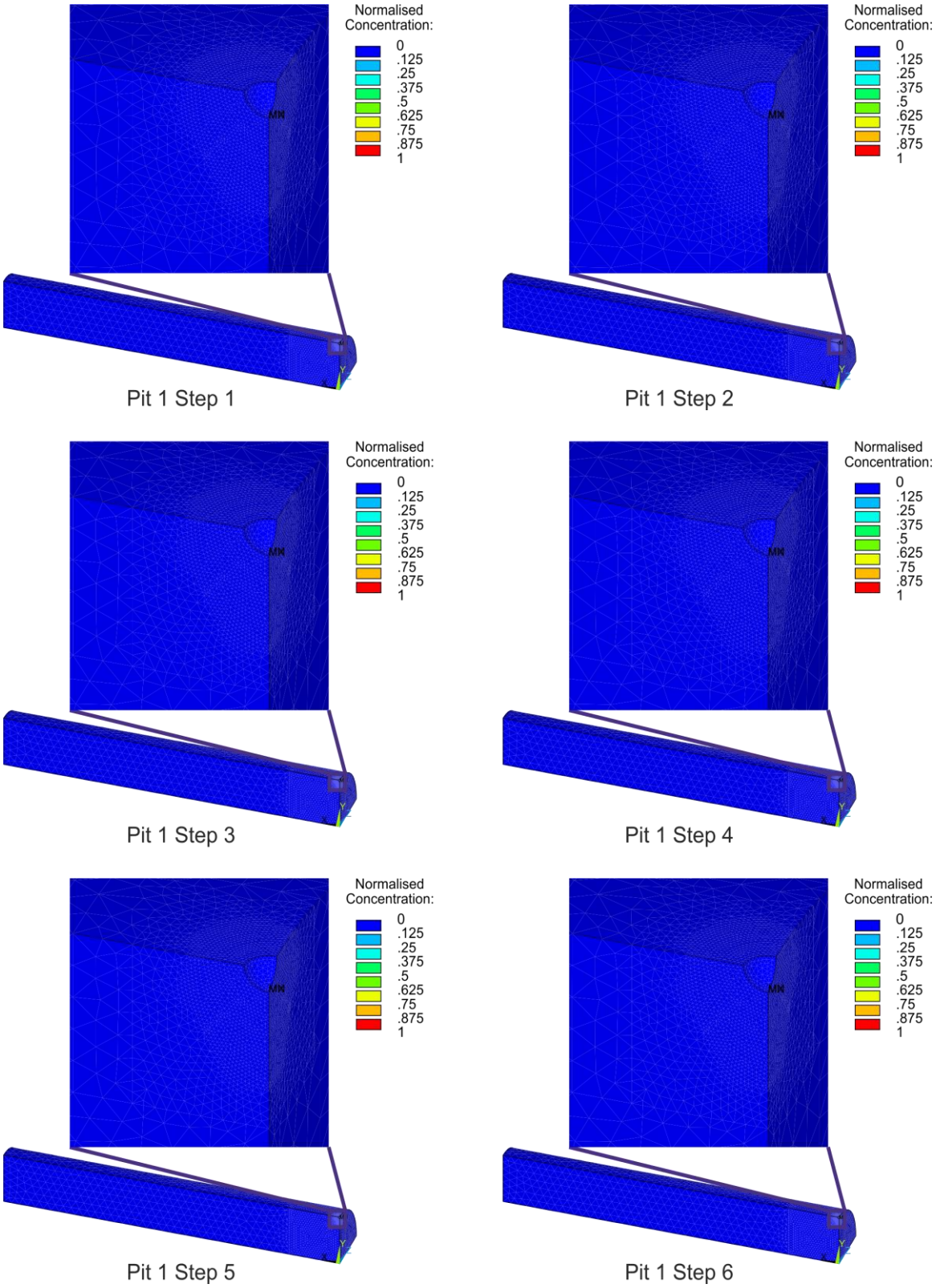

Figure 5.110: Normalised hydrogen concentration for ellipse pit 1.

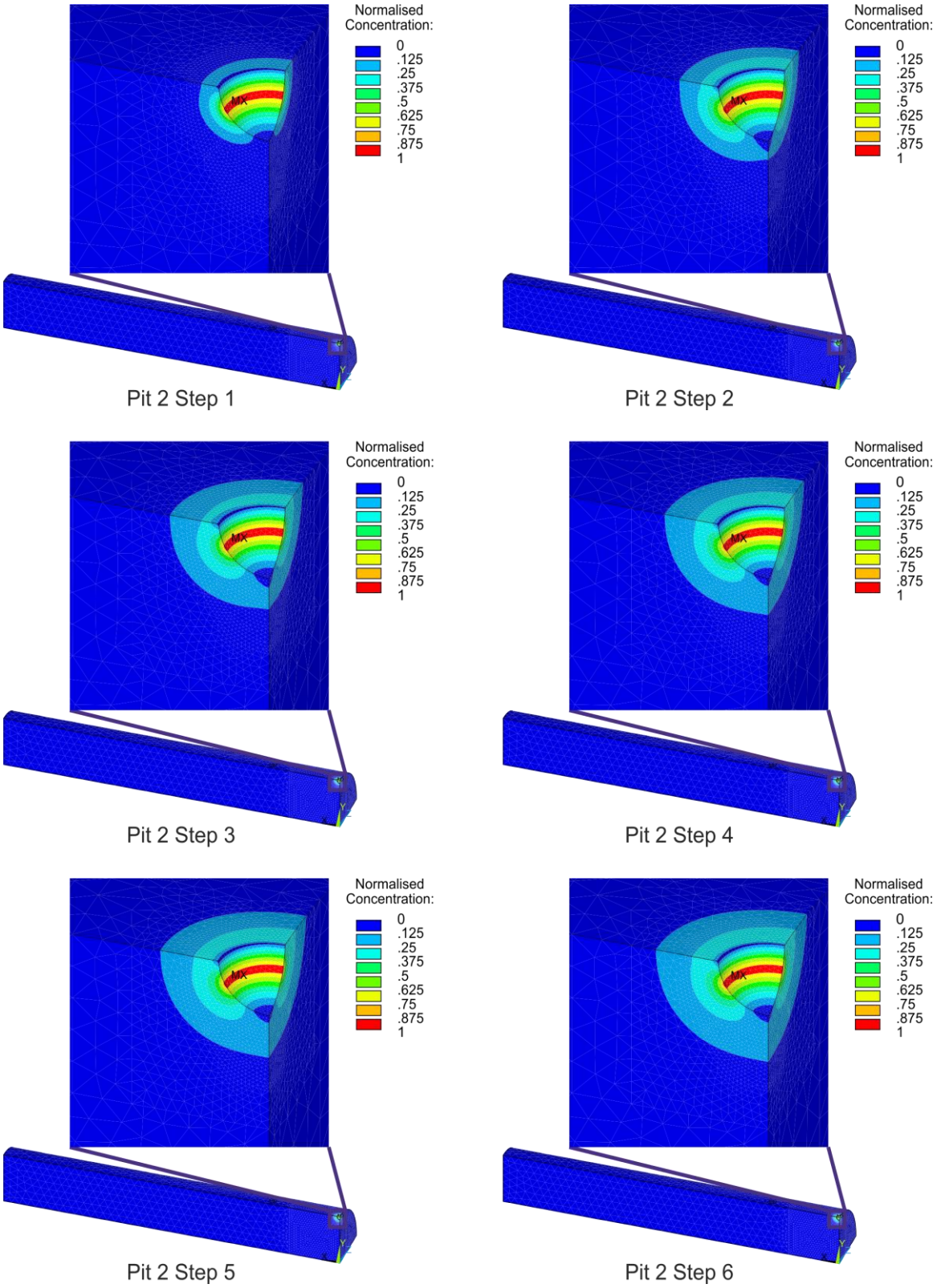

Figure 5.111: Normalised hydrogen concentration for ellipse pit 2.

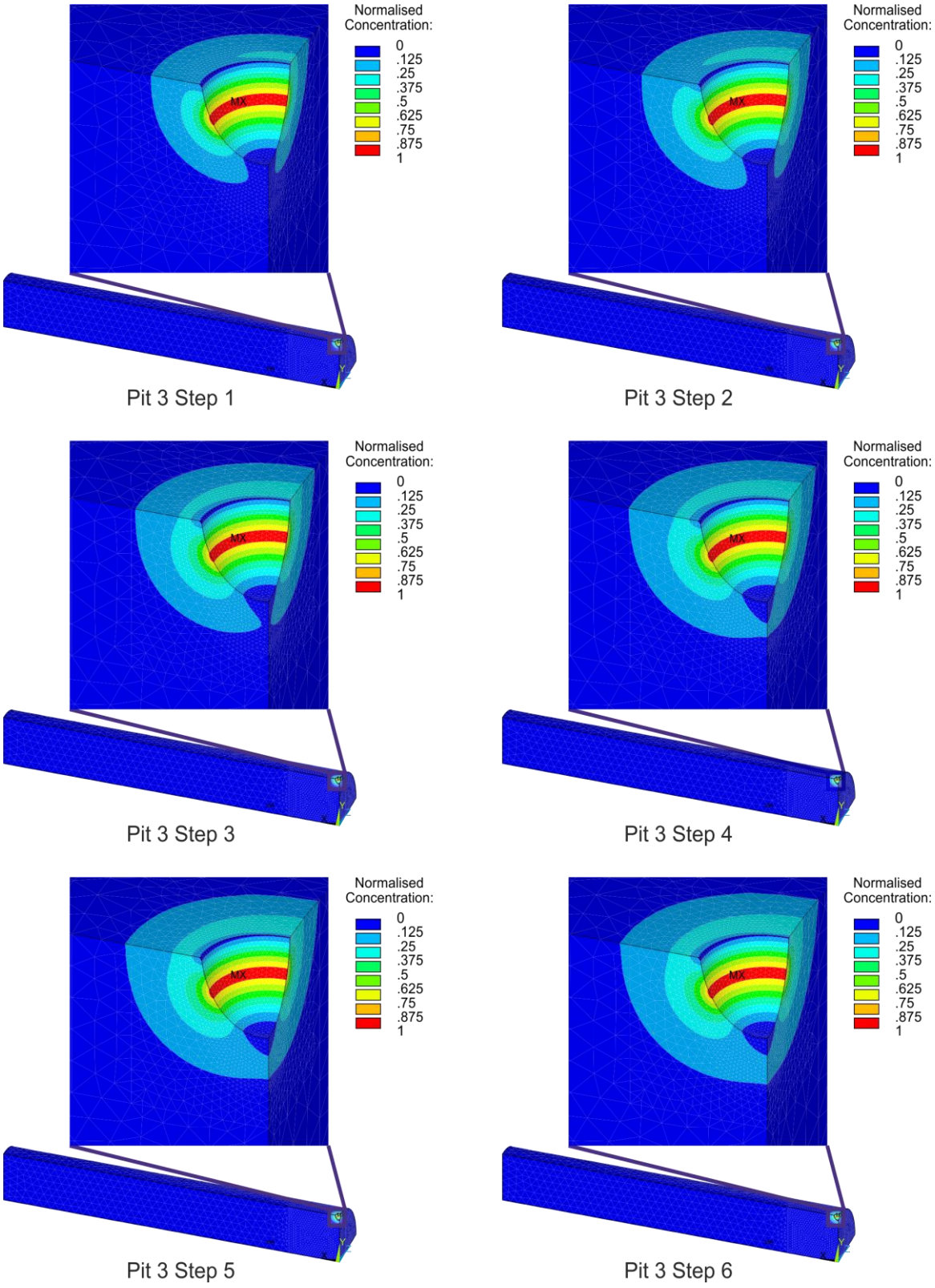

Figure 5.112: Normalised hydrogen concentration for ellipse pit 3.

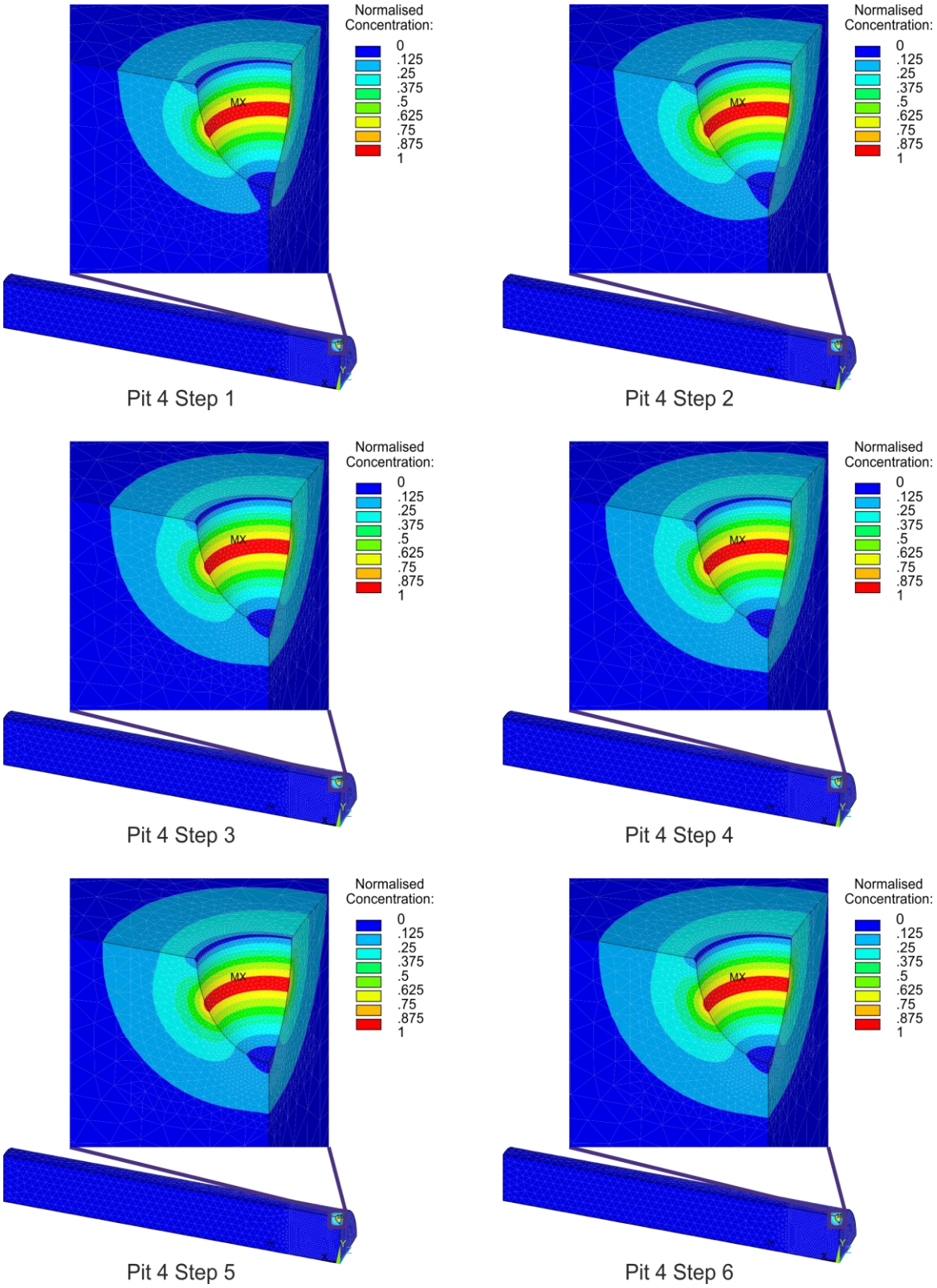

Figure 5.113: Normalised hydrogen concentration for ellipse pit 4.

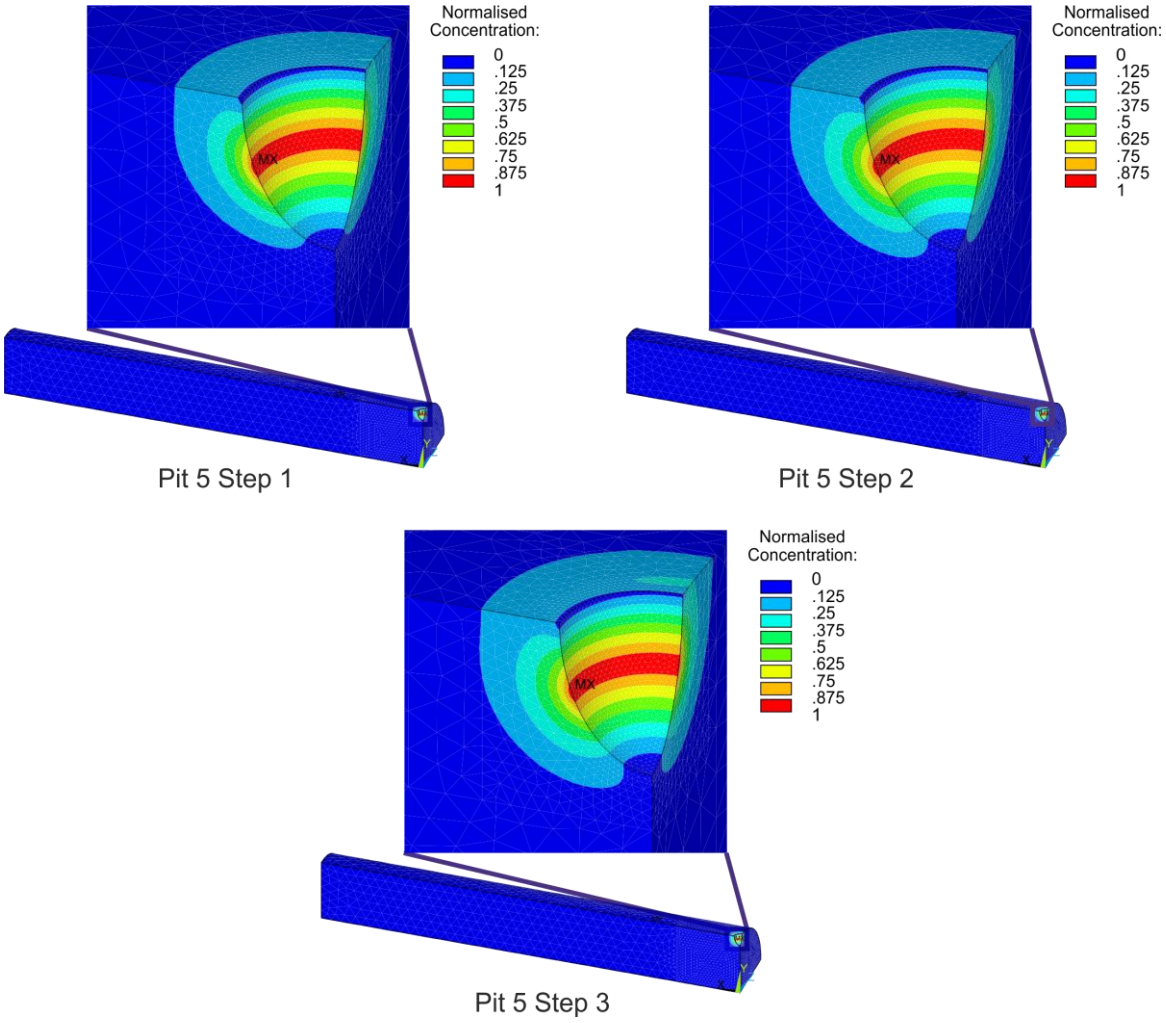

Figure 5.114: Normalised hydrogen concentration for ellipse pit 5.

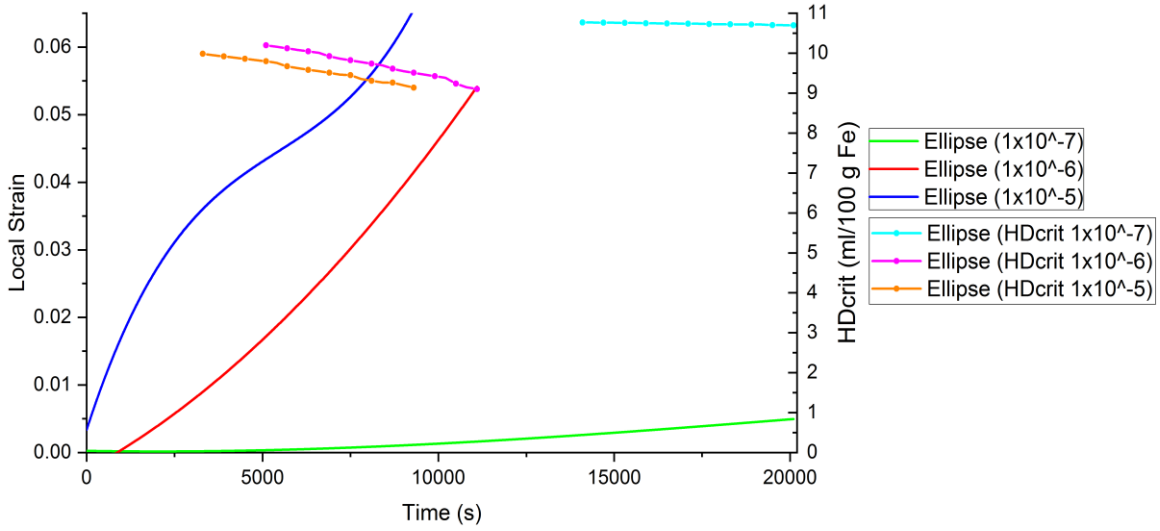

Figure 5.115: Graph of local strain vs time and HDcrit vs time for ellipse pit.

5.3.4 Subsurface Pit

For the subsurface pit however the location of the highest maximum total strain in x-direction varies. For the first pit stage the location is at the pit mouth but as the displacement load increases this location moves to the pit bottom. This may be due to an increase in the local strains in the pit. For the second pit stage the location is at the pit mouth for all displacement loads. For the remaining pit stages the location of the highest maximum total strain in x-direction is the same- where the small pit mouth diameter joins the larger subsurface section of the pit geometry. For the subsurface pit however the location of the highest maximum total strain in x-direction varies, Figure 5.116 to Figure 5.120. For the first pit stage the location is at the pit mouth but as the displacement load increases this location moves towards the pit bottom. This was also observed by Anantha et al. who noticed a pitted specimen had the highest strained location near the pit mouth for specimens loaded to 23% of yield strength but the highest strains were located along the pit walls when the specimens were loaded to 66% of yield strength.

Regarding the subsurface pit geometries in Figure 5.116 to Figure 5.120, the location of the highest maximum total strain in x-direction for pits 2 to 5 are near the pit mouth. For pits 3 to 5 this region is located where the pit mouth intersects with the larger pit body, leading to a sharp edge where strains tend to accumulate. The location of the highest normalised hydrogen concentration, Figure 5.121 to Figure 5.125 is located not in the region of highest maximum total strain in x-direction but in the middle of the larger pit body, where the strains are not as high. Due to the geometry of the pits 3 to 5, the hydrogen diffuses directly into the material and not along the pit geometry. Therefore, in the region of highest maximum total strain in x-direction, the corresponding normalised hydrogen concentration values are towards the lower end of the applied values. However, as the highest maximum total strain in x-direction values are largest for the subsurface pits, the required critical hydrogen concentration value for each pit stage is lowest for all three pit geometries investigated.

The local strain is also presented as a graph in Figure 5.126, for the three different strain rates investigated. Similar to the shallow wide and ellipse pit geometries, this graph again shows how the local strain increases with increasing time for all strain rates, with the strain rate of $1x10^{-5}$ having the highest gradient or steepest slope with the critical hydrogen concentration for each stage when hydrogen is applied to the pit also shown. The critical hydrogen concentration for the corresponding local strain can then be determined which in turn can identify the minimum allowable hydrogen concentration which may be present without the possibility of HAC occurring.

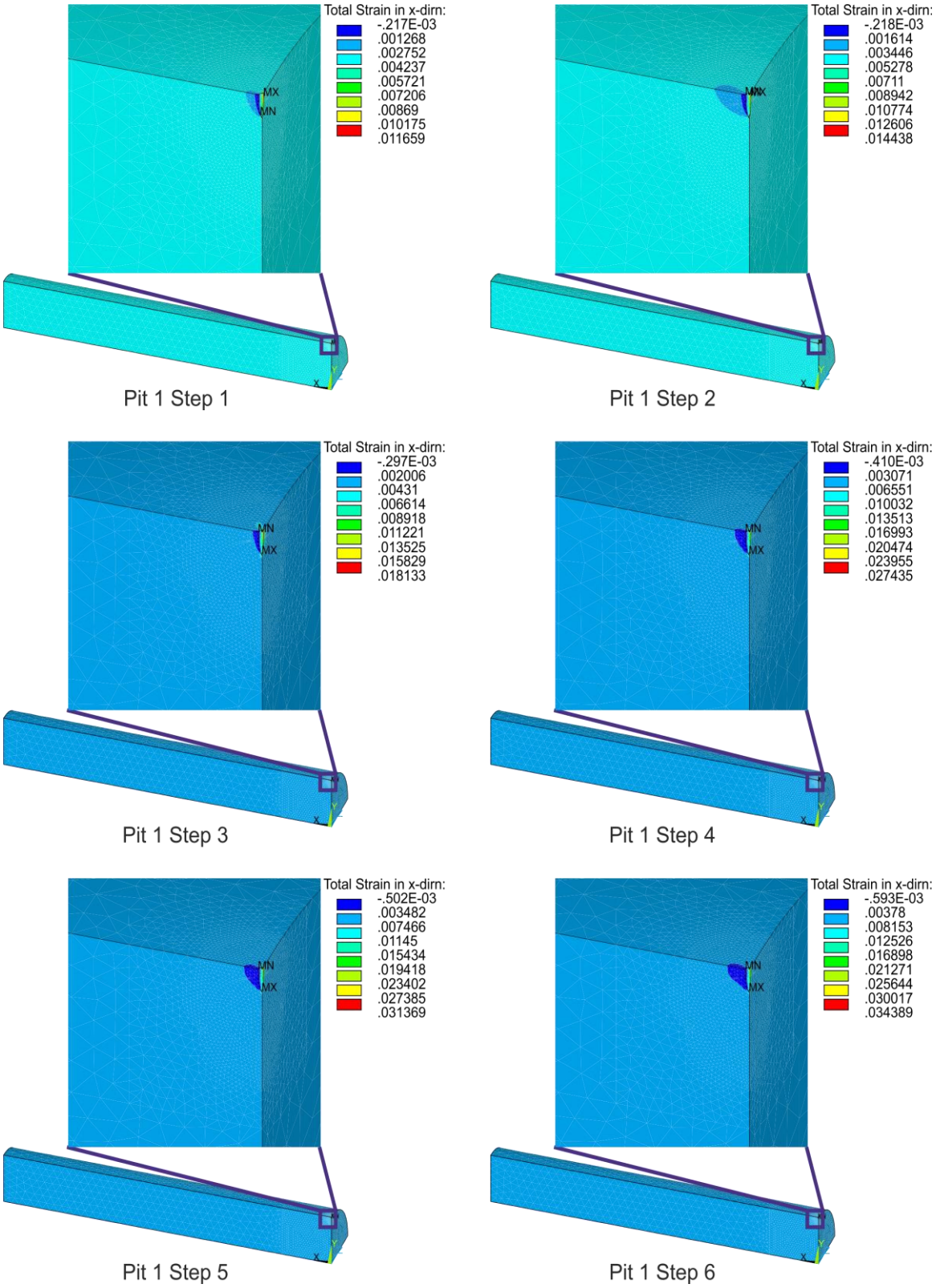

Figure 5.116: Total true strain in x-direction for subsurface pit 1.

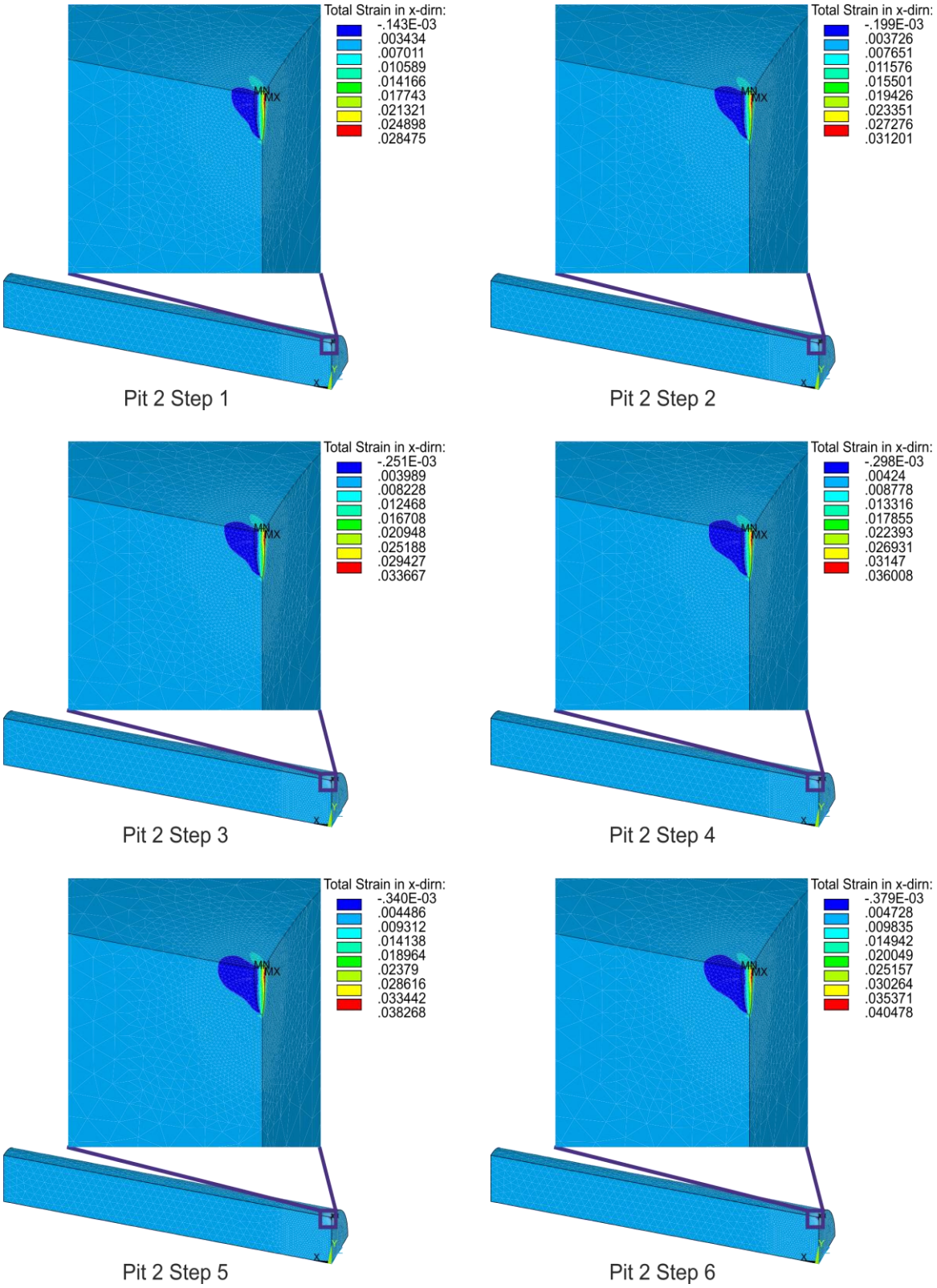

Figure 5.117: Total true strain in x-direction for subsurface pit 2.

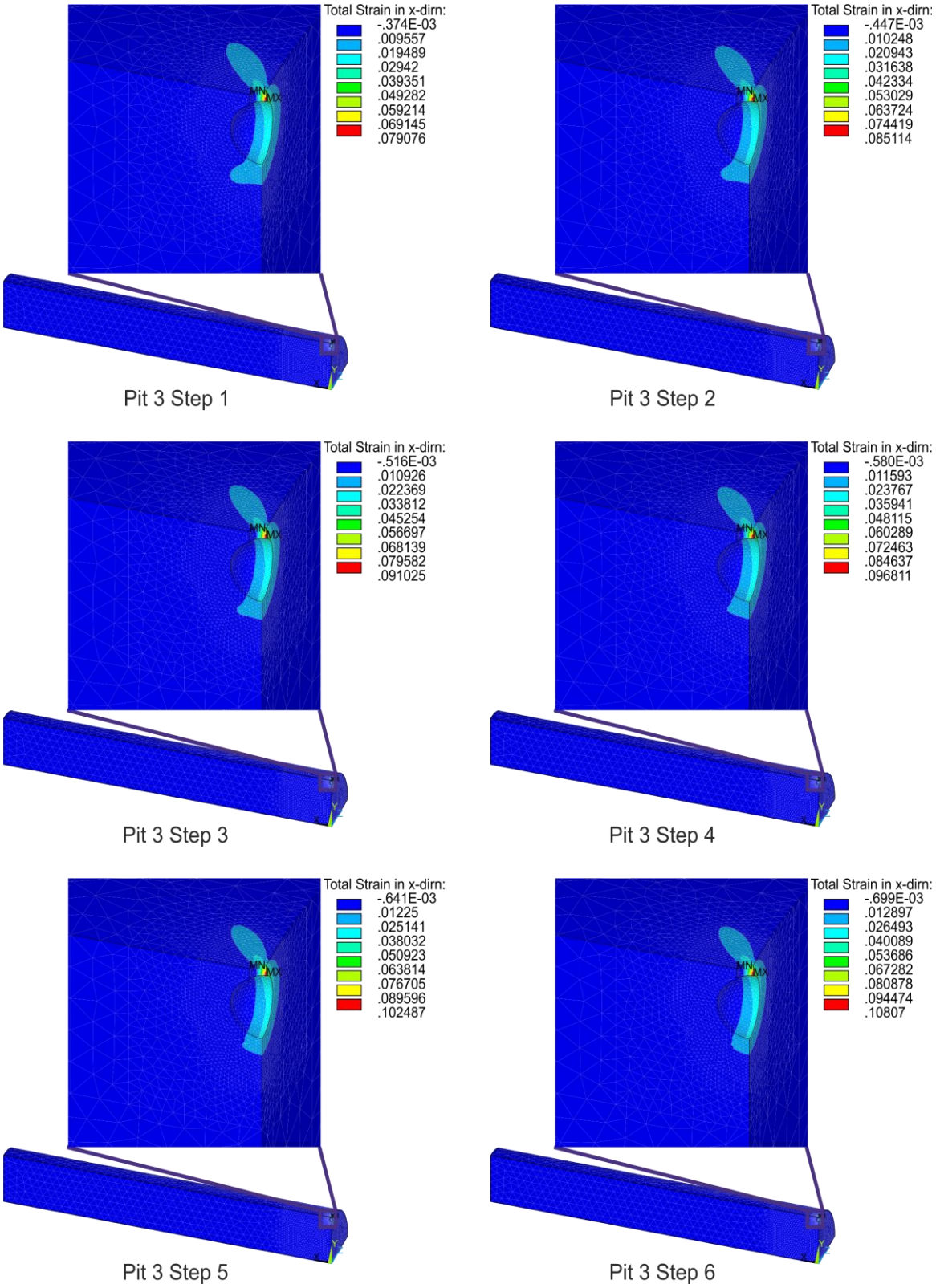

Figure 5.118: Total true strain in x-direction for subsurface pit 3.

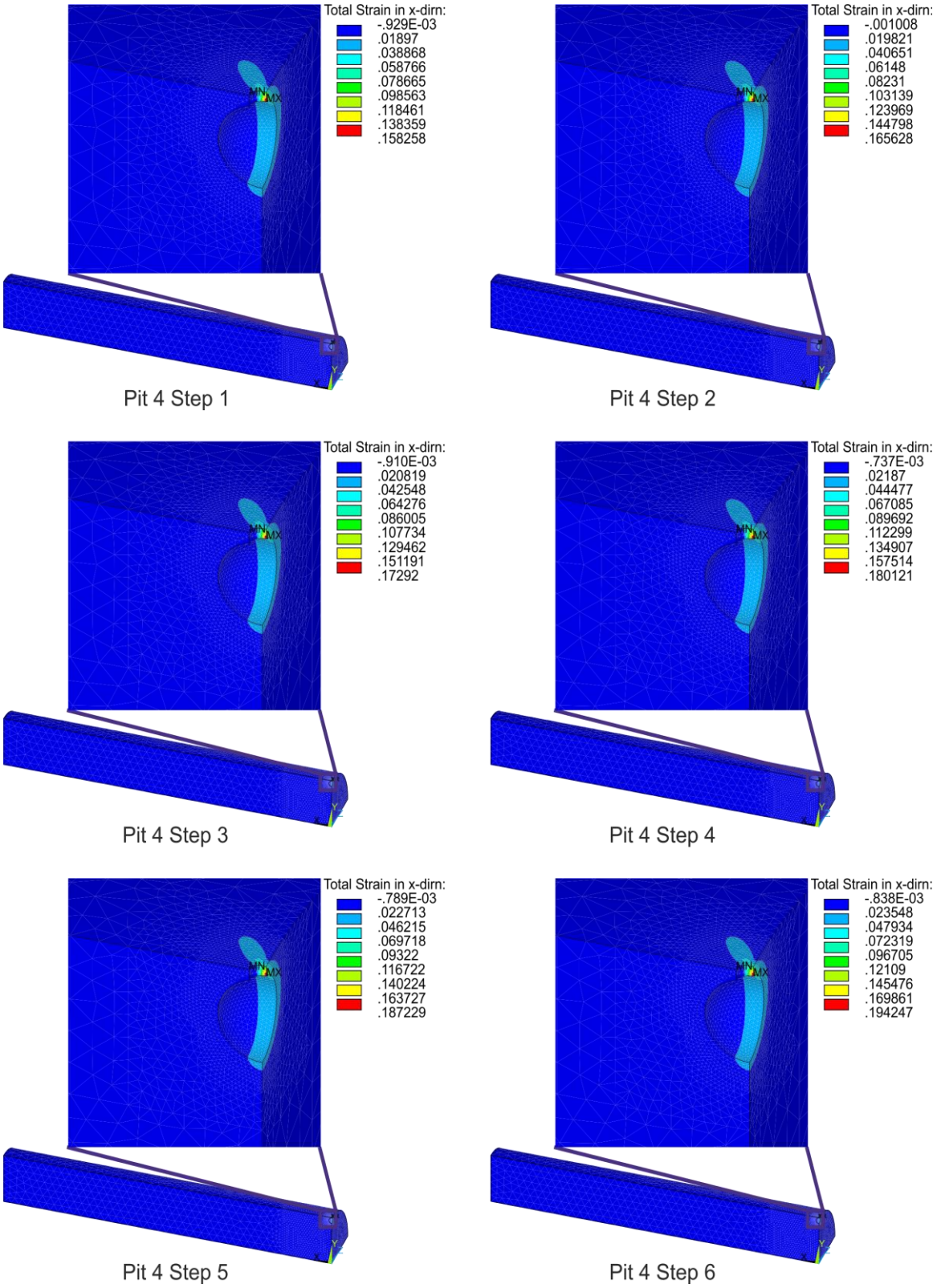

Figure 5.119: Total true strain in x-direction for subsurface pit 4.

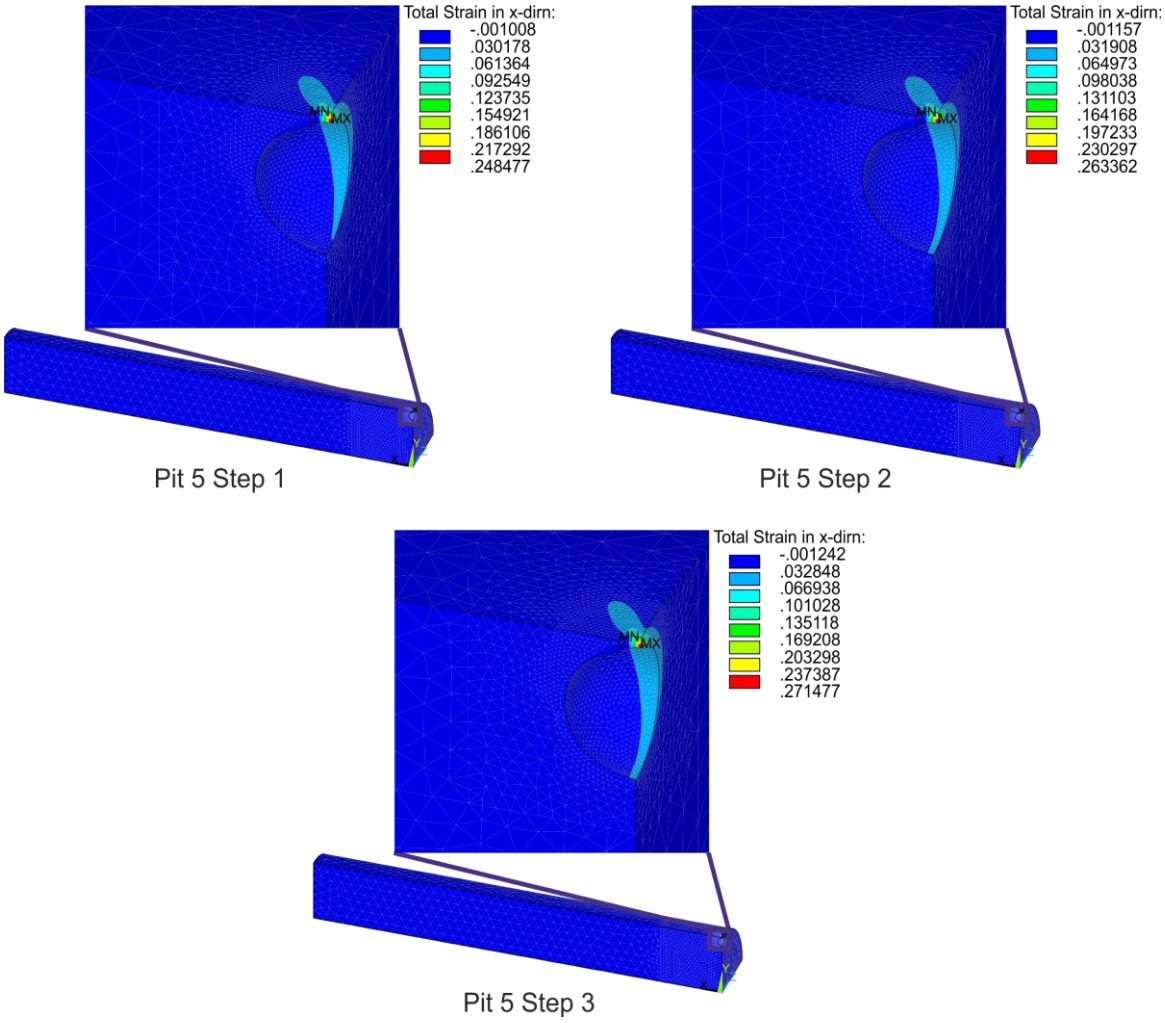

Figure 5.120: Total true strain in x-direction for subsurface pit 5.

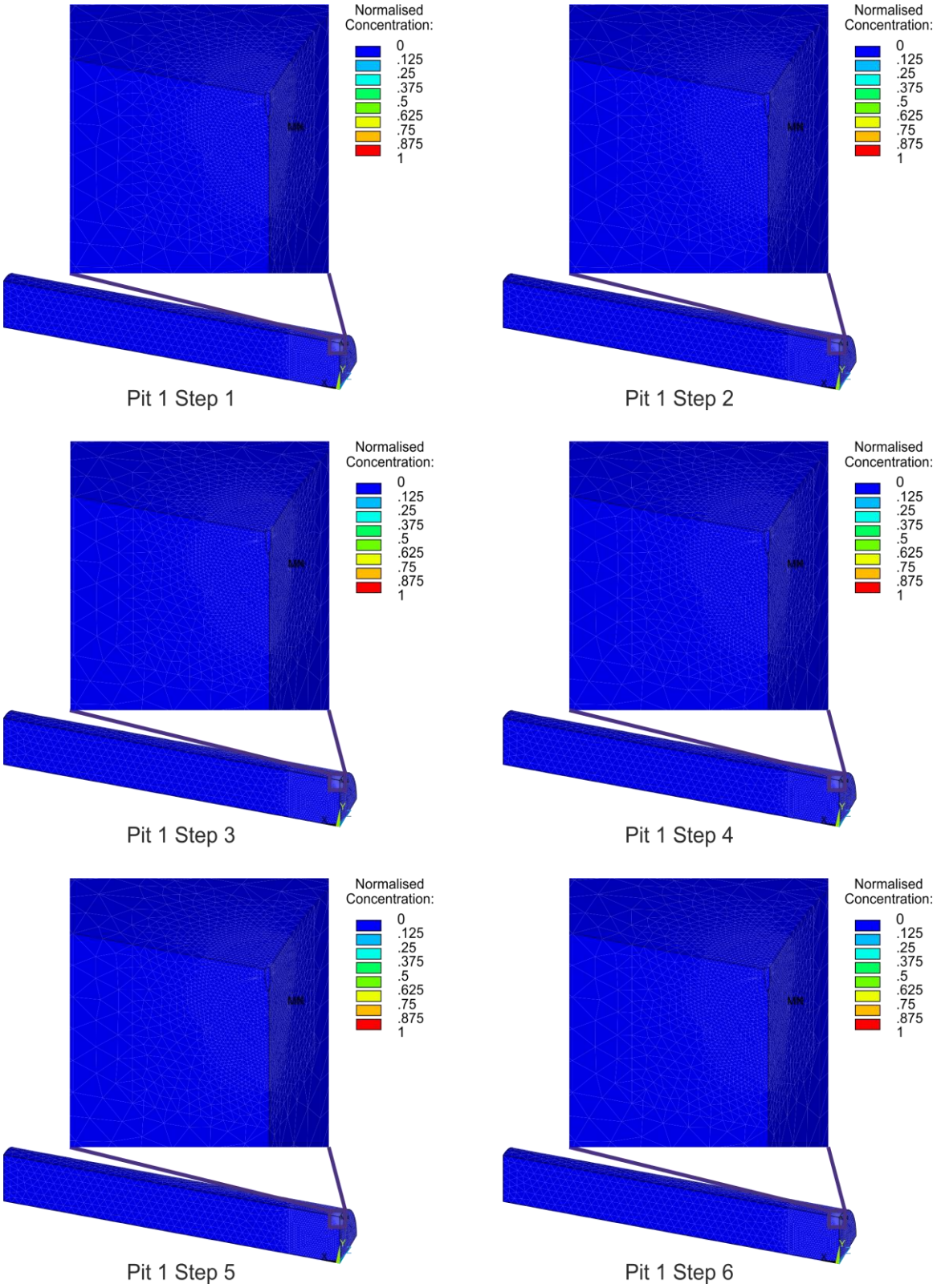

Figure 5.121: Normalised hydrogen concentration for subsurface pit 1.

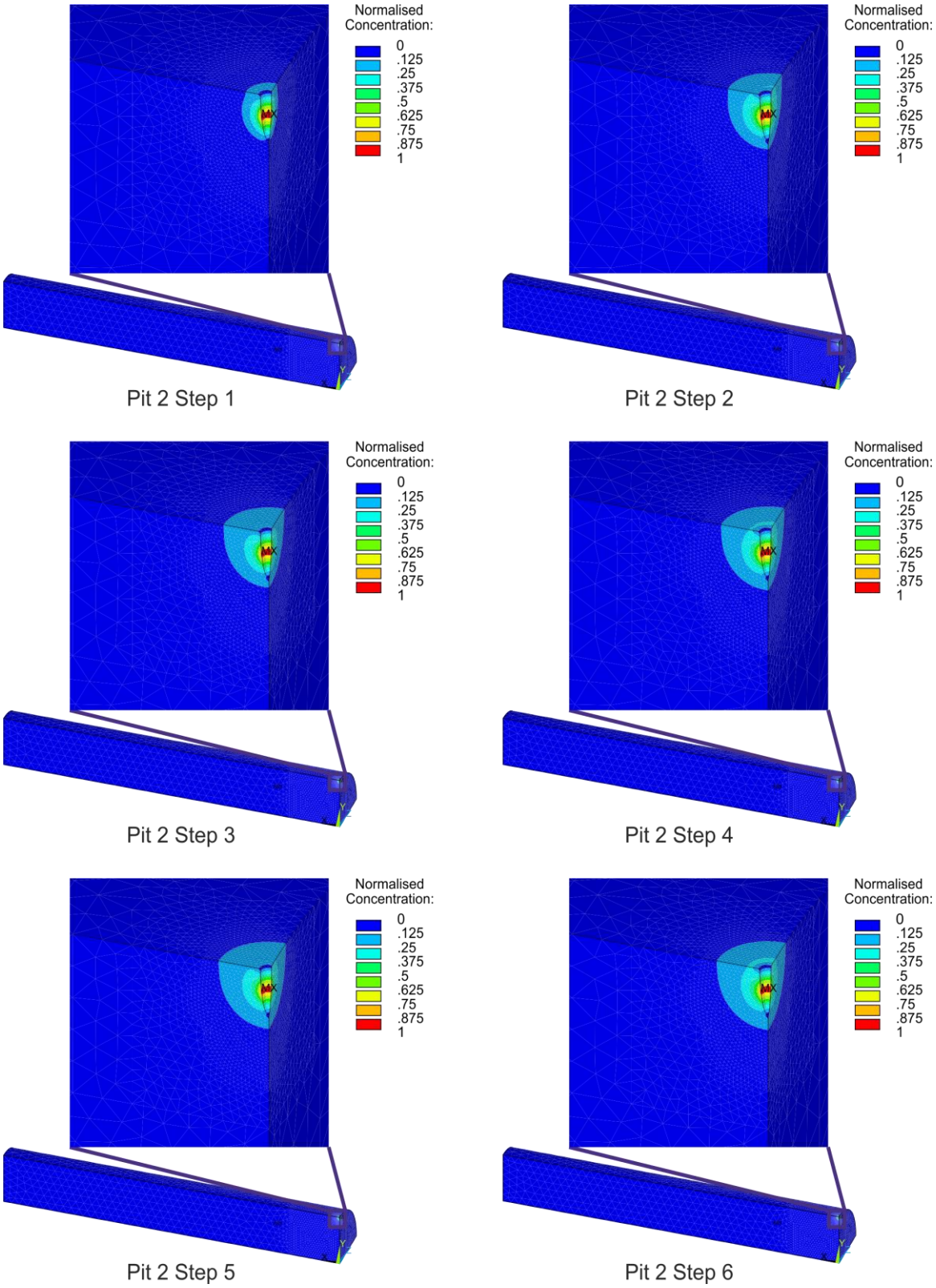

Figure 5.122: Normalised hydrogen concentration for subsurface pit 2.

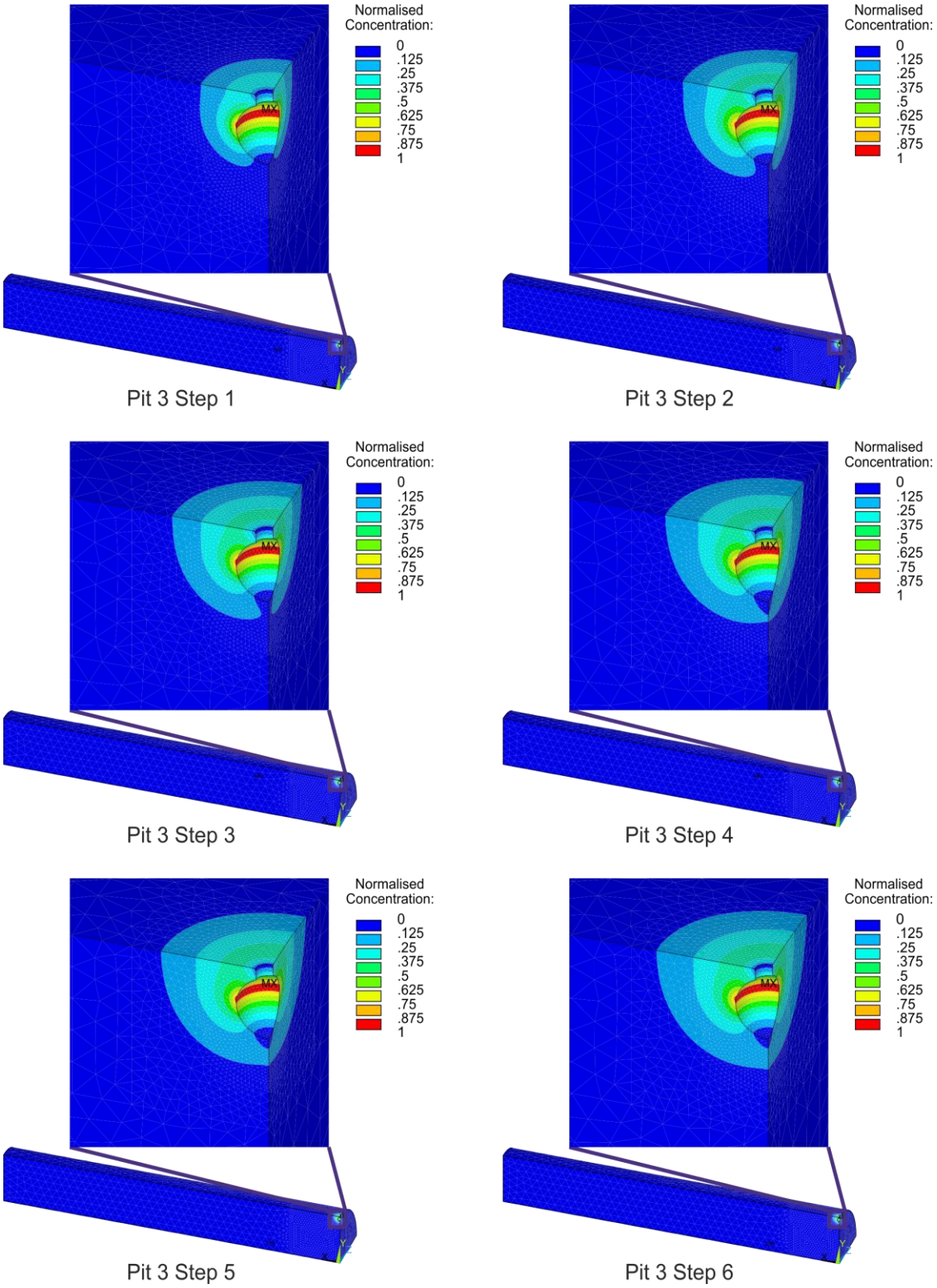

Figure 5.123: Normalised hydrogen concentration for subsurface pit 3.

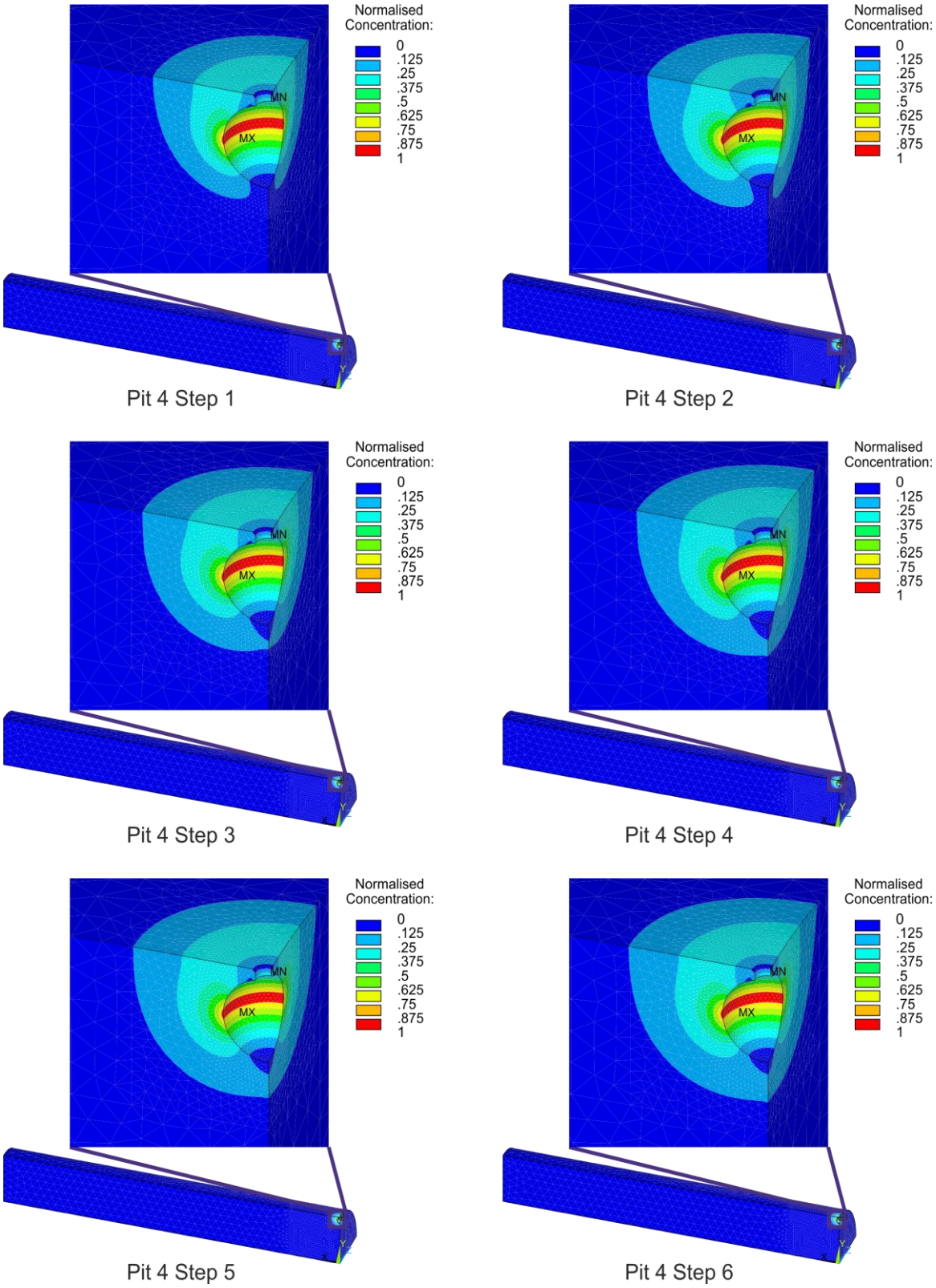

Figure 5.124: Normalised hydrogen concentration for subsurface pit 4.

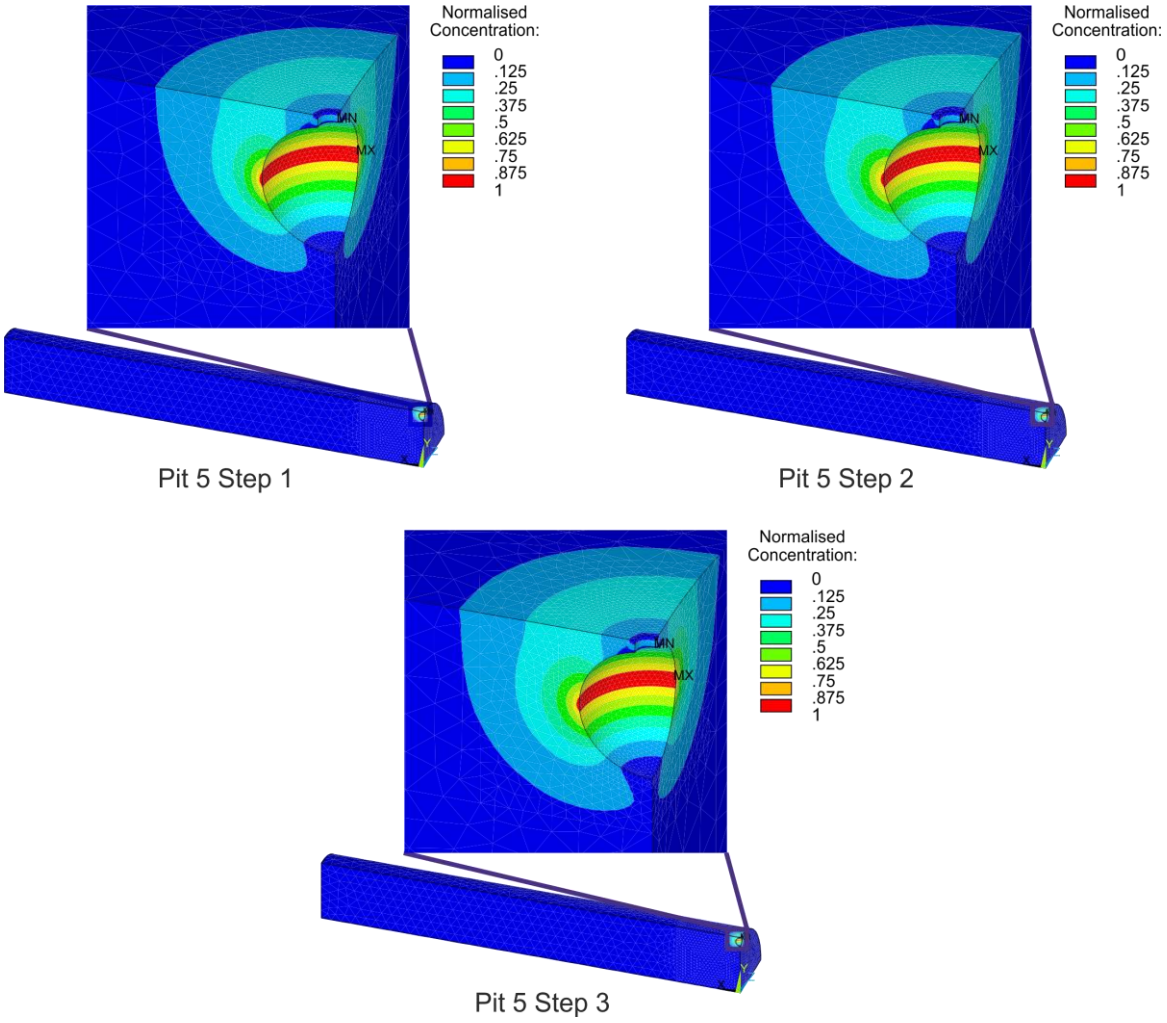

Figure 5.125: Normalised hydrogen concentration for subsurface pit 5.

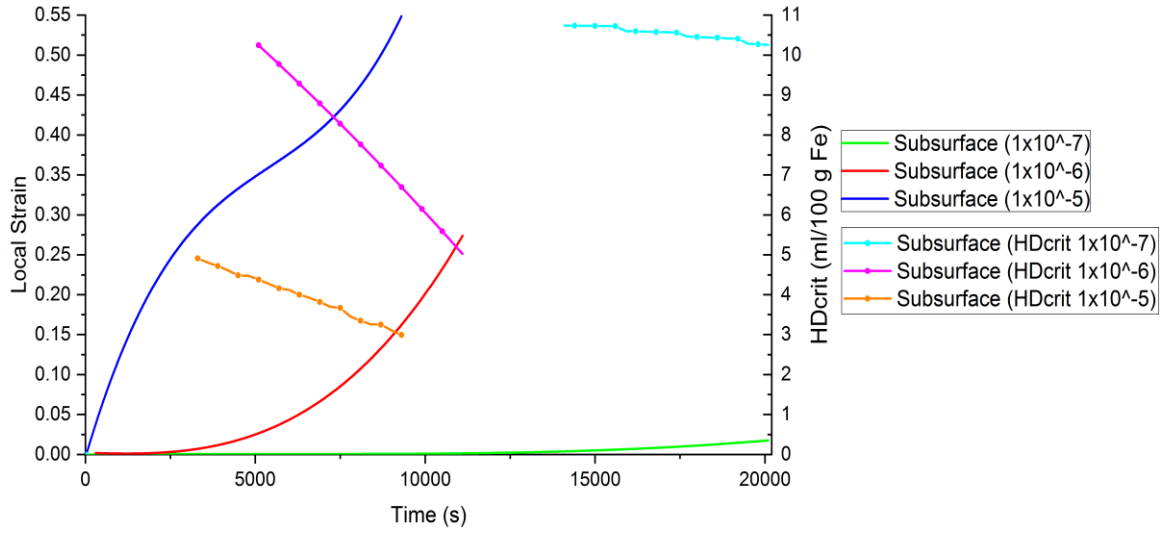

Figure 5.126: Graph of local strain vs time and HDcrit vs time for subsurface pit.

From the present state of investigating combining the structural and diffusion analyses, it can be summarised that:

- *As shown for the shallow wide pit, the shallower the pit the higher the risk of the critical hydrogen concentration being located where the highest maximum total strain in x-direction is also located. However, the deeper the pit then the larger the highest maximum total strain in x-direction values are and in turn, these require a lower critical hydrogen concentration to initiate HAC. This may influence the location of crack initiation as it is the combination of these two factors that determine the crack initiation point which may not occur at the region of highest strains or highest hydrogen concentration, but where the combination of these two factors provide the ideal conditions for crack initiation.*
- *As expected from such consideration, the subsurface pit in Figure 5.126 has the highest local strain values for all strain rates. Correspondingly, this pit geometry also has the lowest HDcrit values. The shallow wide pit has the lowest local strain values, Figure 5.104 and therefor the amount of hydrogen needed in order for HAC to occur is highest for all three pit geometries.*

5.3.5 Approach to Modelling of HAC Initiated in Non-Idealised Pit Geometries

The results mentioned so far are based on 3D idealised pit geometries. However, Jakubowski [302] explains how research was undertaken into the influence of salt water temperature on the corrosion fatigue life of two high carbon steels and it was discovered that the life of the component increased with increasing temperature. This was due to higher temperatures caused hemispherical shaped pits to form and these were less sharp than at lower temperatures. Additionally, at higher temperatures the hydrogen diffusion coefficient is also higher, and the hydrogen produced in the pit is not only absorbed faster but also diffuses through the material faster. Jakubowski also notes that the local stress concentration of a pit is determined by the curvature of the pit strictly in the area where the crack is initiated. Research into the life span of specimens with more smooth pits was also noted and the life span was found to be extended by 50% than those with rough or unpolished pits.

A first approach to determine critical conditions for HAC in non-idealized pit geometries has been carried out within this work [303]. For this approach, asymmetric pit shapes based on pit geometries in the ASM-Handbook [8] have been modelled two-dimensionally, in particular, because such geometries are much more difficult to mesh in respective FE

software. The pit geometries selected were (b), elliptical, (d) subsurface and (e) undercutting from Figure 2.37.

Pit geometry (b) was chosen as this is one of the most commonly modelled pit geometries However an idealised version of this pit is normally modelled and is not very applicable to real life applications. Therefore, a more realistic geometry was created for this work.

Pit geometry (d) was chosen as this pit geometry was determined to have the highest probability of crack initiation occurring subsurface close to the pit mouth region. This is due to the change of geometry in this region which may lead to a build-up of strain in this region. This pit was modelled to investigate if the region near the pit mouth or the pit bottom is the area where crack initiation may occur.

Pit geometry (e) was chosen due to the presence of two pit bottoms in this geometry. This geometry may lead to two areas of high strain concentrations and the interaction between these regions may have an impact on the location of crack initiation and also on the time taken for crack initiation to occur. The three pit geometries used in this work are shown in Figure 5.127.

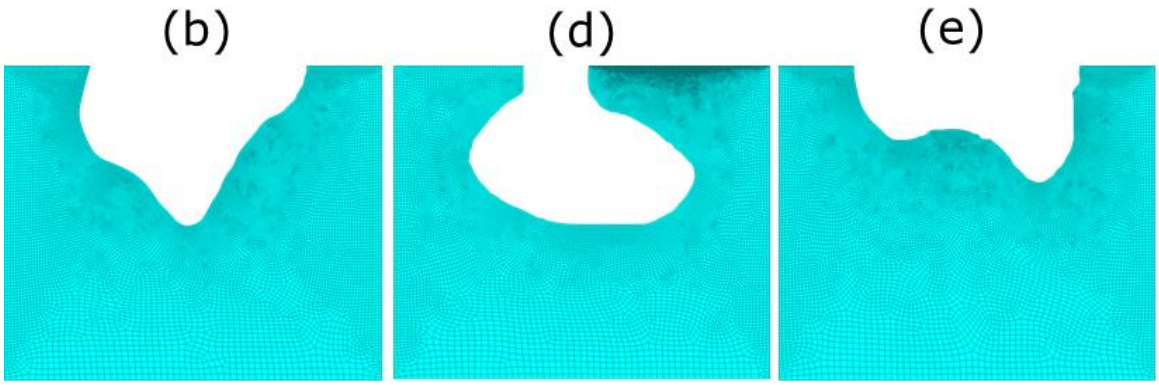

Figure 5.127: The three pit geometries used in the mentioned work and the mesh used in the simulations in the area of interest around the three different pit geometries [303]

The local microstructure selected is the same SMSS homogeneous martensite used in this work. Similar to the work described above, the same bilinear stress strain curves, Figure 4.1 and assumptions, including simulations carried out at room temperature, were also applied to such 2D models. The boundary conditions, element type, model setup are outlined already elsewhere [303] and are briefly summarised here:

Various different boundary conditions with respect to hydrogen entering the material were modelled, which were located on the top surface only, in the pit only, on the top surface and in the pit, from the side of the model and finally from the bottom of the model, as shown in Figure 5.128.

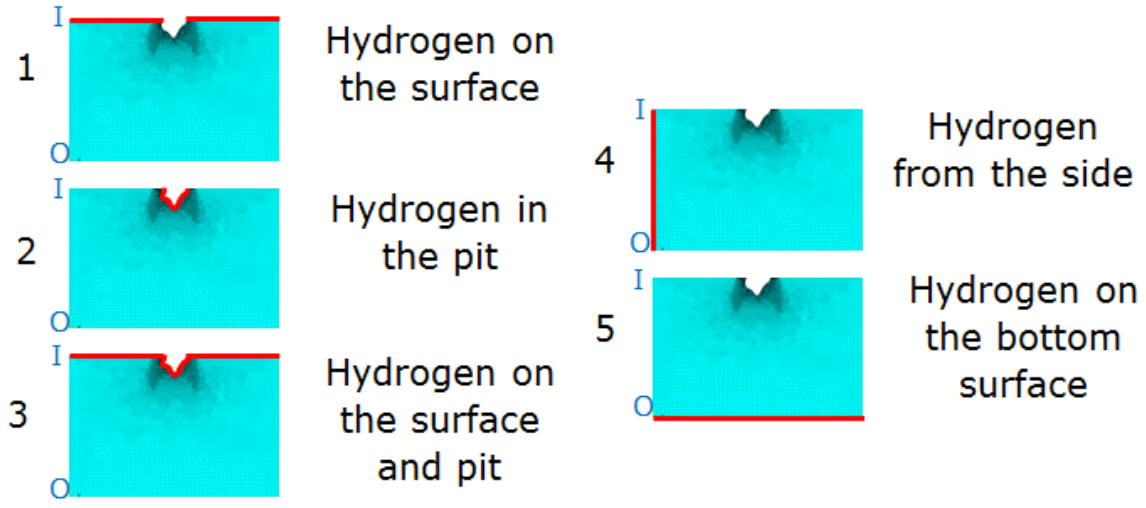

Figure 5.128: Boundary conditions 1 – 5 applied to the model in [303].

The numerical simulation process was divided into four stages- model generation, simulating total true mechanical strain, simulating the hydrogen diffusion and finally, calculating the normalised critical hydrogen diffusion criteria. An example of all four simulation steps for calculating crack initiation in the HAZ, at 100% of yield with a hydrogen concentration of 10 ml·(100gFe)$^{-1}$ applied as a subsurface concentration are shown in Figure 5.129. These results are for a hydrogen concentration applied to the pit only, which is the region which contains the location of the highest total true mechanical strain. This boundary condition produces the same results as the surface and the pit boundary condition due to the hydrogen being applied to the pit area in both models,

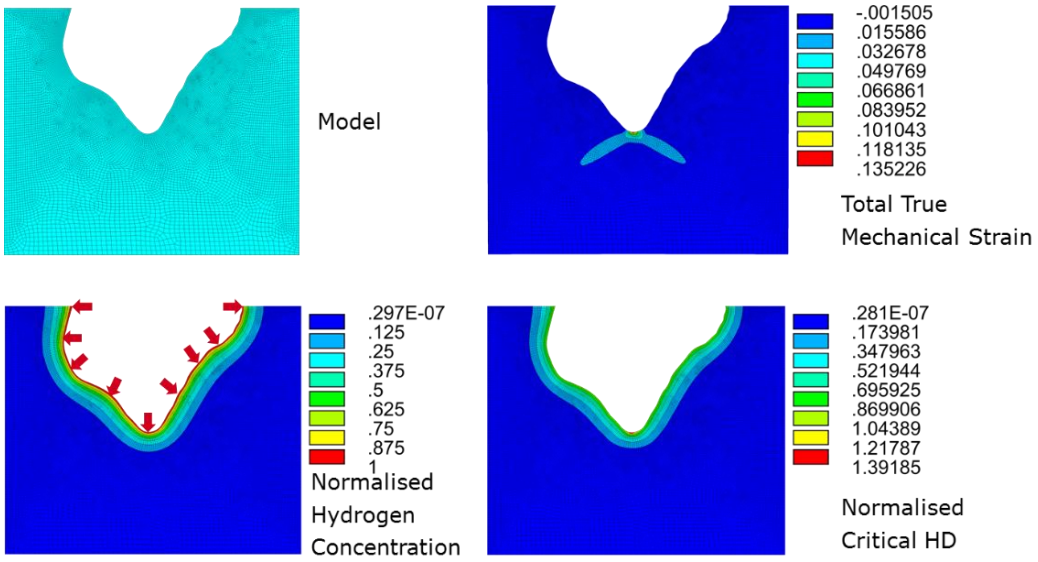

Figure 5.129: Results for the four stages in the simulation process for pit diffusion in the HAZ, at 100% of yield with an applied hydrogen concentration of 10 ml·(100gFe)$^{-1}$, from Madigan et al. [303].

The normalised crack criteria for the five different boundary conditions shown in Figure 5.128 for the HAZ, at 100% of yield with a hydrogen concentration of 10 ml·(100gFe)$^{-1}$ are shown in Figure 5.130. As the cracking criteria are normalised, (the local value of hydrogen diffusion (HD) divided by the critical value of HD, depending on the local strain according to Equations (3.1) and (3.2)) the values range from 0 to 1, with 1 being crack initiation. In order to depict the normalised criteria in the model and show the critical areas, the normalised criteria were applied as a load (temperature) using the element plane77 and the thermal module in ANSYS. Therefore, all the required thermophysical material properties were set to 1 and was solved by applying a load (temperature) to each node in the model. The time step where the combination of strains and hydrogen concentration combined to produce crack initiation for all models was time step 1. This method was only applied to the nodes and elements in the area of interest. This results in a colour print of the critical areas in the model. Cracking was not simulated here, only the area where crack initiation is most likely to occur was determined, as before cracking can be accurately modelled, the conditions which result in crack initiation must first be determined.

It can be seen that crack initiation would begin in boundary conditions 2 and 3 earlier than in boundary condition 1, as this has a lower normalised crack criteria value due to the longer time taken for the hydrogen to diffuse to the area of highest total mechanical strain.

When hydrogen is applied to boundary conditions 2 and 3, failure occurs instantly as the node with the highest strain value is located in this region. This is not true to real life as hydrogen uptake is not an immediate process but a chemical process which occurs over a certain amount of time, gradually building up. If this model was simulated using a gradual increase of hydrogen concentration, then this would be more accurate.

Boundary conditions 4 and 5 in Figure 5.128 show that cracking would not occur for a simulation time of 600,000 seconds with these boundary conditions and a hydrogen subsurface concentration of 10 ml·(100gFe)$^{-1}$ in the HAZ. This is due to the source of the hydrogen being located at the side or bottom of the model, which is significantly further away from the area of the interest, the pit bottom.

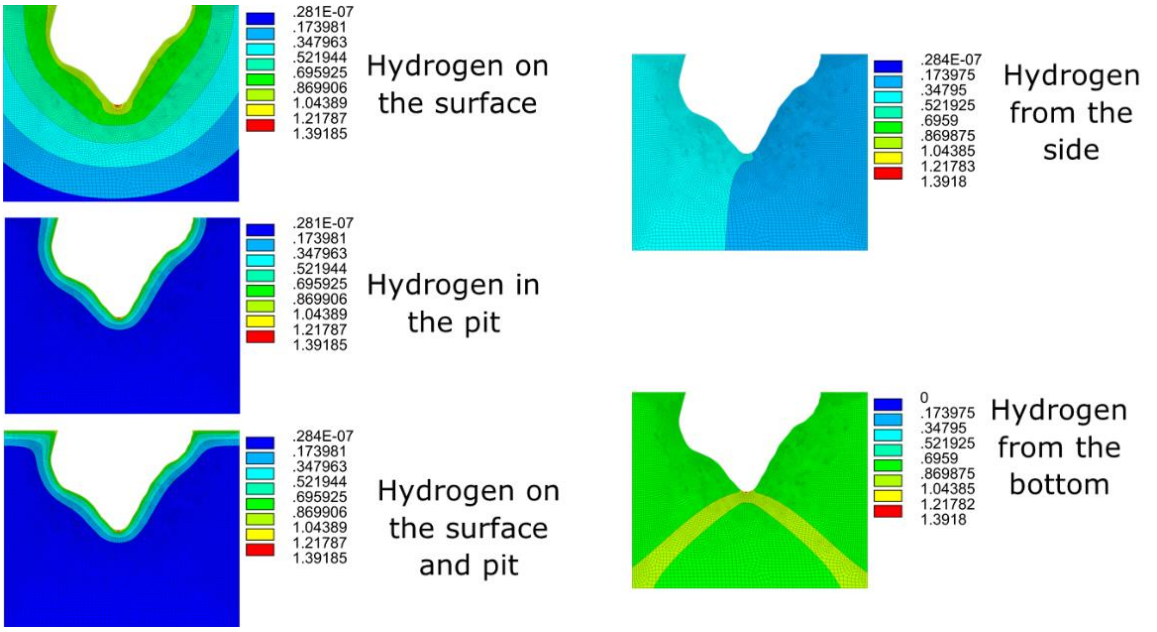

Figure 5.130: Results for five different boundary conditions used in the simulation process in the HAZ, at 100% of yield with a hydrogen concentration of 10 ml·(100gFe)$^{-1}$ [303].

As mentioned previously, three different pit geometries have been investigated, pit geometries “b”, “d” and “e” according to Figure 2.37. The next step of the simulation process was to apply the same loading conditions and hydrogen subsurface concentrations to the pit geometries “d” and “e”, Figure 5.131.

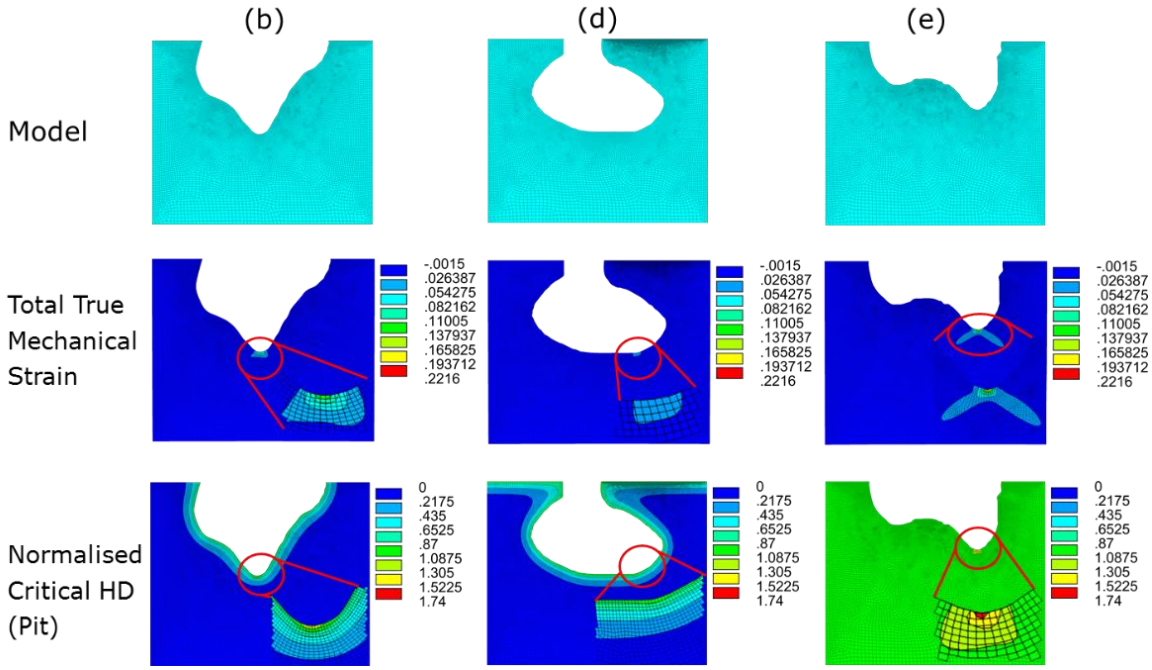

Figure 5.131: Results for the three different pit geometries used in the simulation process in the HAZ, at 100% of yield with a hydrogen concentration of 10 ml·(100gFe)$^{-1}$ applied to the pit, from Madigan et al. [303].

Figure 5.131 gives an overview of the results for all three different pit geometries. The area of highest strain was located in the pit bottom, which is also where the crack criteria is reached, with a hydrogen subsurface concentration of 10 ml·(100gFe)$^{-1}$ applied to the pit only, in the HAZ, at a load of 100% of yield. The same contours were used for displaying the criteria in order to directly compare the three different geometries. For pit geometry “b” the highest normalised critical HD value is 1.39185, for pit geometry “b” is 1.07029 and for pit geometry “e” is 1.74279.

It can also be seen in Figure 5.131 that pit geometry “e” has the highest normalised critical hydrogen diffusion value and pit geometry “d” has the lowest. Therefore, it can be determined that for a hydrogen subsurface concentration of 10 ml·(100gFe)$^{-1}$ applied to the pit only, in the HAZ, at a load of 100% of yield that pit geometry “e” is the pit geometry most susceptible to HAC.

This work shows that the shape of the pit has a significant effect on the location where a crack will initiate in a pit and when this might occur, for the various geometries investigated. This was also investigated by Paneda and Niordson [304] who modelled a 2D plate with pre-existing defects- a notch with root radius 2 and two hemispherical pits, one on the bottom surface and one in the middle of the plate. These pit geometries were idealised pit geometries but were all located on the same plate so the most severe or critical pit geometry would exhibit a crack first. A uniform displacement of 0.0416 µm/s was then applied to the end of the plate and an initial hydrogen concentration of 1 wt ppm was applied throughout the specimen. The crack was found to initiate at the bottom of the notched defect and propagate through to the defect located in the centre of the plate. The crack then continued and merged with a crack which initiated at the smaller surface defect and through cracking occurred. The location of crack initiation in the research by Paneda and Niordson [304], at the bottom of the notched specimen, was the same location as for the pit geometries in Figure 5.131.

From the present state of investigating modelling of HAC initiated in non-idealised pit geometries, it can be summarised that:

- *The location of hydrogen entry into the model is important as cracking will initiate quicker if the hydrogen source is a short distance from the area of highest strains, which in most cases for 2D models will be the pit bottom.*
- *It was found that pit geometry “e” is the pit geometry where cracking will most likely occur under the loading conditions described in this work. The location of this cracking will occur in the bottom of the pit for 2D models. This is due to the highest strain being present in this pit geometry, in comparison with the two other*

geometries, which results in a low critical hydrogen concentration required for crack initiation.

- *However, it has been previously mentioned in this results section that the location of crack initiation when various pit geometries are modelled in 3D and subjected to a normalised hydrogen concentration, may be located at the pit mouth or walls and not at the pit bottom.*

6 Conclusions

From the results outlined in the previous section, the following conclusions can be drawn:

General Structural Analysis

The ultimate strength of a material is most vulnerable to the presence of corrosion pits. This is observed in this current work as the maximum total true strain in x-direction for the 2D and 3D pits subjected to a uniaxial loading condition, Table 5.3 and Table 5.19, are significantly higher than the maximum total true strain in x-direction in the pits when a bending loading condition is applied, Table 5.9 and Table 5.28.

2D Structural Analysis

1) It was found that the plane strain behaviour in the 2D modelling most resembles the maximum total strain in x-direction results from the 3D model, when all element behaviour types were investigated, Table 5.20. The pit geometry modelled for this investigation was the reference pit, which was created specifically for this work and can be seen in Figure 3.2. It is therefore suggested, to use the plane strain instead of plane stress element behaviour type to achieve results for the maximum total strain in x-direction for the pit geometries modelled in this research.
2) For 2D simulations for both UA and bending, for HAZ and BM, the location of the highest strained regions for all the pit geometries occur at the bottom of the pits.
3) The most important geometric aspect of the pit for a 2D uniaxial x-direction displacement was found to be the depth of the pit, with a shallow pit producing lower maximum total true strain in x-direction values in pits. However, for a 2D bending load, the pit mouth diameter was found to be the most important geometric aspect of the pit, with a larger pit mouth diameter producing lower maximum total true strain in x-direction values in pits. The maximum strains in x-direction for the various pit geometries, sorted from lowest to highest were created in Table 5.3 and Table 5.9.
4) The 2D pit geometry also plays an important role in the magnitude of the maximum total true strain in x-direction values in the pit as it seems that the smoother the transition from the pit sides to the pit bottom, the lower the maximum total true strain in x-direction values are in the pits.
5) The presence of the various pit geometries causes a reduction in the load carrying capacity of the material, for both uniaxial and bending loading conditions. All pits caused a reduction in the load carrying capacity, but again the geometry of the pit depends on the severity of this reduction as smooth shallower pits were able to

withstand more load than sharp notched pits before failure, for both loading conditions. It was found that the repassivation pit is the most detrimental pit geometry that may be found during inspections and should be avoided under all circumstances.

3D Structural Analysis

6) The location of the maximum total true strain in the x-direction for the 66% loaded specimens for both uniaxial and bending loading conditions, are located more towards the pit mouth region than the 100% loaded specimens. This indicates that the pit region most susceptible to HAC changes with changing load.
7) The location of the highest maximum strains in x-direction for the bending loading condition occur more towards the pit mouth than for the uniaxial loading condition. Therefore, if HAC were to occur under a bending loading condition the crack might initiate more toward the pit mouth than further along the pit wall, as for the uniaxial loading condition.
8) Similar to the 2D UA loading condition, for the 3D UA loading condition the depth of the pit is again the most important geometric aspect of the pit, with a shallow pit producing lower maximum total true strain in x-direction values in the pits. For a bending load, the pit mouth diameter is the most important geometric aspect of the pit, with a larger pit mouth diameter producing lower maximum total true strain in x-direction values in pits, also for the 3D HAZ bend submodels.
9) The 2D analyses shows that the location of the maximum total true strain in the x-direction occur at the bottom of the pits for all pit geometries. The 3D analyses have a region of high total true strain in the x-direction occurring at the pit bottom and extending up the pit sides to the pit mouth. In these models however, the location of the maximum total true strain in the x-direction for all of the pits do not occur at the bottom of the pits. As the 2D models are lacking the plane perpendicular to the applied load where the maximum total true strains in the x-direction will occur, modelling in 3D produces more accurate information as to the location of the maximum total true strain in the x-direction in the pit geometries.
10) The load carrying capacity of the material with various pits present was found to be higher for the 3D models than the 2D models, resulting in more accurate information for the 3D models. Therefore, for any information on the dependency of mechanical loads with respect to realistic values and on the location in pits, the tables in Section 5.1.2 provide more accurate information. This information is useful to industry and NDT personnel as the pit geometries with the lowest load carrying capacity may need to be monitored or inspected more frequently.

Diffusion Analysis

11) The surface and pit and surface boundary conditions produce similar hydrogen distributions after a certain depth has been reached. This is due to the hydrogen applied to the pit bottom initially being the main source of hydrogen recorded for the surface and pit boundary condition in the vicinity of the pit bottom. The hydrogen applied to the surface then becomes the predominant hydrogen source recorded in the vicinity of the pit bottom, when the surface hydrogen has diffused to the same depth as the pit hydrogen source. As diffusion is time based, the shallower the pit the less time it takes for the hydrogen to diffuse from the surface to the region below the bottom of the pit.
12) The pit depth also influences the hydrogen diffusion as the surface and pit, and surface boundary conditions show the less deep shallow wide pit has consistently higher values than the other two pits. However, when pit depth is no longer a factor, as for the pit boundary condition, the curvature of the pit geometry is the most important factor. The pit hydrogen source diffuses into the material in accordance with the pit geometry. Therefore, for the “flatter”, less steep transition from pit bottom to pit sides in the shallow wide pit, the hydrogen applied to the pit diffuses in a more vertical direction than the other two pit geometries. Therefore, if HAC were to occur then a hydrogen concentration is already present in the region beneath the pit bottom. If the crack initiates on the side of the pit and travels through the material it will reach this hydrogen concentration and may propagate faster as hydrogen no longer needs to diffuse to the crack tip.
13) The pit mouth radius has an effect on diffusion of hydrogen through a material, as shown for the pit varying hydrogen boundary condition. The larger the pit mouth radius the larger the surface area for a normalised hydrogen concentration of 1 resulting in greater diffusion of hydrogen through the material and higher values in all three curves. As the highest concentration occurs at the middle of the pit and the highest total true strains in x-direction for most of the pit geometries occur near the pit mouth, these two regions may cause a crack to initiate at or near the pit mouth as the presence of hydrogen causes crack initiation at lower strains

Combined structural and diffusion analysis

14) From the graphs in Figure 5.104, Figure 5.115 and Figure 5.126 the critical hydrogen concentration for the corresponding local strain and pit geometry can be determined in order to prevent HAC. The minimum allowable hydrogen concentration for the various pit geometries for the local strains mentioned in this work are then known. This is important information as during inspections if a pit is

found then the global hydrogen concentration present can be recorded and monitored.

15) If hydrogen enters the model the location of entry is important as cracking will initiate quickly if the source of hydrogen is a short distance from the area of highest strains, which in most cases for the 2D model will be the pit bottom but for 3D the location is close to the pit mouth.
16) For the 2D analysis it was determined that pit geometry “e”, the pit geometry with two pit bottoms from Figure 5.127, is the pit geometry most likely to initiate cracking under the loading conditions described, which will occur in the bottom of the pit. This is as a result of the highest strain being present in this geometry in comparison with the two other geometries investigated, which results in a low critical hydrogen concentration needed for crack initiation.

7 Perspectives

The perspectives resulting from the present work have been divided into future research to be performed with respect to the pitting corrosion process and with respect to the three local influences on HAC:

Pitting Corrosion Process

In this work pit initiation and growth were modelled using times provided by literature. The process of pitting corrosion could be modelled more accurately if the electrochemistry of the pit was also considered. Such a model of the corrosion process has been developed by Hoffmeister and Böllinghaus. This model could be adapted and included in the simulation from Step 3 in this work to provide a more accurate model which includes the electrochemistry of the pitted region.

Pit geometry

It is however not possible to measure the local strain in a pit, especially on the internal wall of an in service pipeline. The tension forces are measured in a pipeline during pipelaying to ensure they are within the design requirements, but once the pipeline is laid there is no inspection method to accurately record the local, or global, strains present in the pipeline. Also, is not possible to measure the hydrogen concentration in a pit during inspections.

It is likewise difficult to get an exact image of the geometries of corrosion pits during inspections, but the width, length and depth of pits on the internal surface of a pipeline can be recorded during pigging inspections. From this information an estimation of the pit geometry can be made, especially if it is shallow wide (the depth is less than the width) or an ellipse shape (if the depth is greater than the width). The subsurface pit geometry is more difficult to detect, and it would be required to know if the metal cap is still in place over the pit mouth, which gives the subsurface pit geometry the narrow pit mouth diameter. By estimating the pit geometry however, it may be possible to detect if increased inspection and monitoring activities need to be undertaken, especially if the subsurface pit geometry is detected. It is currently very difficult to detect if corrosion or defects are present on the outside of offshore pipelines. A company called Halfwave based in Oslo, Norway has developed a remote vehicle operated mountable inspection tool, called ARTEMIS, for external inspections of subsea assets including rigid and flexible pipelines, flowlines and risers. A major advantage of this new technology is that the coating does not need to be removed for inspection. This may be used to detect if pitting corrosion is present on the outside of the pipelines and risers, which may be as a result of the cathodic protection not functioning as required. ARTEMIS uses acoustic inspecting technology which is able to

determine wall thickness loss and full geometry survey in previously unpiggable pipelines. Using such technology, the geometries of pits present on the outside of offshore pipelines may also be determined during inspection.

The pit geometry is an important factor in determining the possible location of HAC in addition to the local chemistry inside the pit, leading to hydrogen uptake in the pit. Turnbull [298] discovered that the growing pit also has a critical role. It was found that the growing pit generates a dynamic plastic strain and as HAC is dominated by the presence of high plastic strains, the growing pit must also be considered as a factor which causes high strains. Xiang et al. [274] determined that stress analysis of pits has been studied by many researchers but the analysis of plastic strains in pits is explored relatively little. Xiang stated that that dynamic plastic strain is a major condition of stress corrosion crack nucleation and that the growth of pits can be linked to plastic strain.

To measure real pit geometries is a necessary item for future work. However, not all of the occurring pit geometries in reality can be modelled. Numerical modelling of free pit growth dependent on the electrochemical conditions in the pit is only one of the most important next steps.

Additionally, when viewed from the top of the modelling described in this work, it becomes clear that all pit geometries investigated, apart from the notched pit, have a circular pit mouth. However, altering the pit mouth geometry to a more elliptical shape, as represented by the blue, purple and green ellipses in Figure 7.1, may influence the location and magnitude of maximum total true strain in x-direction in the pits. Changing the geometry to a diamond shape, such as after a hardness test or as a result of a dropped object, and loading the specimen may also influence the location and magnitude of maximum total true strain in x-direction in the pits.

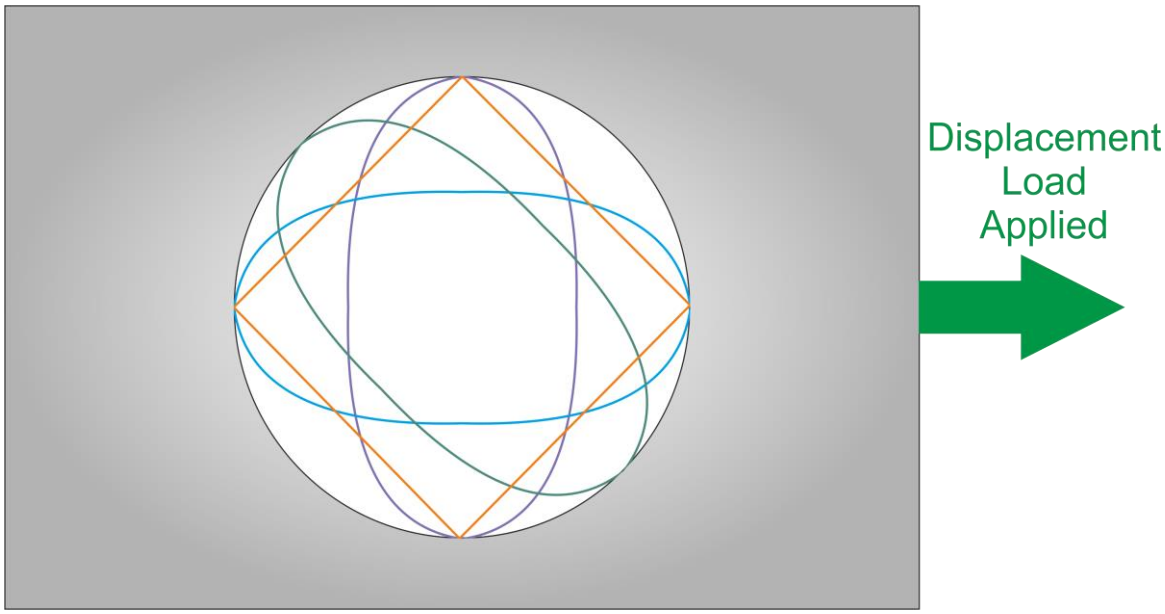

Figure 7.1: Alternative pit mouth geometries.

The pit geometries used in this work are based on those from the ASM corrosion handbook [8], but are smooth, idealised versions of these pits. Mai et al. [12] investigated more “true to life” pit geometries with rough sides in 2D. Eksi [272] then investigated these pit geometries but in 2D instead of 3D. These models could be created, but with the addition of hydrogen and a uniaxial load applied, such as in the third step of this work.

Single pits are modelled in this work, but pitting corrosion normally consists of numerous pits. Therefore, modelling various pit geometries at various locations on the submodel would be more accurate for modelling a real life SSRT with a specimen exposed to a bulk solution. The interaction of two pits located in close proximity to each other and the effect the locations of these pits have on each other for all three stages of this work could also be modelled. This may also help NDT operators, as knowing the interaction between pits may assist in predicting when or if failure might occur, and therefore is an important next step in the continuation of this work.

Local Hydrogen Concentration

If the medium flowing through the pipeline contains H_2S then regular samples must be taken to determine the H_2S content in the medium. This is a requirement to know when selling oil or gas to a supplier. Regular monitoring is also a requirement as it must be verified that the H_2S content is within the allowable limits. From this information the partial pressure of hydrogen can be calculated to determine what percentage of the medium contains hydrogen. It is also possible to calculate the amount of hydrogen present locally in a pit, as undertaken by Hoffmeister. This information can be adapted and included in future models in order to provide more accurate hydrogen distribution models.

Local Microstructure

The effect the combined local mechanical load and hydrogen concentration has on the microstructure could also be investigated. This could be achieved by creating a microscale model and recording the local strain and hydrogen concentration at a certain region of the submodel. These values can then be transferred to the microscale model. A similar methodology as used in this work to transfer loading conditions from quarter or one eight models etc., Section 5.1, can also be applied here.

Creation of a microscale model and applying the various properties, loading conditions and hydrogen from the submodel to the microscale model would give an overview of the three key factors effecting HAC, Figure 2.11 in Section 2.2.3. Various orientations of the microstructure could also be investigated, as the presence of the lath regions in the martensitic microstructure may influence diffusion of hydrogen through the microstructure.

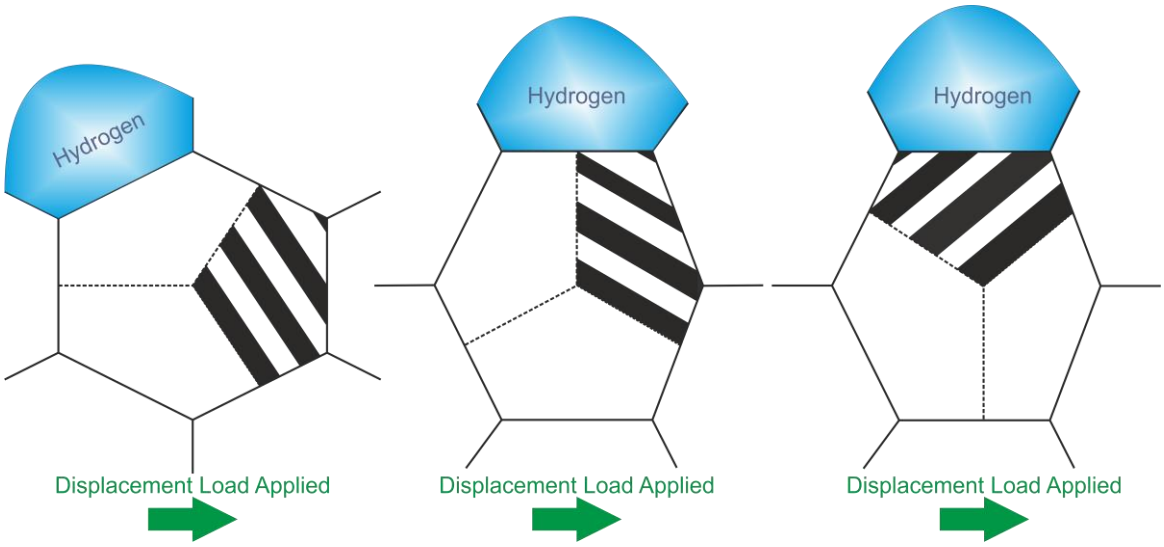

Figure 7.2: Different martensitic microstructure orientations and hydrogen application.

SMSS is a material used in offshore applications, as explained in Chapters 1 and 2, which is a homogeneous material. Duplex stainless steels (DSS) are also used in offshore applications, but are a two phase microstructure material. Therefore, the models and simulations created for this work may be altered to include an inhomogeneous material, such as DSS. This microstructure was previously investigated by Mente [305], Figure 7.3.

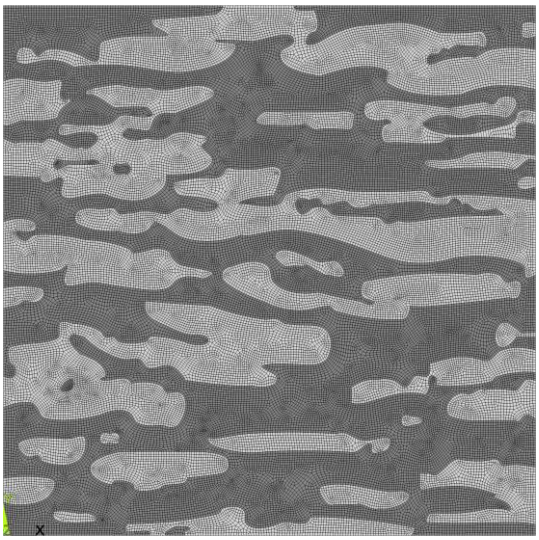

Figure 7.3: Duplex stainless steel microstructure used in previous numerical simulations by Mente [305].

Local Mechanical Load

For HAC to occur there must be a combination of large strains and the presence of hydrogen, which can result in fracture, such as at a notch root, and Sofronis and Lufrano [306] observed cracking to initiate in this region. Anantha et al. [271] found that mobile hydrogen easily follows growing cracks and can accelerate crack growth. As strain fields are located at crack tips, the presence of a highly strained region in a pit provides preferential sites for hydrogen absorption and may result in trapped hydrogen, which causes embrittlement. The presence of hydrogen increases the defect density in the microstructure and impedes dislocation mobility, but also increases stored energy which facilitates brittle film rupture which encourages anodic dissolution. The corrosion and local breakdown potentials were found to reduce when hydrogen uptake occurred. The presence of hydrogen impedes passivation occurring in stainless steels and the surface oxide film is altered. This presence of hydrogen was found to cause acceleration in both corrosion and cracking processes, which Anantha et al. [271] found to be much more pronounced at higher loads.

The loading conditions investigated for this work were uniaxial and bending. A combination of these loading conditions is however also possible as pipelines with long free spans may experience both uniaxial and bending loading conditions. Applying these multiaxial loading conditions may provide more accurate information of the loading conditions experienced by in service pipelines and should be considered in future research.

References

[1] L. Calabrese, M. Galeano, E. Proverbio, D.D. Pietro, F. Cappuccini, A. Donato, Monitoring of 13% Cr martensitic stainless steel corrosion in chloride solution in presence of thiosulphate by acoustic emission technique, Corrosion Science 111 (2016) 151-161.
[2] L. Smith, M. Celant, Martensitic stainless steels in context, Supermartensitic 2002 (2002) 14-20.
[3] G. Cumino, A. Poli, T. Ono, S. Hashizume, K. Yamazaki, L. Scoppio, Supermartensitic 13% Cr large diameter seamless pipes: Mechanical corrosion and weldability properties, Latin American applied research 32(3) (2002) 215-219.
[4] L. Jemblie, V. Olden, P. Mainçon, O.M. Akselsen, Cohesive zone modelling of hydrogen induced cracking on the interface of clad steel pipes, International Journal of Hydrogen Energy 42(47) (2017) 28622-28634.
[5] C.M.J. Lee, R.; Morgan, P.; Weatherhead, R, International Experiences with Cathodic Protection of Offshore Pipelines and Flowlines, TWI, 207.
[6] K. Leinum, B.H. Leinum, E.B. Heier, A. Serednicki, O.E. Gjørv, T. Myre, B. Søgård, L.H. Moen, B.E. Sogstad, M.O. Saugerud, Material Risk– Ageing offshore installations, DNV, 2006.
[7] E. Hörnlund, Sævik, Olystein, Hinderaker, Rolf H., Ersdal, Gerhard, Ageing of Materials, (48227) (2008) 285-292.
[8] A. International, ASM Handbook- Corrosion, ASM International1992.
[9] M.A.O. Alum, Localized Pitting Corrosion of Super Duplex Stainless Steel in a Sea Water Application: Practical Case of When Chlorination was Not to Blame, SPE Nigeria Annual International Conference and Exhibition, Society of Petroleum Engineers, Lagos, Nigeria, 2017, p. 9.
[10] G. Frankel, Pitting corrosion of metals a review of the critical factors, Journal of the Electrochemical society 145(6) (1998) 2186-2198.
[11] J. Paik, J. Lee, M. Ko, Ultimate compressive strength of plate elements with pit corrosion wastage, Proceedings of the Institution of Mechanical Engineers, Part M: Journal of Engineering for the Maritime Environment 217(4) (2003) 185-200.
[12] W. Mai, S. Soghrati, A phase field model for simulating the stress corrosion cracking initiated from pits, Corrosion Science 125(Supplement C) (2017) 87-98.
[13] W. Mai, S. Soghrati, R.G. Buchheit, A phase field model for simulating the pitting corrosion, Corrosion Science 110(Supplement C) (2016) 157-166.
[14] J. Hoehbusch, S. Bucher, H. Haensel, J. Scholten, Evaluation of the fatigue strength of multiphase pump components under corrosive conditions using a short crack fracture mechanics approach, Engineering Failure Analysis 47 (2015) 265-272.
[15] T. Boellinghaus, E. Viyanit, Numerical Simulation of Hydrogen Assisted Cracking in Girth Welds of SMSS Pipelines - Report I, in: H.C. (Ed.) (Ed.), Mathematical Modelling of Weld Phenomena 6, Maney Publishing, Seggau, Austria, 2002, pp. 839-855.
[16] E. Viyanit, Numerical simulation of hydrogen assisted cracking in supermartensitic stainless steel welds Fachbereich Maschinenbau, Helmut-Schmidt-University/University of the Federal Armed Forces Hamburg, Hamburg, Germany, 2005, p. 170.
[17] J. Raoul, Use and application of high-performance steels for steel structures, Iabse2005.
[18] C.O.A. Olsson, D. Landolt, Passive films on stainless steels—chemistry, structure and growth, Electrochimica Acta 48(9) (2003) 1093-1104.
[19] H. Bhadeshia, R. Honeycombe, Steels: microstructure and properties, Butterworth-Heinemann2017.
[20] P. Monnartz, Beitrag zum Studium der Eisen-Chromlegierungen unter besonderer Berücksichtigung der Säurebeständigkeit (Iron-chromium alloys with special consideration of resistance to acids), Metallurgie 8 (1911).
[21] EN-10020, Definition and classification of grades of steel, 2000.
[22] J.R. Davis, Alloy digest sourcebook: stainless steels, ASM international2000.

[23] K.H. Lo, C.H. Shek, J.K.L. Lai, Recent developments in stainless steels, Materials Science and Engineering: R: Reports 65(4) (2009) 39-104.
[24] D.P. Koistinen, R.E. Marburger, A general equation prescribing the extent of the austenite-martensite transformation in pure iron-carbon alloys and plain carbon steels, Acta Metallurgica 7(1) (1959) 59-60.
[25] P. Sofronis, I. Robertson, Viable Mechanisms of Hydrogen Embrittlement—A Review, AIP Conference Proceedings, AIP, 2006, pp. 64-70.
[26] J.C. Lippold, D.J. Kotecki, Welding metallurgy and weldability of stainless steels, Wiley-Interscience2005.
[27] Y. Mine, K. Hirashita, H. Takashima, M. Matsuda, K. Takashima, Micro-tension behaviour of lath martensite structures of carbon steel, Materials Science and Engineering: A 560 (2013) 535-544.
[28] J. Morris, C. Kinney, K. Pytlewski, Y. Adachi, Microstructure and cleavage in lath martensitic steels, Science and Technology of Advanced Materials 14 (2013) 014208.
[29] L.a.C. Smith, M, Martensitic stainless steel flowlines – Do they pay?, Supermartensitic Stainless Steels, Brussels, Belgium, 1999, p. 66.
[30] T.G. Gooch, Heat treatment of welded 13%Cr-4%Ni martensitic stainless steels for sour service, 1995.
[31] K. Kondo, M. Ueda, K. Ogawa, H. Amaya, H. Hirata, H. Takabe, Y. Miyazaki, Alloy design of super 13 Cr martensitic stainless steel(development of super 13 Cr martensitic stainless steel for line pipe-1), Supermartensitic Stainless Steels'99 (1999) 11-18.
[32] C. Barbosa, I. Abud, Recent developments on martensitic stainless steels for oil and gas production, Recent Patents on Corrosion Science 3(1) (2013) 27-38.
[33] G. Rabensteiner, J. Toesch, E. Folkhard, E. Perteneder, M. Schabereiter, Metallurgie der Schweissung nichtrostender Stähle, Springer Vienna2017.
[34] S. Marcelin, N. Pébère, S. Régnier, Electrochemical characterisation of a martensitic stainless steel in a neutral chloride solution, Electrochimica Acta 87 (2013) 32-40.
[35] L. Schäfer, Influence of delta ferrite and dendritic carbides on the impact and tensile properties of a martensitic chromium steel, Journal of Nuclear Materials 258-263 (1998) 1336-1339.
[36] S.S.M. Tavares, B.B. Almeida, D.A.L. Corrêa, J.M. Pardal, Failure of super 13Cr stainless steel due to excessive hardness in the welded joint, Engineering Failure Analysis 91 (2018) 92-98.
[37] C.T. Kwok, K.H. Lo, F.T. Cheng, H.C. Man, Effect of processing conditions on the corrosion performance of laser surface-melted AISI 440C martensitic stainless steel, Surface and Coatings Technology 166(2) (2003) 221-230.
[38] I. Olefjord, L. Wegrelius, Surface analysis of passive state, Corrosion Science 31 (1990) 89-98.
[39] E. Ladanova, J.K. Solberg, T. Rogne, Carbide precipitation in HAZ of multipass welds in titanium containing and titanium free supermartensitic stainless steels Part 2 – Weld simulation studies, Corrosion Engineering, Science and Technology 41(2) (2006) 152-160.
[40] J.M. Aquino, C.A. Della Rovere, S.E. Kuri, Intergranular corrosion susceptibility in supermartensitic stainless steel weldments, Corrosion Science 51(10) (2009) 2316-2323.
[41] F. Hull, Delta ferrite and martnesite formation in stainless steels, Welding journal 52(5) (1973) 193.
[42] F.B. Neto, A. Garbogini, T. AP, Nitrogen bearing martensitic stainless steels: Microstructure and properties, ISIJ international 36(7) (1996) 840-845.
[43] C.X. Li, T. Bell, Corrosion properties of plasma nitrided AISI 410 martensitic stainless steel in 3.5% NaCl and 1% HCl aqueous solutions, Corrosion Science 48(8) (2006) 2036-2049.
[44] H. Geng, X. Wu, H. Wang, Y. Min, Effects of copper content on the machinability and corrosion resistance of martensitic stainless steel, Journal of Materials Science 43(1) (2008) 83-87.
[45] M.J. Al-Saeedi, D. Al-Enezi, M. Sounderrajan, A.K. Saxena, G.K. Gumballi, D.C. McKinnell, First Implementation of CRA Casing in Sour HPHT Reservoirs in Deep Wells

in Kuwait, North Africa Technical Conference and Exhibition, Society of Petroleum Engineers, Cairo, Egypt, 2013, p. 12.
[46] Y. Al-Salali, H. Al-Bader, V.S. Duggirala, A. Manimaran, S. Packirisamy, A. Al-ibrahim, A. Rajkhowa, Challenges in Testing and Completion of Highly Sour HPHT Reservoir in the State of Kuwait, SPE Middle East Oil and Gas Show and Conference, Society of Petroleum Engineers, Manama, Bahrain, 2013, p. 9.
[47] Y. Shumakov, A. Williams, G. Hetherington, B. Davidson, T.M. Whittle, A New Benchmark in HPHT Operations: Safe and Successful Well Testing On the Jackdaw Gas Condensate Field in the North Sea, UK, SPE Bergen One Day Seminar, Society of Petroleum Engineers, Bergen, Norway, 2014, p. 17.
[48] H.B. Skeels, API 17TR8: HPHT Design Guideline for Subsea Equipment, Offshore Technology Conference, Offshore Technology Conference, Houston, Texas, 2014, p. 13.
[49] N. Sridhar, R. Thodla, F. Gui, L. Cao, A. Anderko, Corrosion-resistant alloy testing and selection for oil and gas production, Corrosion Engineering, Science and Technology 53(sup1) (2018) 75-89.
[50] A.N. MR0175/ISO, Petroleum and natural gas industries — Materials for use in H2S containing environments in oil and gas production — Part 3: Cracking-resistant CRAs (corrosion-resistant alloys) and other alloys, 2015.
[51] L.T. Popoola, A.S. Grema, G.K. Latinwo, B. Gutti, A.S. Balogun, Corrosion problems during oil and gas production and its mitigation, International Journal of Industrial Chemistry 4(1) (2013) 35.
[52] P. Rajeev, A. Surendranathan, C.S. Murthy, Corrosion mitigation of the oil well steels using organic inhibitors–a review, Mater. Environ. Sci 3(5) (2012) 856-869.
[53] W. Graeme, Corrosion protection of metals in marine environment, Metal Corrosion Protection, Chemistry (2010) 2191-1363.
[54] P.R. Rhodes, Environment-Assisted Cracking of Corrosion-Resistant Alloys in Oil and Gas Production Environments: A Review, Corrosion 57(11) (2001) 44.
[55] R. Hill, A.L. Perez, 26 - New steels and corrosion-resistant alloys, in: A.M. El-Sherik (Ed.), Trends in Oil and Gas Corrosion Research and Technologies, Woodhead Publishing, Boston, 2017, pp. 613-626.
[56] K. Kondo, K. Ogawa, H. Amaya, H. Ohtani, M. Ueda, Development of Weldable Super 13Cr Martensitic Stainless Steel For Flowline, The Twelfth International Offshore and Polar Engineering Conference, International Society of Offshore and Polar Engineers, Kitakyushu, Japan, 2002, p. 7.
[57] H. Van der Winden, P. Toussaint, L. Coudreuse, Past, present and future of weldable supermartensitic alloys, Proceedings of Second International Conference of Supermartensitic Stainless Steels, 2002, pp. 3-4.
[58] P. Toussaint, B. Hoerner, V. Ligier, B. Bonnefois, L. Coudreuse, Latest evolutions in material properties assessment of supermartensitic stainless steels as considered by a material fabricator, Stainless Steel World 16 (2004) 19-26.
[59] S. Olsen, Kvaale, P.E., Enerhaug, J., Experience in the use of EFC-17 for qualification of super martensitic stainless steel girth welds, Supermartensitic Stainless Steels, 1999 Belgian Welding Institute Brussels, Belgium, 1999, pp. 84-87.
[60] A. Turnbull, A. Griffiths, Corrosion and Cracking of Weldable 13 Cr Martensitic Stainless Steels: A Review, National Physical Laboratory2002.
[61] O. Akselsen, R. Aune, Cathodic hydrogen effects in welding of supermartensitic stainless steel, International conference: advanced metallic materials and their joining, Bratislava, Slovakia, 2004.
[62] P.D. Bilmes, M. Solari, C.L. Llorente, Characteristics and effects of austenite resulting from tempering of 13Cr–NiMo martensitic steel weld metals, Materials Characterization 46(4) (2001) 285-296.
[63] B. EL, Hydrogen transport in duplex stainless steels, NTNU, 1996.

[64] A. Bojack, L. Zhao, P.F. Morris, J. Sietsma, In-situ determination of austenite and martensite formation in 13Cr6Ni2Mo supermartensitic stainless steel, Materials Characterization 71 (2012) 77-86.
[65] J. Hubáčková, V. Číhal, K. Mazanec, Two-Stage Tempering of steel 13% Cr6% Ni, Materialwissenschaft und Werkstofftechnik 15(12) (1984) 411-415.
[66] V. Olden, C. Thaulow, R. Johnsen, Modelling of hydrogen diffusion and hydrogen induced cracking in supermartensitic and duplex stainless steels, Materials & Design 29(10) (2008) 1934-1948.
[67] A. Dalmau, C. Richard, A. Igual – Muñoz, Degradation mechanisms in martensitic stainless steels: Wear, corrosion and tribocorrosion appraisal, Tribology International 121 (2018) 167-179.
[68] B. Fultz, J. Morris, The mechanical stability of precipitated austenite in 9Ni steel, Metallurgical Transactions A 16(12) (1985) 2251-2256.
[69] D. Frear, J. Morris, A study of the effect of precipitated austenite on the fracture of a ferritic cryogenic steel, J Metallurgical Transactions A 17(2) (1986) 243-252.
[70] A.G.Haynes, Some Factors Governing the Metallurgy and Weldability of 13%Cr and Newer Cr-Ni Martensitic Stainless Steels, Brussels : Belgian welding institute1999.
[71] A.P. Institute, API RP 571: Damage Mechanisms Affecting Fixed Equipment in the Refining Industry, 2003, pp. 30-53.
[72] E. Ladanova, J. Solberg, T. Rogne, Carbide precipitation in HAZ of multipass welds in titanium containing and titanium free supermartensitic stainless steels part 1–proposed precipitation mechanisms, Corrosion engineering, science technology 41(2) (2006) 143-151.
[73] H. Nakamichi, K. Sato, Y. Miyata, M. Kimura, K. Masamura, Quantitative analysis of Cr-depleted zone morphology in low carbon martensitic stainless steel using FE-(S)TEM, Corrosion Science 50(2) (2008) 309-315.
[74] T. Böllinghaus, T. Kannengießer, C. Jochum, I. Stiebe-Springer, Effect of filler material selection on stress strain build up and stress corrosion cracking resistance of welded supermartensitic stainless steel pipes, NACE International, Houston, Texas, 2002.
[75] D.-n. Zou, Y. Han, W. Zhang, X.-d. Fang, Influence of Tempering Process on Mechanical Properties of 00Cr13Ni4Mo Supermartensitic Stainless Steel, Journal of Iron and Steel Research, International 17(8) (2010) 50-54.
[76] S.S.M. Tavares, I.N. Bastos, J.M. Pardal, T.R. Montenegro, M.R. da Silva, Slow strain rate tensile test results of new multiphase 17%Cr stainless steel under hydrogen cathodic charging, International Journal of Hydrogen Energy 40(47) (2015) 16992-16999.
[77] G.F. da Silva, S.S.M. Tavares, J.M. Pardal, M.R. Silva, H.F.G. de Abreu, Influence of heat treatments on toughness and sensitization of a Ti-alloyed supermartensitic stainless steel, Journal of Materials Engineering 46(24) (2011) 7737.
[78] C. Gesnouin, A. Hazarabedian, P. Bruzzoni, J. Ovejero-García, P. Bilmes, C. Llorente, Effect of post-weld heat treatment on the microstructure and hydrogen permeation of 13CrNiMo steels, Corrosion Science 46(7) (2004) 1633-1647.
[79] H. Nakagawa, T. Miyazaki, Effect of retained austenite on the microstructure and mechanical properties of martensitic precipitation hardening stainless steel, Journal of materials science 34(16) (1999) 3901-3908.
[80] M. Chellappan, K. Lingadurai, P. Sathiya, Characterization and Optimization of TIG welded supermartensitic stainless steel using TOPSIS, Materials Today: Proceedings 4(2, Part A) (2017) 1662-1669.
[81] Z. Sebastián, H. Svoboda, M. Ramini, E. Surian, L. A. De Vedia, Improving Supermartensitic Stainless Steel Weld Metal Toughness, 2012.
[82] J.E. Ramirez, Weldability evaluation of supermartensitic stainless pipe steels, 2007.
[83] D. Thibault, P. Bocher, M. Thomas, Residual stress and microstructure in welds of 13%Cr–4%Ni martensitic stainless steel, Journal of Materials Processing Technology 209(4) (2009) 2195-2202.

[84] S. Tavares, C. Ribeiro Rodrigues, J. Pardal, E.s. Barbosa, H. Abreu, Effects of Post Weld Heat Treatments on the Microstructure and Mechanical Properties of Dissimilar Weld of Supermartensitic Stainless Steel, 2014.
[85] H.T. Lee, J.L. Wu, Correlation between corrosion resistance properties and thermal cycles experienced by gas tungsten arc welding and laser beam welding Alloy 690 butt weldments, Corrosion Science 51(4) (2009) 733-743.
[86] J. Aquino, C. Della Rovere, S. Kuri, Localized corrosion susceptibility of supermartensitic stainless steel in welded joints, Corrosion 64(1) (2008) 35-39.
[87] T. Hara, H. Asahi, Conditions under which cracks occur in modified 13% chromium steel in wet hydrogen sulfide environments, J Corrosion 56(5) (2000) 533-542.
[88] M. Goldschmitz, L. Karlsson, R. Pedersen, S. Rigdal, Van Den Broek, Developments in the welding of supermartensitic stainless steels: recent developments and applications, Welding international 18(7) (2004) 543-549.
[89] S.B. Dunkerton, A. Johansen, S. Frich, Radial Friction Welding for Offshore Pipelines, 1987.
[90] C.A. Della Rovere, C.R. Ribeiro, R. Silva, N.G. Alcântara, S.E. Kuri, Local mechanical properties of radial friction welded supermartensitic stainless steel pipes, Materials & Design (1980-2015) 56 (2014) 423-427.
[91] C.A. Della Rovere, J.M. Aquino, C.R. Ribeiro, R. Silva, N.G. Alcântara, S.E. Kuri, Corrosion behavior of radial friction welded supermartensitic stainless steel pipes, Materials & Design (1980-2015) 65 (2015) 318-327.
[92] A. Taha, P. Sofronis, A micromechanics approach to the study of hydrogen transport and embrittlement, Engineering Fracture Mechanics 68(6) (2001) 803-837.
[93] M. Djukic, G. Bakic, V. Šijački-Žeravčić, A. Sedmak, B. Rajicic, Hydrogen Embrittlement of Industrial Components: Prediction, Prevention, and Models, Corrosion 72 (2016) 943-961.
[94] ISO, EN ISO 6520-1:2007 Welding and allied processes - Classification of geometric imperfections in metallic materials – Part 1: Fusion welding, 2007.
[95] N. Narita, C.J. Altstetter, H.K. Birnbaum, Hydrogen-related phase transformations in austenitic stainless steels, Metallurgical Transactions A 13(8) (1982) 1355-1365.
[96] P. Rozenak, R. Bergman, X-ray phase analysis of martensitic transformations in austenitic stainless steels electrochemically charged with hydrogen, Materials Science and Engineering: A 437(2) (2006) 366-378.
[97] D.G. Ulmer, C.J. Altstetter, Hydrogen-induced strain localization and failure of austenitic stainless steels at high hydrogen concentrations, Acta Metallurgica et Materialia 39(6) (1991) 1237-1248.
[98] D.G. Ulmer, C.J. Altstetter, Phase relations in the hydrogen-austenite system, Acta Metallurgica et Materialia 41(7) (1993) 2235-2241.
[99] H.W. King, Structure of the pure metals, North-Holland Publishing Company, Amsterdam, 1965.
[100] M.Smialowski, Hydrogen in Steel, Pergamon Press, Oxford, 1962.
[101] H.H. Johnson, Hydrogen in iron, Metallurgical and Materials Transactions A 19(10) (1988) 2371-2387.
[102] A. Turnbull, Perspectives on hydrogen uptake, diffusion and trapping, International Journal of Hydrogen Energy 40(47) (2015) 16961-16970.
[103] Th. Boellinghaus, H. Hoffmeister, K. Feuerstake, H. Alzer, J. Krewinkel, Finite element calculation of hydrogen uptake and diffusion in martensitic stainless steel welds, in: H.H. Cerjak (Ed.) Mathematical Modelling of Weld Phenomena 4, The Institute of Materials, Seggau, Österreich, 1998, pp. 355–378.
[104] T. Boellinghaus, H. Hoffmeister, Numerical Model for Hydrogen-Assisted Cracking, CORROSION 56(6) (2000) 611-622.
[105] A. Barnoush, Hydrogen embrittlement, revisited by in situ electrochemical nanoindentation, (2009).

[106] S.L. Amey, G.M. Michal, J.H. Payer, Modeling hydrogen entry and exit in metals exposed to multiple charging processes, Metallurgical Materials Transactions A 25(4) (1994) 723-731.
[107] P. Bruzzoni, R. Garavaglia, Anodic iron oxide films and their effect on the hydrogen permeation through steel, Corrosion Science 33(11) (1992) 1797-1807.
[108] R.H. Song, S. Pyun, R. Oriani, Hydrogen Permeation Through the Passivation Film on Iron by Time-Lag Method, Journal of the Electrochemical Society 137(6) (1990) 1703-1706.
[109] T.H. Nam, J.G. Kim, Y.S. Choi, Electrochemical hydrogen discharge of high-strength low alloy steel for high-pressure gaseous hydrogen storage tank: Effect of discharging temperature, International Journal of Hydrogen Energy 38(2) (2013) 999-1003.
[110] M. Enomoto, D. Hirakami, T. Tarui, Modeling thermal desorption analysis of hydrogen in steel, ISIJ international 46(9) (2006) 1381-1387.
[111] M. Charca Samuel, N.C. Uwakweh Oswald, A. Agarwala Vinod, Comparative Study of Hydrogen Transport Behaviors in ARMCO-Fe and AF1410 Steels, Corrosion Reviews, 2007, p. 377.
[112] D. Figueroa, M.J. Robinson, Hydrogen transport and embrittlement in 300M and AerMet100 ultra high strength steels, Corrosion Science 52(5) (2010) 1593-1602.
[113] M.R. Louthan, R.G. Derrick, Hydrogen transport in austenitic stainless steel, Corrosion Science 15(6) (1975) 565-577.
[114] C. Örnek, P. Reccagni, U. Kivisäkk, E. Bettini, D.L. Engelberg, J. Pan, Hydrogen embrittlement of super duplex stainless steel – Towards understanding the effects of microstructure and strain, International Journal of Hydrogen Energy 43(27) (2018) 12543-12555.
[115] R. Silverstein, D. Eliezer, Mechanisms of hydrogen trapping in austenitic, duplex, and super martensitic stainless steels, Journal of Alloys and Compounds 720 (2017) 451-459.
[116] S. Brauser, T. Kannengiesser, Hydrogen absorption of different welded duplex steels, International Journal of Hydrogen Energy 35(9) (2010) 4368-4374.
[117] T. Boellinghaus, H. Hoffmeister, C. Middel, Scatterbands for hydrogen diffusion coefficients in steels having a ferritic or martensitic microstructure and steels having an austenitic microstructure at room temperature, Welding in the World 1(37) (1996) 16-23.
[118] D.M. Seeger, Wasserstoffaufnahme und -diffusion in Schweißnahtgefügen hochfester Stähle, Wirtschaftsverl. NW, Verlag für Neue Wiss.2005.
[119] C. Hurtado Noreña, P. Bruzzoni, Effect of microstructure on hydrogen diffusion and trapping in a modified 9%Cr–1%Mo steel, Materials Science and Engineering: A 527(3) (2010) 410-416.
[120] K.G. Solheim, J.K. Solberg, J. Walmsley, F. Rosenqvist, T.H. Bjørnå, The role of retained austenite in hydrogen embrittlement of supermartensitic stainless steel, Engineering Failure Analysis 34 (2013) 140-149.
[121] D.L. Cummings, D.A. Blackburn, The effect of pressure modulation on the flow of gas through a solid membrane: Surface inhibition and internal traps, Metallurgical Transactions A 16(6) (1985) 1013-1024.
[122] R.N. Iyer, H.W. Pickering, M. Zamanzadeh, A mechanistic analysis of hydrogen entry into metals during cathodic hydrogen charging, Pennsylvania State University Park Dept. of Materials Science NCE, 1988.
[123] R.N. Iyer, H.W. Pickering, M. Zamanzadeh, Analysis of Hydrogen Evolution and Entry into Metals for the Discharge-Recombination Process, Journal of the Electrochemical Society 136(9) (1989) 2463-2470.
[124] G.M. Pressouyre, I.M. Bernstein, A quantitative analysis of hydrogen trapping, Metallurgical Transactions A 9(11) (1978) 1571-1580.
[125] P. Sofronis, R.M. McMeeking, Numerical analysis of hydrogen transport near a blunting crack tip, Journal of the Mechanics and Physics of Solids 37(3) (1989) 317-350.

[126] J. Tien, A.W. Thompson, I.M. Bernstein, R.J. Richards, Hydrogen transport by dislocations, Metallurgical Transactions A 7(6) (1976) 821-829.
[127] M. Uhlemann, B.G. Pound, Diffusivity, solubility and trapping behavior of hydrogen in alloys 600, 690tt and 800, Corrosion Science 40(4) (1998) 645-662.
[128] T.-Y. Zhang, W.-Y. Chu, C.-M. Hsiao, Tetragonal distortion field of hydrogen atoms in iron, Metallurgical Transactions A 16(9) (1985) 1649-1653.
[129] J. Crank, The mathematics of diffusion, Clarendon Press, Oxford [England], 1975.
[130] P. Shewmon, Diffusion in solids, Springer2016.
[131] Th.Boellinghaus, Wasserstoffunterstützte Schäden in metallischen Strukturwerkstoffen, Hamburg, 1999.
[132] A. Pundt, R. Kirchheim, Hydrogen in metals: microstructural aspects, Annu. Rev. Mater. Res. 36 (2006) 555-608.
[133] A. McNabb, P.K. Foster, A new analysis of the diffusion of hydrogen in iron and ferritic steels, Transactions of the Metallurgical Society of AIME 227 (1963) 618-627.
[134] R.A. Oriani, The diffusion and trapping of hydrogen in steel, Acta metallurgica 18(1) (1970) 147-157.
[135] R.B. McLellan, Thermodynamics and diffusion behavior of interstitial solute atoms in non-perfect solvent crystals, Acta Metallurgica 27(10) (1979) 1655-1663.
[136] G.M. Pressouyre, A classification of hydrogen traps in steel, Metallurgical Transactions A 10(10) (1979) 1571-1573.
[137] J.P. Hirth, Effects of hydrogen on the properties of iron and steel, Metallurgical Transactions A 11(6) (1980) 861-890.
[138] D. Eliezer, Y. Nissim, T. Kannengiesser, Effects of Shielding with Various Hydrogen-Argon Mixtures on Supermartensitic Stainless Steel TIG Welds, 2010.
[139] A.H.M. Krom, A. Bakker, Hydrogen trapping models in steel, Metallurgical Materials Transactions B 31(6) (2000) 1475-1482.
[140] G.M. Pressouyre, Trap theory of Hydrogen embrittlement, Acta Metallurgica 28(7) (1980) 895-911.
[141] A.-A. Iris, Duplex Stainless Steels: Brief History and Some Recent Alloys, Recent Patents on Mechanical Engineering 1(1) (2008) 51-57.
[142] M.R. Louthan, G.R. Caskey, J.A. Donovan, D.E. Rawl, Hydrogen embrittlement of metals, Materials Science and Engineering 10 (1972) 357-368.
[143] P. Bastien, P. Azou, Effect of Hydrogen on the Deformation and Fracture of Iron and Steel in Simple Tension, The First World Metallurgical Congress ASM, Cleveland, Ohio, 1951.
[144] E.A. Groshart, Design and Finish Requirements of High Strength Steels, Metal Finishing 82 (1984) 49.
[145] A. Barnoush, H. Vehoff, Hydrogen embrittlement of aluminum in aqueous environments examined by in situ electrochemical nanoindentation, Scripta Materialia 58(9) (2008) 747-750.
[146] C.L. Briant, Z.F. Wang, N. Chollocoop, Hydrogen embrittlement of commercial purity titanium, Corrosion Science 44(8) (2002) 1875-1888.
[147] E. Tal-Gutelmacher, D. Eliezer, The hydrogen embrittlement of titanium-based alloys, JOM 57(9) (2005) 46-49.
[148] S.A. Shipilov, Catastrophic failures due to environment-assisted cracking of metals: Case histories, Canadian Inst of Mining, Metallurgy and Petroleum, Canada, 1999.
[149] M. Seita, J.P. Hanson, S. Gradečak, M.J. Demkowicz, The dual role of coherent twin boundaries in hydrogen embrittlement, Nature Communications 6 (2015) 6164.
[150] I.M. Robertson, P. Sofronis, A. Nagao, M.L. Martin, S. Wang, D.W. Gross, K.E. Nygren, Hydrogen Embrittlement Understood, Metallurgical Materials Transactions A 46(6) (2015) 2323-2341.
[151] M. Dadfarnia, P. Novak, D.C. Ahn, J.B. Liu, P. Sofronis, D.D. Johnson, I.M. Robertson, Recent advances in the study of structural materials compatibility with hydrogen, Advanced Materials 22(10) (2010) 1128-1135.

[152] R.A. Oriani, A mechanistic theory of hydrogen embrittlement of steels, Berichte der Bunsengesellschaft für physikalische Chemie 76(8) (1972) 848-857.
[153] A. Barnoush, H. Vehoff, Recent developments in the study of hydrogen embrittlement: Hydrogen effect on dislocation nucleation, Acta Materialia 58(16) (2010) 5274-5285.
[154] H.K. Birnbaum, P. Sofronis, Hydrogen-enhanced localized plasticity—a mechanism for hydrogen-related fracture, Materials Science and Engineering: A 176(1) (1994) 191-202.
[155] J. Lufrano, P. Sofronis, H.K. Birnbaum, Modeling of hydrogen transport and elastically accommodated hydride formation near a crack tip, Journal of the Mechanics and Physics of Solids 44(2) (1996) 179-205.
[156] S.P. Lynch, Environmentally assisted cracking: Overview of evidence for an adsorption-induced localised-slip process, Acta Metallurgica 36(10) (1988) 2639-2661.
[157] S.P. Lynch, Mechanisms of hydrogen assisted cracking - A review, 2003.
[158] A.R. Troiano, The role of hydrogen and other interstitials in the mechanical behavior of metals, Metallography, Microstructure, and Analysis 5(6) (2016) 557-569.
[159] E. Sirois, H. Birnbaum, Effects of hydrogen and carbon on thermally activated deformation in nickel, Acta metallurgica et materialia 40(6) (1992) 1377-1385.
[160] H.G. Nelson, Hydrogen embrittlement, Treatise on Materials Science & Technology, Elsevier1983, pp. 275-359.
[161] S. Lynch, Hydrogen embrittlement phenomena and mechanisms, Corrosion Reviews 30 (2012) 105-123.
[162] C.D. Beachem, A new model for hydrogen-assisted cracking (hydrogen "embrittlement"), Metallurgical Materials Transactions B 3(2) (1972) 441-455.
[163] I.M. Robertson, P. Sofronis, A. Nagao, M.L. Martin, S. Wang, D.W. Gross, K.E. Nygren, Hydrogen Embrittlement Understood, Metallurgical and Materials Transactions A 46(6) (2015) 2323-2341.
[164] D. Delafosse, T. Magnin, Hydrogen induced plasticity in stress corrosion cracking of engineering systems, Engineering Fracture Mechanics 68(6) (2001) 693-729.
[165] M.L. Martin, J.A. Fenske, G.S. Liu, P. Sofronis, I.M. Robertson, On the formation and nature of quasi-cleavage fracture surfaces in hydrogen embrittled steels, Acta Materialia 59(4) (2011) 1601-1606.
[166] S.P. Lynch, A fractographic study of gaseous hydrogen embrittlement and liquid-metal embrittlement in a tempered-martensitic steel, Acta Metallurgica 32(1) (1984) 79-90.
[167] A. Barnoush, M. Asgari, R. Johnsen, Resolving the hydrogen effect on dislocation nucleation and mobility by electrochemical nanoindentation, Scripta Materialia 66(6) (2012) 414-417.
[168] A. Barnoush, H. Vehoff, Electrochemical nanoindentation: A new approach to probe hydrogen/deformation interaction, Scripta materialia 55(2) (2006) 195-198.
[169] D. Broek, Elementary engineering fracture mechanics, Springer Science & Business Media2012.
[170] G.E. Dieter, Mechanical metallurgy, McGraw-Hill1986.
[171] F.P. Ford, Quantitative Prediction of Environmentally Assisted Cracking, Corrosion 52(5) (1996) 375-395.
[172] J.P. Hirth, Theories of Hydrogen-Induced Cracking of Steels, Hydrogen Embrittlement Stress Corrosion Cracking (1980) 29-41.
[173] T. Asaoka, G. Lapasset, M. Aucouturier, P. Lacombe, Observation of Hydrogen Trapping in Fe-0.15 Wt% Ti Alloy by High Resolution Autoradiography, Corrosion 34(2) (1978) 39-47.
[174] T. Michler, J. Naumann, Microstructural aspects upon hydrogen environment embrittlement of various bcc steels, International journal of hydrogen energy 35(2) (2010) 821-832.
[175] T.H. Boellinghaus, H. Reuter, L. , Material properties of as delivered and quenched modified martensitic stainless steels dependent on hydrogen concentration,

Supermartensitic Stainless Steels '99, Proceedings, Belgian Welding Institute Brussels, BE, 1999, pp. 264 - 271.
[176] D. Lidbury, The estimation of crack tip strain rate parameters characterizing environment assisted crack growth data, Embrittlement by the Localized Crack Environment (1983) 149-172.
[177] J. Toribio, The use of precracked and notched slow strain rate specimens, Slow Strain Rate Testing for the Evaluation of Environmentally Induced Cracking: Research and Engineering Applications, ASTM International1993.
[178] D.R. McIntyre, C.P. Dillon, D.C. McIntyre, Forms of Corrosion: Recognition and Prevention, NACE International1997.
[179] P.R. Roberge, Corrosion Engineering Principles and Practice, 1 (2005).
[180] M.G. Fontana, Corrosion engineering, Tata McGraw-Hill Education2005.
[181] G. Burstein, C. Liu, R. Souto, S. Vines, Origins of pitting corrosion, Corrosion Engineering, Science and Technology 39(1) (2004) 25-30.
[182] G. Butler, P. Stretton, J.G. Beynon, Initiation and Growth of Pits on High-Purity Iron and its Alloys with Chromium and Copper in Neutral Chloride Solutions, British Corrosion Journal 7(4) (1972) 168-173.
[183] R.E. Melchers, Pitting Corrosion of Mild Steel in Marine Immersion Environment—Part 2: Variability of Maximum Pit Depth, 60(10) (2004) 937-944.
[184] R.E. Melchers, Statistical Characterization of Pitting Corrosion—Part 1: Data Analysis, 61(7) (2005) 655-664.
[185] H. Hoffmeister, T. Boellinghaus, Modeling of Combined Anodic Dissolution/Hydrogen-Assisted Stress Corrosion Cracking of Low-Alloyed Power Plant Steels in High-Temperature Water Environments, Corrosion 70 (2014) 563-578.
[186] D. Shifler, Corrosion performance and testing of materials in marine environments, 2005.
[187] K.R. Threthewey, P.R. Roberge, Modelling Aqueous Corrosion: From Individual Pits to System Management, Springer Netherlands1994.
[188] B.J. Little, J.S. Lee, Microbiologically Influenced Corrosion, Wiley2007.
[189] H.J. Choi, D. Warnken, F.I. Al Beheiri, N.S. Al-Bannai, Field Corrosion Assessment of L80 Carbon Steel Downhole Production Tubing at Khuff Gas Wells, CORROSION 2006, NACE International, San Diego, California, 2006, p. 10.
[190] J.K. Paik, J.M. Lee, M.J. Ko, Ultimate shear strength of plate elements with pit corrosion wastage, Thin-Walled Structures 42(8) (2004) 1161-1176.
[191] Y. Wang, J.A. Wharton, R.A. Shenoi, Ultimate strength assessment of steel stiffened plate structures with grooving corrosion damage, Engineering Structures 94 (2015) 29-42.
[192] Y. Wang, J.A. Wharton, R.A. Shenoi, Ultimate strength analysis of aged steel-plated structures exposed to marine corrosion damage: A review, Corrosion Science 86 (2014) 42-60.
[193] S. Sultana, Y. Wang, A.J. Sobey, J.A. Wharton, R.A. Shenoi, Influence of corrosion on the ultimate compressive strength of steel plates and stiffened panels, Thin-Walled Structures 96 (2015) 95-104.
[194] K. Sachidananda, K.D. Singh, Numerical study of fixed ended lean duplex stainless steel (LDSS) flat oval hollow stub column under pure axial compression, Thin-Walled Structures 96 (2015) 105-119.
[195] S. Saad-Eldeen, Y. Garbatov, C. Guedes Soares, Ultimate strength assessment of corroded box girders, Ocean Engineering 58 (2013) 35-47.
[196] G. Malumbela, M. Alexander, P. Moyo, Variation of steel loss and its effect on the ultimate flexural capacity of RC beams corroded and repaired under load, Construction and Building Materials 24(6) (2010) 1051-1059.
[197] A. Rahbar-Ranji, Ultimate strength of corroded steel plates with irregular surfaces under in-plane compression, Ocean Engineering 54 (2012) 261-269.
[198] F. Tang, Z. Lin, G. Chen, W. Yi, Three-dimensional corrosion pit measurement and statistical mechanical degradation analysis of deformed steel bars subjected to accelerated corrosion, Construction and Building Materials 70 (2014) 104-117.

[199] Y. Zhang, Y. Huang, Y. Wei, Ultimate strength experiment of hull structural plate with pitting corrosion damage under unaxial compression, Ocean Engineering 130 (2017) 103-114.
[200] D. Ok, Y. Pu, A. Incecik, Artificial neural networks and their application to assessment of ultimate strength of plates with pitting corrosion, Ocean Engineering 34(17) (2007) 2222-2230.
[201] Y. Zhang, Y. Huang, Q. Zhang, G. Liu, Ultimate strength of hull structural plate with pitting corrosion damnification under combined loading, Ocean Engineering 116 (2016) 273-285.
[202] A. Kahyarian, M. Singer, S. Nesic, Modeling of uniform CO2 corrosion of mild steel in gas transportation systems: A review, Journal of Natural Gas Science and Engineering 29 (2016) 530-549.
[203] R.R. Fessler, Pipeline corrosion, Report, US Department of Transportation Pipeline Hazardous Materials Safety Administration, Baker, Evanston, IL (2008).
[204] A.M. El-Sherik, Trends in Oil and Gas Corrosion Research and Technologies: Production and Transmission, Elsevier Science2017.
[205] D. GL, DNVGL-RP-F116: Integrity management of submarine pipeline systems.
[206] M. Cerit, Numerical investigation on torsional stress concentration factor at the semi elliptical corrosion pit, Corrosion Science 67 (2013) 225-232.
[207] D. Rivas, F. Caleyo, A. Valor, J.M. Hallen, Extreme value analysis applied to pitting corrosion experiments in low carbon steel: Comparison of block maxima and peak over threshold approaches, Corrosion Science 50(11) (2008) 3193-3204.
[208] A. Valor, F. Caleyo, J.M. Hallen, J.C. Velázquez, Reliability assessment of buried pipelines based on different corrosion rate models, Corrosion Science 66 (2013) 78-87.
[209] I.A. Chaves, R.E. Melchers, Pitting corrosion in pipeline steel weld zones, Corrosion Science 53(12) (2011) 4026-4032.
[210] T.A. Netto, U.S. Ferraz, A. Botto, On the effect of corrosion defects on the collapse pressure of pipelines, International Journal of Solids and Structures 44(22) (2007) 7597-7614.
[211] T.A. Netto, A simple procedure for the prediction of the collapse pressure of pipelines with narrow and long corrosion defects — Correlation with new experimental data, Applied Ocean Research 32(1) (2010) 132-134.
[212] N. Sakakibara, S. Kyriakides, E. Corona, Collapse of partially corroded or worn pipe under external pressure, International Journal of Mechanical Sciences 50(12) (2008) 1586-1597.
[213] P. Marcus, Corrosion mechanisms in theory and practice, CRC press2011.
[214] H.-H. Strehblow, P. Marcus, Mechanisms of pitting corrosion, Corrosion mechanisms in theory; practice 8 (1995) 201.
[215] A.N.S. Institute, Manual for determining the remaining strength of corroded pipelines: A supplement to ANSI/ASME B31 code for pressure piping, N.Y: American Society of Mechanical Engineers, New York, 1985.
[216] DNVGL, DNVGL-RP-F101: Corroded Pipelines, 2017.
[217] R.M. Pidaparti, A.S. Rao, Analysis of pits induced stresses due to metal corrosion, Corrosion Science 50(7) (2008) 1932-1938.
[218] R. Eiber, J. Kiefner, Failures of pipelines, ASM International (2002) 695-706.
[219] R.J. Bertin, J.E. Abdalla Filho, R.D. Machado, Stress analysis of corrosion pits present on curved and plane surfaces considering plasticity, Mecánica Computacional XXIX (2010).
[220] Z.T. Mu, D.H. Chen, Z.T. Zhu, B. Ye, The stress concentration factor of different corrosion pits shape, Advanced Materials Research, Trans Tech Publ, 2011, pp. 1115-1119.
[221] A. Turnbull, L. Wright, L. Crocker, New insight into the pit-to-crack transition from finite element analysis of the stress and strain distribution around a corrosion pit, Corrosion Science 52(4) (2010) 1492-1498.

[222] A. Rajabipour, R.E. Melchers, A numerical study of damage caused by combined pitting corrosion and axial stress in steel pipes, Corrosion Science 76 (2013) 292-301.
[223] T. Nakai, H. Matsushita, N. Yamamoto, Effect of pitting corrosion on local strength of hold frames of bulk carriers (2nd Report)—Lateral-distortional buckling and local face buckling, Marine Structures 17(8) (2004) 612-641.
[224] Y. Huang, Y. Zhang, G. Liu, Q. Zhang, Ultimate strength assessment of hull structural plate with pitting corrosion damnification under biaxial compression, Ocean Engineering 37(17) (2010) 1503-1512.
[225] W. Yu, Corrosion Effects on the Ductile Fracture, Strength and Reliability of Membranes, Plates and Shells, (2009).
[226] J. Armitt, R. Holmes, M. Manning, D. Meadowcroft, E. Metcalfe, Spalling of steam-grown oxide from superheater and reheater tube steels. Technical planning study 76-655. Final report, Central Electricity Research Labs., Leatherhead (UK), 1978.
[227] J. Robertson, M. Manning, Limits to adherence of oxide scales, Materials Science and Technology 6(1) (1990) 81-92.
[228] Z. Szklarska-Smialowska, Pitting Corrosion of Metals, NACE, Houston, TX, 1986.
[229] B.F.B. R.W. Staehle, J. Kruger, A. Agarwal (Eds.), Localized Corrosion, NACE-3, Houston, TX, 1974.
[230] U.B. H. Isaacs, J. Kruger, S. Smialowska (Eds.), Advances in Localized Corrosion, NACE-9, Houston, TX, 1990.
[231] R.M. Pidaparti, R.R. Patel, Correlation between corrosion pits and stresses in Al alloys, Materials Letters 62(30) (2008) 4497-4499.
[232] H.S.I. R.C. Newman, B. Alman, Corrosion 38 (1982) 261.
[233] R.W.S. Z. Fang, Corrosion 55, (1999) 355.
[234] N.U. Obeyesekere, 9 - Pitting corrosion, in: A.M. El-Sherik (Ed.), Trends in Oil and Gas Corrosion Research and Technologies, Woodhead Publishing, Boston, 2017, pp. 215-248.
[235] M. Rifai, H. Miyamoto, H. Fujiwara, Effects of Strain Energy and Grain Size on Corrosion Resistance of Ultrafine Grained Fe-20%Cr Steels with Extremely low C and N Fabricated by ECAP, 2015.
[236] G.S. Frankel, J. Electrochem. Soc., 145 2186 (1998).
[237] E. McCafferty, Introduction to Corrosion Science, 2010.
[238] C. Kato, Y. Otoguro, S. Kado, Y. Hisamatsu, Grooving corrosion in electric resistance welded steel pipe in sea water, Corrosion Science 18(1) (1978) 61-74.
[239] H.-H. Huang, W.T. Tsai, J.T. Lee, Electrochemical Behavior of A516 Carbon Steel in Solutions Containing Hydrogen Sulfide, 1996.
[240] P.D. Bilmes, C.L. Llorente, C.M. Méndez, C.A. Gervasi, Microstructure, heat treatment and pitting corrosion of 13CrNiMo plate and weld metals, Corrosion Science 51(4) (2009) 876-881.
[241] N.M.A. Eid, Localized corrosion at welds in structural steel under desalination plant conditions Part I: Effect of surface roughness and type of welding electrode, Desalination 73 (1989) 397-406.
[242] J. Enerhaug, G. Ø., U. Steinsmo, Factors affecting initiation of pitting corrosion in super martensitic stainless steel weldments, Science Technology of welding Joining 6(5) (2001) 330-338.
[243] T. Böllinghaus, E. Viyanit, Numerical Simulations of Hydrogen-Assisted Cracking in Girth Welds of Supermartensitic Stainless Steel Pipelines - Report II, in: H. Cerjak, H.K.D.H. Bhadeshia, E. Kozeschnik (Eds.), Mathematical Modelling of Weld Phenomena 7, Verlag der Technischen Universitat Graz, Seggau, Austria, 2005, pp. 847-874.
[244] T. Boellinghaus, E. Steppan, T. Mente, Hydrogen Assisted Cracking of a Subsea-Flowline, in: T. Boellinghaus, J.C. Lippold, C.E. Cross (Eds.), Cracking Phenomena in Welds IV, Springer International Publishing, Cham, 2016, pp. 361-379.
[245] C.T. Kwok, S.L. Fong, F.T. Cheng, H.C. Man, Pitting and galvanic corrosion behavior of laser-welded stainless steels, Journal of Materials Processing Technology 176(1) (2006) 168-178.

[246] D. GL, DNVGL-CG-0182: Allowable thickness diminution for hull, 2016.
[247] Y. Kondo, Prediction of Fatigue Crack Initiation Life Based on Pit Growth, 1989.
[248] D.A. Horner, B.J. Connolly, S. Zhou, L. Crocker, A. Turnbull, Novel images of the evolution of stress corrosion cracks from corrosion pits, Corrosion Science 53(11) (2011) 3466-3485.
[249] C. Patel, T. Pyle, V. Rollins, Corrosion–fatigue crack initiation in metals, Nature 266(5602) (1977) 517-518.
[250] R. Ebara, Corrosion fatigue crack initiation behavior of stainless steels, Procedia Engineering 2(1) (2010) 1297-1306.
[251] D. Hoeppner, Model for prediction of fatigue lives based upon a pitting corrosion fatigue Process, ASTM STP 675, 1979.
[252] M. Müller, Theoretical Considerations on Corrosion Fatigue Crack Initiation, 1982.
[253] A. Turnbull, Current Understanding of Environment-Induced Cracking of Steam Turbine Steels, 64(5) (2008) 420-438.
[254] A. Turnbull, S. Zhou, Pit to crack transition in stress corrosion cracking of a steam turbine disc steel, Corrosion Science 46(5) (2004) 1239-1264.
[255] C. Liu, D. Macdonald, Prediction of Failures of Low-Pressure Steam Turbine Disks, 1997.
[256] A. Turnbull, L.N. McCartney, S. Zhou, Modelling of the evolution of stress corrosion cracks from corrosion pits, Scripta Materialia 54(4) (2006) 575-578.
[257] A. Turnbull, L.N. McCartney, S. Zhou, A model to predict the evolution of pitting corrosion and the pit-to-crack transition incorporating statistically distributed input parameters, Corrosion Science 48(8) (2006) 2084-2105.
[258] A. Turnbull, S. Zhou, L. Orkney, N. McCormick, Visualization of stress corrosion cracks emerging from pits, Corrosion 62(7) (2006) 555-558.
[259] B. Connolly, D. Horner, S. Fox, A. Davenport, C. Padovani, S. Zhou, A. Turnbull, M. Preuss, N. Stevens, T. Marrow, X-ray microtomography studies of localised corrosion and transitions to stress corrosion cracking, Materials science and technology 22(9) (2006) 1076-1085.
[260] A. Davenport, C. Padovani, B. J. Connolly, N. Stevens, T. A. W. Beale, A. Groso, M. Stampanoni, Synchrotron X-Ray Microtomography Study of the Role of Y in Corrosion of Magnesium Alloy WE43, 2007.
[261] T.J. Marrow, L. Babout, B.J. Connolly, D. Engelberg, G. Johnson, J.Y. Buffiere, P.J. Withers, R.C. Newman, High-resolution, in-situ, tomographic observations of stress corrosion cracking, in: S.A. Shipilov, R.H. Jones, J.M. Olive, R.B. Rebak (Eds.), Environment-Induced Cracking of Materials, Elsevier, Amsterdam, 2008, pp. 439-447.
[262] T.J. Marrow, L. Babout, A.P. Jivkov, P. Wood, D. Engelberg, N. Stevens, P.J. Withers, R.C. Newman, Three dimensional observations and modelling of intergranular stress corrosion cracking in austenitic stainless steel, Journal of Nuclear Materials 352(1) (2006) 62-74.
[263] L. Babout, T. Marrow, D. Engelberg, P. Withers, X-ray microtomographic observation of intergranular stress corrosion cracking in sensitised austenitic stainless steel, 2006.
[264] A. Guvenilir, T.M. Breunig, J.H. Kinney, S.R. Stock, Direct observation of crack opening as a function of applied load in the interior of a notched tensile sample of Al・Li 2090, Acta Materialia 45(5) (1997) 1977-1987.
[265] H. Toda, I. Sinclair, J.Y. Buffière, E. Maire, K.H. Khor, P. Gregson, T. Kobayashi, A 3D measurement procedure for internal local crack driving forces via synchrotron X-ray microtomography, Acta Materialia 52(5) (2004) 1305-1317.
[266] M. Cerit, K. Genel, S. Eksi, Numerical investigation on stress concentration of corrosion pit, Engineering Failure Analysis 16(7) (2009) 2467-2472.
[267] K.J. Miller, R.F. Smith, Third lnt. Conf. on Mechanical Behavior of Materials, Pergamon Press, Cambridge, England, 1980, pp. 109-37.
[268] Y. Kondo, Prediction of Fatigue Crack Initiation Life Based on Pit Growth, CORROSION 45(1) (1989) 7-11.

[269] A. Turnbull, D.A. Horner, B.J. Connolly, Challenges in modelling the evolution of stress corrosion cracks from pits, Engineering Fracture Mechanics 76(5) (2009) 633-640.
[270] J. Bhandari, F. Khan, R. Abbassi, V. Garaniya, R. Ojeda, Modelling of pitting corrosion in marine and offshore steel structures – A technical review, Journal of Loss Prevention in the Process Industries 37(Supplement C) (2015) 39-62.
[271] K. Hariramabadran Anantha, C. Örnek, S. Ejnermark, A. Thuvander, A. Medvedeva, J. Sjöström, J. Pan, Experimental and modelling study of the effect of tempering on the susceptibility to environment-assisted cracking of AISI 420 martensitic stainless steel, Corrosion Science 148 (2019) 83-93.
[272] S. Ekşi, Numerical calculation of stress concentration of various subsurface and undercutting pit types, Materials Testing 60(7-8) (2018) 687-690.
[273] H. Wang, E.-H. Han, Computational simulation of corrosion pit interactions under mechanochemical effects using a cellular automaton/finite element model, Corrosion Science 103(Supplement C) (2016) 305-311.
[274] L. Xiang, J. Pan, S. Chen, Analysis on the stress corrosion crack inception based on pit shape and size of the FV520B tensile specimen, Results in Physics 9 (2018) 463-470.
[275] M. Cerit, Corrosion pit-induced stress concentration in spherical pressure vessel, Thin-Walled Structures 136 (2019) 106-112.
[276] M. Mehlich, H. Hoffmeister, T. Böllinghaus, C. Münster, Potentiostatic threshold potentials of stainless steels, E3S Web of Conferences 121 (2019) 01010.
[277] R. Wei, X. Chen, Z. Ai, Y. Jin, Experimental study and numerical simulation on the SSCC in FV520B stainless steel exposed to H2S+Cl− Environment, International Journal of Hydrogen Energy 43(18) (2018) 9059-9067.
[278] L. Anand, Y. Mao, B. Talamini, On modeling fracture of ferritic steels due to hydrogen embrittlement, Journal of the Mechanics and Physics of Solids 122 (2019) 280-314.
[279] A. Díaz, J.M. Alegre, I.I. Cuesta, Numerical simulation of hydrogen embrittlement and local triaxiality effects in notched specimens, Theoretical and Applied Fracture Mechanics 90 (2017) 294-302.
[280] J. Nicholls, D. Hall, P. Tortorelli, Hardness and modulus measurements on oxide scales, Materials at high temperatures 12(2-3) (1994) 141-150.
[281] P.F. Tortorelli, Mechanical properties of chromia scales, Journal de Physique IV Colloque 3 (1993).
[282] L. Calabrese, L. Bonaccorsi, M. Galeano, E. Proverbio, D. Di Pietro, F. Cappuccini, Identification of damage evolution during SCC on 17-4 PH stainless steel by combining electrochemical noise and acoustic emission techniques, Corrosion Science 98 (2015) 573-584.
[283] S. Scheiner, C. Hellmich, Stable pitting corrosion of stainless steel as diffusion-controlled dissolution process with a sharp moving electrode boundary, Corrosion Science 49(2) (2007) 319-346.
[284] Y.P. Kim, M. Fregonese, H. Mazille, D. Féron, G. Santarini, Ability of acoustic emission technique for detection and monitoring of crevice corrosion on 304L austenitic stainless steel, NDT & E International 36(8) (2003) 553-562.
[285] M. Fregonese, H. Idrissi, H. Mazille, L. Renaud, Y. Cetre, Monitoring pitting corrosion of AISI 316L austenitic stainless steel by acoustic emission technique: Choice of representative acoustic parameters, Journal of Materials Science 36(3) (2001) 557-563.
[286] J.O. Park, M. Verhoff, R. Alkire, Microscopic behavior of single corrosion pits: the effect of thiosulfate on corrosion of stainless steel in NaCl, Electrochimica Acta 42(20) (1997) 3281-3291.
[287] M. Fregonese, H. Idrissi, H. Mazille, L. Renaud, Y. Cetre, Initiation and propagation steps in pitting corrosion of austenitic stainless steels: monitoring by acoustic emission, Corrosion Science 43(4) (2001) 627-641.
[288] H. Mazille, R. Rothea, C. Tronel, An acoustic emission technique for monitoring pitting corrosion of austenitic stainless steels, Corrosion Science 37(9) (1995) 1365-1375.

[289] N.S. TM, Laboratory testing of metals for resistance to sulfide stress cracking and stress corrosion cracking in H2S environments, Houston, TX: NACE, NACE International The Corrosion Society, 2005.
[290] T.T. Allen, Introduction to Engineering Statistics and Six Sigma: Statistical Quality Control and Design of Experiments and Systems, Springer London2006.
[291] M. Mehlich, Schwellenpotentiale martensitischer Chromstähle, Hamburg, 2019.
[292] J.A. Goldak, M. Akhlaghi, Computational welding mechanics, Springer, New York, 2005.
[293] E. Madenci, I. Guven, The finite element method and applications in engineering using ANSYS®, Springer2015.
[294] ANSYS-Documentation (Help): User Handbook ANSYS, Canonsburg, 2016.
[295] ASME, Power Piping, B31.1, The American Society of Mechanical Engineers, 2018.
[296] Y.Y. Chen, Y.M. Liou, H.C. Shih, Stress corrosion cracking of type 321 stainless steels in simulated petrochemical process environments containing hydrogen sulfide and chloride, Materials Science and Engineering: A 407(1) (2005) 114-126.
[297] T. Boellinghaus, H. Hoffmeister, Hydrogen permeation in a low carbon martensitic stainless steel exposed to H2S containing brines at free corrosion, CONF-990401, NACE International, NACE International, Houston, TX (United States), Houston, TX (United States), 1999.
[298] A. Turnbull, Corrosion pitting and environmentally assisted small crack growth, Proceedings of the Royal Society A: Mathematical, Physical and Engineering Sciences 470(2169) (2014) 20140254.
[299] T. Nakai, H. Matsushita, N. Yamamoto, Effect of pitting corrosion on the ultimate strength of steel plates subjected to in-plane compression and bending, Journal of Marine Science and Technology 11(1) (2006) 52-64.
[300] J. Capelle, J. Gilgert, I. Dmytrakh, G. Pluvinage, Sensitivity of pipelines with steel API X52 to hydrogen embrittlement, International Journal of Hydrogen Energy 33(24) (2008) 7630-7641.
[301] J. Capelle, J. Gilgert, I. Dmytrakh, G. Pluvinage, The effect of hydrogen concentration on fracture of pipeline steels in presence of a notch, Engineering Fracture Mechanics 78(2) (2011) 364-373.
[302] M. Jakubowski, Influence of Pitting Corrosion on Fatigue and Corrosion Fatigue of Ship and Offshore Structures, Part II: Load - Pit - Crack Interaction, Polish Maritime Research 22 (2015).
[303] M. Madigan, T. Mente, T. Böllinghaus, Numerical simulation of hydrogen assisted stress corrosion cracking originating from pits, 12th International Seminar “Numerical Analysis of Weldability”, Seggau, Austria, 2018.
[304] E. Martínez-Pañeda, A. Golahmar, C.F. Niordson, A phase field formulation for hydrogen assisted cracking, Computer Methods in Applied Mechanics and Engineering 342 (2018) 742-761.
[305] T. Mente, Numerische Simulation der wasserstoffunterstützten Rissbildung in austenitisch-ferritischen Duplexstählen, Fakultät für Maschinenbau, Otto-von-Guericke-Universität Magdeburg, 2015, p. 163.
[306] P. Sofronis, J. Lufrano, Interaction of local elastoplasticity with hydrogen: embrittlement effects, Materials Science and Engineering: A 260(1-2) (1999) 41-47.

Abbreviations

AIDE	Adsorption Induced Dislocation Emission
ASM	American Society for Metals
BCC	Body Centered Cubic
BCT	Body Centered Tetragonal
BISO	Bilinear Isotropic Hardening Specifications
BM	Base Material
CCT	Critical Crevice Temperature
CP	Cathodic Protection
Cr	Chromium
CRA	Corrosion Resistant Alloy
Cu	Copper
DCB	Double Cantilever Beam
DNV	Det Norske Veritas
DNV GL	Det Norske Veritas Germanischer Lloyd
DoF	Degrees of Freedom
DSS	Duplex Stainless Steel
EB	Electron Beam
Fe	Iron
FEA	Finite Element Analysis
FEM	Finite Element Method
FCC	Face Centered Cubic
GMAW	Gas Metal Arc Welding
HAC	Hydrogen Assisted Cracking
HASCC	Hydrogen Assisted Stress Corrosion Cracking
HAZ	Heat Affected Zone
HD	Hydrogen Diffusion
HE	Hydrogen Embrittlement
HEDE	Hydrogen Enhanced De-Cohesion
HELP	Hydrogen Enhanced Localised Plasticity
HIC	Hydrogen Induced Cracking
HPHT	High Pressure High Temperature
HSLA	High Strength Low Alloy

HSU	Helmut Schmidt University
IG	Intergranular
IGSCC	Intergranular Stress Corrosion Cracking
Mn	Manganese
Mo	Molybdenum
MSS	Martensitic Stainless Steel
MVC	MicroVoid Coalescence
NACE	National Association of Corrosion Engineers
N	Nitrogen
Ni	Nickel
OCP	Open Circuit Potential
OCTG	Oil Country Tubular Goods
PREN	Pitting Resistance Equivalent Number
PWHT	Post Weld Heat Treatment
QC	Quasi-Cleavage
RF	Radial Friction
SAW	Submerged Arc Welding
SCC	Stress Corrosion Cracking
SMSS	Super Martensitic Stainless Steel
SSC	Sulphide Stress Cracking
SSRT	Slow Strain Rate Test
TC	Transcrystalline
TEM	Transmission Electron Microscopy
TIG	Tungsten Inert Gas
TG	Transgranular
TRIP	Transformation Induced Plasticity
TTF	Time to Failure
TWI	The Welding Institute
UA	Uniaxial
UTS	Ultimate Tensile Strength
V	Vanadium
W	Tungsten
WM	Weld Metal
XPS	X-ray photoelectron spectra

List of symbols

Latin Characters:

Symbol:	Unit:	Description:
a	[mm]	Actual crack length
a^3_{smm}	[mm]	Crack distance advanced by the movement of vacancies
A_{c1}	[°C]	Temperature where austenite begins to form during heating
c	[-]	Hardening index
C	[mol/m^3]	Concentration
C_{ref}	[ppm]	Reference concentration
C_{sat}	[ppm]	Saturated concentration of the material
$\bar{C}$	[-]	Normalised concentration
d	[mm]	Membrane thickness
$[D]$	[-]	Compliance matrix equations based on Hooke's Law
$\left(\frac{dc}{dt}\right)_{crack}$	[µmm/s]	Crack growth rate
$\left(\frac{dc}{dt}\right)_{pit}$	[µmm/s]	Pit growth rate
D_{eff}	[mm^2/s]	Effective hydrogen diffusion coefficient
D_{H_0}	[mm^2/s]	Hydrogen diffusion coefficient in the normal state
D_{met}	[mm^2/s]	Surface self-diffusion coefficient
E	[GPa]	Young's Modulus
E_A	[kJ/mol]	Activation energy for hydrogen diffusion
$E_{B\,Trap}$	[kJ/mol]	Hydrogen free energy in the trap
E_{cor}	[mV]	Pitting potential where corrosion is initiated
$E_{Lattice}$	[kJ/mol]	Lattice interstitial sites
E_m	[GPa]	Young's modulus of the substrate metal
E_{pit}	[mV]	Critical pitting potential
E_r	[mV]	Repassivation potential
f	[-]	Coefficient of friction
$\{f\}$	[-]	Column vector of elemental nodal forces
f_M	[%]	Fresh Martensite
F	[C/mol]	Faraday's constant (96485.33289(59) C mol^{-1})
$\{F\}$	[-]	Column vector of global nodal forces

F_m	[-]	Maximum cohesive resistive force of iron atoms
G	[MPa]	Shear modulus
G	[-]	Diffusing substance generation rate per unit volume
H	[-]	Plastic hardening at the beginning of the increment
H_{Ab}	[-]	Hydrogen absorbed at the specimen surface
H_{Ad}	[-]	Hydrogen adsorbed at the specimen surface
H^+_{Bulk}	[-]	Hydrogen present in the bulk solution
HD	[ml/100 g Fe]	Hydrogen concentration
HD_{crit}	[ml/100 g Fe]	Critical hydrogen concentration
$H^+_{Surface}$	[-]	Hydrogen present on the surface of the material
i	[A/m^2]	Applied current density
j	[mm]	Jump distance for crack propagation
$\{J\}$	[-]	Diffusion flux vector
J_H	[mol/m^2/s]	Hydrogen flux through the steel membrane
k	[-]	Diminution coefficient (0.7 – 0.8)
k	[J/K]	Boltzmann's constant (1.380x10^{-23}J/K)
k_1	[/s]	Specific rate constant
$[k]$	[-]	Element stiffness matrix
$[K]$	[-]	Global stiffness matrix
K_I	[MPa m$^{1/2}$]	Stress intensity factor of Mode I
K_{IC}	[MPa m$^{1/2}$]	Critical stress intensity factor of Mode I
K_{lid}	[-]	Lidbury's constant factor
K_{TH}	[MPa m$^{1/2}$]	Threshold stress intensity value
ΔK	[MPa m$^{1/2}$]	Stress intensity factor
ΔK_{th}	[MPa m$^{1/2}$]	Threshold stress intensity factor
L_{smm}	[mm]	Diffusion distance of vacancies
Me	[-]	Metal
M_{Fe}	[g/mole]	Atomic weight of steels (≈ 65 g/mole)
M_s	[^{o}C]	Martensite start temperature
n	[-]	Number of metal atoms per unit area of the cracking plane
N_i	[-]	Shape functions
Q	[eV]	Barrier energy for hydrogen diffusion
Q_f	[-]	Oxidation charge passed the rupture event

R	[J/mol·K]	Universal gas constant (8.314 J/mol·K)
R_m	[MPa]	Tensile strength
$R_{p0.2}$	[MPa]	0.2% of yield stress
t	[seconds]	Time
t_{min}	[mm]	Minimum thickness
t_{orig}	[mm]	Original "as built" thickness
T	[K]	Absolute temperature or Tempering temperature
T	[^{o}C]	Room temperature
T_B	[^{o}C]	Ductile to brittle transition temperature
$\{u\}$	[-]	Column vector of unknown element nodal displacements.
u , v , w	[-]	Gaussian displacements
u_i, v_i, w_i	[-]	Nodal displacements
$\{U\}$	[-]	Column vector of nodal displacements
$\{v\}$	[-]	Transport velocity vector
W	[J]	Work
x, y, z	[-]	Cartesian coordinates
Z_{Fe}	[-]	Valence electron of dissolved species

Greek Characters:

Symbol:	Unit:	Description:
$\{\beta\}$	[-]	Vector of coefficients of diffusion expansion
δW	[-]	Total virtual work
δW_{ext}	[-]	Internal virtual work
δW_{int}	[-]	External virtual work
∇	[-]	Gradient/ divergence operator
∇C	[-]	Concentration change
$\Delta\varepsilon_{eq}^{pl}$	[-]	Increment of equivalent plastic strain
ε	[-]	Strain in the oxide
$\{\varepsilon\}$	[-]	Total strain vector
$\dot{\varepsilon}_{ct}$	[-]	Strain rate at the crack tip
$\{\varepsilon^{di}\}$	[-]	Diffusion strain vector
$\{\varepsilon^{el}\}$	[-]	Elastic strain vector

ε_{frac}	[-]	Fracture strain of the material
$\dot{\varepsilon}_{glob}$	[-]	Global strain rate
$\dot{\varepsilon}_{loc}$	[-]	Local strain rate ahead of the crack tip
ε_m	[-]	Strain in the substrate metal
ε_{true}	[-]	True strain
ε_{ys}	[-]	Yield strain of the material
ε_{eq}^{cr}	[-]	Equivalent creep strain
ε_{eq}^{el}	[-]	Equivalent elastic strain
ε_{eq}^{tm}	[-]	Equivalent total mechanical strain
ρ_{Fe}	[kg/m^3]	Density of steels
σ	[MPa]	Stress
$\{\sigma\}$	[-]	Stress vector
σ_{crit}	[MPa]	Critical tensile stress, Mode I required for crack to propagate
σ_{ct}	[MPa]	Tensile stress at the crack tip
σ_{eq}	[MPa]	Equivalent stress
σ_m	[MPa]	Stress in the substrate metal
σ'_{max}	[Mpa]	Maximum local tensile stress ahead of the crack tip
σ_y	[MPa]	Yield stress
σ_{ys}	[MPa]	Yield Stress of the material
τ_{xy}	[MPa]	Shear stress in the x-y plane

List of Figures

List of Tables

Appendix A

2D 66% Displacement Applied to HAZ Model

Table A. 1: Displacement values applied to 2D UA HAZ submodel and resulting total true strain and stress results for 66% of yield stress.

Displacement (x) (mm)	Total true strain in x-direction	Stress in X-direction (MPa)	% Yield
0.033302	0.0027	575	66

Table A.2: Lowest maximum total true strain in x-direction to highest for all seven pit geometries in the 2D UA HAZ submodel and the pit aspect ratios loaded to 66% of yield stress.

Pit Geometry	Maximum Total true strain in the x-direction	Pit Aspect Ratio
Unpitted	0.0027	-
Shallow Wide	0.007131	0.3
Spherical	0.012588	0.5
Reference	0.012714	0.5
Subsurface	0.021298	10
Ellipse	0.025461	0.83
Notched	0.139994	0.83
Repassivation	0.418690	0.83

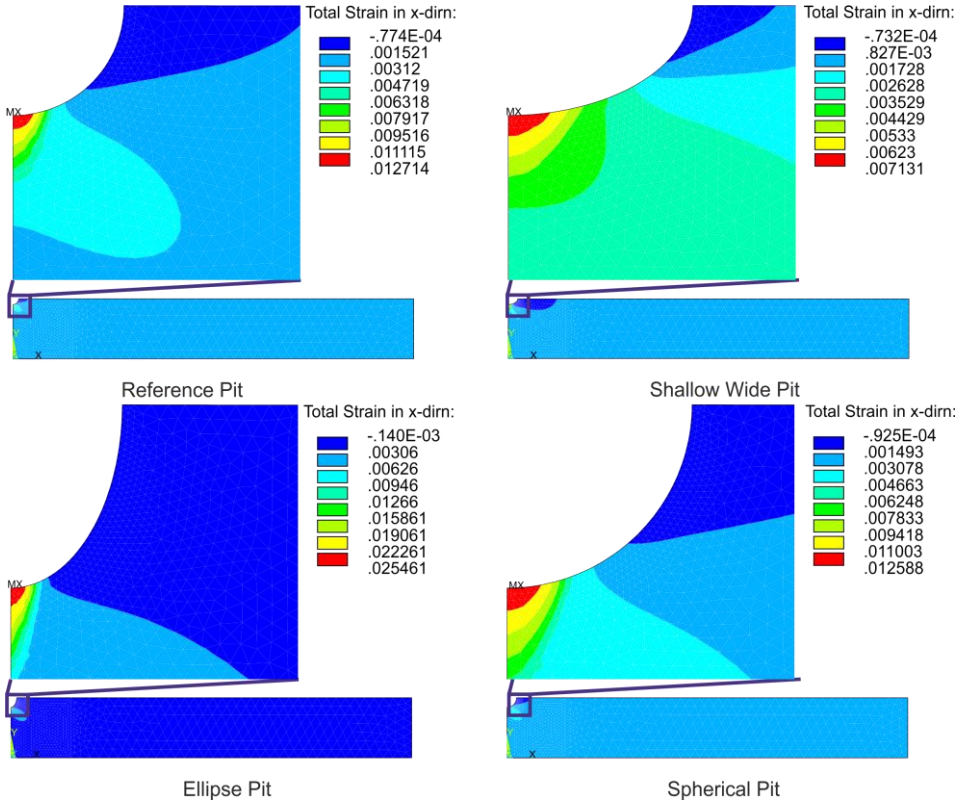

Figure A.1: 2D UA HAZ submodel with reference, shallow wide, ellipse and spherical pits total true strain in x-direction results for 66% load applied.

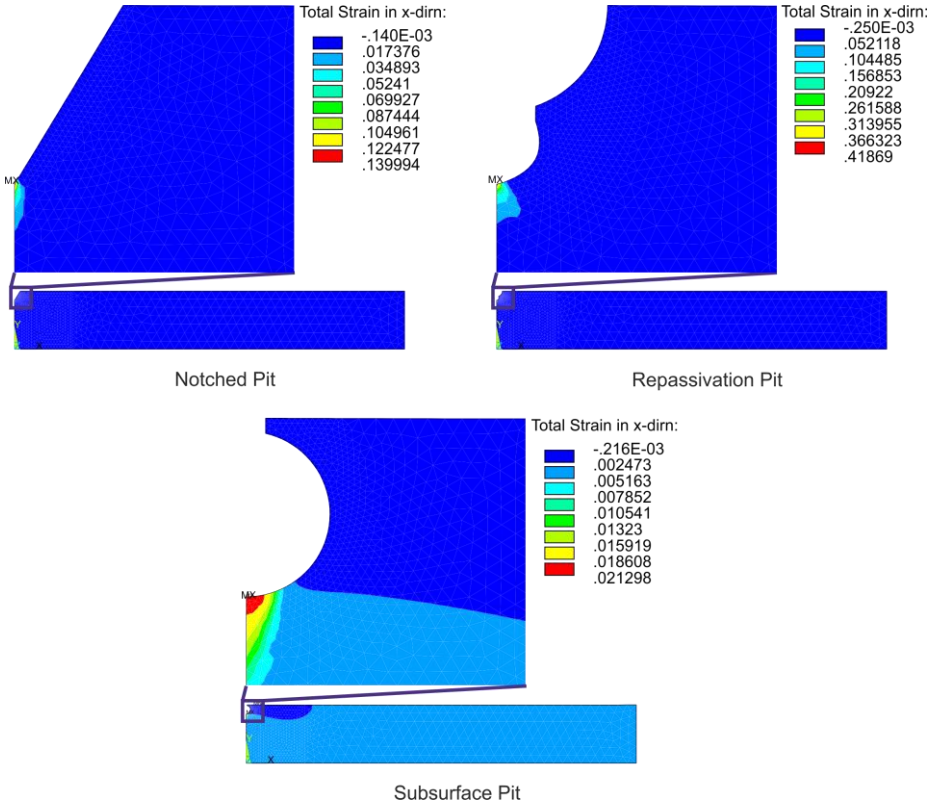

Figure A.2: 2D UA HAZ submodel with notched, repassivation and subsurface pits total true strain in x-direction results for 66% load applied.

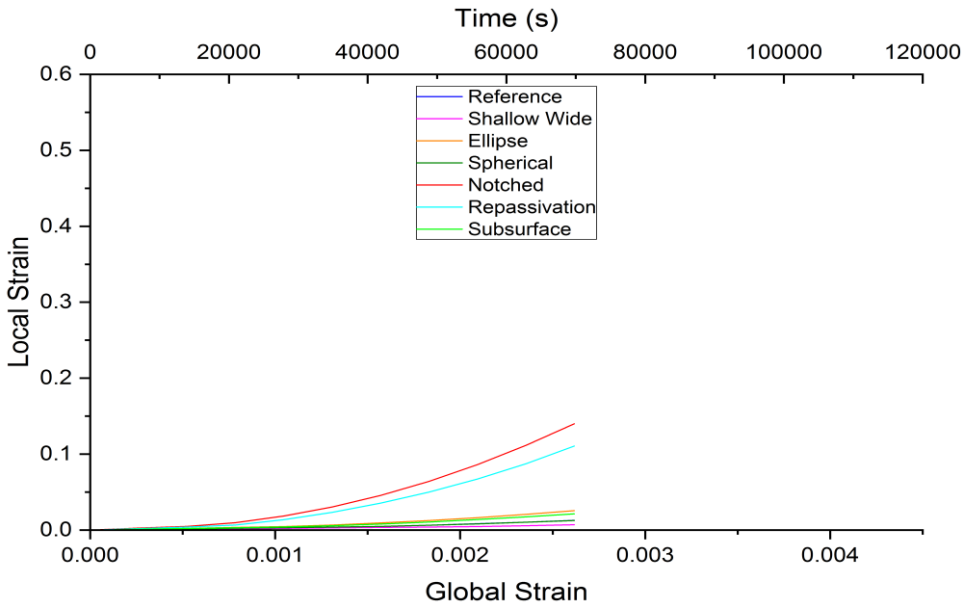

Figure A.3:Graph of global vs local strains for all pit geometries 2D 66% HAZ UA submodel.

Table A. 3: Displacement values applied to 2D HAZ bend submodel and resulting total true strain and stress results for 66% of yield stress.

Displacement (x) (mm)	Total true strain in x-direction	Stress in X-direction (MPa)	% Yield
0.094137	0.00244	513	67

Table A.4: Lowest maximum total true strain in x-direction to highest for all seven pit geometries in the 2D HAZ bend submodel and the pit aspect ratios loaded to 66% of yield stress.

Pit Geometry	Maximum Total true strain in the x-direction	Pit Aspect Ratio
Unpitted	0.00244	-
Shallow Wide	0.006711	0.3
Spherical	0.010919	0.5
Reference	0.012140	0.5
Subsurface	0.018725	10
Ellipse	0.022551	0.83
Repassivation	0.097145	0.83
Notched	0.125509	0.83

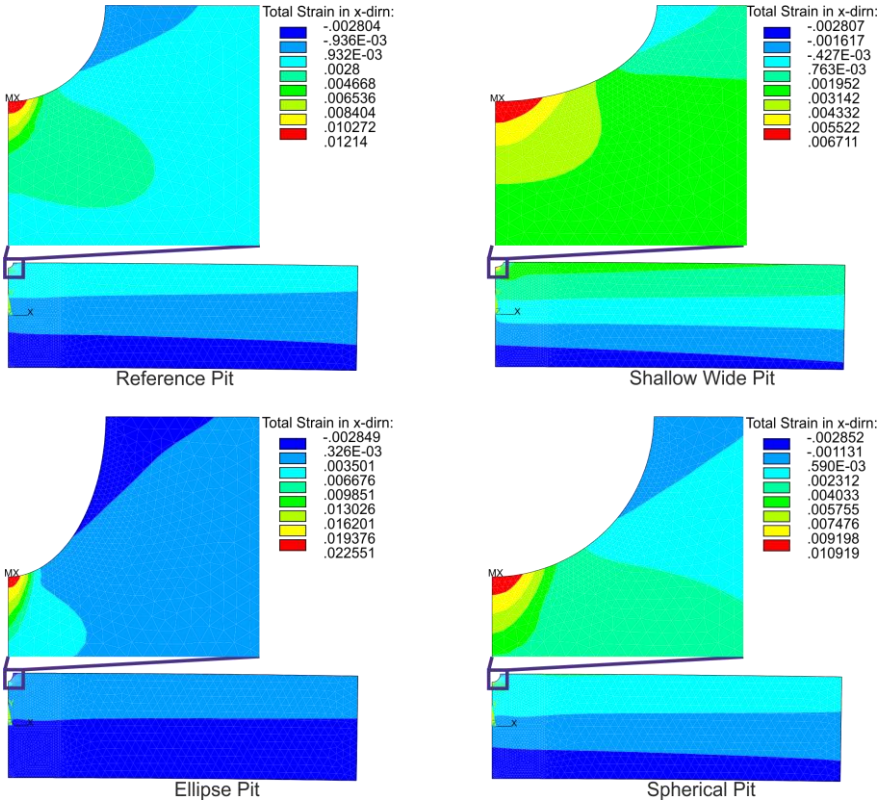

Figure A.4: 2D HAZ bend submodel with reference, shallow wide, ellipse and spherical pits total true strain in x-direction results for 66% load applied.

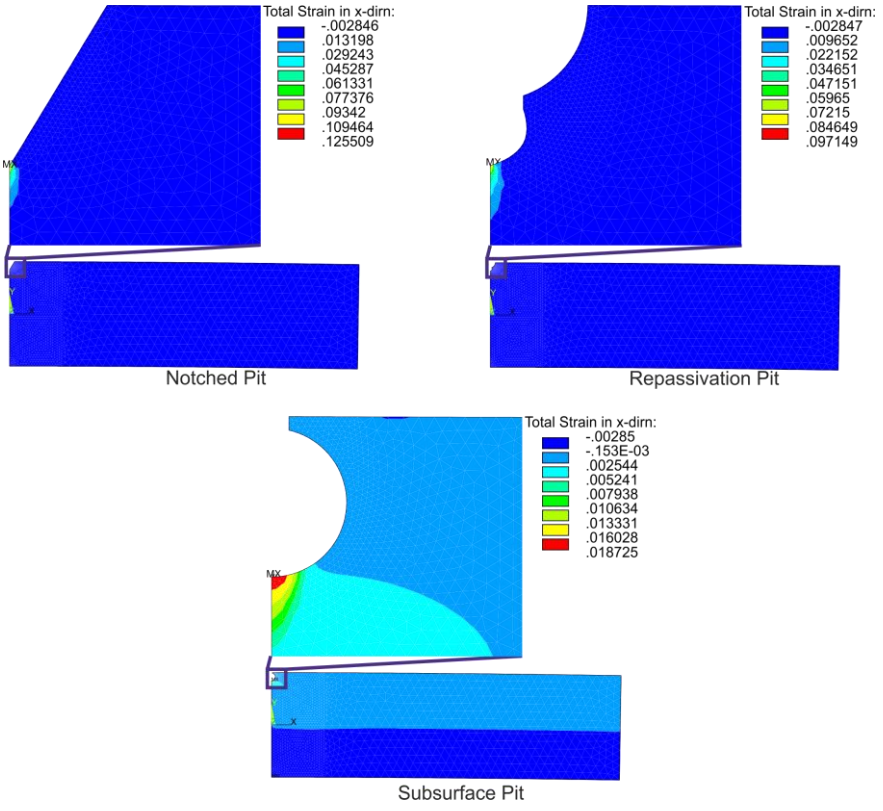

Figure A.5: 2D HAZ bend submodel with notched, repassivation and subsurface pits total true strain in x-direction results for 66% load applied.

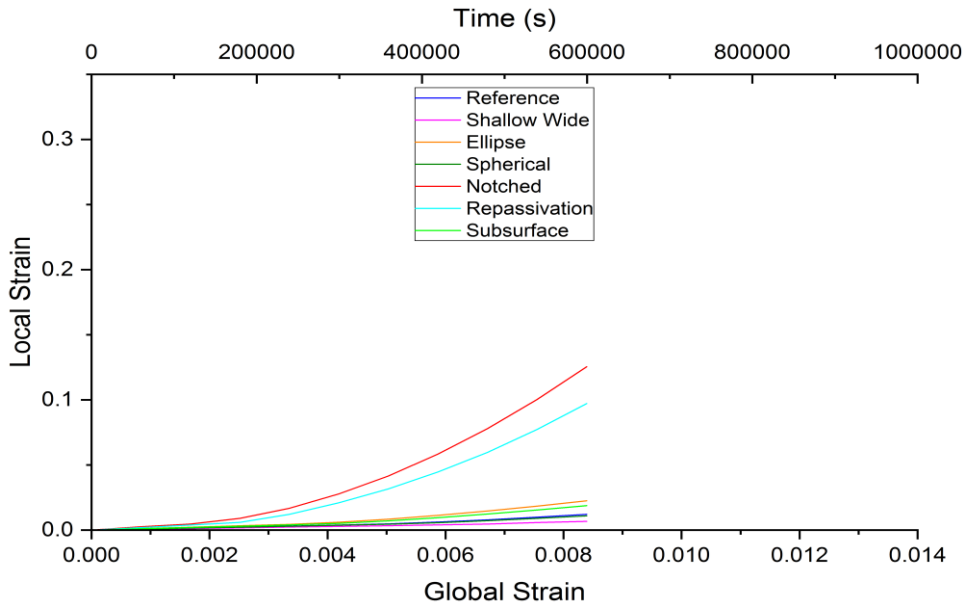

Figure A.6:Graph of global vs local strains for all pit geometries 2D 66% HAZ bend submodel.

3D Uniaxial Structural Analysis for Unpitted Base Material (BM)

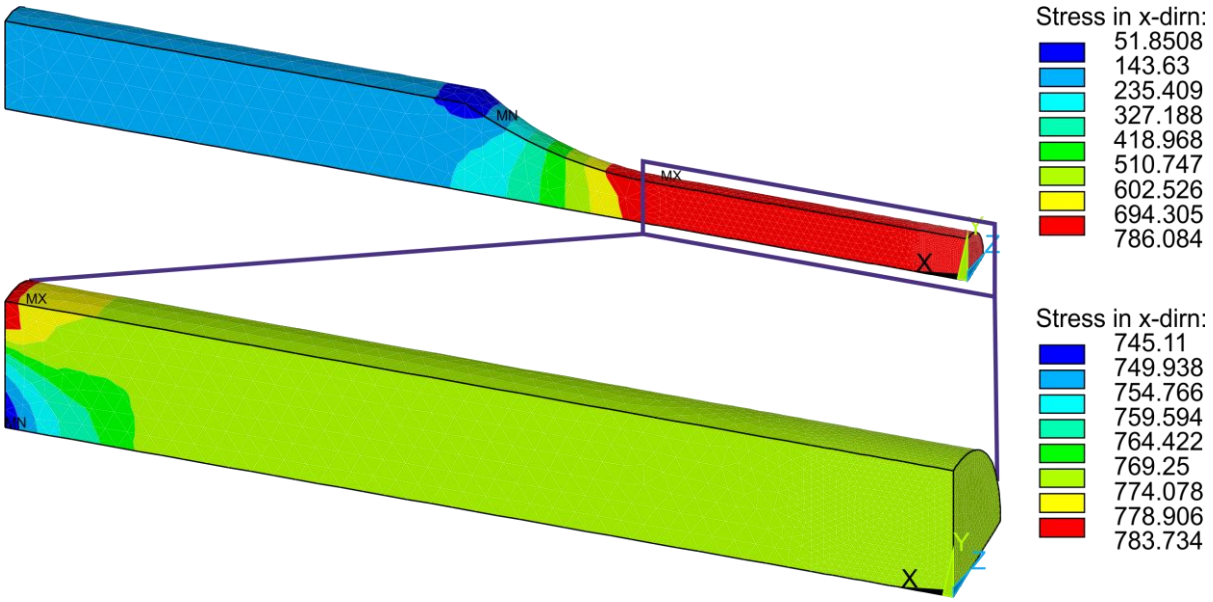

Figure A.7: 3D one eight model maximum stress in x-direction for 100% of BM yield stress applied as uniaxial displacement to 2D model and selected gauge length region shown on the 3D one eight model.

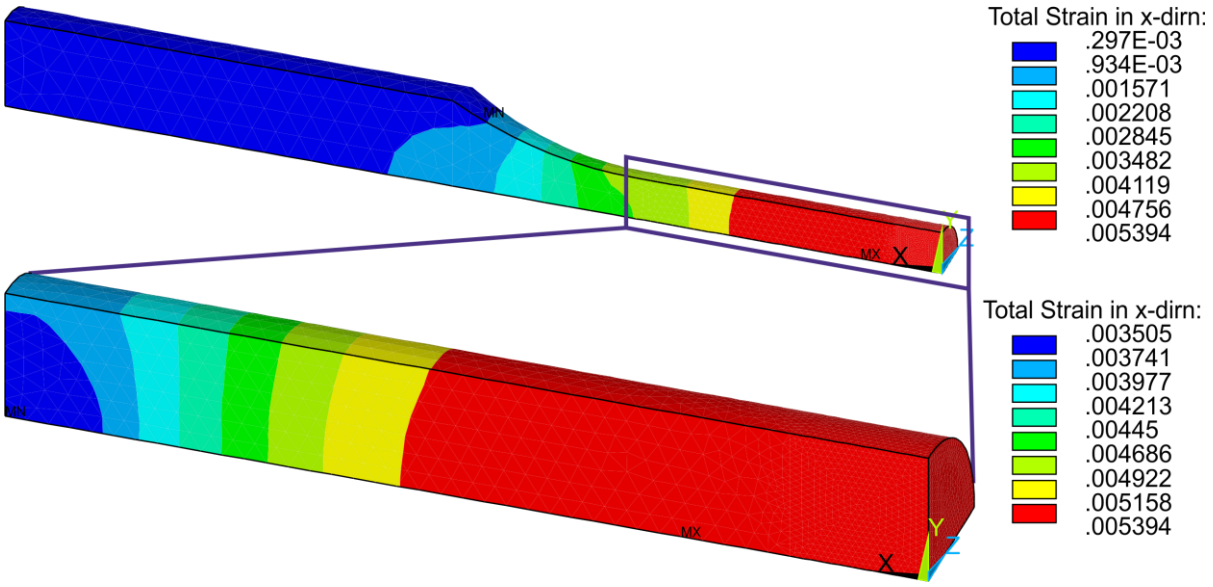

Figure A.8: 3D one eight model maximum total true strain in x-direction for 100% of BM yield stress applied as uniaxial displacement to 2D model and selected gauge length region shown on the 3D one eight model.

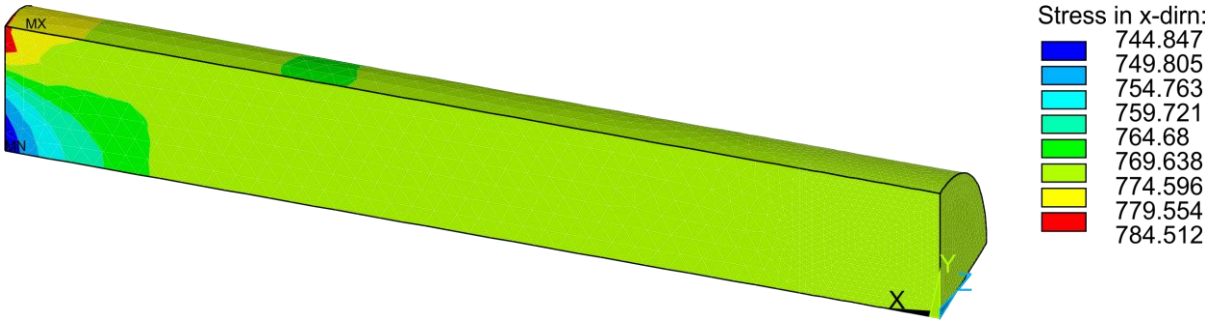

Figure A.9: 3D UA submodel maximum stress in x-direction for 100% of BM yield stress applied as uniaxial displacement to 2D model.

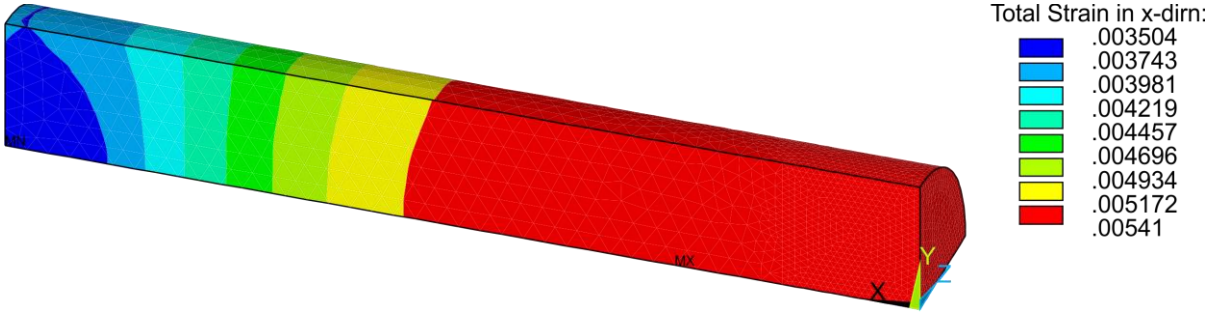

Figure A.10: 3D UA submodel maximum total true strain in x-direction for 100% of BM yield stress applied as uniaxial displacement to 2D model.

Table A.5: Displacement values applied to 3D BM UA one quarter model and resulting total true strain and stress results.

Displacement (x) (mm)	Total true strain in x-direction	Stress in X-direction (MPa)	% Yield
0.0966	0.0054	786	102

Table A.6: Displacement values applied to 3D BM UA submodel and resulting total true strain and stress results.

Displacement (x) (mm)	Total true strain in x-direction	Stress in X-direction (MPa)	% Yield
0.062602	0.00541	785	102

3D Uniaxial Structural Analysis for Pitted Base Material (BM)

Table A.7: Lowest maximum total true strain in x-direction to highest for all seven pit geometries in the uniaxially loaded 3D BM UA submodel and the pit aspect ratios.

Pit Geometry	Maximum Total true strain in the x-direction	Pit Aspect Ratio
Unpitted	0.00541	-
Shallow Wide	0.024881	0.3
Reference	0.027254	0.5
Spherical	0.039662	0.5
Ellipse	0.044170	0.83
Repassivation	0.078978	0.83
Notched	0.143586	0.83
Subsurface	0.209971	10

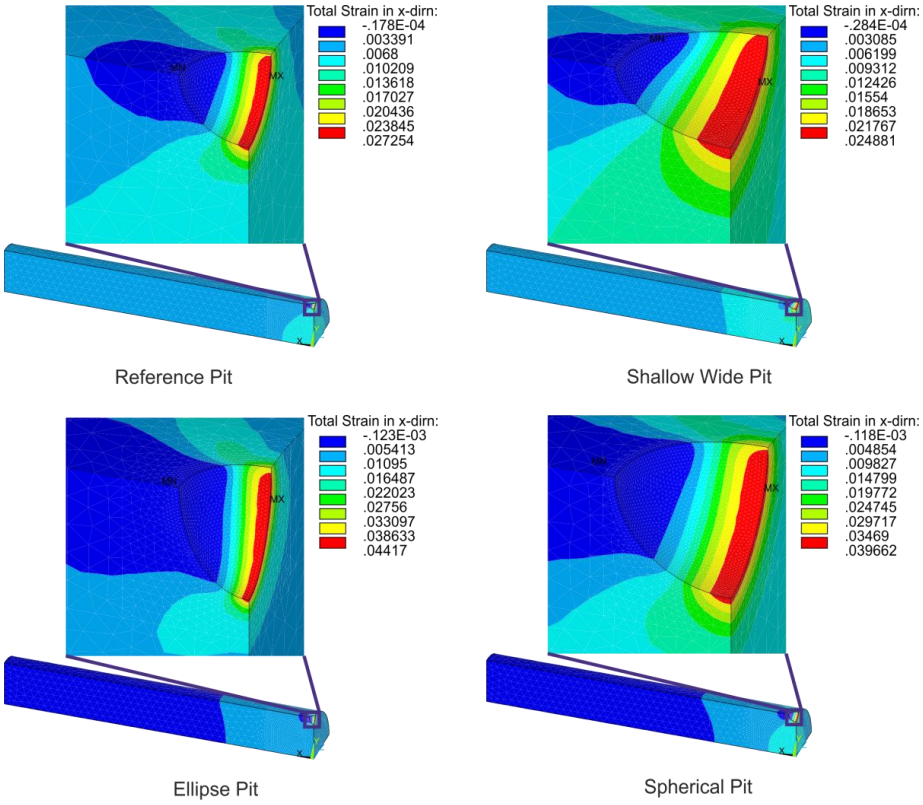

Figure A.11: 3D BM UA submodel with reference, shallow wide, ellipse and spherical pits total true strain in x-direction results.

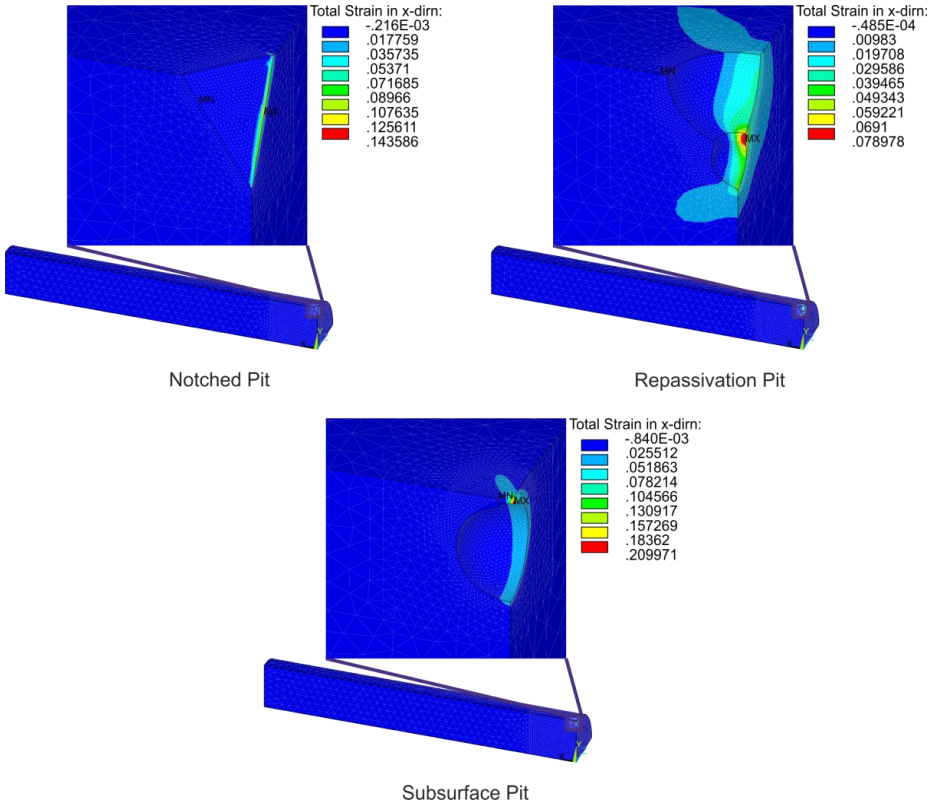

Figure A.12: 2D UA BM submodel with notched, repassivation and subsurface pits total true strain in x-direction results.

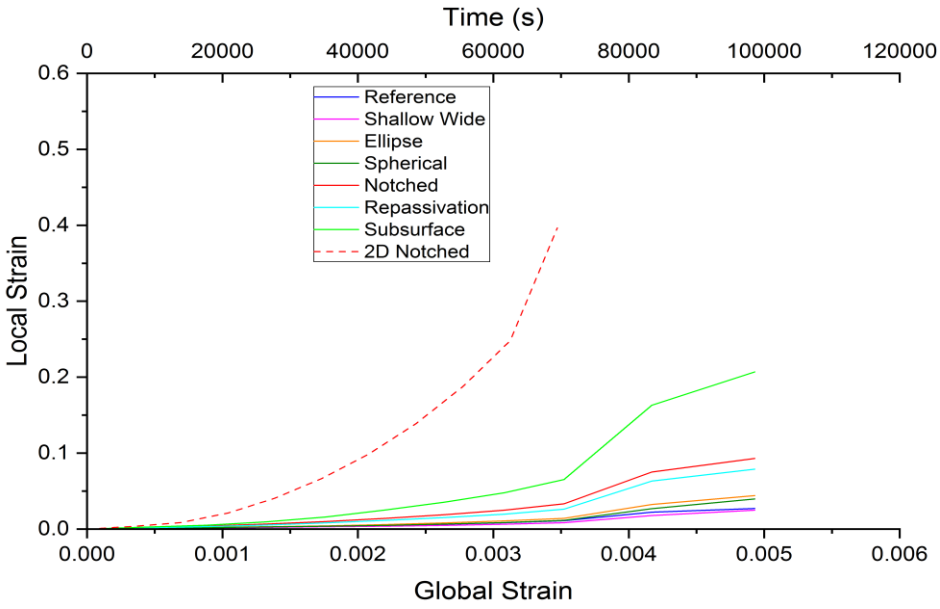

Figure A. 13: Graph of global vs local strains for all pit geometries in the 3D BM UA submodel.

3D Bending Structural Analysis for Unpitted Base Material (BM)

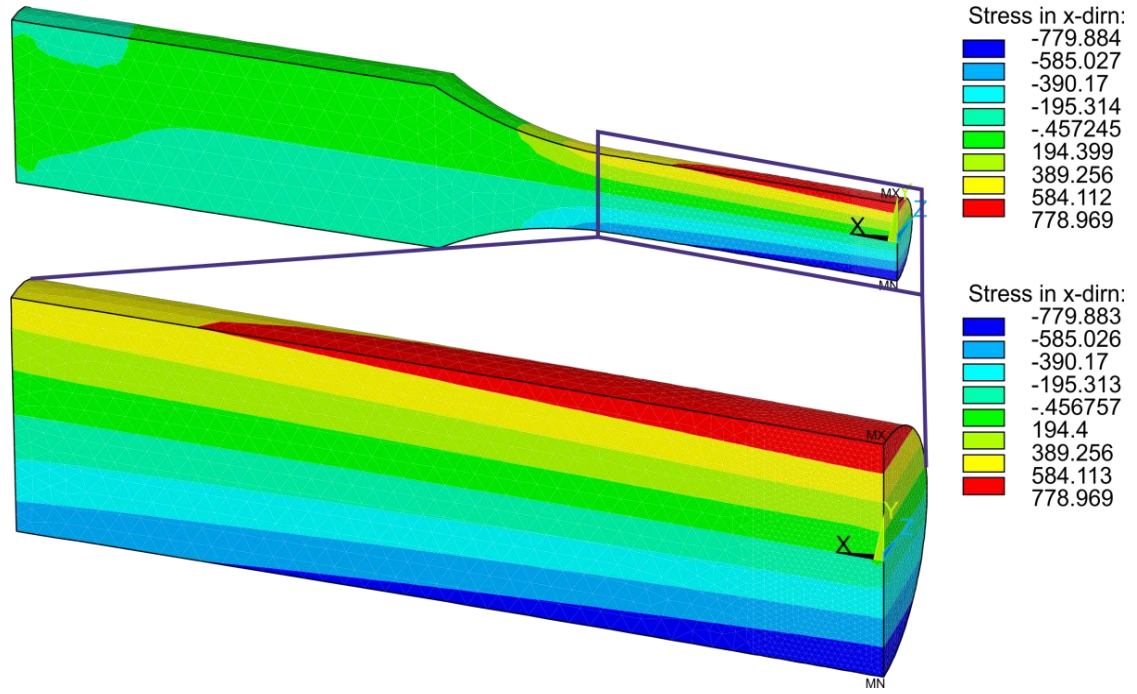

Figure A.14: One quarter model maximum stress result for 100% of BM yield stress applied as bending displacement and selected gauge length region shown on the full half specimen.

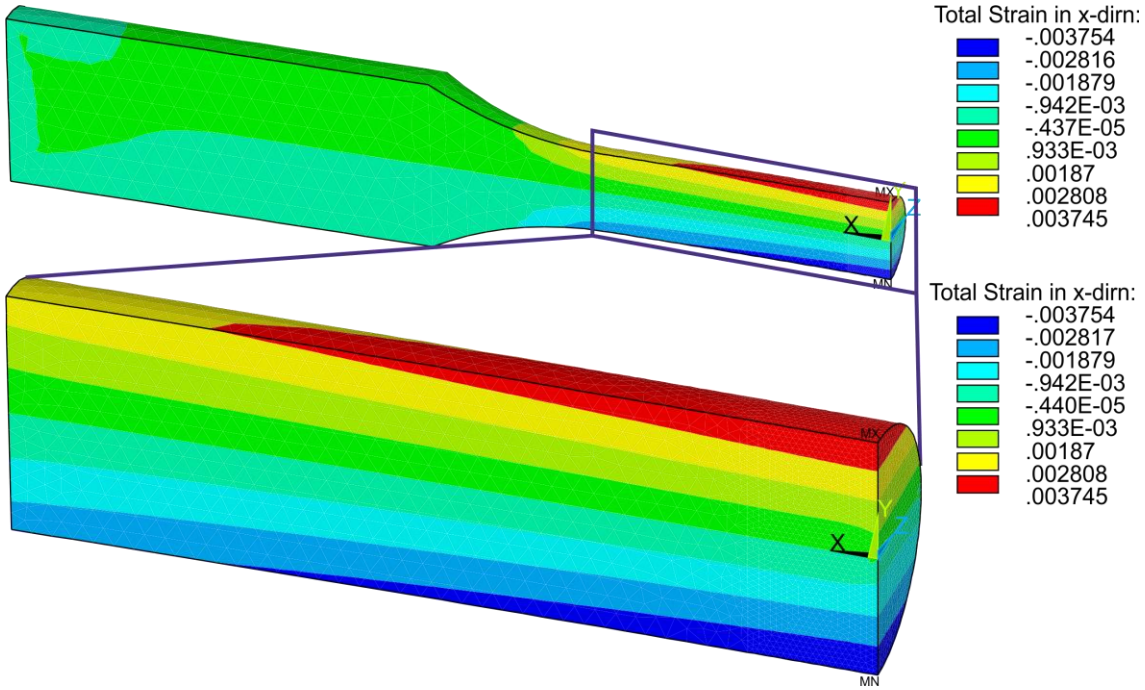

Figure A.15: One quarter model maximum total true strain result for 100% of BM yield stress applied as bending displacement and selected gauge length region shown on the full half specimen.

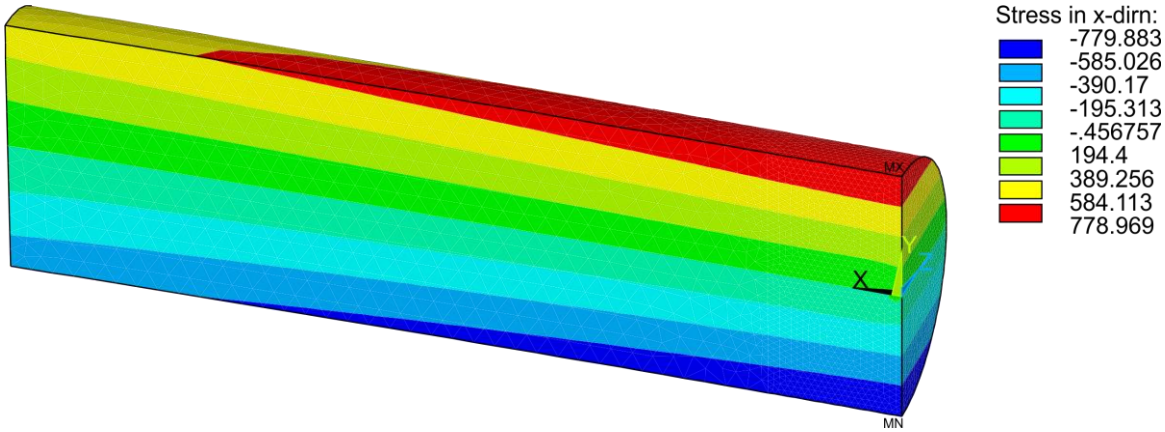

Figure A.16: Submodel maximum stress result for 100% of yield stress applied as bending displacement to BM one quarter model.

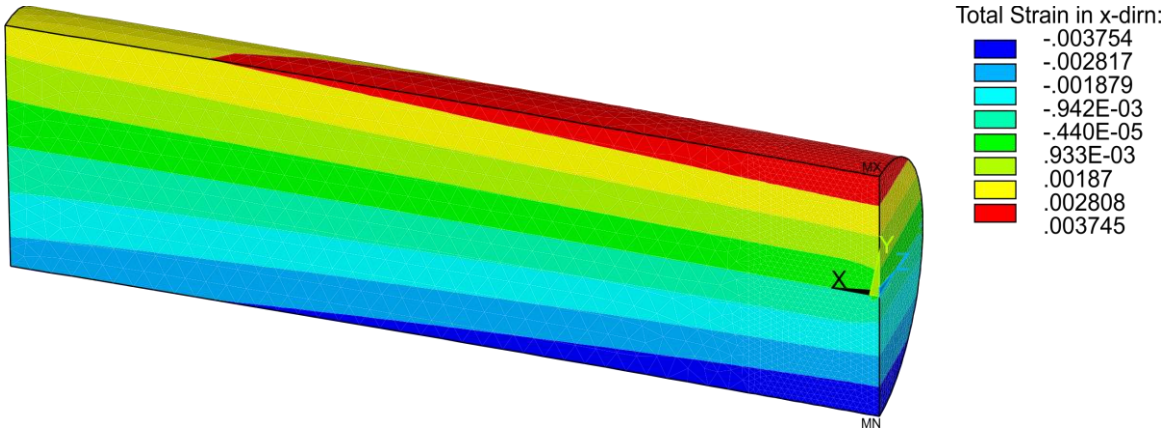

Figure A.17: Submodel maximum total true strain result for 100% of yield stress applied as bending displacement to BM one quarter model.

Table A.8: Displacement values applied to 3D BM bend one quarter model and resulting total true strain and stress results.

Displacement (x) (mm)	Total true strain in x-direction	Stress in X-direction (MPa)	% Yield
0.809	0.0038	779	101

Table A.9: Displacement values applied to 3D BM bend submodel and resulting total true strain and stress results.

Displacement (x) (mm)	Total true strain in x-direction	Stress in X-direction (MPa)	% Yield
0.145311	0.0038	779	101

3D Bending Structural Analysis for Pitted Base Material (BM)

Table A.10: Lowest maximum total true strain in x-direction to highest for all seven pit geometries in the bending loaded 3D BM bend submodel and the pit aspect ratios.

Pit Geometry	Maximum Total true strain in the x-direction	Pit Aspect Ratio
Unpitted	0.0038	-
Shallow Wide	0.008357	0.3
Spherical	0.010993	0.5
Reference	0.011266	0.5
Ellipse	0.014127	0.83
Repassivation	0.024685	0.83
Notched	0.054478	0.83
Subsurface	0.069844	10

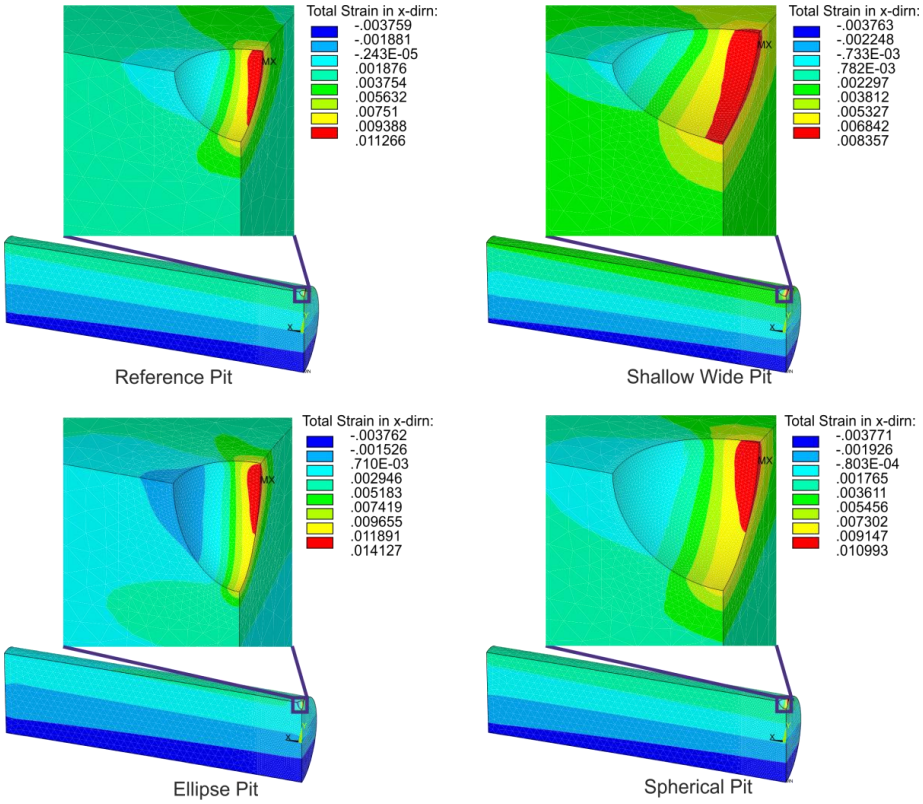

Figure A.18: 3D BM UA submodel with reference, shallow wide, ellipse and spherical pits total true strain in x-direction results.

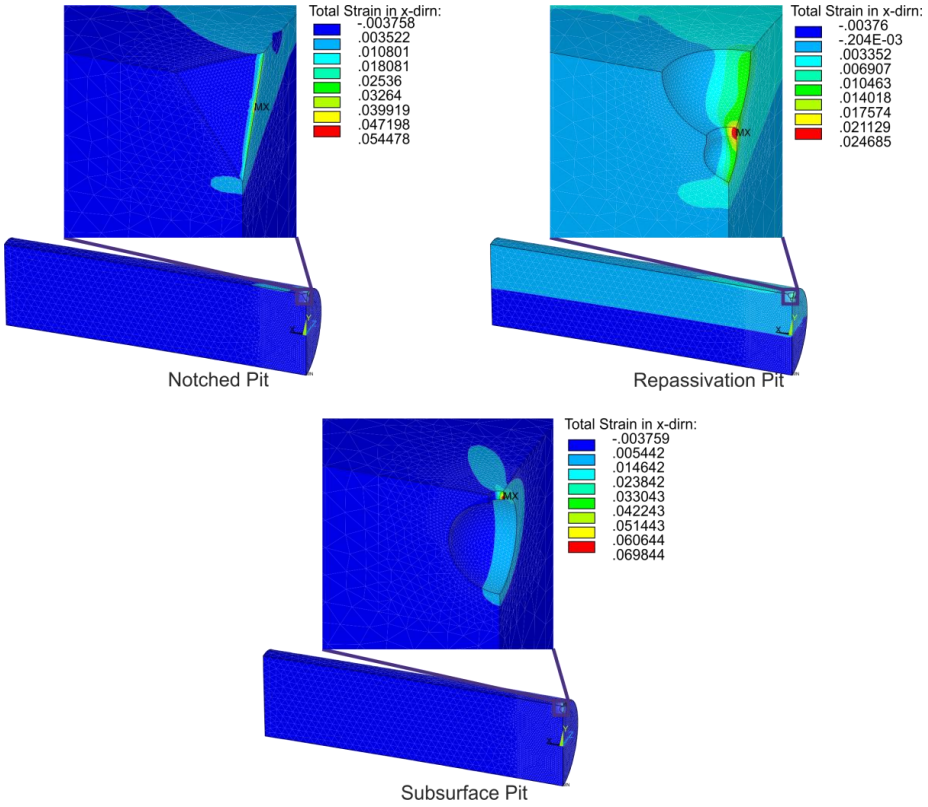

Figure A.19: 3D BM UA submodel with notched, repassivation and subsurface pits total true strain in x-direction results.

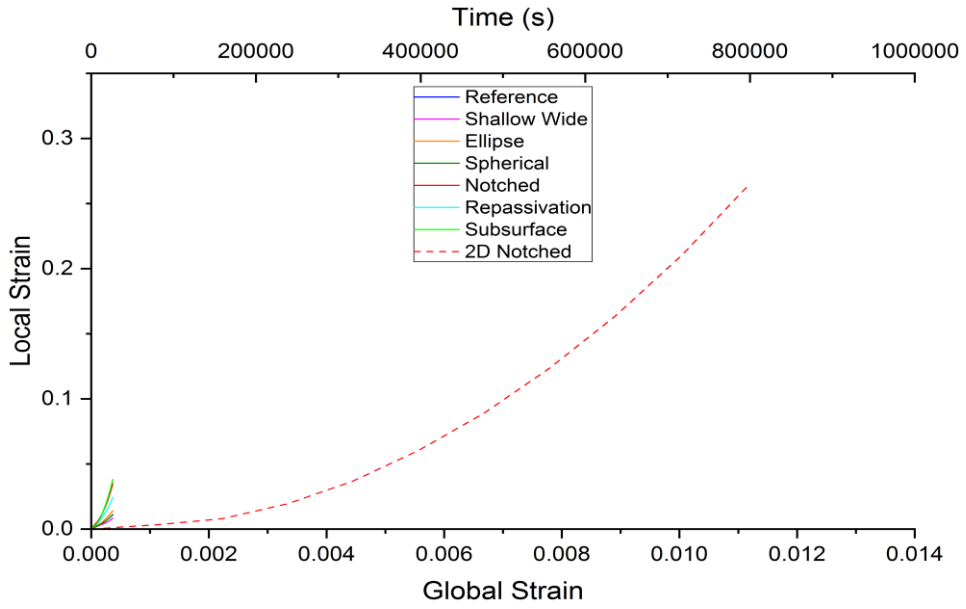

Figure A. 20: Graph of global vs local strains for all pit geometries in 3D BM bend submodel.

3D 66% Displacement Applied to HAZ Model

Table A. 11: Displacement values applied to 3D HAZ UA one quarter model and resulting total true strain and stress results for 66% of yield stress.

Displacement (x) (mm)	Total true strain in x-direction	Stress in X-direction (MPa)	% Yield
0.042131	0.0034	721	83

Table A. 12: Lowest maximum total true strain in x-direction to highest for all seven pit geometries in the bending loaded 3D HAZ UD submodel and the pit aspect ratios loaded to 66% of yield stress.

Pit Geometry	Maximum Total true strain in the x-direction	Pit Aspect Ratio
Unpitted	0.0034	-
Shallow Wide	0.006630	0.3
Reference	0.008696	0.5
Spherical	0.008995	0.5
Ellipse	0.011202	0.83
Repassivation	0.020620	0.83
Notched	0.042865	0.83
Subsurface	0.050384	10

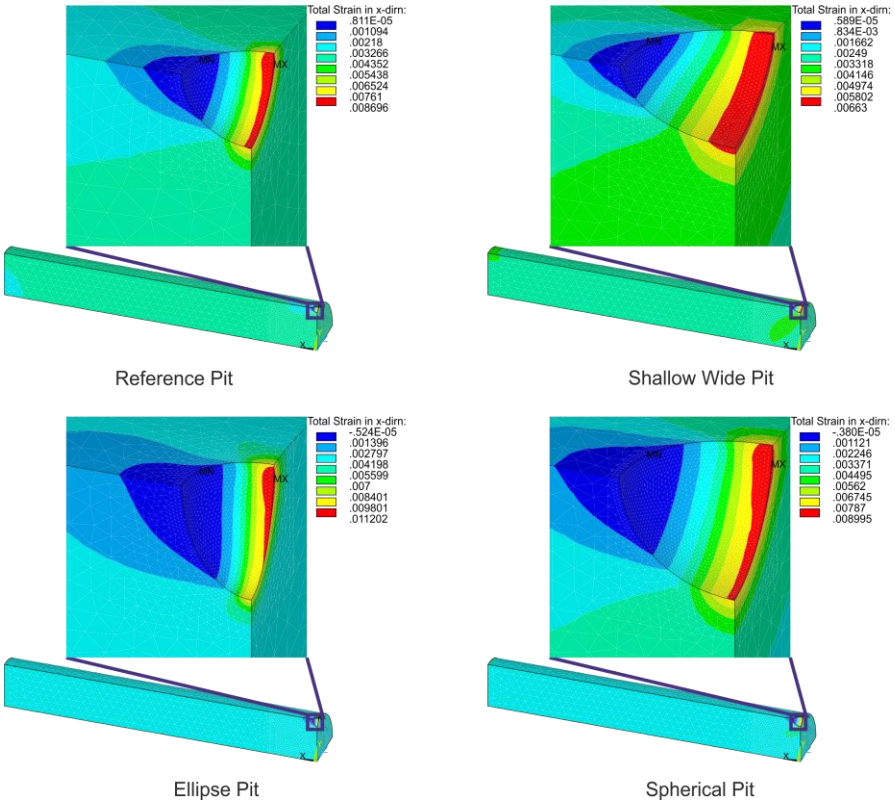

Figure A.21: 3D HAZ UA submodel with reference, shallow wide, ellipse and spherical pits total true strain in x-direction results.

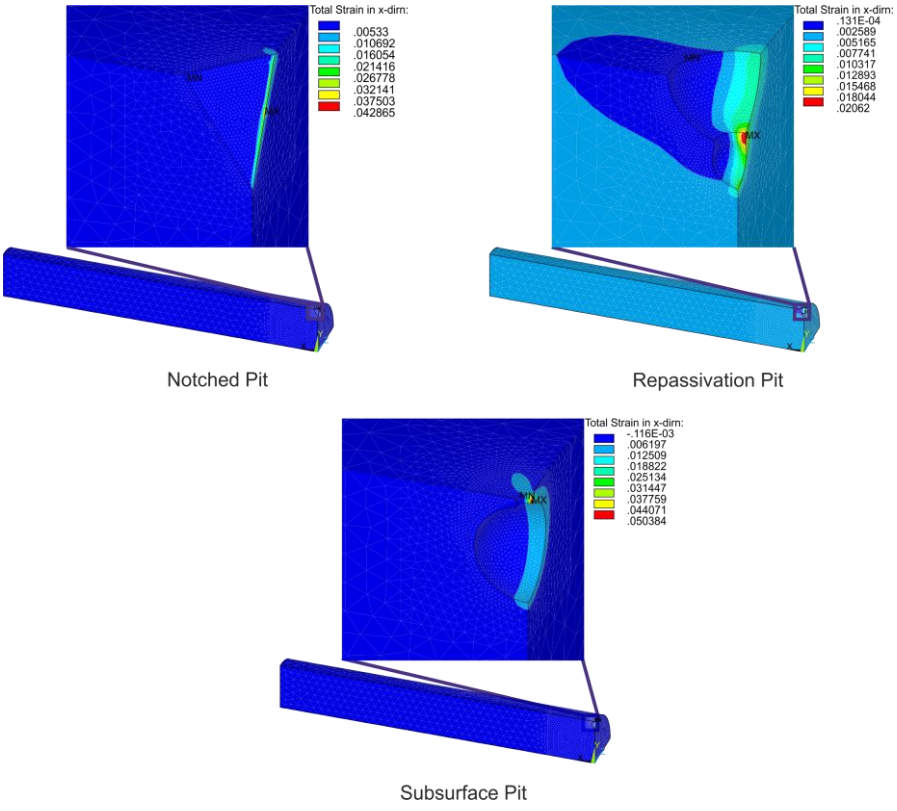

Figure A.22: 2D UA HAZ submodel with notched, repassivation and subsurface pits total true strain in x-direction results.

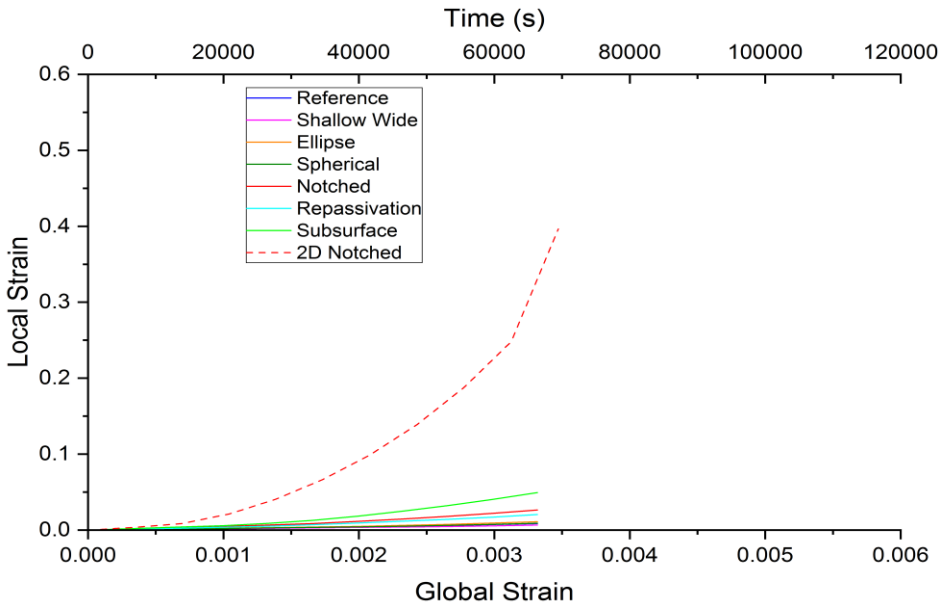

Figure A. 23: Graph of global vs local strains for all pit geometries 3D 66% HAZ UA submodel.

Table A. 13: Displacement values applied to 3D HAZ bend one quarter model and resulting total true strain and stress results for 66% of yield stress.

Displacement (y) (mm)	Total true strain in x-direction	Stress in X-direction (MPa)	% Yield
0.109374	0.0028	597	69

Table A. 14: Lowest maximum total true strain in x-direction to highest for all seven pit geometries in the bending loaded 3D HAZ bend submodel and the pit aspect ratios loaded to 66% of yield stress.

Pit Geometry	Maximum Total true strain in the x-direction	Pit Aspect Ratio
Unpitted	0.0028	-
Shallow Wide	0.004930	0.3
Reference	0.006412	0.5
Spherical	0.006435	0.5
Ellipse	0.008027	0.83
Repassivation	0.013857	0.83
Notched	0.029353	0.83
Subsurface	0.034564	10

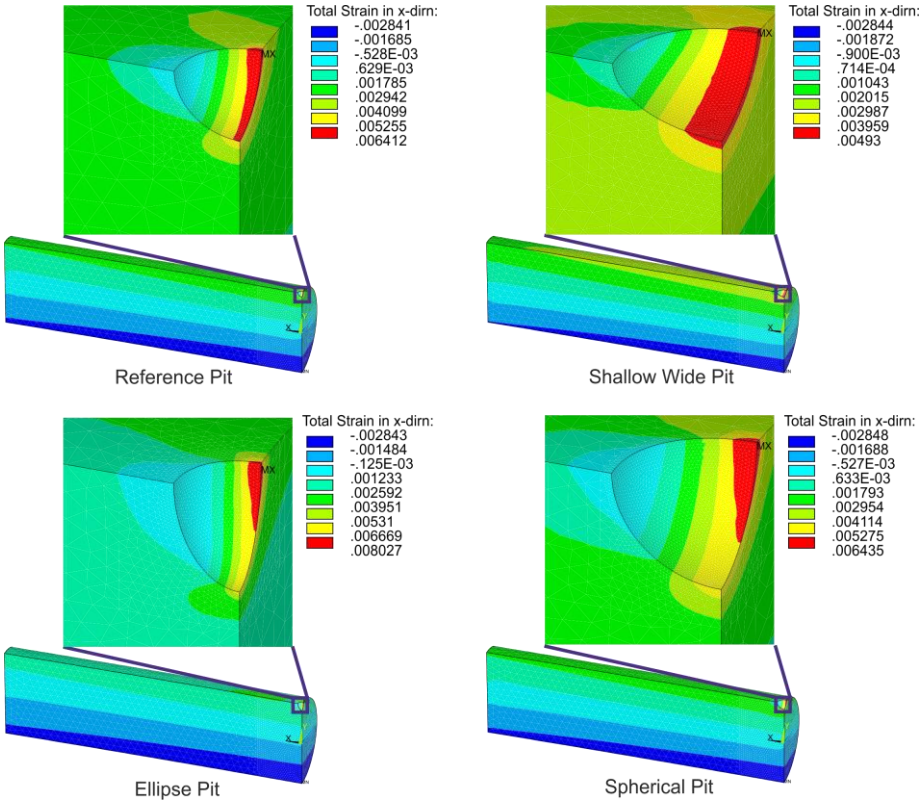

Figure A.24: 3D HAZ UA submodel with reference, shallow wide, ellipse and spherical pits total true strain in x-direction results.

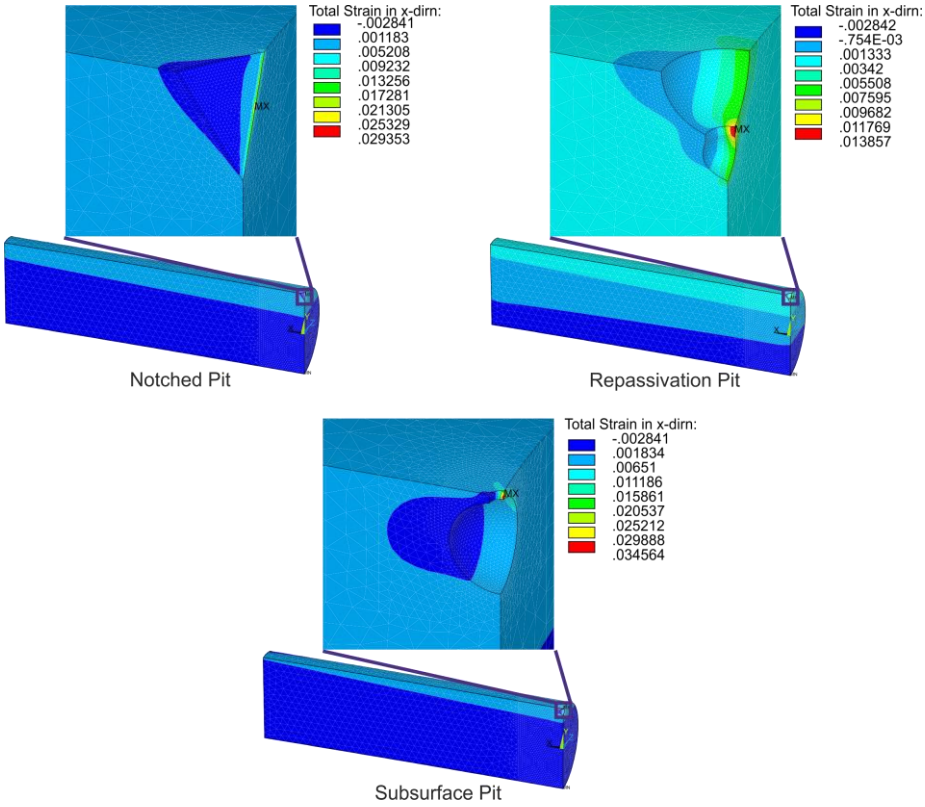

Figure A.25: 2D UA HAZ submodel with notched, repassivation and subsurface pits total true strain in x-direction results.

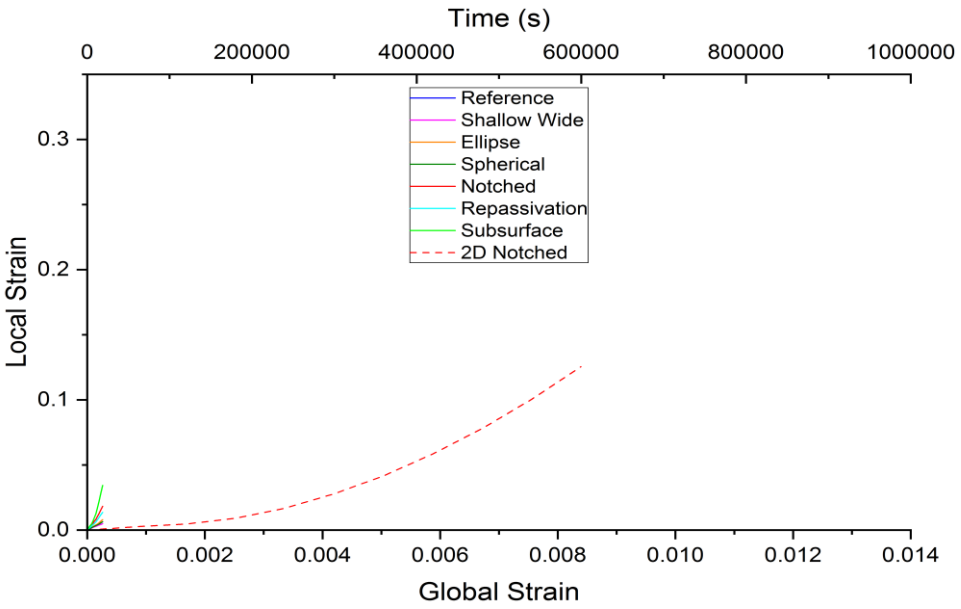

Figure A.26:Graph of global vs local strains for all pit geometries 3D 66% HAZ bend submodel.

Appendix B

Surface Hydrogen Boundary Condition

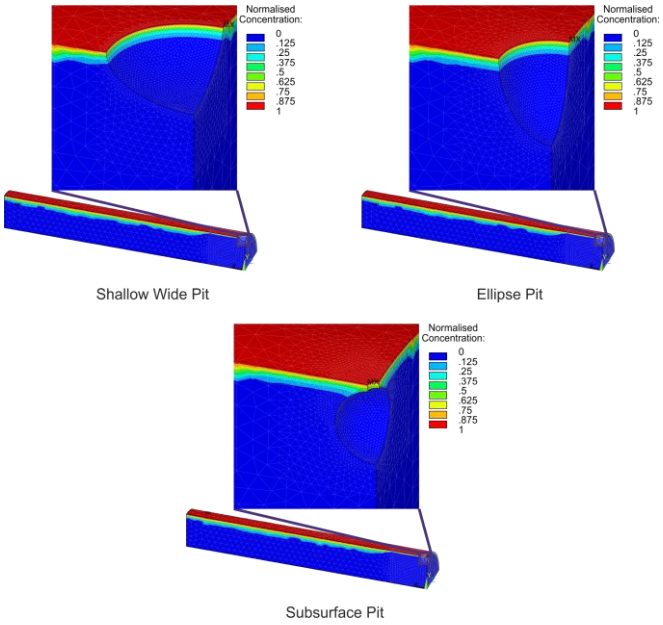

Figure B.1: Shallow wide, ellipse and subsurface pits normalised hydrogen concentration models exposed to a normalised hydrogen concentration applied to the surface.

Pit Hydrogen Boundary Condition

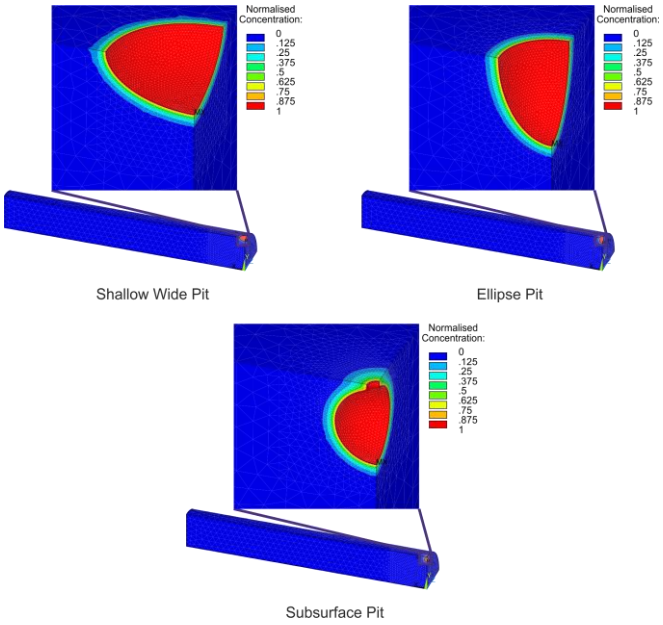

Figure B. 2: Shallow wide, ellipse and subsurface pits normalised hydrogen concentration models exposed to a normalised hydrogen concentration applied to the surface and pit.

Surface and Pit Hydrogen Boundary Condition

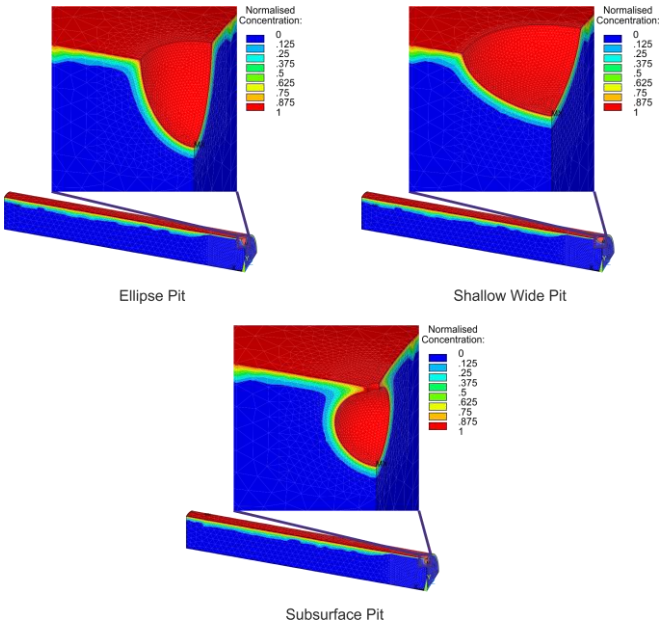

Figure B. 3: Shallow wide, ellipse and subsurface pits normalised hydrogen concentration models exposed to a normalised hydrogen concentration applied to the surface and pit.

Pit Varying Hydrogen Concentration Boundary Condition

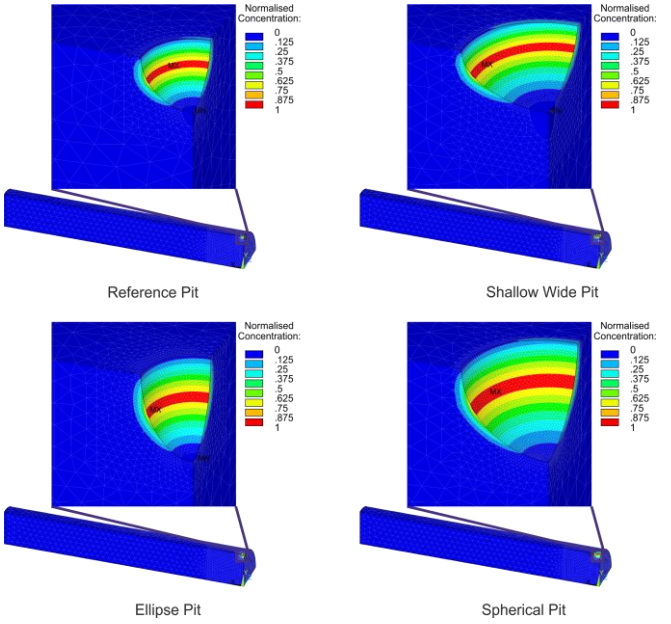

Figure B. 4: Reference, shallow wide, ellipse and spherical pit geometries exposed to a varying normalised hydrogen concentration after 20 days.

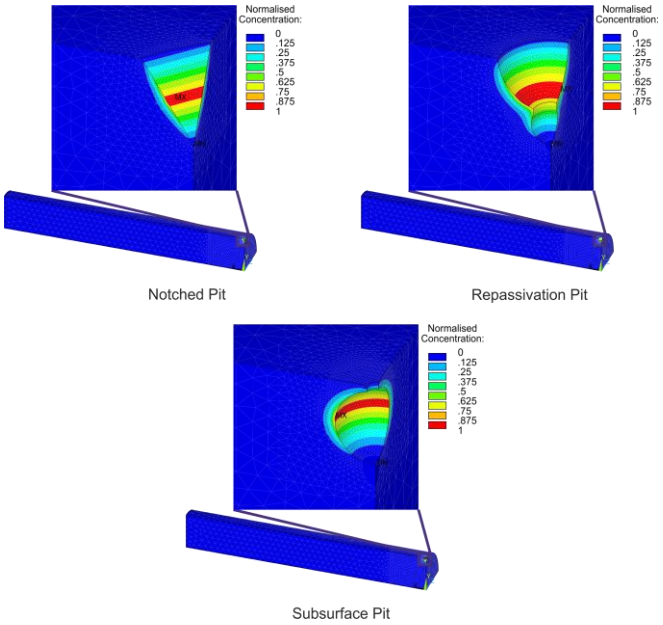

Figure B. 5: Notched, repassivation and subsurface pit geometries exposed to a varying normalised hydrogen concentration after 20 days.

Conferences

1) Numerical Analysis of Weldability 2018, Graz Austria, Numerical Simulation of Hydrogen Assisted Stress Corrosion Cracking Originating from Pits, 2018.

Curriculum Vitae

Name:	Maria Cristine Madigan
Date of Birth:	8th June 1987
Place of Birth:	Limerick, Ireland
Nationality:	Irish

Education:

09/2011 – 05/2013	University of Limerick, Ireland Master of Science in Advanced Materials
09/2004 – 05/2008	University of Limerick, Ireland Bachelor of Engineering in Mechanical Engineering
09/1999 – 06/2005	St. Josephs Convent of Mercy, Abbeyfeale, Co. Limerick

Professional Experience:

09/2008 – Present	Engineer, DNV GL, Høvik, Norway
10/2016 - Present	Doctoral student at Bundesanstalt für Materialforschung und -prüfung (BAM) in Berlin (10/2016 – 12/2019)
09/2006 – 02/2007	Internship at Schwarz Pharma, Shannon, Ireland
06/2006 – 09/2006	Internship at Amphenol Tuchel Electronics, Heilbronn, Germany